SHORT PAPERS IN—

Astrogeology

Dispersion and diffusion studies

Economic geology

Geochemistry of water

Geomorphology

Geophysics

Ground water

Hydrologic instrumentation

Mineralogy

Paleogeomorphology

Paleontology

Petrology and petrography

Pleistocene geology

Quality of water

Sedimentation

Stratigraphy

Structural geology

Surface water

Topographic survey equipment

GEOLOGICAL SURVEY RESEARCH 1969

Chapter D

GEOLOGICAL SURVEY PROFESSIONAL PAPER 650–D

GEOLOGICAL SURVEY RESEARCH 1969

Chapter D

GEOLOGICAL SURVEY PROFESSIONAL PAPER 650–D

Scientific notes and summaries of investigations in geology, hydrology, and related fields

UNITED STATES GOVERNMENT PRINTING OFFICE, WASHINGTON: 1969

UNITED STATES DEPARTMENT OF THE INTERIOR

WALTER J. HICKEL, Secretary

GEOLOGICAL SURVEY

William T. Pecora, Director

For sale by the Superintendent of Documents, U.S. Government Printing Office
Washington, D.C. 20402 – Price $3.75

CONTENTS

GEOLOGIC STUDIES

GEOLOGICAL SURVEY RESEARCH 1969

This collection of 45 short papers is the third published chapter of "Geological Survey Research 1969." The papers report on scientific and economic results of current work by members of the Geologic, Topographic, and Water Resources Divisions of the U.S. Geological Survey.

Chapter A, to be published later in the year, will present a summary of significant results of work done during fiscal year 1969, together with lists of investigations in progress, reports published, cooperating agencies, and Geological Survey offices.

"Geological Survey Research 1969" is the tenth volume of the annual series Geological Survey Research. The nine volumes already published are listed below, with their series designations.

Geological Survey Research 1960—Prof. Paper 400
Geological Survey Research 1961—Prof. Paper 424
Geological Survey Research 1962—Prof. Paper 450
Geological Survey Research 1963—Prof. Paper 475
Geological Survey Research 1964—Prof. Paper 501
Geological Survey Research 1965—Prof. Paper 525
Geological Survey Research 1966—Prof. Paper 550
Geological Survey Research 1967—Prof. Paper 575
Geological Survey Research 1968—Prof. Paper 600

RECONNAISSANCE GEOLOGY OF THE MOUNT EDGECUMBE VOLCANIC FIELD, KRUZOF ISLAND, SOUTHEASTERN ALASKA

By DAVID A. BREW, L. J. PATRICK MUFFLER,
and ROBERT A. LONEY, Menlo Park, Calif.

Abstract.—The postglacial Mount Edgecumbe volcanic field contains at least 14 rock units ranging in composition from olivine-augite basalt to augite-bearing quartz latite. Mesozoic graywacke and slate and Tertiary granitic intrusions underlie the gently dipping basalt which forms the base of the pile. Andesite and basaltic andesite overlie the basalt near Mount Edgecumbe and, in turn, they are probably overlain by the dacitic rocks which make up the composite cone of Mount Edgecumbe proper and by dacite flows and cinder cones on its southwest flank. Mount Edgecumbe and a nearby remnant of a similar cone are cut by latite domes. The remnant is now the site of a caldera 1.6 kilometers in diameter and 240 meters deep. Widespread dacite(?) lapilli and ash probably resulted from explosive eruptions during the formation of the composite cones. Nine chemical analyses define a smooth compositional trend that correlates with the relative age of the map units. The magma series is calc-alkaline and has a close relationship to the high-alumina basalt series.

Mount Edgecumbe is an inactive volcano 26 kilometers west of Sitka, Alaska (figs. 1, 2, and 3). The mountain is part of a Pleistocene and Holocene volcanic field that covers about 260 square kilometers on the southern end of Kruzof Island. The field consists of gently dipping flows, composite cones, and air-fall ash and lapilli. Augite basalt seems to be the most common rock type; olivine basalt, basaltic andesite, hypersthene dacite, and quartz latite are also present.

With the exception of Quaternary(?) vents on Lisianski Inlet, Chichagof Island (Rossman, 1959, p. 186), there are no known Holocene volcanic areas within 240 km of Mount Edgecumbe (Brew, Loney, and Muffler, 1966). The scattered vents of interior British Columbia are 240 to 320 km away (Little, 1962); those of southern southeastern Alaska are 320 km distant; and the volcanic seamounts of the Gulf of Alaska, a few of which could be Holocene, are also at least 320 km away. The volcanic field is far distant from those in the Aleutian Islands (Coats, 1950) and the Wrangell Mountains (fig. 1).

The Mount Edgecumbe volcanic field is closer to the continental margin (as defined by the 100-fathom contour) than are the volcanoes of the interior conterminous United States, Canada, and Alaska, and is even closer than most Aleutian volcanoes (fig. 1). Thus the Mount Edgecumbe field may provide an informational link between the continental volcanoes and the volcanic seamounts of the Gulf of Alaska (Engel and Engel, 1963).

Unsubstantiated (and probably inaccurate) accounts of volcanic activity at Mount Edgecumbe within historic time have been summarized by Becker (1898, p. 13). Two radiocarbon dates provide evidence about the absolute age of the major eruptions of Mount Edgecumbe. One date, from peat underlying an ash layer near Juneau, suggests that large-scale ash and lapilli eruptions from Mount Edgecumbe occurred about 9000 Before Present (Heusser, 1960, p. 97, 184). This date is in good agreement with one of 8750±300 B. P. for rooted wood at the base of a peat layer that overlies the Mount Edgecumbe ash at Sitka (R. W. Lemke, U.S. Geological Survey, oral commun., 1966).

The Mount Edgecumbe volcanic field has been visited by few geologists. William Libbey, Jr., a geographer, visited the field in 1884 (Libbey, 1886, p. 283–286), and H. F. Reid climbed Mount Edgecumbe in 1892 (Cushing, 1897). F. E. Wright, of the U.S. Geological Survey, climbed the volcano in 1904 and studied some of the rocks but never published his results. Adolph Knopf, also of the Geological Survey, visited the east side of the field briefly in 1910 (Knopf, 1912, p. 14) and described a specimen of the most common flow rock. Berg and Hinckley (1963, p. O14–O15) mapped the northeast corner of the field and described the major features briefly.

U.S. GEOL. SURVEY PROF. PAPER 650-D, PAGES D1-D18

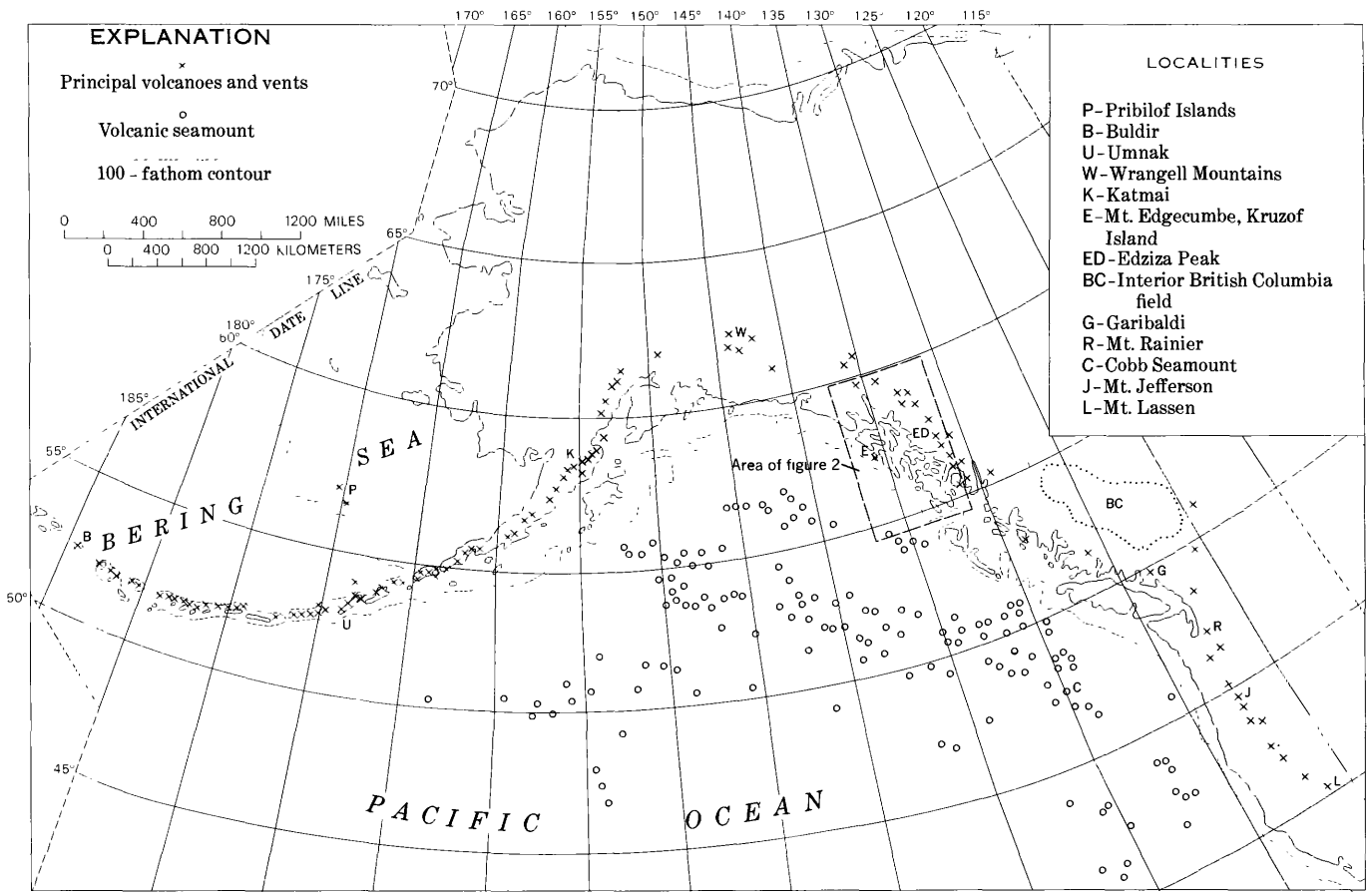

FIGURE 1.—Map of northeastern Pacific region, showing location of some Plio-Pleistocene, Pleistocene, and Holocene volcanoes (x), volcanic seamounts (o), 100-fathom contour (short dashes), and outline of figure 2.

The present study is based on reconnaissance mapping of the shoreline in August 1961 by R. A. Loney and D. A. Brew, with some additional data provided by H. C. Berg and J. S. Pomeroy, and on reconnaissance mapping of the shoreline and island interior in June and August 1962 by D. A. Brew and L. J. P. Muffler. A preliminary photogeologic map of the island was compiled by J. S. Pomeroy and combined with field data by L. J. P. Muffler in 1962. Preliminary petrographic examinations by H. C. Berg in 1961 were used in the preparation of a preliminary map covering the area (Loney and others, 1963). The petrographic studies were completed by D. A. Brew. Some preliminary results of our studies were reported by Brew, Muffler, and Loney (1966).

In the petrographic study of the Edgecumbe Volcanics, flat-stage methods were used in examining both thin sections and grain mounts. Precise mafic mineral determinations have not been made, although refractive indices of olivine and clinopyroxene were measured in some specimens. Determinative curves from Tröger (1959) were used. Plagioclase compositions were obtained from extinction-angle data and checked in high-dispersion oils, using the method of Emmons and Gates (1948) and the curves of Tsuboi (1923). Modal values were estimated visually from thin sections. The volcanic rocks were classified by means of Peterson's (1961) criteria. In addition, the rock names are modified by prefixing the names of the most important mafic minerals in the specimen. Thus an olivine-bearing augite basalt is a basalt containing more than about 10 percent augite and less than 10 percent olivine in the phenocrystic and groundmass phases taken together. Nine chemical analyses were obtained to verify the compositional classification of critical specimens and to provide a basis for better comparison of this volcanic field with others. Semiquantitative spectrographic analyses for 50 elements were also obtained from these nine specimens (Heropoulos and Mays, 1969).

This brief report cannot do justice to the complicated eruptive and petrogenetic history of the Mount Edgecumbe volcanic field, but it summarizes our present interpretations and hopefully will encourage a detailed study of the area.

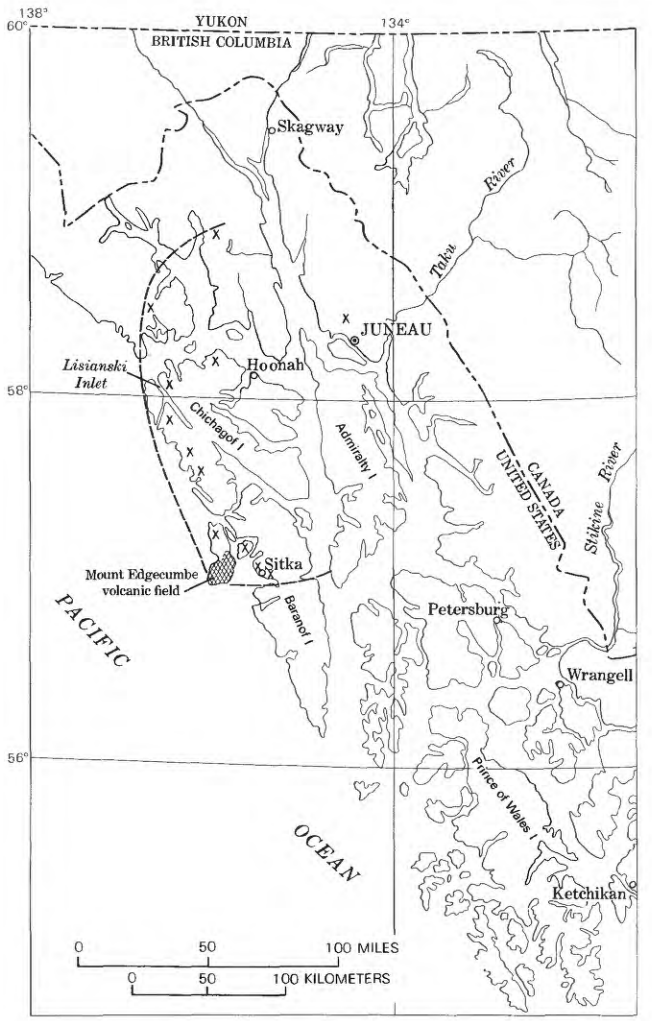

FIGURE 2.—Map of southeastern Alaska, showing location of Mount Edgecumbe volcanic field. Localities where Mount Edgecumbe ash is known to have been deposited are indicated by X. Dashed line is inferred limit of Mount Edgecumbe ash.

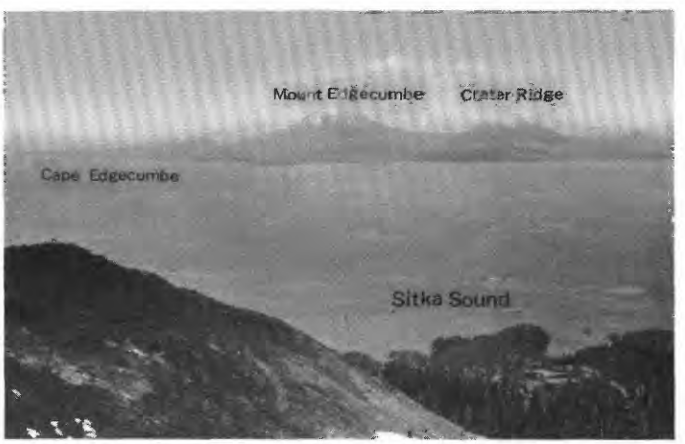

FIGURE 3.—Mount Edgecumbe volcanic field viewed from 29 km southeast across Sitka Sound. Mount Edgecumbe is 976 m high. The part of Kruzof Island shown in the photograph is about 16 km from left to right.

We thank James G. Smith and Donald A. Swanson for critically reviewing the manuscript.

STRATIGRAPHY AND PETROGRAPHY

Basement rocks

The volcanic rocks of the Mount Edgecumbe volcanic field were extruded onto a glacially planed surface of Mesozoic graywacke and slate that had been intruded by Tertiary granitic rocks (fig. 4). The graywacke and slate are part of the Sitka Graywacke (Berg and Hinckley, 1963, p. O12–O14; Loney and others, 1963, p. 5; Loney and others, 1964). Unmetamorphosed Sitka Graywacke consists of highly folded thin- to medium-bedded dark-gray graywacke interlayered with dark-gray slate. Although exposed only on the Vitskari Rocks and Vitskari Island (east of Low Island, fig. 4), unmetamorphosed Sitka Graywacke probably underlies the southern third of the volcanic field. The Sitka Graywacke in the northern part of the volcanic field has been thermally metamorphosed to biotite-plagioclase-quartz hornfels and schist, garnet-biotite-plagioclase-quartz hornfels, cordierite-biotite-plagioclase-quartz hornfels, and chlorite-plagioclase-quartz hornfels and schist. These thermally metamorphosed rocks are well exposed along the east shore of Kruzof Island, where they are locally highly sheared, mostly along north and northwest trends, and range in strike from west-northwest to north. Steeply dipping dikes of porphyritic basalt are exposed where the covering volcanics have been stripped off along the shore by wave erosion. The dikes are 1 to 15 meters wide and trend either about north-south or east-west.

The intrusions which thermally metamorphosed the Sitka Graywacke in Tertiary time (Loney and others, 1967) consist of light-gray medium-grained biotite granodiorite, biotite adamellite, and biotite granite (Loney and others, 1963, table 1) and probably underlie a third of the volcanic pile. The presence of granodiorite clasts among the ejecta at the summit of Mount Edgecumbe and as boulders in streams draining from wholly volcanic areas south of Shelikof Bay indicates that the magma conduits in those areas are at least partly within the intrusive rock.

Edgecumbe Volcanics

The volcanic rocks of southern Kruzof Island, named the Edgecumbe Volcanics by Berg and Hinckley (1963, p. O14–O15), are unglaciated and rest uncomformably on a low-relief glaciated surface that truncates all rocks older than the volcanic rocks. The volcanic rocks are overlain by alluvial deposits north and east of Shelikof Bay (fig. 4).

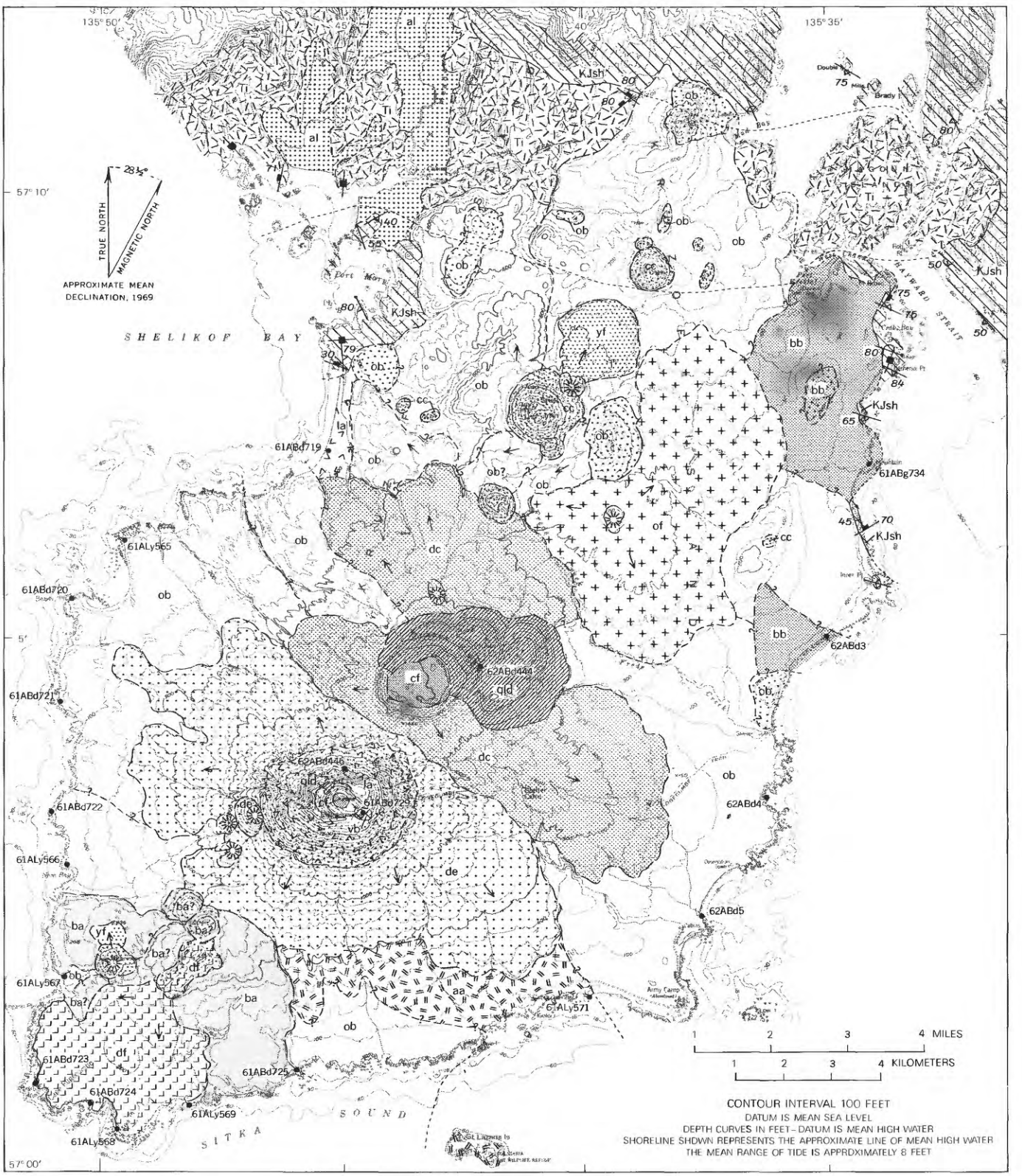

Base from U.S. Geological Survey
Sitka A-5 and A-6, 1951

Geology by D. A. Brew, R. A. Loney, L. J. P. Muffler, H. C. Berg, J. S. Pomeroy, and D. W. Hinckley, 1960–62

FIGURE 4.—Reconnaissance geologic map of the Mount Edgecumbe volcanic field, Kruzof Island, southeastern Alaska.

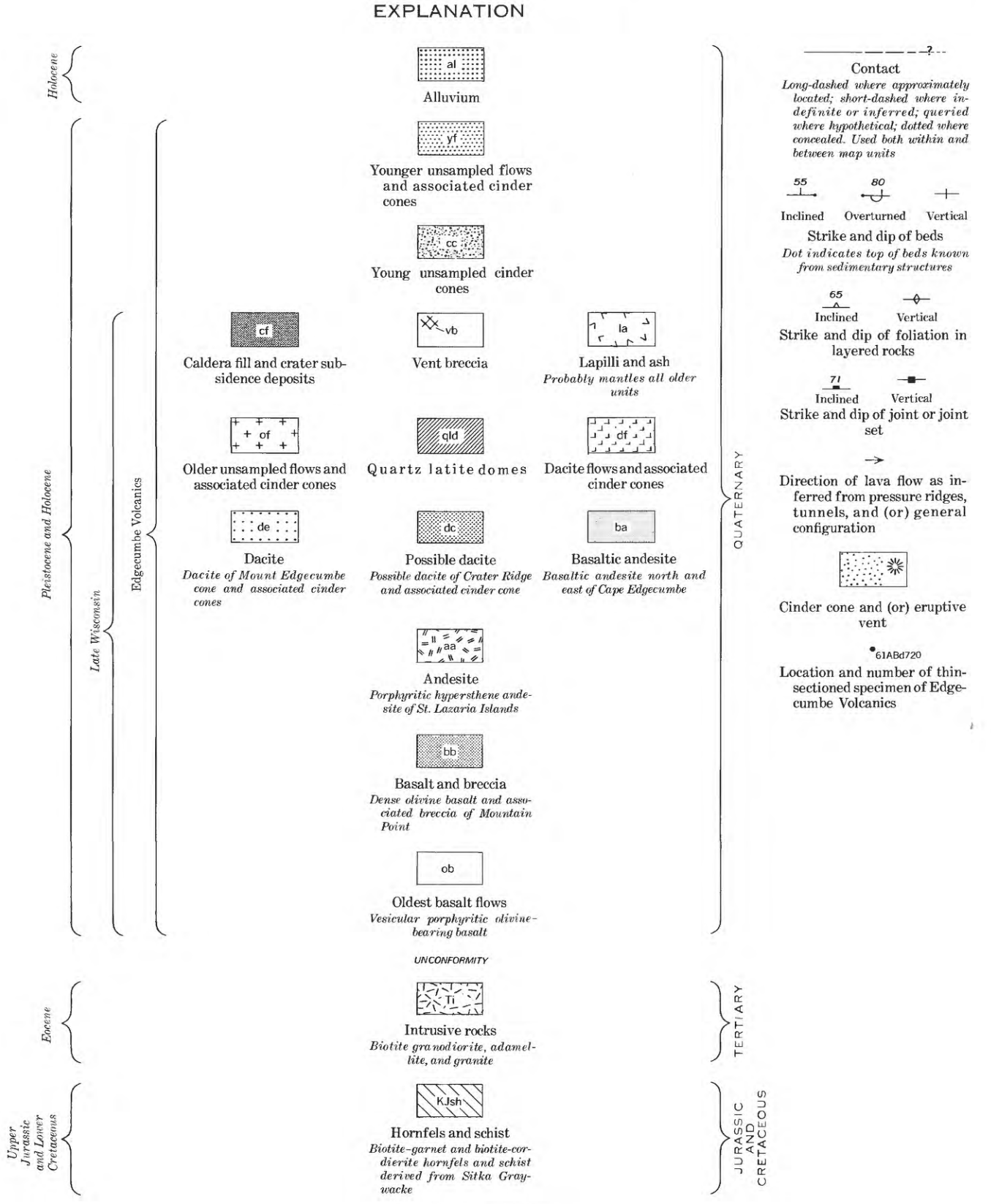
EXPLANATION
Holocene
Pleistocene and Holocene
Late Wisconsin
Edgecumbe Volcanics
QUATERNARY
al
Alluvium
yf
Younger unsampled flows and associated cinder cones
cc
Young unsampled cinder cones
cf
Caldera fill and crater subsidence deposits
vb
Vent breccia
la
Lapilli and ash
Probably mantles all older units
of
Older unsampled flows and associated cinder cones
qld
Quartz latite domes
df
Dacite flows and associated cinder cones
de
Dacite
Dacite of Mount Edgecumbe cone and associated cinder cones
dc
Possible dacite
Possible dacite of Crater Ridge and associated cinder cone
ba
Basaltic andesite
Basaltic andesite north and east of Cape Edgecumbe
aa
Andesite
Porphyritic hypersthene andesite of St. Lazaria Islands
bb
Basalt and breccia
Dense olivine basalt and associated breccia of Mountain Point
ob
Oldest basalt flows
Vesicular porphyritic olivine-bearing basalt
UNCONFORMITY
Eocene
TERTIARY
Ti
Intrusive rocks
Biotite granodiorite, adamellite, and granite
Upper Jurassic and Lower Cretaceous
JURASSIC AND CRETACEOUS
KJsh
Hornfels and schist
Biotite-garnet and biotite-cordierite hornfels and schist derived from Sitka Graywacke
Contact
Long-dashed where approximately located; short-dashed where indefinite or inferred; queried where hypothetical; dotted where concealed. Used both within and between map units
55
80
Inclined
Overturned
Vertical
Strike and dip of beds
Dot indicates top of beds known from sedimentary structures
65
Inclined
Vertical
Strike and dip of foliation in layered rocks
71
Inclined
Vertical
Strike and dip of joint or joint set
Direction of lava flow as inferred from pressure ridges, tunnels, and (or) general configuration
Cinder cone and (or) eruptive vent
61ABd720
Location and number of thin-sectioned specimen of Edgecumbe Volcanics

FIGURE 4.—(CON.)

The Edgecumbe Volcanics contains flows, minor intercalated breccias, cinder cones, and steep-sided domes. The volcanic field is dominated by one large composite volcanic cone, Mount Edgecumbe, and also contains a collapsed composite cone, Crater Ridge, and several smaller cinder cones, all of which stand above a broad base made up of many thin flows. Both composite cones and all but the youngest lava flows appear to be mantled by unconsolidated lapilli and ash.

The major vents are alined in a narrow 24-km-long belt that trends N. 30° E. Some of the youngest activity appears to have been concentrated near the southwestern tip of the island, but the overall eruptive sequence indicates no systematic change of active vent locations.

We have subdivided the Edgecumbe Volcanics into 14 units (table 1; figs. 4 and 5); their stratigraphy and petrography are treated separately below.

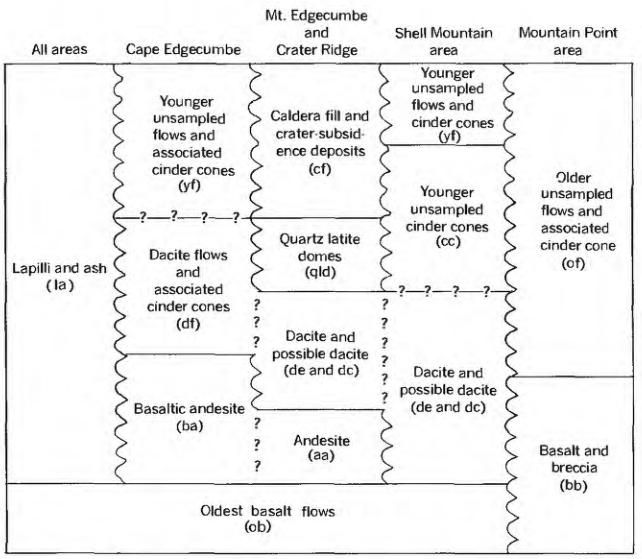

FIGURE 5.—Correlation chart showing reconnaissance subdivision of Edgecumbe Volcanics. Vertical position in chart shows probable place in eruptive sequence. Solid lines indicate stratigraphic relation known. Queried solid lines indicate stratigraphic position inferred. Wavy vertical lines separate geographic groups of units whose mutual relations are not known. Queries along vertical lines indicate possible correlation between units in adjacent columns. Lowercase letters in parentheses are map symbols used on figure 4. Vent breccia (vb of fig. 4) not shown on chart because of uncertainty of its age relation to crater fill and crater subsidence deposits.

Oldest basalt flows.—Most of the broad platform that underlies the spectacular composite cones of southern Kruzof Island consists of medium-gray vesicular porphyroaphanitic olivine-bearing augite basalt flows (fig. 4). These flows are characterized by 10–30 percent vesicles, 5–40 percent plagioclase phenocrysts, and scattered olivine phenocrysts 0.5–1 millimeter in diameter. Individual flows range from 0.5 m to a few meters in thickness and commonly have chilled bottoms and highly vesicular oxidized pahoehoe tops. Other features include (1) well-developed polygonal columns 0.3–1.2 m across and (2) abundant pressure domes and ridges up to a few hundred meters in maximum dimension and as much as 2 m high. The flanks of these domes and ridges have dips as steep as 50°.

Other rock types have been locally included in the "oldest basalt flows" unit (fig. 4). Interlayered breccia and medium- to dark-gray slightly vesicular basalt occur about 1 mile northeast of Beaver Point on the west coast of the island. Both the basalt flow and the fragments in the breccia are slightly porphyritic olivine-bearing augite basalt. The breccia fragments range from 2 centimeters to 1 meter in maximum dimension, and some bomblike fragments were noted. A sequence of pahoehoe flows with minor breccia layers has also been included in the map unit north of Neva Bay. These flows are composed of light- to medium-gray porphyritic to microporphyritic vesicular olivine-augite basalt. The flows contrast with those typical of the "oldest basalt flows" unit because of their slightly greater olivine content, poorer columnar jointing, thinness (average 30–50 cm), and relatively small (3-m diameter) domes. The breccia interlayers are 2–6 m thick and consist of angular to subangular fragments, 1 cm to 1 m in diameter, of flow-rock lithic type in a soft fine-grained tuff matrix.

Another group of flows included in the "oldest basalt flows" unit occurs along the shore due south of Mount Edgecumbe. These flows are light- to medium-gray, coarsely vesicular, microporphyritic augite-bearing olivine basalt. They are further characterized by polygonal columns 0.5–1 m in diameter, small domes, and rare pahoehoe tops; single flows are probably a few meters thick.

Petrographic characteristics of thin-sectioned specimens from the "oldest basalt flows" are given in table 1. These flows are typified texturally by vesicularity, abundant phenocrysts, and intergranular groundmass textures. The low amount of olivine phenocrysts and the consistent olivine and plagioclase compositions (table 1) are important. A consistent range of clinopyroxene compositions was not obtained from the optical data, and the mineral is therefore reported simply as augite, although most is probably diopsidic augite and some is subcalcic augite.

Fine grain size made it difficult to determine compositions and proportions of groundmass olivine and clinopyroxene and to determine the presence or absence of reaction relations around olivine phenocrysts.

Several significant petrographic features common to all specimens are not shown in table 1 and are therefore noted here. Plagioclase phenocrysts commonly are progressively zoned over a range of 30 percent An from core to rim with conspicuous oscillatory zoning near the rims. Their composition in table 1 is representative of the "outer core" and is practically an average for the phenocryst. In some of the specimens, the phenocryst outlines are irregular owing to reaction with the groundmass material after crystallization or with the magma.

Another striking feature of some of these basalts is the presence of glomeroporphyritic clots of plagioclase and mafic crystals as large as 1 cm in diameter.

Minerals derived from olivine after crystallization are described in table 1 simply as an orange-brown or red-brown secondary mineral. Probably this late product is "bowlingite" or "iddingsite." Chlorophaeite present in a few specimens is included with the glass in table 1.

Three samples (61ABd720, 61ABd725b, and 61ALy-566) of the "oldest flows" were analyzed chemically (columns 2, 3, and 4, table 2).

Basalt and breccia.—A lithologically distinct unit consisting of volcanic breccia overlain by dense massive lava flows is exposed in two areas along the east shore of Kruzof Island. Between Port Krestof and Mountain Point the unit rests uncomformably on hornfels derived from the Sitka Graywacke. South of Inner Point the unit has been interpreted from photogeologic evidence to rest on the "oldest basalt flows," but the evidence is poor. The stretch of shore separating the northern and southern exposures is made up of hornfels overlain by "oldest basalt flows."

The relations of the "basalt and breccia" unit to the other rock units in the volcanic field are not clear from the available reconnaissance data. The unit is considered younger than the "oldest basalt flows" (fig. 5) and probably older than the "older unsampled flows," but could antedate or be coeval with the "oldest basalt flows" unit.

The lower part of the "basalt and breccia" unit is volcanic breccia consisting of bomblike or pillowlike fragments of vitrophyre and dense nonvesicular slightly porphyritic olivine basalt as much as 75 cm in maximum dimension in a poorly sorted matrix of irregularly shaped breccia fragments and tuff. The breccia is variable in thickness and locally contains fragments that appear to be weathered fine-grained graywacke; this latter feature suggests that subaerially weathered debris was incorporated in the breccia during movement. The "basalt and breccia" unit may have been erupted, at least in part, from a dissected cone about 2.4 km northwest of Mountain Point.

Flows of olivine basalt compositionally similar to the large fragments in the breccia overlie the breccia. The flows are subhorizontally layered, massive, dense, fine grained, and generally nonvesicular. In places erosional remnants of the flows rise above the breccia and superficially resemble dikes.

The augite-bearing olivine and olivine-augite basalts are characterized by the absence or near absence of vesicles and phenocrysts (table 1). The available petrographic data suggest that this unit may contain a variety of rock types and, perhaps, compositions. One sample (61ABg734d) from the "basalt and breccia" unit was analyzed chemically (column 1, table 2).

Andesite.—A distinctive unit of subhorizontal andesite flows is well exposed along the shore near Lava and Goloi Islands and on St. Lazaria Islands (fig. 4). These flows probably came from near Mount Edgecumbe. The andesitic composition suggests affinity with rocks of Mount Edgecumbe rather than with the "oldest basalt flows," which the andesites are interpreted to overlie and which they resemble in outcrop.

The unit consists of nonvesicular, highly porphyritic, dark-gray olivine-bearing hypersthene andesite or basaltic andesite flows a few meters thick. The andesites have excellently developed joint columns about 30 cm in diameter that are oriented perpendicular to flow surfaces. The andesite flows are also characterized by abundant domes as much as 15 m across and a few meters high, and the columns appear to radiate from many centers beneath the domes. Locally the flanks of the domes dip as steeply as 40°.

Petrographic features of the andesite (table 1) include the following: abundant broken plagioclase phenocrysts and microphenocrysts that are partly replaced by an epidotelike mineral, synneusis-twinned plagioclase phenocrysts, glomeroporphyritic clots of plagioclase and locally corroded pigeonitic augite, hypersthene apparently intergrown with clinopyroxene and plagioclase, and rare quartz xenocrysts.

One sample (61Ly571) of this andesite unit was analyzed chemically (column 6, table 2). Comparison of the analysis with Nockolds' (1954) averages suggests that the rock is best called an andesite.

Basaltic andesite.—Low on the southwest flank of Mount Edgecumbe are rocks mapped separately (fig. 4) as basaltic andesite. The flows probably originated from now slightly dissected cinder cones at elevations between 700 and 1,200 feet and spread over the southwestern part of Kruzof Island. They rest on the "oldest basalt flows" unit on the south side of the island and between Engano Point and Neva Bay on the west side

TABLE 1.—*Petrographic characteristics of thin-section specimens from*

[Specimen locations shown on figure 4. Asterisk (*) indicates chemically analyzed specimen. Abbreviations—General: Comp., composition; Tr., trace; V, very. Mineral: m, medium;

Specimen No.	Rock name	Texture							Composition (percent)					
		General (percent)		Specific		Average phenocryst size (mm)			Plagioclase				Olivine	
									Phenocrysts		Groundmass		Phenocrysts	
		Vesicles	Phenocrysts	Whole rock	Groundmass	Plagioclase	Olivine	Pyroxene	Total	An content	Total	An content	Total	Fa content
OLDEST BASALT FLOWS (ob)														
Typical flows														
61ABd720*	Vesicular porphyritic olivine-bearing augite basalt.	≈25	42	Porphyro-aphanitic.	Intergranular	1×3	0.6	.....	30	50–60	46	50–55	8	5–10
61ABd721b	do	≈15	25	do	Intergranular to micro-ophitic.	1×5	1×1.7	.....	22	57	52	57	3	12–15
62ABd5	do	≈30–40	40	do	Intergranular	1×3	0.6	.....	35	61	30	48	5	15–25
62ABd4	Vesicular porphyritic augite-olivine basalt.	≈35	28	do	do	0.8×3.5	0.5	.....	25	62	35	54	3	15–20
Less typical breccia fragment														
61ALy565a	Vesicular porphyritic olivine-bearing augite basalt.	≈10	10	Porphyro-aphanitic.	Intergranular to felty.	1×3	2	.....	6	60	47	60	3	20–23
Other flows														
61ABd722a	Vesicular porphyritic olivine-augite basalt.	≈20	22	Porphyro-aphanitic.	Intergranular and intersertal.	0.5×1	0.8	.....	12	70	15	54	10	15
61ALy566*	Vesicular microporphyritic augite-olivine basalt.	≈10	.....	Microporphyro-aphanitic.	Felty intergranular to intersertal.	.....	.....	.....	5	48	55	51	3	15
61ABd725b*	Vesicular microporphyritic olivine basalt.	≈15	.....	do	Intergranular to intersertal.	.....	.....	.....	2	60	56	48	3	10–15
BASALT AND BRECCIA (bb)														
61ABg734a*	Olivine-pigeonitic augite basalt.	.....	.....	Aphanitic	Microophitic to intersertal.	.....	.....	.....	.....	.....	53	59	.....	.....
62ABd3	Slightly vesicular porphyritic olivine basalt.	≈5	7	Vitrophyric	Hyalopilitic	.....	0.7–3.0	.....	.....	.....	47	56	7	10–15
ANDESITE (aa)														
61ALy571*	Porphyritic hypersthene basaltic(?) andesite.[1]	.....	40	Vitrophyric	Hyalopilitic	0.75	0.2–0.6	0.2–0.6	30	65	20	46	2	10–20
BASALTIC ANDESITE (ba)														
61ALy567a*	Porphyritic olivine-bearing pigeonite basaltic andesite.[1]	.....	20	Porphyro-aphanitic.	Felty intersertal.	0.5×1	1	0.5	15	58	38	50	4	15–25
61ALy567b	Porphyritic hypersthene-bearing olivine basalt or basaltic andesite.	<2	25	do	Felty intergranular.	2	0.7	0.6	18	60	49	54	5	10
61ALy569a	Slightly vesicular porphyritic olivine-bearing pigeonite basalt or basaltic andesite.	≈5	15	do	Felty intersertal.	0.4×0.8	0.9	?	9	52	50	52	3	0–5
61ALy569c	Slightly vesicular porphyritic olivine-bearing pigeonite basaltic andesite.	<5	20	do	Felty intersertal to pilotaxitic.	0.6×1	0.6	0.6	16	53	20	48?	4	15
61ABd725c	Slightly vesicular porphyritic olivine-bearing pigeonite?-augite basaltic andesite.	10	20	do	Felty intersertal.	0.8	0.3	1.5	15	55	50	47–55	1	15

See footnotes at end of table.

the Edgecumbe Volcanics, Kruzof Island, southeastern Alaska

Pg, subcalcic augite; Di, diopside; Hy, hypersthene; Au, augite; Mg, magnetite; Il, ilmenite; Hm, hematite. Color: or, orange; br, brown; gn, green; gy, gray; dk, dark; lt, light]

Composition (percent)																Remarks
Olivine		Clinopyroxene				Orthopyroxene				Opaque minerals		Glass		Secondary minerals		
Groundmass		Phenocrysts		Groundmass		Phenocrysts		Groundmass								
Total	Fa content	Total	Comp.	Total	Comp.	Total	Comp.	Total	Comp.	Total	Type	Total	Description	Total	Description	
OLDEST BASALT FLOWS (ob)																
Typical flows																
1	12	4	Pg?	9	Pg?					1	Mg?	1		Tr.	Or br	
2	12–15	15	Ti rich							3	Mg, Il?	3	Murky	Tr.	do	Probable reaction around olivine.
3	15–25	5	Di?	15	Di?					5	Mg?			2	do	
15	5–15			16						5	do	Tr.?		1	do	No reaction around olivine.
Less typical breccia fragment																
1	23	1	Di?	25	Au					10	Mg?	5	Devitrified.			Possible reaction around olivine.
Other flows																
Tr.	15			27	Di?					20	Mg?	10		Tr.	Red br	No reaction around olivine.
12	15–20			12	do					7	do	6	Dk br, murky.	Tr.	Gn, or-br.	Olivine has magnetite+clinopyroxene rims; microphenocryst composition is given.
24	10–15			5	Pg?					3	do	6	do			Possible reaction around olivine; microphenocryst composition is given.
BASALT AND BRECCIA (bb)																
17	10–15			20	Pg			1	Hy	5	Mg	4	Br, gn, devitrified.	1	Gn chlorite?	
10	10–15			4	Au							32	V dk br			No reaction around olivine.
ANDESITE (aa)																
		2?	Pg?			6	Hy	5	Hy?	15	Mg?	18	Dk	2	Murky	10 percent plagioclase microphenocrysts included with phenocrysts; 5 percent hypersthene microphenocrysts included with groundmass; one quartz phenocryst noted.
BASALTIC ANDESITE (ba)																
		1	Pg?	25	Pg					2	Mg?	15	Br, gy, murky.			Olivine has clinopyroxene rims; excellent flow alinement around phenocrysts.
4?		1	Au	15	Au	1	Hy	?		4	do	3	M br			Olivine has clinopyroxene rims; proportion of orthopyroxene may be > given; one exotic sphene grain noted.
1?		3	Pg?	20	Pg					8	do	15	Lt m br	1	Chlorophaeite.	Possibly two generations of plagioclase phenocrysts; olivine has clinopyroxene+magnetite rims; 5 percent "late alkalies" in groundmass.
1?		4	Pg?	43	Pg?					8	do	8	M br			Plagioclase and olivine phenocrysts reacting with groundmass.
		4	Pg	10	Au					10	do	10	Dk br			Plagioclase, olivine, and pigeonite phenocrysts reacting with groundmass.

TABLE 1.—*Petrographic characteristics of thin-section specimens from*

[Specimen locations shown on figure 4. Asterisk (*) indicates chemically analyzed specimen. Abbreviations—General: Comp., composition; Tr., trace; V, very. Mineral: m, medium;

Specimen No.	Rock name	Texture							Composition (percent)					
		General (percent)		Specific		Average phenocryst size (mm)			Plagioclase				Olivine	
									Phenocrysts		Groundmass		Phenocrysts	
		Vesicles	Phenocrysts	Whole rock	Groundmass	Plagioclase	Olivine	Pyroxene	Total	An content	Total	An content	Total	Fa content
DACITE (de)														
62ABd446*...	Slightly vesicular porphyritic augite andesite(?) [2]	≈8	25	Porphyro-aphanitic.	Hyalopilitic...	0.2	.....	0.4	17	55	43	43	.....	
DACITE FLOWS (df)														
61ABd723a...	Lineated porphyritic pyroxene andesite or trachyandesite.	.....	5	Porphyro-aphanitic.	Pilotaxitic.....	1	.....		[3] 3	64	40	43	.....	
61ABd723d*..	Porphyritic augite-hypersthene andesite or trachyandesite. [2]	.....	7	....do....	.....do.....	.....	.....		[5] 4	78	40	35	.....	
61ABd724c...	Vesicular porphyritic hypersthene-augite andesite?	20	4	....do.....	Hyalopilitic...	0.5×1	.....		3	46	[8] 55	47	.....	
61ALy568....	Porphyritic hypersthene-augite andesite or trachyandesite.	.....	8	....do.....	Pilotaxitic.....	0.3×0.8	.....	0.3×0.5	[9] 5	53	23	33	.....	
QUARTZ LATITE DOMES (qld)														
62ABd444*...	Banded porphyritic augite-bearing andesite or trachyandesite. [10]	≈2	5	Vitrophyric	Felty hyalopilitic.	0.5×1	.....	0.3×1	4	46?	40	37	.....	
VENT BRECCIA (vb)														
61ALy729b...	Vesicular porphyritic augite-bearing andesite? or trachyandesite?	15	25	Porphyro-aphanitic.	Intersertal to intergranular.	.....			[11] 10	50	35	35–39	.....	
LAPILLI AND ASH (la)														
61ABd719–1..	Pyroxene- and plagioclase-bearing pumice.	40	5	Holohyaline.....		0.3×1	.....		5	.....				
61ABd719–2..	Hypersthene- and plagioclase-bearing pumice.	50	4	....do.....		.....			2	33	.....		.....	

[1] Andesite on basis of chemical analysis.
[2] Dacite on basis of chemical analysis.
[3] Twenty percent microphenocrysts of An_{49} and An_{55} (two generations).
[4] Two percent augite microphenocrysts also.
[5] Ten percent microphenocrysts of An_{53} and An_{38} also.
[6] One percent augite microphenocrysts also.

the Edgecumbe Volcanics, Kruzof Island, southeastern Alaska—Continued

Pg, subcalcic augite; Di, diopside; Hy, hypersthene; Au, augite; Mg, magnetite; Il, ilmenite; Hm, hematite. Color: or, orange; br, brown; gn, green; gy, gray; dk, dark; lt, light]

Composition (percent)																Remarks
Olivine		Clinopyroxene				Orthopyroxene				Opaque minerals		Glass		Secondary minerals		
Groundmass		Phenocrysts		Groundmass		Phenocrysts		Groundmass								
Total	Fa content	Total	Comp.	Total	Comp.	Total	Comp.	Total	Comp.	Total	Type	Total	Description	Total	Description	
DACITE (de)																
		7	Au	10	Au	1?				7	Mg?	15	Devitrified?			Proportion of orthopyroxene may be greater than given.
DACITE FLOWS (df)																
		[4] 2	Au	12	Au	2	Hy			15	Mg?	6	Gy br			
		[6] 1	Au	28	Au	[7] 2	Hy			8	do	5	Murky			
				10	?	1	Hy			6	do	25	Br, murky.			
		1	Au	15	Au	2	Hy			12	do	12	Lt-m-br			Hypersthene has narrow reaction rim with groundmass; most mafic phenocrysts in glomeroporphyritic clots.
QUARTZ LATITE DOMES (qld)																
		Tr.	Au							10	Mg?, Il?	45	Devitrified.	4	Hm	1 percent of opaques are phenocrysts.
VENT BRECCIA (vb)																
		5	Pg?	15	Au	10	Hy			10	Mg?	5	Gy br			Plagioclase phenocrysts broken and reacted; hypersthene phenocrysts have reaction rim with groundmass.
LAPILLI AND ASH (la)																
		7								2	Mg?	93	Colorless			
						2	Hy					94	Lt br			2 percent lithic fragments (also dark-brown vesicular glass with plagioclase phenocrysts).

[7] One percent hypersthene microphenocrysts also.
[8] Actually microphenocrysts.
[9] Thirty percent microphenocrysts of An_{60}? also.
[10] Quartz latite on basis of chemical analysis.
[11] Ten percent microphenocrysts of An_{50} also.

and are overlain by the "dacite flow and associated cinder cone" unit and some of the "younger unsampled flows." The relation to the "andesite" unit, which the basaltic andesite also contacts, is unclear.

The rocks of this unit are porphyroaphanitic olivine-bearing pigeonite basaltic andesites (table 1). They are nonvesicular to slightly (10 percent) vesicular and commonly contain 15–20 percent phenocrysts (mostly plagioclase) that are 1–2 mm long. Some vitrophyres and breccias are interbedded with the usual flow rocks. In general the unit is characterized by dense light- to medium-gray cliff-forming flows.

The andesites are notable for well-developed felty textures and reaction relations betwen phenocrysts and the groundmass. The flow-alined plagioclase laths of the groundmass neatly surround the phenocrysts, which have been rotated into the flow planes together with flattened and collapsed vesicles.

The phenocrysts occur singly or in glomeroporphyritic clots and show clear evidence of reaction with the groundmass material. Plagioclase phenocrysts are commonly sieved with small crystals of mafic minerals and have corroded outer margins. Olivine and subcalcic augite phenocrysts have thin selvages of augite with or without magnetite granules. Flat-stage optical data suggest the presence of both subcalcic and calcic augite as phenocrysts and groundmass minerals in most of the basaltic andesites, as in many other rocks from the Mount Edgecumbe volcanic field.

One basaltic andesite (61ALy567a) was analyzed chemically (column 5, table 2), and comparison of its analysis and norm with Nockolds' (1954) average andesite suggests that the rock is an andesite, although the mode shows basaltic affinities.

FIGURE 6.—Aerial view of Mount Edgecumbe from the southeast. Light-colored lapilli and ash on upper unforested flanks are underlain by outward-dipping lava and tuff layers. Photograph by U.S. Navy.

Dacite and possible dacite.—The composite cone of Mount Edgecumbe consists of alternating meter-thick dacite flows and airfall tuff layers here called the "dacite" unit. The deposits around the former vent at Crater Ridge are probably similar and are here referred to the "possible dacite" unit. The "possible dacite" is known only from aerial observation and from a few thin sections of specimens collected at unspecified localities by F. E. Wright in 1904; the available field and petrographic evidence supports their temporal and compositional similarity to the deposits of Mount Edgecumbe.

The Mount Edgecumbe dacite flows and airfall tuff deposits are well exposed on the rim of the summit crater (figs. 4 and 6), where they dip outward from a point close to the northwest part of the rim. Many individual lava and tuff units are present; in general, the purplish-gray-weathering airfall tuff layers predominate over the medium-gray-weathering flows. The lava flows are slightly vesicular, porphyritic augite dacites and hypersthene-augite dacites characterized by well-developed flow features, including vesicle trains, and by oxidized flow tops.

The alternating lava flow and tuff layers are mantled on the outer slopes, and locally within the summit crater, by the distinctive yellow and orange "lapilli and ash" unit; they are intruded by a small quartz latite(?) dome on the northwest rim near the apex of the projected layers. The sides of the summit crater are obscured by rubble and talus in many places (fig. 8).

Some petrographic features of a typical dacite from Mount Edgecumbe cone are summarized in table 1. Other notable features include broken phenocrysts of zoned plagioclase that show blotchy alteration to a claylike mineral. Optical properties suggest that both orthopyroxene and clinopyroxene (augite and subcalcic augite) are present.

The rock looks like an andesite, on the basis of color, hyalopilitic groundmass texture, and general contrast with the basalts. However, a chemically analyzed sample (62ABd446; column 7, table 2) is a dacite by comparison with Nockolds' (1954) averages.

Quartz latite domes.—The dacitic lava flows and tuff layers of Mount Edgecumbe and Crater Ridge were intruded by two viscous steep-sided quartz latite domes.

The largest of these masses covers about 6.5 sq km on Crater Ridge (fig. 7) and the hills directly east of the ridge. It consists of locally vesicular or amygdaloidal, gray- and reddish-brown-weathering aphanitic, augite-bearing quartz latite. The detailed internal structure of this vertically flow-layered dome is not known, but it is probably a composite of at least three contiguous masses which rose more or less synchronously. The

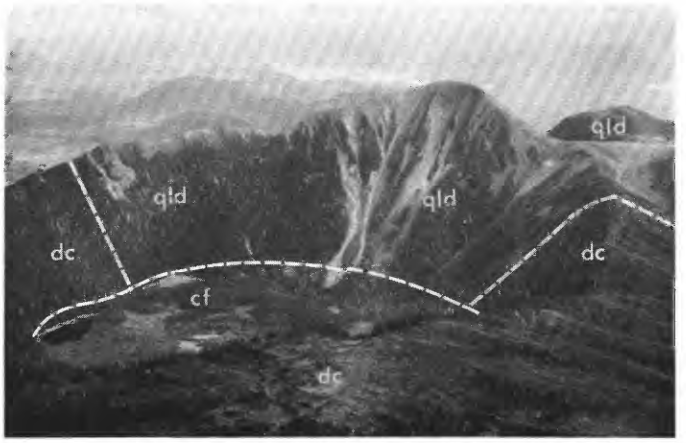

FIGURE 7.—Crater Ridge and Crater Ridge caldera viewed from Mount Edgecumbe, Kruzof Island, southeastern Alaska. The quartz latite dome (qld) makes up all but the left-hand part of Crater Ridge. Possible dacite unit (dc) and caldera fill unit (cf) shown also. Shell Mountain and other cinder cones are visible in the distance beyond the ridge.

FIGURE 8.—Aerial view of summit crater of Mount Edgecumbe, Kruzof Island, southeastern Alaska, from the southeast. The crater is filled largely by colluvium derived from the dacite and tuff layers which form the cone. "Lapilli and ash" unit (la) at left and right overlies "dacite" unit (de), which is intruded by quartz latite(?) (qld) at right center. Possible vent breccia (vb) is exposed in a small area. Photograph by U.S. Navy.

domal complex probably was about 0.65 sq km larger before collapse of the Crater Ridge caldera.

A second quartz latite dome forms a gray-weathering outcrop about 300 m in diameter on the west-northwest rim of Mount Edgecumbe (fig. 8). It clearly truncates the radially dipping tuff and lava-flow deposits of the composite cone. The attitudes of these deposits suggest that their vent was close to, and may be plugged by, the dome.

The quartz latite contains only a few percent of plagioclase and other phenocrysts in a felty groundmass (table 1). The material surrounding the alined plagioclase laths of the groundmass is anisotropic, probably devitrified glass. The banding in the quartz latite is caused by streaks and irregular splotches of hematite and, to a lesser extent, opaque minerals more or less parallel to the flow alinement in the groundmass.

Comparison of a chemical analysis (table 2, column 9) and norm with those of the average dellenite (quartz latite), rhyodacite, and rhyolite obsidian of Nockolds (1954) suggests that the rock is a quartz latite or a rhyodacite.

Dacite flows and associated cinder cones.—The "basaltic andesite" unit on the southwestern tip of Kruzof Island is overlain by about 13 sq km of cliff-forming dacite flows, which crop out continuously from near Engano Point to beyond Sitka Point. The exposures are best visited at low tide because the surf breaks against the sea cliffs at all other times.

The lower part of the unit includes medium-dark-gray and grayish-brown, strikingly layered flows; its upper part is made up of dense reddish-gray flows and minor breccia and tuff. Some of the dense flows and breccias were deposited on an irregular (erosional?) surface cut across the layered flows.

All four rock specimens studied in thin section contain a few percent of corroded plagioclase phenocrysts, and accompanying phenocrysts of augite and hypersthene have narrow reaction zones. Perhaps the most striking microscopic feature of these rocks is the presence of abundant microphenocrysts intermediate in size (and, for plagioclase, intermediate in composition) between phenocrysts and groundmass minerals. The microphenocrysts are generally well alined in a felty texture, and groundmass plagioclase laths are also well alined in some specimens.

The specimens studied were classified as nonvesicular porphyroaphanitic hypersthene-bearing augite andesites or trachyandesites on the basis of their microscopic features (table 1), but comparision (table 2, column 8) with Nockolds' (1954) average suggests a dacitic composition.

Older unsampled flows and associated cinder cone.—About 20 sq km of gentle terrain southeast and east of Shell Mountain was mapped photogeologically as "older unsampled flows and associated cinder cone" (fig. 4). The unit has a shieldlike form and appears to have been erupted from near a partly dissected cinder cone. The unit is interpreted to rest on the "oldest basalt flows" and "basalt and breccia" units, and it may

be constrained on the southwest by "possible dacite" flows which emanated from Crater Ridge.

Caldera fill and crater subsidence deposits.—The deposits partly filling the caldera at Crater Ridge and the summit crater of Mount Edgecumbe are poorly known. The Mount Edgecumbe crater appears to be filled mostly by colluvium derived from the crater walls (fig. 7). The debris in Crater Ridge caldera was described by F. E. Wright (unpub. notes, 1904) as a jumble of great angular blocks of lava, and the mound near the north wall of the caldera was described as consisting of blocks of slightly scoriaceous lava 0.9–9.0 m in diameter. Wright described the caldera floor as swampy in places and noted that the shallow lake on the west side bubbled locally at irregular intervals. The bubbles are of nonflammable gas according to Wright and are definitely not marsh gas.

The caldera of Crater Ridge in particular is worth further study. As shown on figure 4, it is 1.6 km in diameter at the rim, 1.1 km in average diameter at the floor, and about 240 m deep. The volume is calculated to be 1.4 cubic kilometers. Truncation of the quartz latite dome by the caldera suggests that it formed by collapse, but conclusive evidence is lacking. Figure 5 and the explanation of figure 4 reflect the inexact dating of the caldera formation. Our reconnaissance data do not provide the age relation between the "lapilli and ash" unit and the formation of the caldera.

Vent breccia.—A small area on the southeast rim of Mount Edgecumbe is underlain by glassy volcanic breccia which truncates the layered deposits of the cone (figs. 4 and 8). The breccia is interpreted to fill a vent. It is reddish-brown weathering, contains about 25 percent angular, 0.2–5-cm-long fragments of dacite(?) and vesicular porphyroaphanitic hypersthene-augite dacite in a flow-banded, dark-red and black glassy matrix. About 10 percent of the rock consists of angular voids.

The one specimen studied in thin section (table 1) is a clast in the vent breccia and is somewhat similar to the dacitic rocks from elsewhere on Mount Edgecumbe. It is notable mainly for its high content (10 percent) of hypersthene phenocrysts, the presence of plagioclase microphenocrysts in addition to the groundmass and phenocrystic plagioclase, and the reaction relations around hypersthene and plagioclase phenocrysts.

In addition to the rock fragments, the glassy breccia matrix also encloses scattered small (less than 1 mm) plagioclase phenocrysts of about An_{37} composition.

Lapilli and ash.—The distribution of the "lapilli and ash" unit shown in figure 4 is misleading because the only outcrop areas shown are the most conspicuous ones noted. Probably almost all the volcanic field and adjacent basement rock areas are or were mantled by this unit; large areas of unknown size inland from the south and east shores of the island are known to have a thick ash blanket.

The lapilli and ash deposits noted during the mapping range from zero to 5–6 m in thickness on the lower parts of the island and may be more than 15 m thick on the higher parts of Mount Edgecumbe (fig. 7).

The lapilli and ash weather reddish orange and yellowish brown at different localities and consist almost entirely of siliceous pumice and (or) scoria with less than 5 percent phenocrysts and lithic fragments. The two specimens studied in thin section (table 1) are very vesicular glassy rocks with minor content of plagioclase and pyroxene crystals and lithic fragments. The refractive index of the glass is about 1.51 to 1.52, indicating a silica content of 65 to 68 percent according to the general curve of Huber and Rinehart (1966). Hence the rocks may be dacites.

Young and younger unsampled cinder cones and flows.—The two youngest volcanic units shown on figure 4 are known only from aerial photographs and distant aerial observations. The "young unsampled cinder cones" making up Shell Mountain and nearby smaller cones are distinguished from other, apparently older cones by their undissected forms. As interpreted, all the young cones rest on the "oldest basalt flows" unit and one also apparently overlaps onto the "possible dacite" unit of Crater Ridge.

The "younger unsampled flows and associated cinder cones" were mapped separately because they are undissected and are not covered by thick vegetation, as are all the other volcanic units.

Alluvium

The areas shown on figure 4 as "alluvium" are broad valleys filled with sand and gravel of probable local derivation. These areas were not examined in detail, and it is probable that many are underlain at shallow depths by the "lapilli and ash" unit.

PETROGENESIS

The Mount Edgecumbe volcanic field is nearly ideal for the study of petrogenetic relationships within a single magma series for the following reasons: (1) there is wide variation of rock type, from basalt containing 48 percent SiO_2 to quartz latite containing almost 70 percent SiO_2; (2) the relatively short duration of activity and the clear temporal separation from earlier magmatic activity (that is, the mesozonal intrusions of middle Tertiary time) obviate many interpretive problems that can arise in a complex area such

as the Cascade Range (Hopson and others, 1967); (3) the geographic isolation from other Holocene volcanic centers eliminates problems of mixing or contamination with other magma series; and (4) the geomorphic features are varied and well preserved and consequently are useful in establishing stratigraphic succession.

The reconnaissance nature of our fieldwork and the lack of precise determinations of phenocryst and groundmass compositions preclude setting up a detailed petrologic model for the Mount Edgecumbe volcanic field. However, the available data do permit a few tentative conclusions and a comparison with other volcanic series.

The chemical analyses (table 2) define a relatively smooth compositional trend (figs. 9 and 10) that we interpret as reflecting differentiation in a subjacent magma chamber. The trend from basalt to quartz latite also correlates with sequence of eruption, as

TABLE 2.—*Chemical analyses and CIPW norms of specimens from the Edgecumbe Volcanics, Kruzof Island, Alaska*

[Analyses 1 and 3-7 by P. L. D. Elmore, S. D. Botts, Lowell Artis, D. Taylor, G. W. Chloe, H. Smith, and J. L. Glenn using rapid-rock techniques (Shapiro and Brannock, 1962) supplemented by atomic absorption. Analyses 2, 8, and 9 by A. C. Bettiga using X-ray spectroscopy for SiO_2, Al_2O_3, CaO (Nos. 8 and 9 only), TiO_2, MnO, and total iron, by L. B. Beatty using wet chemistry for FeO, MgO (No. 2 only), CaO (No. 2 only), Na_2O, K_2O, H_2O+, H_2O-, P_2O_5, and CO_2, and by R. E. Mays using quantitative spectrographic analysis for MgO (Nos. 8 and 9 only)]

Number	1	2	3	4	5	6	7	8	9
Chemical analysis									
SiO_2	48.0	50.0	51.3	52.6	53.8	56.7	59.5	60.4	69.5
Al_2O_3	17.3	17.4	18.1	18.4	18.1	17.7	17.5	16.9	15.2
Fe_2O_3	2.1	2.3	2.0	2.8	1.5	1.0	1.2	1.8	3.2
FeO	6.5	6.2	6.1	5.5	6.1	6.2	4.7	4.9	.33
MgO	9.6	7.1	6.5	5.6	5.2	4.2	3.6	2.6	.42
CaO	11.0	10.8	10.2	9.0	9.1	7.0	6.8	5.5	2.3
Na_2O	2.5	3.4	3.3	3.4	3.8	3.5	4.2	4.8	5.0
K_2O	.13	.20	.25	.47	.40	1.3	.81	1.2	2.1
H_2O-	.77	.12	.10	.12	.04	.08	.09	.05	.25
H_2O+	1.0	.26	.51	.48	.26	.64	.39	.07	.85
TiO_2	.79	1.1	1.1	1.1	.98	1.1	.74	.96	.32
P_2O_5	.13	.30	.34	.35	.39	.40	.32	.37	.10
MnO	.17	.18	.16	.16	.16	.15	.12	.13	.12
CO_2	<.05	<.05	<.05	<.05	<.05	<.05	<.05	.06	<.05
Total	100	99.4	100	100	100	100	100	99.7	99.7
Specific density:									
Powder	2.94	----	2.91	2.88	2.89	2.78	2.78	----	----
Bulk	2.88	----	2.50	2.60	2.63	2.69	2.48	----	----
CIPW norms									
Q			0.1	3.5	2.6	7.9	11.1	11.4	27.2
C									.9
or	0.8	1.2	1.5	2.8	2.4	7.7	4.8	7.1	12.4
ab	21.2	28.8	27.9	28.8	32.2	29.6	35.5	40.6	42.3
an	35.6	31.6	33.8	33.6	31.1	28.7	26.5	21.0	10.4
wo	7.4	8.2	5.9	3.5	4.6	1.3	2.0	1.4	----
en	11.6	11.0	16.2	13.9	13.0	10.5	9.0	6.5	1.0
fs	4.5	5.0	8.0	6.3	8.6	9.0	6.6	6.2	----
fo	8.6	4.7	----	----	----	----	----	----	----
fa	3.7	2.3	----	----	----	----	----	----	----
mt	3.0	3.3	2.9	4.1	2.2	1.5	1.7	2.6	.5
il	1.5	2.1	2.1	2.1	1.9	2.1	1.4	1.8	.6
ap	.3	.7	.8	.8	.9	.9	.8	.9	.2
cc	<.1	<.1	<.1	<.1	<.1	<.1	<.1	.1	<.1
Total	98.3	99.0	99.3	99.5	99.6	99.3	99.5	99.6	98.6
di	14.3	15.9	11.5	6.9	9.1	2.5	4.0	2.9	----
hy	9.2	8.3	18.6	16.9	17.2	18.2	13.7	11.2	1.0
ol	12.3	7.0	----	----	----	----	----	----	----

1. 61ABg734a. Olivine-pigeonitic augite basalt from "Basalt and breccia" unit.
2. 61ABd720. Porphyritic olivine-bearing augite basalt from "Oldest basalt flows" unit.
3. 61ABd725b. Microporphyritic olivine basalt from "Oldest basalt flows" unit.
4. 61ALy566. Microporphyritic augite-olivine basalt from "Oldest basalt flows" unit.
5. 61ALy567a. Porphyritic olivine-bearing pigeonite basaltic andesite from "Basaltic andesite" unit.
6. 61ALy571. Porphyritic hypersthene basaltic(?) andesite from "Andesite" unit.
7. 62ABd446. Porphyritic augite dacite from "Dacite and possible dacite" unit.
8. 61ABd723d. Porphyritic pyroxene dacite from "Dacite flows and associated cinder cones" unit.
9. 62ABd444. Porphyritic augite-bearing quartz latite from "Quartz latite domes" unit.

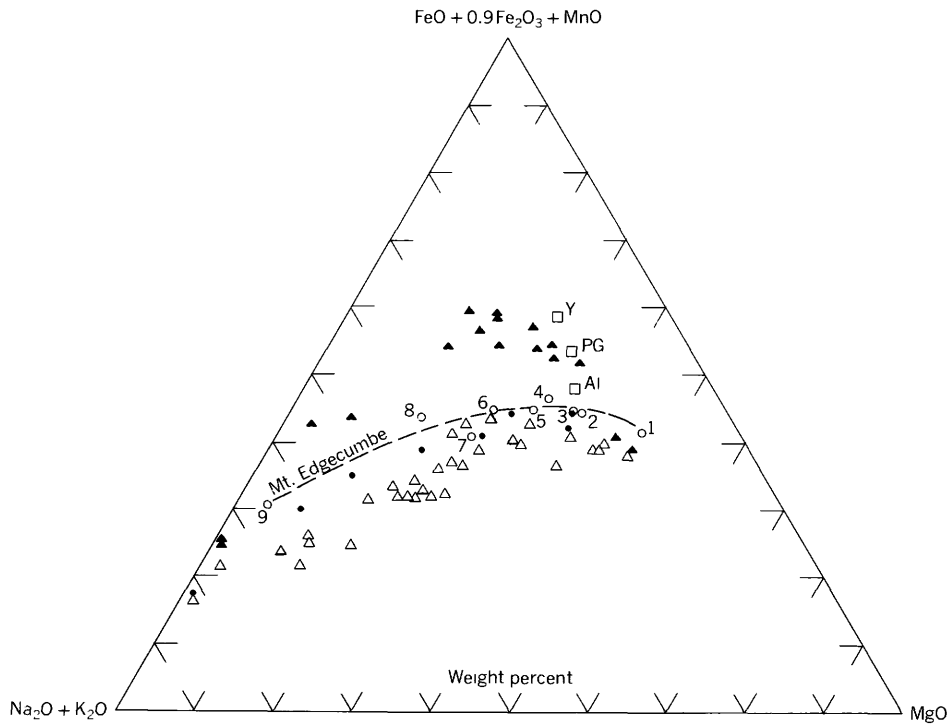

FIGURE 9.—AFM diagram comparing Mount Edgecumbe rocks with selected volcanic rocks from the Pacific coast of North America. Open circles, Mount Edgecumbe (numbers refer to columns of table 2). Closed circles, Mount Jefferson (Greene, 1968). Open triangles, Mount Lassen (Williams, 1932). Closed triangles, aphyric lavas and groundmasses, northeastern Umnak Island, Aleutian Islands, Alaska (Byers, 1961). Open squares, magma types of Waters (1962); Y, Yakima type; PG, Picture Gorge type; Al, high-alumina type from the Oregon Plateaus and Cascade Range.

deduced from the field criteria (fig. 5). The younger rocks are closer to the AF side of the AFM diagram (fig. 9) and richer in silica (fig. 10). The apparent exception is No. 1, the basalt lowest in silica and highest in MgO. If the admittedly tentative stratigraphic assignment is correct (p. D7), this sample was extruded later than the "oldest basalt flows" (samples 2, 3, and 4, table 2).

Many of the analyzed specimens from the Mount Edgecumbe field are porphyritic, and, as Bowen (1956) has emphasized, the composition of a porphyritic rock may or may not represent the composition of a liquid, depending on the gain or loss of crystals during crystallization. Smooth variation on diagrams such as figures 9 and 10 is commonly taken to indicate close approximation of the rocks to liquids. Efforts to correct the Mount Edgecumbe chemical data for phenocryst content, by use of data from table 1, scattered the data points and considerably distorted the simple AFM variation of the uncorrected analyses. We therefore conclude that the porphyritic rocks closely approximate a liquid.

The chemical variation displayed by the Mount Edgecumbe series is similar to that displayed by many

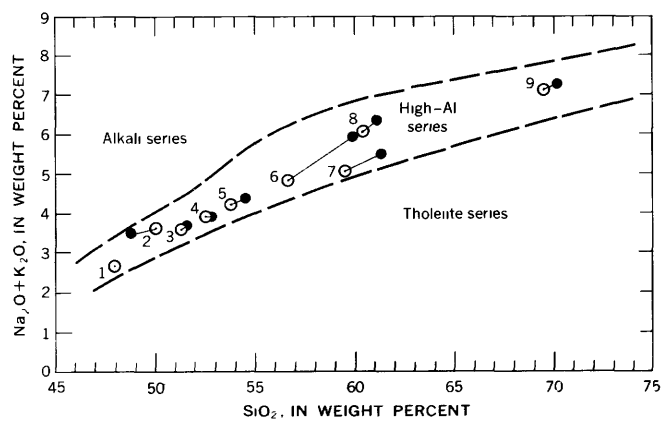

FIGURE 10.—Variation of Na_2O+K_2O with SiO_2 in the Edgecumbe volcanic series. Open circles, Na_2O+K_2O uncorrected for phenocrysts. Closed circles, composition of groundmass as calculated by subtraction of phenocrysts. Dashed lines are boundaries of magma series of Kuno (1965). Numbers refer to columns of table 2.

circum-Pacific volcanic suites (fig. 11). The alkali-lime index of the Mount Edgecumbe series is 60–61, thus falling within the calc-alkalic subdivision of Peacock (1931). This index is lower than that of the calcic High Cascades magma series (61–64), but higher than that

of the calc-alkalic Oregon Plateaus series (55–58; LeMasurier, 1968).

The variation curve of the Mount Edgecumbe series in the AFM diagram shows a relative low iron content that is characteristic of calc-alkaline volcanic series (Nockolds and Allen, 1953) (fig. 9). The data suggest that the various calc-alkaline series plotted in figure 9 differ systematically in Fe/Mg+alk ratio, the Lassen series having the smallest ratio and the Umnak series the largest.

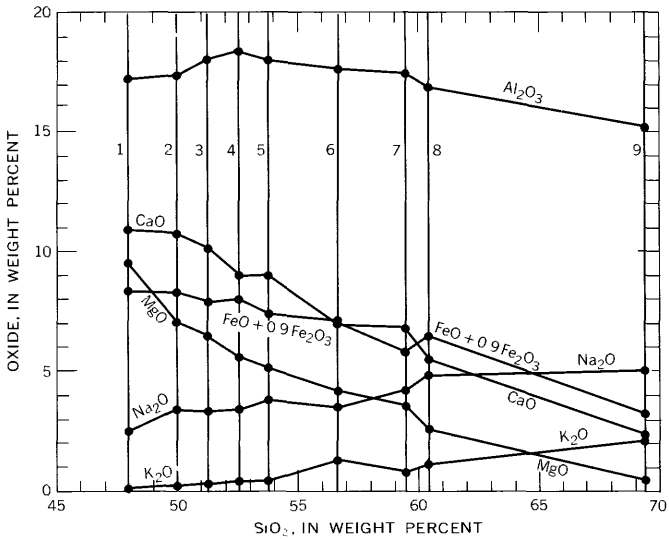

FIGURE 11.—Variation of major oxides with SiO_2 in the Edgecumbe volcanic series. Numbers refer to columns of table 2.

The differences among the series in figure 9 cannot be evaluated simply, for the various series are not comparable as to the manner in which the phenocrysts were treated in the evaluation of the raw analyses. The variation curves for Mount Lassen, Mount Jefferson, and Mount Edgecumbe are probably comparable, because they are for whole rocks, many of which are porphyritic, and have not been corrected for phenocryst content. The Umnak data, on the other hand, are from aphyric lavas or have been corrected for phenocryst content (Byers, 1961). Recalculation of the Mount Edgecumbe data for phenocryst content reduces, but does not eliminate, the difference between the Mount Edgecumbe series and the Umnak series.

Interpretation of the Mount Edgecumbe data in the framework of Kuno (1960, 1965) shows that all the analyses fall within the high-alumina basalt series (fig. 10). Correction for phenocryst content and composition (as above) shifts all the analyses within the high-alumina field. The exception, 61ABd720, is the sample rich in olivine and plagioclase phenocrysts. The basalts of Mount Edgecumbe are also compared in figure 9 with the three basalt types of Waters (1962) from the Columbia Plateau and Cascade Range in Oregon. The Edgecumbe basalts are closer to his high-alumina Cascade basalts than the Yakima and Picture Gorge Basalts of the Columbia Plateau.

The chemical correspondence of the Edgecumbe basalts to high-alumina basalt is compatible with their petrographic characteristics. However, neither the chemical nor the petrographic data indicate definitely whether the Edgecumbe basalts are alkalic basalt or whether they are tholeiite, according to the criteria of Macdonald and Katsura (1964). The "oldest basalt flows" (p. D6–D7) contain sporadic phenocrysts of olivine rimmed by grains of clinopyroxene and magnetite. This apparent reaction relationship, together with the occurrence of at least some subcalcic augite, suggests a tholeiite affinity when one uses the criteria of Macdonald and Katsura. On the other hand, the abundant groundmass olivine suggests an alkalic affinity.

REFERENCES

Becker, G. F., 1898, Reconnaissance of the gold fields of southern Alaska, with some notes on general geology: U.S. Geol. Survey 18th Ann. Rept., pt. 3, p. 1–86.

Berg, H. C., and Hinckley, D. W., 1963, Reconnaissance geology of northern Baranof Island, Alaska: U.S. Geol. Survey Bull. 1141–O, 24 p.

Bowen, N. L., 1956, The evolution of the igneous rocks: New York, Dover Publications, 332 p.

Brew, D. A., Loney, R. A., and Muffler, L. J. P., 1966, Tectonic history of southeastern Alaska: Canadian Inst. Mining and Metallurgy Spec. Vol. 8, p. 149–170.

Brew, D. A., Muffler, L. J. P., and Loney, R. A., 1966, Eruptive history of the Mount Edgecumbe volcanic field, Kruzof Island, southeastern Alaska [abs.]: Alaskan Science Conf., 16th, Juneau, 1965, Proc., p. 115–116.

Byers, F. M., Jr., 1961, Petrology of three volcanic suites, Umnak and Bogoslof Islands, Aleutian Islands, Alaska: Geol. Soc. America Bull., v. 72, no. 1, p. 93–128.

Coats, R. R., 1950, Volcanic activity in the Aleutian Arc: U.S. Geol. Survey Bull. 974–B, p. 35–49.

Cushing, H. P., 1897, Note on hypersthene-andesite from Mount Edgecumbe, Alaska: Am. Geologist, v. 20, no. 3, p. 156–158.

Emmons, R. C., and Gates, R. M., 1948, The use of Becke line colors in refractive index determination: Am. Mineralogist, v. 33, no. 9–10, p. 612–618.

Engel, C. G., and Engel, A. E. J., 1963, Basalts dredged from the northeastern Pacific Ocean: Science, v. 140, no. 3573, p. 1321–1324.

Greene, R. C., 1968, Petrography and petrology of volcanic rocks in the Mount Jefferson area, High Cascade Range, Oregon: U.S. Geol. Survey Bull. 1251–G, 48 p.

Heropoulos, Chris, and Mays, R. E., 1969, Semiquantitative spectrographic analyses of nine specimens from the Mount Edgecumbe volcanic field, Kruzof Island, southeastern Alaska: U.S. Geol. Survey open-file rept, 3 p.

Heusser, C. J., 1960, Late Pleistocene environments of North Pacific, North America: Am. Geog. Soc. Spec. Pub. 35, 308 p.

Hopson, C. A., Cater, F. W., Crowder, D. F., Engels, J. C., and Tabor, R. W., 1967, Anatectic origin of Cascade volcanic rocks, northwestern United States [abs.]: Internat. Union Geology and Geophysics Assoc. Symposium, Seismology and Physics of Earth's Interior, Zurich, Switzerland, Oct. 1967.

Huber, N. K., and Rinehart, C. D., 1966, Some relationships between the refractive index of fused glass beads and the petrologic affinity of volcanic rock suites: Geol. Soc. America Bull., v. 77, no. 1, p. 101–110.

Knopf, Adolph, 1912, The Sitka mining district, Alaska: U.S. Geol. Survey Bull. 504, 32 p.

Kuno, Hisashi, 1960, High-alumina basalt: Jour. Petrology [Oxford], v. 1, p. 121–145.

——— 1965, Fractionation trends of basalt magmas in lava flows: Jour. Petrology [Oxford], v. 6, p. 302–321.

LeMasurier, W. E., 1968, Crystallization behavior of basalt magma, Santa Rosa Range, Nevada: Geol. Soc. America Bull., v. 79, no. 8, p. 949–972.

Libbey, William, Jr., 1886, Some of the geographical features of southeastern Alaska: Am. Geog. Soc. Bull., v. 18, no. 4, p. 279–300.

Little, H. W., 1962, Geological map of British Columbia: Canada Geol. Survey Map 932A, 2nd ed., 1:1,267,200.

Loney, R. A., Berg, H. C., Pomeroy, J. S., and Brew, D. A., 1963, Baranof Island, Alaska: U.S. Geol. Survey Misc. Geol. Inv. Map I-388, scale 1:250,000.

Loney, R. A., Brew, D. A., and Lanphere, M. A., 1967, Post-Paleozoic radiometric ages and their relevance to fault movements, northern southeastern Alaska: Geol. Soc. America Bull., v. 78, no. 4, p. 511–526.

Loney, R. A., Pomeroy, J. S., Brew, D. A., and Muffler, L. J. P., 1964, Reconnaissance geologic map of Baranof and Kruzof Islands, Alaska: U.S. Geol. Survey Misc. Geol. Inv. Map I-411, scale 1:250,000.

Macdonald, G. A., and Katsura, T., 1964, Chemical composition of Hawaiian lavas: Jour. Petrology [Oxford], v. 5, no. 1, p. 82–133.

Nockolds, S. R., 1954, Average chemical compositions of some igneous rocks: Geol. Soc. America Bull., v. 65, no. 10, p. 1007–1032.

Nockholds, S. R., and Allen, R., 1953, The geochemistry of some igneous rock series, pt. 1: Geochim. et Cosmochim. Acta, v. 4, p. 105–142.

Peacock, M. A., 1931, Classification of igneous rock series: Jour. Geology, v. 39, no. 1, p. 54–67.

Peterson, D. W., 1961, Descriptive modal classification of igneous rocks [AGI Data sheet 23]: GeoTimes, v. 5, no. 6, p. 30–36.

Rossman, D. L., 1959, Geology and ore deposits of northwestern Chichagof Island, Alaska: U.S. Geol. Survey Bull. 1058-E, p. 139–216.

Shapiro, Leonard, and Brannock, W. W., 1962, Rapid analysis of silicate, carbonate, and phosphate rocks: U.S. Geol. Survey Bull. 1144-A, p. A1–A56.

Tröger, W. E., 1959, Optische Bestimmung der gesteinsbildenden Minerale, pt. I, Bestimmungstabellen: Stuttgart, E. Schweizerbart'sche Verlagsbuchhandlung, 147 p.

Tsuboi, Seitarô, 1923, A dispersion method of determining plagioclases in cleavage flakes: Mineralog. Mag. [Great Britain] v. 20, p. 108–122.

Waters, A. C., 1962, Basalt magma types and their tectonic association—Pacific Northwest of the United States, *in* The crust of the Pacific Basin: Am. Geophys. Union Geophys. Mon. 6 (NAS-NRC Pub. 1035), p. 158–170.

Williams, Howell, 1932, Geology of the Lassen Volcanic National Park, California: California Univ., Dept. Geol. Sci. Bull., v. 21, no. 8, p. 195–385.

CONCENTRIC STRUCTURE IN ELONGATE PILLOWS, AMADOR COUNTY, CALIFORNIA

By WENDELL A. DUFFIELD, Hawaiian Volcano Observatory, Hawaii National Park, Hawaii

Abstract.—A porphyritic pillow lava crops out in the pre-Cenozoic bedrock complex of the western foothills of the Sierra Nevada, Amador County, Calif. Its form and structures suggest that the pillows are interconnected, and that they formed on a slope when a magma-crystal mixture flowed into and then through them as local rupture of chilled skins gave rise to new pillows. Field evidence that suggests this mode of formation is (1) the pillows are elongate, (2) their long axes are alined, and (3) large tabular phenocrysts are uniformly parallel to pillow walls from skins to cores. Both the concentric structure and calculations which describe flow through a cylindrical conduit argue that the movement of material through the pillows was effectively laminar. This mode of formation for pillows is generally the same as that proposed by J. V. Lewis in 1914 and J. G. Jones in 1968; the concentric structures within pillows add new support for their idea.

Since pillow lavas were first recognized and described, their genesis and significance have become controversial topics, and multiple theories for their origin have evolved (see Lewis, 1914; Zavaritsky, 1960; and Snyder and Fraser, 1963).

This report describes a distinctive pillow lava whose form and structures suggest a specific mode of formation. The interpretation developed is similar to the idea of digital advance of a lava flow as suggested by Lewis (1914) and Jones (1968), and, as Jones (1968, p. 487) pointed out, this model probably has general application to pillow lavas with certain morphologic and structural features.

Acknowledgments.—Norman MacLeod, Howard Wilshire, and Robert V. Sharp reviewed the manuscript and offered useful suggestions for its revision. Robert V. Sharp was also a coworker in the field while gathering data for this study.

GEOLOGIC SETTING

The pillow lava described in this report forms part of the folded and faulted pre-Tertiary bedrock complex of the western foothills of the Sierra Nevada (fig. 1). It is one of the few mappable stratigraphic markers in a steeply dipping section of volcanic rocks which are sandwiched between Paleozoic(?) and Jurassic(?) sedimentary and metasedimentary units. Volcanic rocks below (that is, west of) the pillow lava are primarily breccias of augite porphyry. Those above it are fine- to coarse-grained bedded tuff and breccia, massive augite porphyry, and a digitated tabular body of feldspar porphyry which is similar to the pillow lava in many respects. Although the original mineralogy of these volcanic rocks is generally altered, relict structures and textures and fresh augite phenocrysts suggest that the unaltered rocks were andesitic to basaltic in composition. Knopf (1929, p. 16) analyzed a massive augite porphyry from a locality a few miles south of the pillow lava and reported that it had the composition of a basalt.

DESCRIPTION OF THE PILLOW LAVA

The outcrop pattern of the pillow lava is cigar shaped and trends nearly parallel to the contacts of the larger volcanic unit within which it occurs. The maximum width of outcrop is 850 feet, the average width is about 400 feet, and the length along strike is 3 miles. As the entire volcanic unit forms a steeply dipping homocline, width of outcrop is approximately equal to stratigraphic thickness. The surface upon which the pillows formed now strikes N. 25° W. and dips 70°–80° eastward; flattened and draped bases of the pillows, together with graded beds in the overlying tuffs, show that the section has not been overturned.

Most outcrops on drainage divides are small and are separated by tens to hundreds of feet, and often only part of a single pillow is exposed. Consequently, the nature of the northern and southern terminations is poorly known. For lack of compelling evidence to the contrary, these terminations are assumed to represent the original extremities of the lava rather than later structural or erosional features. The most northerly

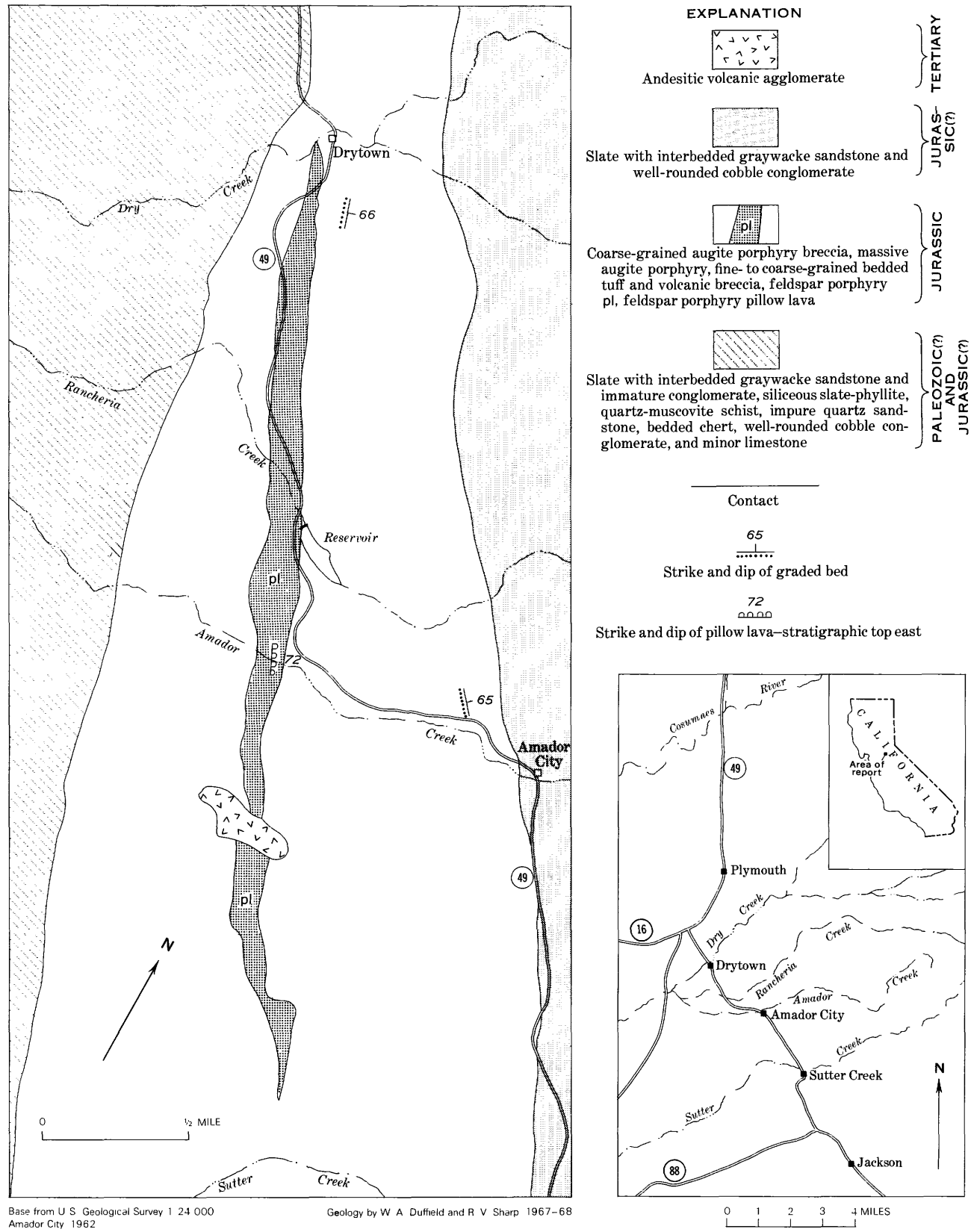

FIGURE 1.—Maps showing the area near State Highway 49 in Amador County, Calif., and generalized geology of the Amador City–Drytown area.

outcrop (in Dry Creek) is more vesicular than other exposures and may well represent the vesiculated edge of the flow. However, the detailed geology in the vicinity of Drytown is quite complex, and a faulted northern termination cannot be ruled out.

Pillow structure is best exposed in Amador and Rancheria Creeks (fig. 1), and is generally seen on gently dipping joint surfaces (fig. 2). Average diameters of the pillows at such outcrops range from 1 foot to 5 feet, but are most commonly 3 feet. The length of the pillows is generally unknown because of the type of exposures available for examination, but a few measurements indicate that some are at least three to four times as long as they are wide. This is a minimum range for the relative elongation.

The long axes of the pillows are parallel. This orientation was determined by general observations at outcrops and by locating the intersection of measured attitudes of pillow skins and tabular phenocrysts which parallel the skins. The lineation so determined plunges 70° in the direction N. 40° E. Before the volcanic section was tilted to its present position, this lineation of pillows probably dipped much less steeply.

The appearance and texture of the pillow lava are distinctive because of the presence of many large feldspar phenocrysts. These crystals are square to slightly rectangular tablets measuring 1 to 1¼ inches wide and 1/16 to 3/16 inch thick. They constitute 10–20 volume percent of an average pillow. On weathered surfaces they usually stand out in relief as euhedral pale-green crystals in a tan matrix, but locally they have weathered away leaving the rock with a pitted surface. On fresh surfaces they form euhedral green outlines in a gray mesostasis. Augite phenocrysts are also common, but they are smaller, less abundant, and much less conspicuous.

In virtually every pillow, the major faces of the feldspar phenocrysts are parallel to the skin. In cross section, this presents a concentric arrangement of crystals about the long axis of a pillow (fig. 3). The degree to which this fabric is developed does not appear to correlate with distance from the skin, for phenocrysts near the core of a pillow are generally as well oriented as those near the skin. Vesicles, typically about 3/32 inch in average diameter, are present in some pillows and are flattened parallel to the fabric of the pheno-

FIGURE 2.—Elongate pillows exposed in cross section on gently dipping joints on the bank of Amador Creek. The average diameter is about 3 feet.

FIGURE 3.—Rock slab showing the concentric arrangement of feldspar phenocrysts in cross section of a pillow. The long axis of the pillow is almost perpendicular to the page, and it passes through the point about which the fabric is concentric. An unusually large complex phenocryst occurs at this point. None of the skin of the pillow is present on this fragment. The circular area of lichen in the lower central part of the slab is about 1 1/16 inches in diameter.

crysts. These vesicles only account for a few percent by volume of a pillow; they are commonly filled with chlorite or carbonate.

The skin of an average pillow is about 1 inch thick and is darker than the interior. Phenocrysts are distributed evenly across both skin and interior. Where present, the vesicles are not in the skin but are more or less evenly distributed in the interior. Rarely, the core of a pillow is filled with quartz or, even more rarely, with a deep-green aphanitic material, but otherwise the nonphenocrystic interior of the pillow appears quite homogeneous.

The original mineralogy can only be inferred from relict textures and approximate bulk compositions of related volcanic rocks in the vicinity. The feldspar phenocrysts are thoroughly altered, and only their original outlines are now visible. In thin section, the areas between feldspar phenocrysts appear to have been occupied by an intergranular mixture of plagioclase laths, roughly equant grains of augite, and perhaps some glass. Except for some of the pyroxene, this material also has been pervasively altered. X-ray diffractometer patterns of both phenocrysts and groundmass show that white mica is the most abundant mineral. Minor amounts of albite, epidote, and chlorite also appear on some of the patterns.

FORMATION OF THE PILLOWS AND THEIR CONCENTRIC STRUCTURE

Any theory of how the pillows formed must account for (1) the parallel arrangement of the long axes of the pillows, and (2) the preferred orientation of the feldspar tablets. The first feature seems best explained by digital advance of a lava flow down a slope. This mode of formation requires that pillows be interconnected; for at a set of limiting conditions, likely determined by the rigidity of the skin, the viscosity of the magma, and the rate at which new magma is introduced, a growing pillow ruptures locally and gives birth to a new pillow.

The distinctive alinement of tabular phenocrysts suggests that there was laminar flow of a crystal-magma mixture through elongate pillows with a velocity which decreased toward the skin. This type of flow is thought to orient the major faces of tabular particles parallel to the flow laminae (Mackin, 1947, p. 27) or, in this situation, to the pillow skins. Ideally, the crystals come to rest in a zone that progressively migrates inward as a pillow cools and solidifies so that the degree of orientation is equally well developed throughout.

This orienting mechanism for flow through a cylindrical tube is shown graphically in figure 4. If flow is

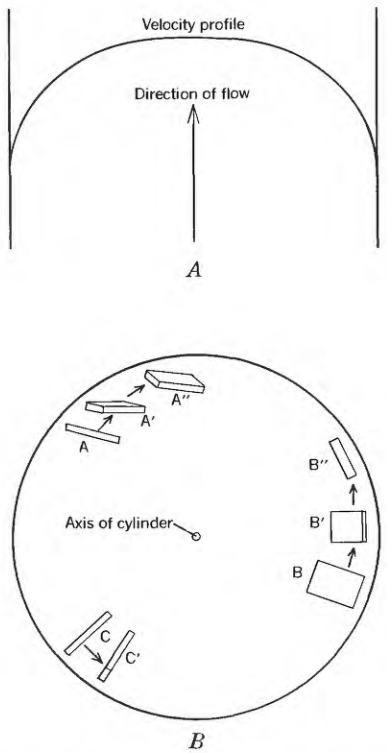

FIGURE 4.—Ideal laminar, velocity-gradient flow through a cylinder and how it rotates tabular particles. *A*, Generalized velocity profile across a cylinder. *B*, Flow is perpendicular to the page and away from the reader. The three particles will rotate about axes which lie in the plane of the page and are tangential to equal-velocity surfaces. Particles *A* and *B* will move through positions *A'* and *B'* to *A''* and *B''*, and so on during flow, as their major faces approach parallelism to surfaces of equal velocity. The major faces of particle *C* will remain perpendicular to equal-velocity surfaces while the crystal rotates about an axis which is at right angles to these faces.

effectively laminar, then surfaces of equal velocity form a set of nested cylinders, coaxial with the circular tube. Tabular crystals which extend across the velocity gradient are rotated toward a position of stability (that is, with major faces tangential to the surfaces of equal velocity). However, crystals whose major faces parallel planes which contain the axis and a radius of the cylinder are not rotated toward this position. Such a crystal may turn on an axis which is perpendicular to its major faces, but theoretically this is its only possible rotation.

This special case need not detract from the general model if the initial orientation of crystals is random. Also, in actual laminar flow of lava through an elongate pillow, surfaces of equal velocity would probably be irregular enough (perhaps through departures of the pillow from a truly cylindrical shape and the presence

of relatively small scale turbulence) to "catch up" these crystals and start them rotating toward a preferred position. A similar effect might be caused by variations in the shapes of the crystals.

Test for laminar flow

If flow through the pillows was turbulent, the preferred orientation of phenocrysts remains unexplained and the model is invalid. Intuitively, the preferred orientation itself is strong evidence for laminar flow, but with the data now available on viscosities of basaltic and andesitic melts (see Clark, 1966; and Shaw and others, 1968), an independent test for laminar flow may be made by determining the probable Reynolds number for basaltic magma flowing through elongate pillows. To compute the Reynolds number, several simplifying assumptions must be made. The calculations are based on flow through a pillow with only a thin solid rind. The effect of crystallization on the radius of the pillow and consequently on the predicted type of flow can be assessed by assuming progressively smaller radii, and it is easy to show that the maximum radius provides the critical limiting condition.An equation for the streamlined flow of an incompressible fluid through a circular pipe is used. This equation is the Hagen-Poiseuille law (see McAdams, 1954, p. 148; and Shaw, 1965, p. 137–138):

$$Q=\frac{\pi P a^4}{8\eta l} \tag{1}$$

where Q is the volume rate of flow for a fluid of viscosity η through a cylinder with radius a and length l, and P is the pressure gradient which drives the flow.

The elongate pillows are good approximations of cylinders, and the magma-crystal mixture must have been nearly incompressible, although vesicles suggest that a minor amount of exsolved vapor phase was present during flow in some pillows. The pressure gradient, P, is attributed entirely to the effect of gravity on the vertical distance between the "top" and "bottom" ends of a pillow. This provides the minimum pressure gradient, to which a force of extrusion might add. However, if extrusion were very forceful, pillows would tend to brecciate or perhaps never form.

The Reynolds number, R_e, is related to the Hagen-Poiseuille expression through

$$R_e=\frac{2pQ}{\pi a\eta}, \tag{2}$$

where p is the density of the fluid, and the other parameters have their usual meanings. Combining equations 1 and 2:

$$R_e=\frac{pPa^3}{4\eta^2 l}. \tag{3}$$

The critical Reynolds number for circular pipes has been determined experimentally and is about 2×10^3 (see McAdams, 1954, table 6–2). Thus laminar flow should obtain for all values of R_e less than 2×10^3.

For the pillows being considered here, equation 3 may be rewritten as

$$R_e\approx K\frac{P}{\eta^2 l}, \tag{4}$$

where K is a constant. The density of the fluid (basaltic to andesitic magma), making a very generous allowance for uncertainty, should be between 2.0 and 3.0 grams per cubic centimeter; and the radius, a, of a pillow is fixed at about 50 centimeters by field data. Thus, to the nearest order of magnitude, K is 10^5.

The limiting condition for laminar flow may now be tested by substituting 2×10^3 for R_e and 10^5 for K in equation 4. The expression reduces to

$$\eta^2\approx 50\frac{P}{l},$$

and since $P=lp \sin\theta$, where θ is the angle of the pipe (elongate pillow) with the horizontal, the final expression is

$$\eta^2\approx 100 \sin\theta. \tag{5}$$

Discussion

Figure 5 shows the relationship of equation 5 graphically. All values of $\sin\theta$ and η on the convex side of the curve are in the field of laminar flow. If the calculations are valid for the pillow lava, then turbulent flow would have been possible only if the viscosity of the magma had been 10 poises or less—a very unlikely condition for andesitic to basaltic lava somewhat below its liquidus temperature. Most reported viscosities for andesitic and basaltic melts range from 10^3 to 10^5 poises (see Macdonald, 1963; Clark, 1966; Shaw and others, 1968); Shaw and others (1968, p. 263), however, reported a viscosity of 400 poises for an Hawaiian tholeiitic lava at its liquidus (1,200°C) and 100 poises at 1,300°C. But even these relatively low values do not violate the calculated criteria for laminar flow.

The Hagen-Poiseuille equation assumes flow of an incompressible Newtonian fluid through a smooth-walled pipe at constant temperature; probably none of these conditions was entirely satisfied as the pillow lava formed—especially the condition of constant temperature. For while magma flowed through a pillow, there must have been a temperature gradient in cross section and a steady decrease in absolute temperature throughout. This situation would have caused a similar viscosity gradient and an increase in viscosity through time. Intuitively, such departures from the ideal conditions for the calculations should not destroy a laminar, velocity-gradient flow regime. They might actually

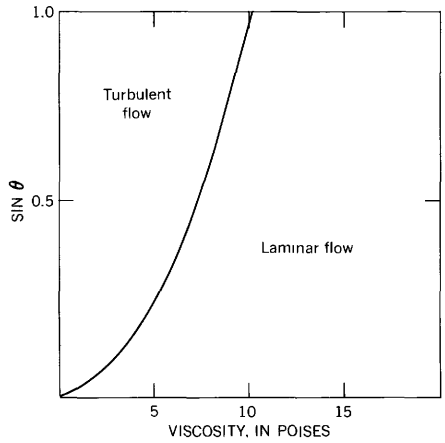

FIGURE 5.—Graph of $\eta^2 = 100 \sin \theta$. This expresses the boundary between laminar and turbulent flow through a pipe under the conditions described in the text. The area on the convex side of the curve is the field of laminar flow. η and θ are defined in text.

facilitate formation of flow structures by steepening the velocity gradient over that of an isothermal environment.

There are many other problem in connection with the analysis of flow through the pillows. For instance, the effect of water in a submarine eruption was purposely ignored in the calculations; for even though field evidence (such as associated marine fossils and graded beds) suggests a submarine environment, it is not conclusive. Pillow forms may also develop from subaerial flows (see Jones, 1968, pl. 5). But with other conditions being unchanged, the correction for an eruption in water would increase the size of the field of laminar flow, and therefore would not change the implications of figure 5. At best, the calculations provide only a first approximation to the flow regime for the pillow lava. Nevertheless the relatively low limiting value of viscosity on the large field of laminar flow suggests that turbulent flow would only have resulted from rather exceptional conditions (such as superheated melt), and the geological evidence argues aginst such an unusual situation.

Other considerations

The digital advance mode of formation assumes feeder necks between pillows, yet the pillows of this report show no interconnections. Like the elusive "ends" of pillows, this may well simply result from the type and limited amount of outcrop available for study. However, if pillows never were joined, then at least two other possibilities must be considered:

(1) Discrete pillow-sized bodies of lava were forcibly erupted through water (or air).

(2) Discrete pillow-sized bodies of lava were erupted less violently and collected at the base of a slope.

With the former type of eruption, even if pillows were originally elongate (an unlikely circumstance), it is difficult to imagine how they would settle in a preferred orientation rather than as a completely disordered mass. With the latter type of eruption, elongate pillows might indeed collect with their longest axes perpendicular to the direction of slope. And even if the original bodies were spherical, such spheres might deform into elongate shapes as they roll down a slope—if they do not first become too rigid.

But neither of these hypothetical types of eruptions provides a good explanation for the concentric structures within pillows. Some investigators (Reid and Dewey, 1908, p. 267; Lewis, 1914, p. 647) have suggested that similar structures in other pillow lavas were formed through ballooning—either by the exsolution of a vapor phase from the melt or by the continued introduction of lava into the yet unruptured pillows. As vesicles are volumetrically minor for the pillows under examination here, inflation by a vapor phase could not have been important; and ballooning through continued introduction of lava cannot account for the fabric throughout each pillow. A rolling-kneading motion might produce a fabric parallel to the skins of pillows. However for our purposes, virtually every pillow would have had to roll or flatten enough to orient the phenocrysts and to orient them equally as well at the core as at the skin of the pillow.

It is also noteworthy that despite the proposed flow of a magma-crystal mixture through elongate pillows, there is no apparent concentration of crystals toward the axes of the pillows, such as might be expected from the experiments of Bhattacharji and Smith (1964) and Bhattacharji (1967). This is perhaps due to the relatively rapid cooling and crystallization that the pillows must have experienced. This suggestion may be borne out if future work shows that an axial concentration of phenocrysts, which is thought to result from a migration toward areas of relatively high flow velocity, is found only in environments where cooling and crystallization were slow compared to movement of material through its geological conduit. It might also be that flow through any one pillow or set of connected pillows was not sustained long enough for axial migration to occur. But for the present, the apparent contradiction remains unexplained.

CONCLUSIONS

I conclude that elongate pillows formed on a slope and were fed by and served as feeders for other pillows. The length of individual pillows is unknown. Intra-

pillow structures suggest that flow was laminar; and subject to many recognized limitations, the calculations describing flow through a cylinder also support this suggestion. I agree with Jones's conclusion (1968, p. 487) regarding the importance and meaning of the form and fabric displayed in pillow lavas, and I further propose that structures within individual pillows may well provide information as important as interpillow relationships.

REFERENCES

Bhattacharji, Somdev, 1967, Mechanics of flow differentiation in ultramafic and mafic sills: Jour. Geology, v. 75, no. 1, p. 101–112.

Bhattacharji, Somdev, and Smith, C. H., 1964, Flowage differentiation: Science, v. 145, no. 3628, p. 150–153.

Clark, S. P., Jr., 1966, Viscosity, *in* Clark, S. J., Jr., ed., Handbook of physical constants: Geol. Soc. America Mem. 97, p. 291–300.

Jones, J. G., 1968, Pillow lava and pahoehoe: Jour. Geology, v. 76, no. 4, p. 485–488.

Knopf, Adolph, 1929, The Mother Lode system of California: U.S. Geol. Survey Prof. Paper 157, 88 p.

Lewis, J. V., 1914, Origin of pillow lavas: Geol. Soc. America Bull., v. 25, p. 591–654.

Macdonald, G. A., 1963, Physical properties of erupting Hawaiian magmas: Geol. Soc. America Bull., v. 74, no. 8, p. 1071–1077.

Mackin, J. H., 1947, Some structural features of the intrusions in the Iron Springs district [Utah]: Utah Geol. Soc. Guidebook, no. 2, 62 p.

McAdams, W. H., 1954, Heat transmission: New York, McGraw-Hill Book Co., Inc., 532 p.

Reid, Clement, and Dewey, Henry, 1908, The origin of the pillow-lava near Port Isaac in Cornwall: Geol. Soc. London Quart. Jour., v. 64, p. 264–272.

Shaw, H. R., 1965, Comments on viscosity, crystal settling, and convection in granitic magmas: Am. Jour. Sci., v. 263, no. 2, p. 120–152.

Shaw, H. R., Peck, D. L., Wright, T. L., and Okamura, R. T., 1968, The viscosity of basaltic magma—An analysis of field measurements in Makaopuhi lava lake, Hawaii: Am. Jour. Sci., v. 266, no. 4, p. 225–264.

Snyder, G. L., and Fraser, G. D., 1963, Pillowed lavas, 2—A review of selected recent literature: U.S. Geol. Survey Prof. Paper 454–C, 7 p.

Zavaritsky, V. A., 1960, The spilite-keratophyre formation in the region of the Blyava deposit in the Ural Mountains: Internat. Geology Rev., v. 2, no. 7, p. 551–576.

AIRFALL ASH AND PUMICE LAPILLI DEPOSITS FROM CENTRAL PUMICE CONE, NEWBERRY CALDERA, OREGON

By MICHAEL W. HIGGINS, Beltsville, Md.

Abstract.—There are two airfall ash and pumice lapilli deposits from Central Pumice Cone, Newberry Caldera, Oreg. The older deposit is poorly exposed, and its extent is unclear. The younger deposit is more distinctive, widespread, and valuable for relative dating. It can be divided into (1) a main pumice fall, consisting chiefly of ungraded pumice lapilli, that extends 20–40 miles from the caldera; and (2) an overlying unit of as many as five graded ash falls, consisting of pumice and lithic fragments, confined to within about 3 miles of the caldera. Wood beneath the main pumice fall has a carbon-14 age of 1,720±250 years. China Hat and East Butte, east of the volcano and once thought to be cones, are actually domes of pre-Mazama age and did not contribute material to the younger deposits from Newberry Volcano. What Wilcox considered pumice from a China Hat vent is part of the main pumice fall of the younger deposit.

Mount Newberry is a large shield volcano which rises from the basalt plateaus of central Oregon about 40 miles (64 kilometers) east of the Cascade crest and just south of Bend (fig. 1). At the summit of the shield is Newberry Caldera[1], a large, complex, nested caldera with two large lakes and numerous small cones and other eruptive features on its floor (Higgins and Waters, 1967). Central Pumice Cone (fig. 2) is one of the most conspicuous of these features. It occupies approximately the center of the caldera and rises more than 700 feet (214 meters) from a strip of land separating the lakes. Ash and pumice erupted from Central Pumice Cone form deposits that cover the eastern part of the caldera, the eastern and southeastern parts of the shield, and large areas east and southeast of Newberry Volcano (Walker, 1951; Walker and others, 1967; Williams, 1942). One of these deposits is an easily recognizable datum plane that should be valuable for relative dating of geologic features and archaeological sites. However, its physical characteristics are not well known and its precise age has only recently been determined. Moreover, there has been confusion regarding the source of this ash and pumice blanket.

This blanket deposit is the second or younger of two known unwelded airfall ash and pumice lapilli deposits from Newberry volcano, here informally called Newberry ash deposit No. 1 and Newberry ash and pumice deposit No. 2. Deposit No. 2 is thicker and areally more extensive than the first, and is relatively undissected. Therefore, there are relatively few exposures of the older or first deposit, its shape and extent are unclear,

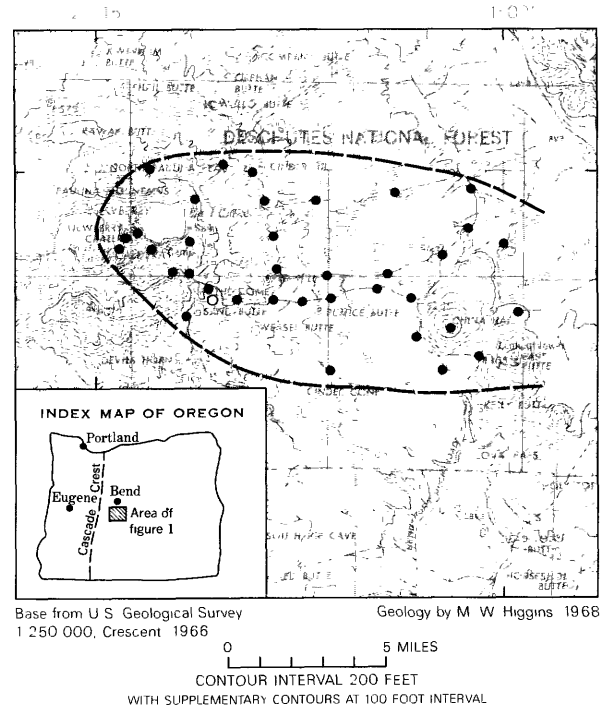

FIGURE 1.—Index map showing part of the Newberry shield volcano and geographic features mentioned in the text. The dashed line represents the 2-inch (5 cm) isopach of Newberry ash and pumice deposit No. 2. Dots show sample and measurement localities. Open circle shows the locality of the carbon-14 sample.

[1] The official geographic name of this caldera is Newberry Crater. However, it was named at a time when no distinction was made between craters and calderas (Russell, 1905). Since it is undoubtedly a caldera and not a crater, according to present usage of these terms (see Williams, 1941), it will be referred to in this paper as Newberry Caldera.

FIGURE 2.—Oblique aerial photograph of the central part of Newberry Caldera, looking south-southeast. Central Pumice Cone, CP, is in the center of the view. It is symmetrical, especially in an east-west (left-right) direction and rises more than 700 feet (214 m) above East Lake. The Dome, D, a basaltic cinder cone covered by pumice of Newberry ash and pumice deposit No. 2, is seen at the upper left. (Oregon Dept. Geology and Mineral Industries photograph.)

and its value as a datum plane is low. This paper gives only a limited description of the first deposit. The main purposes of the paper are to: (1) describe the younger deposit, Newberry ash and pumice deposit No. 2, and define its physical characteristics; (2) show how it varies with distance from the source; (3) delimit its source; (4) give its age; (5) attempt to reconstruct the manner of eruption; and (6) make inferences about the weather at the time of eruption and deposition. It is hoped that, besides adding to the growing knowledge of characteristics of airfall deposits in general, the information will enable geologists, paleontologists, and archaeologists to make more precise use of the second deposit as a datum plane.

The age of Newberry ash and pumice deposit No. 2 is 1,720±250 years (carbon-14 dating). The deposit can be used as a datum plane which, in conjunction with the Mazama ash of Powers and Wilcox (1964, p. 1335) (about 6,600 years in age), forms a valuable tool for relative-age dating of recent volcanic, tectonic, paleontologic, and archaeologic features.

Acknowledgments.—A. C. Waters supervised the dissertation from which this paper is, in large part, adapted, spent several days of each field season with me, and was always available for discussions throughout the 2½ years of the study. He was also chiefly responsible for my obtaining the research grant and fellowship which financed a large part of the study. Without his help, suggestions, and continued encouragement this study would have been impossible.

Field expenses for 1966 were provided by a research grant from the University of California, Santa Barbara. During the 1967 field season I was supported by the U.S. Geological Survey. Financial support for laboratory work was provided by a National Aeronautics and Space Administration traineeship.

I also wish to thank Mr. and Mrs. Rod Davis and Mr. and Mrs. Gus Larkin, of Portland, Oreg., who generously loaned their camp and equipment for the summer of 1966; Mr. Larry Lermo, of Bend, Oreg., who flew me over the caldera and shield without charge; and Mr. and Mrs. M. G. Apel, of Bend, Oreg., who provided me with room and meals, boats, equipment, and information during the summer of 1967.

G. W. Walker, C. D. Rinehart, and R. E. Wilcox read and greatly improved the manuscript.

NEWBERRY ASH DEPOSIT NO. 1

Newberry ash deposit No. 1 is found in Newberry Caldera and as far east of the caldera as the base of China Hat (fig. 1). In the caldera it is a crudely graded deposit 3–7 feet (1–2 m) thick. Near the base of China Hat, about 8 miles (13 km) from the caldera, it is up to 4 feet (1.2 m) thick where locally concentrated by wind or water but is exposed only in a few deep roadcuts.

In the caldera, 85–95 percent of this deposit consists of pieces of white to buff pumice ranging in size from about 0.2 millimeter to about 1.5 mm; most of the pumice fragments are very close to 1 mm. Tiny lithic fragments and broken crystals of feldspar (same size range as the pumice fragments) make up most of the remaining 5–15 percent of the deposit. The deposit is well sorted in its upper parts and would appear ungraded except for a zone about 1 foot (30.5 centimeters) thick near the base, in which lithic fragments are concentrated. Most of these fragments are gray to black obsidian, but some are platy rhyolite and basalt. The fragments in the basal zone are as large as 3 cm in diameter, but average about 1–2 cm.

Near China Hat the pumice is about the same size as in the caldera exposures, but there is less crystalline material and most of the crystals present are less than 0.5 mm in size. Moreover, lithic fragments larger than 0.4 mm are rare and the deposit appears ungraded. Locally a thin soil horizon is present at the top of ash deposit No. 1 and beneath deposit No. 2 (fig. 3), apparently indicating a relatively long time span between the two deposits.

The No. 1 ash deposit is absent from the western, southern, and northern parts of the volcano and from the western part of the caldera. Its precise source is unknown, but from what can be seen of its distribution, it most likely came from Central Pumice Cone.

359-403 O—69——3

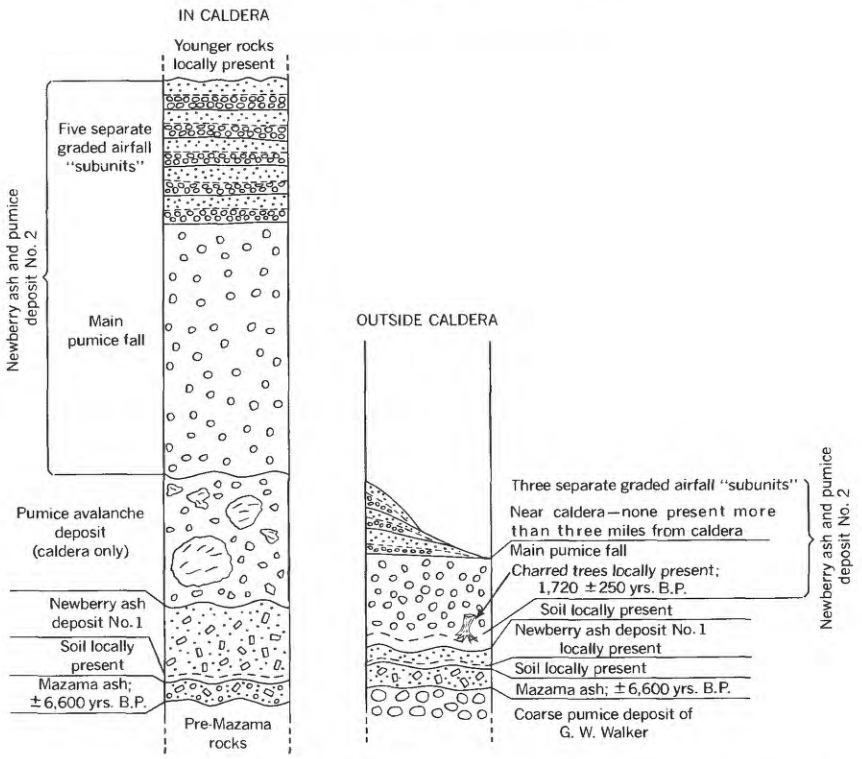

FIGURE 3.—Stratigraphic relations of the Newberry ash and pumice deposits and other deposits within and outside the Newberry Caldera.

NEWBERRY ASH AND PUMICE DEPOSIT NO. 2

Newberry ash and pumice deposit No. 2 is composed of a sequence of related pumice fall and pumice- and ash-fall deposits and could be called a multiple fall unit (Healy and others, 1964; Nakamura, 1960). The characteristics of the deposit suggest that it was erupted rapidly in a strong and constant west-northwest wind. The sequence or unit is divisible into two main parts: an early, thick, ungraded pumice fall and a younger composite layer composed of as many as five separate well-graded pumice ash falls (fig. 3). The upper five graded ash-fall layers were probably erupted during waning, intermittent eruptive activity. The thick pumice fall will hereafter be referred to as the main pumice fall. Wilcox (1965, p. 810, fig. 2) referred to this pumice as "Newberry pumice." All the material came from Central Pumice Cone.

The main pumice fall extends as an elliptical blanket for at least 20 miles (32 km) to the east of Newberry Caldera and is present in water-wind concentrated deposits as far as 35–40 miles (56–64 km) from the caldera (Peterson, 1965, p. 28; Walker and others, 1967; Walker, 1951). At its thickest point, on the southeast wall of the caldera, this blanket of pumice is 18–20 feet (5.5–6.1 m). It thins to about 1 foot (30.5 cm) east of China Hat (fig. 4). The deposit is remarkably restricted in lateral extent.

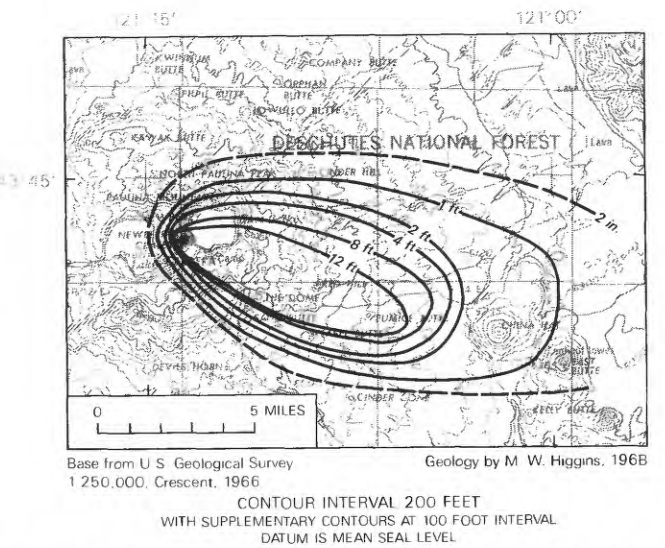

FIGURE 4.—Reconnaissance isopach map showing the thickness and distribution of Newberry ash and pumice deposit No. 2. The dot marks the vent in Central Pumice Cone.

The main pumice fall is composed of fragments ranging in size from about 1 mm to about 7 cm; the majority are in the 2–4 cm range. Size of the pumice

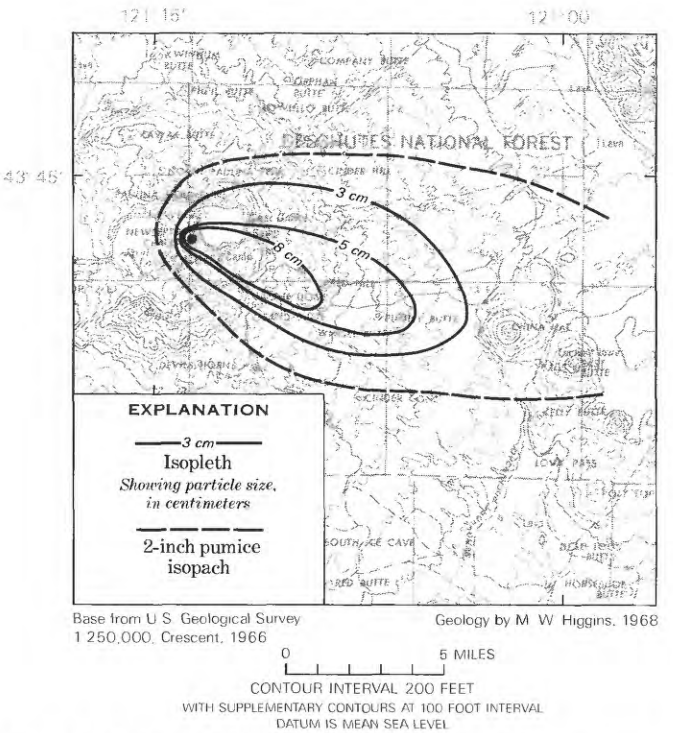

FIGURE 5.—Reconnaissance isopleth map showing maximum extent of selected pumice particle sizes for the main pumice fall of Newberry ash and pumice deposit No. 2.

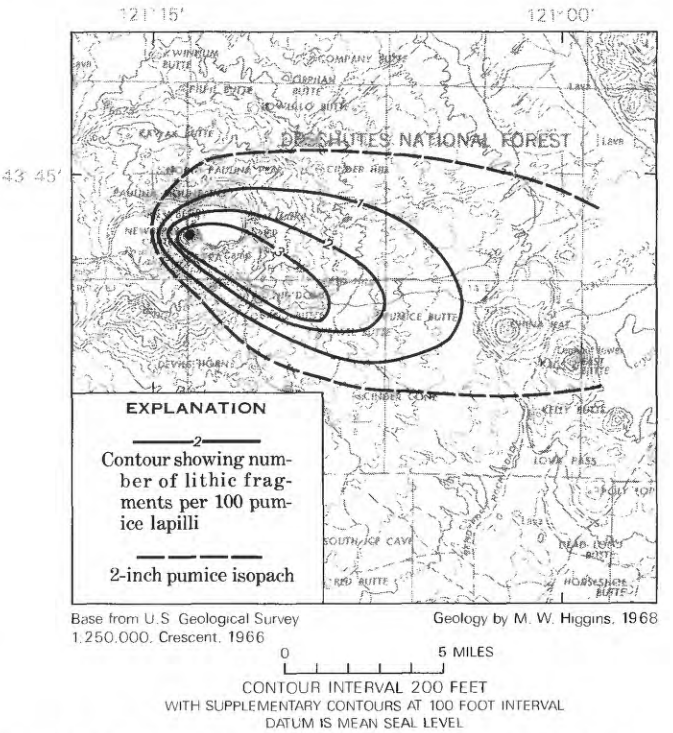

FIGURE 6.—Reconnaissance map showing number of lithic fragments per 100 pumice lapilli in the main pumice fall of Newberry ash and pumice deposit No. 2.

fragments decreases with distance from the source (fig. 5). Lithic fragments are relatively abundant close to the source (approximately 1–3 percent by volume) but decrease in abundance with distance from the source and are very rare in peripheral areas (fig. 6). The majority of the lithic fragments are chips of black and gray obsidian that are generally pumiceous, but some fragments of platy rhyolites, andesites, and basalt are locally present. The size of the lithic fragments is, in general, about half that of the pumice, but they are about equal in weight.

The main pumice-fall deposit contains crystals and crystal fragments of plagioclase, clinopyroxene, orthopyroxene, and basaltic hornblende, but such crystals are rare and are absent in many outcrops. Table 1 gives data on these minerals.

Above the main pumice fall in the caldera are as many as five separate airfall "subunits" (fig. 3). Each of these is 3–10 inches (7.6–25.4 cm) thick and is composed of a lower part consisting of angular and subangular pumice lapilli and a minor amount of interstitial ash-size particles, and an upper part consisting of medium to very fine ash-size particles. In addition, the lower part generally is relatively rich (up to 10 percent by volume) in lithic fragments, chiefly obsidian chips about one-half or one-third the size of, but about the same weight as, the pumice lapilli. By contrast, the upper part of each fall is largely free of lithic fragments. The boundary between upper and lower parts of each fall is sharp.

Five of these airfall subunits are present in the caldera near the source, but away from the source the number decreases. Only three subunits are present near the top of the southeast wall of the caldera; two are present about 1 mile (1.6 km) southeast of the rim; and only one is present about 2 miles (3.2 km) from the rim. About 3 miles (4.8 km) southeast of the caldera rim the airfall subunits are absent. Thickness of these subunits also decreases away from the source. About 1½ miles (2.4 km) from the rim, the two subunits present are each only about 2–4 inches (5–10 cm) thick. The size of fragments in the lower parts of the subunits also decreases away from the source.

Index of refraction

Wilcox (1965, p. 810, fig. 2, column 4) determined the refractive index of pumice from the Newberry pumice fall to have a range of about 1.492 to about 1.499, with the most "prominent index" about 1.494 to about 1.498. In the present study, similar refractive-index data were obtained from 24 samples of pumice and 5 obsidian chips from Newberry ash and pumice deposit No. 2 (table 2). The pumice index measurements were made on "fresh" glass from centers of

TABLE 1.—*Data on minerals from the main pumice fall of Newberry ash and pumice deposit No. 2, Newberry Volcano area, Oregon*

[Refractive index and 2*V* determined on the universal stage]

Mineral	Size (mm)	Refractive index	2*V*	Composition		Number of measurements
				Universal stage (max extinction angle)	Reference source	
Plagioclase	0.05–0.7	(n_x) 1.544–1.547±0.001		An_{30-37}	An_{31-37}[1]	37
Clinopyroxene	0.02–0.5	(n_y) 1.689±0.002	(z) 55–56		Salite or high-lime augite.[2]	6
Orthopyroxene	0.1	(n_y) 1.689–1.699±0.001	(x) 56–58		Ferrohypersthene En_{32-37}.[2]	5
Basaltic hornblende (very rare)	1	(n_z) 1.670±0.003				1

[1] Slemmons (1962, pl. 12).
[2] Deer, Howie, and Zussman (1963).

TABLE 2.—*Refractive index* (n) *of pumice and obsidian from the main pumice fall of Newberry ash and pumice deposit No. 2, Newberry Volcano area, Oregon*

[Indices: range 1.490–1.502; most common 1.494–1.497; all ±0.001]

Pumice						Obsidian	
No.	*n*	No.	*n*	No.	*n*	No.	*n*
1	1.495	9	1.494	17	1.494	25	1.500
2	1.494	10	1.490	18	1.502	26	1.499
3	1.498	11	1.493	19	1.500	27	1.498
4	1.496	12	1.496	19	1.499	28	1.502
5	1.499	13	1.491	21	1.495	29	1.501
6	1.495	14	1.501	22	2.497		
7	1.495	15	1.496	23	1.499		
8	1.497	16	1.493	24	1.494		

lapilli. On the curves of Huber and Rinehart (1966), my data would correspond to silica percentages of about 70–74 percent.

Conditions of eruption and deposition

The overall distribution of ash-fall material (fig. 4), the size distribution of pumice fragments (fig. 5), and the distribution of lithic fragments (fig. 6) indicate that a strong west-northwest wind prevailed during the eruptive episode that resulted in Newberry ash and pumice deposit No. 2. Prevailing winds at the present time are also from west-northwest; commonly they rise, or the wind velocity increases, between about 6:00 a.m. and 9:00 a.m. and abate by about 9:00 p.m. On the assumption that wind conditions have not changed appreciably since Newberry ash and pumice deposit No. 2 was erupted, the ash fall, or at least the main pumice-fall part, would appear to have been erupted during a period of only 12 to 15 hours. The ungraded nature of the main pumice fall may also indicate rapid eruption. The relative paucity of fines and the fair degree of sorting are supporting evidence of strong winds. An alternative interpretation for the pattern of distribution is a directed eruption. If the blast of pumice had been directed at a low angle, it would have piled up against the wall of the caldera, creating thick near-vent accumulations of hot pumice highly susceptible to welding or sintering. However, no such welded or sintered tuff has been recognized. There is a welded tuff in the wall sequence of Newberry Caldera, but it is at least 6,600 years old (Higgins and Waters, 1968) and it predates the creation of the caldera. A low-angle directed blast would also probably preclude deposition of ash far from the caldera rim. Moreover, Central Pumice Cone, from which Newberry ash and pumice deposit No. 2 was erupted, is nearly symmetrical, particularly on the eastern and western sides in line with the principal axis of the elliptical eruptive blanket (figs. 2, 4). A symmetrical cone is indicative of near-vertical eruption rather than a low-angle directed blast.

The only hypothesis befitting the observed characteristics of the deposit and the symmetry of Central Pumice Cone is that the pumice now making up the main pumice-fall sheet was blown nearly straight up from the vent, but that not far above the vent this ascending stream was bent east-southeastward by strong and constant west-northwest wind; the finer particles were blown for great distances from the volcano, but the very rapidly erupting, copious lapilli began to fall almost as soon as they were away from the vent, the larger and heavier particles falling first, and formed the main pumice-fall part of the deposit.

Whether the graded upper "sub-unit" sequence represents waning wind, waning energy of eruption, or intermittent activity cannot be definitely determined. But if wind velocity had decreased, ash beds should be present at least a short distance west of Central Pumice Cone; they are not. Probably a combination of waning and more widely spaced eruptive activity best fits the characteristics observed as well as the known patterns of activity at other volcanoes. After the large volume of pumice of the main pumice fall had

been ejected, eruptive activity probably slowed, lost energy, and became intermittent.

Age and importance

Locally the main pumice fall buried small trees. A carbon-14 age of 1,720±250 years (Lab. No. W–2168, Field No. CH-C, U.S. Geol. Survey) was determined by Meyer Rubin, of the U.S. Geological Survey, for some of the charred wood collected from a deep cut near The Dome (fig. 1).

In addition to its value as a wind strength and direction indicator, the ash and pumice deposit is important as a means of dating geologic features in the area. Any of the features covered by the deposit must be older than about 1,700 years, and, conversely, any not covered (where it can be shown that the ash was never present) must be younger than about 1,700 years. When considered in conjunction with the Mazama ash (age about 6,600 years; see Wilcox, 1965), this datum plane can be used effectively to relatively date the numerous volcanic and tectonic features in the area of the deposit.

Source

Field relations, shape, and characteristics of the deposit (figs. 3, 4, and 5) show that the source must have been Central Pumice Cone. Moreover, the refractive index of pumice on Central Pumice Cone matches that of the deposit. Nevertheless, there has been much confusion regarding the source of the ash and pumice blanket.

Williams (1935, p. 273) wrote:

> In general, the cover of pumice is thickest on the southeastern slope of the volcano. One cause may be that the prevalent winds at the time of explosion were from the northwest. Equally important, however is the fact that *there were other sources of pumice than those within the caldera;* viz., *China Hat and East Butte, two large cones,* a short distance from the east base of the volcano. [italics mine]

At the time Williams wrote (1935) he had not made his classic study of the Crater Lake Caldera (1942) and must not have recognized the Mazama ash. Both China Hat and East Butte (fig. 1) are rhyolite domes, not cones, and neither shows any evidence of late pyroclastic eruptions.[2] More important, both China Hat and East Butte are covered by Mazama ash and by the main pumice fall of Newberry ash and pumice deposit No. 2, and therefore there is no possibility that they contributed pyroclastic material to the pumice fall from Newberry.

In his paper "Volcanic-ash Chronology," Wilcox (1965, p. 810, fig. 2, column 5) listed the characteristics of a pumice deposit at China Hat and inferred (p. 810, fig. 2 and p. 808, fig. 1) it to be from a separate China Hat vent. He determined the range of refractive index for this pumice to be from about 1.498 to about 1.502, with the "prominent index" at about 1.493 to about 1.498. He found "rare phenocrysts" of plagioclase in the deposit, but did not find clinopyroxene, orthopyroxene, amphibole, or biotite. The refractive index of this pumice fits my data for the main pumice fall of Newberry ash and pumice deposit No. 2 (table 2) very well, and at this distance from the Central Pumice Cone vent, clinopyroxene and orthopyroxene are extremely rare in the main pumice fall and the plagioclase content very low. There are four deposits of pyroclastic material around China Hat: (1) old (pre-Mazama) coarse pumice from an unknown source, (2) Mazama ash, (3) Newberry ash deposit No. 1, and (4) the main pumice fall of Newberry ash and pumice deposit No. 2. The very coarse, highly inflated, honey to amber pumice described by Walker (see footnote 2) is exposed only in deep cuts and lies beneath the Mazama ash. It would be hard to confuse with the younger deposits. Certainly Wilcox would have recognized the Mazama ash, because he has been one of its principal investigators (Wilcox, 1965; Powers and Wilox, 1964). Moreover, its characteristics (Williams, 1942, p. 68–79; Powers and Wilcox, 1964; Wilcox, 1965) are so completely different from those he listed for the material at China Hat (Wilcox, 1965, p. 810) and from the two Newberry deposits that to confuse them would be unlikely. Therefore, the material at China Hat that Wilcox measured is almost certainly part of one of the Newberry deposits. Since Newberry ash deposit No. 1 is exposed only in a few very deep cuts, the material Wilcox measured very probably belongs to the main pumice fall of Newberry ash and pumice deposit No. 2.

[2] G. W. Walker (written commun., 1968) has found "very coarse and highly inflated pumice lumps of honey to amber color in old logging railroad cuts near the southwest base of East Butte," which he thinks "could possibly be old pumice perhaps related to vents at either East Butte or China Hat that were subsequently filled with domes." These deposits would be pre-Mazama in age, and would not be at the same horizon as the Newberry ash and pumice deposits.

REFERENCES

Deer, W. A., Howie, R. A., and Zussman, J., 1963, Rock-forming minerals; v. 2, Chain silicates: London, Longmans, Green and Co., Ltd., New York, John Wiley and Sons, Inc., 379 p.

Healy, J., Vucetich, C. G., and Pullar, W. A., 1964, Stratigraphy and chronology of Taupo and Rotorua volcanic ash: New Zealand Geol. Survey Bull. 73, 88 p.

Higgins, M. W., and Waters, A. C., 1967, Newberry Caldera, Oregon—A preliminary report: Ore Bin, v. 29, no. 3, p. 37–60.

——— 1968, Newberry Caldera field trip—The caldera wall sequence, p. 59–77 *in* Andesite Conference guidebook: Oregon Dept. Geology and Mineral Industries Bull. 62, 107 p.

Huber, N. K., and Rinehart, C. D., 1966, Some relationships between refractive index of fused glass beads and petro-

logic affinity of volcanic rock suites: Geol. Soc. America Bull., v. 77, p. 101–110.

Nakamura, K., 1960, Stratigraphic studies of the pyroclastics of Oshima Volcano, Izu, deposited during the last fifteen centuries; I. Cyclic activity of "Main craters" and absolute chronology of the pyroclastic sediments: Univ. Tokyo, Sci. Rept. Colln. Gen. Education, v. 10, p. 125–145.

Peterson, N. V., 1965, Newberry Volcano area field trip, p. 11–18 *in* Peterson, N. V., and Groh, E. A., eds., Lunar Geological Field Conference guidebook: Oregon Dept. Geology and Mineral Industries Bull. 57, 51 p.

Powers, H. A., and Wilcox, R. E., 1964, Volcanic ash from Mount Mazama (Crater Lake) and from Glacier Peak: Science, v. 144, p. 1334–1336.

Russell, I. C., 1905, Preliminary report on the geology and water resources of central Oregon: U.S. Geol. Survey Bull. 138 p.

Slemmons, D. B., 1962, Determination of volcanic and plutonic plagioclase using a three- or four-axis universal stage—Revision of Turner method: Geol. Soc. America Spec. Paper 69, 64 p.

Walker, G. W., 1951, Pumice deposits of the Klamath Indian Reservation, Klamath County, Oregon: U.S. Geol. Survey Circ. 128, 6 p.

Walker, G. W., Peterson, N. V., and Greene, R. C., 1967, Reconnaissance geologic map of the east half of the Crescent quadrangle, Lake, Deschutes, and Crook Counties, Oregon: U.S. Geol. Survey Misc. Geol. Inv. Map I–493.

Wilcox, R. E., 1965, Volcanic-ash chronology, p. 807–816 *in* Wright, H. E., and Frey, D. G., eds., The Quaternary of the United States: Princeton, N.J., Princeton Univ. Press, 922 p.

Williams, Howel, 1935, Newberry Volcano of central Oregon: Geol. Soc. America Bull., v. 46, p. 253–304.

——— 1941, Calderas and their origin: California Univ. Dept. Geol. Sci. Bull., v. 25, no. 6, p. 239–346.

——— 1942, The geology of Crater Lake National Park: Carnegie Inst. Washington Pub. 540, 162 p.

SIMILARITY OF CENOZOIC IGNEOUS ACTIVITY IN THE SAN JUAN AND ELK MOUNTAINS, COLORADO, AND ITS REGIONAL SIGNIFICANCE

By PETER W. LIPMAN, FELIX E. MUTSCHLER, BRUCE BRYANT, and THOMAS A. STEVEN, Denver, Colo.

Abstract.—Upper Cenozoic igneous rocks of the San Juan Mountains region are predominantly volcanic, whereas those of the Elk Mountains region are largely epizonal plutonic; yet the age and sequence of petrologic types are strikingly similar in the two areas. In both, rocks of intermediate composition were emplaced in large volume during the Oligocene; these were followed during the Miocene, Pliocene, and Pleistocene by a less voluminous bimodal assemblage of mafic and silicic rocks. This sequence seems to characterize middle and late Cenozoic igneous activity of much of the southern Rocky Mountains, with the change from intermediate to bimodal igneous activity coinciding approximately with beginning of block faulting related to late Cenozoic crustal extension.

Recent geologic and isotopic-age studies of Tertiary igneous rocks in the southern Rocky Mountains have required major revisions in the Cenozoic history of the region. Data available to 1967 have been summarized by Steven and Epis (1968), who conclude that most volcanic rocks in south-central Colorado were once parts of a single composite Oligocene volcanic field that was fragmented by block faulting and erosion in Miocene and later time. Our work, still in progress, substantiates and extends this interpretation. Not only the age of igneous activity but also the petrologic character of the rocks can be correlated over large areas, and consistent changes in magma chemistry which occurred with time over much of the southern Rocky Mountains region can be detected.

In this paper we make a preliminary attempt to compare middle and late Cenozoic igneous activity of two representative areas in the southern Rocky Mountains for which new petrologic and geochronologic data are especially abundant. One—the San Juan Mountains region—is predominantly volcanic, whereas the other—the Elk Mountains region—is predominantly epizonal plutonic. Nevertheless, the sequence of igneous activity, spanning early Oligocene to recent times, is strikingly similar. In both areas the earlier igneous rocks are predominantly intermediate in composition, and the younger rocks are a bimodal assemblage of mafic and silicic rocks. Late Cretaceous and early Tertiary ("Laramide") igneous activity, although represented in both areas, is not discussed in this paper.

SAN JUAN MOUNTAINS REGION

The San Juan volcanic field, which covers about 25,000 square kilometers in southwestern Colorado (fig. 1), and which is well known through the classic study of Larsen and Cross (1956), constitutes the largest erosional remnant of the composite Oligocene volcanic fields discussed by Steven and Epis (1968). The volcanic history postulated for the region by Larsen and Cross (1956) has been significantly modified, however, by recent regional stratigraphic and isotopic age studies (Steven and Ratté, 1964; Steven and others, 1967; Luedke and Burbank, 1963, 1968; Lipman and Steven, 1969), and current data indicate a relatively simple evolution of igneous activity throughout the San Juan Mountains region. In late Oligocene time, initial eruptions of intermediate lavas and breccias gave way to voluminous quartz latite and low-silica rhyolite ash-flow tuffs, and from Miocene time through the Pleistocene, volcanism was characterized by a bimodal assemblage of basalt and rhyolite.

Early intermediate lavas and breccias

Everywhere in the San Juan volcanic field the initial volcanism erupted alkali andesite, rhyodacite, and mafic quartz latite lavas and breccias from numerous local volcanic centers. A few centers underwent a greater range of local differentiation and produced rocks ranging from basaltic andesite to rhyolite (Lipman, 1968). Basalt is absent or extremely sparse. The early intermediate lavas and breccias have been assigned to numerous local formations, the most voluminous of which are the San Juan Formation and Lake Fork

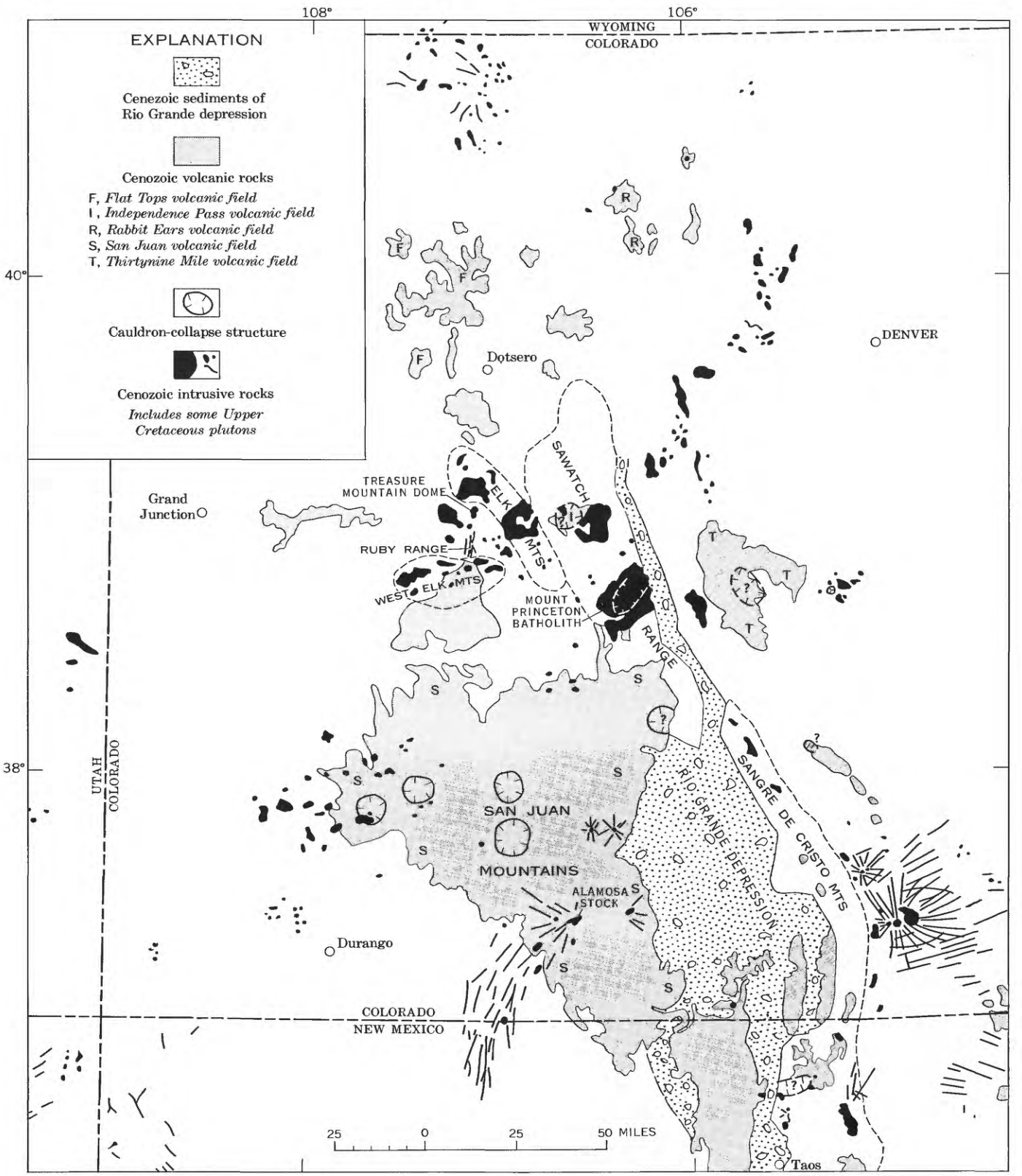

FIGURE 1.—Index map, showing location of San Juan volcanic field, Elk Mountains region, and other areas referred to in text. Modified from Cohee (1961).

Formation in the western part of the field, the West Elk Breccia in the northern part, and the Conejos Formation in the eastern and southeastern parts.

Isotopic age studies currently in progress indicate that most of the intermediate rocks formed during the relatively restricted interval of from 30 to 35 million years (P. W. Lipman and H. H. Mehnert, unpub. data). However, some of these rocks may have formed earlier, and petrologically similar rocks continued to be erupted in diminished volume during the succeeding several million years while the voluminous more silicic ash-flow tuffs were being erupted. The early intermediate rocks were originally deposited over more than 25,000 km^2 and probably had a volume of at least 40,000 km^3.

A histogram of SiO_2 contents of available analyses of the early lavas and breccias (fig. 2*A*) has a mean of 60 percent SiO_2, with a positive skewness toward more silicic compositions. The analyzed samples are, however, biased in favor of extreme compositions, and the volumetric predominance of intermediate-composition rocks is greater than indicated.

Ash-flow tuffs

About 30 m.y. ago eruption of intermediate lavas waned, and major volcanic activity changed to explosive ash-flow eruptions of quartz latite and low-silica rhyolite that persisted until about 26 m.y. ago (Steven and others, 1967; P. W. Lipman and H. H. Mehnert, unpub. data). Source areas for the ash flows were large cauldron complexes (fig. 1) in the central and western San Juan Mountains (Steven and Lipman, 1968; Luedke and Burbank, 1968). The original extent of the ash-flow tuffs was similar to that of the intermediate lavas (about 25,000 km^2), but their volume was only about half as great (about 20,000 km^3). Some individual ash-flow sheets were very large, spreading over as much as 15,000 km^2, with volumes as great as 2,000 km^3.

A histogram of SiO_2 contents of available analyses of the ash-flow tuffs (fig. 2*B*) displays a broad maximum from about 64 to 74 percent SiO_2 with few values beyond. This broad maximum reflects mainly the nonsystematic alternation of rhyolitic and quartz latitic ash-flow sheets. Also, compositional zonations within some individual sheets, becoming more mafic upward, indicate eruption from vertically zoned magma chambers in which rhyolite overlay quartz latite (Ratté and Steven, 1964). Three zoned sheets display variations that nearly bracket the compositional range of the entire sequence of ash-flow sheets (fig. 2*B*).

Later intermediate-silicic lava flows and breccias are interlayered with and overlie the ash-flow sequence locally but are greatly subordinate in volume (fig. 2*C*). Some of the lavas, which occur adjacent to cauldron-collapse structures, petrographically and chemically resemble the ash-flow tuffs and are clearly genetically related to the pyroclastic eruptions. Other lavas, generally somewhat more mafic, are distinguishable only by stratigraphic position from the intermediate lavas that preceded the ash-flow eruptions, and appear to represent a continuation and waning of this phase. Most of the intermediate lavas of both types are older than 26 m.y. (Steven and others, 1967; P. W. Lipman and H. H. Mehnert, unpub. data).

Shallow plutons

A few small epizonal porphyritic stocks and laccoliths intrude the volcanic pile, especially in the northern, western, and southeastern parts of the volcanic field. Most of these were indicated by Larsen and Cross (1956, pl. 1) as having the same age as the early intermediate lavas and breccias, but stocks intrude lower units of the ash-flow sequence in both the western (Bromfield, 1967, p. 57) and southeastern San Juan Mountains. The largest exposed intrusive body in the San Juan volcanic field, the Alamosa stock (Larsen and Cross, 1956, p. 108), has been dated at 29 m.y. by K-Ar methods (P. W. Lipman and H. H. Mehnert, unpub. data), and many other stocks are probably in the range 26–30 m.y., contemporaneous with the ash-flow eruptions. The intrusive rocks are mainly monzonites and granodiorites, chemically similar to the intermediate lavas and breccias, and distinctly less silicic than the concurrently emplaced ash-flow tuffs (fig. 2*D*).

Late basalts and rhyolites

In the early Miocene the character of volcanism changed notably. Whereas the Oligocene volcanics are predominantly intermediate lavas and somewhat more silicic ash-flow tuffs, the younger rocks are largely a bimodal association of basalt and silicic alkali rhyolite. The basaltic rocks (Hinsdale Formation) are mainly alkalic olivine basalt flows, relatively high in SiO_2 and trending into basaltic andesite; contaminated basaltic rocks that contain xenocrysts of quartz and alkali feldspar are abundant (Doe and others, 1969). The rhyolites consist of small scattered volcanic necks, plug domes, and one small ash-flow sheet, all characterized by high SiO_2 content (fig. 2*E*). Basalt and rhyolite were erupted intermittently through the Miocene and Pliocene, forming a widespread thin veneer over the older volcanic terrane. The oldest dated basalt is 24 m.y. (P. W. Lipman and H. H. Mehnert, unpub. data); flows as young as Pleistocene occur in northern New Mexico, at the south end of the volcanic field

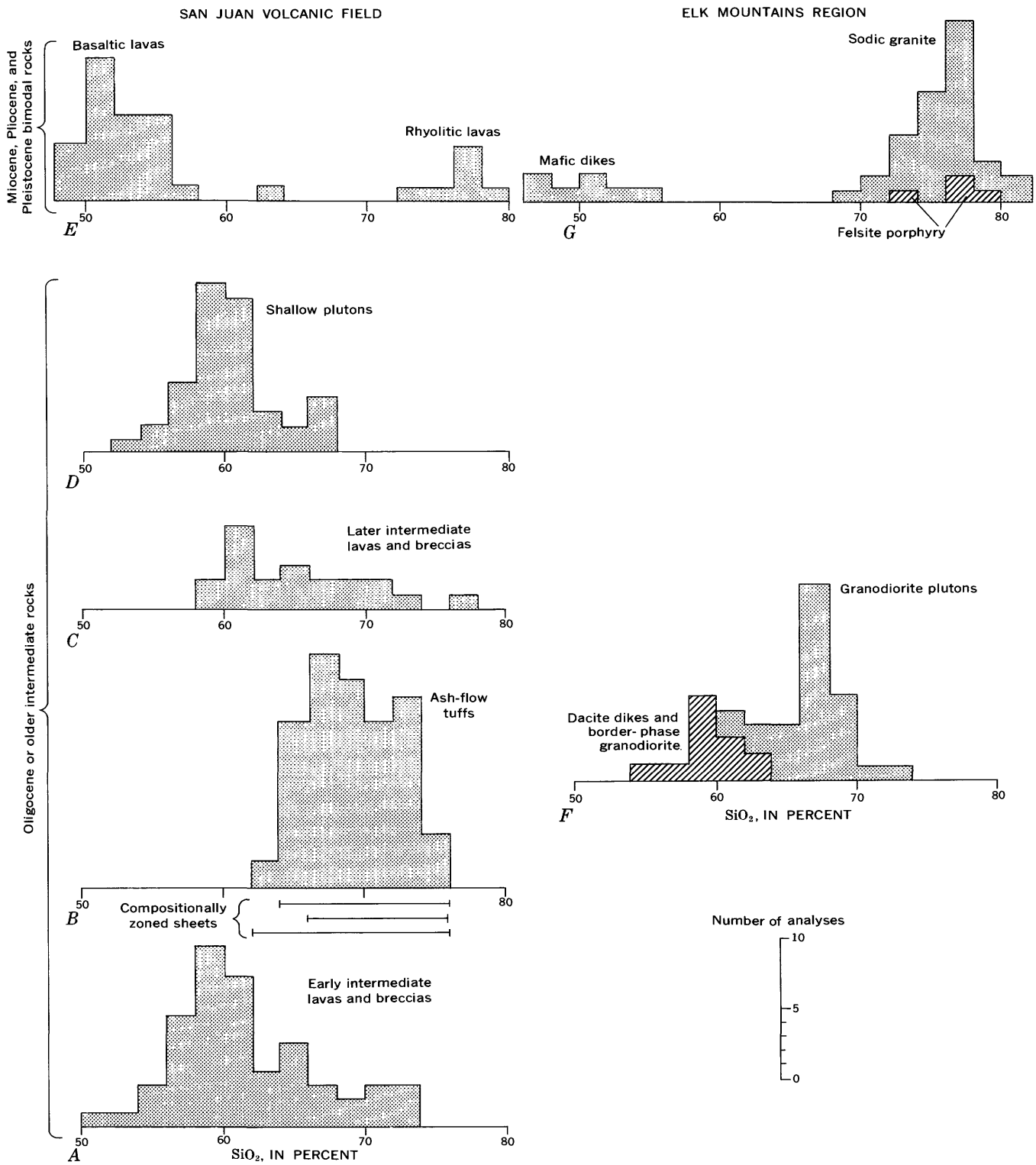

FIGURE 2.—Histograms of SiO_2 contents for major rock units of the San Juan volcanic field and Elk Mountains region. Interval for SiO_2 is 2 percent. Plotted from analyses calculated to 100 percent free of volatiles. Analyses from Larsen and Cross (1956); Bromfield (1967); Ratté and Steven (1967); Steven and Ratté (1960); Olson, Hedlund, and Hansen (1968); Godwin and Gaskill (1964); Doe, Lipman, Hedge, and Kurasawa (1969); Varnes (1963); F. E. Mutschler (unpub. data, 1969); and P. W. Lipman (unpub. data).

(Bingler, 1968). The basalt flows, now much eroded, probably originally covered 15,000–20,000 km^2, but total volume may have been no more than 1,000 km^3; the rhyolites were relatively minor, with an initial area of a few hundred square kilometers and volume of a few tens of cubic kilometers.

ELK MOUNTAINS REGION

The Elk Mountains region as used in this report includes the Elk Mountains, Ruby Range, Treasure Mountain dome, and West Elk Mountains (fig. 1).

Upper Cenozoic igneous rocks of the Elk Mountains region are mostly intrusive and, on the basis of field relations, petrographic similarities, and isotopic age determinations, can be divided into three general groups: (1) granodioritic plutons of Oligocene age, (2) Miocene and Pilocene(?) mafic dikes, and (3) a sodic granite stock of latest Miocene or earliest Pliocene age.

Granodioritic plutons

Stocks, laccoliths, sills, and dikes consisting mainly of granodiorite and granodiorite porphyry intrude rocks as young as the Eocene Wasatch Formation in the Elk Mountains region and have yielded radiometric ages of 29.0–34.4 m.y. (Obradovich and others, 1969). These rocks make up the greatest volume of exposed intrusive rocks in the region.

Some of the smaller granodioritic stocks of the Ruby Range and western Elk Mountains have borders of more mafic granodiorite. These borders have compositions similar to hornblendic and dacitic dikes in the West Elk Mountains (Gaskill and Godwin, 1966; Gaskill and others, 1967) and in the Elk Mountains (Bryant, 1969). These compositional differences are evident in a SiO_2 histogram (fig. 2*F*), in which the main peak at about 68 percent SiO_2 represents the volumetrically preponderant interior facies of the intrusions, and the smaller peak at about 60 percent SiO_2 represents the more mafic border facies and the dacite dikes. The mafic border rocks clearly represent early phases of the intrusions, as they are cut by more silicic dikes of interior-type granodiorite. Granodiorite porphyry plutons in the western Elk Mountains region locally contain xenoliths of quartz diorite which F. E. Mutschler (unpub. data) has interpreted as products of early crystallization at depth. The quartz diorite xenoliths and the progression from the early mafic border facies of the stocks to the interior granodiorites that form the bulk of the exposed plutons both suggest that the initial undifferentiated Oligocene magmas had relatively mafic intermediate compositions.

In the West Elk Mountains the dacite dikes cut intrusives related to the stocks, but in the Elk Mountains similar dikes are no younger than the large granodiorite plutons and are probably of the same age.

Mafic dikes

Small gabbro porphyry and lamprophyre dikes cut the Oligocene granodiorites in the Elk Mountains region. These are provisionally thought to be Miocene and early Pliocene in age, as they are petrographically and chemically similar to radiometrically dated Miocene and Pliocene basalts of the Flat Tops Primitive Area to the north (E. E. Larson, oral commun., 1968). Mafic igneous activity in the southern Rocky Mountains appears to have occurred intermittently from the Miocene nearly to the present. Basalt flows occupy a variety of physiographic positions in the major drainages, and the youngest known flows, in the bottom of the Colorado River valley near Dotsero, Colo., have been dated at about 4,000 years B.P. (Giegengack, 1962).

Most of the mafic dikes are somewhat altered, and are low in SiO_2 and high in CO_2 and H_2O. When calculated free of volatiles, however, analyses of these rocks cluster at about 50 percent SiO_2 (fig. 2*G*) similar to typical alkali olivine basalts of the San Juan Mountains region (fig. 2*E*) to the south and the Flat Tops area to the north.

Sodic granite and related rocks

At Treasure Mountain (fig. 1) a distinctive sodic granite stock has intruded Precambrian and Paleozoic rocks, producing a dome in the country rocks about 6 miles in diameter with structural relief of about 6,000 feet. The pluton contains a variety of compositionally similar facies whose textures range from coarse grained equigranular to fine grained seriate porphyritic. Some textural variants, that indicate abrupt quenching during late stages of crystallization, may reflect roof-rock rupture, perhaps with explosive volcanic venting (F. E. Mutschler, unpub. data, 1969).

The granite of Treasure Mountain, which is much more silicic than the Oligocene intrusions (fig. 2*F*, *G*), has yielded K-Ar ages of about 12.5 m.y. (Obradovich and others, 1969).

Highly altered felsite porphyries, which are chemically similar to the granite of Treasure Mountain, occur as small dikes, sills, and breccia pipes in the Elk Mountains region. Some of these are genetically related to the granite of Treasure Mountain, but some others are probably as old as Oligocene.

Possible volcanic venting

Some of the intrusive rocks of the Elk Mountains region probably served as feeders for volcanic deposits now largely removed by erosion, and this region may have constituted an important part of the composite volcanic field of the southern Rocky Mountains discussed by Steven and Epis (1968). In composition the Elk Mountains plutons most closely resemble the less silicic ash-flow tuffs in the San Juan Mountains sequence, but the mafic border facies resembles the early intermediate lavas and breccias and the shallow San Juan plutons.

The West Elk Breccia (Olson and others, 1968), which is continuous with the early intermediate lavas and breccias of the western San Juan Mountains, was probably derived from vents related to granodiorite plutons of the West Elk Mountains. These granodiorite plutons, which are more silicic than the volcanic breccias they intrude, apparently represent late differentiates of larger underlying magma bodies that were predominantly more mafic during eruption of the West Elk Breccia. The low silica border zones and inclusions within some Elk Mountains plutons also indicate that the magmas underwent some differentiation, during emplacement to their exposed crustal level, that is comparable, on a small scale, to the more extensively differentiated magma sources of the compositionally zoned San Juan ash flows.

In contrast with the San Juan Mountains region, a significant feature of the Elk Mountains region is the apparent absence of eroded equivalents of cauldron-collapse structures, such as ring-dike complexes. This suggests that ash-flow eruptions, abundant in late Oligocene volcanism of the San Juan Mountains region, were minor or absent farther north. However, in the Sawatch Range east and southeast of the Elk Mountains, deeply eroded cauldron complexes are probably present near Independence Pass and in the Mount Princeton area (fig. 1). At Independence Pass an ash-flow sequence several thousand feet thick is preserved in a block about 5 miles across that is downfaulted in Precambrian rocks and is intruded by a granodioritic porphyry dated at 34 m.y. (Obradovich and others, 1969). In the Mount Princeton area in the southern Sawatch Range, Dings and Robinson (1957, pl. 1) have mapped a composite stock of intrusive quartz latite porphyry, Mount Aetna Quartz Monzonite Porphyry, and volcanic breccia about 3 miles across that may represent the roots of a Tertiary volcano. Two dikes of the Mount Aetna Porphyry extend out from the stock and partly enclose an elliptical mass of older Mount Princeton Quartz Monzonite nearly 10 miles long and 7 miles wide, and appear to form an incomplete ring dike. None of these rocks have been dated radiometrically, but some and perhaps all may be Oligocene in age.

The Miocene and Pliocene(?) mafic dikes of the Elk Mountains may have been feeders for basalt flows such as those preserved to the northeast, west, and south. Whether or not these dikes actually fed flows, basalt flows clearly were widespread in the vicinity of the Elk Mountains in the Miocene and Pliocene, and are analogous in composition and age to the Hinsdale basalts of the San Juan Mountains region.

Textural features suggest that the sodic granite of Treasure Mountain vented (F. E. Mutschler, unpub. data, 1969), but any near-source volcanic deposits have been removed by erosion. In any case, the volumetrically rather minor high-silica igneous rocks of Treasure Mountain, together with the basalts at Flat Tops, constitute a contemporaneous bimodal suite very similar to that of the San Juan volcanic field (E. E. Larson, M. Ozima, and F. E. Mutschler, oral commun., 1968).

DISCUSSION

Upper Cenozoic igneous rocks of the San Juan Mountains region are predominantly volcanic, whereas those of the Elk Mountains region are largely epizonal plutonic. Yet both the timing of igneous activity and the sequence of petrologic types are strikingly similar for the two regions. In both, igneous activity was most intense during the same brief period in late Oligocene time and produced large volumes of intermediate composition rocks and genetically related somewhat more silicic differentiates. In both regions subsequent igneous activity in the Miocene and Pliocene was not so intense and produced lesser volumes of bimodal mafic and highly silicic rocks that contrast markedly with the intermediate older rocks.

In addition to the general similarities in age and sequence of igneous activity between San Juan Mountains and Elk Mountains regions, the chemical variations among the suites of igneous rocks follow very similar trends. This is most evident from simple SiO_2-variation diagrams (fig. 3, p. D40–D41). These diagrams include almost all available chemical data for the two areas. Omitted from the diagrams are a few analyses of obviously altered rocks, as indicated by petrographic study or by high CO_2 content. Some of the scatter in the plotted analyses is also certainly the result of less conspicuous alteration, but no analyses have been omitted simply because they deviate from the generalized trends. Rocks of all ages from the San Juan volcanic field, considered together over the entire range from basalt to rhyolite, define a typical calc-

alkalic trend (fig. 3*A*), as has been generally recognized since the petrologic studies of Larsen (1938). In the Elk Mountains region, the gabbro porphyries, granodiorites, and granite define similar trends (fig. 3*B*). In the Elk Mountains suite K_2O and perhaps TiO_2 are slightly lower and CaO and P_2O_5 may be slightly higher, especially at intermediate SiO_2 contents; otherwise the trends are indistinguishable within the scatter of the data. Similar plots of total Fe, MgO, and Al_2O_3, that were omitted for reasons of space, show even smaller differences between the two regions.

Less abundant petrologic and geochronologic data indicate generally similar sequences of igneous activity, from earlier predominantly intermediate rocks to later bimodal suites of mafic and silicic rocks, in many other parts of the southern Rocky Mountains region and adjacent parts of the Basin and Range province, including most of the areas cited by Steven and Epis (1968) as constituting parts of the large composite Oligocene volcanic field. This sequence of igneous activity appears to be approximately valid for volcanics of the Rabbit Ears area (Izett, 1966, 1968) and for the Thirtynine Mile volcanic field (Epis and Chapin, 1968, and oral commun., 1968) in Colorado as well as for the southern Sangre de Cristo Mountains of Colorado and New Mexico (C. L. Pillmore, oral commun., 1968). Rocks of similar age and sequence are also common over a large part of central New Mexico, including the Mogollon Plateau (Elston and others, 1968), the Blue Range (Ratté and others, 1969), the Black Range (Kuellmer, 1954), the Puertecito area (Tonking, 1957), and the Santa Rita area (Jones and others, 1967). A general progression in Tertiary volcanic rocks of New Mexico, andesite-rhyolite-basalt, was in fact noted many years ago (Lindgren and others, 1910, p. 42–46).

The marked contrast between early intermediate magmas and later bimodal mafic-silicic magmas in the southern Rocky Mountains implies either different conditions of magma generation or processes of differentiation for the two suites. In southern Colorado this petrologic change coincides approximately in time with initial structural development of the Rio Grande depression, a major rift that is a local expression of widespread late Cenozoic crustal extension in western North America (Lipman and Steven, 1969). Similar progressions from predominantly intermediate to bimodal basalt-rhyolite volcanism, approximately concurrent with initiation of late Tertiary crustal extension, appear characteristic of Cenozoic volcanism for much of the Western Interior of the United States.

REFERENCES

Bingler, E. C., 1968, Geology and mineral resources of Rio Arriba County, New Mexico: New Mexico Bur. Mines and Mineral Resources Bull. 91, 158 p.

Bromfield, C. S., 1967, Geology of the Mount Wilson quadrangle, western San Juan Mountains, Colorado: U.S. Geol. Survey Bull. 1227, 100 p.

Bryant, Bruce, 1969, Geologic map of the Maroon Bells quadrangle, Pitkin and Gunnison Counties, Colorado: U.S. Geol. Survey Geol. Quad. Map GQ–788.

Cohee, G. V., chm., 1961, Tectonic map of the United States—Exclusive of Alaska and Hawaii: U.S. Geol. Survey and Am. Assoc. Petroleum Geologists [1962].

Dings, M. G., and Robinson, C. S., 1957, Geology and ore deposits of the Garfield quadrangle, Colorado: U.S. Geol. Survey Prof. Paper 289, 110 p.

Doe, B. R., Lipman, P. W., Hedge, C. E., and Kurasawa, Hajime, 1969, Primitive and contaminated basalts from the southern Rocky Mountains, U.S.A.: Earth and Planetary Sci. Letters, v. 21, p. 142–156.

Elston, W. E., Coney, P. J., and Rhodes, R. C., 1968, A progress report on the Mogollon Plateau volcanic province, southwestern New Mexico: Colorado School Mines Quart., v. 63, no. 3, p. 261–287.

Epis, R. C., and Chapin, C. E., 1968, Geologic history of the Thirtynine Mile volcanic field, central Colorado: Colorado School Mines Quart., v. 63, no. 3, p. 51–85.

Gaskill, D. L., and Godwin, L. H., 1966, Geologic map of the Marble quadrangle, Gunnison and Pitkin Counties, Colorado: U.S. Geol. Survey Geol. Quad. Map GQ–512.

Gaskill, D. L., Godwin, L. H., and Mutschler, F. E., 1967, Geologic map of the Oh-be-joyful quadrangle, Gunnison County, Colorado: U.S. Geol. Survey Geol. Quad. Map GQ–578.

Giegengack, R. F., 1962, Recent volcanism near Dotsero, Colorado: Colorado Univ. unpub. M.S. thesis, 43 p.

Godwin, L. H., and Gaskill, D. L., 1964, Post-Paleocene West Elk laccolithic cluster, west-central Colorado, *in* Geological Survey Research 1964: U.S. Geol. Survey Prof. Paper 501–C, p. C66–C68.

Izett, G. A., 1966, Tertiary extrusive volcanic rocks in Middle Park, Grand County, Colorado, *in* Geological Survey Research 1966: U.S. Geol. Survey Prof. Paper 550–B, p. B42–B46.

——— 1968, Geology of the Hot Sulphur Springs quadrangle, Grand County, Colorado: U.S. Geol. Survey Prof. Paper 586, 79 p.

Jones, W. R., Hernon, R. M., and Moore, S. L., 1967, General geology of Santa Rita quadrangle, Grant County, New Mexico: U.S. Geol. Survey Prof. Paper 555, 144 p.

Kuellmer, F. J., 1954, Geologic section of the Black Range at Kingston, New Mexico; New Mexico Bur. Mines and Mineral Resources Bull. 33, 100 p.

Larsen, E. S., 1938, Some new variation diagrams for groups of igneous rocks: Jour. Geology, v. 46, no. 3, pt. 2, p. 505–520.

Larsen, E. S., Jr., and Cross, C. W., 1956, Geology and petrology of the San Juan region, southwestern Colorado: U.S. Geol. Survey Prof. Paper 258, 303 p.

Lindgren, Waldemar, Graton, L. C., and Gordon, C. H., 1910, The ore deposits of New Mexico: U.S. Geol. Survey Prof. Paper 68, 361 p.

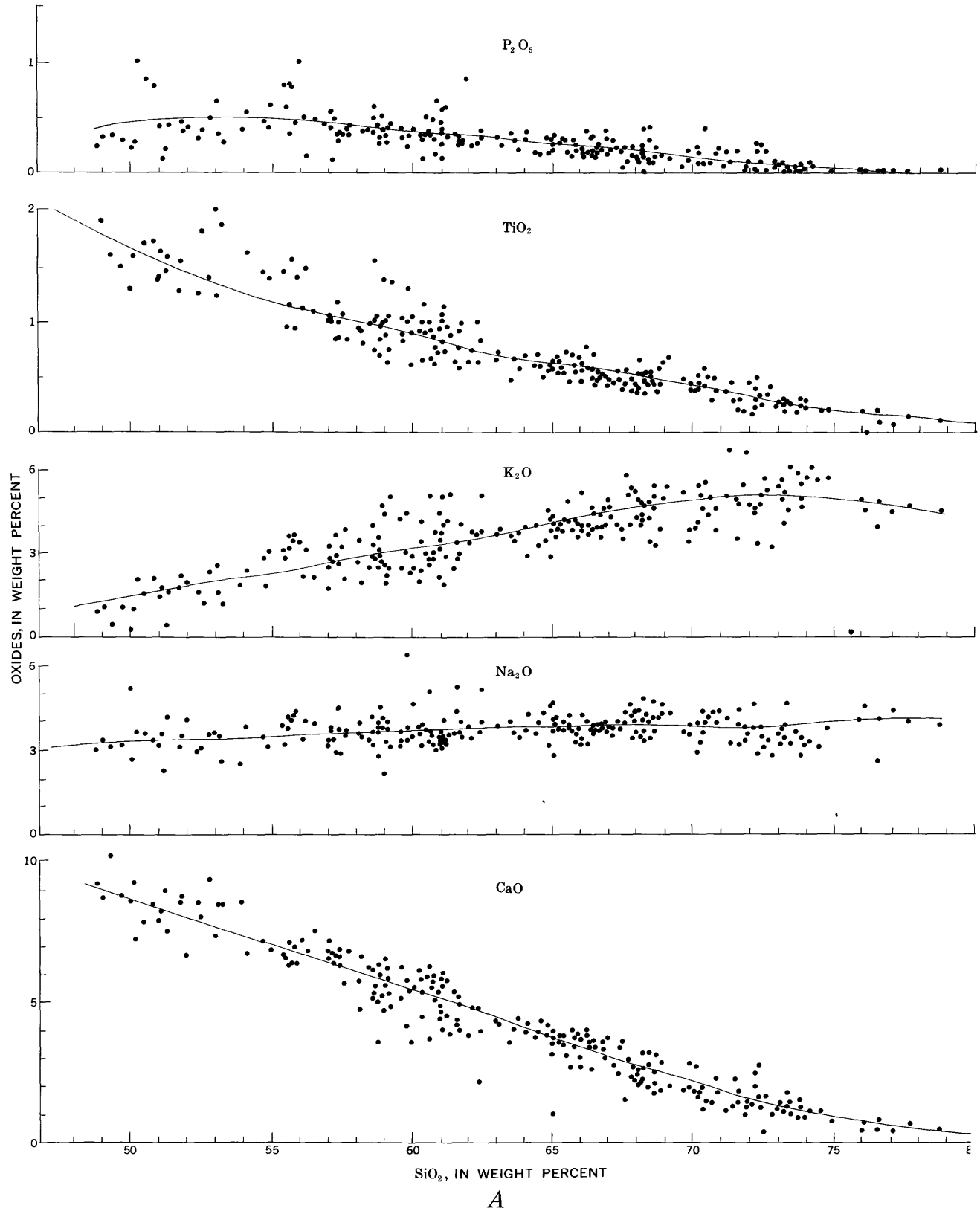

FIGURE 3.—SiO_2 variation diagrams for major volcanic units of the San Juan volcanic field (*A*), and for igneous rocks of the Elk Mountains region (*B*). Approximate trend lines were drawn by inspection for the San Juan data (*A*); these same trends are juxtaposed on the Elk Mountains data (*B*). All analyses were recalculated to 100 percent on a volatile-free basis. Analyses from same sources as those of figure 2.

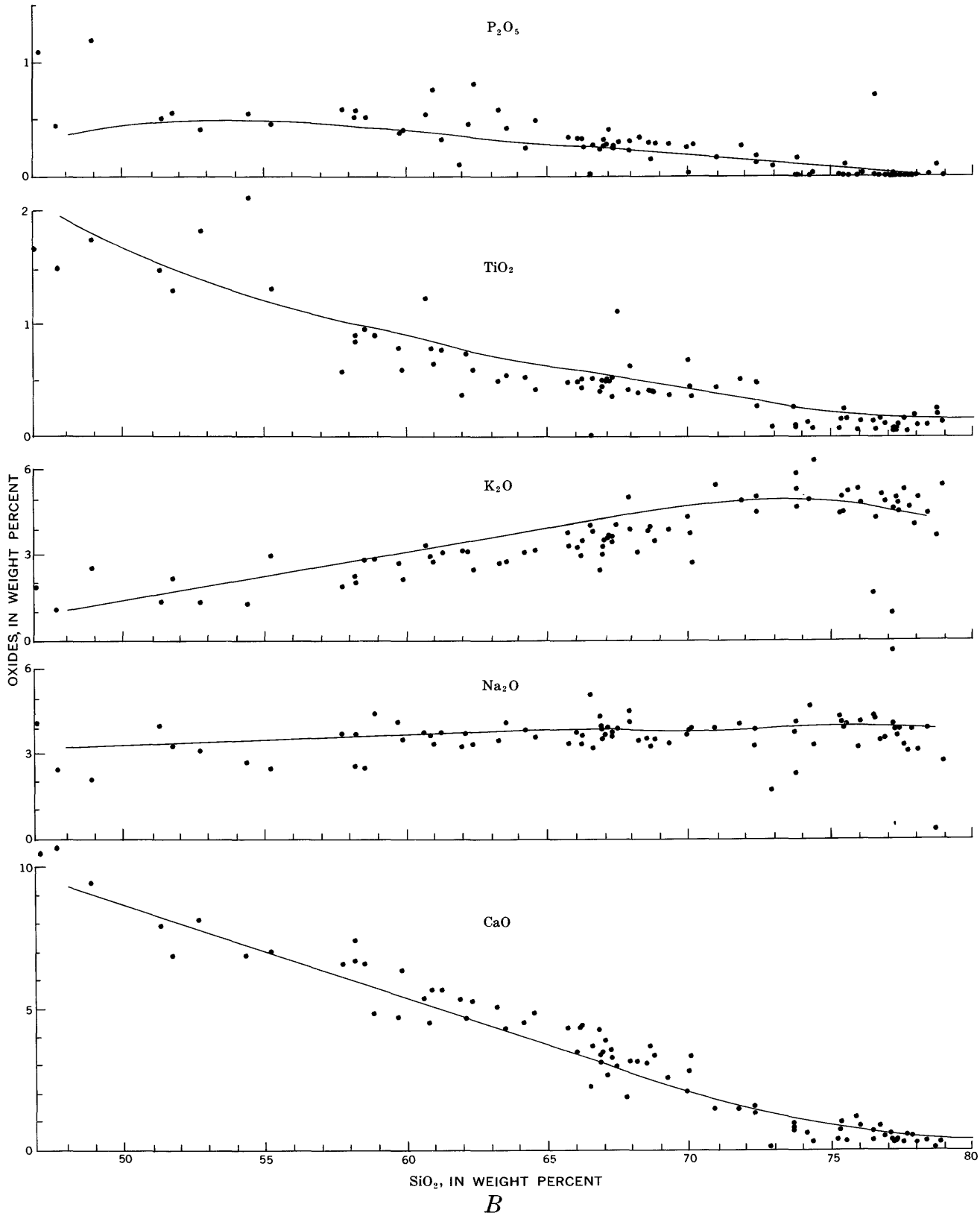

B

FIGURE 3 (CON.)

Lipman, P. W., 1968, Geology of Summer Coon volcanic center, eastern San Juan Mountains, Colorado: Colorado School Mines Quart., v. 63, no. 3, p. 211–236.

Lipman, P. W., and Steven, T. A., 1969, Petrologic evolution of the San Juan volcanic field, southwestern Colorado, U.S.A. [abs.]: Oxford, England, Internat. Symposium Volcanology, Program 1969. [In press]

Luedke, R. G., and Burbank, W. S., 1963, Tertiary volcanic stratigraphy in the western San Juan Mountains, Colorado: Art. 70 *in* U.S. Geol. Survey Prof. Paper 475–C, p. C39–C44.

——— 1968, Volcanism and cauldron development in the western San Juan Mountains, Colorado: Colorado School Mines Quart., v. 63, no. 3, p. 175–208.

Obradovich, J. D., Mutschler, F. E., and Bryant, Bruce, 1969, K-Ar ages bearing on the igneous and tectonic history of the Elk Mountains and vicinity, Colorado—A preliminary report: Geol. Soc. America Bull., v. 80, no. 9, p. 1749–1756.

Olson, J. C., Hedlund, D. C., and Hansen, W. R., 1968, Tertiary volcanic stratigraphy in the Powderhorn-Black Canyon region, Gunnison and Montrose Counties, Colorado: U.S. Geol. Survey Bull. 1251–C, p. C1–C29.

Ratté, J. C., Landis, E. R., Gaskill, D. L., and Damon, P. E., 1969, Geology of the Blue Range Primitive Area, Arizona-New Mexico, *in* Abstracts for 1968: Geol. Soc. America Spec. Paper 121, p. 549.

Ratté, J. C., and Steven, T. A., 1964, Magmatic differentiation in a volcanic sequence related to the Creede caldera, Colorado: Art. 131 *in* U.S. Geol. Survey Prof. Paper 475–D, p. D49–D53.

——— 1967, Ash flows and related volcanic rocks associated with the Creede caldera, San Juan Mountains, Colorado: U.S. Geol. Survey Prof. Paper 524–H, p. H1–H58.

Steven, T. A., and Epis, R. C., 1968, Oligocene volcanism in south-central Colorado: Colorado School Mines Quart., v. 63, no. 3, p. 241–258.

Steven, T. A., and Lipman, P. W., 1968, Central San Juan cauldron complex, Colorado [abs]: Colorado School Mines Quart., v. 63, no. 3, p. 209.

Steven, T. A., Mehnert, H. H., Obradovich, J. D., 1967, Age of volcanic activity in the San Juan Mountains, Colorado, *in* Geological Survey Research 1967: U.S. Geol. Survey Prof. Paper 575–D, p. D47–D55.

Steven, T. A., and Ratté, J. C., 1960, Geology and ore deposits of the Summitville district, San Juan Mountains, Colorado: U.S. Geol. Survey Prof. Paper 343, 70 p.

——— 1964, Revised Tertiary volcanic sequence in the central San Juan Mountains, Colorado: Art. 132 *in* U.S. Geol. Survey Prof. Paper 475–D, p. D54–D63.

Tonking, W. H., 1957, Geology of Puertecito quadrangle, Socorro County, New Mexico: New Mexico Bur. Mines and Mineral Resources Bull. 41, 67 p.

Varnes, D. J., 1963, Geology and ore deposits of the South Silverton mining area, San Juan County, Colorado: U.S. Geol. Survey Prof. Paper 378–A, p. A1–A56.

ULTRAMAFIC XENOLITHS IN BASALT, NYE COUNTY, NEVADA

By NEWELL J. TRASK, Menlo Park, Calif.

Work done in cooperation with the National Aeronautics and Space Administration

Abstract.—Lherzolites from ejecta and flows around two vents in central Nevada are moderately to strongly deformed; olivine-rich wehrlites and dunites are intensely deformed; and clinopyroxene-rich wehrlites, clinopyroxenites, and gabbros are undeformed to only slightly deformed. The olivine-rich wehrlites contain striking large, black, glassy clinopyroxene grains some of which are broken and invaded by fine-grained recrystallized olivine. The lherzolite probably came from the upper mantle; the clinopyroxene-rich wehrlite, and clinopyroxenite may have formed in the lower crust as cumulates from the magma that produced some nearby basalt flows older than the host rock; source of the highly deformed olivine-rich wehrlite and dunite is not clear.

Ultramafic and mafic xenoliths are abundant in basaltic flows and ejecta around two small conical vents near Black Rock Summit in the southern part of the Pancake Range, northern Nye County, Nev. One of the volcanic flows was described by Vitaliano and Harvey (1965), who noted the presence in it of large (8 centimeters) individual crystals of pyroxene, olivine, and plagioclase. Polycrystalline aggregates of lherzolite, wehrlite, dunite, pyroxenite, and gabbro up to 15 cm in length are present in this flow, in a second flow to the south, and in the ejecta around the vents at the heads of both flows. These xenoliths have a wide variety of compositions and textures; deformation textures are especially conspicuous. They represent a hitherto unreported occurrence in the circumpacific belt of ultramafic inclusions in basalts described by Forbes and Kuno (1965).

Acknowledgments.—This report is part of a study of basaltic craters and lava fields done on behalf of the National Aeronautics and Space Administration under contract No. R–66.

GEOLOGIC SETTING

The inclusion-bearing rocks lie within a relatively small field of basaltic flows, cinder cones, and cinder-and-spatter cones in an elevated valley in the southwest part of the Pancake Range. The basalt field is crossed by U.S. Route 6 midway between Tonopah and Ely (fig. 1). Most of the field lies within an elongate area, 10 by 30 kilometers, trending northeast, and several of the vents are alined along northeast-trending lineaments (fig. 1). The youngest flows poured out on relatively young playa deposits in the undrained valleys and may be as young as Holocene (fig. 2). The inclusion-bearing flows are among the youngest of the basalts.

Most of the vents within the basalt field are steep cinder cones and cinder-and-spatter cones. Two of the vents are maars; one just to the south of the southern inclusion-bearing flow is known as Grandfather's Chair (fig. 1), and a second, 7 km south of the area of figure 1, is known as Lunar Crater. The maars have rims of palagonite tuff; only a few small ultramafic xenoliths have been found to date in the ejecta surrounding them.

The basalt field is surrounded by older Tertiary ignimbrites of the type described by Cook (1965). The generally circular plan of the elevated valley containing the basalts and the surrounding hills of ignimbrite has led some workers (E. B. Ekren and others, personal commun., 1967) to the conclusion that the entire structure is a caldera similar to others in the Basin and Range province of western Nevada (Christiansen and others, 1965). The basalt field is included in a geologic map of northern Nye County, Nev., by Kleinhampl and Ziony (1967). A detailed study of the basalts and their relation to the surrounding ignimbrites has been made by Scott (1969).

HOST ROCKS

Both cones around which inclusions are found are elongate in a northeast direction and have been breached on the northwest side. Both measure approxi-

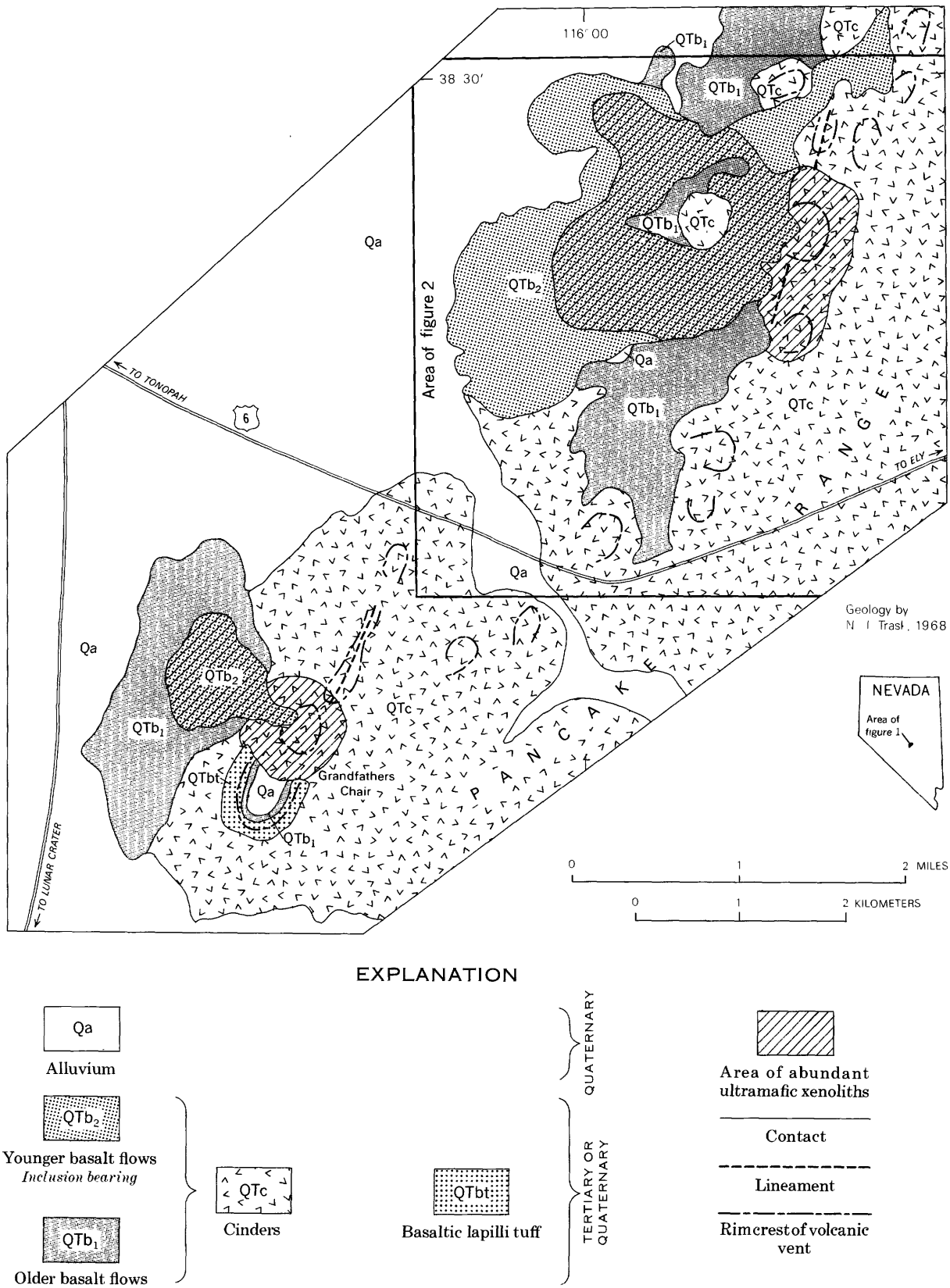

FIGURE 1.—Geologic sketch map of part of the basalt field in the southern Pancake Range, showing areas with abundant ultramafic inclusions.

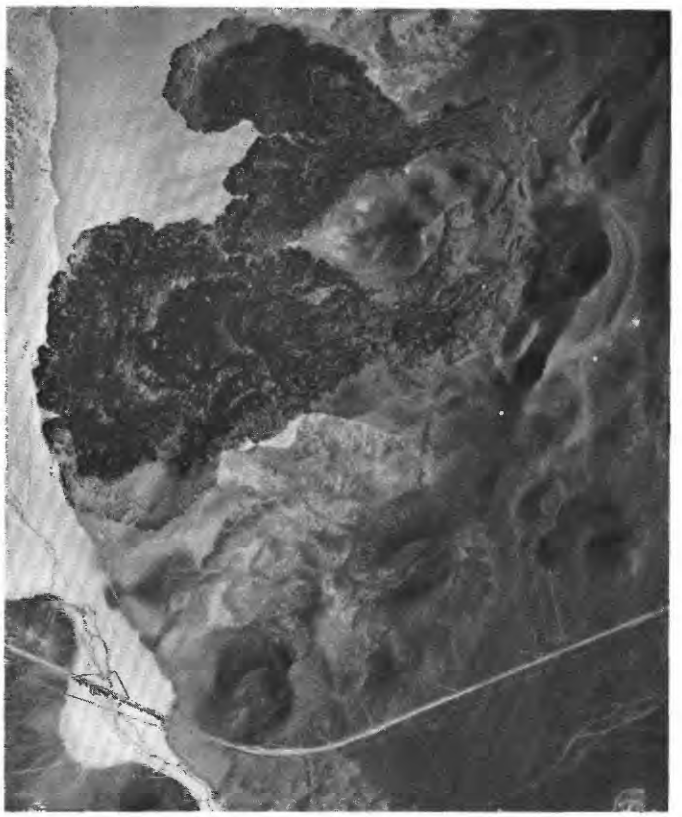

FIGURE 2.—Aerial view of youngest flows in southern Pancake Range basalt field. North is toward top of photograph. Area of photograph shown in figure 1.

mately 1,200 × 700 meters at the base. At least three small lava flows issued from each vent and extend 1 to 3 km to the northwest. Other flows, similar in freshness and appearance to those which issued from the northern vent, came from a northeast-trending fissure north of the vent. The northern flows are extremely jagged and have on their surfaces monolithic blocks of oxidized spatter and pyroclastic material sheathed with dense dark-gray basalt. Vitaliano and Harvey (1965) interpreted these blocks as fragments of the crater wall torn loose at the time it was breached, but the blocks may also have originated as a form of squeezeup or broken pressure ridge. The flows from the southern vent are considerably smoother than those from the northern vent, and the large monolithic blocks of pyroclastic material are lacking.

The flows and pyroclastics at both vents are black vesicular basalts except in areas of abundant spatter, where they are red. They are composed of a brown to black glassy groundmass with microphenocrysts of plagioclase, clinopyroxene, olivine, and opaque minerals. Xenocrysts, ranging in size from 0.5 millimeters to 8 centimeters, are abundant and consist mostly of ragged deformed olivine, clinopyroxene crystals with corroded, spongy cores and overgrowths of euhedral salite, and corroded plagioclase. A few anhedral grains of spinel and orthopyroxene are present in the host. Some spinel is surrounded by a corona of plagioclase at its contact with the host, and some is altered to an opaque mineral. The orthopyroxene is surrounded by a corona of fine-grained olivine.

TABLE 1.—*Bulk chemical analyses and molecular norms of basalt from southern Pancake Range, Nye County, Nev.*

[Analyst: C. L. Parker, U.S. Geological Survey, Denver, Colo., 1968]

	LC–48	LC–109
Chemical analyses (weight percent)		
SiO_2	44. 41	47. 24
Al_2O_3	15. 45	16. 52
Fe_2O_3	2. 74	3. 38
FeO	8. 66	8. 75
MgO	8. 74	6. 30
CaO	10. 49	8. 42
Na_2O	3. 99	4. 15
K_2O	1. 80	1. 52
H_2O+	. 11	. 12
H_2O-	. 01	. 06
TiO_2	2. 34	2. 40
P_2O_5	. 73	. 51
MnO	. 22	. 19
Cr_2O_3	. 06	. 02
Total	99. 75	99. 58
Molecular norms		
or	10. 63	8. 99
ab	8. 24	26. 50
an	19. 12	22. 14
ne	13. 62	4. 53
di	22. 45	12. 25
ol	15. 26	14. 14
mt	3. 97	4. 91
il	4. 44	4. 56
ap	1. 73	1. 21
Total	99. 46	99. 23

The xenocrysts in the host rock make the results of bulk chemical analyses subject to some uncertainty. Xenoliths and individual grains larger than 2 mm in diameter were avoided in selecting material for analysis, but smaller grains foreign to the magma were undoubtedly included. The analysis and norm of typical younger inclusion-bearing basalt (LC–48, table 1) is very similar to the analysis published by Vitaliano and Harvey (1965). No modal nepheline has been detected, but occult nepheline may be present in the very fine grained groundmass. The rock would be classed as a basanitoid as defined by MacDonald and Katsura (1964, p. 86). The older basalt flows (fig. 1), underlying the inclusion-bearing basalts, are apparently free of xenocrysts but contain 5 percent olivine as phenocrysts. The analysis and norm of this rock (LC–109, table 1) show that it would be classed as an alkali-olivine basalt as defined by MacDonald and

Katsura (1964, p. 89); its chemistry may be more typical of uncontaminated magma in this basalt field.

XENOLITHS

The xenoliths occur as cores of bombs, as blocks in the mounds and monoliths of spatter, and as inclusions in flows. Most are rounded; they range in size from microscopic aggregates to 15 cm in length. All are relatively fresh, but some of the pyroxene-rich and hornblende-rich xenoliths are highly friable.

The major assemblages of the inclusion suite are:

olivine-orthopyroxene-clinopyroxene-spinel
olivine-clinopyroxene-spinel
olivine-clinopyroxene
olivine
olivine-clinopyroxene-spinel-plagioclase
clinopyroxene-spinel
olivine-clinopyroxene-spinel-plagioclase-hornblende-biotite.

Estimated mineral proportions in 150 inclusions from the northern vent and flows of figure 1 are shown in figure 3, a plot similar to those of Jackson (1968). Fields A and B in figure 3 enclose compositions of two distinct types of xenoliths. The relatively few remaining inclusions have a wide range of composition; textural characteristics also set them apart from the rocks of fields A and B.

Olivine-rich lherzolite makes up field A. Olivine in these inclusions is light green; orthopyroxene is dark-gray bronzite altered at the contact with the host basalt to a mosaic of fine-grained olivine; clinopyroxene is emerald-green diopside in grains generally less than 1 mm across. Brown spinel is an accessory constituent in nearly all the lherzolites. Deformation of the olivines in the lherzolites is for the most part moderate with subparallel bands of different extinction position in almost every grain. Raleigh (1968) interpreted identical features in experimentally and naturally deformed peridotites as kink-band boundaries. A few of the

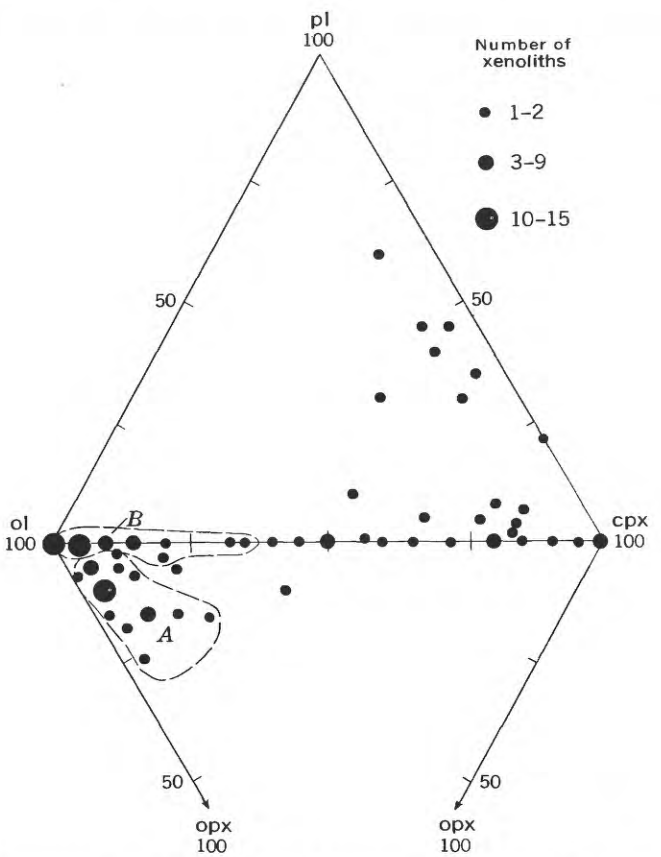

FIGURE 3.—Triangular plots of proportions of minerals in 150 xenoliths from ejecta and flows around the northern inclusion-bearing vent in figure 1. Size of dot indicates number of xenoliths. Abbreviations: cpx, clinopyroxene; ol, olivine; opx, orthopyroxene; pl, plagioclase.

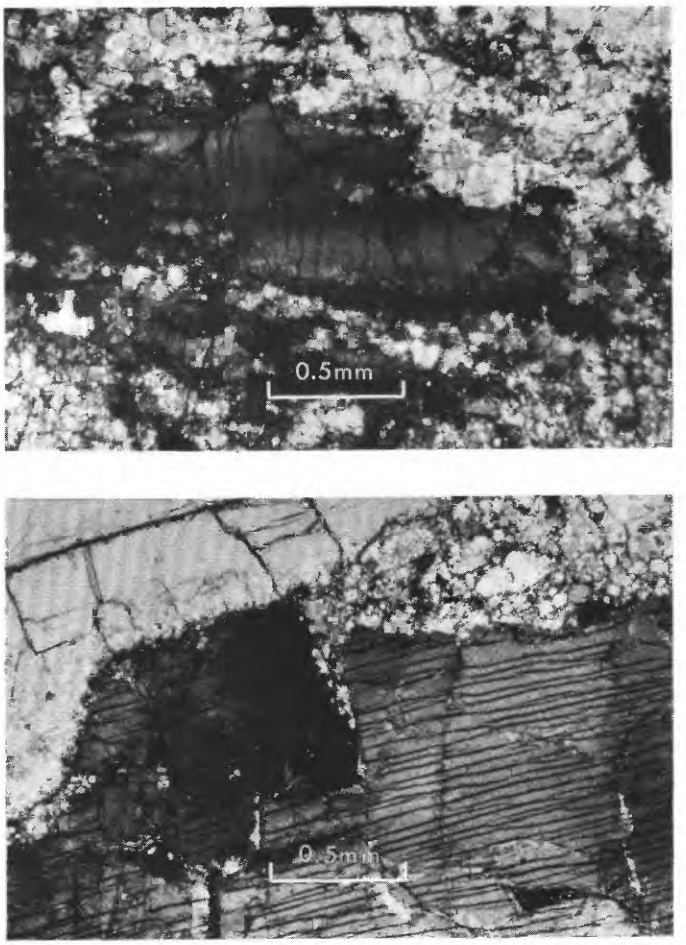

FIGURE 4.—Photomicrographs of inclusions from the southern Pancake Range. Crossed polarizers. Top, deformed lherzolite. Grain of olivine-α (see text) with kink bands (east-west) surrounded and in part cut by mosaic of olivine-β. Bottom, deformed olivine-rich wehrlite. Dark-gray mineral with cleavage is clinopyroxene, deformed, partially broken, and invaded by olivine-β.

lherzolites have large elongate olivine grains with well-developed kink bands surrounded by a mosaic of smaller (<1 mm), equidimensional olivine grains lacking kink bands (fig. 4, top). Jackson (1968) termed these two types of olivine in Hawaiian lherzolites "olivine-α" and "olivine-β", respectively. Segments which originally belonged to the same olivine-α grain and which extinguish at only slightly different angles are separated by septa of olivine-β in some lherzolites. Many grains of orthopyroxene and clinopyroxene have marked undulatory extinction, although discrete kink-band boundaries are lacking. Like the lherzolites from Dish Hill, Calif., but unlike those from Hawaii and many other localities (White, 1966), none of the pyroxenes in the lherzolites from the Pancake Range have exsolution lamellae.

The inclusions of field B consist of olivine-rich wehrlites and dunites, most with intense deformation textures. The olivine in these inclusions is light olive; the clinopyroxene occurs as large black glassy grains up to 4 cm in length; spinel is lacking. Mosaics of olivine-β surrounding olivine-α are present in every inclusion of this group, and some specimens consist almost entirely of olivine-β. The clinopyroxene is less deformed than the olivine, but some grains have marked undulatory extinction. Other grains show evidence of mechanical breakup, and stringers of the fine-grained olivine lie within the cracks (fig. 4, bottom). Thin lamellae of orthopyroxene are present in some of the large grains of clinopyroxene. Several inclusions have fair to good foliation defined by elongate olivine grains and thin bands of fine-grained pyroxene.

In addition to kink-band boundaries, many olivine grains in the olivine-rich lherzolites and wehrlites have good cleavage parallel to (010), and a few show deformed cleavage. Well-developed cleavage has been reported in olivine from several intrusive dunite bodies (Kuroda and Shimoda, 1967).

Wehrlite, clinopyroxene-rich wehrlite, clinopyroxenite, and gabbro make up the rest of the inclusion suite. Their compositions vary over wide limits (fig. 3); in several inclusions, olivine-rich and clinopyroxene-rich compositions are interlayered. In addition to the components shown in figure 3, some of these xenoliths contain as much as 20 percent hornblende poikilitically enclosing olivine and clinopyroxene, as much as 15 percent biotite, and as much as 15 percent green spinel. These inclusions are much less deformed than the olivine-rich lherzolites and wehrlites, and the dunites. Only a few olivine grains have well-developed kink-band boundaries. Many of the clinopyroxene-rich wehrlites are loosely packed and have extensive veinlets and apophyses of glass with plagioclase phenocrysts from the host basalt. The clinopyroxene in some of the wehrlites appears to be titansalite with violet pleochroism. The clinopyroxenites consist of glassy black augite with as much as 10 percent green spinel. Exsolution lamellae of orthopyroxene are common in the clinopyroxene of the clinopyroxene-rich wehrlites and clinopyroxenites.

ORIGIN OF THE XENOLITHS

The pronounced deformation textures in the ultramafic xenoliths of the Pancake Range and in other localities (Jackson, 1968; Aoki, 1968; McGetchin and Hoare, 1968; Ernst, 1967; White, 1966; Foster and others, 1966; Talbot and others, 1963; Wilshire and Binns, 1961; and Ross and others, 1954) have been reproduced by experimental deformation of olivine in the solid state at high temperatures and pressures (Raleigh, 1968; Jorgensen and Raleigh, 1968.) Thus the highly deformed inclusions must have come from deformed preexisting rocks, and not from cumulates subject only to gravitational stresses. Whether such textures can form in cumulates undergoing shearing stresses at the margins of an ascending magma body is not certain, but the intensity of the deformation would seem to preclude such an origin. The deformation in the xenoliths as a whole in this area is apparently more intense than that in many other xenolith localities and closely resembles the deformation textures in intrusive dunite masses (Ragan, 1963; Raleigh, 1965).

Spinel-bearing lherzolites are stable at mantle depths in this part of the western United States (MacGregor, 1968, p. 3741). Thus the moderately to strongly deformed lherzolites of the Pancake Range are probably samples of the mantle, though they may be the residue left after extensive partial melting of original mantle material. The olivine-rich wehrlites and the dunites are more strongly deformed than the lherzolites and apparently suffered extensive recrystallization of olivine and mechanical mixing of olivine-β and pyroxenes. Whether they also came from the mantle is uncertain; they could be part of a hybrid peridotite body that intruded either the crust or mantle.

The clinopyroxene-rich wehrlites, clinopyroxenites, and gabbros have much less intense deformation textures, and some of them may be cumulates derived from the magma that formed older basalts in the field (compare Aoki, 1968). Recent experimental work with liquids of basaltic composition at moderate to high pressures (Green and Ringwood, 1967, p. 156) indicates that large amounts of pyroxene and olivine crystallize before the appearance of plagioclase. If the magma had differentiated during ascent, cumulates rich in these minerals should have formed. Separation of cumulates rich in clinopyroxene and olivine should

result in enrichment of the residual liquid in alumina (Green and Ringwood, 1967, p. 156). Several basalt flows especially rich in plagioclase phenocrysts occur near the south end of the basalt field and lie stratigraphically below the inclusion-bearing basalts; they may represent the liquid produced by differentiation at moderate depths (15 to 35 km) during which the olivine and clinopyroxene were removed from the magma. Eruption in the reverse sequence would then produce first the plagioclase-rich flows and later wehrlite as inclusions in the youngest flows.

The large individual crystals of olivine and clinopyroxene in the inclusion-bearing basalts, described earlier by Vitaliano and Harvey (1965), were probably derived partly by attrition of the xenoliths. Many of the crystals of olivine show evidence of deformation. Some of the large black glassy crystals of aluminous clinopyroxene are deformed and are similar to the clinopyroxene in the highly deformed olivine-rich wehrlites. Others are undeformed and resemble clinopyroxene from the clinopyroxene-rich wehrlites and pyroxenites. All of the larger xenocrysts of clinopyroxene have euhedral rims of salite derived from the host magma. Large black crystals of pyroxene are common at many localities where ultramafic xenoliths occur in basalts (Green and Ringwood, 1967, p. 185; Aoki, 1968, p. 253). At least some of them are also probably xenocrysts rather than phenocrysts that crystallized from the enclosing magma.

REFERENCES

Aoki, Ken-ichiro, 1968, Petrogenesis of ultrabasic and basic inclusions in alkali basalts. Iki Island, Japan: Am. Mineralogist, v. 53, nos. 1–2, p. 241–256.

Christiansen, R. L., Lipman, P. W., Orkild, P. P., and Byers, F. M. Jr., 1965, Structure of the Timber Mountain caldera, southern Nevada, and its relation to Basin-Range structure, *in* Geological Survey Research 1965: U.S. Geol. Survey Prof. Paper 525–B, p. B43–B48.

Cook, E. F., 1965, Stratigraphy of Tertiary volcanic rocks in eastern Nevada: Nevada Bur. Mines Rept. 11, 61 p.

Ernst, Theodor, 1967, Olivine nodules and the composition of the Earth's mantle; *in* Runcorn, S. K., ed., Mantles of the Earth and terrestrial planets: New York, Interscience, p. 321–328.

Forbes, R. B., and Kuno, Hisashi, 1965, The regional petrology of peridotite inclusions and basaltic host rocks, *in* Smith, C. H., and Sorgenfrei, Theodor, eds., The upper mantle symposium, New Delhi, 1964: Copenhagen, Det Berlinsgke Bogtrykkeri, p. 161–179.

Foster, H. L., Forbes, R. B., and Ragan, D. M., 1966, Granulite and peridotite inclusions from Prindle Volcano, Yukon-Tanana upland, Alaska, *in* Geological Survey Research 1966: U.S. Geol. Survey Prof. Paper 550–B, p. B115–B119.

Green, D. H., and Ringwood, A. E., 1967, The genesis of basaltic magmas: Contr. Mineralogy and Petrology, v. 15, no. 2, p. 103–190.

Jackson, E. D., 1968, The character of the lower crust and upper mantle beneath the Hawaiian Islands, *in* Proceedings of Section 1—Upper mantle (geological processes): Internat. Geol. Cong. 23d, Prague, 1968, Rept. p. 135–150.

Jorgensen, D. B., and Raleigh, C. B., 1968, Fabrics of naturally and experimentally recrystallized olivine [abs.]: Geol. Soc. America, Cordilleran Sect., 64th Ann. Mtg., Program, p. 71.

Kleinhampl, F. J. and Ziony, J. I., 1967, Preliminary geologic map of northern Nye County, Nevada: U.S. Geol. Survey map, open-file rept.

Kuroda, Yoshimasu, and Shimoda, Susumu, 1967, Olivine with well-developed cleavages—its geological and mineralogical meanings: Jour. Geol. Soc. Japan, v. 73, no. 8, p. 377–388.

MacDonald, G. A., and Katsura, Takashi, 1964, Chemical composition of Hawaiian lavas: Jour. Petrology, v. 5, pt. 1, p. 83–133.

MacGregor, I. D., 1968, Mafic and ultramafic inclusions as indicators of the depth of origin of basaltic magmas: Jour. Geophys. Research, v. 73, no. 12, p. 3737–3745.

McGetchin, T. R. and Hoare, J. M., 1968, A micaceous-spinel-lherzolite fragment from Nanwaksjiak Crater, Nunivak Island, Alaska [abs.]: American Geophys. Union Trans., v. 49, no. 4, p. 760.

Ragan, D. M., 1963, Emplacement of the Twin Sisters dunite, Washington: Am. Jour. Sci., v. 261, no. 6, p. 549–565.

Raleigh, C. B., 1965, Structure and petrology of an alpine peridotite on Cypress Island, Washington, U.S.A.: Beitr. Mineralogie u. Petrographie, v. 11, p. 719–741.

——— 1968, Mechanisms of plastic deformation of olivine: Jour. Geophys. Research, v. 73, no. 16, p. 5391–5406.

Ross, C. S., Foster, M. D., and Myers, A. T., 1954, Origin of dunites and of olivine-rich inclusions in basaltic rocks: Am. Mineralogist, v. 39, nos. 7–8, p. 693–737.

Scott, D. H., 1969, The geology of the southern Pancake Range and the Lunar Crater volcanic field, Nye County, Nevada: Univ. California at Los Angeles, Ph. D. thesis, 127 p.

Talbot, J. L., Hobbs, B. E., Wilshire, H. G., and Sweatman, T. R., 1963, Xenoliths and xenocrysts from lavas of the Kerguelen Archipelago: Am. Mineralogist, v. 48, nos. 1–2, p. 159–179.

Vitaliano, C. J., and Harvey, R. D., 1965, Alkali basalt from Nye County, Nevada: Am. Mineralogist, v. 50, nos. 1–2, p. 73–84.

White, R. W., 1966, Ultramafic inclusions in basaltic rocks from Hawaii: Contr. Mineralogy and Petrology, v. 12, no. 3, p. 245–314.

Wilshire, H. G., and Binns, R. A., 1961, Basic and ultrabasic xenoliths from volcanic rocks of New South Wales: Jour. Petrology v. 2, no. 2, p. 185–208.

THE CHITISTONE AND NIZINA LIMESTONES OF PART OF THE SOUTHERN WRANGELL MOUNTAINS, ALASKA—A PRELIMINARY REPORT STRESSING CARBONATE PETROGRAPHY AND DEPOSITIONAL ENVIRONMENTS

By AUGUSTUS K. ARMSTRONG, E. M. MacKEVETT, JR.,
and N. J. SILBERLING,[1] Menlo Park, Calif.

Abstract.—Carbonate petrographic and related studies of the Chitistone and Nizina Limestones in parts of the southern Wrangell Mountains, Alaska, provide new information on the depositional history, lithology, extent, and fauna of the formations. The Upper Triassic carbonates, about 3,500 feet in maximum thickness, disconformably overlie the Nikolai Greenstone and conformably underlie the McCarthy Formation. Beds of the Chitistone Limestone reflect intertidal and supratidal conditions followed by low-energy restricted shallow-water marine deposition interspersed with high-energy shoaling-water deposition. Carbonates of the overlying Nizina Limestone formed in deeper water on the basinal slope of the drowned Chitistone carbonate platform and, during the later stages, on shallow carbonate shelves. A rapid rise in sea level terminated the carbonate deposition. Inferences on the depositional environments are corroborated by the distribution and nature of the fossils. Possibly the large Kennecott copper deposits in the lower part of the Chitistone Limestone are genetically related to thermal brines associated with the intertidal-supratidal rocks.

This report stresses petrographic studies that were made to clarify the depositional history of the Late Triassic Chitistone and Nizina Limestones. These two limestone formations are exposed intermittently throughout a northwest-trending belt about 65 miles long and 15 miles wide along the southern flank of the Wrangell Mountains (fig. 1), Alaska.

The investigations included measuring and sampling six stratigraphic sections as well as relevant laboratory studies by Armstrong, quadrangle mapping and related studies of the southern Wrangell Mountains under the direction of MacKevett, and biostratigraphic studies in the field and laboratory by Silberling. The investigations are considered to be preliminary inasmuch as only parts of the carbonate terrane were sampled and studied extensively.

[1] N. J. Silberling, also of Stanford University, Palo Alto, Calif.

The carbonate rocks studied in most detail form bold outcrops on the east side of Green Butte in the McCarthy B-5 and C-5 quadrangles (figs. 1 and 2). Other exposures carefully studied are located (1) near Boulder Creek in the McCarthy B-4 quadrangle, (2) northeast of Nikolai Creek in the McCarthy B-5 quadrangle, (3) near the Kennecott mines in the McCarthy C-5 quadrangle, (4) south of Hidden Creek in the McCarthy C-6 quadrangle, and (5) south of the Kuskulana Glacier in the McCarthy C-7 quadrangle (fig. 1).

About 200 thin sections and numerous sawed and polished rock samples were examined in the laboratory. Calcite-dolomite ratios were determined by staining with alizarine red S, using the method described by Friedman (1959).

The main objectives of the investigations were (1) to describe the carbonate petrography of the Chitistone and Nizina Limestones, (2) to determine their depositional environments and possibly document the carbonate depositional cycles, (3) to ascertain possible relationships between the carbonate rocks and the localization of the Kennecott copper lodes, and (4) to compare the carbonate rocks with other ancient and modern carbonate sequences. The classification of carbonate rocks used in this report is from Dunham (1962) and is shown in table 1.

Additional information on the distribution and general properties of the Chitistone and Nizina Limestones may be found in reports by Moffit (1938) and MacKevett (1963, 1965a, 1965b, and 1969). The sequence and age of some of the more diagnostic fossils from the Triassic rocks of the Wrangell Mountains are summarized in a report by Silberling and Tozer (1968, p. 48).

The sedimentary features and structures used to delineate intertidal and supratidal facies are described

U.S. GEOL. SURVEY PROF. PAPER 650-D, PAGES D49-D62

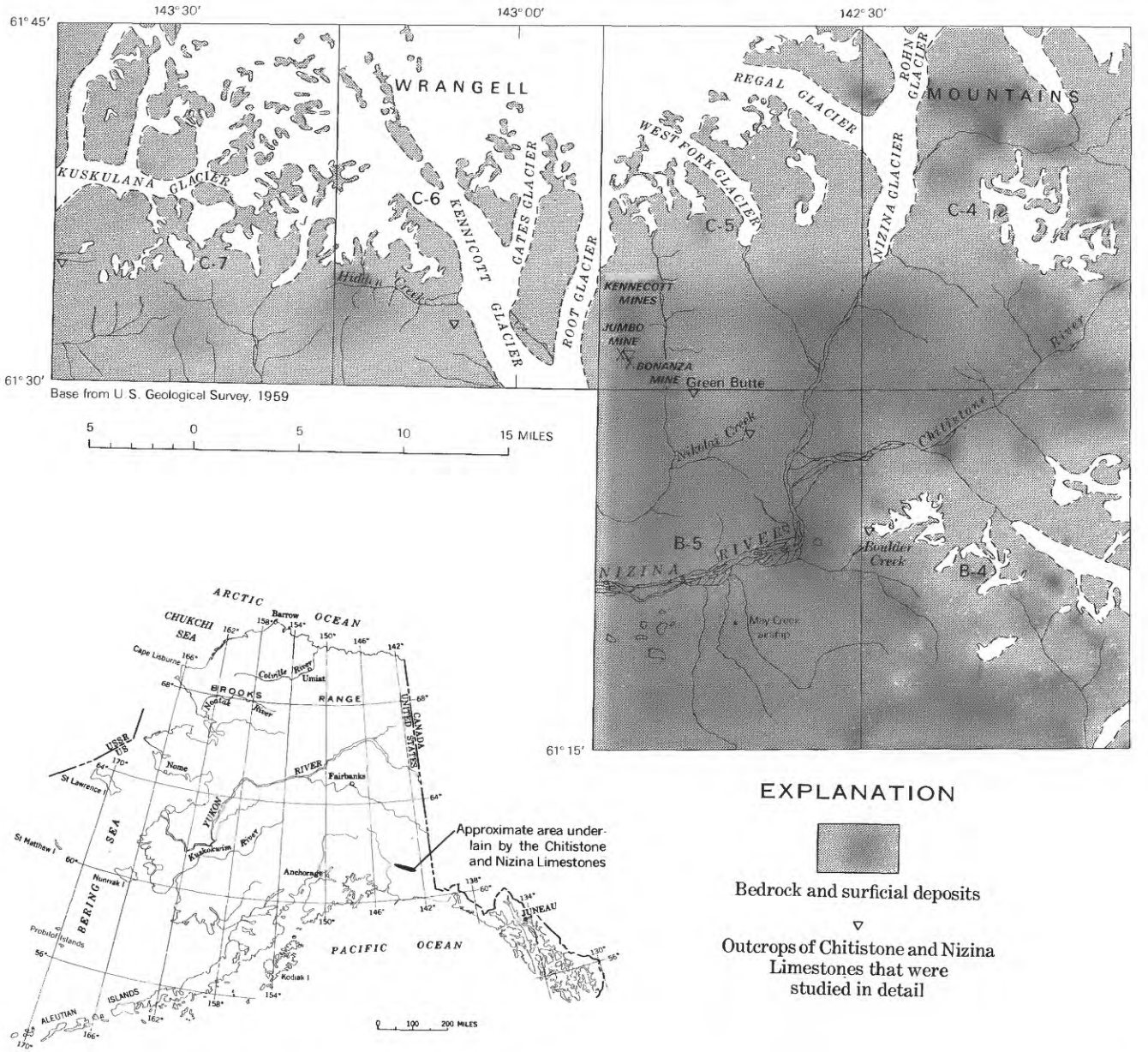

FIGURE 1.—Map of Alaska showing the approximate area underlain by the Chitistone and Nizina Limestones, and map of part of the McCarthy 1° by 3° quadrangle showing locations of the carbonate rocks studied.

in detail by Fischer (1964), Logan, Rezak, and Ginsburg (1964), Shinn, Ginsburg, and Floyd (1965), Illing, Wells, and Taylor (1965), Roehl (1967), Wilson (1967c), and Shinn (1968a); sedimentary and textural features used to define shallow marine and shelf carbonates are described by Purdy (1963), Ball (1967), and Wilson (1967a, 1967b); and the criteria for toe-of-the-slope and basinal sediments are described by Wilson (1967c) and McDaniel and Pray (1967). Detailed descriptions of these sedimentary features and how they are formed are not given in this report; the interested reader is referred to the publications listed above for details.

GENERAL DESCRIPTION AND RELATIONS

The Chitistone and Nizina Limestones form a stratigraphic sequence about 3,500 feet in maximum thickness along the southern flank of the Wrangell Mountains (fig. 1). Rohn (1900, p. 425) named the rocks of this Upper Triassic sequence the Chitistone Limestone, but subsequently Martin (1916, p. 693) applied the name Nizina Limestone to the generally thinner bedded

FIGURE 2.—Photograph of the east face of Green Butte. Locations of the measured and sampled sections shown on figure 8 are indicated by black lines and section numbers. Contact between Chitistone Limestone and the underlying Nikolai Greenstone is shown on left-hand side. Triassic carbonate section is about 3,500 feet thick. Classification of carbonate rocks is from Dunham (1962) and is shown in table 1. Trng, Nikolai Greenstone; Trc, Chitistone Limestone; Trnz, Nizina Limestone; mdst, Lime mudstone; wkst, wackstone; pkst, packstone; gnst, grainstone.

TABLE 1.—*Classification of carbonate rocks according to depositional texture*

[From Dunham, 1962, p. 117]

Depositional texture recognizable					Depositional texture not recognizable
Original components not bound together during deposition				Original components were bound together during deposition . . . as shown by intergrown skeletal matter, lamination contrary to gravity, or sediment-floored cavities that are roofed over by organic or questionably organic matter and are too large to be interstices.	Crystalline carbonate (Subdivide according to classifications designed to bear on physical texture or diagenesis.)
Contains mud (particles of clay and fine silt size)			Lacks mud and is grain supported.		
Mud supported		Grain supported.			
Less than 10 percent grains.	More than 10 percent grains.				
Mudstone	Wackestone	Packstone	Grainstone	Boundstone	

and darker rocks that constitute the upper part of the sequence. The thickness of the entire carbonate sequence and its two constituent formations differs widely; generally the Chitistone Limestone is the thicker of the two units. The Chitistone Limestone disconformably overlies the Nikolai Greenstone of late Middle and (or) early Late Triassic age. At some places the top of the greenstone is marked by a weathered zone a few inches thick. Contacts between the Chitistone and the overlying Nizina Limestone generally are broadly gradational, but locally, as near Green Butte (fig. 7), they are sharp. The Nizina Limestone is conformably overlain by the McCarthy Formation of Late Triassic and Early Jurassic age.

The Chitistone Limestone commonly consists of bedding units between 2 and 20 feet thick that form bold cliffs marked by a few caves and related solution cavities. It is mainly light, medium, or olive gray on both fresh and weathered surfaces and consists of limestone with subordinate dolomite and a few chert nodules.

The Nizina Limestone consists of limestone with subordinate chert lenses and nodules and rare grains of dolomite. Characteristic beds of the Nizina Lime-

FIGURE 3.—Dolomitic lime mudstone with algal mat chips (*A*), vugs and birdseye structures (*B*), pellets (*C*), and clasts (*D*). Collected 190 feet above the base of the Chitistone Limestone, Nikolai Creek. Shinn, Ginsburg, and Lloyd (1965, p. 119, fig. 7) illustrate a specimen similar to this from the Holocene intertidal zone of Andros Island, Bahamas.

stone range from ½ to 3 feet in thickness. They form bold outcrops but generally are more subdued than the cliffs of the Chitistone Limestone. Most of the Nizina Limestone is medium or dark gray when fresh and diverse shades of brown when weathered.

Mapping in the McCarthy B-4 quadrangle (E. M. MacKevett, Jr., and James G. Smith, unpublished data) and in the McCarthy A-4 quadrangle (Miller and MacColl, 1964), as well as supplementary paleontologic studies of the meager fauna by Silberling, indicates that contacts between the Chitistone and Nizina Limestones and between the Nizina Limestone and the McCarthy Formation transgress time boundaries.

CARBONATE PETROGRAPHY AND SEDIMENTARY STRUCTURES

Detailed petrographic studies of the Chitistone and Nizina Limestones provide information on the sedimentary history of the carbonate rocks. Much information can be deduced by comparing their properties with those of other carbonate sequences that have been studied in detail.

The basal Chitistone Limestone is marked locally by a layer of yellowish-weathering shaly limestone between 1 and 4 inches thick that is overlain by a 1- to 3-foot-thick argillaceous lime mudstone with numerous worm-tube casts and trails. Where the shaly limestone is absent, the argillaceous limestone forms the basal unit. Fossil-fragment and ooid packstones and grainstones overlie the lime mudstone and predominate throughout the lower 100 feet of the Chitistone Limestone (fig. 6*A*). Lime mudstone, dolomitic mudstone, and dolomite composed of rhombs between 100 and 200 microns long are the dominant rocks throughout the 100- to 300-foot section above the base of the Chitistone Limestone (fig. 6*B*). Most of these rocks contain well-developed birdseye structures (fig. 3) like those studied by Shinn (1968a). He believed them to be restricted to intertidal and supratidal environments. These rocks also contain algal mat chips, stromatolites, and desiccated storm layers (figs. 3 and 4)—features that according to Shinn, Ginsburg, and Lloyd (1965) and Illing, Wells, and Taylor (1965) clearly indicate intertidal or supratidal environments. The sedimentary structures indicative of such environments for the 100- to 300-foot section above the base of the Chitistone Limestone are geographically widespread. They were found in almost all the carbonate sections throughout a northwest-trending belt more than 40 miles long. Parts of this section represent an extensive intertidal-supratidal carbonate facies comparable

FIGURE 4.—Algal mat chips (*A*) and stromatolites (*B*) in a dolomitic lime mudstone, 270 feet above the base of the Chitistone Limestone, Boulder Creek. Sedimentary features of this specimen are similar to supratidal features shown by Illing, Wells, and Taylor (1965, p. 98, fig. 5) for Holocene cores taken from Sebkha Faishakn, Persian Gulf.

to the modern sebkha-wadi complex of the Trucial Coast of the Persian Gulf (Illing and others, 1965).

In most of the exposures studied, particularly those at Green Butte and south of Hidden Creek (fig. 1), about 300 feet of ooid packstone and echinoderm- and mollusk-rich wackestone directly overly the intertidal-supratidal rocks. These relatively high-energy packstones and wackestones indicate marine transgression. They are overlain by a sequence of 700 to 1,000 feet of clotted lime mudstone (fig. 6*C*) and wackestone that contains abraded and broken fragments of mollusks, ostracodes, and echinoderms. These rocks are gray to dark gray and occur in beds between 3 and 15 feet thick that contain about 5 percent nodular black chert. They are believd to represent shallow-water restricted marine shelf sedimentation.

Crossbedded packstone and grainstone more than 100 feet thick overlie the lime mudstone sequence in the middle part of the Chitistone section near Green Butte (fig. 5). This massive unit is composed of rounded fragments, generally between 0.4 and 1 millimeter in diameter, consisting of echinoderms, mollusks, brachio-

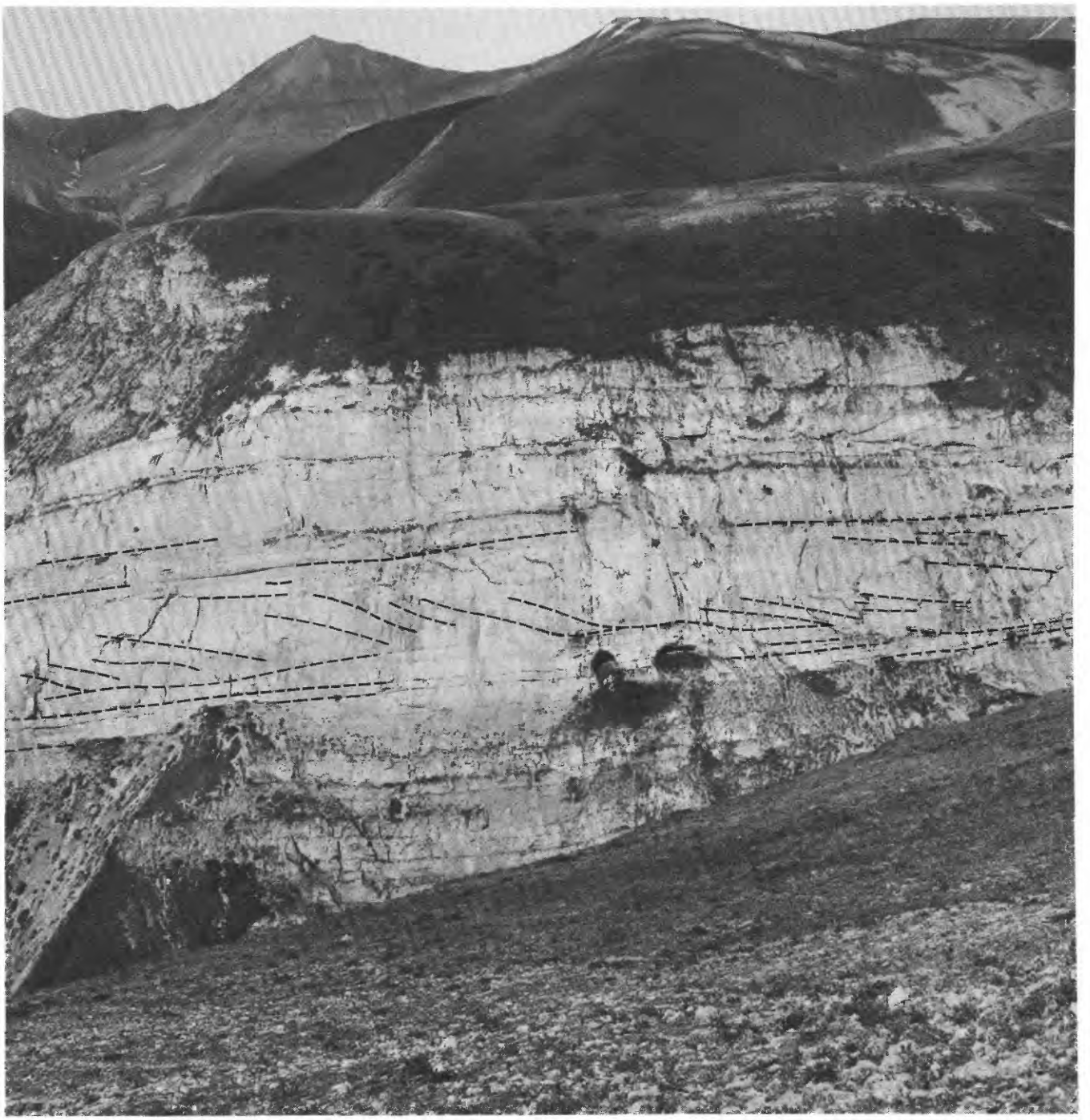

FIGURE 5.—Crossbedded oolitic grainstones, about 100 feet thick (between upper and lower dashed lines), in the central part of the Chitistone Limestone. Photograph was taken east of Green Butte. Photomicrograph of a rock specimen taken from the center of this bed is shown on figure 6*D*.

pods, calcareous algae, ooids, oolites, and large rounded lithoclasts as much as 5 mm in diameter (fig. 6*D*). On the top and bottom are horizontally stratified beds. Oolites are subordinate to rounded and sorted fossil fragments in the crossbedded sections. Except for the low percentage of oolites, the crossbedded rocks are analogous in thickness and structure to the tidal bars of calcareous sands on the modern Bahama platform that were described by Ball (1967, p. 563–571, fig. 19).

The upper part of the Chitistone Limestone above the massive crossbedded calcareous rocks is predomi-

nantly light- to dark-gray clotted lime mudstone and echinoderm-mollusk wackestone (fig. 6*E*). These beds contain three significant zones, each generally less than 100 feet thick, of packstone and grainstone (fig. 8). Two of these zones are about 200 and 400 feet above the crossbedded rocks and are composed of ooid-pelletoid-lithoclast packstone. The other zone is about 100 feet below the top of the Chitistone Limestone and consists of oolite grainstone (fig. 6*F*). All three of these zones contain grain-supported oolitic-coated particles and reflect excellent sorting—features indicative of high-energy shoaling-water depositional environments.

The lime mudstones are believed to have been deposited in shallow waters, possibly with restricted circulation, in a low-energy environment. This concept is suggested by their massive bedding and restricted fauna. Thin-section studies show that the lime mudstones are generally clotted and have undergone extensive churning by burrowing organisms (Shinn, 1968b). The massive beds of lime mudstone swell and pinch, thus suggesting that they are preserved lime mudbanks and mounds similar to those found in the shallow waters of Florida Bay. The calcareous fossil remains, with some notable exceptions, are small broken fragments, generally less than 1 mm long. The uppermost 50 feet of the Chitistone Limestone is composed of micropelletoidal grainstone.

Photographs (figs. 2 and 7) show that the lower half of the Nizina Limestone, which is mainly micropelletoidal grainstone (fig. 6*G*), contains long, lenticular, light-gray carbonate tongues. Petrographic studies show them to be lime mudstone and wackestone.

Micropelletoidal grainstones can be formed in, and are indicative of, two divergent facies. They are documented as coming from the toe-of-the-slope environment by McDaniel and Pray (1967) and Wilson (1967c) and from the open-platform environment, behind the shoaling facies and in front of the lime mudstone facies, by Wilson (1967a, p. 240, 284, pl. 3, fig. 1) and Armstrong (1967, p. 12).

An unequivocal interpretation of the environment of deposition is not possible for these pelletoidal grainstones. The writers, on the basis of field evidence, prefer the concept of a toe-of-slope environment of deposition. This preference is based on the following features: the beds are generally 6 inches to 2 feet thick, are gray in color, and contain lenticular dark-gray chert nodules and minor amounts of disseminated pyrite. The sedimentary features within the beds are small-scale crossbeds. The upper and lower surfaces of the beds may have slight undulations or oscillatory ripple marks.

Within the grainstone beds and parallel to the bedding, thin-shelled gastropods and relatively large open-sea types of pelecypods are preserved.

At Green Butte the contact between the Chitistone and Nizina Limestones is marked by pronounced lithologic and topographic changes. Thick-bedded shoaling-water lime mudstone and oolitic packstone of the Chitistone Limestone are in juxtaposition with thinner bedded, dark-gray micropelletoid grainstone of the Nizina Limestone. The present-day differences in topographic expression reflect the sharp contrast in depositional environments.

The uppermost 500 feet of Nizina Limestone near Green Butte consists predominantly of clotted lime mudstones and wackestones that contain fragments of echinoderms and mollusks. The measured section at Green Butte contains two zones of high-energy shoaling-water carbonates, each about 20 to 30 feet thick. One of the zones is about 480 feet below the top of the formation and the other about 220 feet below the top. These zones consist of grainstones and packstones that are composed of grains (0.5 to 1 mm in diameter) of rounded and coated ooids, oolites, lithoclasts, and fossil fragments including echinoderms, mollusks, foraminifers, and solenoporaceae algae. The carbonate grains are well sorted and are generally cemented by sparry calcite. The typical lime mudstone and wackestone (fig. 6*H*) of the upper part of the Nizina Limestone is dark gray and weathers brown. It forms beds between 2 and 10 feet thick and is associated with dark-gray chert nodules and lenses that are as much as 18 inches long and 5 inches thick. These rocks are believed to be the products of shallow-water shelf deposition. A 2- to 4-foot-thick bed of lime mudstone and wackestone near the top of the Nizina Limestone contains abundant disseminated pyrite and scattered echinoderm and mollusk fragments; 20 to 40 percent of the bed is black chert that forms lenses several feet long.

DEPOSITIONAL HISTORY AND CARBONATE CYCLES

Deposition of the Late Triassic carbonates commenced after a gentle widespread submergence of the continental basalt platform of Nikolai Greenstone. Early stages of the Chitistone Limestone indicate that deposition took place under widespread intertidal and supratidal conditions. Subsequently a shallow sea transgressed over the intertidal and supratidal deposits, and the bulk of the Chitistone carbonates accumulated. These rocks reflect low-energy restricted shallow-water shelf deposition interspersed with intermittent high-energy shoaling-water deposition.

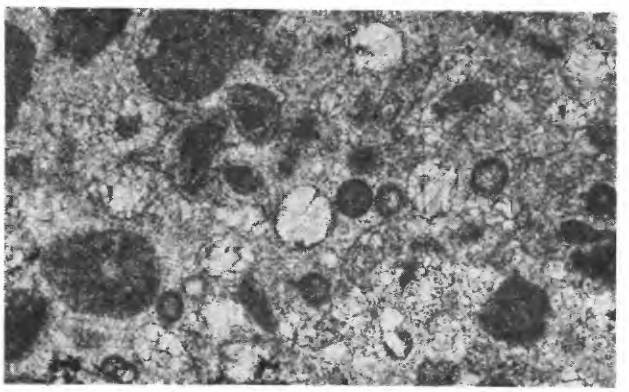

A

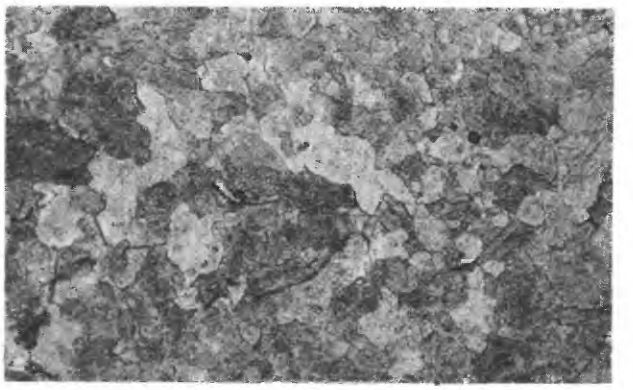

B

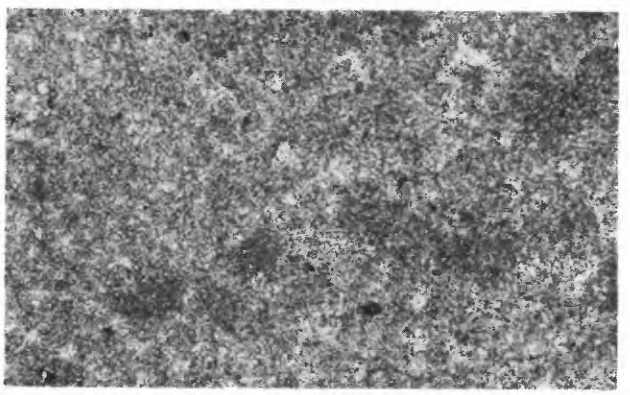

C

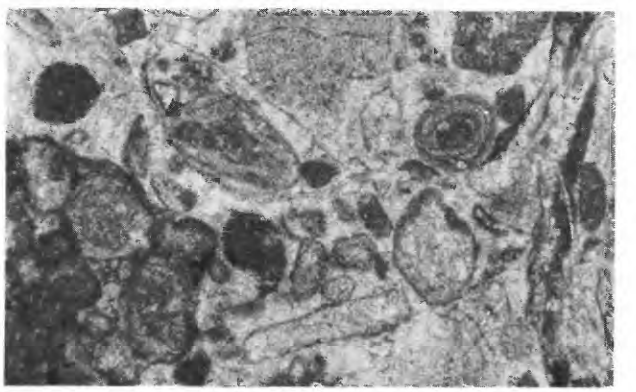

D

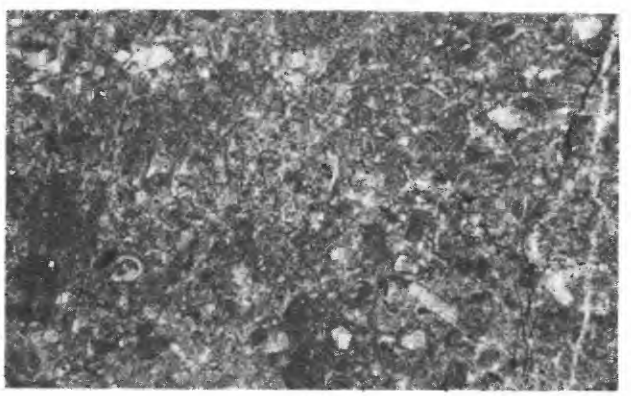

E

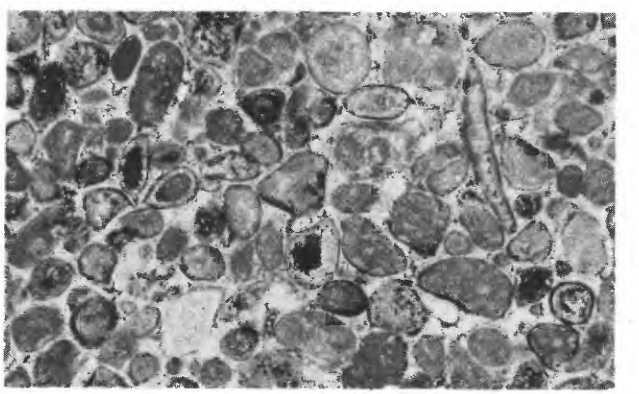

F

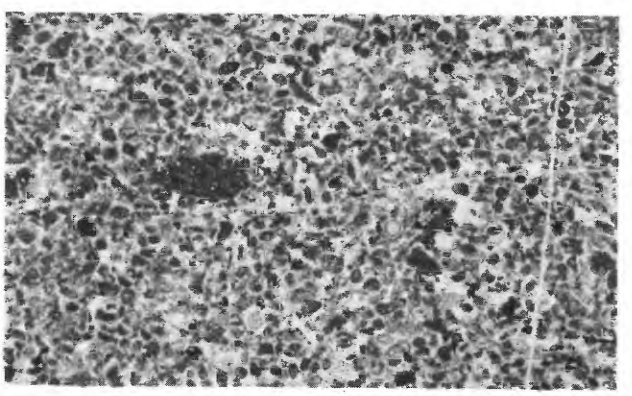

G

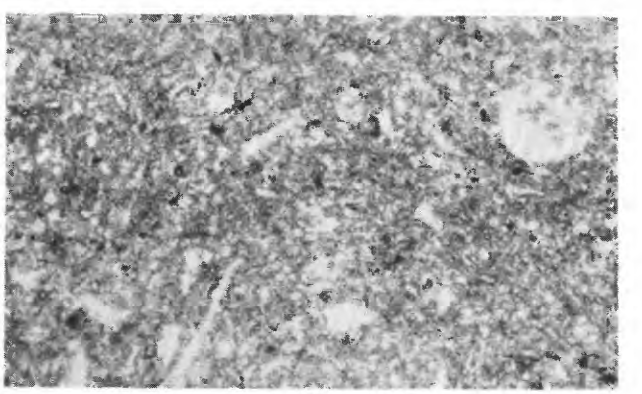

H

FIGURE 6.

Sedimentation of the Nizina Limestone commenced with the deposition of deeper water micropelletoid grainstone on the slope of the drowned Chitistone carbonate shelf platform. Most of the younger rocks probably were deposited in shallow- to shoaling-water environments typical of shelf carbonate deposits. Within the Nizina Limestone the shift in carbonate facies with time (figs. 2, 6*H*, 8) is believed to represent progradation of a shallow-water shelf carbonate facies over the deeper water slope carbonates of the lower part of the formation. The contact between the Nizina Limestone and the McCarthy Formation probably represents a rapid drowning of the Nizina carbonate shelf to a depth where carbonate production ceased. The dominant rocks near the base of the McCarthy Formation are dark-gray to black fissile shales and bedbed cherts. The shales are carbonaceous and contain scattered silt-size quartz grains; siliceous biogenic detritus (radiolarians and sponge spicules) are locally abundant. These are interpreted as indicating deep-water, starved basin sedimentation for the McCarthy Formation.

The Chitistone and Nizina Limestones may contain six incomplete carbonate depositional cycles (fig. 8). Five of these represent shallow-water shelf deposits formed during Chitistone time. Subsidence in general was slightly greater than carbonate production. Carbonate production clearly outstripped subsidence only during deposition of the lower 300 feet of the Chitistone Limestone; regional development of the intertidal-supratidal (sebkha-wadi complex of Illings and others, 1965) facies was the result. Carbonate cycles 2, 3, 4, and 5 represent subsidence and consist of ooid and oolite grainstones and packstones. The bases of cycles 3, 4, and 5 are lime mudstone on oolitic crossbedded grainstone (fig. 8).

The sharp contact between the Nizina and Chitistone Limestones at Green Butte marks the beginning of carbonate cycle 6. This cycle may reflect the partial drowning of the shallow-water Chitistone carbonate shelf and the deposition of micropelletoidal grainstone on a deeper water carbonate slope or apron. An alternate interpretation could be that the micropelletoid grainstone was deposited behind the shoaling-water facies and in front of the lime mud facies (figs. 8, 9).

MEGAFOSSILS

In addition to providing a means of dating the Chitistone and Nizina Limestones, the nature and occurrence of invertebrate megafossils in these formations tend to confirm their sedimentary history.

In this part of the Wrangell Mountains, calcareous megafossils are virtually absent in the basal few hundred feet of the Chitistone—the intertidal deposits. In the higher parts of the Chitistone that are interpreted as open to restricted platform deposits, megafossils are scarce, even though comminuted shelly debris forms a substantial proportion of the carbonate rock. Bottom-dwelling organisms are represented mainly by sporadic and isolated gastropods and ostreid pelecypods. Ammonites, mostly arcestids and haloritids, associated with the shells of halobiid pelecypods are also found in this part of the section, but in stratigraphically restricted concentrations. All these mollusks are free-swimming, floating, or attached-floating organisms that inhabited the open sea, and their occurrence suggests the occasional influx of normal marine waters into the restricted and inhospitable environment of the shelf platform. A fauna of this kind, comprising *Tropites* cf. *T. welleri* Smith, *Arcestes*, and *Halobia* cf. *H. superba* Mojsisovics, was collected about 500 feet above the base of the Chitistone at Green Butte (USGS Mesozoic loc. M1707) and is indicative of a late Karnian age.

By far the most fossiliferous rocks of the Chitistone-Nizina succession are found at the transition between these two formations. At this horizon in the Green Butte section several beds contain highly diverse,

FIGURE 6.—Photomicrographs, plane polarized light. All thin sections are from the Green Butte section. Stratigraphic location of each specimen is shown on figure 8. The suggested environment of deposition for each sample is shown in the "facies" line of figure 9. *A*, Pelletoid-ooid-echinoderm packstone. The lime mud between the particles has undergone aggrading neomorphism and is composed of 50- to 125-micron-size crystals of calcite. The specimen was collected near the Green Butte mine, 6 feet above the Nikolai Greenstone–Chitistone Limestone contact. *B*, Dolomite. Dolomite rhombs are from 200 to 400 microns in size. Specimen was collected some 230 feet above the base of the Chitistone Limestone in association with intertidal-supratidal sedimentary features. *C*, Lime mudstone with clotted pellets. The lime mudstone is composed of 5- to 10-micron-size crystals of calcite. Rare fossil fragments are ostracodes and calcispheres. This is one of the more abundant carbonate types of the Chitistone Limestone. Specimen was collected 460 feet above the base of the Chitistone Limestone. *D*, Echinoderm-mollusk-ooid-oolite-lithoclast grainstone. The specimen was collected at about the center of the crossbeded calcareous sand bed shown on figure 5. This bed is near the middle part of the Chitistone Limestone. *E*, Ostracode-echinoderm wackestones. Clotted pellets and abraded fragments of ostracodes and echinoderms suggest extensive churning by burrowing organisms. This carbonate rock type is characteristic of the upper half of the Chitistone Limestone. *F*, Ooid-oolite grainstone. Typical particles are 350 to 500 microns in diameter. Centers of the majority of ooids and oolites are composed of lime mud. Some oolites have echinoderm or mollusk fragments for centers. Specimen was collected near the top of the Chitistone Limestone. *G*, Micropelletoid grainstone. Pellets are 100 to 150 microns in diameter and have a 10- to 15-micron-thick coating. Particles also of mollusks, echinoderms, and foraminifers are present. Also present are 100- to 150-micron grains of detrital quartz. Specimen was collected 300 feet above the base of the Nizina Limestone. *H*, Echinoderm-mollusk wackestone. Clotted pellets and broken fossil fragments suggest extensive burrowing. Specimen was collected 125 feet from the top of the Nizina Limestone.

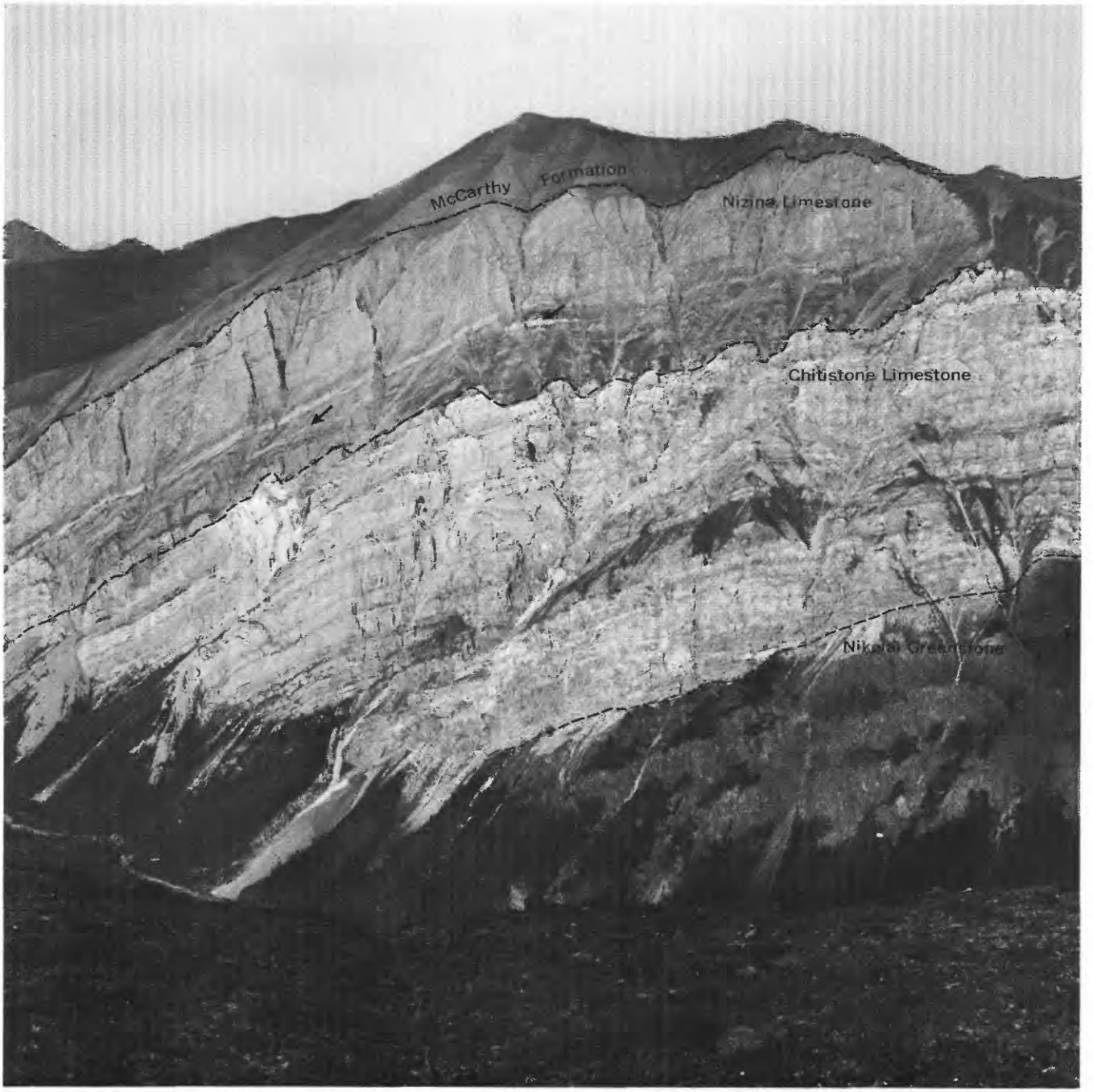

FIGURE 7.—The west face of Green Butte as viewed from the hills west of McCarthy Creek. The arrows point to light-gray limestone tongues which are believed to have been formed by submarine penecontemporaneous slides downslope from a carbonate shelf into the basinal micropelletoid grainstones in the lower part of the Nizina Limestone. Relief on the west face is 3,545 feet.

partly silicified concentrations of invertebrate megafossils that represent a latest Karnian or earliest Norian age (Silberling and Tozer, 1968, p. 48). Collections from this locality (USGS Mesozoic loc. M1708) include about 70 specifically distinct taxa of marine invertebrates, such as many different kinds of gastropods and pelecypods; several kinds of brachiopods; a variety of colonial corals and spongiomorphs; a few ammonites, nautiloids, and coleoids; crinoid columnals; echinoid spines; and calcareous worm tubes. These fossils occur as tightly packed aggregates of delicate shells, both broken and unbroken, mixed with many fragments of corals and spongiomorphs, which suggests that they accumulated more or less in

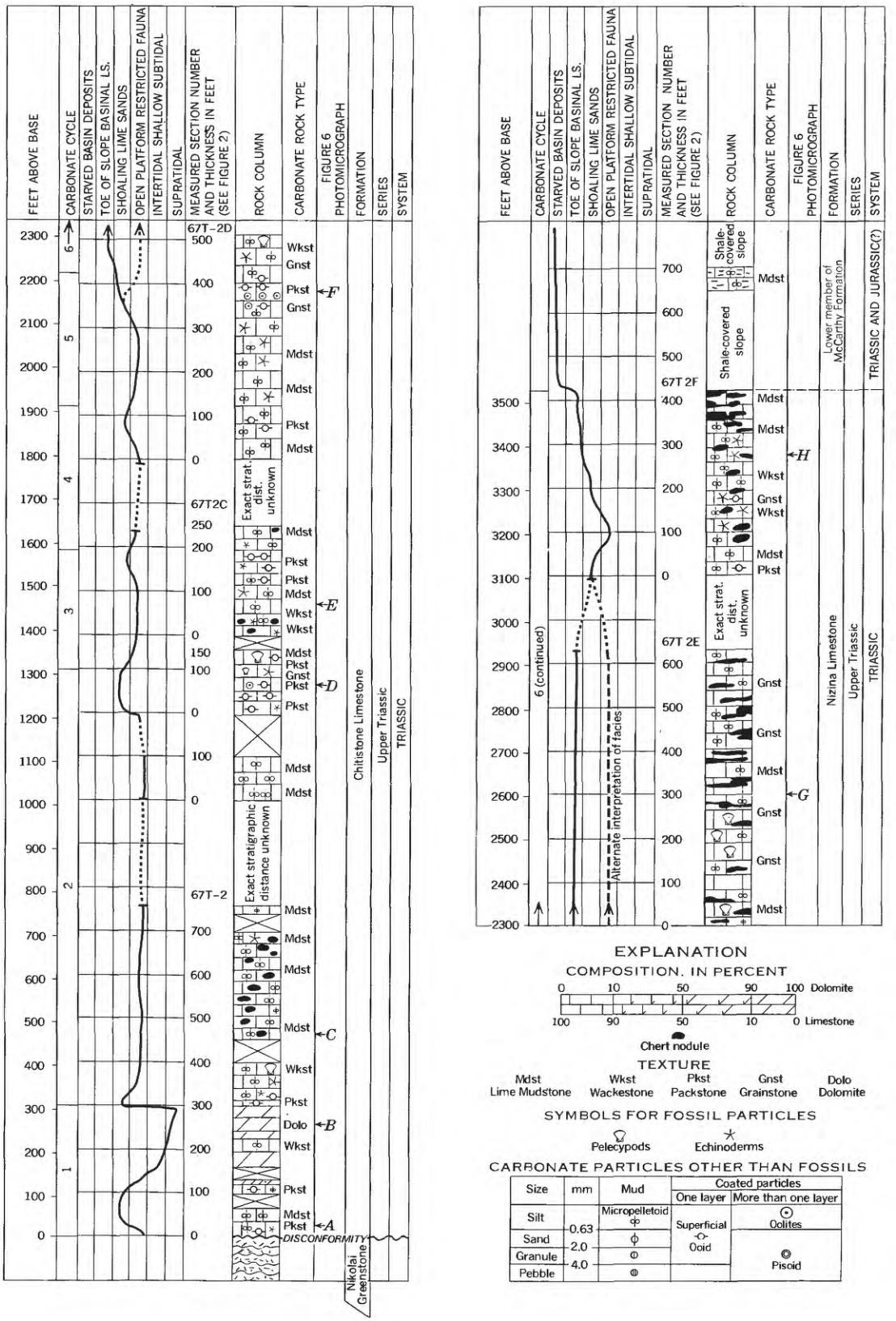

FIGURE 8.—Composite Upper Triassic stratigraphic section at Green Butte. Location of each of the stratigraphic segments is shown on figure 2. The environmental interpretation is shown to the left of the rock column, and the possible carbonate cycles are also listed. To the right of the rock column the stratigraphic positions of the photomicrographs shown on figure 6 are listed.

place and have not been extensively reworked or redeposited by submarine sliding. Similar, though taxonomically less diverse, occurrences have also been found elsewhere in the McCarthy quadrangle in the basal part of the Nizina Limestone.

At Green Butte this fauna occurs about 100 feet above the well-sorted oolitic beds which are near the top of the Chitistone Limestone. These beds are believed to be shoal lime sands deposited at the seaward edge of the carbonate platform. The fauna is found in the lower part of the slope basinal limestones and appears to represent the assemblage that flourished in the shallow waters just seaward from the lime sand shoals where the greatest abundance and diversity of marine life would be expected to occur (Purdy, 1963, p. 495, fig. 4).

In the higher parts of the Nizina Limestone, megafossils are not uncommon, though rarely are they well preserved. Brachiopods, gastropods, ammonites, and pelecypods were collected from a number of localities during the present study and in the course of the geologic mapping. Among the pelecypods, floating or attached-floating shells of *Halobia* are well represented, as are certain bottom-dwelling forms, especially those tentatively referred to as *Gryphaea*.

In the beds transitional from the Nizina into the overlying shales and cherts of the McCarthy Formation a few miles northeast of Green Butte (at USGS Mesozoic loc. M1695), a poorly preserved ammonite fauna includes the distinctive genus *Pterotoceras*—an early middle Norian age form. Thus the 3,500 feet of Upper Triassic carbonate rocks of the Chitistone and Nizina Limestones in this part of the Wrangell Mountains ranges in age from late Karnian through the early part of the Norian.

DEPOSITIONAL MODEL

The Chitistone and Nizina Limestones are lithologically and stratigraphically similar to many other carbonate sequences of various ages in other parts of the world. They are composed predominantly of lime mud and particles formed of lime mud. They record deposition on a broad slowly subsiding carbonate platform separated from an offshore submarine slope by a relatively narrow partial barrier of shoal lime sands. Although shelly marine life flourished on the seaward edge of the lime shoals and contributed much fine-grained calcareous detritus to the shoals and platform, organic reefs evidently were not developed at the platform edge. On the platform, shoreward of the shoals, the environment was evidently inhospitable to most kinds of marine invertebrate animals.

The Chitistone and Nizina Limestones have not yet been studied over a large enough area to determine the paleogeography of the carbonate shelf on which they were deposited, but some measure of its dimensions is suggested by the occurrence of correlative carbonate rocks to the east in nearby parts of the Yukon Territory, Canada. The 500 feet of limestone in the Mush Lake Group, which is exposed 100 to 140 miles east of the Kennecott district, is correlated by Muller (1967, p. 50, 54) with the Chitistone and Nizina Limestones and is described as being mostly massive, indistinctly bedded, yellowish- and reddish-weathering limestone including some gypsum and anhydrite. The occurrence of evaporites in these rocks suggests that they represent the far inshore part of the carbonate platform.

A modern analog of this Upper Triassic carbonate shelf, but possibly on a smaller scale, is the area of deposition of lime mud sediments in Florida Bay which extends some 150 miles east of the seaward western edge of the Florida Platform (Ball, 1967, p. 577–579). A similar, but somewhat poorer, model is the area of deposition of lime mud and soft pellet lime mud in the shallow waters on the west side of the Bahama Banks adjacent to Andros Island (Purdy, 1963, fig. 1). The bulk of the lime mudstone in these modern carbonate deposits may be formed of the clay-size (less than 15 micron) particles produced in the tissue of shallow-water green algae like *Penicillus* (Stockman and others, 1967).

A model of a long ramp platform illustrating the various depositional environments for the Chitistone and Nizina Limestones is shown on figure 9. The significant or diagnostic rock types found in each environment are also shown. The thickness of any one carbonate facies at any given geographic location depends upon the rate of subsidence and the rate of carbonate deposition. For example, the shoaling sand belt shown on figure 9 would move to the right or landward, with a rise of sea level, and to the left or seaward with a fall of sea level. Equilibrium between the rate of subsidence and the rate of carbonate production would result in a very thick section of shoaling-water carbonate sand. (For further discussion of these principles see Macqueen and Bamber, 1968, p. 266–269; Armstrong, 1967, p. 9–11; Wilson, 1967c; Ginsburg, 1966; Kinsman, 1966.)

CARBONATE ROCKS NEAR THE KENNECOTT MINES—POSSIBLE RELATION TO ORE DEPOSITION

The large copper deposits at the Kennecott mines are localized in the lowermost few hundred feet of the Chitistone Limestone—a localization that suggests a strong stratigraphic influence. Between 1908 and 1938,

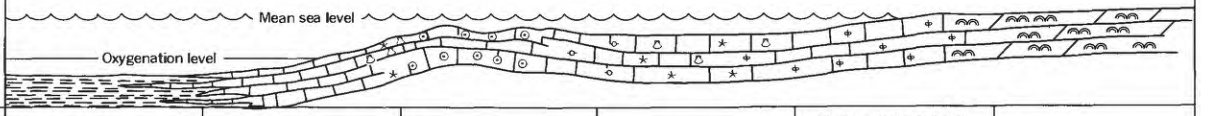

FACIES	Starved-basin shales, radiolarian cherts	Toe-of-slope basinal limestones	Shoal lime sands	Open platform limited fauna	Shallow, restricted subtidal marine, tidal channels, intertidal	Supratidal, sebkhas, and ponds
LITHOLOGY	Dark-gray to black shales	Dark lime mudstone, micropelletoid grainstones	Light-colored limestones, fossil fragments, oolitic	Lime mudstones, clotted fossilferous wackestones, micropelletoid grainstones	Clotted lime mudstones, dolomitic, and dolomites	Stromatolitic, birdseye lime mudstones, dolomites
PHOTOMICROGRAPHS OF LITHOLOGY, FIGURE 6	None	*G*	*A,D,F*	*E,H,G*	*B,C*	(See figures 3,4)
BEDDING AND SEDIMENTARY STRUCTURES	Fissile shales	Fine laminae, microcut-and-fill structures, rare burrows	Small to massive crossbeds	Burrows	Burrows, birdseye structures, algal chips, stromatolites, tidal channel cut and fills	Birdseye structures, algal chips, stromatolites
SECONDARY INTERBEDDED TERRIGENOUS CLASTICS	Dark shale, silt-size quartz sand	Rare silt-size and smaller quartz sand	None	None	None	None
FORAMINIFERS	None to rare	Common	Common	Common	None	None
OSTRACODES	None	Rare	Rare	Common	Common	None
GASTROPODS	Rare	Rare to common	Common	Common	Rare	None
PELECYPODS	Rare to common	Common	Common	Common	Rare	None
AMMONITES	Rare to common	Rare to common	None	Rare	None	None
ECHINODERMS	None	Rare to common	Common	Common	Rare	None

FIGURE 9.—Depositional model for the Upper Triassic carbonate facies. (No horizontal scale intended.)

when the mines were operated on a large scale, they were among the world's leading copper producers and were noted for the size and tenor of their chalcocite-rich lodes.

The carbonate rocks of the lower parts of the Chitistone Limestone were investigated near the two largest Kennecott mines, the Bonanza and the Jumbo (fig. 1). The lowermost 70 feet of Chitistone Limestone at these mines consists of lime mudstone and an underlying 4-inch-thick layer of shaly limestone. Calcitic pellets are dominant in the mudstone and are between 10 and 20 microns in diameter. The lime mudstone here is petrographically similar to lime mudstones elsewhere near the base of the Chitistone Limestone. Similarities are found in the size and shape of the pellets and in the content of fragmented calcispheres, echinoderms, and mullusks. It differs from other Chitistone lime mudstones in containing abundant disseminated pyrite and a few scattered copper minerals.

The rocks between 70 and 350 feet above the base of the Chitistone Limestone near the Bonanza and Jumbo mines are markedly different from those studied elsewhere. They consist of dolomite composed of rhombs, from 100 to 200 microns long, and calcite pore fillings. The dolomite is massive and contains numerous lithoclasts and breccia zones that probably are of tectonic origin. Most of the ore was localized in the dolomite, although some extends downward into the lime mudstone. Most of the dolomite is believed to have been deposited from hydrothermal solutions moving through an extensive breccia zone. Consequently, the lithologic and sedimentary features of the rocks that originally occupied this zone have been either obliterated or replaced. Probably these rocks were originally intertidal and supratidal phases, similar to rocks in the lower part of the other Chitistone successions elsewhere. Conceivably both the ore deposition and the pyritization were related to the hydrothermal activity that produced the dolomitization.

Study of the depositional environment of the Chitistone Limestone and the distinctive properties of the host rock for the Kennecott ores could provide significant information about the genesis of the Kennecott deposits. An attractive speculation is that thermal brines played dominant roles in the ore formation. The importance of such brines as metal carriers has recently been emphasized by several geologists, notably White (1967, 1968) and Davidson (1965). Such brines are potent solvents of copper and many other metals, and they conceivably could also carry sulfur derived from supratidal evaporite deposits. Supratidal environments would be favorable sites for the generation of these brines. The brines could have been heated and mobilized during the major regional orogeny, near the close of the Jurassic or in the Early Cretaceous, or during the early stages of the extensive Tertiary vulcanism

when Wrangell Lava was erupted and the plutons were emplaced. The thermal brines could have acquired their copper by migrating through parts of the copper-rich subjacent Nikolai Greenstone and subsequently rising to the brecciated dolomite, where conditions were favorable for ore deposition.

REFERENCES

Armstrong, A. K., 1967, Biostratigraphy and carbonate facies of the Mississippian Arroyo Penasco Formation, north-central Mexico: New Mexico Bur. Mines and Mineral Resources Mem. 20, 80 p., 10 pls., 45 figs.

Ball, M. M., 1967, Carbonate sand bodies of Florida and the Bahamas: Jour. Sed. Petrology, v. 37, no. 2, p. 556–591, figs. 1–40.

Davidson, C. F., 1965, A possible mode of origin of strata-bound copper ores: Econ. Geology, v. 60, p. 942–954.

Dunham, R. J., 1962, Classification of carbonate rocks according to deposition texture, *in* Classification of carbonate rocks—A symposium: Am. Assoc. Petroleum Geologists Mem. 1, p. 108–121.

Fischer, A. G., 1964, The Lofer cyclothems of the Alpine Triassic, *in* Merriam, D. F., Symposium on cyclic sedimentation: Kansas Geol. Survey Bull., v. 169, no. 1, p. 107–149.

Friedman, G. M., 1959, Identification of carbonate minerals by staining methods: Jour. Sed. Petrology, v. 29, no. 1, p. 87–97.

Ginsberg, R. N., 1966, Introduction to Recent sedimentation, [9 leaves] *in* South Florida carbonate sediments, *of* Pt. 3, Recent carbonate environments: Soc. Econ. Paleontologists and Mineralogists, Permian Basin Sec., 11th Ann. Mtg., Midland, Tex., 1966, Carbonate Seminar [manual].

Illing, L. V., Wells, A. J., and Taylor, J. C. M., 1965, Penecontemporary dolomite in the Persian Gulf, *in* Pray, L. C., and Murray, R. C., eds., Dolomitization and limestone diagenesis, a symposium: Soc. Econ. Paleontologists and Mineralogists Spec. Pub. 13, p. 89–111.

Kinsman, D. J. J., 1966, Intertidal and supratidal sedimentation—penecontemporaneous dolomitization, [2 leaves] *in* Outline and Notes for lecture 3, *of* Pt. 3, Recent carbonate environments: Soc. Econ. Paleontologists and Mineralogists, Permian Basin Sec., 11th Ann. Mtg., Midland, Tex., 1966, Carbonate Seminar [manual].

Logan, B. W., Rezak, R., and Ginsburg, R. N., 1964, Classification and environmental significance of algal stromatolites: Jour. Geology, v. 72, no. 1, p. 68–83, 5 figs.

McDaniel, P. N., and Pray, L. C., 1967, Bank to basin transition in Permian (Leonardian) carbonates, Guadalupe Mountains, Texas [abs.]: Am. Assoc. Petroleum Geologists Bull., v. 51, no. 3, p. 474.

MacKevett, E. M., Jr., 1963, Preliminary geologic map of the McCarthy C-5 quadrangle, Alaska: U.S. Geol. Survey Misc. Geol. Inv. Map I–406, scale 1:63,360.

——— 1965a, Preliminary geologic map of the McCarthy B-5 quadrangle, Alaska: U.S. Geol. Survey Misc. Geol. Inv. Map I–438, scale 1:63,360.

——— 1965b, Preliminary geologic map of the McCarthy C-6 quadrangle, Alaska: U.S. Geol. Survey Misc. Geol. Inv. Map I–444, scale 1:63,360.

MacKevett, E. M., Jr., 1969, Geologic map of the McCarthy C-4 quadrangle, Alaska: U.S. Geol. Survey Geol. Quad. Map GQ–844, scale 1:63.360. [In press]

Macqueen, R. W., and Bamber, E. W., 1968, Stratigraphy and facies relationships of the Upper Mississippian Mount Head Formation, Rocky Mountains and Foothills, southwestern Alberta: Canadian Petroleum Geology Bull., v. 16, no. 3, p. 225–287.

Martin, G. C., 1916, Triassic rocks of Alaska: Geol. Soc. America Bull., v. 27, p. 685–718.

Miller, D. J., and MacColl, R. S., 1964, Geologic map and sections of the northern part of the McCarthy A-4 quadrangle, Alaska: U.S. Geol. Survey Misc. Geol. Inv. Map I-410, scale 1:63,360.

Moffit, F. H., 1938, Geology of the Chitina Valley and adjacent area, Alaska: U.S. Geol. Survey Bull. 894, 137 p.

Muller, J. E., 1967, Kluane Lake map area, Yukon Territory (11fG, 115F E½): Canada Geol. Survey Mem. 340, 137 p.

Purdy, E. G., 1963, Recent calcium carbonate facies of the Great Bahama Bank—[Pt.] 2, Sedimentary facies: Jour. Geology, v. 71, no. 4, p. 472–497.

Roehl, P. O., 1967, Stony Mountain (Ordovician) and Interlake (Silurian) facies analogs of Recent low-energy marine and subaerial carbonates, Bahamas: Am. Assoc. Petroleum Geologists Bull., v. 51, no. 10, p. 1979–2032.

Rohn, Oscar, 1900, A reconnaissance of the Chitina River and the Skolai Mountains, Alaska: U.S. Geol. Survey 21st Ann. Rept., pt. 2, p. 399–440.

Shinn, E. A., 1968a, Practical significance of birdseye structures in carbonate rocks: Jour. Sed. Petrology, v. 38, no. 1, p. 215–223, figs. 1–13.

——— 1968b, Burrowing in recent lime sediments of Florida and the Bahamas: Jour. Paleontology, v. 42, no. 4, p. 879–894, pls. 109–112, figs. 1–17.

Shinn, E. A., Ginsburg, R. N., and Lloyd, R. M., 1965, Recent supratidal dolomite from Andros Island, Bahamas, *in* Pray, L. C., and Murray, R. C., eds., Dolomitization and limestone diagenesis, a symposium: Soc. Econ. Paleontologists and Mineralogists Spec. Pub. 13, p. 112–123.

Silberling, N. J., and Tozer, E. T., 1968, Biostratigraphic classification of the marine Triassic in North America: Geol. Soc. America Spec. Paper 110, 63 p.

Stockman, K. W., Ginsburg, R. N., and Shinn, E. A., 1967, The production of lime mud by algae in south Florida: Jour. Sed. Petrology, v. 37, no. 2, p. 633–648, figs. 1–14.

White, D. E., 1967, Mercury and base metal deposits with associated thermal and mineral waters, *in* Barnes, H. L., ed., Geochemistry of hydrothermal ore deposits: New York, Holt, Rinehart and Winston, Inc., p. 575–631.

——— 1968, Environments of generation of some base-metal ore deposits: Econ. Geology, v. 63, no. 4, p. 301–335.

Wilson, J. L., 1967a, Carbonate-evaporite cycles in Lower Duperow Formation of Williston Basin: Canadian Petroleum Geology Bull., v. 15, no. 3, p. 230–312, 22 pls., 14 figs.

———1967b, Cyclic and reciprocal sedimentation in Virgilian strata of southern New Mexico: Geol. Soc. America Bull., v. 78, no. 7, p. 805–818, 4 pls., 4 figs.

——— 1967c, Microfacies and sedimentary structures in deeper-water lime mudstones [abs.]: Am. Assoc. Petroleum Geologists Bull., v. 51, no. 3, p. 485–486.

PINK COPPER-BEARING PREHNITE FROM ISLE ROYALE NATIONAL PARK, MICHIGAN

By N. KING HUBER, Menlo Park, Calif.

Abstract.—Pink prehnite, occurring as amygdules in Keweenawan lava flows in Isle Royale National Park and elsewhere in the Lake Superior region, has commonly been misidentified as thomsonite, which it superficially resembles. The pink color of the prehnite is due to internal reflections from finely disseminated native copper inclusions.

Isle Royale has long been considered an important source for thomsonite, a mineral that in the Lake Superior region commonly produces attractive gemstones. Mineralogic studies, carried out as part of a broader geologic study of Isle Royale National Park in cooperation with the U.S. National Park Service, indicate that material often called thomsonite is actually a pink copper-bearing prehnite. The pink prehnite has a radiating fibrous habit and occurs as amygdules in volcanic flows of Keweenawan age as does much of the thomsonite of the Lake Superior region. Although the pink prehnite superficially resembles thomsonite, it does not develop the spectacular patterns and color variations present in gem quality thomsonite, which explains why "Isle Royale thomsonites" have always been considered to be of inferior gem quality (W. J. Bingham, lapidary, oral commun., 1967).

Prehnite is an abundant secondary mineral in lava flows of the Keweenawan Series in the Lake Superior region. It occurs as amygdule fillings, crosscutting veins, and as replacement of earlier minerals or rock. Most of the prehnite has the normal pale-green to white color characteristic of this mineral, but where it occurs in amygdules it is commonly light to dark pink or variously mottled in pink and green. On Isle Royale such amygdules occur in flows throughout the stratigraphic section but appear to be especially abundant in amygdaloidal flow tops at only two horizons, over 5,000 feet apart stratigraphically.

The prehnite amygdules, which most commonly range in size from ½ to 1 centimeter, are more resistant to weathering than the volcanic matrix within which they have formed. As a result, the rock outcrops and beach pebbles often have a knobby appearance, the amygdules projecting above the general surface of the matrix (fig. 1). Where the prehnite amygdules weather free from the matrix, they may make up a fair percentage of the fine gravel on beaches near the prehnite-bearing outcrops.

The amygdules in figure 2 are typical and illustrate the radiating fibrous habit of the prehnite, with the occasional development of "eyes." From samples collected throughout the park it is clear that the anomalous pink color of the prehnite and the color intensity are related to the distribution and grain size of native copper inclusions.

The purposes of this report are to point out that prehnite (on Isle Royale) has previously been mis-

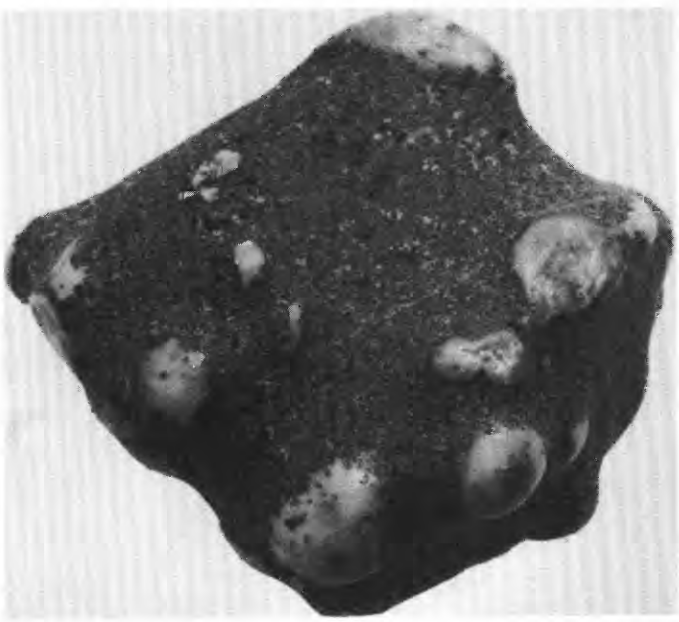

FIGURE 1.—Beach pebble derived from basaltic lava flow containing pink prehnite amygdules. Long dimension of pebble is 5 cm.

U.S. GEOL. SURVEY PROF. PAPER 650–D, PAGES D63–D68

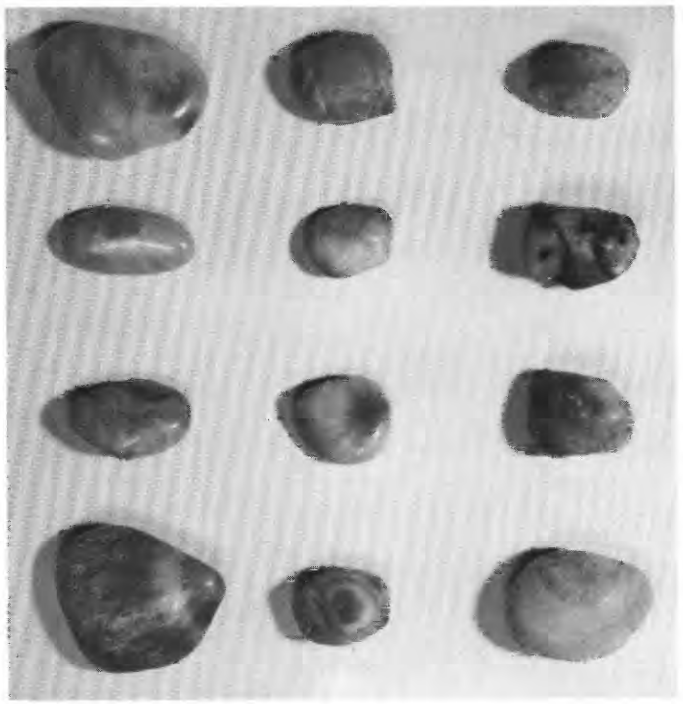

FIGURE 2.—Pink prehnite amygdules from beach on Shaw Island in Isle Royale National Park. Note radiating fibrous structure with development of "eyes." Largest amygdule is 2 cm across.

identified as thomsonite and to present some data on the quantity and distribution of native copper in some pink prehnite amygdules from Isle Royale National Park.

Acknowledgments.—It was extremely difficult to obtain meaningful black and white photomicrographs of the prehnite amygdules with native copper inclusions. The present photomicrographs are the results of the patient effort of Norman Prime, of the U.S. Geological Survey photographic laboratory.

HISTORICAL BACKGROUND

The pink copper-bearing prehnite, with its radiating fibrous habit and development of "eyes," has commonly been mistaken for thomsonite, which it superficially resembles. Dobell (1966) points out that although pink prehnite pebbles from beaches on the Keweenaw Peninsula of Michigan are commonly confused with thomsonite, they can be readily distinguished from thomsonite on the basis of specific gravity and hardness. Prehnite also tends to be somewhat more translucent than thomsonite, and, with experience, the two minerals can usually be differentiated visually. Nevertheless, prehnite pebbles continue to be sold as thomsonite in some rock shops.

With specific reference to Isle Royale, confusion of pink prehnite with thomsonite can be traced at least as far back as 1898. In his classic report on Isle Royale, Lane (1898, p. 165) states that, "* * * thomsonite is a very common zeolite on the island * * *," and notes (1898, p. 207) that, "* * * thomsonite amygdules * * * are abundantly collected on the beaches * * *." The beaches mentioned are along the north coast of the island where one of the pink-prehnite-bearing amygdaloidal zones is exposed. Indeed, one such beach was called Thomsonite Beach on Lane's geologic map and continues to be so labeled on the current (1957) U.S. Geological Survey topographic map of Isle Royale. Pink prehnite is abundant on these beaches and in adjacent outcrops, but a search during the present study yielded only a few pebbles containing thomsonite amygdules and a few free thomsonite amygdules. Thomsonite was not found in outcrop, and the source of the material, although probably local, remains uncertain in this glaciated terrane.

It is somewhat surprising that Lane fell into this error as he did recognize pink prehnite elsewhere on the island (1898, p. 165), and admitted that he had not seen thomsonite in the many thin sections examined by him (1898, p. 168). He was aware of the similarity of the two minerals, however, for he later stated (1911, p. 125) that, "In casual examination of drill cores I may have often confused this [thomsonite] with a pink fibrous radiating prehnite which also occurs * * *."

Because much thomsonite from the Lake Superior region (especially that from Grand Marais, Minn.) makes attractive gems when cut en cabochon, it has been avidly searched for by collectors, and abundant references to it can be found in the popular literature. Only a few specific references to Isle Royale will be mentioned here.

In 1931, Fred Dustin, who was primarily engaged in archeological studies of Isle Royale, published a paper entitled, "Gems of Isle Royale, Michigan," in which thomsonite is described as being abundant, possibly following Lane. This paper, as the first to cite detailed locality data for collecting, may be responsible for entrenching the belief that pink prehnite at these localities was thomsonite and helped to perpetuate the continuing misidentification of the prehnite. It also undoubtedly accounts for some errors in mineral identifications in the museum collection of the National Park Service.

Waite (1961), who also visited Isle Royale, cites Dustin's localities, as well as some additional ones, as sources of thomsonite. Neither Lane, Dustin, nor Waite present any substantiating data for their thomsonite identifications; they all appear to have been visual

ones. In their defense, I shall admit that during my first summer on the island, prior to making any definitive tests on material collected, I, too, misidentified the pink prehnite as thomsonite, having collected thomsonite at Grand Marais, Minn., in my youth.

Most recent popular gemology books that include thomsonite also cite Isle Royale as an abundant source (for example, Pearl, 1964; Sinkankas, 1959). These books by their nature are largely compilations, however, and errors such as this can usually be traced back to earlier references. Sinkankas does indeed list Dustin's article in his bibliography, and the localities cited are identical with those of Dustin. The technical literature also continues to bear incorrect references to thomsonite on Isle Royale, based at least in part on earlier reports (for example, Stoiber and Davidson, 1959, table 1). All of the "thomsonite" localities cited in the literature for Isle Royale were visited during the course of the present study. At each one, pink prehnite amygdules were abundant; thomsonite was found only rarely.

Reinforcing the conclusion that pink prehnite has been mistaken for thomsonite on Isle Royale is the fact that most writers, including Dustin and Waite, describe green prehnite (and sometimes yellowish or whitish) from the island but never pink prehnite (except for Lane). In addition, Waite (1961, p. 450) states that "Isle Royale thomsonites" are inclined to more uniform shades than thomsonite from Grand Marais, Minn., a comparison that is quite valid for pink prehnite and Minnesota thomsonite.

Thomsonite occurs on the Keneenaw Peninsula, some 40 miles to the southeast of Isle Royale, in flows stratigraphically equivalent to those on the island (Butler and Burbank, 1929; Stoiber and Davidson, 1959; Cornwall, 1954; and other local geologic quadrangle maps), and at a famous collecting locality near Grand Marais, Minn., some 50 miles southwest of the island, in flows stratigraphically below those on the island (Hey, 1932; Hanley, 1939). Thus it would not be surprising to find abundant thomsonite on Isle Royale; therefore some of the reports of its occurrence there are difficult to evaluate. For example, Kraus and Slawson (1947, p. 268) illustrate specimens said to be thomsonite and to have come from Isle Royale. There are additional specimens of authentic thomsonite in the National Park Service museum collection, but as locality data for these donated specimens are not available, their point of origin is uncertain; their appearance is similar to Grand Marais material. In the present study, the only thomsonite found consists of amygdules in a few pebbles and a few loose amygdules from the north shore of the island; its identification was substantiated by X-ray diffraction analysis. It is clear that thomsonite is not as common on Isle Royale as the earlier literature would suggest, and that pink prehnite has often been mistaken for thomsonite.

In summary, table 1 indicates some criteria for readily distinguishing between prehnite and thomsonite of similar appearances; X-ray diffraction patterns are, of course, also diagnostic.

TABLE 1.—*Criteria for distinguishing between prehnite and thomsonite of similar appearance* [1]

	Prehnite	Thomsonite
Hardness	6–6½	5–5½
Specific gravity	2. 80–2. 95	2. 25–2. 40
Refractive index	1. 614–1. 665	1. 511–1. 545

[1] Data from Winchell (1951).

Misidentifications notwithstanding, the existence of fibrous pink prehnite, as well as some idea of the nature of its coloring, was noted very early in studies of Isle Royale geology. J. W. Foster and J. D. Whitney, in the first comprehensive report on the geology of the Lake Superior region, describe pebbles of fibrous "faint flesh-red" prehnite (1851, p. 106–107). They attributed the color, however, to a "suboxide of copper," rather than to native copper. They present an analysis of one specimen indicating 1.04 percent "suboxide of copper." The rest of the analysis compares quite favorably with modern analyses of prehnite.

Lane recognized that the pink color of the prehnite amygdules was due to very fine inclusions of native copper. In his Isle Royale report (1898, p. 165), he refers to a specimen of prehnite, "* * * which shows copper crystals under the microscope, [and] shows a light-flesh-pink color to the naked eye." In his 1911 report on the Keweenaw series of Michigan, there are 13 entries under the index heading, "Prehnite, pink, copper bearing" (Lane, 1911, p. 975), and there are numerous other references to pink prehnite in the text. For example, on page 847, he notes that "* * * prehnite and datolite * * * both frequently occur in nature colored pink with finely divided copper."

PREHNITE WITH NATIVE COPPER

Isle Royale National Park includes a large island, Isle Royale, and numerous smaller islands. Pink prehnite amygdules were collected from the upper prehnite amygdaloidal zone on one of the smaller islands, Shaw Island, and green prehnite with euhedral crystal terminations, occurring in vuggy veins with quartz and calcite, was collected from adjacent Tooker's Island. Both contain native copper, but in the pink prehnite the copper is finely disseminated throughout, whereas

in the green prehnitic vein material the copper is in larger irregular masses with virtually no fine dispersed material. X-ray diffraction curves for the pink and the green prehnite are virtually identical (table 2). The many pink prehnite amygdules examined from various localities in the park have similar X-ray patterns and physical properties, and all fall within ranges indicated in table 1, except for specific gravity, which is often somewhat higher than the indicated maximum of 2.95 (up to 3.07 as determined by Jolly balance on entire amygdule). The higher specific gravities are usually obtained on darker pink material having more readily visible particles of copper (specific gravity of pure prehnite will be increased by about 0.06 for each percent of copper content).

TABLE 2.—*X-ray diffraction powder data for prehnite*
[Copper radiation]

1		2		3	
d (angstroms)	I/I_1	*d* (angstroms)	I/I_1	*d* (angstroms)	I/I_1
		9.30		9.30	
5.28	10	5.28		5.29	
4.60	20	4.62		4.66	
4.15	10	4.14		4.16	
3.53	10	3.54		3.55	
3.48	90	3.48	Major peak.	3.49	Major peak.
3.28	60	3.29		3.31	
3.08	100	3.08	Major peak.	3.09	Major peak.
2.81	30	2.81		2.82	
2.62	5	2.63		2.64	
2.55	100	2.56	Major peak.	2.57	Major peak.
2.37	40	2.36		2.37	
2.31	40	2.31	Major peak.	2.32	Major peak.
2.07	20	2.07		2.08	
1.93	30	1.93		1.94	
1.84	20	1.85		1.86	
1.77	70	1.77	Major peak.	1.78	Major peak.
1.69	5	1.70		1.70	
1.66	20	1.66		1.66	
1.64	20	1.64		1.64	
1.54	40	1.54		1.55	

1. Colorless prehnite, Ashcroft, British Columbia (Nuffield, 1943; ASTM No. 7–333).
2. Pink prehnite, Shaw Island, Isle Royale National Park, Mich.
3. Green prehnite, Tooker's Island, Isle Royale National Park, Mich.

Samples 2 and 3: Cu$K\alpha$ radiation, Ni filter ($\lambda = 1.5418$ A). Pattern taken with North American Philips X-ray diffractometer internally standardized with quartz.

The ideal chemical formula for prehnite is $Ca_2Al_2Si_3O_{10}(OH)_2$; it generally shows little variation in composition. The only appreciable substitutions are iron for aluminum and sometimes a small replacement of silicon by aluminum (Deer and others, 1962). In the literature examined, the only trace-element analysis of a "normal" prehnite that indicates copper to be present is of a sample that contains 60 parts per million (0.006 percent) of copper from near Davos, Switzerland (Peters, 1963, table 10).

Semiquantitative spectrographic analysis of a combined sample of six pink (slightly lighter than 5*R*6/2 of the "Rock-color Chart," Goddard, 1948) amygdules from Shaw Island indicates that elements not in the ideal formula (except iron and copper) are present in no more than trace amounts (table 3). Iron, at about 1 percent, is not visible under the microscope as oxide

TABLE 3.—*Semiquantitative spectrographic analysis of pink prehnite*

[Sample consisted of six similar-appearing pink prehnite amygdules from beach on Shaw Island, Isle Royale National Park, Mich. Laboratory No. M–105026. Results are reported in percent to the nearest number in the series 1, 0.7, 0.5, 0.3, 0.2, 0.15, and 0.1, which represent approximate midpoints of interval data on a geometric scale. The assigned interval for semiquantitative results will include the quantitative value about 30 percent of the time. Only elements reported present are listed in this table. M, major constituent, greater than 10 percent. Analyst: Harry Bastron]

Element	Weight percent	Element	Weight percent
Si	M	Ag	0.0005
Al	10	B	.02
Fe	1	Ba	.0015
Mg	.07	Cu	[1] 1.5
Ca	M(15)	Ga	.001
Na	.03	Sr	.005
Ti	.0007	V	.0015
Mn	.05		

[1] X-ray fluorescence analysis yielded 0.85 percent Cu. Analyst: Brent Fabbi.

inclusions and may substitute for aluminum in the mineral lattice. Similar iron content is reported for pale-green and colorless prehnite (Deer and others, 1962, table 44), so iron present at this order of magnitude seems to have little effect on color. Minute inclusions of native copper, on the other hand, are present in the amygdules. X-ray fluorescence analysis (probably a somewhat more accurate method in this range than the semiquantitative spectrographic analysis) yielded a copper content of 0.85 percent. Prehnite amygdules of this shade of pink thus appear to contain about 1 percent copper. Prehnite with visibly greater amounts of finely divided copper than the analyzed material can be as dark as grayish red (5*R*4/2).

Figure 3 illustrates the nature of the grain size and distribution of copper inclusions in an amygdule from Shaw Island similar in appearance to the ones analyzed. The matrix is entirely prehnite; the chevron pattern results from the intersection of two radiating fibrous bundles of prehnite. The dark specks are inclusions of native copper at or near the surface of the polished specimen; the light specks are internal reflections from native copper inclusions below the surface. The light area to the left of the chevron contains larger copper inclusions and is milky white; the rest of the area is various shades of pink. Very fine, rather uniformly disseminated copper occurs only in the pink area. The different gray tones in the chevron are due

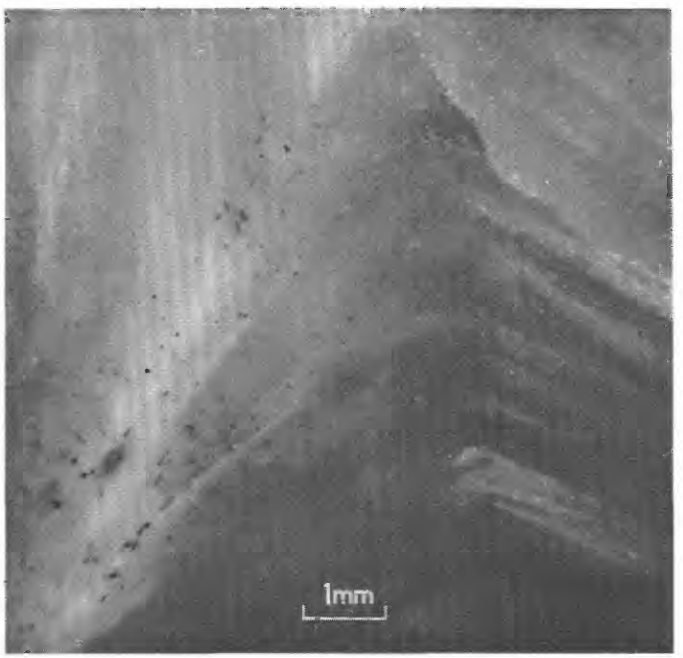

FIGURE 3.—Photomicrograph of native copper inclusions in prehnite amygdule. Dark specks are inclusions at or near the surface of the polished specimen; light specks are internal reflections from native copper inclusions below the surface. Inclined reflected light.

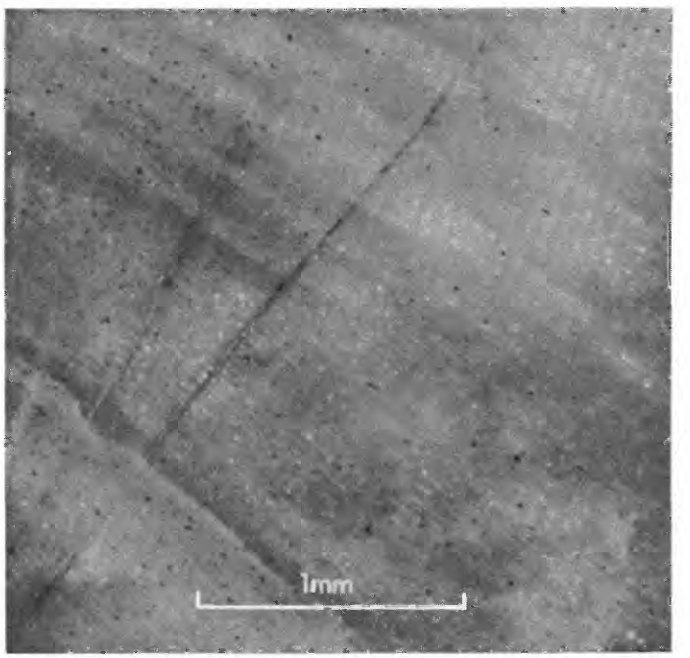

FIGURE 4.—Photomicrograph of native copper inclusions in prehnite amygdule. Preferred orientation of inclusions parallels fibrous structure of prehnite. Note copper concentrations in crosscutting seams. Inclined reflected light. Same specimen as figure 3.

to differences in orientation of internal reflections from the inclined light source on the copper inclusions alined parallel with the prehnite fibers, rather than to differences in copper content. Figures 4 and 5 illustrate, at higher magnification, the preferred orientation of native copper inclusions as controlled by the fibrous structure of the prehnite. Concentrations of copper are sometimes also present along thin seams crosscutting the prehnite fibers (fig. 4).

Pink copper-bearing prehnite is not altogether unique to the Lake Superior region. Surdam (1968) has recently described pink prehnite amygdules in lava flows of the Triassic Karmutsen Group on Vancouver Island, British Columbia. He also concluded that the pink color of the amygdaloidal prehnite is caused by finely disseminated blebs of native copper, which form contemporaneously with the formation of the prehnite. Several spectrographic analyses of the amygdules showed an average copper content greater than 1 percent. The description of the Canadian pink prehnite is very similar to that of the material from Isle Royale and the Keweenaw Peninsula of Michigan.

Lane (1898, p. 217) long ago observed that, "If there is one mineral with which the copper is more particularly associated than with others it is prehnite * * *." While this may be an overgeneralization with respect to the major economic deposits on the Keweenaw Peninsula (Stoiber and Davidson, 1959), as well as to many of the abandoned mines and prospects on Isle Royale, virtually all of the prehnitic veins and prehnite amygdules on Isle Royale contain some disseminated copper. Spatial relations also indicate that the

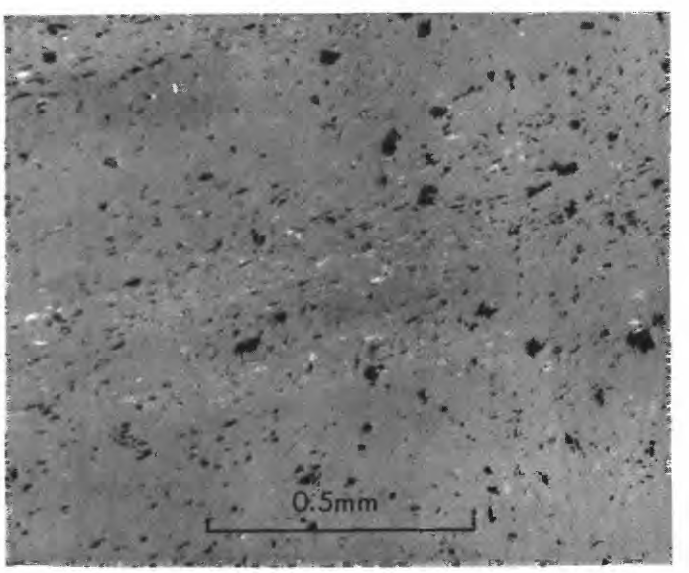

FIGURE 5.—Photomicrograph of native copper inclusions in prehnite amygdule. Preferred orientation of inclusions parallels fibrous structure of prehnite. Vertical reflected light. Copper appears more abundant in this photomicrograph than in the others because the inclusions appear dark much farther below the surface of the specimen than with inclined reflected light. Same specimen as figure 3.

deposition of the native copper was contemporaneous with that of the prehnite, and, that when the copper is very fine and evenly disseminated within the prehnite, internal reflections from the copper inclusions lend a pink color to the prehnite.

REFERENCES

Butler, B. S., and Burbank, W. S. (in collaboration with Broderick, T. M., and others), 1929, The copper deposits of Michigan: U.S. Geol. Survey Prof. Paper 144, 238 p.

Cornwall, H. R., 1954, Bedrock geology of the Lake Medora quadrangle, Michigan: U.S. Geol. Survey Geol. Quad. Map GQ–52, scale 1:24,000.

Deer, W. A., Howie, R. A., and Zussman, J., 1962, Sheet silicates, v. 3 *of* Rock-forming minerals: New York, John Wiley and Sons, 270 p.

Dobell, J. P., 1966, Thomsonite and prehnite—similar but distinguishable: Earth Sci., v. 19, no. 2, p. 60–61.

Dustin, Fred, 1931, The gems of Isle Royale, Michigan: Michigan Acad. Sci., Arts, and Letters, Papers, v. 16, p. 383–398.

Foster, J. W., and Whitney, J. D., 1851, Report on the geology of the Lake Superior land district; pt. 2, The iron region, together with the general geology: U.S. 32d Cong., Spec. sess., Senate Executive Doc. 4, 406 p.

Goddard, E. N., chm., and others, 1948, Rock-color chart: Washington, D.C., Natl. Research Council, repr. Geol. Soc. America, 1951.

Hanley, F. B., 1939, Minnesota's Thomsonite Beach: Rocks and Minerals, v. 14, no. 12, p. 371–376.

Hey, M. H., 1932, Studies on the zeolites; pt. 2, Thomsonite (including faroelite) and gonnardite: Mineralog. Mag., v. 23, p. 51–125.

Kraus, E. H., and Slawson, C. B., 1947, Gems and gem materials, 5th ed.: New York, McGraw-Hill Book Co., Inc., 332 p.

Lane, A. C., 1898, Geological report on Isle Royale, Michigan: Michigan Geol. Survey, v. 6, pt. 1, 281 p.

——— 1911, The Keweenaw Series of Michigan: Michigan Geol. Survey Pub. 6, Geol. Ser. 4, v. 1 and 2, 983 p.

Nuffield, E. W., 1943, Prehnite from Ashcroft, British Columbia: Toronto Univ. Studies, Geol. Ser. 48, p. 49–64.

Pearl, R. M., 1964, American gem trails: New York, McGraw-Hill Book Co., 173 p.

Peters, Tjerk, 1963, Mineralogie und petrographie des Totalpserpentins bei Davos: Schweizer. Mineralog. u. Petrog. Mitt., v. 43, no. 2, p. 529–684.

Sinkankas, John, 1959, Gemstones of North America: Princeton, N.J., D. Van Nostrand Co., 675 p.

Stoiber, R. E., and Davidson, E. S., 1959, Amygdule mineral zoning in the Portage Lake lava series, Michigan copper district—pt. 1: Econ. Geology, v. 54, no. 7, p. 1250–1277; pt. 2, no. 8, p. 1444–1460.

Surdam, R. C., 1968, Origin of native copper and hematite in the Karmutsen Group, Vancouver Island, B.C.: Econ. Geology, v. 63, no. 8, p. 961–966.

Waite, G. G., 1961, Gemstones along Lake Superior shores—Ontario—Michigan—Minnesota: Lapidary Jour., v. 15, no. 4 p. 434–451.

Winchell, A. N., and Winchell, Horace, 1951, Elements of optical mineralogy—an introduction to microscopic petrography, pt. 2, Descriptions of minerals, 4th ed.: New York, John Wiley and Sons, 551 p.

AUTHIGENIC FLUORITE IN PLIOCENE LACUSTRINE ROCKS NEAR ROME, MALHEUR COUNTY, OREGON

By RICHARD A. SHEPPARD and ARTHUR J. GUDE 3d, Denver, Colo.

Abstract.—Fluorite occurs as submicroscopic, nearly spherical grains in tuff, tuffaceous mudstone, and mudstone of an unnamed lacustrine deposit in southeastern Oregon. The fluorite is nonuniformly distributed in the upper 60 feet of the deposit. The content of fluorite is generally less than 5 percent, but it is as much as 16 percent in the lower part of a conspicuous zeolitic tuff. Fluorite probably formed during diagenesis in sediments that had been deposited in an alkaline, saline lake.

Fluorite has long been known to occur in sedimentary rocks, although its origin was generally attributed to the same mineralization that produced the commonly associated metallic ore deposits. Kazakov and Sokolova (1950) cited many occurrences of fluorite in sedimentary rocks that range in age from Cambrian to Cretaceous. The rocks are chiefly marine carbonates and evaporites, and the fluorite was considered either a primary precipitate from saline water or a diagenetic product. Experimental work by Kazakov and Sokolova indicated that fluorite could precipitate from sea water that was concentrated three to four times.

The fluorite deposit described herein occurs in Pliocene lacustrine rocks that have not been subjected to hydrothermal activity. Fluorite was first recognized in these rocks by Studer (1967) during a study of the zeolitic tuffs.

DESCRIPTION AND MINERALOGY OF THE FLUORITE-BEARING ROCKS

The fluorite-bearing strata are part of an unnamed lacustrine and fluviatile deposit that crops out along the Owyhee River and its tributaries near Rome, in southeastern Oregon. This deposit contains the Rome fauna of Wilson (1937), who considered the fauna to be Pliocene in age. Walker and Repenning (1966) mapped the deposit during their geologic reconnaissance of the Jordan Valley quadrangle. The deposit is nearly flat lying and is locally overlain unconformably by basalt and sedimentary rocks of Pliocene and Pleistocene age.

The fluorite-bearing strata are restricted to the upper lacustrine part of the deposit and underlie an area of about 7 square miles, chiefly between Crooked Creek and the Owyhee River (fig.1). A conspicuous gray and yellow zeolitic tuff unit (fig. 2) marks the top of the fluorite-bearing rocks and is herein termed the "marker tuff." Fluorite has been identified in mudstone, tuffaceous mudstone, and zeolitic tuff collected as much as 36 feet stratigraphically beneath the marker tuff; however, only the zeolitic marker tuff seems to have a consistently high fluorite content.

The zeolitic marker tuff consists of three subunits that total as much as 23 feet in thickness. The original

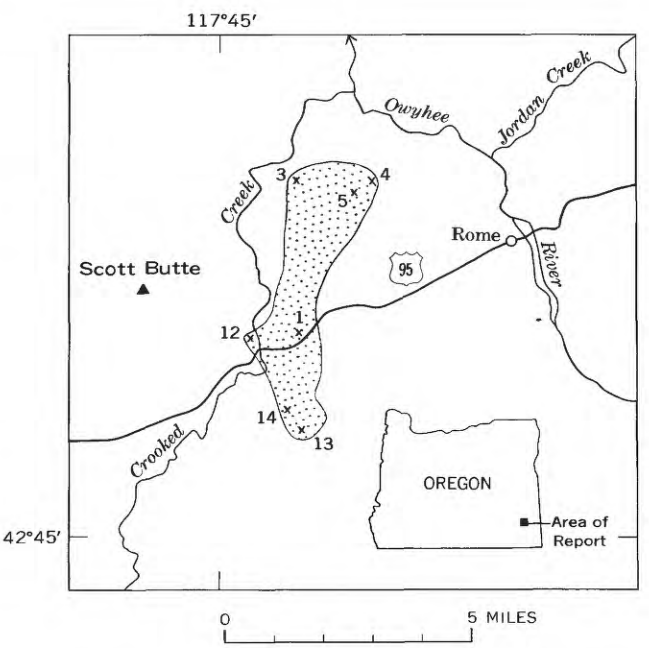

FIGURE 1.—Index map showing the distribution of fluorite-bearing rocks (stippled) near Rome, Oreg. X, sample locality.

FIGURE 2.—Zeolitic marker tuff on north side of U.S. Route 95, about 0.75 mile northeast of Crooked Creek. The marker tuff consists of ledge-forming lower gray (L) and middle yellow (M) subunits and a less resistant upper gray (U) subunit. A green vuggy bed occurs in the upper third of the lower gray subunit. The marker tuff grades into tuffaceous mudstone below the feet of the standing figure.

thickness was greater than 23 feet because an unknown thickness of tuff was eroded prior to the deposition of upper Pliocene and Pleistocene sediments. The subunits are well exposed and easily distinguished on the north side of the roadcut for U.S. Route 95, about 0.75 mile northeast of Crooked Creek. A very resistant yellow to orange layer near the middle of the tuff unit separates the predominantly light-gray tuff into lower and upper subunits. Both gray subunits break with a blocky to conchoidal fracture and contain abundant saline-mineral molds. A thin bed of green vuggy tuff occurs locally in the upper third of the lower gray subunit. The lower subunit is gradational into the underlying green tuffaceous mudstone.

Mudstone and tuffaceous mudstone beneath the marker tuff are green and break with a subconchoidal to conchoidal fracture. These rocks are commonly concealed by a characteristic punky "popcorn" coating, several inches thick, formed by weathering of expandable clay minerals in the mudstone.

The mineralogy (table 1) of the fluorite-bearing rocks was determined by study of X-ray diffractometer patterns of powdered bulk samples. The tuffs consist chiefly of zeolites, clay minerals, quartz, potassium feldspar, and calcite. The tuffs originally consisted mainly of silicic shards and minor crystal fragments. During diagenesis the vitric material reacted with saline and alkaline pore water to form zeolites and the associated silicate minerals. Relict vitroclastic texture is well preserved in some tuff but vague in others. Although most constituents in the mudstones are probably detrital, some of the silicate minerals are undoubtedly authigenic, having formed from original vitric material or precursor silicate minerals during diagenesis.

The abundance and distribution of the fluorite were determined by chemical and X-ray techniques. Fluorite seems to impart to the lacustrine rocks no recognizable physical property that would indicate its presence. Electron micrographs (fig. 3) show that the fluorite occurs as nearly spherical grains. The grains have a rough surface and are less than 1 micron in diameter. No crystal faces were recognized on the fluorite grains.

An attempt was made, without success, to separate the fluorite from a sample of the zeolitic marker tuff with a heavy-liquid mixture of bromoform and acetone. However, some success was achieved by size fractionation utilizing a centrifugal decantation method after disaggregation of the crushed sample in an ultrasonic bath. Fluorite was concentrated in the small size fractions. The bulk sample originally contained about 10 percent fluorite, but the less-than-1μ fraction contained about 40 percent fluorite.

Table 1 gives the fluorine and calculated fluorite contents for the marker tuff and for mudstone and tuff beneath the marker tuff. Fluorine was determined by a distillation-volumetric method, and the fluorite content was then calculated from the analyzed fluorine content, with the assumption that all the analyzed fluorine is in fluorite. Rock-forming clay minerals and zeolites from sedimentary environments generally contain less than 0.1 percent fluorine, according to unpublished analytical data in the files of the U.S. Geo-

TABLE 1.—*Mineralogic composition, fluorine content, and calculated fluorite content of lacustrine rocks near Rome, Oreg.*

[Fluorine determined by J. M. Gardner and W. D. Goss by a distillation-volumetric method. Mineral composition determined from X-ray-diffractometer patterns of powdered bulk samples. Abbreviations: Ca, Calcite; Cl, clinoptilolite; E, erionite; F, fluorite; G, glass; I, 10-angstrom clay mineral; K, potassium feldspar; Md, mordenite; Mt, 14-angstrom clay mineral; O, opal; Ph, phillipsite; Q, quartz. Minerals listed in order of decreasing abundance]

Sample locality (fig. 1)	Lithology	Sample	Sample position (in feet above or below base of marker tuff)	Fluorine (weight percent)	Fluorite (calculated weight percent)	Mineral composition
1	Tuff, marker, upper gray	W	20.5 above	0.62	1.3	Md, Ca, I, Mt, Q, F
		V	18.5 above	2.38	4.9	Md, I, F, Cl, Mt
		U	15.0 above	.63	1.3	Md, Q, Cl, F
	Tuff, marker, middle yellow	T	14.5 above	.05	.1	Cl, E, I, Mt
		S	12.6 above	<.03	0	E, Cl
		R	11.7 above	.07	.1	Cl, Ph, K
		Q	11.6 above	<.03	0	Cl, Ph, I, Mt
		P	11.5 above	.03	.1	Cl, Ph, Mt
		N	11.1 above	.05	.1	Cl, Ph, Mt
		M	10.6 above	.07	.1	Cl, Ph
	Tuff, marker, lower gray	L	10.5 above	.15	.3	Md, Mt, I, Q, Ca
		K	9.2 above	.63	1.3	Md, Ca, Q, F
		J	7.5 above	1.38	2.8	Cl, K, I, Mt, F
		I	7.3 above	1.05	2.2	Cl, K, F
		H	7.0 above	.76	1.6	Ph, Mt, K, I, F
		G	6.7 above	8.00	16.4	Md, K, F, Mt, I, Cl
		F	3.5 above	.59	1.2	Md, Q, Ca, Mt, F
		E	1.7 above	.15	.3	Md, Q, Ca, Mt
		D	At base	4.62	9.5	Md, K, Mt, I, Q, F
	Tuffaceous mudstone	C	0.2 below	2.16	4.4	I, K, Q, Mt, F
		B	1.0 below	2.44	5.0	K, I, Mt, F
		A	2.5 below	.79	1.6	K, I, Mt, F
		X	5.0 below	.23	.5	K, I, Mt, Ca, F
		Y	16.4 below	.24	.5	K, I, Mt, Ca, F
		Z	22.4 below	.39	.8	K, I, Mt, Ca, F
	Tuff	AA	23.5 below	.72	1.5	Q, I, Mt, Cl, Ca, F
	Mudstone	BB	24.2 below	2.85	5.8	Mt, Ca, Q, I, K, F
	Tuff	CC	24.7 below	.94	1.9	Q, I, K, Cl, F
	Mudstone	DD	25.5 below	1.86	3.8	Q, I, Mt, Cl, K, F, Ca
	Tuff	EE	26.1 below	1.04	2.1	Q, I, Mt, K, F
3	Tuff, marker, upper gray	H	17.5 above	4.96	10.2	Md, F, Q
	Tuff, marker, middle yellow	G	10.5 above	.22	.4	Ph, Cl, I, F
	Tuff, marker, lower gray	F	8.3 above	5.60	11.5	Md, F, K, Mt, I
		E	7.1 above	2.27	4.7	K, I, Cl, Mt, F
		D	3.8 above	1.17	2.4	Md, Q, F
		C	0.5 above	.05	.1	Ph, Cl, Mt, I
	Tuffaceous mudstone	B	1.6 below	1.20	2.5	K, Mt, I, F
		A	5.8 below	.79	1.6	K, I, Mt, F
4	Tuff, marker, upper gray	F	15.9 above	1.76	3.6	Md, O, Mt, Q, F
	Tuff, marker, middle yellow	E	8.3 above	1.24	2.5	Cl, Mt, Ph, I, F
	Tuff, marker, lower gray	DU	5.5 above	2.11	4.3	K, I, Mt, Cl, F
		DL	3.0 above	1.38	2.8	I, Mt, K, Cl, F
		CU	1.5 above	2.66	5.5	I, Mt, Cl, E, F
		CL	0.5 above	3.34	6.9	I, Mt, Cl, Md, E, F
	Tuff	B	8.5 below	.16	.3	Ph, Mt, I
		A	13.5 below	.26	.5	E, Ph, Mt, I, Cl, F
5	Tuff, marker, lower gray	C	5.0 above	.19	.4	Md, Mt
		B	3.3 above	.09	.2	Ph, Mt, I, Cl
		A	1.5 above	1.22	2.5	Md, Q, F
12	Tuff, marker, middle yellow	G	15.3 above	.12	.2	E, Cl, Mt, I
		F	13.4 above	.03	.1	Cl, Ph, Mt
	Tuff, marker, lower gray	E	13.0 above	.19	.4	Md, Ca, Mt, Q, I
		D	7.0 above	1.84	3.8	Md, Ca, Q, F
		C	2.0 above	2.05	4.2	K, Md, Mt, I, F
	Tuffaceous mudstone	B	0.1 below	1.25	2.6	K, I, Mt, F
		A	3.0 below	.21	.4	K, I, Mt, Ca, F
	Tuff	H	24.0 below	2.03	4.2	Q, K, Mt, I, F, Cl
		I	34.5 below	2.27	4.7	K, I, Mt, Cl, F, E
13	Tuff, marker, middle yellow	B	11.0 above	.06	.1	E, Cl
	Tuff, marker, lower gray	A	3.5 above	1.67	3.4	Q, Md, F
14	Tuff, marker, upper gray	G	10.5 above	.27	.6	O, Md, Q, F
	Tuff, marker, middle yellow	F	7.2 above	.05	.1	G, E, Mt, I
		E	5.7 above	.05	.1	Cl, Ph
	Tuff, marker, lower gray	D	5.4 above	4.20	8.6	Md, O, Q, F
		C	3.0 above	2.96	6.1	Md, Ca, I, F
		B	0.2 above	.80	1.6	Ca, Md, Q, F
	Tuffaceous mudstone	A	0.5 below	.83	1.7	Q, K, I, F

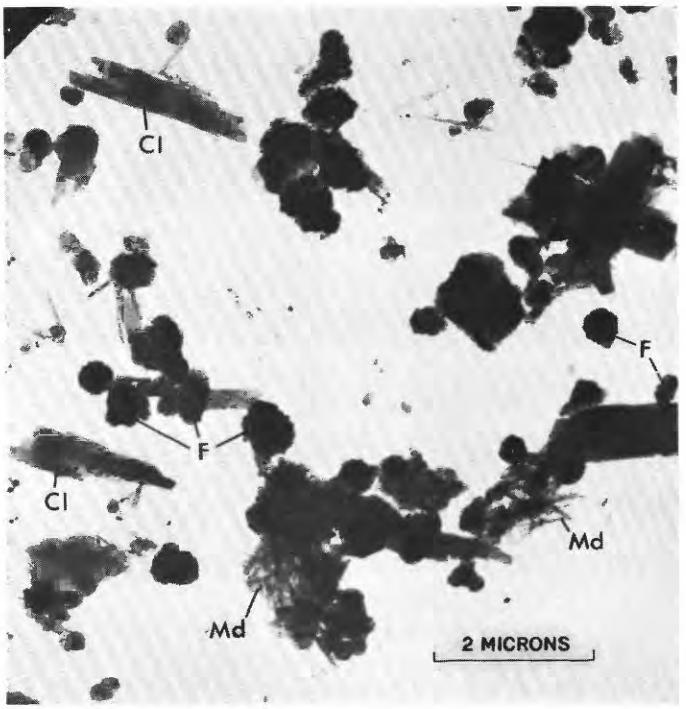

FIGURE 3.—Electron micrograph showing fluorite (F), clinoptilolite (Cl), and mordenite (Md) in the marker tuff. The fluorite was concentrated by disaggregation and size fractionation. Micrograph by Paul D. Blackmon.

logical Survey. Thus, the calculated fluorite content for the samples listed in table 1 could be as much as 0.2 percent too high. Those samples that show 0.2 percent or less calculated fluorite may not contain any fluorite. All the analyzed fluorine could be in clay minerals and zeolites.

Studies of X-ray diffractometer patterns of splits of the analyzed samples show a good correlation between the intensity of the (220) peak for fluorite and the fluorite content as calculated from the analyzed fluorine content (fig. 4). The correlation is supporting evidence that most of the analyzed fluorine is in fluorite because the samples include tuff and mudstone and show a variation in mineralogic composition (table 1).

The calculated fluorite content for sampled tuff is 0.0–16.4 percent, whereas for sampled mudstone and tuffaceous mudstone it is 0.4–5.8 percent. The fluorite is apparently nonuniformly disseminated; however, the lower gray subunit of the marker tuff generally has a high fluorite content, and the upper half of this subunit commonly has the highest content. The yellow middle subunit of the marker tuff seems to have a consistently low fluorite content. Although the range for the yellow subunit is 0.0–2.5 percent, most samples contain less than 0.2 percent fluorite.

Tuff, tuffaceous mudstone, and tuffaceous sandstone samples that were collected more than 40 feet stratigraphically below the marker tuff show only small amounts of fluorine. The calculated fluorite content for these rocks ranges from 0.1 to 0.3 percent; however, most of the analyzed fluorine is probably in clay minerals and zeolites rather than in fluorite. Fluorite was not detected in X-ray diffractometer patterns of powdered bulk samples. Brown lacustrine mudstone that unconformably overlies the marker tuff likewise contains negligible fluorine.

GENESIS OF THE FLUORITE

There is no evidence that the Pliocene lacustrine rocks near Rome were affected by hydrothermal activity. Zeolites, potassium feldspar, and at least some of the clay minerals formed during diagenesis. Fluorite also probably formed during diagenesis, but its restricted occurrence in the upper part of the lacustrine sequence may have been due to an exceptional concentration of fluorine in the lake water at the time of deposition. The relationship of fluorite to the other minerals in the lacustrine rocks is difficult to ascertain because of the minute size of the fluorite.

The occurrence of saline mineral molds and the assemblage of authigenic silicate minerals indicate a saline, alkaline depositional environment for the fluorite-bearing lacustrine rocks. Zeolites such as clinoptilolite and mordenite occur in altered silicic tuffs that were deposited in either fresh or saline water, but zeolites such as erionite and phillipsite are found almost exclusively in saline lake deposits (Hay, 1966, p. 67; Sheppard and Gude, 1968). Authigenic potassium feldspar in the tuffs and mudstones is also indicative of a highly saline depositional environment.

In addition to being saline, the lake water in which the fluorite-bearing strata were deposited must have been enriched in fluorine. Most fresh-water lakes have less than 1 part per million of fluorine (Livingstone, 1963, p. G41), but concentrated lake waters can have considerably higher fluorine contents. The fluorine content is generally limited by the availability of calcium to form fluorite. Lakes that are unusually high in fluorine content are commonly sodium carbonate-bicarbonate in composition and are located in volcanic terranes. Baker (1958, p. 58) reported high fluorine contents for water in lakes of the Gregory Rift Valley in Kenya: Lake Elementeita, 1,627 ppm; Lake Nakuru, 1,400 ppm; and Lake Hannington, 1,170 ppm. Brine from Lake Magadi, another rift valley lake, contains 1,270 ppm of fluorine (Hay, 1966, p. 33) and negligible calcium.

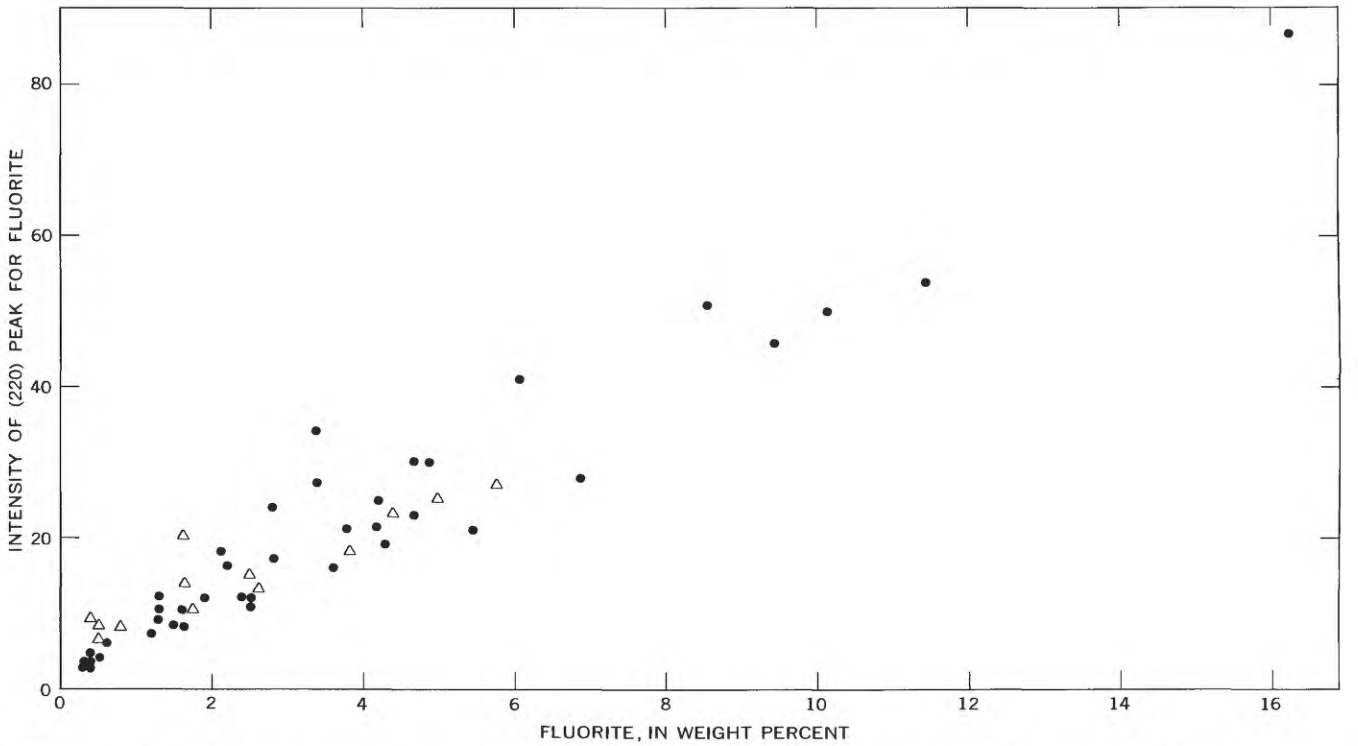

FIGURE 4.—Scatter diagram showing the correlation between the intensity of the (220) peak for fluorite and the fluorite content as calculated from the analyzed fluorine content. Intensity is peak height, in chart divisions, above background. Dot, tuff; triangle, mudstone and tuffaceous mudstone.

Knowledge of the distribution of fluorides in the deposits of Lake Magadi may give a clue to the genesis of fluorite in the lacustrine rocks near Rome. Lake Magadi contains a vast deposit of trona ($Na_2CO_3 \cdot NaHCO_3 \cdot 2H_2O$), which has been mined since 1916 (Baker, 1968, p. 69). Trona in the upper part of the evaporite series commonly contains about 1–2 percent villiaumite (NaF) (Baker, 1958, p. 78); however, the trona locally contains as much as 22 percent villiaumite (Walter Rouse, written commun., 1967). Fluorite was identified by R. L. Hay (written commun. 1967) in the 96- to 112-foot interval of a core from borehole B at Lake Magadi. The fluorite occurs in trona and claystone of the lower part of the evaporite series and makes up as much as 6 percent of the sampled core. Villiaumite was not identified in the fluorite bearing part of the core.

Inasmuch as villiaumite, along with trona, presently precipitates from the Lake Magadi brine (H. P. Eugster, oral commun. 1968), the fluorite in the lower part of the evaporite series may have formed from villiaumite during diagenesis by a solution-precipitation mechanism. The solubility of villiaumite at 25°C is more than three orders of magnitude greater than that of fluorite (Kazakov and Sokolova, 1950). Interstitial water may have dissolved the villiaumite in the buried sediments and affected the precipitation of fluorite. Calcium in the interstitial water could have been derived outside the depositional basin or from solution of minor amounts of a calcium-bearing saline mineral, such as gaylussite ($CaCO_3 \cdot Na_2CO_3 \cdot 5H_2O$), in the lake sediments.

Although there is no evidence of villiaumite in the lacustrine rocks near Rome, the genesis of the fluorite there may have been similar to that proposed for fluorite at Lake Magadi. Solution of villiaumite and precipitation of fluorite were probably facilitated by calcium-bearing water that infiltrated the lacustrine rocks after deposition. Some redistribution of fluorine probably occured during the solution of villiaumite, and the present distribution of fluorite was controlled by the porosity and permeability of the host rock and the availability of calcium. The formation of fluorite probably postdates the authigenesis of the zeolites, although there is no substantiating textural evidence.

ECONOMIC CONSIDERATIONS

The fluorite deposit near Rome is of much lower grade than that currently mined by the fluorspar industry. The highest grade material is about half the grade considered economically minable in the United States. However, the Pliocene rocks contain a sizable quantity of fluorite at shallow depths. The tonnage of fluorite near Rome is conservatively estimated at 12

million tons, but analyses are insufficient to indicate the tonnages of fluorite-bearing rock in the various grades. The fine grain size and the disseminated character of the fluorite probably prohibit commercial recovery by mechanical techniques.

Fluorite and the zeolites near Rome are potential resources. The zeolites have been extensively prospected by private companies, but as of 1968 none had been mined. If the zeolitic tuffs are mined, fluorine could perhaps be chemically extracted during processing of the zeolites.

Fluorite deposits such as the one near Rome have seemingly been overlooked by the fluorspar industry. Perhaps fluorite deposits of similar origin but higher grade will be found elsewhere in rocks that were deposited in a saline lacustrine environment.

REFERENCES

Baker, B. H., 1958, Geology of the Magadi area; degree sheet 51, S.W. quarter: Kenya Geol. Survey Rept. 42, 81 p.

Hay, R. L., 1966, Zeolites and zeolitic reactions in sedimentary rocks: Geol. Soc. America Spec. Paper 85, 130 p.

Kazakov, A. V., and Sokolova, E. I., 1950, Usloviya obrazovaniya flyuorita v osadochnykh porodakh (flynoritovaya sistema) [Conditions of the formation of fluorite in sedimentary rocks.]: Akad. Nauk SSSR Geol. Inst. Trudy, v. 114, Geol. Ser. 40, p. 22–64 [English trans., U.S. Geol. Survey TEI–386, 76 p., 1951].

Livingstone, D. A., 1963, Chemical composition of rivers and lakes, *in* Fleischer, Michael, ed., Data of geochemistry, 6th ed.: U.S. Geol. Survey Prof. Paper 440–G, p. G1–G64.

Sheppard, R. A., and Gude, A. J., 3d, 1968, Distribution and genesis of authigenic silicate minerals in tuffs of Pleistocene Lake Tecopa, Inyo County, California: U.S. Geol. Survey Prof. Paper 597, 38 p.

Studer, H. P., 1967, Mineral analysis of natural zeolite deposits [abs.], *in* Bailey, S. W., ed., Clays and clay minerals—Clay Minerals Conf., 15th, Pittsburgh, Pa., 1966, Proc.: New York Pergamon Press (Internat. Ser. Mons. Earth Sci., v. 27), p. 187.

Walker, G. W., and Repenning, C. A., 1966, Reconnaissance geologic map of the west half of the Jordan Valley quadrangle, Malheur County, Oregon: U.S. Geol. Survey Misc. Geol. Inv. Map I–457.

Wilson, R. W., 1937, New middle Pliocene rodent and lagomorph faunas from Oregon and California, *in* Studies on Cenozoic vertebrates of western North America: Carnegie Inst. Washington Pub. 487, p. 1–19 [1938].

TWINNING IN BARBOSALITE FROM THE SAPUCAIA PEGMATITE MINE, MINAS GERAIS, BRAZIL

By MARIE LOUISE LINDBERG SMITH, Washington, D.C.

Abstract.—Crystals of barbosalite, $Fe^{+2}Fe_2^{+3}(PO_4)_2(OH)_2$, monoclinic $P2_1/c$, $a=7.25$ A, $b=7.46$ A, $c=7.49$ A, $\beta=120°15'$, from the Sapucaia pegmatite mine, Minas Gerais, Brazil, are twinned with *ab* the composition plane. The crystal structure of barbosalite is based upon triple groups of ferric iron-ferrous iron-ferric iron-oxygen octahedra linked together through corner-shared hydroxyls and corner-shared oxygens of phosphate groups. Each triple group is separated by a vacant octahedral site. Twinning is explained on the basis of a crystallographic interruption in the order of filling of 3 out of 4 octahedral sites. The operation of twinning involves a rotation twin axis, parallel c^*, through hydroxyl and phosphorus on the composition plane, *ab*, at $z=\frac{1}{4}$. If the rotation is repeated at every second phosphorus-hydroxyl plane, the stacking sequence will have tetragonal symmetry. An ordered occupancy of octahedral sites is proposed for tetragonal manganoan lipscombite, $(Fe^{+2},Mn^{+2})Fe_2^{+3}(PO_4)_2(OH)_2$, $P4_12_12$, $a=7.40$ A, $c=12.81$ A, also found at the Sapucaia pegmatite mine.

Twin crystals of barbosalite, $Fe^{+2}Fe_2^{+3}(PO_4)_2(OH)_2$, the ferrous-ferric analog of lazulite, $MgAl_2(PO_4)_2(OH)_2$, and of scorzalite, $Fe^{+2}Al_2(PO_4)_2(OH)_2$ (Pecora and Fahey, 1950), have recently been discovered from the Sapucaia pegmatite mine, Minas Gerais, Brazil. The original description of barbosalite was based upon massive material intimately intergrown with tavorite, $LiFePO_4(OH)$, and with other secondary phosphate minerals (Lindberg and Pecora, 1954, 1955). A trial crystal structure common to barbosalite, lazulite, and scorzalite has been established (Lindberg and Christ, 1959). The present paper offers an interpretation of the twinning based upon the crystal structures of the minerals of the lazulite-scorzalite-barbosalite series and the structure of the related synthetic compound, tetragonal iron lazulite, $Fe_7(PO_4)_4(OH)_4$ (Katz and Lipscomb, 1951). Synthetic tetragonal iron lazulite has a defect structure with 7 out of 8 octahedral sites statistically occupied. Three out of four octahedral sites are occupied in an ordered way in barbosalite. When the order of occupancy is crystallographically interrupted a twinned crystal results. An ordered occupancy of 3 out of 4 octahedral sites is proposed for manganoan lipscombite, $(Fe^{+2},Mn^{+2})Fe^{+3}_2(PO_4)_2(OH)_2$, a tetragonal mineral occurring with barbosalite at the Sapucaia pegmatite mine.

Acknowledgments.—The interpretation of twinning in barbosalite in the present paper is based upon the published description of the trial structure common to lazulite, scorzalite, and barbosalite, coauthored by Charles L. Christ, of the U.S. Geological Survey. Appreciation is expressed to Charles L. Christ for guidance and for the many concepts in the present paper which cannot truly be separated from earlier joint studies, and to Daniel Appleman for suggestions. Appreciation is also expressed to William T. Pecora, of the U.S. Geological Survey, for his making available for study the phosphate mineral suite from the Sapucaia pegmatite mine and to George Switzer, of the U.S. National Museum, for supplementing the original suite with additional specimens.

MORPHOLOGY

Crystals of barbosalite are monoclinic, pseudotetragonal. They are twinned with each of the two members of the twin equally and symmetrically developed (fig. 1). Lindberg and Christ (1959) obtained unit-cell parameters from the twinned crystals used in the present study. They chose a monoclinic cell, with space group $P2_1/c$, $a=7.25$ A, $b=7.46$ A, $c=7.49$ A, $\beta=120°15'$. In this orientation the (001) plane of barbosalite corresponds to the (001) planes of related tetragonal compounds, synthetic iron lazulite and manganoan lipscombite. The pseudotetragonal cell of barbosalite, given by the transformation from the monoclinic cell 100/010/102, has space group $B2_1/d$ and cell dimensions $a=7.25$ A, $b=7.46$ A, $c=12.94$ A, $\beta=91°20'$.

Berry (1948) and Palache, Berman, and Frondel (1951, p. 911) refer to an alternative pseudotetragonal

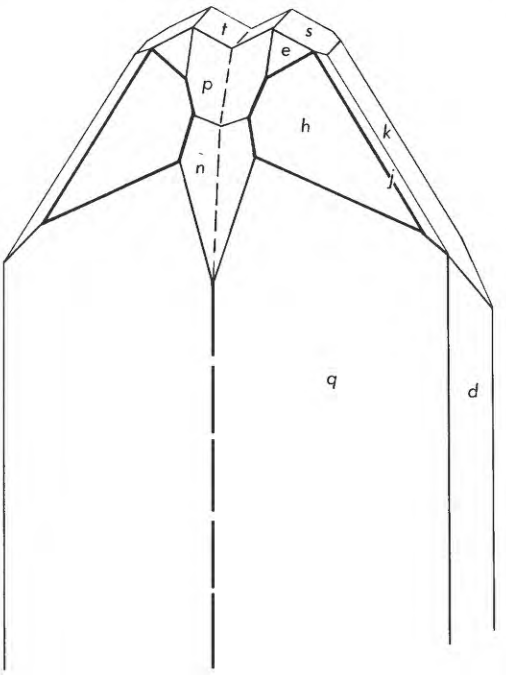

FIGURE 1.—The twinned crystal of barbosalite used to obtain $0kl$ intensity data is shown with the trace of the composition and twinning plane (001) vertical (dashed); the a-axis is vertical, and the b-axis is forward.

setting for the lazulite group with space group $B2_1/a$ which they call the "morphological" unit cell. The transformation from the $P2_1/c$ monoclinic cell of barbosalite to a $B2_1/a$ cell with $\beta>90°$ is $001/010/\bar{2}0\bar{1}$. The same transformation produces a $B2_1/a$ cell with $\beta<90°$ for lazulite and scorzalite. Conversely the transformation 001/010/201 gives a $B2_1/a$ cell with $\beta>90°$ for lazulite and scorzalite, but, $<90°$ for barbosalite. Palache, Berman and Frondel give an incorrect transformation from the $B2_1/a$ cell to a $P2_1/n$ cell. For simplicity, the $P2_1/c$ monoclinic cell described above is used through this paper.

Examination of Buerger precession photographs of the $h0l$ net of barbosalite reveals that the crystal is twinned, and that the twin operation is a rotation of 180° around the c^* reciprocal lattice axis (fig. 2). Directions referred to in this study are labeled on the figure. The observed crystal forms (fig. 1) suggest a composition plane parallel to (001). The crystal forms t, p, and n are reentrant and striated, and yield signals which cannot be measured accurately on the optical goniometer. Forms k, s, j, e, and h are not reentrant and give good signals. The crystallographic elements and angle table calculated from the X-ray cell data and the observed morphology are indexed in table 1.

RELATIONSHIP OF CRYSTAL STRUCTURE TO TWINNING

The crystal structure common to the minerals lazulite, scorzalite, and barbosalite was described by Lindberg and Christ (1959) as follows:

> The structure consists of the packing together of metal ion-oxygen octahedra and phosphate tetrahedra. The phosphorus is bonded to four non-equivalent oxygens. The proton present is assigned to the fifth independent oxygen. A magnesium-oxygen octahedron and two aluminum-oxygen octahedra share faces to form triple groups. These triple groups are linked together through corner-shared hydroxyls and through corner-shared oxygen of the phosphate groups. Each corner of a tetrahedral phosphate group is shared with a corner of an octahedral group in such a way as to tie the octahedral groups together laterally into sheets and the sheets together into a three-dimensional edifice.

The triple groups of octahedra in barbosalite are iron bearing. The ferrous iron-oxygen octahedron in barbosalite corresponds crystallographically to the magnesium-oxygen octahedron of lazulite, and the two ferric iron-oxygen octahedra in barbosalite to the two aluminum-oxygen octahedra of lazulite, respectively. The crystal structure is illustrated in figure 3.

In order to understand the mechanism of twinning in barbosalite, it is necessary to examine the structure in more detail. The octahedrally coordinated cations lie on planes at $z\approx0$ and $z\approx\frac{1}{2}$, while the P and OH ions lie on planes at $z\approx\frac{1}{4}$ and $z\approx\frac{3}{4}$. We may thus speak of "octahedral layers" and "P–OH" layers. The octahedral layers are composed of diagonal chains of octahedra, running parallel to $[\bar{1}10]$ in the layer at $z\approx0$ and parallel to [110] in the layer at $z\approx\frac{1}{2}$. Along the chains, the sequence of cations Fe^{+3}-Fe^{+2}-Fe^{+3}-vacancy is repeated. In the P–OH^{-1} layers the P-tetrahedrons are oriented with 180° rotation axis approximately parallel with c*. The four closest oxygen neighbors of OH^{-1} also form an OH^{-1} tetrahedron similarly oriented.

The bonding between the P–OH layers and the octahedral layers can be seen in figure 3. Certain of the octahedra were omitted to reveal the details of the structure. Each P tetrahedron shares corners with a Fe^{+3} octahedron and a Fe^{+2} octahedron in one triple group and a Fe^{+3} octahedron and a vacant octahedron in a parallel triple group in the same octahedral layer; the other two corners are shared in the next octahedral layer with a Fe^{+3} octahedron and a Fe^{+2} octahedron in one triple group and a Fe^{+3} octahedron and a vacant octahedron in a parallel triple group. The OH^{-1} ions are shared by a Fe^{+2} and a Fe^{+3} octahedron in one octahedral layer, and by a Fe^{+3} and a vacant octahedron in the adjacent octahedral layer.

Twinning may now be described as equivalent to the following growth process. Consider the crystal growing by laying down successive octahedral layers.

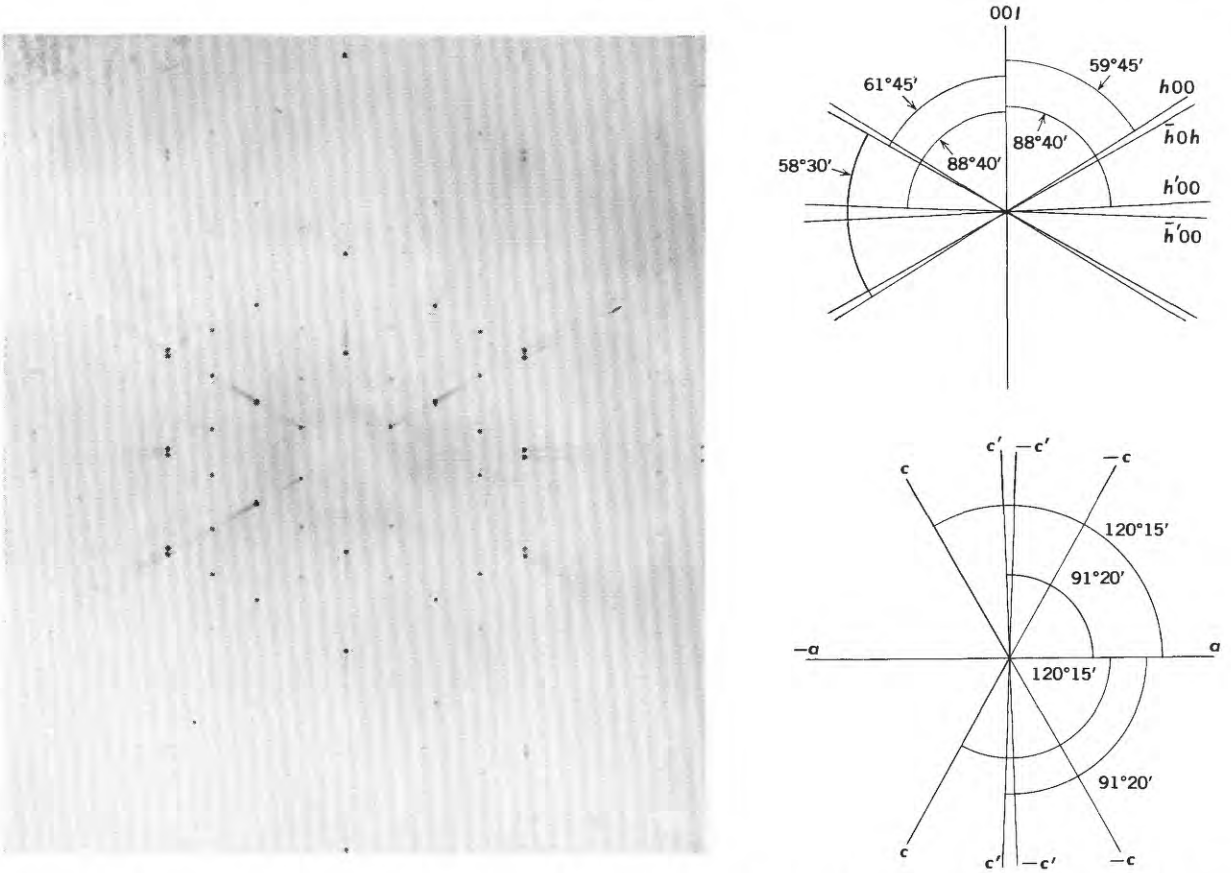

FIGURE 2.—Precession photograph (left) of twinned $h0l$ zone, barbosalite (Mo/Zr radiation); corresponding directions in reciprocal cell (upper right) and in direct cell (lower right). Primed directions $h'00$ and c' refer to the $B2_1/d$ setting; nonprimed directions $h00$, $\bar{h}0h$ and c refer to the $P2_1/c$ setting. The c^* and a axes remain in the same directions in the two settings.

TABLE 1.—*Crystallographic elements and angle table for barbosalite*

Monoclinic prismatic $2/m$ space group $P2_1/c$
$a=7.25$ A, $b=7.46$ A, $c=7.49$ A; $\beta=120°15'$
$a:b:c=0.9718:1:1.0040$; $\beta=120°15'$; $p_0:q_0:r_0=1.0331:0.8673:1$
$r_2:p_2:q_2=1.1530:1.1912:1$; $\mu=59°45'$; $p'_0=1.1960$, $q'_0=1.004$, $x'_0=0.5832$

	Crystal form	Calculated from X-ray data						Measured data, $P2_1/c$ orientation of unit cell [1]				
								(010) polar			(001) polar	
		ϕ	ρ	ϕ_2	$\rho_2=B$	C	A	Optical goniometer signal	ϕ_2	$\rho_2=B$	Optical goniometer signal	C
d	011	30°09′	49°16′	59°45′	49°04′	40°56′	67°38′	Fair	(*)	49°00′	Good	40°55′
q	021	16 12	64 26	59 45	29 59	60 02	75 25	Fair	(*)	30 05	Good	60 05
y	101	90 00	60 40	29 20	90 00	30 26	29 20	Multiple	(*)	90 00	Multiple	(*)
t	100	90 00	90 00	0 00	90 00	59 45	----------	Multiple	(*)	90 00	Multiple	(*)
k	$\bar{1}02$	−90 00	0 51	90 51	90 00	31 05	90 51	Good	91°03′	90 05	Multiple	30 55
s	$\bar{1}01$	−90 00	31 30	121 30	90 00	61 45	121 30	Good	121 35	89 55	Good	62 00
f	111	60 34	63 55	29 20	63 49	39 18	64 40	Multiple	(*)	----------	Multiple	(*)
p	110	49 59	90 00	0 00	49 59	67 18	40 01	Multiple	(*)	----------	Multiple	(*
j	$\bar{1}12$	−1 41	26 40	90 51	63 21	40 04	90 45	Good	91 03	63 28 to 63 33	Good	39 50
e	$\bar{1}11$	−31 24	49 38	121 30	49 26	68 56	113 23	Good	121 25	49 34 to 49 40	Fair	68 38
g	121	41 33	69 33	29 20	45 28	52 04	51 34	Multiple	(*)	----------	Multiple	(*)
h	122	−0 51	45 07	90 51	44 54	52 50	90 36	Good	(*)	----------	Multiple	(*)
n	$\bar{4}81$	−27 37	83 42	166 37	28 16	82 06	117 26	Multiple	(*)	----------	Multiple	(*)
v	$\bar{4}83$	−20 42	70 44	135 20	27 59	83 30	109 29	Good	135 25	28 02	Not observed	

[1] Only the nonreentrant crystal faces give good signals by optical goniometry. An angle table, calculated from the unit-cell data from precession camera techniques, shows an average deviation between calculated and measured angles of 0°10′ if negative indices (hkl) are assigned to the nonreentrant forms k,s,j,e,h, and v or 0°53′ if positive indices are assigned to these same forms. Reentrant forms y, t, f, p and n are striated and give multiple signals by optical goniometry;* indicates that the crystal form has been identified by deviations between measured and calculated angles less than ±1°, if the best of the multiple signals are considered. Forms y, f, g, and v are line faces not shown on figure 1.

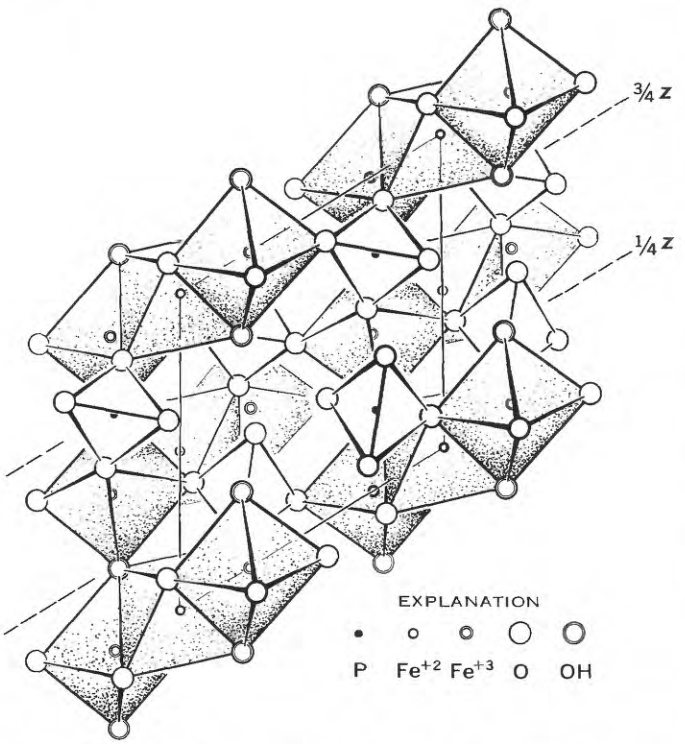

FIGURE 3.—Structure common to lazulite, scorzalite, and barbosalite, illustrated for barbosalite. The view is along [010]; unit cell is outlined by the parallelogram, the origin being taken at the lower right-hand corner with z vertical and positive upward, and x at 121° away from z and positive to the left. Certain of the polyhedra are omitted in order to reveal details of the structure. Drawing by H. T. Evans, Jr., from Lindberg and Christ (1959).

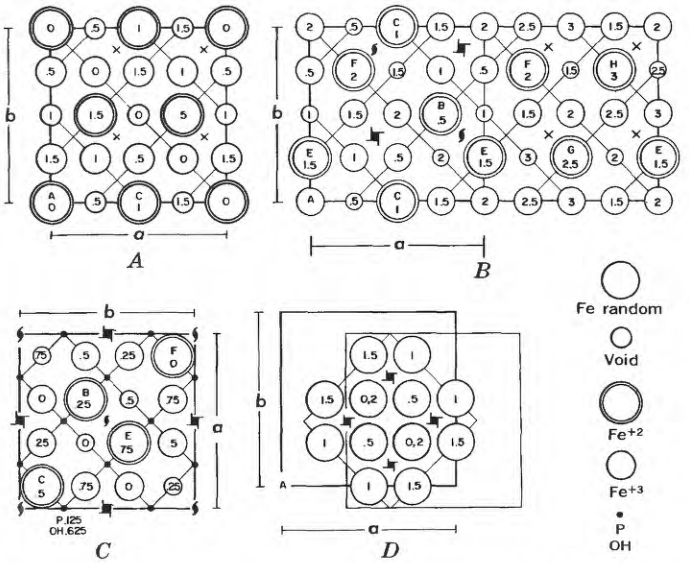

FIGURE 4.—Diagrams showing atomic structure of barbosalite, manganoan lipscombite, and iron lazulite. *A*, projection down c* of four layers of Fe octahedra on *ab* of barbosalite. Orientation of chains of octahedra indicated by diagonal joins parallel [$\bar{1}$10] or [110]. *B*, stacking sequence of twinned crystal; left, two layers below twin plane ($z=1¼$) in stacking sequence of untwinned crystal (pseudosymmetry elements shown do not extend beyond the two layers on each side of the composition plane), and two layers above twin plane in stacking sequences of twinned crystal; right, four layers, in stacking sequence of twinned crystal. *C*, suggested arrangement of triple groups in manganoan lipscombite, $P4_12_12$, z in fractions of tetragonal $c \approx$ monoclinic $2d_{001}$. *D*, iron octahedra of tetragonal iron lazulite (small diagonal base) projected on *ab* of barbosalite; height z in fractions of monoclinic d_{001}; 7 out of 8 octahedra filled randomly. Compare the filling of nonequivalent octahedral sites in barbosalite and in manganoan lipscombite with the operation of equivalent 4_1 axes in tetragonal iron lazulite.

At some point, let a mistake occur such that an octahedral layer is produced with all the cations shifted one octahedron in the same direction along the chains, relative to the previous layers. Then let subsequent growth occur normally, relative to this shifted layer. The bonding to the P and OH^{-1} ions between the last octahedral layer in the original orientation and the shifted layer has virtually the same character as in the untwinned crystal, with regard to the number and kinds of octahedra involved. If the process of twinning is thought of in this way, then the composition plane will pass through a P-OH^{-1} layer. A more usual explanation of the process of twinning makes use of some atom or coordination polyhedra which can play a common role in the original crystal and in the twinned counterpart by some symmetry operation. The 180° rotation axes of the P-tetrahedrons and the OH^{-1} tetrahedrons may be utilized in this manner. The structural relationship between the twinned and untwinned crystal is shown in figure 4.

Figure 4*A* shows the original untwinned crystal structure projected down c*, normal to the layers. Note that because of the value of β ($\approx$ 120°) successive sheets are displaced so that the identical layers at $z=0$ and $z=2$ superimpose exactly, while at $z=1$ the layer is shifted by ½a in projection. Figure 4*B* is obtained by applying the twin operation to figure 4*A*, assuming the composition plane to be at $z=1¼$. It can be seen that this is, indeed, equivalent to shifting all the cations in the octahedral layer at $z=1½$ by one octahedron in the [$\bar{1}$10] direction, and then letting the crystal grow in an orientation related to the original orientation by a 180° rotation around c*, the normal to the sheet.

MANGANOAN LIPSCOMBITE

Manganoan lipscombite (Fe^{+2}, Mn^{+2})$Fe_2^{+3}(PO_4)_2(OH)_2$ from the Sapucaia pegmatite mine, Minas Gerais, Brazil (Lindberg and Pecora, 1958; Lindberg, 1962) is a tetragonal mineral with $a=7.40$ A, $c=12.81$ A; space group $P4_12_12$. If the $h0l$ and $0kl$ X-ray diffraction patterns of monoclinic barbosalite are superimposed, a "synthetic" pattern results in which the distribution of the observed reflections has a striking

resemblance to that observed on the *h0l* and *0kl* patterns of manganoan lipscombite. A possible structural interpretation of manganoan lipscombite is shown in figure 4*C*.

The structure proposed for manganoan lipscombite is derived from that of barbosalite by systematic twinning at every second P–OH layer by a 180° rotation axis through P and OH^{-1} on the composition planes. As seen in figure 4*B*, this stacking sequence produces pseudo 4_1 and pseudo 2_1 axes. In figure 4*C*, the projection of these four layers is translated in the *ab* plane so that the suggested 4_1 and 2_1 axes coincide with their emergence in $P4_12_12$, the space group given above for manganoan lipscombite. The height *z* of the triple groups above the *ab* plane is renumbered in fractions of tetragonal *c*. Then *x* and *y* are so directed that Fe^{+2}, which must occupy special positions in 4(*a*), has *x* and *y* coordinates consistent with *z*. The suggested coordinates for the 4 Fe^{+2} in 4(*a*) are $x=\frac{1}{8}$, $y=\frac{1}{8}$, $z=0$; for 8 Fe^{+3} in 8(*b*) are $x=\frac{3}{8}$, $y=\frac{7}{8}$, $z=0$; of 8 P in 8(*b*) are $x=0$, $y=\frac{3}{4}$, $z=\frac{1}{8}$, and so forth.

The term "tetragonal iron lazulite" is used herein to denote the synthesized compound for which Katz and Lipscomb have determined the crystal structure. Gheith (1953) renamed this product lipscombite. Barbosalite (Lindberg and Pecora, 1954) had not yet been described. Gheith synthesized more than 100 samples under various laboratory conditions. He concluded that both tetragonal and monoclinic dimorphs form under identical conditions, and that "no prediction can be made as to whether the product will be lipscombite or ferrous ferric lazulite" (barbosalite). Once the monoclinic form is synthesized it may be converted to the tetragonal compound at temperatures between 110° and 290°C; above 290°C no ferrous iron remains (Gheith, 1953).

The structure proposed for manganoan lipscombite differs from that of tetragonal iron lazulite (Katz and Lipscomb, 1951) only in the filling of octahedral sites. Tetragonal iron lazulite has a defect structure with 7 out of 8 octahedral sites occupied statistically. These form randomly broken diagonal chains of octahedra, with smaller cell base *a* than in barbosalite or in manganoan lipscombite. In figure 4*D* the iron octahedra of tetragonal iron lazulite are shown projected on the *ab* plane of barbosalite (origin at *A*, *z* in fractions of monoclinic d_{001}). A chemical analysis ot tetragonal iron lazulite is lacking, but the suggested structure requires the formula $Fe^{+2}{}_5Fe^{+3}{}_2(PO_4)_4(OH)_4$.

CONCLUSIONS

The crystal structure of barbosalite, of tetragonal iron lazulite, and the suggested crystal structure of manganoan lipscombite consist of P–OH^{-1} layers and of iron octahedra layers. The iron octahedra form broken diagonal chains, parallel [$\bar{1}$10] (of barbosalite) in one metal layer and parallel [110] in the next layer. In tetragonal iron lazulite 7 out of 8 positions in the chains of octahedra are occupied randomly, with consequent formation of a smaller unit-cell base ($a/\sqrt{2}$). In barbosalite and in manganoan lipscombite 3 out of 4 octahedral sites are occupied by ordered triple groups of Fe^{+3}—Fe^{+2}—Fe^{+3} octahedra.

REFERENCES

Berry, L. G., 1948, Structural crystallography of lazulite, scorzalite, and vezelyite [abs.]: Am. Mineralogist, v. 33, p. 750.

Gheith, M. A., 1953, Lipscombite, a new synthetic "iron-lazulite": Am. Mineralogist, v. 38, p. 612–628.

Katz, Lewis, and Lipscomb, W. N., 1951, The crystal structure of iron lazulite, a synthetic mineral related to lazulite: Acta Cryst., v. 4, p. 345–348.

Lindberg, M. L., 1962, Manganoan lipscombite from the Sapucaia pegmatite mine, Minas Gerais, Brazil; first occurrence of lipscombite in nature: Am. Mineralogist, v. 47, p. 353–359.

Lindberg, M. L., and Christ, C. L., 1959, Crystal structures of the isostructural minerals lazulite, scorzalite, and barbosalite: Acta Cryst., v. 12, p. 695–696.

Lindberg, M. L., and Pecora, W. T., 1954, Tavorite and barbosalite, two new phosphate minerals from Minas Gerais, Brazil: Science, v. 119, p. 739.

——— 1955, Tavorite and barbosalite, two new phosphate minerals from Minas Gerais, Brazil: Am. Mineralogist, v. 40, p. 952–966.

——— 1958, Phosphate minerals from the Sapucaia pegmatite mine, Minas Gerais: Soc. Brasileira Geologia Bol., v. 7, no. 2, p. 5–14.

Palache, Charles, Berman, Harry, and Frondel, Clifford, 1951, The system of mineralogy of James Dwight Dana and Edward Salisbury Dana, v. 2, 7th ed.: New York, John Wiley and Sons, 1123 p.

Pecora, W. T., and Fahey, J. J., 1950, The lazulite-scorzalite isomorphous series: Am. Mineralogist, v. 35, p. 1–18.

AUTHIGENIC LAUMONTITE IN ARKOSIC ROCKS OF EOCENE AGE IN THE SPANISH PEAKS AREA, LAS ANIMAS COUNTY, COLORADO

By JAMES D. VINE, Denver, Colo.

Abstract.—Authigenic laumontite makes up as much as 25 percent of some beds of arkosic sandstone and conglomerate in the Cuchara and Huerfano Formations of Eocene age along the south flanks of the Spanish Peaks, Las Animas County, Colo. This calcium-rich zeolite replaces the micaceous minerals of the matrix and the potassium feldspar grains of the framework in rocks that were intruded by the Spanish Peaks stocks and dikes. The full extent and chemical nature of the alteration have not yet been determined.

As much as one-quarter of the mineral grains and matrix of arkosic sandstone and conglomerate in the Huerfano and Cuchara Formations of Eocene age has been replaced by authigenic laumontite in the Spanish Peaks area, Las Animas County, Colo. (fig. 1). Laumontite is a hydrous calcium-aluminum silicate characteristic of the zeolite facies of low-grade regional metamorphism in New Zealand (Coombs and others, 1959).

The occurrence of laumontite in the arkosic rocks of the Spanish Peaks area was discovered during routine X-ray diffraction analyses of Eocene fluviatile sandstones collected throughout the Rocky Mountains region. Five of six sandstone and conglomerate samples collected adjacent to the Aguilar-Apishapa Pass road on the south flank of the Spanish Peaks contained laumontite, as shown in table 1, whereas none of the samples collected from these same units in the Huerfano Park area 30 to 35 miles to the northwest contained laumontite. Alteration was not suspected at the time the samples were collected, as there was nothing unusual about the appearance of the rocks in outcrop. Sandstone and conglomerate beds in the Huerfano Formation are typically pale red to maroon, whereas those in the Cuchara Formation are more commonly yellowish gray to pale orange.

Eocene sedimentary rocks in the Spanish Peaks area have been intruded by stocks and dikes that, according to Johnson (1968), range in composition from silicic to ultrabasic; the most common rock type is syenodiorite. These igneous rocks were probably emplaced at various intervals during late Eocene or early Oligocene time, for the Huerfano Formation is the youngest sedimentary unit that was cut (Johnson, 1968, p. G7). Evidence is lacking to suggest that the Eocene sedimen-

TABLE 1.—*Mineral composition of selected rocks from the Spanish Peaks area, Las Animas County, Colo.*

[X-ray diffraction peak heights measured in inches of deflection for the principal reflection. Data derived from hand-ground pelletized samples scanned routinely from 2° to 60° 2θ at a rate of 2° per minute on a Norelco X-ray diffractometer; Cu$K\alpha$ radiation; 48 kilovolts and 20 milliamperes. Peak heights were measured above background by using the principal peak for each mineral species, as follows: 9.51 A for laumontite, 3.33 A for quartz, 3.24 A for potassium feldspar, and 3.19 A for plagioclase. Dashes indicate peak not detected]

Sample No.	Formation and rock type	Minerals (relative intensity)						
		Clay minerals			Laumontite	Quartz	Feldspar	
		14 A	10 A	7 A			Potassium	Plagioclase
1	Huerfano Formation, conglomerate	0.2	0.5	0.2	0.2	6.9	3.3	3.2
2	do	.3	----	----	1.5	7.8	.1	2.0
3	Huerfano Formation, sandstone	.1	.4	----	.2	8.1	3.8	3.8
4	do	.2	.4	.2	----	7.4	4.0	2.4
5	Cuchara Formation, sandstone	.1	----	----	1.3	8.1	.2	3.3
6	do	----	----	----	1.8	7.9	----	3.4
6 (light) [1]	do	----	----	----	4.4	2.7	----	1.6
108 [2]	Syenodiorite porphyry dike	3	----	----	.5	----	----	4.6

[1] Light fraction having specific gravity of about 2.5 to obtain laumontite concentrate.
[2] See reference to locality 108 in Johnson (1968, p. G23 and pl. 1).

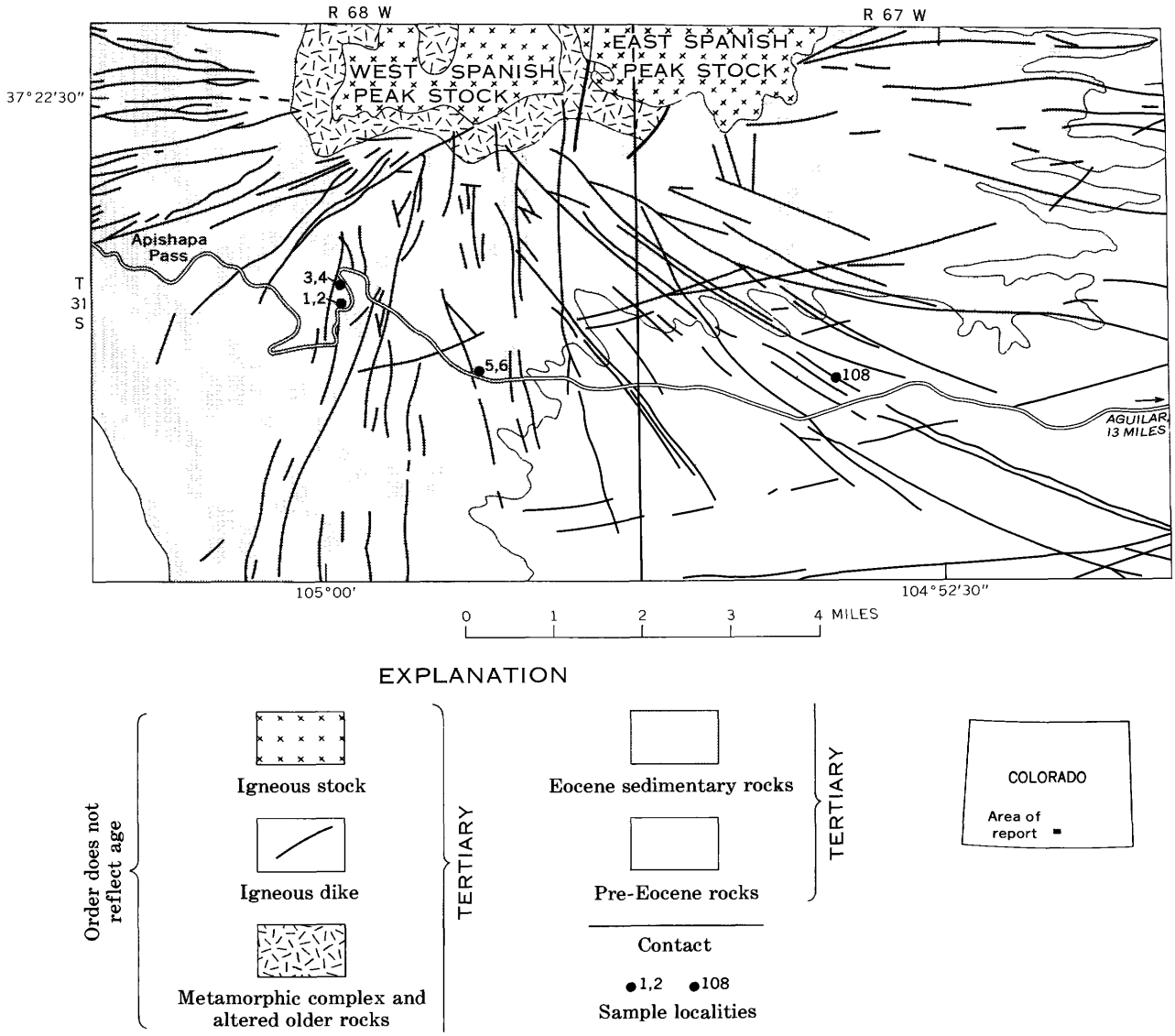

FIGURE 1.—Generalized geologic map of south flank of Spanish Peaks area. Sandstone samples from localities 2, 5, and 6 contain abundant laumontite replacement of potassium feldspar and matrix. The syenodiorite dike at locality 108 also contains laumontite. Modified from Johnson, Wood, and Harbour (1958) and Johnson (1968).

tary rocks were deeply buried at the time of intrusion or that the laumontite-bearing rocks were ever buried more than a few thousand feet.

Laumontite replaces micaceous minerals in the matrix of arkosic sandstone and conglomerate and partly or completely replaces framework grains of feldspar in the more highly altered samples. One sample (No. 4) from the Huerfano Formation is cemented with hematite, but no laumontite was detected by the X-ray analysis or by examination of the thin section. The mineral composition of the framework grains of sample 4 may therefore reflect the original composition of the other samples as well. If so, a marked reduction in the amount of potassium feldspar in the laumontite-bearing samples is indicated. A sample (No. 6) of sandstone from the Cuchara Formation contains the most laumontite and no detectable potassium feldspar or clay minerals. A split of sample 6 was separated in a bromoform-acetone mixture with a specific gravity of about 2.5 in order to obtain a concentrate of laumontite (specific gravity less than 2.4) in the float fraction. An X-ray diffractogram of this light fraction of sample 6 is shown on figure 2, and the mineral composition compared with the other samples is given in table 1. An estimate of the remaining quartz and feldspar in this light fraction by Leonard G. Schultz (oral commun., 1969) indicates that there may be about 65 percent laumontite in the con-

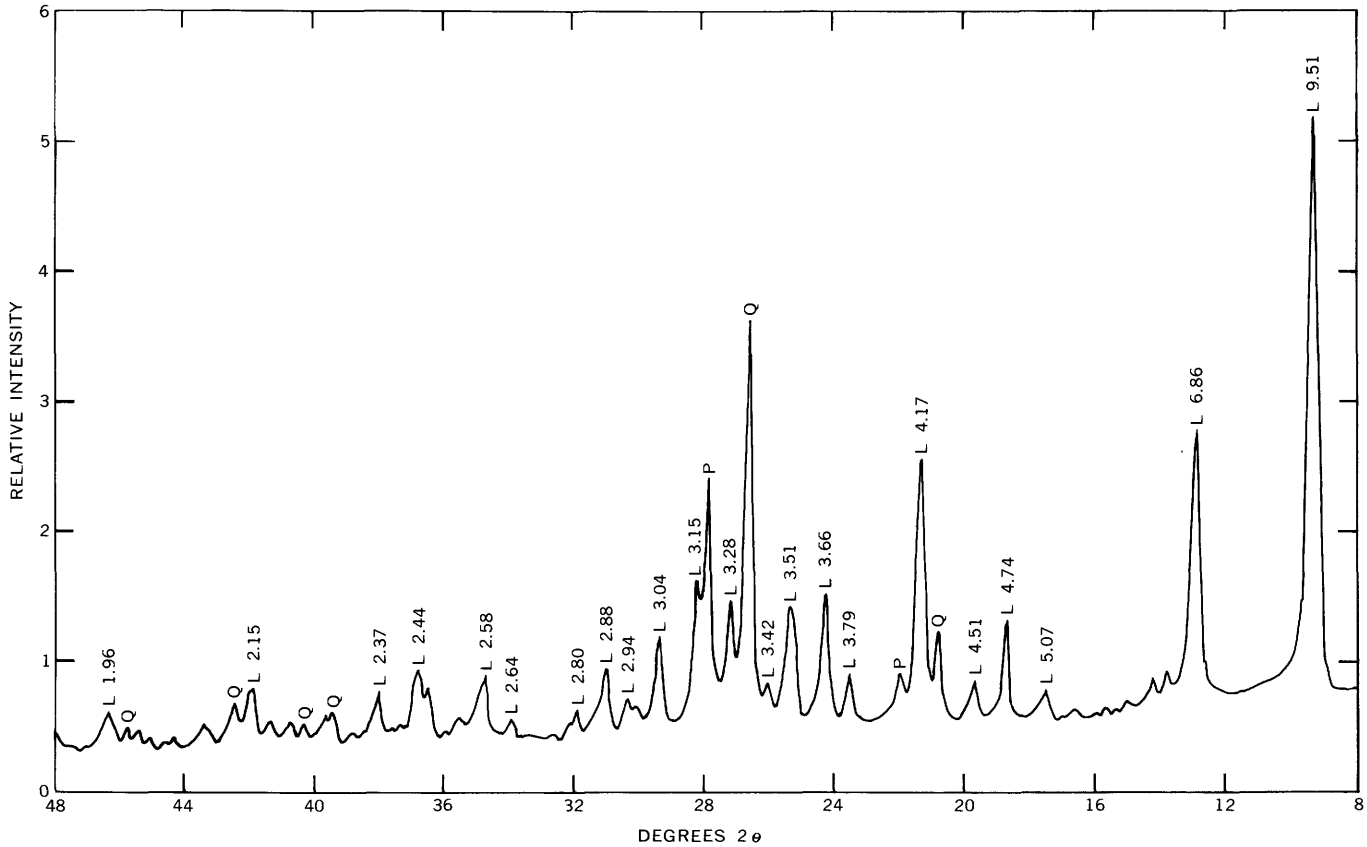

FIGURE 2.—X-ray diffractometer pattern of the float fraction of a laumontite-bearing sandstone separated in heavy liquid with a specific gravity of about 2.5. *Q*, quartz; *P*, plagioclase; and *L*, laumontite (*d* spacings in angstrom units). Cu$K\alpha$: $\lambda = 1.5418$ Å. Sample 6 (light) in table 1.

centrate. Comparison of X-ray peak heights in the concentrate and in the original sample indicates a composition of about 25 percent laumontite for the original sample.

Examination of the sandstone and conglomerate samples in thin section by petrographic microscope indicates the occurrence of laumontite as a massive cement that (1) has replaced much of the matrix minerals, and (2) has partially to completely replaced feldspar grains. Little or no microcline remains in the more highly altered samples, whereas the plagioclase grains, chiefly oligoclase, show incomplete replacement by laumontite. Areas of laumontite replacement are characterized by a pale-yellowish-gray birefringence and wavy extinction in polarized light. Two cleavage directions at nearly right angles to each other are clearly visible under high magnification.

A sample of syenodiorite porphyry supplied by R. B. Johnson from a radial dike at his locality 108 (Johnson, 1968, p. G23 and pl. 1) contains laumontite that has replaced the original rock constituents in spheroidal areas as much as 15 millimeters across. The spheroidal concentrations are similar to the occurrence of laumontite in Tertiary volcanic rocks in the Mount Rainier area, Washington, as described by Fiske, Hopson, and Waters (1963, p. 32–36).

Although no chemical analyses were available at the time of this writing, the replacement of potassium feldspar by a calcium zeolite suggests a massive transportation of major elements. Such massive transfer, if it did occur, would indicate a zonal pattern of alteration centered on the Spanish Peaks intrusions. Detailed study is required to further delineate the area of alteration and to determine the chemical compositions of the zones.

The occurrence of authigenic laumontite in sedimentary rocks has been reported from many geosynclinal rock sequences. For example, Kaley and Hanson (1955) describe laumontite as a cement in a feldspathic sandstone of Miocene age recovered by drilling in the San Joaquin Valley, Calif. Moreover, B. M. Madsen and K. J. Murata (written commun., 1969) have found laumontite in outcrops of Miocene rocks near San Jose, Calif. In many areas the laumontite is associated with the alteration of volcanic material in the sedimentary sequence. In southwestern Grant County,

Oreg., Dickinson (1962) described replacement by laumontite as one phase in the alteration of pyroclastic marine Jurassic rocks along the South Fork John Day River. Brown and Thayer (1963) also recognized a laumontite stage in the zeolitic alteration of a thick sequence of Upper Triassic and Lower Jurassic strata in the Aldrich Mountains of Oregon. The laumontite occurs there chiefly in rocks of volcanic origin. Laumontite was recognized in Cretaceous sandstone in western Alaska by Hoare, Condon, and Patton (1964) who suggested that tuffaceous material of siliceous or intermediate composition was a prerequisite for its formation. They also note, however, that the altered, laumontitic rocks there contain only a trace of potassium feldspar, whereas the unaltered rocks contain 5 to 20 percent potassium feldspar. In New Zealand, laumontite is characteristic of tuffaceous graywackes that have been buried 17,000 to 30,000 feet. Coombs, Ellis, Fyfe, and Taylor (1959) recognized laumontitic rock as a facies of low-grade metamorphism that bridges the gap between ordinary diagenesis and conventional metamorphic facies.

The occurrence of laumontite in arkosic Eocene rocks of the Spanish Peaks area is noteworthy for the following reasons: (1) The micaceous minerals of the matrix and framework grains of potassium feldspar are most readily replaced by laumontite; (2) vitric material is not a precursor of the laumontite; and (3) alteration appears to be localized near the Spanish Peaks intrusive complex, which probably supplied the heat required for hydrothermal alteration at a relatively shallow depth.

REFERENCES

Brown, C. E., and Thayer, T. P., 1963, Low-grade mineral facies in Upper Triassic and Lower Jurassic rocks of the Aldrich Mountains, Oregon: Jour. Sed. Petrology, v. 33, no. 2, p. 411–425.

Coombs, D. S., Ellis, A. J., Fyfe, W. S., and Taylor, A. M. 1959, The zeolite facies, with comments on the interpretation of hydrothermal syntheses: Geochim. et Cosmochim. Acta, v. 17, no. 1–2, p. 53–107.

Dickinson, W. R., 1962, Petrology and diagenesis of Jurassic andesitic strata in central Oregon: Am. Jour. Sci., v. 260, no. 7, p. 481–500.

Fiske, R. S., Hopson, C. A., and Waters, A. C., 1963, Geology of Mount Rainier National Park, Washington: U.S. Geol. Survey Prof. Paper 444, 93 p. [1964].

Hoare, J. M., Condon, W. H., and Patton, W. W., Jr., 1964, Occurrence and origin of laumontite in Cretaceous sedimentary rocks in western Alaska, *in* Geological Survey Research 1964: U.S. Geol. Survey Prof. Paper 501–C, p. C74–C78.

Johnson, R. B., 1968, Geology of the igneous rocks of the Spanish Peaks region, Colorado: U.S. Geol. Survey Prof. Paper 594–G, p. G1–G47.

Johnson, R. B., Wood, G. H., Jr., and Harbour, R. L., 1958, Preliminary geologic map of the northern part of the Raton Mesa region and Huerfano Park in parts of Las Animas, Huerfano, and Custer Counties, Colorado: U.S. Geol. Survey Oil and Gas Inv. Map OM-183.

Kaley, M. E., and Hanson, R. F., 1955, Laumontite and leonhardite cement in Miocene sandstone from a well in San Joaquin Valley, California: Am. Mineralogist, v. 40, nos. 9–10, p. 923–925.

MINERALOGY AND GEOCHEMISTRY OF FLUORAPATITE FROM CERRO DE MERCADO, DURANGO, MEXICO

By. E. J. YOUNG, A. T. MYERS, ELAINE L. MUNSON, and NANCY M. CONKLIN, Denver, Colo.

Abstract.—Fluorapatite from Cerro de Mercado has been known to mineral collectors throughout the world for its yellow color, transparency, and perfect crystal form. Because this fluorapatite was considered for use as a phosphate reference standard in spectrochemical laboratories of the U.S. Geological Survey, knowledge of its complete chemical composition and physical properties became necessary. The fluorapatite principally contains rare earths, but it also contains a rather large number of minor elements, its formula being $Ca_{9.83}Na_{0.08}Sr_{0.01}RE_{0.09}(PO_4)_{5.87}(SO_4)_{0.05}(CO_3)_{0.01}(SiO_4)_{0.06}(AsO_4)_{0.01}F_{1.90}Cl_{0.12}(OH)_{0.01}$. Although the apatite is intimately associated with martite, no FeO was found by chemical analysis, and Fe_2O_3 was found in the amount of only 0.06 percent. Physical properties of the analyzed apatite are: $\omega = 1.6362 \pm 0.0005$, $\epsilon = 1.6326 \pm 0.0005$; $a = 9.391 \pm 0.001$ A, $c = 6.878 \pm 0.002$ A; measured specific gravity (22°C) is 3.216, calculated density (22°C) is 3.219; magnetic susceptibility is -0.078×10^{-6} emu/g.

Fluorapatite occurs in many different associations; one of the more common occurrences is in intimate association with iron ores related to igneous rocks. From a geochemical point of view, iron ores related to igneous rocks may be divided into two types: (1) the type characterized by iron only, containing magnetite, martite, or hematite, or any combination of the three; and (2) the type characterized by iron and titanium, containing titaniferous magnetite or ilmenite, or both, and occasionally rutile. Some of the more notable fluorapatite-bearing type 1 deposits, in addition to the Cerro de Mercado, are those from the Mineville district, New York (McKeown and Klemic, 1956); Iron Mountain, Mo. (Crane, 1912); Iron Springs district, Utah, and Barth, Nev. (Shawe and others, 1962); Kiirunavaara, Sweden (Geijer, 1931, 1967); several localities in the Urals (Boldyrev, 1930; Sumin, 1957); and several localities in Chile (Geijer, 1967), including a magnetite "flow" (Park, 1961). To the authors' knowledge, fluorapatites in all these iron ore deposits contain at least 1 percent rare-earth oxides, except, perhaps, those from Iron Mountain, Mo., and Barth, Nev., and those from Chile, for which there are no relevant data. Sparse data on fluorapatite from the type 2 deposits, in which both Fe and Ti are major elements, suggest that the rare-earth content of these fluorapatites is appreciably less. A fluorapatite from Colombia, South America, intimately associated with ilmenite, contains 0.30 percent rare-earth oxides (N. M. Conklin and A. T. Myers, unpub. data, 1967). Fluorapatites from nelsonite (apatite plus rutile or ilmenite) in Virginia (Ross, 1941), from titaniferous magnetite in the Lake Sanford area, New York (Stephenson, 1945), and from ilmenite deposits in Quebec (Gillson, 1932) are not reported to contain rare earths, but analytical data for these deposits are meager or nonexistent.

Acknowledgments.—In addition to the many analysts who have contributed to this study, and who are cited in the text or tables, we would like to express our appreciation to engineer Luis Garcia Gutierrez of Durango, Mexico, who very kindly guided us through Cerro de Mercado.

Special thanks are also given to Walter Coleman, of the U.S. Geological Survey, who provided us with most of the samples of fluorapatite.

GEOLOGIC BACKGROUND

The Cerro de Mercado (also called Iron Mountain), near the city of Durango, is the largest deposit of iron ore in Mexico. Its name is derived from that of Captain Gines Vasquez del Mercado, who set out from Guadalajara in 1552 to search for gold and silver and was led to the hill by reports of its being a mountain of gold. The mountain rises abruptly to a height of 600 feet[1] above its base of approximately 6,260 feet

[1] This information is slightly different from that in the abstract by Young and others (1968), and it supersedes the data in their abstract.

altitude and is roughly 1 mile long and a third of a mile wide. High-grade martite outcrops form six prominent knobs on the mountain. Between these knobs and forming most of the mass of the mountain are several extrusive rocks, consisting of latite, rhyolite, and rhyolite tuff, all of which are Tertiary in age. The ore bodies of martite are tabular and almost flat lying and have a maximum thickness of 200 feet. In 1950, iron ore reserves for this deposit were estimated at 25–50 million tons. The deposit was studied extensively by Salinas, Gonzales, Santillan, Acevedo, and Martinez Quintero (1923) and the mineralogy and geology were described by Foshag (1929). Flores Reyes (1950) recounted the various theories of origin of the deposit and concluded that the deposit is a result of replacement by iron-bearing fluids.

MODE OF OCCURRENCE OF THE FLUORAPATITE AND ASSOCIATED MINERALS

Fluorapatite crystals are found throughout the martite in several modes of occurrence. The chief mode of occurrence is in fissures or cavities in the martite, less commonly embedded in martite. Locally, where the ore is soft, apatite occurs in veinlets. Another mode of occurrence is in association with quartz, chalcedony, and sepiolite. Commonly, small crystals of martite are observed intergrown with apatite crystals. Paulick and Newesely (1968) illustrated such intergrowths and other microintergrowths with iron oxides and concluded that the apatite crystallized simultaneously with the iron ore. Generally the finest gemstone quality fluorapatite is as much as ½ to 1 inch long by ¼ to ½ inch wide. Rarely, some crystals may reach about 2 inches in length. Both prismatic and pyramidal faces are well developed.

Foshag (1929) mentioned a colorless apatite, dahllite, and a rose-red to lavender botryoidal unknown phosphate as being found at Peñascos de la Industria (southwestern extremity of Cerro de Mercado). Some small colorless crystals of fluorapatite found by us at Peñascos de la Industria are spectrographically similar to the larger yellow ones. Dahllite and the unknown rose-red phosphate were not found by us, but the occurrence of the secondary calcium-aluminum phosphate, crandallite, previously unreported, was confirmed by X-ray analysis. The crandallite was found at Peñascos de la Industria as a soft, white, earthy material in association with calcite crystals.

Martite (hematite) is the major ore mineral and is mostly massive, but it may occur in octahedrons as much as 3 inches across. X-ray analysis of the octahedrons shows the presence also of trace amounts of goethite and magnetite. Other minerals recorded from Cerro de Mercado are augite, hyalite, barite, and titanite.

PHOSPHATE SPECTROGRAPHIC STANDARD

Because some of the fluorapatite from Cerro de Mercado is highly transparent and is free of inclusions, it was decided that these crystals would make a much-needed phosphate reference standard for the U.S. Geological Survey spectrographic laboratories. From more than 500 grams of crystals, 23.5g was chosen for analysis because of virtual freedom from inclusions and mineral coatings. Figure 1 shows the analyzed crystals. Small chips were taken from each of the 51 crystals that comprised this select group, called DM-A, for physical analysis. The chips and crystals were then ultrasonically cleaned, and the crystals were crushed in a boron carbide mortar for chemical and spectrographic analyses.

FIGURE 1.—DM–A, select group of crystals of fluorapatite from Cerro de Mercado, Durango, Mexico, used for chemical, spectrographic, and physical analyses. The group constitutes 23.5 g of crystals chosen for their purity from more than 500 g.

Seemingly slightly less pure crystals, in the amount of about 400 g, were ultrasonically cleaned, and then crushed in an alumina ball mill. This group of crystals, called DM-B, provided the phosphate reference spectrographic standard now used in the U.S. Geological Survey. DM-B was analyzed by four spectrographers and was found to be virtually indistinguishable from DM-A as shown in table 1.

PHYSICAL PROPERTIES

Color, fluorescence, dichroism

The lemon-yellow crystals of fluorapatite fom Cerro de Mercado (fig. 1) are world famous for their clarity and purity of color. Using the "Munsell Book of Color" (Munsell Color Co., 1929), we determined the color of many crystals as yellow, green-yellow (*Y-GY* 8/6).

TABLE 1.—*Trace-element analyses of fluorapatite from Cerro de Mercado, Durango, Mexico*

[DM-A, group of purest crystals, provided the chemical, spectrographic, and physical analyses; DM-B, group of crystals, provided spectrographic reference standard; DM-D, crystals collected by A. T. Myers and E. J. Young in 1967; DM-E, colorless crystals collected by A. T. Myers and E. J. Young in 1967. Abbreviations: OS, optical spectrography; AA, atomic absorption; XF, X-ray fluorescence; Nd., not determined. Precision of quantitative spectrographic analysis is ±15 percent. Semiquantitative spectrographic results are reported to the nearest number in the series 1, 0.7, 0.5, 0.3, 0.2, 0.15, and 0.1, which represent approximate midpoints of group data on a geometric scale. The precision of a reported value is approximately plus or minus one bracket at 68 percent, or two brackets at 95 percent confidence. Elements (with detection limits in parts per million) looked for but not found: Ag, Be (1); Pd (2); Co, Mo (3); Ga (5); Bi, Ge, In, Nb, Pb, Sn (10); Au, B (20); Pt, Re, Tl (50); Hf, W (100); Sb, Ta (200); Te (2,000); Hg (10,000). Analysts are from the U.S. Geological Survey, except for Niilo Lounamaa, who is from Typpi oy, Oulu, Finland]

	DM-A			DM-B				DM-D	DM-E
	Quantitative analyses (N. M. Conklin)	(C. Huffman, Jr.)	Semiquantitative analyses (N. M. Conklin)	Quantitative analyses (C. Waring)	(N. Lounamaa)	Semiquantitative analyses (H. Worthing)	(C. Heropoulos)	Semiquantitative analyses (N. M. Conklin)	
	OS	AA	OS	OS	AA and XF	OS	OS	OS	
	Analysis, in parts per million								
Si	1, 600	Nd.	Nd.	1, 800	Nd.	2, 000	1, 500	1, 500	1, 500
Al	Nd.	Nd.	<500	220	Nd.	300	200	<500	<500
Fe	Nd.	350	500	400	Nd.	300	700	700	500
Mg	Nd.	140	300	200	Nd.	150	150	300	300
Na	Nd.	2, 400	3, 000	1, 500	Nd.	1, 500	3, 000	3, 000	3, 000
K	Nd.	<30	Nd.	<100	Nd.	<30	Nd.	Nd.	Nd.
Ti	Nd.	Nd.	<2	<100	Nd.	<. 8	70	<2	<2
Mn	130	100	Nd.	100	Nd.	100	100	100	100
As	600	Nd.	Nd.	<1, 000	Nd.	700	<200	700	1, 500
Ba	<3	Nd.	Nd.	2	Nd.	2	7	<2	<2
Cd	Nd.	<10	<50	Nd.	Nd.	<10	<50	<50	<50
Cr	Nd.	Nd.	<1	<1	Nd.	<. 8	<1	<1	<1
Cu	<1	Nd.	Nd.	. 9	Nd.	. 5	<1	<1	<1
Li	Nd.	Nd.	<100	<10	Nd.	3	<200	<100	<100
Ni	Nd.	Nd.	<3	Nd.	Nd.	<30	5	<3	<3
Sc	Nd.	Nd.	<5	<100	Nd.	<10	<2	<5	<5
Sr	580	440	Nd.	750	Nd.	700	1, 000	500	500
Th	Nd.	Nd.	300	<100	Nd.	70	<150	<300	300
V	40	Nd.	Nd.	40	Nd.	30	50	30	30
Zn	Nd.	10	<200	Nd.	Nd.	<100	<100	<200	<200
Zr	23	Nd.	Nd.	25	Nd.	20	<5	<10	<10
Ce	4, 700	Nd.	Nd.	7, 000	4, 150 (XF)	7, 000	5, 000	7, 000	7, 000
La	4, 200	Nd.	Nd.	6, 400	3, 330 (XF)	7, 000	5, 000	2, 000	3, 000
Nd	2, 000	Nd.	Nd.	2, 000	1, 230 (XF)	1, 500	2, 000	1, 500	1, 500
Pr	<1, 000	Nd.	Nd.	800	540 (XF)	700	1, 000	<1, 000	<1. 000
Sm	300	Nd.	Nd.	200	Nd.	200	300	300	500
Eu	<100	Nd.	Nd.	<100	17 (AA)	20	<50	<100	<100
Y	760	Nd.	Nd.	1, 000	670 (AA)	1, 000	1, 000	700	700
Gd	200	Nd.	Nd.	300	<110 (AA)	200	200	150	200
Tb	100	Nd.	Nd.	100	Nd.	200	<100	<100	<100
Dy	150	Nd.	Nd.	100	90 (AA)	100	100	150	200
Ho	30	Nd.	Nd.	40	10 (AA)	50	70	30	50
Er	100	Nd.	Nd.	100	35 (AA)	100	100	50	70
Tm	<20	Nd.	Nd.	10	7 (AA)	10	<10	<20	<20
Yb	50	Nd.	Nd.	80	23 (AA)	70	70	30	50
Lu	<40	Nd.	Nd.	<100	Nd.	<10	<15	<40	<40
	Analysis, in percent								
ΣRE_2O_3	1. 58	Nd.	Nd.	2. 12	1. 3	2. 13	1. 74	1. 48	1. 65

NOTE: Quantitative analysis for Th and U by isotope-dilution technique was done by J. N. Rosholt, U.S. Geological Survey. Results, in parts per million, are:

	DM-A	DM-B	DM-D
Th	201±6	238±12	167±17
U	11. 0±0. 2	12. 3±0. 2	9. 7±0. 2

Fluorescence is extremely weak in shortwave ultraviolet light (table 2). Dichroism is also extremely weak, detectable only in crystals that are at least 5 millimeters thick; ω is pale yellow and ϵ is pale light gray; $\omega > \epsilon$. Paulick and Newesely (1968) reported the apatite from Cerro de Mercado to be anomalously biaxial with $2V$ as much as 10°.

Absorption spectra

Absorption spectra (table 2) in the visible region are weakly shown by thick crystals.

TABLE 2.—*Physical properties of DM–A, fluorapatite from Cerro de Mercado, Durango, Mexico*

Color	*Y–GY*8/6 (yellow, green-yellow).
Dichroism	ω, pale yellow; ϵ, pale light gray; $\omega > \epsilon$ (detectable only in crystals that are at least 5 mm thick).
Fluorescence (20°C), under shortwave ultraviolet light (254 mμ).	607 ± 4 mμ; pale pinkish orange, very weak.
Absorption spectra:	
ω	Yellow: 573 mμ, weak broad band; 579–597 mμ, very weak band.
ϵ	Yellow: 573 mμ, weak diffuse line. 577–579 mμ, weak diffuse band. 583–584 mμ, weak diffuse band. Yellow-orange: 591 mμ, weak diffuse line.
Magnetic susceptibility 27°C	-0.078×10^{-6} emu/g; diamagnetic.
Lattice constants:	
a	9.391 ± 0.001 A
c	6.878 ± 0.002 A
c/a	0.7324
Volume	525.3 ± 0.1 A³
Density (22°C):	
Measured	3.216 ± 0.002 g/cm³
Calculated	3.219 g/cm³
Refractive indices:	
ω	1.6362 ± 0.0005
ϵ	1.6326 ± 0.0005 $\omega - \epsilon = 0.0036$
ω	1.6359 (average of 21 other crystals, determined directly on Abbé refractometer).
Birefringence	0.0037 (average of 15 other crystals determined by Ehringhaus compensator).

Magnetic susceptibility

Magnetic susceptibility of this apatite is very low, as should be expected because of the very low iron and manganese content. F. E. Senftle (written commun., 1968), of the U.S. Geological Survey, measured its magnetic susceptibility in a quartz helix magnetic susceptibility balance. (See method in Senftle and others, 1958.) Room-temperature (27°C) susceptibility was found to be -0.078×10^{-6} emu/g (fig. 2). As far as the authors know, this is the first time the magnetic susceptibility of apatite has been found to be diamagnetic (negative values are diamagnetic, positive ones are paramagnetic) at room temperature.

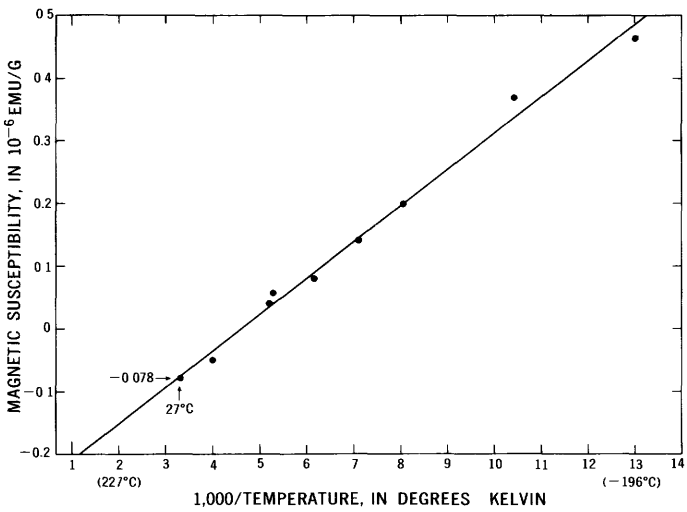

FIGURE 2.—Magnetic susceptibility in emu/g of DM–A, fluorapatite from Cerro de Mercado, Durango, Mexico. Measured by F. E. Senftle, U.S. Geological Survey.

Measurements of susceptibility made by the senior author by means of the Frantz isodynamic separator gave a best value of $+0.0045 \times 10^{-6}$ emu/g (22°C). The difference between this value and Senftle's value indicates that the Frantz separator should not be used for measurements of minerals having very low magnetic susceptibility.

Lattice constants and interplanar spacings

X-ray diffractometry was done at a chart speed of ¼° 2θ per minute using CaF_2 as internal standard. The resulting observational data were handled by the computer program of Evans, Appleman, and Handwerker (1963). See table 3, this report. Lattice constants are $a = 9.391 \pm 0.001$ A; $c = 6.878 \pm 0.002$ A; volume $= 525.3 \pm 0.1$ A³; $c/a = 0.7324$. A more precise determination of the lattice constants of a sample of apatite from Cerro de Mercado by H. T. Evans and D. E. Appleman (1962, unpub. data) gave $a = 9.3923 \pm 0.0003$ A; $c = 6.8821 \pm 0.0005$ A; volume $= 525.77$ A³; $c/a = 0.7327$. Paulick and Newesely (1968) reported the following lattice constants from Cerro de Mercado apatite: $a = 9.40 \pm 0.01$ A; $c = 6.87 \pm 0.01$ A; volume $= 525.7$ A³; $c/a = 0.731$.

Density

The average of three determinations of density done by a combined suspension pycnometer method (Young and Munson, 1966) was 3.216 ± 0.002 g/cm³ (22°C). The average of six determinations done on a newly calibrated specific gravity balance was $3.215_4 \pm 0.002$ g/cm³ (22°C). The calculated density based on the chemical composition and the unit cell constants is 3.218_7 g/cm³ (22°C). Thus calculated and measured densities differ by only ≈0.003 g/cm³.

TABLE 3.—*X-ray powder data for DM-A, fluorapatite from Cerro de Mercado, Durango, Mexico*

[Cu$K\alpha_1$ radiation, Ni filter (λ=1.5405)]

hkl	Intensity	*d* spacing (in angstroms)	
		Measured	Calculated [1]
100	7	8. 12	8. 13
101	5	5. 24	5. 25
200	6	4. 059	4. 066
111	8	3. 870	3. 878
002	46	3. 434	3. 439
102	18	3. 163	3. 167
210	16	3. 072	3. 074
211	100	2. 803	2. 806
112	34	2. 773	2. 774
300	39	2. 708	2. 711
202	23	2. 625	2. 626
301	5	2. 520	2. 522
212	5	2. 292	2. 292
310	15	2. 255	2. 256
221	2	2. 221	2. 222
311	7	2. 143	2. 143
113	4	2. 061	2. 060
203	3	1. 998	1. 997
222	15	1. 939	1. 939
312	9	1. 886	1. 886
320	4	1. 865	1. 866
213	28	1. 838	1. 838
321	11	1. 801	1. 801
410	6	1. 775	1. 775
313	2	1. 607	1. 608
420	3	1. 537	1. 537
502	12	1. 471	1. 470
304	5	1. 453	1. 452
323	5	1. 448	1. 447
511	6	1. 429	1. 429
332	4	1. 425	1. 425
512	2	1. 345	1. 344
423	6	1. 276	1. 277
610	2	1. 240	1. 240
513	4	1 232	1. 232
522	3	1. 218	1. 218

[1] Determined by D. E. Appleman using a computer-based least-squares refinement method.

Paulick and Newesely (1968) reported a pycnometrically determined density of 3.237±0.003 g/cm³ (22°C) for the apatite from Cerro de Mercado, whereas their calculated density (from X-ray data) was 3.214 g/cm³ (22°C). They attributed the higher measured density to the finely dispersed inclusions which had densities considerably higher than the density of the apatite.

The density calculated from the lattice constants of Evans and Appleman is 3.2159 g/cm³, which is very close to our measured average density of 3.2157 g/cm³. This raises the question of how much variation in lattice constants occurs in Cerro de Mercado apatite, and whether more precise work on different samples would answer the question.

Optical data

Refractive indices were obtained by the immersion method involving temperature variation (Young and Munson, 1966) on fragments of the crystals selected for chemical analysis. In addition, refractive index ω was determined on 21 other crystals by means of the Abbé refractometer. Finally, a rotatable calcite compensator (Ehringhaus) was used to measure the birefringence of 15 crystals. Small quartz crystals of varying thickness were used to calibrate the compensator. The range of birefringences from compensator measurements is 0.0035_9 to 0.0038_8, $\Delta=0.0002_9$. The wider range encountered for refractive index ω is 1.6352 to 1.6370, $\Delta=0.0018$, in the 21 crystals. For the chemically analyzed DM-A, the range for ω was 1.6356 to 1.6366 ($\Delta=0.001$) for 10 fragments, yielding an average of $\omega=1.6362$ and $\epsilon=1.6326$.

Paulick and Newesely (1968) reported similar refractive indices for Cerro de Mercado apatite—$\omega=1.6364$ and $\epsilon=1.6327$.

CHEMICAL PROPERTIES

The earliest chemical analysis available is by A. R. Martinez Quintero (in Salinas and others, 1923). As shown in table 4, the analysis is undoubtedly erroneous, as no rare earths or even fluorine is listed. The high Fe_2O_3 content can definitely be attributed to martite impurity. A later chemical analysis by the late Ivan Barlow (unpub. data, 1950), of the U.S. Geological Survey, is also shown in table 4. No rare earths were reported. Spectrographic analyses by Cruft (1966) and Paulick and Newesely (1968) are listed in table 5.

TABLE 4.—*Previous chemical analyses, in percent, of fluorapatite from Cerro de Mercado, Durango, Mexico*

[Tr., trace]

Analysis by A. R. Martinez Quintero (in Salinas and others, 1923)		Analysis by Ivan Barlow (unpub. data, 1950)	
CaO	53. 01	CaO	55. 68
MgO	. 35	MgO	. 68
P_2O_5	44. 36	P_2O_5	41. 04
Fe_2O_3	. 99	V_2O_5	0
SiO_2	. 77	CO_2	. 03
Cl	. 39	F	3. 50
H_2O^+	. 44	Cl	Tr.
H_2O^-	. 19	H_2O^+	. 13
	100. 50	H_2O^-	0
Less O	0. 09		101. 06
	100. 41	Less O	1. 47
			99. 59

Our work shows that there are 16 chemical components in the fluorapatite from Cerro de Mercado that have a weight percent of at least 0.01, if we count the rare-earth oxides as a unit and discount the traces of MgO, Fe_2O_3, and Al_2O_3 as impurities. The complete analysis is shown in table 6 and the distribution of the rare earths in table 1. The calculated formula is $Ca_{9.83}Na_{0.09}Sr_{0.01}Re_{0.09}(PO_4)_{5.87}(SO_4)_{0.05}(SiO_4)_{0.06}(AsO_4)_{0.01}(CO_3)_{0.01}F_{1.90}Cl_{0.12}(OH)_{0.01}$.

TABLE 5.—*Previous spectrographic analyses of fluorapatite from Cerro de Mercado, Durango, Mexico*

[X, secondary constituent; Tr., trace; Nf., looked for but not found; Nd., not determined]

	Analysis by Cruft (1966) (ppm)	Analysis by Paulick and Newesely (1968)		Remarks on all data by Paulick and Newesely (1968)
		Crystal powder, average	Optically clear crystal fragments	
Si	1, 379	Tr.	Nf.	(1)
Al	69	Tr.	Nf.	(2)
V	Tr.	Nf.	Nf.	(3)
Mg	Tr.	Tr.	Tr.	(4)
Ni	Tr.	Tr.	Nf.	(5)
Cu	1. 7	Tr.	Nf.	(3)
Fe	1, 200	X	Nf.	(6)
Zr	Tr.	Nf.	Nf.	(3)
Mn	269	X	Nf.	(5)
Y	1, 083	X	Tr.	(4)
Ce	4, 433	X	X	(4)
Sr	[7] 8, 898	Nf.	Nf.	(4)
La	5, 129	X	X	(4)
Ba	Tr.	Nf.	Nf.	(4)
Na	Nd.	Tr.	Tr.	(4)
As	Nd.	Tr.	Nf.	(3)

[1] Inclusion (SiO_2).
[2] Inclusion.
[3] Inclusion(?).
[4] Lattice substitution.
[5] Inclusion (magnetite).
[6] Inclusion (magnetite, hematite, goethite).
[7] This value for Sr is about 14 times higher than the average obtained by the analysts in table 1, and is therefore suspect.

CRYSTAL CHEMISTRY AND GEOCHEMISTRY

Relation of omega index of refraction to chemical composition

The effect of chemical composition on the omega index of refraction, ω, of the Cerro de Mercado apatite is shown in the following calculation where the sum of the products of the weight percentages of the chemical components and factors (Young, 1965) are added to the omega index of pure fluorapatite to obtain a calculated omega index:

Cl	0. 41×0. 0054=	0. 00221
Rare-earth oxides (including ThO_2)	1. 45× . 0018=	. 00261
SO_3	. 37× . 0003=	. 00011
H_2O+	. 01× . 0091=	. 00009
MnO [1]	. 01× . 0020=	. 00002
SrO	. 07× . 0001=	. 00001
Total		0. 00505
ω, pure fluorapatite		1. 6325
ω, calculated		1. 6376

[1] Factor for MnO is from Young, Sheridan, and Munson (1966).

The measured ω of the fluorapatite from Cerro de Mercado is 1.6362; the calculated ω is therefore 0.0014 too high. Because chlorine and the rare-earth oxides are the only components that significantly affect ω, we might suspect that their factors are too high, or else that an unaccounted-for component tends to depress ω. Sodium may be depressing ω in this case, but many more careful analyses of apatite will be necessary before we can be sure.

Rule of Gladstone and Dale

The mean index of the apatite from Cerro de Mercado calculated by the rule of Gladstone and Dale, $\frac{(n-1)}{d}=K$, where n is the mean index of refraction, d is the density, and K is the total specific refractive energy of a mineral, is 0.0204 higher than the measured mean index. For the apatite from Cerro de Mercado, $K=0.20380$; $d=3.216$; $dK+1=1.6554$; and the mean index of the mineral, $\frac{2\omega+\epsilon}{3}=1.6350$. This discrepancy and other data (Young and Munson, 1966) suggest that the published specific refractive energy values for CaO or P_2O_5, or both, are too high, at least for apatite.

Geochemistry

In the following discussion, the ions found in apatite from Cerro de Mercado are placed in four categories:

(1) Ions considered to be contaminants,
(2) Ions which replace Ca^{+2},
(3) Ions which replace P^{+5}, and
(4) Ions which replace F^{-1}.

In pure fluorapatite, 60 percent of the calcium is surrounded by seven anions (7-fold coordination) and 40 percent of the calcium is surrounded by nine anions (9-fold coordination) (Beevers and McIntyre, 1946). In most tabulations of ionic sizes, such as those by Green (1959), ionic radii are given only for even-numbered coordinations, such as 6, 8, and 10. To transform the ionic radius of an element from one coordination number to another, the relation $\frac{r_p}{r_m}=\left(\frac{p}{m}\right)^{1/n-1}$ must be used (Wells, 1962), where r_p and r_m are the apparent radii for coordination numbers p and m, and $n\approx 9$. Thus, to transform the ionic radius of an ion whose radius is known for 6-fold coordination to the radius in 7-fold coordination, the radius for 6-fold coordination would have to be multiplied by $(7/6)^{1/8}=1.0195$.

In table 7, which is given as a basis for discussion of the fluorapatite from Cerro de Mercado, relevant ionic radii (with size differential from host ion), best estimates of the ion content in fluorapatite and martite, as well as the Clarkes, and enrichment or impoverishment factors in the fluorapatite are listed for each ion.

1. *Ions considered to be contaminants.*—Mg^{+2}, Fe^{+3}, and Al^{+3}. Each of these ions differs in size from the host Ca^{+2} by at least 34 percent, and each impoverishment factor (with respect to its Clarke) is more than 100.

2. *Ions which replace* Ca^{+2}.—Of the alkali metals, Na^{+1} is greatly in excess of K^{+1} in the fluorapatite; the impoverishment factor for K^{+1} with respect to its Clarke is 21 times that of Na^{+1}. This shows the effect of the large ionic size of K^{+1} (35 percent $>Ca^{+2}$) as compared with that of Na^{+1} (2 percent $<Ca^{+2}$).

The copper content of the apatite is very low ($\approx$0.5 ppm), giving copper an impoverishment factor of almost

TABLE 6.—*Analysis of DM–A, fluorapatite from Cerro de Mercado, Durango, Mexico*

[Abbreviations: D, discounted as impurity; Na., not applicable. Br and I contents are each less than 10 ppm by X-ray fluorescence analysis, J. S. Wahlberg, analyst. Analyses are wet chemical and were determined by ElaineMunson, unless otherwise indicated; H_2O+ content determined by Penfield method. SiO_2, SrO, As_2O_5, and V_2O_5 contents were determined by quantitative spectrographic methods, N.M. Conklin, analyst; ThO_2 content by isotope dilution method, J. N. Rosholt, analyst; CO_2 content by gasometric method, I. C. Frost, analyst]

	Weight percent	Weight percent recalculated to 100 percent	Ratios	Metal equivalent	Oxygen equivalent	Atoms per unit cell [1]
CaO [2]	54.02	54.13	0.9652	0.9652	0.9652	9.83
P_2O_5	40.78	40.86	.2879	.5758	1.4395	5.87
Na_2O	.23	.23	.0037	.0074	.0037	.08
K_2O	.01	.01	.0001	.0002	.0001	[3]
MgO [4]	.01	D	D	D	D	D
FeO	0					
Fe_2O_3 [4]	.06	D	D	D	D	D
Al_2O_3 [4]	.07	D	D	D	D	D
MnO	.01	.01	.0001	.0001	.0001	[3]
SrO	.07	.07	.0007	.0007	.0007	.01
RE_2O_3	1.43	1.43	.0044	.0088	.0132	.09
ThO_2	.02	.02	.0001	.0001	.0002	[3]
SiO_2 [5]	.34	.34	.0057	.0057	.0114	.06
As_2O_5	.09	.09	.0004	.0008	.0020	.01
V_2O_5	.01	.01	.0001	.0002	.0005	[3]
CO_2	.05	.05	.0011	.0011	.0022	.01
SO_3	.37	.37	.0046	.0046	.0138	.05
F	3.53	3.54	.1863	Na.	.0932	1.90
Cl	.41	.41	.0116	Na.	.0058	.12
H_2O+	.01	.01	.0006	.0012	.0006	.01
H_2O-	0					
Insoluble residue	0					
Subtotal	101.52	101.58				
Less O	1.58	1.58				
Total	99.94	100.00				

[1] Calculated on the basis of 26(O, F, Cl, OH) in the unit cell. Formula: $Ca_{9.83}Na_{0.08}Sr_{0.01}RE_{0.09}(PO_4)_{5.87}(SO_4)_{0.05}(SiO_4)_{0.06}(AsO_4)_{0.01}(CO_3)_{0.01}F_{1.90}Cl_{0.12}(OH)_{0.01}$. Mol. wt 1,018.6. Valence balance: sum of (+) charges=20.03=sum of (−) charges.
[2] Reported as 54.08±0.1 percent by atomic absorption method, Claude Huffman, Jr., analyst.
[3] Less than 0.01.
[4] Considered to be an impurity.
[5] Soluble.

TABLE 7.—*Replacement ions in fluorapatite from Cerro de Mercado, Durango, Mexico*

[Ionic radii are based on Green (1959). Percent size differential for ionic radii is given in parentheses. Nd., not determined; Indet., indeterminate. Analysts: (B) N. M. Conklin, (C) Claude Waring, (D) Helen Worthing, (F) Christopher Heropoulos, (G) J. N. Rosholt, (H) J. S. Wahlberg, (J) I. C. Frost, (K) Claude Huffman, Jr., (L) E. L. Munson, (M) E. J. Fennelly]

Ion	Ionic radii (in angstroms)		Ion content (in parts per million)			Enrichment (+) [1] or impoverishment (−) factors of ion	
	Coordination					With respect to martite	With respect to Clarke
	7-fold	9-fold	In fluorapatite [2]	In martite [3]	Clarke [4]		
Ca^{+2} (host)	1.01	1.04	38.6×10^4 (L)	850	2.96×10^4	454 (+)	13 (+)
Considered to be contaminants:							
Mg^{+2}	.67 (−34)	.69 (−34)	60 (L)	3,000	1.87×10^4	50 (−)	312 (−)
[5] Fe^{+3}	.65 (−36)	.67 (−36)	420 (L)	70×10^4	4.65×10^4	1,670 (−)	111 (−)
[6] Al^{+3}	.52 (−49)	.54 (−48)	370 (L)	2,000	8.05×10^4	5.4 (−)	218 (−)
Substitutions for Ca^{+2}:							
Li^{+1}	.69 (−32)	.72 (−31)	≈3 (D)	<100	32	<33 (−)	≈11 (−)
Na^{+1}	.99 (−2)	1.02 (−2)	1,700 (L)	<500	2.5×10^4	>3.4 (+)	14.7 (−)
K^{+1}	1.36 (+35)	1.40 (+35)	80 (L)	Nd.	2.5×10^4	Indet.	313 (−)
Cu^{+1}	.98 (−3)	1.02 (−2)	.5 (D)	3	47	6 (−)	94 (−)
Cu^{+2}	.77 (−24)	.80 (−23)	.5 (D)	3	47	6 (−)	94 (−)
Sr^{+2}	1.14 (+13)	1.18 (+13)	580 (B)	10	340	58 (+)	1.7 (+)
Ba^{+2}	1.37 (+36)	1.41 (+36)	2 (C, D)	15	650	7.5 (−)	325 (−)
Zn^{+2}	.75 (−26)	.78 (−25)	10 (K)	<200	83	<20 (−)	8.3 (−)
Cd^{+2}	.99 (−2)	1.03 (−1)	<10 (D, K)	<50	.13	Indet.	<77 (+?)
Mn^{+2}	.82 (−19)	.84 (−19)	80 (L)	200	1,000	2.5 (−)	13 (−)
Fe^{+2}	.75 (−26)	.78 (−25)	<100 (L)	70×10^4	4.65×10^4	>7,000 (−)	>465 (−)
Ni^{+2}	.70 (−31)	.73 (−30)	<3 (B)	100	58	>33 (−)	>19 (−)

See footnotes at end of table.

TABLE 7.—*Replacement ions in fluorapatite from Cerro de Mercado, Durango, Mexico*—Continued

Ion	Ionic radii (in angstroms)		Ion content (in parts per million)			Enrichment (+) [1] or impoverishment (−) factors of ion	
	Coordination		In fluorapatite [2]	In martite [3]	Clarke [4]	With respect to martite	With respect to Clarke
	7-fold	9-fold					
Ca^{+2} (host)—Con.							
Substitutions for Ca^{+2}—Con.							
Sc^{+3}	.83 (−18)	.85 (−18)	<5 (B)	7	10	>1.5 (−)	>2 (−)
La^{+3}	1.16 (+15)	1.20 (+15)	4,200 (B)	<30	29	>140 (+)	145 (+)
Ce^{+3}	1.09 (+8)	1.13 (+9)	4,700 (B)	<150	70	>31 (+)	67 (+)
Pr^{+3}	1.08 (+7)	1.12 (+8)	800 (C)	<100	9	>8 (+)	89 (+)
Nd^{+3}	1.06 (+5)	1.10 (+6)	2,000 (B, C, F)	<70	37	>29 (+)	54 (+)
Sm^{+3}	1.02 (+1)	1.06 (+2)	300 (B, F)	<100	8	>3 (+)	38 (+)
Eu^{+3}	1.00 (−1)	1.04 (0)	20 (D)	<100	1.3	<5 (−?)	15 (+)
Y^{+3}	.94 (−7)	.97 (−7)	760 (B)	<10	29	>76 (+)	26 (+)
Gd^{+3}	.99 (−2)	1.03 (−1)	200 (B, D, F)	<50	8	>4 (+)	25 (+)
Tb^{+3}	.94 (−7)	.97 (−7)	100 (B, C)	<300	4.3	<3 (−?)	23 (+)
Dy^{+3}	.93 (−8)	.96 (−8)	150 (B)	<50	5	>3 (+)	30 (+)
Ho^{+3}	.92 (−9)	.95 (−9)	30 (B)	<20	1.7	>1.5 (+)	18 (+)
Er^{+3}	.90 (−11)	.94 (−10)	100 (B, C, D, F)	<50	3.3	>2 (+)	30 (+)
Tm^{+3}	.89 (−12)	.92 (−12)	10 (C, D)	<20	.27	<2 (−?)	37 (+)
Yb^{+3}	.88 (−13)	.90 (−13)	50 (B)	<1	.33	>50 (+)	150 (+)
Lu^{+3}	.87 (−14)	.89 (−14)	≈10 (D)	<30	.8	<3 (−?)	≈13 (+)
Ti^{+4}	.77 (−24)	.80 (−23)	<.8 (D)	5,000	4,500	>6,250 (−)	>5,630 (−)
Zr^{+4}	.81 (−20)	.83 (−20)	23 (B)	<10	170	>2.3 (+)	7.4 (−)
Th^{+4}	1.04 (+3)	1.08 (+4)	200 (G)	5.7 (G)	13	35 (+)	15.4 (+)
U^{+4}	.99 (−2)	1.02 (−2)	11 (G)	.52 (G)	2.5	21 (+)	4.4 (+)
	Ionic radii 4-fold coordination						
P^{+5} (host)	0.33		17.8×10^{4} (L)	1,500 (H)	930	119 (+)	192 (+)
Substitutions for P^{+5}:							
C^{+4}	.16 (−52)		137 (J)	Nd.	230	Indet.	1.7 (−)
Si^{+4}	.40 (+21)		1,600 (B)	3,000	29.5×10^{4}	1.9 (−)	184 (−)
As^{+5}	.44 (+33)		600 (B)	[7] <10 (M)	1.7	>60 (+)	350 (+)
V^{+5}	.56 (+70)		40 (B, C)	1,500	90	38 (−)	2.2 (−)
S^{+6}	.29 (−12)		1,480 (L)	200 (H)	470	7.4 (+)	3.2 (+)
Cr^{+6}	.49 (+48)		<.8 (D)	3	83	>3.8 (−)	>104 (−)
	Ionic radii						
F^{-1} (host)	1.36		3.53×10^{4} (L)	Nd.	660	Indet.	53.5 (+)
Substitutions for F^{-1}:							
$(OH)^{-1}$	1.40 (+3)		190 (L)	Nd.	2.36×10^{4}	Indet.	124 (−)
Cl^{-1}	1.81 (+33)		4,100 (L)	Nd.	170	Indet.	24 (+)
Br^{-1}	1.96 (+44)		<10 (H)	Nd.	2.1	Indet.	<4.8 (+?)
I^{-1}	2.20 (+62)		<10 (H)	Nd.	.4	Indet.	<25 (+?)

[1] Enrichment factor is the number of times an element (ion) is more abundant in the apatite than it is in the martite or with respect to its Clarke. Impoverishment factor is the inverse.
[2] Values of elements (ions) in the fluorapatite are considered to be the truest values.
[3] Values of elements (ions) in the martite were determined by semiquantitative spectrographic analyses by N. M. Conklin, except as otherwise noted.
[4] Clarkes (crustal abundances) are from Vinogradov (1962), except the Clarke for OH, which is from Mason (1958).
[5] For simplicity, when an ion is being considered, all the element is considered to be in that ion's valent state; for example, when the ion is Fe^{+3}, all the iron in the crust (Clarke) and all the iron in the martite is considered to be in the trivalent state.
[6] If Al^{+3} substitutes for P^{+5} (4-fold coordination), the size differential would be Al^{+3}=0.49 A (+48 percent).
[7] Gutzeit method.

100 with respect to its Clarke, despite the fact that the martite contains more copper (3 ppm). This suggests to us that copper entered the apatite as the divalent ion whose radius size is less favorable than that of monovalent for replacement of Ca^{+2}.

Sr^{+2} and Ba^{+2} also illustrate very well the difficulty a large ion has in entering the apatite lattice. Although the martite contains slightly more barium than strontium, the impoverishment factor for Ba (with respect to its Clarke) is over 300, whereas Sr is enriched (with respect to its Clarke) almost twice.

Probably the most remarkable fact we have learned about this apatite is the inability of Fe^{+2} to enter the lattice. Despite crystallization within an iron ore host,

no Fe^{+2} (<100 ppm) was found in the apatite by chemical analysis, leading to an impoverishment factor (with respect to its Clarke) of >465. The impoverishment factor with respect to the martite host is >7,000. Clearly, iron has been excluded from the apatite so thoroughly that apatite analyses reporting iron, at least from igneous iron ore deposits, should be considered carefully before being accepted.

In contrast to iron, all the rare earths show exceptional ability to be scavenged or concentrated by the apatite, especially since rare earths could not be detected in the martite. As is usual in apatite, the Ce earths predominate over the Y earths. The Ce group elements (Ce, La, Pr, Nd, Sm, Eu) total 1.20 weight percent; the Y group elements (Y, Yb, Gd, Tb, Dy, Ho, Er, Tm, Lu) total 0.14 weight percent, yielding a Ce group/Y group ratio of 8.6. This is considerably lower than the ratio of 17.25 for the fluor-chlor-oxy-apatite from pegmatite described by Young and Munson (1966).

Ti^{+4} is fairly abundant in the martite (5,000 ppm), yet there is only <0.8 ppm Ti^{+4} in the apatite. By contrast, there is <10 ppm Zr^{+4} in the martite, but the apatite contains 23 ppm. The fact that the Ti^{+4} ion is only slightly smaller than the Zr^{+4} ion does not seem reason enough for the extreme impoverishment of Ti^{+4} in the apatite. Th^{+4} and U^{+4} are both very close to Ca^{+2} in ionic size and also show enrichment factors, indicating favorableness for replacement when ionic size differentials are small. The strong affinity of apatite for thorium and uranium is emphasized by the small amounts of thorium and uranium in the martite (5.7 ppm Th and 0.5 ppm U, both values being less than their respective Clarkes).

3. *Ions which replace* P^{+5}.—Both the pentavalent and hexavalent ions As^{+5} and S^{+6} replace P^{+5} successfully enough to show enrichment factors. In view of the enrichment of 350 for As (with respect to its Clarke), apparently a size differential of +33 percent is tolerated easily for 4-fold coordination, whereas for 7- or 9-fold coordination such a large size differential virtually excludes entry.

V^{+5}, despite the large size differential (+70 percent), replaces P^{+5} more successfully than Cr^{+5} (+48 percent), but this may be the result of more available V, the martite containing 1,500 ppm V, but only 3 ppm Cr.

4. *Ions which replace* F^{-1}.—The martite offers a very anhydrous environment, hence the sparsity of water found in the apatite is not surprising. Cl^{-1} shows enrichment, but contents of Br^{-1} and I^{-1} were not determined adequately enough to indicate trends.

REFERENCES

Beevers, C. A., and McIntyre, D. B., 1946, The atomic structure of fluor-apatite and its relation to that of tooth and bone material: Mineralog. Mag., v. 27, no. 194, p. 254–257.

Boldyrev, A. K., 1930, Les apatites de Lebiajia et du Mont Wyssokaya dans l'Oural [The apatites of Lebiajia and Mount Wyssokaya in the Urals]: Comité géol. Matériaux géologie gén. et appl., Leningrad, no. 142, p. 1–56.

Crane, G. W., 1912, The iron ores of Missouri: Missouri Bur. Geology and Mines, 2d ser., v. 10, 434 p.

Cruft, E. F., 1966, Minor elements in igneous and metamorphic apatite: Geochim. et Cosmochim. Acta, v. 30, no. 4, p. 375–398.

Evans, H. T., Jr., Appleman, D. E., and Handwerker, D. S., 1963, The least squares refinement of crystal unit cells with powder diffraction data by an automatic computer indexing method [abs.]: Am. Cryst. Assoc. Program and Abs. 1963 Ann. Mtg., E–10, p. 42–43.

Flores Reyes, Teodoro, 1950, Geologic and structural environment of the iron ore deposits of Mexico: Econ. Geology, v. 45, no. 2, p. 105–126.

Foshag, W. F., 1929, Mineralogy and geology of Cerro Mercado, Durango, Mexico: U.S. Natl. Mus. Proc., v. 74, art. 23, 27 p.

Geijer, Per, 1931, The iron ores of the Kiruna type, geographical distribution, geological characters, and origin: Sveriges Geol. Undersökning Årsb., ser. C, v. 24, no. 4, 39 p.

——— 1967, Internal features of the apatite-bearing magnetite ores: Sveriges Geol. Undersökning Årsb., ser. C, v. 61, no. 9, 32 p.

Gillson, J. L., 1932, Genesis of the ilmenite deposits of St. Urbain, County Charlevoix, Quebec: Econ. Geology, v. 27, no. 6, p. 554–577.

Green, Jack, 1959, Geochemical table of the elements for 1959: Geol. Soc. America Bull., v. 70, no. 9, p. 1127–1183.

McKeown, F. A., and Klemic, Harry, 1956, Rare-earth-bearing apatite at Mineville, Essex County, New York: U.S. Geol. Survey Bull. 1046–B, p. 9–23.

Mason, B. H., 1958, Principles of geochemistry [2d ed.]: New York, John Wiley & Sons, Inc., 310 p.

Munsell Color Co., 1929, Munsell book of color (standard ed.): Baltimore, Munsell Color Co., 2 v.

Park, C. F., Jr., 1961, A magnetite "flow" in northern Chile: Econ. Geology, v. 56, no. 2, p. 431–436.

Paulick, J., and Newesely, H., 1968, Zur Kenntnis der Apatite der Cerro de Mercado, Durango, Mexiko: Neues Jahrb. Mineralogie Monatsh., no. 7, p. 224–235.

Ross, C. S., 1941, Occurrence and origin of the titanium deposits of Nelson and Amherst Counties, Virginia: U.S. Geol. Survey Prof. Paper 198, 59 p.

Salinas, L. S., Gonzalez, Pedro, Santillan, Manuel, Acevedo, Antonio, and Martinez Quintero, A. R., 1923, El Cerro de Mercado, Durango: Inst. Geol. Mexico Bull. 44, 94 p.

Senftle, F. E., Lee, M. D., Monkewicz, A. A., Mayo, J. W., and Pankey, Titus, 1958, Quartz helix magnetic susceptibility balance using the Curie-Cheneveau principle: Rev. Sci. Instruments, v. 29, no. 5, p. 429–432.

Shawe, F. R., Reeves, R. G., and Kral, V. E., 1962, Iron deposits of Nevada—Pt. C, Iron ore deposits of northern Nevada: Nevada Bur. Mines Bull. 53, pt. C, p. 79–130.

Stephenson, R. C., 1945, Titaniferous magnetite deposits of the Lake Sanford area, New York: Am. Inst. Mining Engineers Tech. Pub 1789, Mining Technology, v. 9, no. 1, 25 p.

Sumin, N. G., 1957, Some properties of apatite from skarn-type iron-ore deposits: Akad. Nauk SSSR Trudy Mineral. Muz., no. 8, p. 116–121. [In Russian]

Vinogradov, A. P., 1962, Average contents of chemical elements in the principal types of igneous rocks of the earth's crust: Geochemistry, no. 7, p. 641–664.

Wells, A. F., 1962, Structural inorganic chemistry [3d ed.]: Oxford Univ. Press, 1055 p.

Young, E. J., 1965, Effect of isomorphic substitutions on the omega index of refraction of apatite, *in* Abstracts for 1964: Geol. Soc. America Spec. Paper 82, p. 231.

Young, E. J., and Munson, E. L., 1966, Fluor-chlor-oxy-apatite and sphene from Crystal Lode pegmatite near Eagle, Colorado: Am. Mineralogist, v. 51, nos. 9–10, p. 1476–1493.

Young, E. J., Myers, A. T., Munson, E. L., and Conklin, N. M., 1968, Mineralogy and geochemistry of fluorapatite from Cerro de Mercado, Durango, Mexico, *in* Abstracts for 1967: Geol. Soc. America Spec. Paper 115, p. 245.

Young, E. J., Sheridan, D. M., and Munson, E. L., 1966, Manganese- and strontium-bearing fluorapatite from the Peerless pegmatite, South Dakota: Am. Mineralogist, v. 51, nos. 9–10, p. 1516–1524.

RESIDUAL CLAY DEPOSITS IN ROCKS OF EARLY AND MIDDLE DEVONIAN AGE NEAR KUNKLETOWN, PENNSYLVANIA

By JACK B. EPSTEIN and JOHN W. HOSTERMAN, Beltsville, Md.

Work done in cooperation with the Pennsylvania Geological Survey

Abstract.—Residual white clay deposits and sedimentary rock saprolites occur in complexly folded cherty shaly limestones and limy shales of Early and Middle Devonian age in Cherry and Chestnut Ridges between Kunkletown and Saylorsburg, Monroe County, Pa. The deposits are located southwest of the Wisconsin-age terminal moraine and are believed to have formed during pre-Wisconsin weathering. Comparison of fresh rocks with weathered counterparts shows that in the saprolites calcite and minor dolomite have been removed by leaching, 2M muscovite has altered to M*d* muscovite, and chlorite has been removed with the development of kaolinite. Since 1891, the residual white clay has been used for brick, ceramics, porcelain, electrical insulators, and paint, and is presently used in the manufacture of white cement.

Residual white clay deposits are found in Cherry and Chestnut Ridges between Kunkletown and Saylorsburg, Monroe County, Pa. (fig. 1). The clay is currently being removed from limy shales and shaly limestones of the New Scotland Formation and Shriver Chert of Early Devonian age and Buttermilk Falls Limestone of Willard (1938) of Middle Devonian age. These deposits have been worked since 1891. Characteristics of the clay and the mining history of the clay deposits are described by Peck (1922), Ries, Bayley, and others (1922, p. 111–115), and Leighton (1934, p. 17–19; 1941, p. 183–187). The clay has been used as filler for paper and rubber, and for the manufacture of porcelain, brick, electrical insulators, ceramics, paint, and white cement. The clay is currently used in the manufacture of white cement by the Universal Atlas Cement Co. The following description of the white clay operations near Kunkletown, Pa., was supplied by George F. Smith, geologist, Universal Atlas Cement Division, United States Steel Corp. (written commun., 1967):

Since 1932, Universal Atlas has used clay from the Kunkletown property as a raw material in the manufacture of White Cement at Northampton, Pa. Cement raw materials must be blended to reach certain fixed ratios of SiO_2, Al_2O_3, and CaO before calcining. The silica, alumina, and ferric oxide components of White Cement are obtained from the Kunkletown pits by proper proportioning of the clays found there. White Cement raw-material requirements include a very low Fe_2O_3 content; the Kunkletown clays meet this requirement.

Prospecting starts with air-photo-based contour maps and selection of topographically favorable areas, followed by self-potential and resistivity studies to pinpoint probable low-iron clay bodies. Test drilling, using rotary or driven coring methods, is then used to outline the clay bodies and to determine their actual composition.

Development of the pits requires some additional test drilling or test pits, but day-to-day operations are guided largely by the experience of the supervisors, who use visual clues for silica and iron content. The supervisors are also aided by daily sample reports from the chemical laboratory at Northampton.

These clay pits provide 200 tons of raw material per day. One small power shovel loads the 15-ton trucks for the 22-mile haul to Northampton, where the clay is crushed, ground, made into a slurry, and blended with limestone into cement-kiln feed.

Epstein has investigated these deposits in conjunction with mapping and miscellaneous geologic studies in the Stroudsburg, Wind Gap, Saylorsburg, Kunkletown, Palmerton, and Lehighton 7½-minute quadrangles. The deposits near Kunkletown were investigated as part of a more comprehensive study of the clays in northern Appalachia, including detailed X-ray diffraction and fluorescence analyses by Hosterman. We wish to thank George F. Smith, of Universal Atlas Cement Division of United States Steel Corp., for his cooperation in all phases of the investigation. A. G. Epstein assisted in stratigraphic studies in the area.

STRATIGRAPHY

The clay deposits occur within a heterogeneous assemblage of weathered Upper Silurian through Middle Devonian limestone, shale, siltstone, sandstone,

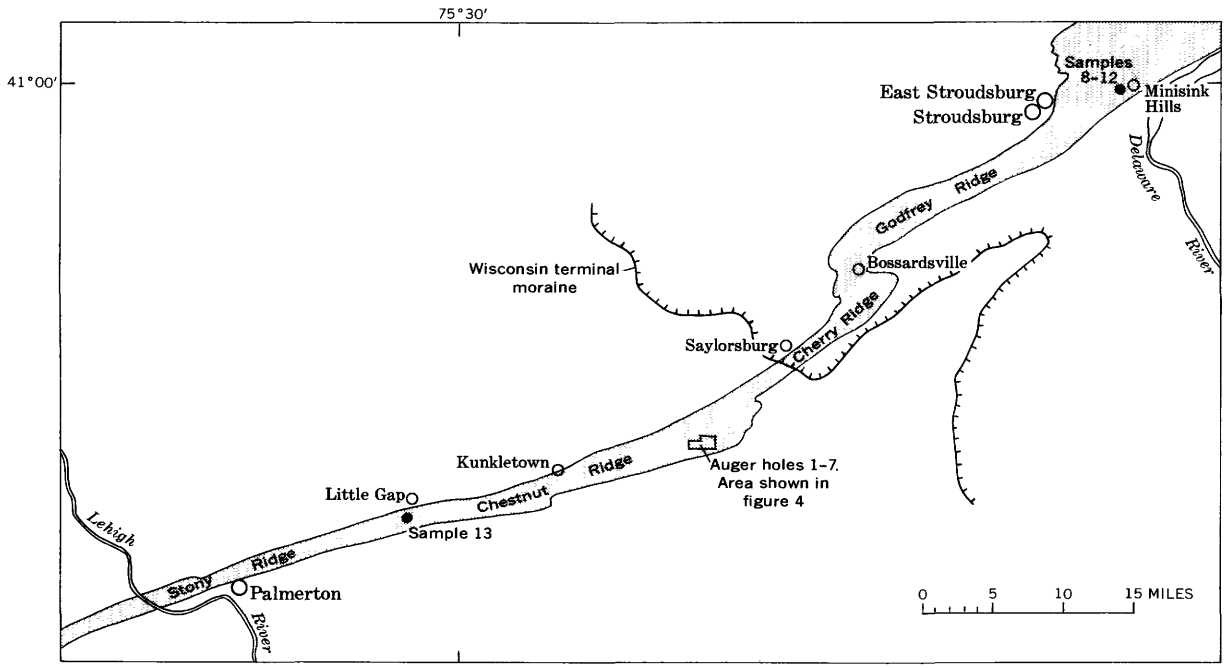

FIGURE 1.—Outcrop belt of Lower and Middle Devonian rocks (shaded area) containing residual clay deposits in eastern Pennsylvania, maximum southwest extent of the Wisconsin glacier, and locations of samples described in this report.

and dolomite (fig. 2). Unweathered outcrops of these rocks are rare west of Bossardsville, Pa., but northeast of Bossardsville fresh rocks crop out in abundance. These have been described by Epstein and others (1967). Several unweathered beds were sampled and are described in table 1. The rocks in the active claypit area are described in figure 3. The clays are probably more than 100 feet thick in many places; and in the pit shown in figure 5, a hole penetrated 182 feet of clay without reaching unweathered rock (G. F. Smith, oral commun., 1969).

Clay has been and is currently being removed from the New Scotland Formation, Shriver Chert of the Oriskany Group, and Buttermilk Falls Limestone. Where fresh, these rocks are generally cherty silty argillaceous limestones and limy shales (table 1). These have been weathered to silty clays and clayey silts. The best clays are white to light gray, but some are stained various shades of red and yellow. In some of the deposits, the chert has not been completely leached and remains as hard nodular impurities. The units in which the clays occur become thinner and less pure (less calcareous and more siliceous and iron stained) westward, so that they are not worked west of Little Gap. Chance (in White, 1882, p. 356) reported 3 to 8 feet of clay in the Esopus Formation (his caudi-galli grit) in the Lehigh Gap area. Willard (1957, p. 2300) reported a similar thin clay at the base of the Esopus in Stony Ridge along the Pennsylvania Turnpike extension, 3.5 miles west of Lehigh Gap. The clay in the Lehigh Gap area is too thin to have any commercial value. To the east, the thickest deposits occur in the Saylorsburg area where they have been extensively worked (Peck, 1922). Farther eastward, beyond Bossardsville and the Wisconsin terminal moraine, no residual clay deposits are found. The most promising areas for prospecting are about two miles east of the presently active area where pit operations should prove most profitable, and between Kunkletown and about one mile west of Saylorsburg, where underground workings might be considered.

STRUCTURAL GEOLOGY

Cherry and Chestnut Ridges are prominent topographic features underlain by complexly folded strata lying north of Blue Mountain in the Valley and Ridge province of eastern Pennsylvania. The folds are generally asymmetric and, depending on the rock types involved, are either concentric or similar. Both flexural and passive mechanisms appear to have been operative. Wavelengths of folds average about 1,000 feet and amplitudes average about 250 feet. Axes generally plunge gently westward, and axial planes dip steeply to gently southward. Locally, axial planes dip gently northward and overturned south-dipping beds can be traced into north-dipping doubly overturned beds

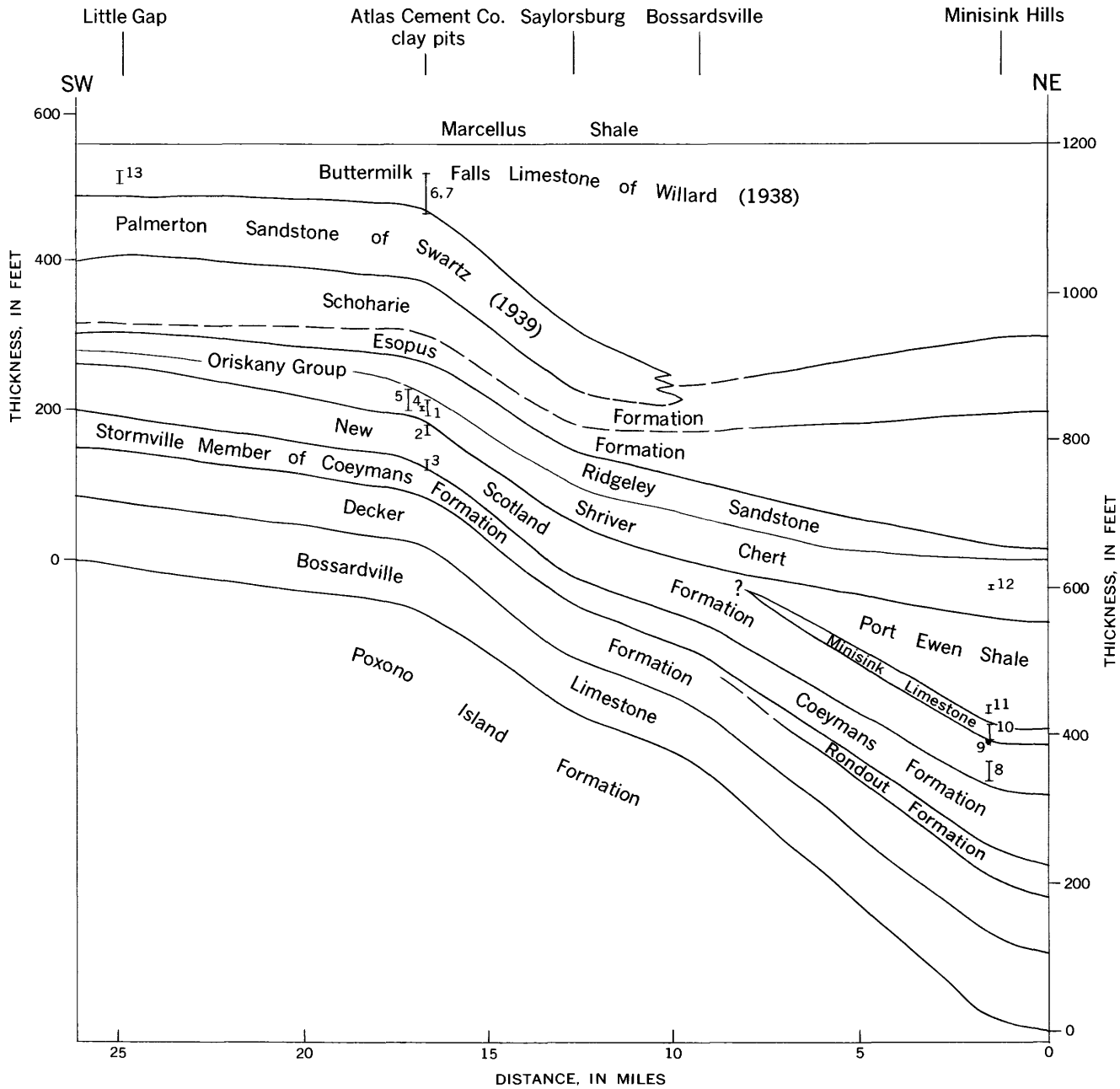

FIGURE 2.—Diagrammatic cross section of Upper Silurian to Middle Devonian strata in eastern Pennsylvania and stratigraphic position of samples (numbered symbols) described in this report (modified from Epstein and Epstein, 1969).

defining antiforms and synforms (figs. 4 and 5, section *B–B'*). Erosion of these folds has produced a complex outcrop pattern, especially east of the area shown in figure 4. Accurate knowledge of the areal distribution of the clay-bearing formations is, therefore, essential for future exploitation.

In the area currently being worked, the clay-bearing units crop out in long narrow belts and are repeated by folding (figs. 4, 5, and 6). Noses are common in the eastern section. Pit operations are confined to the top of the ridge where overburden is not a great problem. Underground mining in the sides of the ridge has not been attempted here as it once was in the Saylorsburg area (Peck, 1922).

MINERALOGY

The mineralogy of seven samples of unweathered bedrock was determined and compared with that of 49 samples from seven auger holes of equivalent weathered rocks in order to determine the mineralog-

TABLE 1.—*Description and analyses of unweathered samples of Lower and Middle Devonian rocks (limy shales and shaly limestones) in easternmost Pennsylvania*

[Rock color designations from Munsell Color Co., Inc., 1929–1960]

Sample No.	Formation	Location	Field description	Semiquantitative analysis based on X-ray diffraction peak-area ratios [1]					Treatment with 3*M* acetic acid	
				Illite 10.0 A(002)	Chlorite 14.2 A(001)	Quartz 4.3 A(100)	Calcite 3.04 A(104)	Dolomite 2.9 A(104)	Soluble (weight	Insoluble percent)
8	Flatbrookville Member of New Scotland Formation.	Northeast bank of Brodhead Creek at Minisink Hills, Pa.; Stroudsburg 7½-minute quadrangle.	Fossiliferous cherty slightly dolomitic calcareous and siliceous shale with about 10 percent lenses, nodules, and beds of medium-dark-gray (N4) fine-grained argillaceous fossiliferous limestone; channel sample from units 8 and 10 (22.5 feet thick) of measured section 15–c, (Epstein and others, 1967, p. 64).	16	5	24	48	7	55	45
9	Maskenozha Member of New Scotland Formation.	Roadcut on southwest side of U.S. Interstate Highway 80, approximately 0.4 mile southwest of Minisink Hills, Pa.; Stroudsburg 7½-minute quadrangle.	Dark-gray (N3) calcareous and siliceous laminated shale; grab sample of float from unit 1 of measured section 15–d, (Epstein and others, 1967, p. 67).	17	7	44	32	----	32	68
10	Minisink Limestone	----do----	Fossiliferous medium-gray (N5) fine-grained argillaceous irregularly bedded limestone with thin calcareous shale interbeds; channel sample from unit 2 (14.0 feet thick) of measured section 15–d, (Epstein and others, 1967, p. 67).	12	7	12	69	----	69	31
11	Port Ewen Shale	----do----	Poorly fossiliferous medium-dark-gray (N4) silty calcareous irregularly laminated shale; channel sample from lower 10 feet of unit 4 of measured section 15–d, (Epstein and others, 1967, p. 67).	24	6	53	17	----	17	83
12	Shriver Chert	----do----	Sparingly fossiliferous medium-dark gray (N4) fine-grained silty calcareous shale; channel sample from upper 5 feet of unit 10 of measured section 15–d, (Epstein and others, 1967, p. 66).	16	6	39	31	8	39	61
13	Buttermilk Falls Limestone of Willard (1938).	Exposure in Stony Ridge about 30 feet west of county road, 1,000 feet southwest of Little Gap, Pa.; Palmerton 7½-minute quadrangle.	Cherty meduim-gray (N5) to dark-gray (N3) fine-grained argillaceous limestone; channel sample from about 20 feet of exposed beds.	6	1	20	73	----	73	27

[1] Percent calcite and dolomite derived from treatment with 3*M* acetic acid; ratios of peak-area heights adjusted to equal soluble weight percent. Ratios of peak-area heights of illite, chlorite, and quartz adjusted to equal insoluble weight percent.

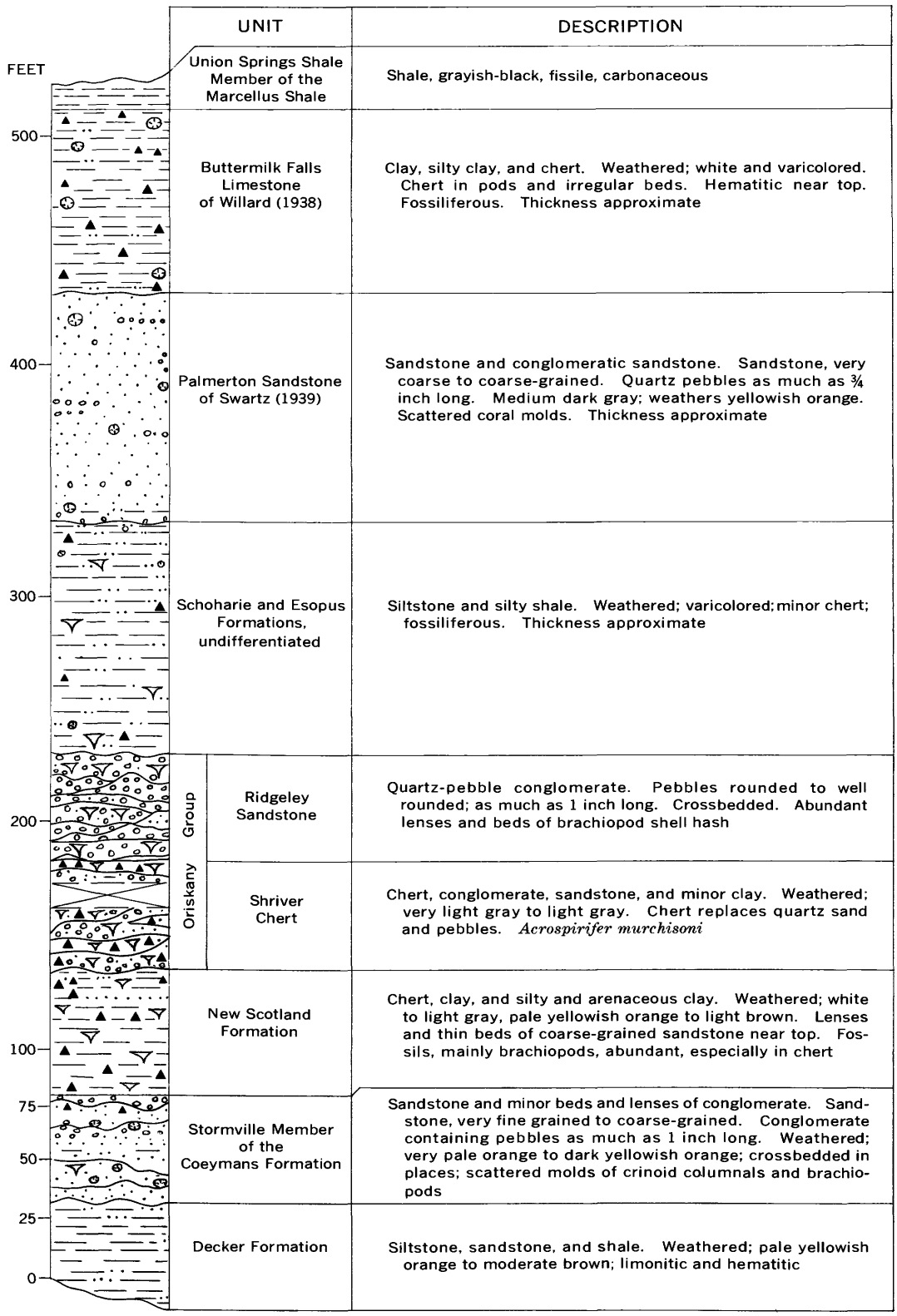

FIGURE 3.—Stratigraphic units exposed in claypits and sandpits of the Universal Atlas Cement Co., near Kunkletown, Pa. Modified from Epstein and Epstein (1967).

ical changes that took place during the formation of the residual clay.

A comparison of the areas of selected peaks of illite (illite is used here to mean a clay-sized muscovite), chlorite, quartz, calcite, and dolomite on X-ray diffraction traces provided a semiquantitative analysis of the unweathered samples (table 1). This semiquantiative analysis method has had widespread use (for example, Schultz, 1964). In addition, the percent of carbonate and noncarbonate minerals was determined by treatment in 3*M* acetic acid. The mineral and chemical compositions of the weathered samples are given in table 2.

Whole-rock samples were prepared for X-ray diffraction by grinding to pass through a 170-mesh screen and pressing the sample into a 1-inch-diameter disk in a hydraulic press for a minimum of 30 seconds at a pressure of 30,000 pounds per square inch. Boric acid and methyl acetate were pressed beneath the sample for support. Clay minerals were concentrated and prepared by allowing a deflocculated suspension of the sample to settle for 2 hours and 3 minutes and carefully siphoning off the upper 10 centimeters which contained particles less than 4 microns in diameter. An oriented aggregate was obtained by sedimenting the siphoned-off suspension onto a 1- by 2- by ¼-inch porous ceramic tile and removing the water by vacuum. Typical X-ray diffraction traces of fresh and weathered Buttermilk Falls Limestone are given in figure 7.

In general, the unweathered samples are cherty argillaceous limestones and limy shales. Chlorite and 2M illite are the dominant clay minerals and occur with quartz, calcite, and minor dolomite (table 1 and fig. 7*A*).

The average mineralogy and composition of the weathered rocks are similar in all stratigraphic units (table 2). Quartz, kaolinite, and M*d* illite are the dominant minerals; chlorite, calcite, and dolomite are not present (fig. 7*C*). The silt and sand fractions of the samples are composed of quartz and chert. The overall average of the X-ray fluorescence analyses (table 3) is remarkably similar to the average of the raw materials removed by Universal Atlas Cement Company from the pits near Kunkletown: 80.8 percent SiO_2, 12.1 percent Al_2O_3, 0.6 percent Fe_2O_3, 0.6 percent CaO, and 0.3 percent MgO (G. F. Smith, written commun., September 1967).

ORIGIN AND AGE OF THE CLAYS

The geological, mineralogical, and chemical data indicate that the clay deposits in the Saylorsburg-Kunkletown area are residual and are products of katamorphic alteration of cherty limy shales and argillaceous limestones. This has generally been known by earlier workers in the area. Intense leaching by downward-percolating water in the New Scotland Formation, Shriver Chert, and Buttermilk Falls Limestone produced three profound changes: (1) chlorite, found in the unweathered rocks, is destroyed during weathering; (2) illite, although its ratio to other clay minerals is approximately the same in weathered and unweathered samples, undergoes a change in crystalline character from a 2M polymorph to an M*d* polymorph upon weathering; and (3) kaolinite, which is found only in the residual clays, forms from the disintegration of chlorite. There seems to be little or no difference in the amount of quartz and chert in the unweathered rock and residual clay. There is, however, an average volume loss of about 50 percent resulting from the leaching of the carbonates. Tectonic and sedimentary features are generally preserved in the clays (Epstein and Epstein, 1969, fig. 56). The clays are, therefore, sedimentary rock saprolites.

Rocks other than those which produced the residual clay deposits are also weathered. Siliceous and calcareous sandstones have been leached to semiconsolidated friable sand; the Oriskany and Palmerton (fig. 6) are two examples. Pure limestones, such as the Bossardville Limestone which crops out on the steep south slope of Cherry and Chestnut Ridges, do not have residual clays on them, probably because their topographic position favors the removal of residual materials, and also because they do not contain enough impurities to have residual clays develop.

It is interesting to speculate on the age of the clays. The deposits occur only southwest of the Wisconsin terminal moraine (fig. 1), and none occur for any considerable distance northeast of the moraine. It is believed they formed during pre-Wisconsin weathering and were stripped away northeast of the terminal moraine during the Wisconsin glacial advance.

It is difficult to ascertain the maximum possible age of the clays. Kaolinite is found along with degraded chlorite and vermiculite in pre-Wisconsin drift, possibly Illinoian in age, in eastern Pennsylvania (Epstein, 1969, and unpub. data). If the drift is Illinoian and has been weathering since the Sangamon Interglaciation, then kaolinite began to form and chlorite began to disappear within the last 100,000 to 300,000 years, according to the figures of Ericson and others (1964). The clays in Chestnut and Cherry Ridges are certainly much older, possibly several million years old.

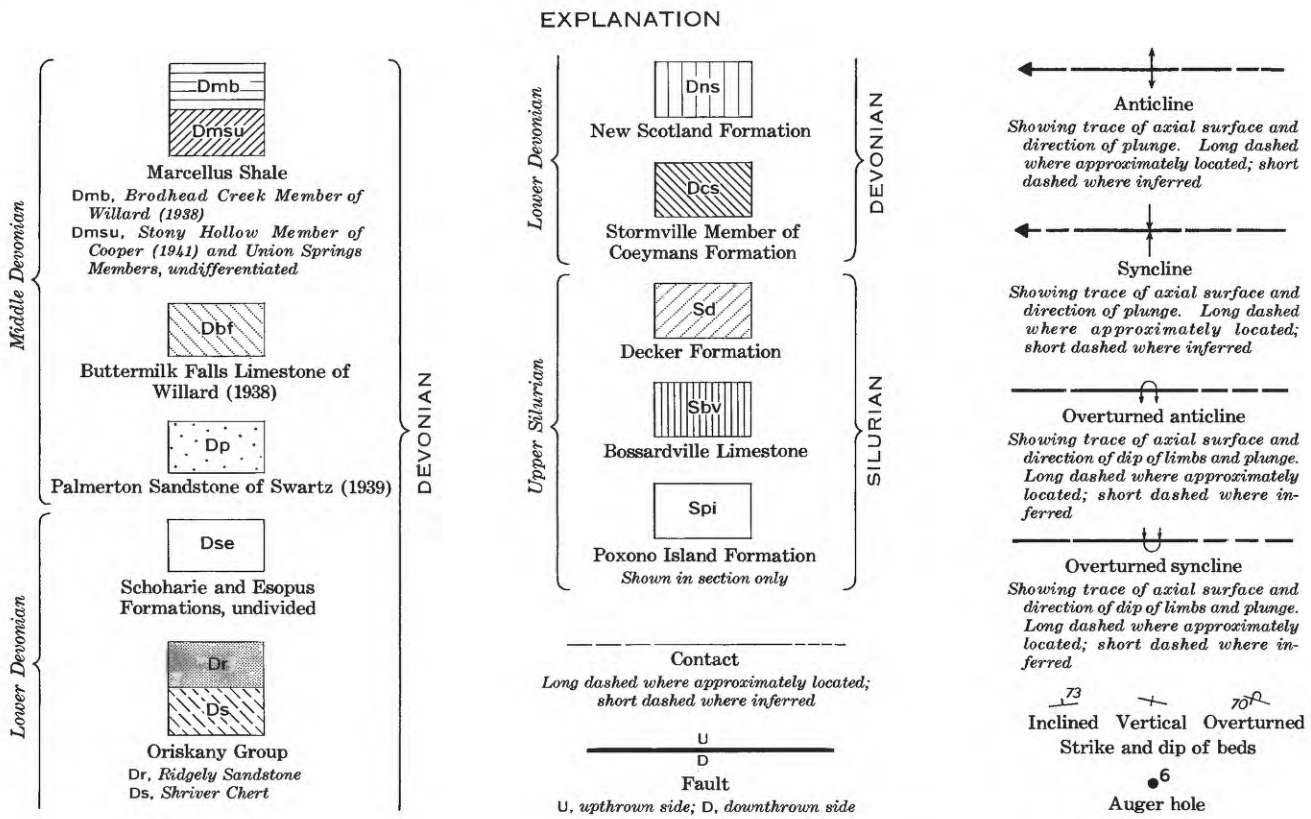

Base from Universal Atlas Cement Division of United States Steel Corporation, Kunkletown, Pennsylvania, 1961. Compiled from aerial photographs by Fairchild Aerial Surveys, 1952

FIGURE 4.—Geologic map of the Universal Atlas Ceme northeast of Kunkletown, Pa., with location of aug are shown in figure 5.

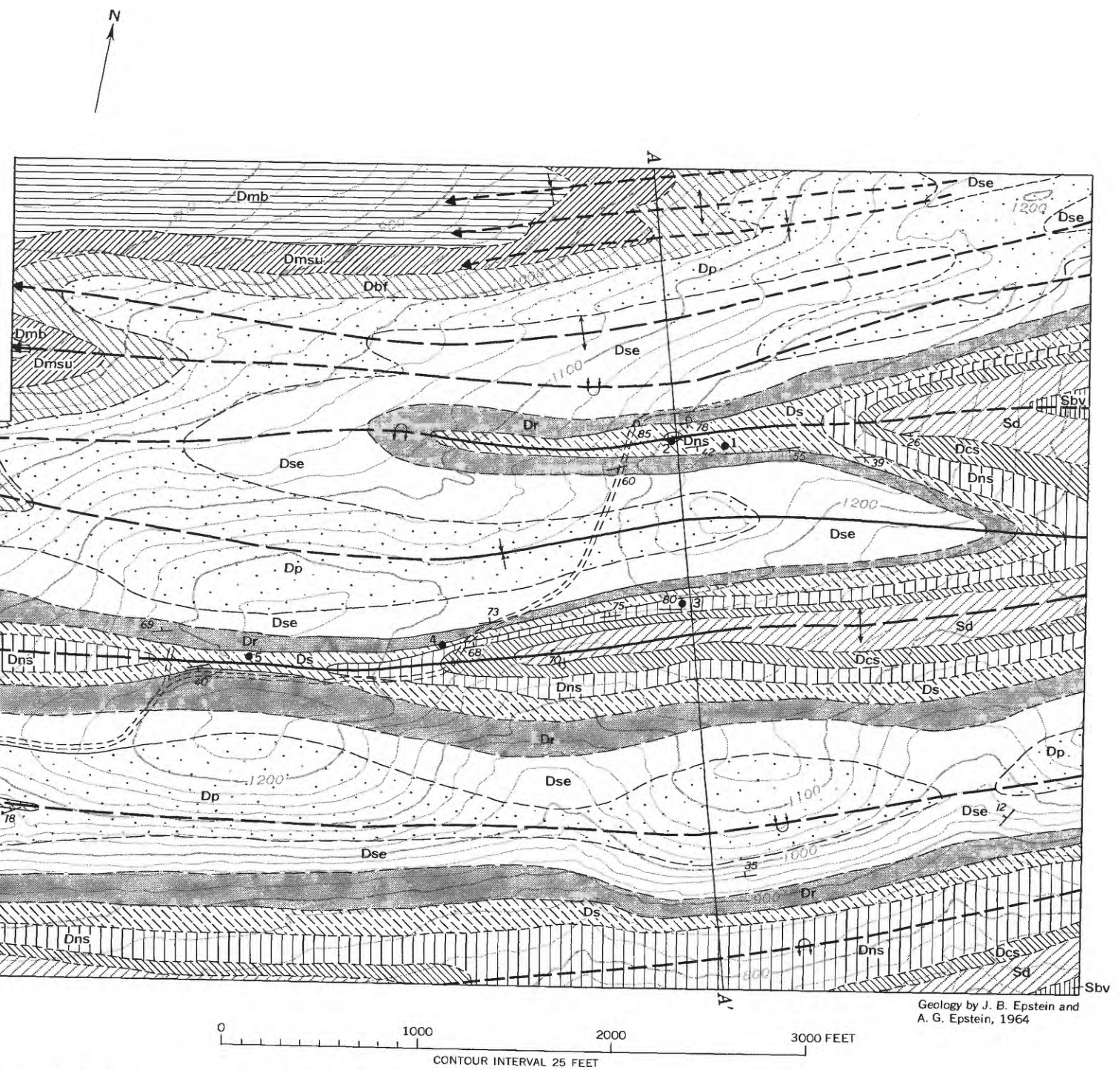

. claypits in Chestnut Ridge, approximately 4 miles north-
les described in table 2. Geologic sections *A–A′* and *B–B′*

TABLE 2.—*Description and analyses of weathered samples from the Universal Atlas Cement Co. claypits near Kunkletown, Pa.*

[Rock color designations from Munsell Color Co., Inc., 1929–1960]

Auger hole number	Formation	Depth (feet)	Number of samples	Description	Grain-size distribution (weight percent)			Peak-area ratio[1] kaolinite:illite		X-ray fluorescence analysis (weight percent)						
					Sand	Silt	Clay			SiO_2	Al_2O_3	Fe_2O_3	CaO	K_2O	TiO_2	Loss on ignition (1,000°C)
1	Shriver Chert	0–36	9	Silty clay, white (*N*9) at top to yellowish gray (10*YR*8/1) at bottom.	6	37	57	4.5	5.5	78	14	0.7	0.2	2.9	0.8	3.6
2	New Scotland Formation.	0–100	14	Silty clay, yellowish white (5*Y*9/1), grayish pink (5*R*7/2), pale orange yellow (10*YR*8/3), and yellowish gray (2.5*Y*8/2).	6	35	59	4.5	5.5	76	14	1.2	.2	3.5	.8	3.3
3	New Scotland Formation.	0–29	3	Silty clay, white (*N*9) at top to yellowish white (5*Y*9/1) at bottom.	7	41	52	3.8	6.2	78	14	.6	.3	3.1	.7	3.9
3	Stormville Member of the Coeymans Formation.	29–30	1	Sand, yellowish brown												
4	Shriver Chert	0–25	3	Silty sandy clay, yellowish white (7.5*Y*9/1) at top, and clayey silt, yellowish white (7.5*Y*9/1) to pale yellow (7.5*Y*9/2) at bottom.	20	45	35	4.8	5.2	88	7.6	.5	.4	1.4	.4	2.0
5	Shriver Chert	0–59	6	Clayey silt, white (*N*9) to pale yellow (7.5*Y*9/2) and silty clay, yellowish white (7.5*Y*9/1).	11	43	46	3.8	6.2	81	12	.6	.3	2.6	.6	2.8
6	Buttermilk Falls Limestone of Willard (1938).	0–55	6	Clayey silt, white (*N*9) and silty clay, white (*N*9), yellowish white (7.5*Y*9/1), and light yellowish brown (10*YR*7/3).	2	40	58	4.2	5.8	78	14	.7	.3	3.2	.7	3.4
6	Palmerton Sandstone of Swartz (1939).	55–64	1	Sandy silty clay, yellowish white (7.5*Y*9/1).	33	24	43	4.8	5.2	85	10	.7	.4	2.1	.5	2.3
7	Buttermilk Falls Limestone.	0–62	8	Silty clay, white (*N*9) to yellowish white (5*Y*9/1).	6	36	58	5.0	5.0	83	11	.5	.3	2.2	.5	2.8
7	Palmerton Sandstone.	62–68	1	Sandy silty clay, yellowish pink (7.5*YR*8/2) at top, and sand, brown, at bottom (not collected).	22	21	57	3.3	6.7	79	12	1.9	.4	2.8	.7	2.7

[1] Semiquantitative analysis based on peak-area ratio of 7.2 A (001) peak of kaolinite and 10.0 A (001) peak of illite.

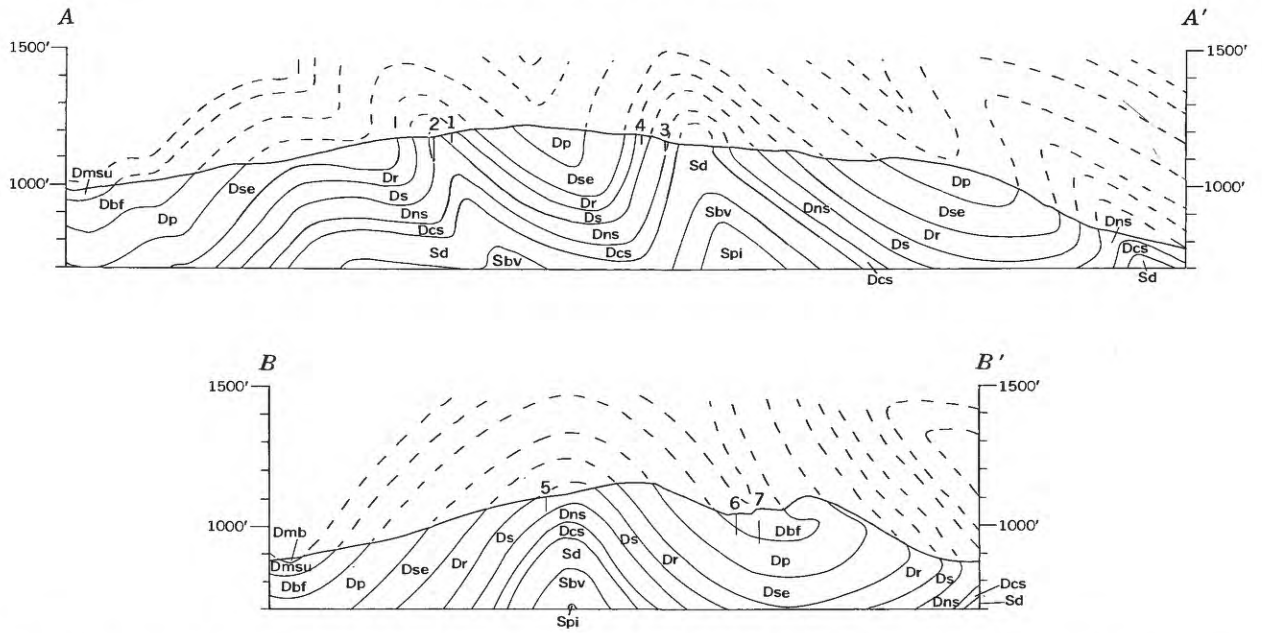

FIGURE 5.—Geologic sections *A–A'* and *B–B'* in the Universal Atlas Cement Co. claypits in Chestnut Ridge, approximately 4 miles north-northwest of Kunkletown, Pa. Location of sections is shown in figure 4. Numbered symbols are auger holes described in table 2.

TABLE 3.—*Average of grain-size distribution, semiquantitative analyses of kaolinite and illite, and X-ray fluorescence analyses of weathered New Scotland Formation, Shriver Chert, and Buttermilk Falls Limestone of Willard (1938) from claypits near Kunkletown, Pa.*

Formation	Number of samples	Auger hole numbers	Grain-size distribution (weight percent)			Peak-area ratio	
			Sand	Silt	Clay	Kaolinite (001)	Illite (001)
New Scotland Formation	17	2, 3	6	36	58	4. 4	5. 6
Shriver Chert	18	1, 4, 5	10	40	50	4. 3	5. 7
Buttermilk Falls Limestone	14	6, 7	4	38	58	4. 7	5. 3
All units	49	1–7	7	38	55	4. 4	5. 6

Formation	X-ray fluorescence analysis (weight percent)						
	SiO_2	Al_2O_3	Fe_2O_3	CaO	K_2O	TiO_2	Loss on ignition (1,000° C)
New Scotland Formation	76	14	1. 1	0. 2	3. 4	0. 8	3. 4
Shriver Chert	81	12	. 5	. 3	2. 6	. 7	3. 1
Buttermilk Falls Limestone	81	12	. 6	. 3	2. 6	. 6	3. 1
All units	79	13	. 7	. 3	2. 9	. 7	3. 2

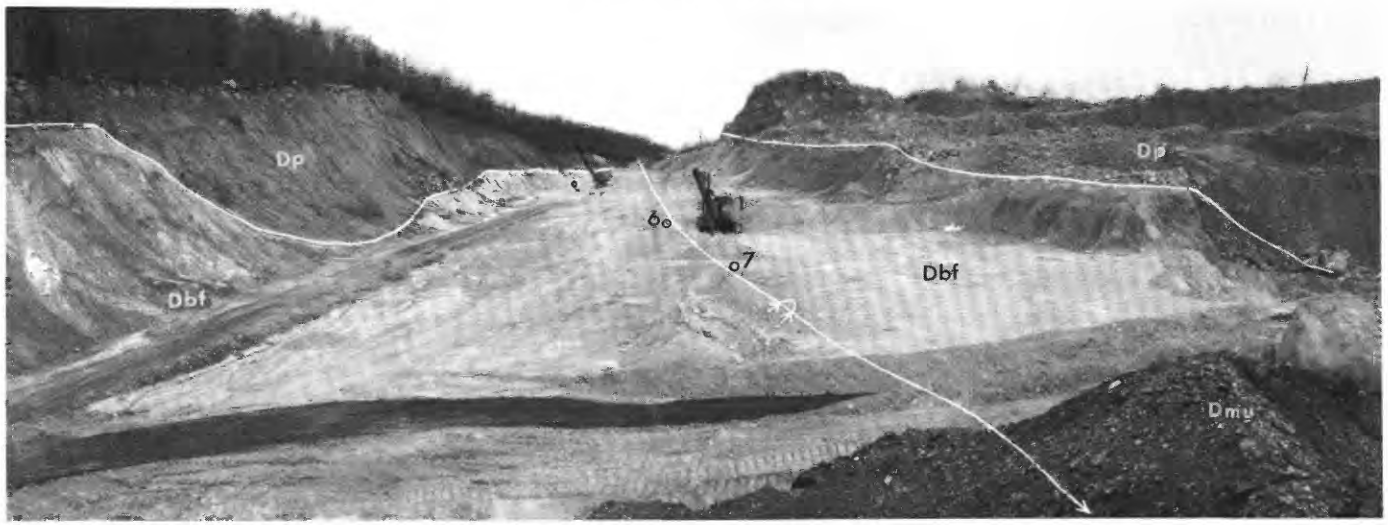

FIGURE 6.—Clay and sand operations in the lower pit of the Universal Atlas Cement Co. near Kunkletown, Pa., showing location of auger holes 6 and 7 (see fig. 4). View eastward from knob of grayish-black Union Springs Shale Member of Marcellus Shale (Dmu) and paralleling axial trace of westward-plunging overturned syncline (figs. 4 and 5, sec. *B–B'*). Palmerton Sandstone of Swartz (1939) (Dp) and Buttermilk Falls Limestone of Willard (1938) (Dbf) dip about 60° S. on left and are overturned about 50° S. on right. Leached sand from the Palmerton is being removed from pit on far right.

If the interpretation of Pierce (1965), that the Great Valley and Valley and Ridge provinces of Pennsylvania have been exposed to subaerial erosion and weathering since the Cretaceous, and possibly earlier, is correct, then this establishes a possible age for the beginning of weathering. This is not to say that the present rocks near Kunkletown have undergone leaching since that time—there has been too much erosional denudation of the earth's surface since then. But it is not unreasonable to suppose that the clays at Kunkletown today are a product of prolonged weathering during several millions of years, and that large amounts of weathered residuum have been removed.

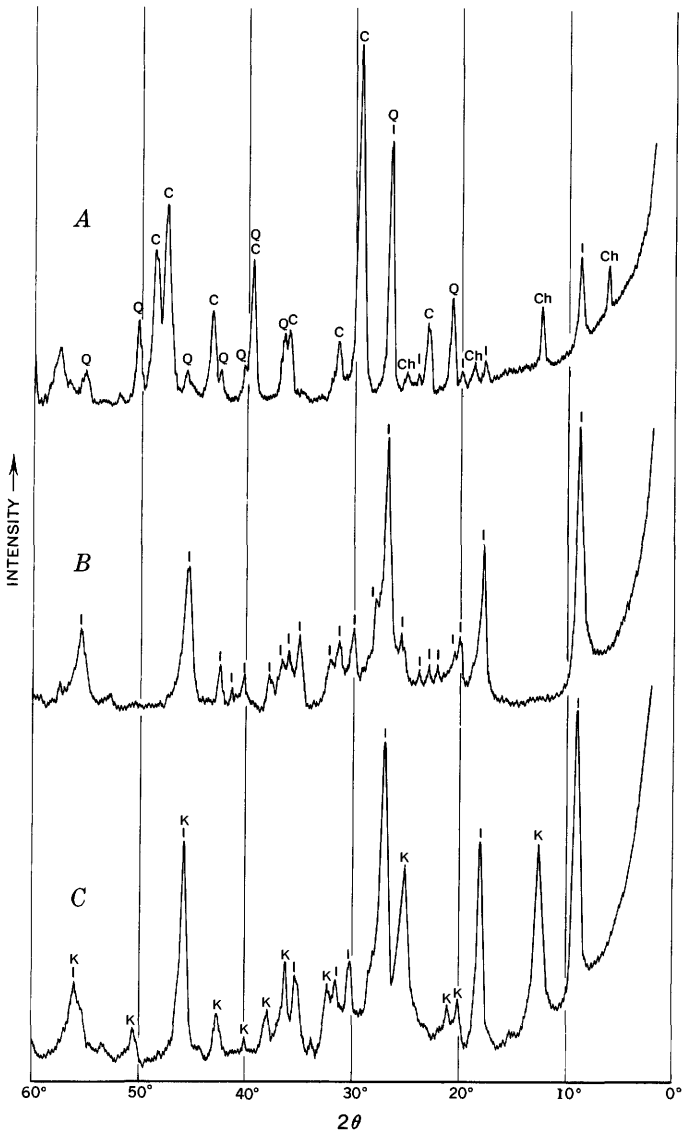

FIGURE 7.—Typical X-ray diffractometer traces of fresh and weathered Buttermilk Falls Limestone of Willard (1938). Cu$K\alpha$ radiation. *A*, Unweathered whole rock (table 1, sample 13); Ch, chlorite; I, illite; Q, quartz; C, calcite. *B*, Same sample as *A;* chlorite and calcite removed by treatment in boiling 6*M* hydrochloric acid for 3 hours; quartz removed by settling out >4 micron particles; I, 2M illite. *C*, Weathered sample from auger hole 7 (table 2); quartz removed by settling out >4 micron particles; I, M*d* illite; K, kaolinite.

REFERENCES

Epstein, A. G., Epstein, J. B., Spink, W. J., and Jennings, D. S., 1967, Upper Silurian and Lower Devonian stratigraphy of northeastern Pennsylvania, New Jersey, and southeasternmost New York: U.S. Geol. Survey Bull. 1243, 74 p.

Epstein, J. B., 1969, Surficial geology of the Stroudsburg quadrangle, Pennsylvania-New Jersey: Pennsylvania Geol. Survey, 4th ser., Bull. G–57 [In press].

Epstein, J. B., and Epstein, A. G., 1967, Geology in the region of the Delaware to Lehigh Water Gaps, Field Conference of Pennsylvania Geologists 32d, East Stroudsburg, Guidebook: Harrisburg, Pa., Pennsylvania Geol. Survey, 89 p.

——— 1969, Geology of the Valley and Ridge Province between Delaware Water Gap and Lehigh Gap, Pennsylvania, *in* Subitzky, Seymour, ed., Geology of selected areas in New Jersey and Pennsylvania—and guidebook of excursions: New Brunswick, N.J., Rutgers Univ. Press [In press].

Ericson, D. B., Ewing, Maurice, and Wollin, Goesta, 1964, The Pleistocene epoch in deep-sea sediments: Science, v. 146, no. 3645, p. 723–732.

Leighton, Henry, 1934, The white clays of Pennsylvania: Pennsylvania Geol. Survey, 4th ser., Prog. Rept. 112, 19 p.

——— 1941, Clay and shale resources in Pennsylvania: Pennsylvania Geol. Survey, 4th ser., Bull. M–23, 245 p.

Munsell Color Co., Inc., 1929–1960, Munsell Book of Color: Baltimore, Md.

Peck, F. B., 1922. White clay deposits at Saylorsburg, Monroe County, Pennsylvania: Pennsylvania Geol. Survey, 4th ser., Bull. 40, 8 p.

Pierce, K. L., 1965, Geomorphic significance of a Cretaceous deposit in the Great Valley of southern Pennsylvania: U.S. Geol. Survey Prof. Paper 525–C, p. C152–C156.

Ries, Heinrich, Bayley, W. S., and others, 1922, High-grade clays of the eastern United States, with notes on some western clays: U.S. Geol. Survey Bull. 708, 314 p.

Schultz, L. G., 1964, Quantitative interpretation of mineralogical composition from X-ray and chemical data for the Pierre Shale: U.S. Geol. Survey Prof. Paper 391–C, 31 p.

Swartz, F. M., 1939, The Keyser Limestone and Helderberg Group, *in* The Devonian of Pennsylvania: Pennsylvania Geol. Survey, 4th ser., Bull. G–19, p. 29–91.

White, I. C., 1882, The geology of Pike and Monroe Counties: Pennsylvania Geol. Survey, 2d Rept., G6, 406 p.

Willard, Bradford, 1938, A Paleozoic section at Delaware Water Gap: Pennsylvania Geol. Survey, 4th ser., Bull. G–11, 35 p.

——— 1957, Devonian section at Bowmanstown, Pennsylvania: Am. Assoc. Petroleum Geologists Bull., v. 41, p. 2298–2311.

THE SECOND LAKE ANTICLINE—A MAJOR STRUCTURE ON THE NORTHWEST LIMB OF THE BOUNDARY MOUNTAIN ANTICLINORIUM, NORTHERN NEW HAMPSHIRE, WEST-CENTRAL MAINE, AND ADJACENT QUEBEC

By DAVID S. HARWOOD, Washington, D.C.

Abstract.—A narrow belt of greenstone, graywacke, and slate in northern New Hampshire, west-central Maine, and adjacent Quebec, previously thought to be Devonian, is correlated with the Dixville Formation (Middle Ordovician) and is inferred to lie in the core of an anticline, the Second Lake anticline, on the northwest limb of the Boundary Mountain anticlinorium. The name Deer Brook syncline is proposed for the belt of Silurian and Devonian rocks that separates, in part, the rocks in the Second Lake anticline from the pre-Silurian rocks in the Boundary Mountain anticlinorium.

The Boundary Mountain anticlinorium (Albee, 1961) trends northeast across northern New Hampshire and west-central Maine (fig. 1). It contains a core of pre-Silurian rocks bounded on the northwest by Silurian and Devonian rocks of the Connecticut Valley-Gaspé synclinorium (Cady, 1960) and on the southeast by Silurian and Devonian rocks of the Moose River synclinorium (Boucot, 1961) (fig. 1) and the Merrimack synclinorium (Osberg and others, 1968) (southeast of area of fig. 1).

The core of the anticlinorium is composed of rocks of known Middle Ordovician age (Harwood and Berry, 1967) and older rocks of probable Middle and Early Ordovician age and possible Late Cambrian age (Green, 1964; 1968) that have been assigned to the Dixville and Albee Formations, the Aziscohos Formation of Green (1964), and the Arnold River Formation of Marleau (1968). North of the 45th parallel, these rocks are predominantly slates, graywackes, and greenstones in the chlorite zone of regional metamorphism; to the south, they are schists, gneisses, and amphibolites in the garnet, staurolite, and sillimanite zones of metamorphism (Green and Guidotti, 1968, fig. 19–5).

The rocks on the northwest flank of the anticlinorium are interbedded slate, metasandstone, and felsic and mafic metavolcanic rocks that have been mapped as the Kidderville Formation of Hatch (1963), the Frontenac Formation (Marleau, 1957, 1959; Green, 1968), and the Seboomook Formation (Marleau, 1959; Green, 1968). All these rocks have been considered to be of Early Devonian age and to form a virtually homoclinal northwest-facing sequence that continues at least as far northwest as the trace of the Frontenac syncline (Marleau, 1959; Green and Guidotti, 1968) (fig. 1).

Stratigraphic and structural evidence presented in this report indicates that at least part of the Kidderville Formation of Hatch (1963) and part of the Frontenac Formation of Marleau (1957) may be pre-Silurian in age and may lie in the core of a subsidiary anticline on the northwest flank of the Boundary Mountain anticlinorium. This interpretation is an alternative to the interpretation of the structure of the northwest limb of the Boundary Mountain anticlinorium recently proposed by Green and Guidotti (1968).

PREVIOUS WORK

Early reports, beginning about 1850, on the age and structural relations of the rocks on the northwest limb of the Boundary Mountain anticlinorium and the Connecticut Valley-Gaspé synclinorium to the northwest have been discussed and synthesized by Cady (1960). The synthesis by Cady (1960) shows a synclinorium of Silurian and Devonian rocks—the Connecticut Valley-Gaspé synclinorium—situated in eastern Vermont and southeastern Quebec between an anticlinorium of pre-Silurian rocks on the west—the Green Mountain anticlinorium—and the Boundary Mountain anticlinorium on the east.

On the northwest limb of the Boundary Mountain anticlinorium in the Woburn area of Quebec (fig. 1), Marleau (1957, 1968) mapped a belt of greenish-gray slate containing lenses of greenstone flanked to the northwest and southeast by interbedded gray slate and

U.S. GEOL. SURVEY PROF. PAPER 650-D, PAGES D106-D115

metasandstone. He retained the name Frontenac Formation of McGerrigle (1935) for the slate and volcanic unit and the name Compton Formation of McGerrigle (1935) for the gray slate and metasandstone to the northwest. The unit of gray slate and metasandstone mapped southeast of the Frontenac Formation by Marleau extends into west-central Maine (Albee, 1961) and is equivalent to the Seboomook Formation (Boucot, 1961) of Early Devonian age. Marleau (1959) located the trace of the Frontenac syncline (fig. 1) on the basis of pillow structures in the lenses of greenstone northeast of Lake Megantic (fig. 1) and correlated the Compton Formation on the northwest limb of this syncline with the Seboomook Formation on the southeast limb. This correlation and structural interpretation required the Compton and Frontenac Formations to be Devonian in age rather than Ordovician as proposed by McGerrigle (1935). Marleau considered the thick greenstone associated with slate, graywacke, and serpentinite that extends southwest of the south end of Lake Megantic (fig. 1) to be equivalent to the thin lenses of greenstone he found elsewhere in the Frontenac Formation and thus to be of Devonian age.

In the Dixville quadrangle (fig. 1), Hatch (1963) mapped a northeast-trending belt of metavolcanic rocks and schists, which he called the Kidderville Formation, northwest of the Dixville Formation of Ordovician age and southeast of the Gile Mountain Formation of Devonian age. He divided the Kidderville into an eastern felsic volcanic member and a western mafic volcanic member. Although Billings (1956) considered the rocks mapped as Kidderville to be the Orfordville Formation (Ordovician) (Hadley, 1942), Hatch (1963, p. 27) assigned a Devonian age to his Kidderville Formation because of its probable continuation to the northeast into rocks mapped as the Seboomook and Frontenac Formations (Devonian) by Marleau (1957). The Kidderville Formation of Hatch (1963) is bounded on the northwest by gray schist, phyllite, quartzite and thin lenses of greenstone assigned by Hatch to the Gile Mountain Formation of Devonian age. Hatch (1963, fig. 4; pl. 1) mapped the trace of his East Colebrook syncline through the middle of the lenses of greenstone and considered the Gile Mountain to be stratigraphically above his Kidderville Formation.

Green (1968) traced the mafic and falsic volcanic members of the Kidderville Formation of Hatch (1963) northeastward into the Frontenac and Seboomook Formations, respectively, as mapped by Marleau (1957) to the international boundary. Green retained the Devonian age for these rocks which he called Frontenac and Seboomook rather than Kidderville. The gray schist, phyllite, quartzite, and lenses of greenstone continuous with rocks assigned to the Gile Mountain Formation by Hatch (1963) were mapped as the Frontenac and Compton Formations by Green (1968). Green (1968) extended the trace of the Frontenac syncline of Marleau southwestward into northern New Hampshire, and correlated the rocks continuous with the mafic member of the Kidderville Formation of Hatch (1963) on the southeast limb of the syncline with lenses of greenstone apparently continuous with those mapped by Marleau (1957) on the northwest limb of the syncline. Green and Guidotti (1968, fig. 19-2), however, show the lenses of greenstone on the northwest limb of the Frontenac syncline to be stratigraphically equivalent to the lenses of greenstone mapped by Hatch (1963) in the Gile Mountain Formation and considered by Hatch (1963, fig. 4) to be younger than his Kidderville Formation.

In a recent summary of the geology of the Boundary Mountain anticlinorium, Green and Guidotti (1968, p. 261) consider the possibility that the mafic member of the Kidderville Formation of Hatch (1963) and the rocks continuous with it could be pre-Silurian, but they dismiss this alternative interpretation because "metabasaltic pillows in this belt indicate younger rocks to the northwest." Green (1968, p. 1628) also cites these pillow structures and the apparent symmetrical distribution of rock units as evidence for the existence and position of the Frontenac syncline.

STRATIGRAPHIC RELATIONS IN THE ARNOLD POND QUADRANGLE

Near marker post 460 on the international boundary (fig. 2), feldspathic graywacke, black slate, and greenstone of the Magalloway Member of Green (1968, p. 1610) of the Dixville Formation underlies a unit of gray calcareous slate containing lenses of limestone and limestone conglomerate. The Magalloway Member (upper graywacke part of Dixville of Harwood and Berry, 1967, p. D20) is considered of Middle Ordovician age. Recrystallized fragments of halysitid corals and other fossils, found by Green (1968, p. 1615) in a lens of limestone above the Magalloway indicate a Late Silurian (Ludlow) age. Although it was not seen in outcrop, the Taconic unconformity is believed to lie at the base of the calcareous slate because of the divergent dips in the Silurian and pre-Silurian rocks and the apparent truncation of a thin layer of greenstone in the Magalloway Member south of Lower Black Pond (fig. 2). The Magalloway Member of Green (1968) is herein adopted as the upper member of the Dixville Formation, and the type locality is designated as on the south slopes of Thrasher Peaks in Parmachenee Township, Maine.

359-403 O—69——8

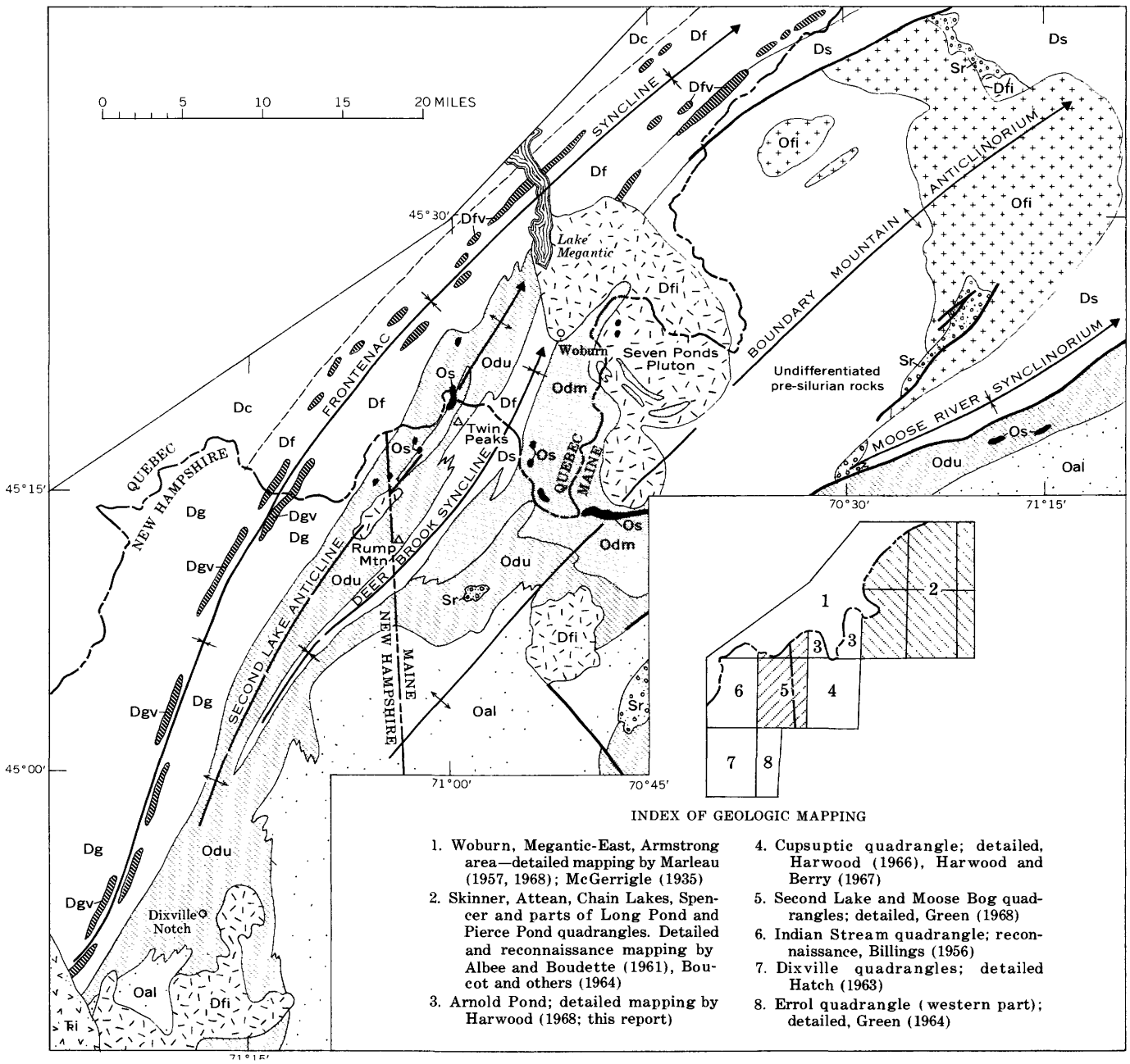

FIGURE 1.—Generalized geologic map of west-central Maine, northern New Hampshire, and adjacent Quebec, Canada, showing the position of the proposed Second Lake anticline and the Deer Brook syncline.

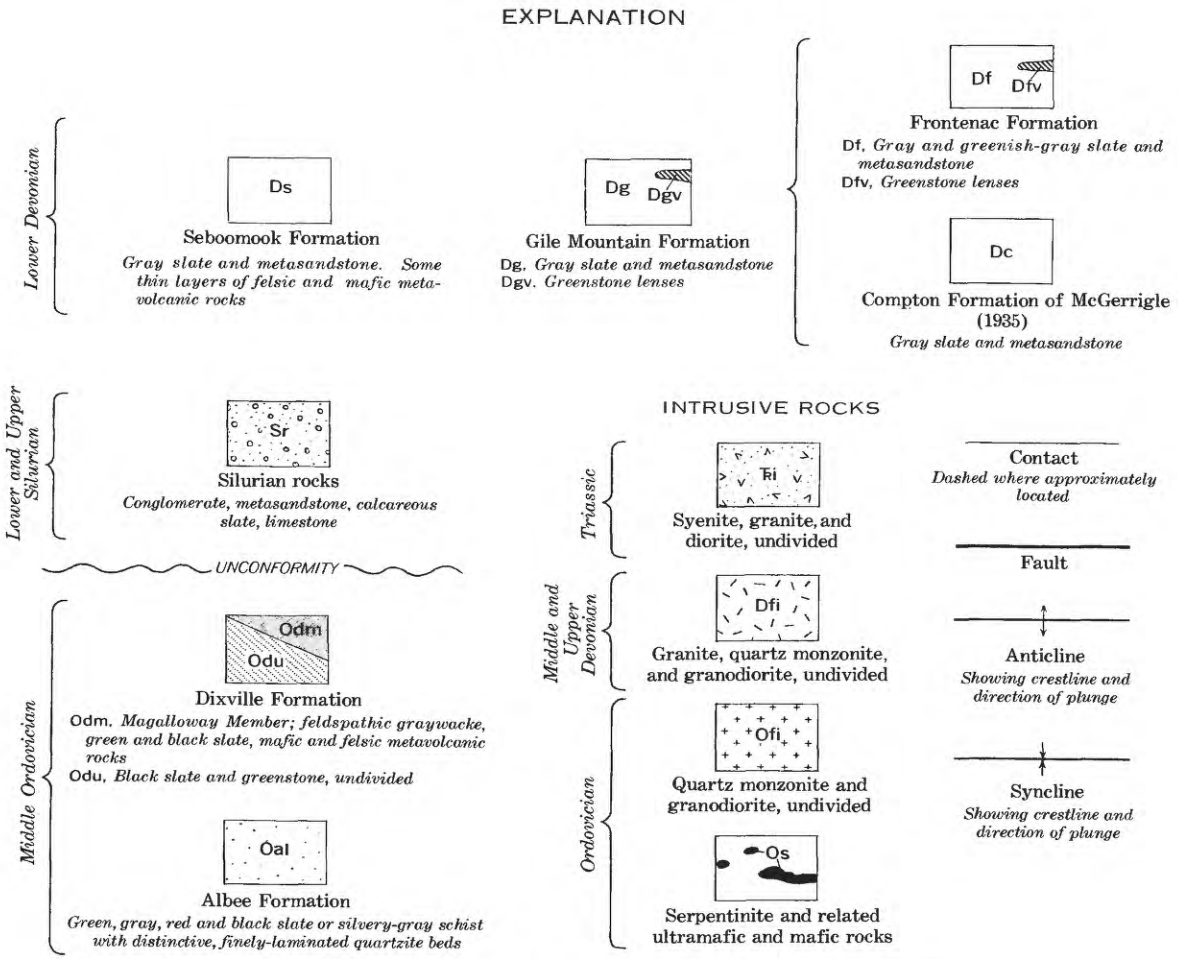

FIGURE 1.

The calcareous slate is conformably overlain by a resistant layer of white to greenish-gray felsic metavolcanic rock from 10 to 80 feet thick. Near the international boundary, the felsic metavolcanic rock grades upward into a discontinuous layer of red slate or into gray slate and metasandstone of the Seboomook Formation. No fossils were found in the red slate and felsic metavolcanic rocks; therefore, they can be dated only as Late Silurian to Early Devonian from their position between the calcareous slate and limestone unit and the Seboomook.

East of Lower Black Pond, the calcareous slate and felsic metavolcanic rocks outline a small syncline succeeded to the northwest by a tight anticline (fig. 2) that exposes feldspathic graywacke and greenstone of the Magalloway Member in its core. The calcareous slate and limestone unit has been removed from the northwest limb of this tight anticline by an inferred high-angle reverse fault, and the felsic metavolcanic rocks are in contact with the greenstone of the Magalloway Member. Southeast of Lower Black Pond (fig. 2), the felsic metavolcanic unit grades upward into green slate and locally calcareous metasiltstone about 75 feet thick. The green slate and calcareous metasiltstone grade upward and laterally into the Seboomook Formation. Southwest of Lower Black Pond, the Seboomook Formation rests directly on the Magalloway Member, either in fault contact or upon the Taconic unconformity, where the felsic metavolcanic rock is missing. Farther southeast, the Seboomook Formation is separated from the Magalloway Member by a discontinuous layer of polymict conglomerate composed of clasts of greenstone, graywacke, and gray siltstone apparently derived from the underlying Magalloway Member. The polymict conglomerate has tentatively been dated as Silurian (Harwood, 1966; Harwood and Berry, 1967).

Northwest of the trace of the Deer Brook syncline (fig. 2), the Seboomook Formation is underlain by green slate and locally calcareous metasiltstone interbedded in variable proportions. The green slate and metasiltstone unit, which is about 3,000 feet thick, is

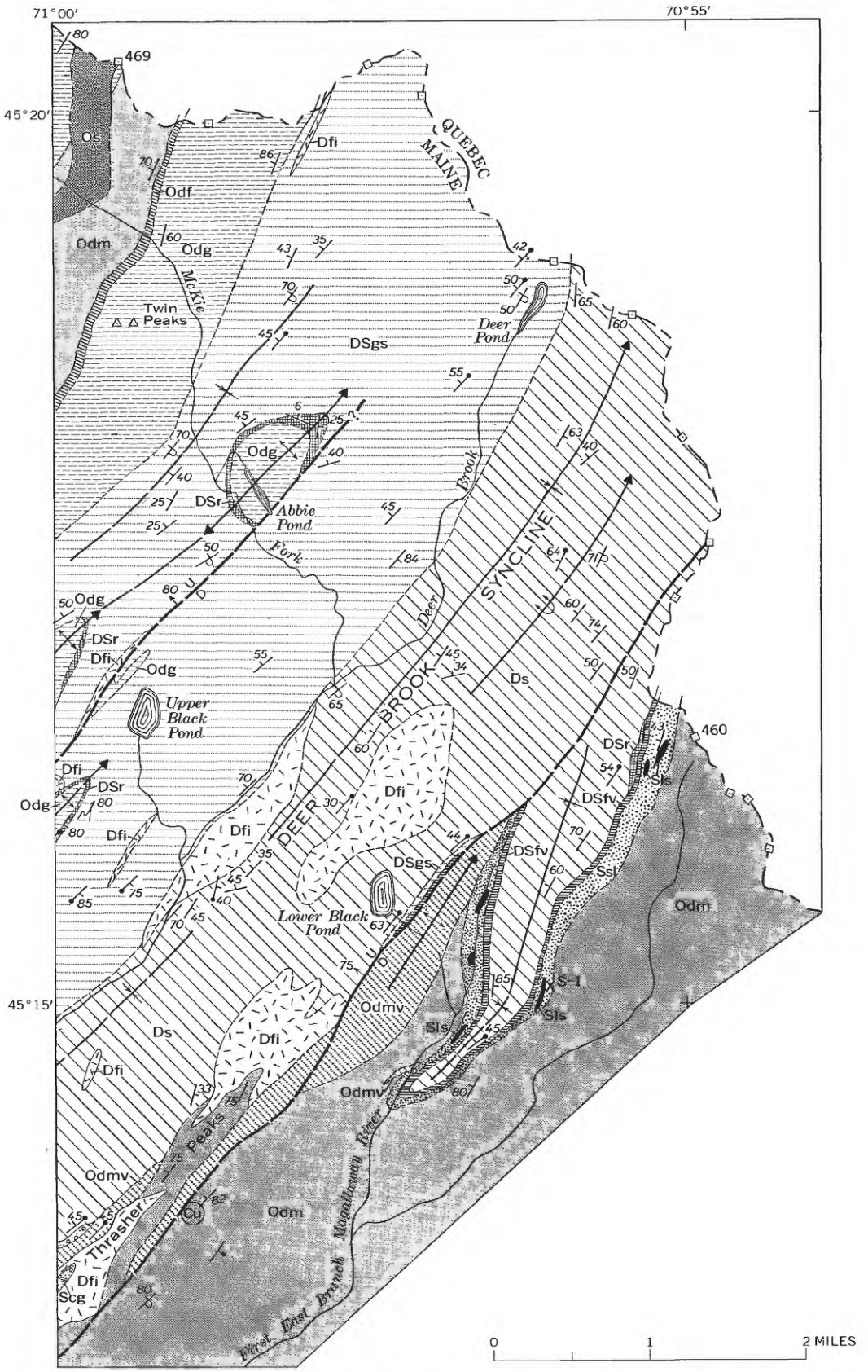

FIGURE 2.—Detailed geologic map of the western part of the Arnold Pond quadrangle and the northwest part of the Cupsuptic quadrangle, west-central Maine.

EXPLANATION

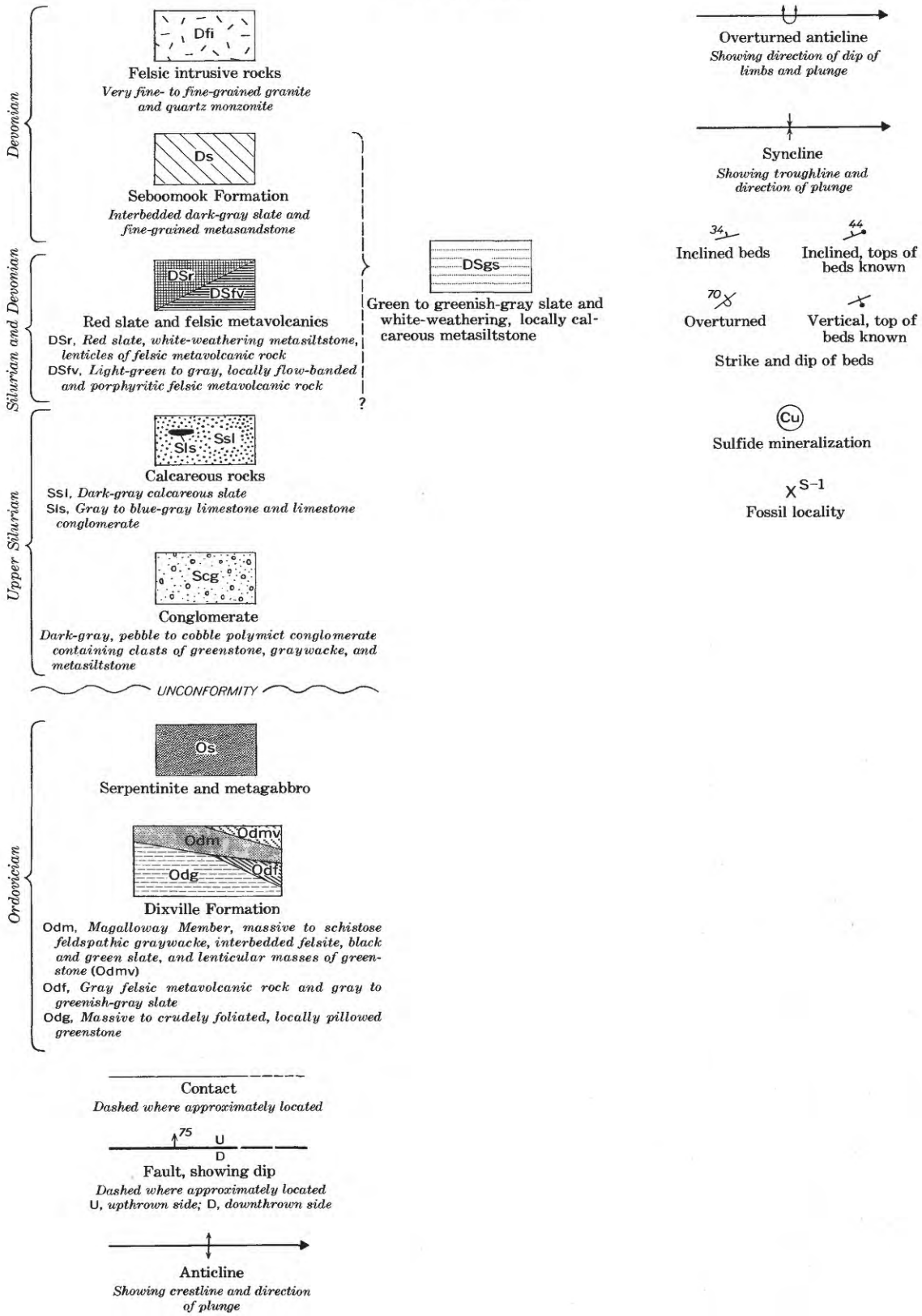

FIGURE 2 (CON.)

lithologically similar to that found below the Seboomook and above the felsic metavolcanic rock at the outlet to Lower Black Pond (fig. 2). Because of the unit's position below the Seboomook it can be no younger than Early Devonian, and it may be in part Silurian in age.

North of Abbie Pond (fig. 2) and southwest of Upper Black Pond (fig. 2), the green slate and metasiltstone are conformably and gradationally underlain by a discontinuous layer of red slate about 150 feet thick. The red slate contains beds of light-gray metasiltstone a few inches thick and discontinuous lenses of white felsic metavolcanic rock also a few inches thick. The contact with the overlying green slate and metasiltstone unit is exposed northeast of Abbie Pond (fig. 2) where the unit is a zone of intermixed red, green, and purplish-gray slate and white weathering metasiltstone about 10 feet thick.

The red slate northeast of Abbie Pond dips gently outward around the nose of a doubly plunging anticline (fig. 2) that contains massive, dark-green, fine- to medium-grained greenstone in its core. The contact between the red slate and the greenstone was not seen northeast of Abbie Pond, but it is exposed along the southeast face of a 15-foot cliff about 4,000 feet southwest of Lower Black Pond (fig. 2). The contact in this area strikes N.50° E., dips 80° SE., and is extremely sharp. Massive and fractured red slate a few inches from the contact grades into a zone of dark-gray magnetite-rich slate ½ inch from the greenstone. The greenstone within ½ inch of the contact is composed of a scaly chlorite and magnetite aggregate, about ½ inch thick, which grades into the normal greenstone. In the red slate, fine laminae of dark-gray, magnetite-rich slate outline crossbeds which indicate that the red slate faces southeast and overlies the greenstone. The chlorite-magnetite-rich layer in the greenstone may be a metamorphosed laterite horizon that was reworked and incorporated into the basal part of the overlying red slate.

Although the greenstone is stratigraphically below the red slate, no fossils have been found in these rocks, and their ages can only be inferred from field relationships. The red slate is tentatively correlated with the patch of red slate and the felsic metavolcanic rocks near marker post 460 on the international boundary (fig. 2). If this correlation is correct, the red slate is Late Silurian to Early Devonian. The overlying green slate and metasiltstone unit probably represents the same time span and may be equivalent, in part, to the Seboomook. The greenstone is no younger than the red slate, and, for reasons discussed below, it is considered to be pre-Silurian and unconformably below the red slate and green slate and metasiltstone unit.

The belt of rocks at Twin Peaks (fig. 2) is composed of about 4,000 feet of massive to foliated greenstone that contains scattered layers of pillowed metabasalt (see Green, 1968, pl. 5, fig. 2) and coarse-grained mafic metavolcanic ejecta. Northwest of Twin Peaks, the greenstone is succeeded by interbedded felsic metavolcanic rock and gray slate about 250 feet thick. The contact between the felsic metavolcanic and slate unit and the greenstone was not observed, but the layering in both units is virtually parallel. Northwest of the felsic metavolcanic and slate unit is about 2,000 feet of medium- to coarse-grained, massive to schistose feldspathic graywacke that contains discontinuous layers of black and green slate and some greenstone. The graywacke is remarkably similar in outcrop appearance and mineralogy to the feldspathic graywacke of the Magalloway Member of the Dixville Formation found in the northern part of the Cupsuptic quadrangle (fig. 1) and described in detail by Harwood (1966) and Green (1968, p. 1610). To the northwest, the feldspathic graywacke is succeeded by a belt of greenstone and interlayered black slate that extends about a mile northwest of the area shown on figure 2 (Green, 1968, pl. 1) and that has an apparent maximum thickness of about 5,000 feet. The contact between the feldspathic graywacke and the greenstone to the northwest is intruded by an elongate body of dark-green, highly fractured serpentinite that contains a thin, discontinuous shell of coarse-grained metagabbro on its eastern side.

The age of the metavolcanic rocks, slate, and feldspathic graywacke in the northwestern part of the area shown on figure 2 is not unequivocally known and represents the basic point of disagreement between the recent interpretation of Green and Guidotti (1968) and this report. Crossbeds in the red slate in contact with the greenstone indicate that the greestone underlies the red slate, and, thus, the greenstone must be no younger than Late Silurian, the infered maximum age of the red slate. Green (1968, p. 1621), however, reports that pillow structures in this belt of greenstone face northwest; therefore, the contact between the red slate and greenstone must be a fault or an unconformity. There is a northeast-trending fault near Upper Black Pond, but this fault apparently offsets both the greenstone and the red slate and does not coincide with the greenstone-red slate contact. The magnetite-rich layer at the red slate-greenstone contact, on the other hand, suggests that the greenstone was weathered subaerially and argues for an unconformity. The metavolcanic rocks, black slate, and feldspathic graywacke

in the northwest part of the area shown on figure 2 are lithologically similar to rocks in the Dixville Formation (Middle Ordovician) found to the southeast in the core of the Boundary Mountain anticlinorium (Harwood, 1966; Harwood and Berry, 1967; Green, 1968). Furthermore, several bodies of serpentinite and related metagabbro, similar to the body shown in the northwest corner of figure 2, intrude the Magalloway Member of the Dixville (and its correlative, the Arnold River Formation of Marleau, 1957, 1968) in the Boundary Mountain anticlinorium (see fig. 1). Chidester (1962) reports that no ultramafic rocks intrude rocks of known Silurian or Devonian age in the northern Appalachians. Therefore, the rocks in the northwest part of the area shown on figure 2 are considered to be equivalent to the Dixville Formation to the southeast and are inferred to be Middle Ordovician.

The evidence cited above leads to the conclusions that the rocks in the northwest part of the Arnold Pond quadrangle (figs. 1 and 2) correlate with the Dixville Formation and lie in the core of an anticline outlined by the base of the Silurian and Devonian rocks. This anticline, herein named the Second Lake anticline (fig. 1) is separated from the Boundary Mountain anticlinorium to the southeast by a syncline of Silurian and Devonian rocks, herein named the Deer Brook syncline. The internal structure of the Second Lake anticline is not well known because of the scarcity of top-facing evidence in most of the rocks. The pre-Silurian rocks in the Boundary Mountain anticlinorium and probably those in the Second Lake anticline were folded, uplifted, and eroded before deposition of the Silurian and Devonian rocks (Harwood, 1966; Harwood and Berry, 1967). The rocks in the core of the Second Lake anticline, therefore, need not be folded into an anticline conformable with the structure outlined by the base of the Silurian and Devonian rocks (the inferred Taconic uncomformity). The Second Lake anticline, like the Boundary Mountain anticlinorium (Albee, 1961, p. C51), is defined by the base of the Silurian and Devonian rocks and not necessarily by its internal structure.

REGIONAL RELATIONSHIPS

The rocks in the Second Lake anticline in the northwest corner of the area shown on figure 2 are continuous with and lithologically similar to rocks described and mapped to the southwest by Hatch (1963) and Green (1968) and to the northeast by Marleau (1957, 1968). These rocks form a continuous northeast-trending belt extending from the southwest part of the Dixville quadrangle (fig. 1) to the south end of Lake Megantic (fig. 1). It is proposed that the stratigraphic and structural relations presented in this report for the northwest part of the Arnold Pond area are valid for this continuous belt of rocks.

The greenstone at Twin Peaks (figs. 1, 2) extends southwestward to Rump Mountain (fig. 1) where Green (1968) reports that it underlies and interfingers with felsic metavolcanic rocks that are apparently continuous with the thin layer of interbedded felsic metavolcanic rocks and slate northwest of Twin Peaks (fig. 2). The feldspathic graywacke, assigned to the Magalloway Member in the Second Lake anticline (fig. 1), continues southwest of the international boundary for 3½ miles, where Green (1968, pl. 1) shows it pinching out between felsic metavolcanic rocks on the southeast and greenstone and black slate on the northwest. The rocks in the core of the Second Lake anticline apparently form a northwest-facing sequence composed of about 4,000 feet of greenstone and felsic metavolcanic rocks on the southeast overlain by 0 to 2,000 feet of feldspathic graywacke, which, in turn, is overlain by about 5,000 feet of greenstone and black slate.

This sequence, which in the northwest part of the Arnold Pond quadrangle was correlated with the Dixville Formation on the basis of lithologic similarity, is concluded to be continuous to the southwest with the Dixville Formation mapped by Hatch (1963, pl. 1) near Dixville Notch (fig. 1). There, the rocks overlie the Albee Formation on the northwest limb of the Bald Head Mountain anticline of Hatch (1963, p. 52; fig. 4).

Green (1968, pl. 1) and Marleau (1968, Woburn area map) show several small bodies of serpentinite and ultramafic rock in the core of the proposed Second Lake anticline. They concluded that the serpentinite and ultramafic bodies were Devonian because they believed that these bodies intruded rocks of Devonian age. Green (1968, p. 1623) suggested that the ultramafic rocks may have been "remobilized older bodies from the Ordovician or even older basement." To the east, however, ultramafic bodies occur as septa in the Seven Ponds pluton (fig. 1) of Devonian age, indicating that they predate the intrusion of the pluton. Utramafic rocks are also abundant in the pre-Silurian rocks south and east of the Seven Ponds pluton (Harwood, 1966; E. L. Boudette, written commun., 1968) but are not known to occur in the Silurian or Devonian rocks. Poole and others (1963) obtained a minimum K/Ar date of 480 m.y. on muscovite from two granite bodies cutting ultramafic rocks in the Thetford Mines-Black Lake area of Quebec, indicating that the ultramafic rocks in that part of the Green Mountain anticlinorium (Cady, 1960) are Ordovician or older. On the basis of these considerations and the findings of Chidester (1962), the rocks transected by the serpentinite

bodies in the proposed Second Lake anticline are more reasonably interpreted to be Ordovician rather than Devonian. N. L. Hatch (written commun., 1969) now concurs in this conclusion.

The southwestern extent of the Deer Brook syncline is not precisely known. The distinctive Silurian calcareous slate and limestone on the southeast limb of the syncline is restricted to the area shown on figure 2, except for a few isolated patches reported by Green (1968, p. 1614, fig. 4). Green (1968, pl. 1) has traced the Seboomook Formation southwest of the Arnold Pond quadrangle (figs. 1, 2) to the 45th parallel and has mapped a discontinuous layer of felsic metavolcanic rock at the base of the Seboomook that may correlate with the felsic metavolcanic rock above the calcareous slate and limestone near marker post 460 on the international boundary (fig. 2). Hatch (1963, p. 20–22) reports scattered beds of gray and black slate, possibly the Seboomook Formation, as far south as Dixville Notch (fig. 1). Green (1968, p. 1618) concluded that metavolcanic rocks and black slate similar to those in the Dixville Formation, but found along the inferred trace of the Deer Brook syncline, were interlayered with the Seboomook, but he could not eliminate the possibility of interfolding. Thus, the Seboomook Formation and the Deer Brook syncline are probably continuous as far southwest as the 45th parallel and may be present somewhat farther south as isolated infolded patches.

The red slate and green slate and metasiltstone on the northwest limb of the Deer Brook syncline have been mapped by Green (1968) to the vicinity of Rump Mountain (fig. 1) where they apparently pinch out beneath the Seboomook Formation. Their disappearance as well as the absence of the calcareous slate, limestone, and felsic metavolcanic rocks on the northwest limb of the Deer Brook syncline suggests that the Seboomook overlaps the older units along the Taconic unconformity or that the southeast limb of the Second Lake anticline is bounded by a major fault.

Similar relations are found along the northwest limb of the Second Lake anticline where gray slate, phyllite, schist, and quartzite of the Gile Mountain Formation and equivalent rocks (part of the Frontenac Formation of Marleau, 1968) rest directly on greenstone and black slate of inferred pre-Silurian age. It is possible that the red and green slate and the calcareous rocks were never deposited on the northwest limb of the Second Lake anticline or that the Gile Mountain Formation overlaps these older rocks along the Taconic unconformity. Alternatively, the contact between the Gile Mountain Formation (and equivalent rocks to the northeast) and the rocks in the proposed Second Lake anticline may be a major fault possibly coextensive with the Monroe fault to the southwest (Eric and others, 1941; Hall, 1959).

The trace of the Frontenac syncline shown on figure 1 is inferred to lie within the belt of greenstone lenses in the Gile Mountain Formation as mapped by Hatch (1963, pl. 1) and in the northwestern part of the Frontenac Formation as mapped by Green (1968, pl. 1) and Marleau (1968, Woburn area map). In this position, the Frontenac syncline is continuous with the East Colebrook syncline of Hatch (1963, fig. 4). The trace of the Frontenac syncline is extended northeastward to join the trace of the syncline shown by Marleau (1968, Woburn area map) northeast of Lake Megantic, with the understanding that the greenstone southwest of the south end of Lake Megantic is probably pre-Silurian in age and stratigraphically below the lenses of greenstone on the southeast limb of the Frontenac syncline northeast of the lake.

CONCLUSIONS

The metavolcanic rocks, slate, and feldspathic graywacke, which are intruded by serpentinite in the northwest part of the Arnold Pond quadrangle (figs. 1 and 2), are stratigraphically below red and green slate of inferred Late Silurian to Early Devonian age, which, in turn, are below the Seboomook Formation of Early Devonian age. This belt of heterogeneous rocks, previously mapped as the Kidderville Formation by Hatch (1963) and part of the Frontenac Formation by Green (1968) and Marleau (1957, 1968), is correlated with the Dixville Formation (Middle Ordovician) and is inferred to lie in the Second Lake anticline outlined by the trace of the Taconic unconformity. The rocks of the Second Lake anticline are separated, in part, from the main belt of the Dixville Formation in the Boundary Mountain anticlinorium (fig. 1) by Silurian and Devonian rocks of the Deer Brook syncline. Correlation of the rocks in the Second Lake anticline with the Dixville Formation and thus with the Ammonoosuc Volcanics and the Partridge Formation (Billings, 1956; Harwood and Berry, 1967) to the southwest offers an explanation for the absence of the Kidderville Formation of Hatch (1963) below the Silurian and Devonian rocks on the east limb of the Connecticut Valley-Gaspé synclinorium in eastern Vermont. Furthermore, the proposed stratigraphic and structural interpretation allows the age of the serpentinite and ultramafic bodies in the Second Lake anticline to be Ordovician, in keeping with the pre-Silurian age of the other known ultramafic bodies in the northern Appalachians.

REFERENCES

Albee, A. L., 1961, Boundary Mountain anticlinorium, west-central Maine and northern New Hampshire: Art. 168 *in* U.S. Geol. Survey Prof. Paper 424–C, p. C51–C54.

Albee, A. L., and Boudette, E. L., 1961, Preliminary geologic map of the Attean quadrangle, Somerset County, Maine: U.S. Geol. Survey open-file report.

Billings, M. P., 1956, Bedrock geology, pt. 2 *of* The geology of New Hampshire: Concord, N.H., New Hampshire State Plan. and Devel. Comm., 203 p.

Boucot, A. J., 1961, Stratigraphy of the Moose River synclinorium, Maine: U.S. Geol. Survey Bull. 1111–E., p. 153–188.

Boucot, A. J., Griscom, Andrew, and Allingham, J. W., 1964, Geologic and aeromagnetic map of northern Maine: U.S. Geol. Survey Geophys. Inv. Map GP-312.

Cady, W. M., 1960, Stratigraphic and geotectonic relations in northern Vermont and southern Quebec: Geol. Soc. America Bull., v. 71, no. 5, p. 531–576.

Chidester, A. H., 1962, Petrology and geochemistry of selected talc-bearing ultramafic rocks and adjacent country rocks in north-central Vermont: U.S. Geol. Survey Prof. Paper 345, 207 p.

Eric, J. H., White, W. S., and Hadley, J. B., 1941, Monroe fault of New Hampshire and Vermont [abs.]: Geol. Soc. America Bull., v. 52, no. 12, pt. 2, p. 1900.

Green, J. C., 1964, Stratigraphy and structure of the Boundary Mountain anticlinorium in the Errol quadrangle, New Hampshire-Maine: Geol. Soc. America Spec. Paper 77, 78 p.

——— 1968, Geology of the Connecticut Lakes-Parmachenee area, New Hampshire and Maine: Geol. Soc. America Bull., v. 79, no. 11, p. 1601–1638.

Green, J. C., and Guidotti, C. V., 1968, Geology of the Boundary Mountain anticlinorium in northern New Hampshire and northwestern Maine, *in* Zen, E-an, White, W. S., Hadley, J. B., and Thompson, J. B., eds., Studies of Appalachian geology—Northern and Maritime: New York, Interscience, p. 225–266.

Hadley, J. B., 1942, Stratigraphy, structure, and petrology of the Mt. Cube area, New Hampshire: Geol. Soc. America Bull., v. 53, no. 1, p. 113–176.

Hall, L. M., 1959, Geology of the St. Johnsbury quadrangle, Vermont and New Hampshire: Vermont Geol. Survey Bull. 13, 105 p.

Harwood, D. S., 1966, Geology of the Cupsuptic quadrangle, Maine: U.S. Geol. Survey open-file rept., 259 p.

——— 1968, Geology of the Arnold Pond quadrangle, Oxford and Franklin Counties, Maine: U.S. Geol. Survey open-file rept., 13 p.

Harwood, D. S., and Berry, W. B. N., 1967, Fossiliferous lower Paleozoic rocks in the Cupsuptic quadrangle, west-central Maine, *in* Geological Survey Research 1967: U.S. Geol. Survey Prof. Paper 575–D, p. D16–D23.

Hatch, N. L., Jr., 1963, Geology of the Dixville quadrangle, New Hampshire: New Hampshire Dept. Resources and Econ. Devel. Bull. 1, 81 p.

McGerrigle, H. W., 1935, Mount Megantic area, southeastern Quebec, and its placer-gold deposits: Quebec Bur. Mines Ann. Rept. 1934, pt. D, p. 63–104.

Marleau, R. A., 1957, Preliminary report on East Megantic and Armstrong areas, electoral districts of Frontenac and Beauce: Quebec Dept. Mines, Geol. Survey Br. Prelim. Rept. 362, 7 p.

——— 1959, Age relations in the Lake Megantic Range, southern Quebec: Geol. Assoc. Canada Proc., v. 11, p. 129–139.

——— 1968, Woburn-East Megantic-Armstrong area, Frontenac and Beauce Counties: Quebec Dept. Nat. Resources Geol. Rept. 131, 55 p.

Osberg, P. H., Moench, R. H., and Warner, Jeffrey, 1968, Stratigraphy of the Merrimack synclinorium in west-central Maine, *in* Zen, E-an, White, W. S., Hadley, J. B., and Thompson, J. B., eds., Studies of Appalachian geology—Northern and Maritime: New York, Interscience, p. 241–253.

Poole, W. H., Béland, J., and Wanless, R. K., 1963, Minimum age of Middle Ordovician rocks in southern Quebec: Geol. Soc. America Bull. v. 74, no. 8, p. 1963–1066.

THE BLUE CUT FAULT, SOUTHEASTERN CALIFORNIA

By ROGER A. HOPE, Menlo Park, Calif.

Abstract.—The Blue Cut fault is one of several east-west faults in a region south of the Mojave Desert and east of the San Andreas fault. Between 3 and 4 miles of left-lateral strike slip accumulated along the Blue Cut fault sometime between the Jurassic and the Quaternary. At its western end, displacements along the fault were probably translated to the Dillon fault which strikes northwest, dips northeast, and has had at least minor reverse-slip movement. At the eastern end, the Blue Cut fault may be displaced more than 11 miles right laterally by the northwest-trending Sheep Hole fault.

In the part of southern California east of the San Andreas fault, the major faults as well as the mountain ranges and valleys generally trend north to northwest. This trend is broken south of the Mojave Desert by the east-west Transverse Ranges (fig. 1, see also Jahns, 1954, p. 11). The shapes of these ranges and the intervening basins are in part due to the presence of several west-trending faults. Reconnaissance mapping indicated that crustal blocks had shifted a mile or more left laterally along several of these faults (Hope, 1966). Two of the longest faults have been studied in more detail. One of these, the Blue Cut fault, is described in this article; the other, the Pinto Mountain fault, has been mapped and described by T. W. Dibblee, Jr. (1967a, 1967b, 1967c, 1968).

EXTENT AND PHYSICAL FEATURES

The Blue Cut fault (Pruss and others, 1959), is named for the Blue Cut, a straight east-west canyon eroded along the fault zone where it crosses the Little San Bernardino Mountains (fig. 1). At its western end, the fault curves slightly and merges with the northwest-trending Dillon fault. East of the Blue Cut, the fault zone is buried under the alluvium of Pleasant Valley, but reappears in El Dorado Canyon in the Hexie Mountains. East of El Dorado Canyon, the position of the Blue Cut fault becomes less certain.

The only good exposures of the fault zone are in and west of the Blue Cut. Here the fault zone is several hundred feet wide and contains interbranching breaks, as well as breaks which splay northwestward (not shown in figure 1 because of the scale of the map). Individual fault surfaces appear to be almost vertical in the Blue Cut, although to the west, steep northward dips occur. In the Blue Cut, gouge zones a few tens of feet thick border the more continuous faults. The two main rock types (foliated quartz monzonite and granodiorite) show differing types of deformation within these gouge zones. The quartz monzonite and associated aplites and pegmatites have been pulverized to produce a loose mixture of very fine white powder and small angular fragments. The granodiorite is more sheared than pulverized, and occasional slickensides can be found.

DISPLACEMENT IN THE LITTLE SAN BERNARDINO AND HEXIE MOUNTAINS

Figure 2 shows the structure and lithic units of the north and south walls of the Blue Cut fault west of Pinto Basin (between points *A* and *B* in fig. 1). The fault surface in figure 2 is assumed to be a vertical plane. Pairs of circled numbers (1 and 1′, 2 and 2′, and so forth) on figure 2 identify corresponding traces formed by the intersection of the segments of an offset geologic surface with the fault surface. Subsurface interpretations have been made by extrapolating surficial orientations of traces at depth (their actual orientations may differ markedly). Corresponding traces in the two walls are nearly parallel, at least at the surface, indicating a lack of significant rotational fault slip. Figure 2 also shows the numbered pairs of offset traces transposed so that the traces in the south wall all intersect at a point. If the two blocks of the fault had behaved rigidly while sliding past one another, the traces in the north wall should intersect at a second point in the diagram of figure 2, and the position of these two points would determine the orientation and magnitude of relative slip along this segment of the fault. The traces in the north wall,

however, intersect within a small area rather than at a point, which suggests that the two blocks did not behave in this ideal manner. Of course, the uncertain orientation of the traces at depth also affects the size of the area of intersections.

Along this segment of the fault, then, the north block slid westward and slightly upward (the average slip line plunges 7°E. in fig. 2 diagram) relative to the south block, and the magnitude of displacement was about 3.7 miles.

WEST END OF THE FAULT

The Blue Cut fault merges to the west with the Dillion fault—a northwest-trending, steeply northeast-dipping fault. Little is known about the time, direction, or magnitude of displacement along the Dillon fault. It dies out at both ends, although one branch terminates at the San Andreas fault at the northwest end. The trace is about 36 miles long, and the Blue Cut fault joins it near the middle. At the northwest end, local reverse slip on the west branch of the Dillon fault has carried gneiss southward over Tertiary fanglomerate (Dibblee, 1967b). This meager evidence suggests that the net displacement on the Dillon fault has not been great—probably amounting to several thousands of feet rather than many miles.

The question is how these two faults have interacted. No offset extension of the Blue Cut fault is found farther west, although exposures are adequate and the terrane has been examined by several geologists. The most reasonable interpretation is that displacements were translated from one fault to the other at their juncture. In order for this to happen, the slip direction along both faults near their juncture must nearly parallel the line of intersection. From the assumed orientations of the two faults (the Dillon fault striking N. 60° W. and dipping 55° NE., the Blue Cut fault striking due west and dipping 90°), the slip direction should trend about due east and plunge 35°. This would require that the movement along the Dillon fault have components of reverse slip and left slip. About 5 miles farther east on the Blue Cut fault, the slip vector apparently plunges only about 7°E. (fig. 2). Such a change in plunge requires a considerable rotation of the north block along the westernmost 5 miles of the fault, and, if this interpretation is correct, the rotation should be found with more detailed mapping.

As the north block of the Blue Cut fault was shoved upward along the Dillon fault, increased horizontal compression may have been partly relieved by east-west shortening in the westernmost part of the block. This could explain why the strike slip measured between traces 5 and 5′ is less than that measured between the traces farther east, and also why the width of the foliated quartz monzonite measured along the fault trace is about 1½ miles less in the north wall than in the south wall (fig. 2). This shortening could easily have been accomplished by small displacements along the numerous shear zones in the north block which more or less parallel the Dillon fault.

EAST END OF THE FAULT

The Blue Cut fault zone extends under Pleasant Valley and through El Dorado Canyon (fig. 1); it may be represented by the Quaternary fault scarps that bound the Hexie Mountains east-southeast of El Dorado Canyon. This branch seems to die out about 10 miles east-southeast of El Dorado Canyon.

Two pieces of evidence suggest that another branch—and probably the main one—extends eastward under Pinto Basin from El Dorado Canyon: (1) A northeast-trending pendant of metasedimentary rocks (fig. 1) appears to be offset at least 3.5 miles left laterally from the central Pinto Mountains to the Eagle Mountains. (2) A west-trending fault bounds low dune-draped hills of late Cenozoic lacustrine beds in the western Pinto Basin and lies approximately on the eastward projected strike of the Blue Cut fault. If a continuation of the Blue Cut fault eastward under Pinto Basin exists, the fault has not moved as recently as the zone of faults which trends east-southeast from El Dorado Canyon, because there are no older alluvial breaks trending due east from this canyon.

The Blue Cut fault probably underlies the western part of Pinto Basin, but it definitely does not cut through the Coxcomb Mountains to the east. At least four hypotheses can explain the eastern termination: (1) The fault dies out under the alluvium of the eastern Pinto Basin (this would mean that 3 to 4 miles of strike slip diminished to zero within 12 miles or less). (2) The fault terminates against the Sheep Hole fault and displacements have been transferred between the two faults, perhaps in a manner similar to that of the Dillon-Blue Cut fault intersection. (3) The fault went through the site of the present Coxcomb Mountains, but prior to emplacement of the granodiorite and uplift of the Coxcomb Mountains (as yet, no extension of this fault has been mapped in the adjacent ranges to the east). (4) The fault is older than the Sheep Hole fault and has been offset by it, perhaps right laterally.

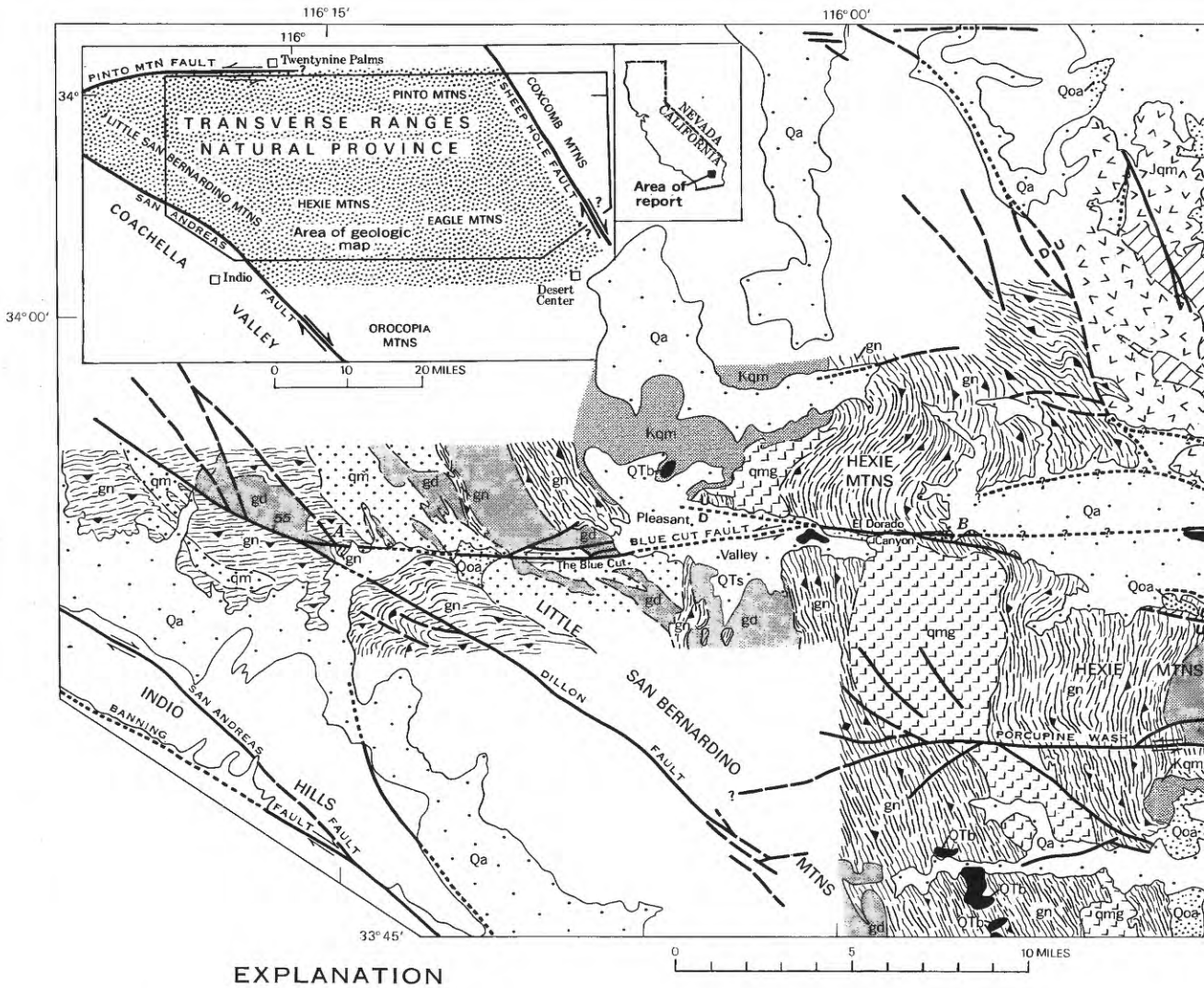

EXPLANATION

SEDIMENTARY AND VOLCANIC ROCKS

Qa — Alluvium

Qoa — Older alluvium, dissected

QUATERNARY

QTb, QTs, QTbs — Volcanic and sedimentary rocks

QTb, *olivine basalt flows (+1 plug)*

QTs, *sedimentary rocks. Includes lacustrine beds*

QTbs, *interbedded flows and sedimentary rocks*

TERTIARY OR QUATERNARY

INTRUSIVE ROCKS

Kqm — Quartz monzonite

CRETACEOUS

KJgd+ — Granodiorite

JURASSIC OR CRETACEOUS

Jqm — Porphyritic quartz monzonite

JURASSIC

qm — Foliated quartz monzonite

gd — Granodiorite

Age unknown

FIGURE 1.—Generalized geologic map of part of th
showing opposing fault-plan

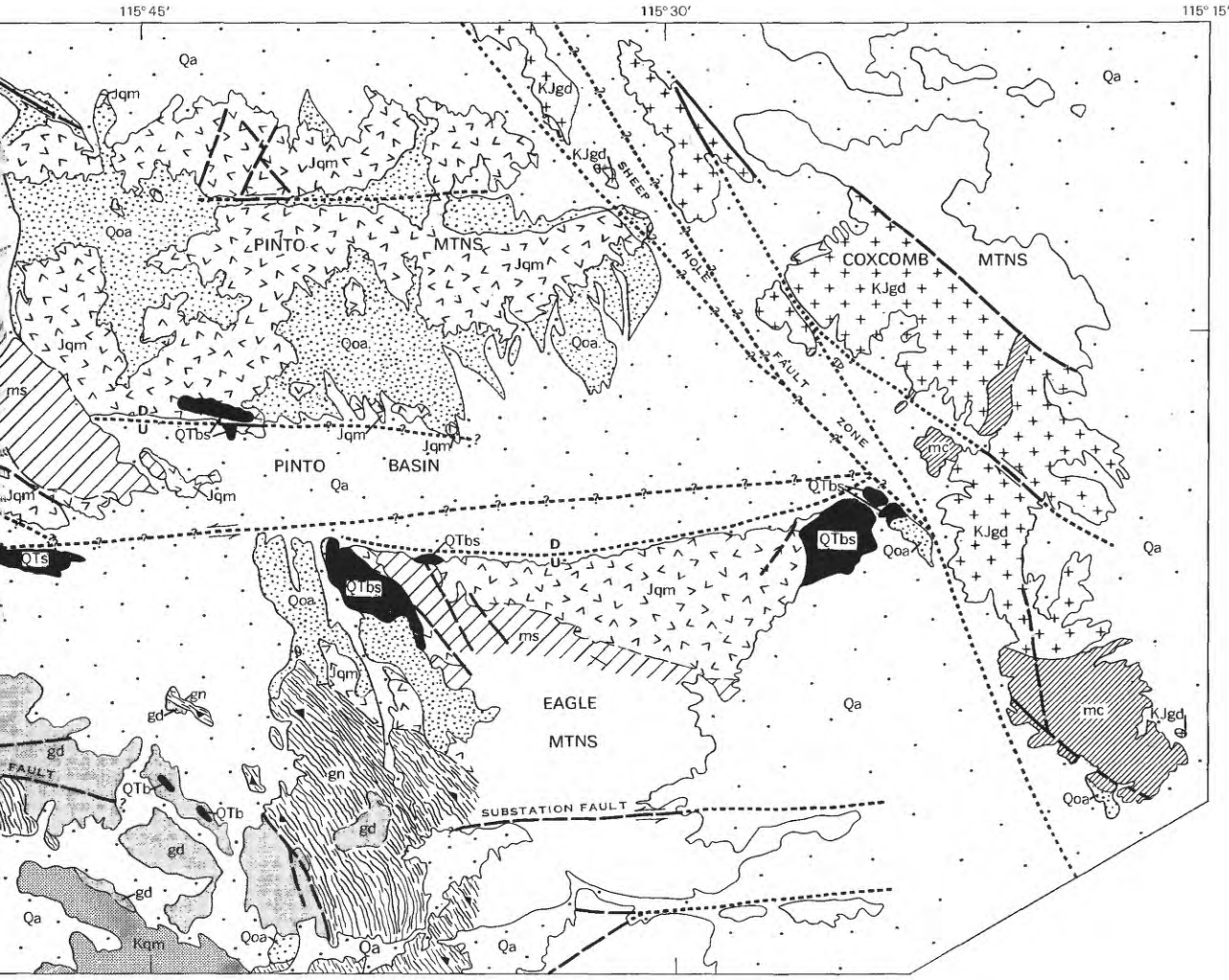

METAMORPHIC ROCKS

mc — McCoy Mountains Formation of Miller (1944)
Metavolcanic and metasedimentary rocks

ms — Metasedimentary rocks, mainly quartzite and marble

PALEOZOIC OR MESOZOIC

qmg — Quartz monzonite gneiss and associated metahornfels

gn — Gneiss, migmatite and minor quartzite, irregular broken lines show general strike of foliation

PRECAMBRIAN (?)

Unmapped bedrock

Contact
Dashed where approximate

55 U D
Fault, showing dip
Dashed where approximately located; queried where doubtful; dotted where concealed. Arrows and letters show relative displacement

eastern Transverse Ranges. See figure 2 for cross sections
surfaces between points *A* and *B*.

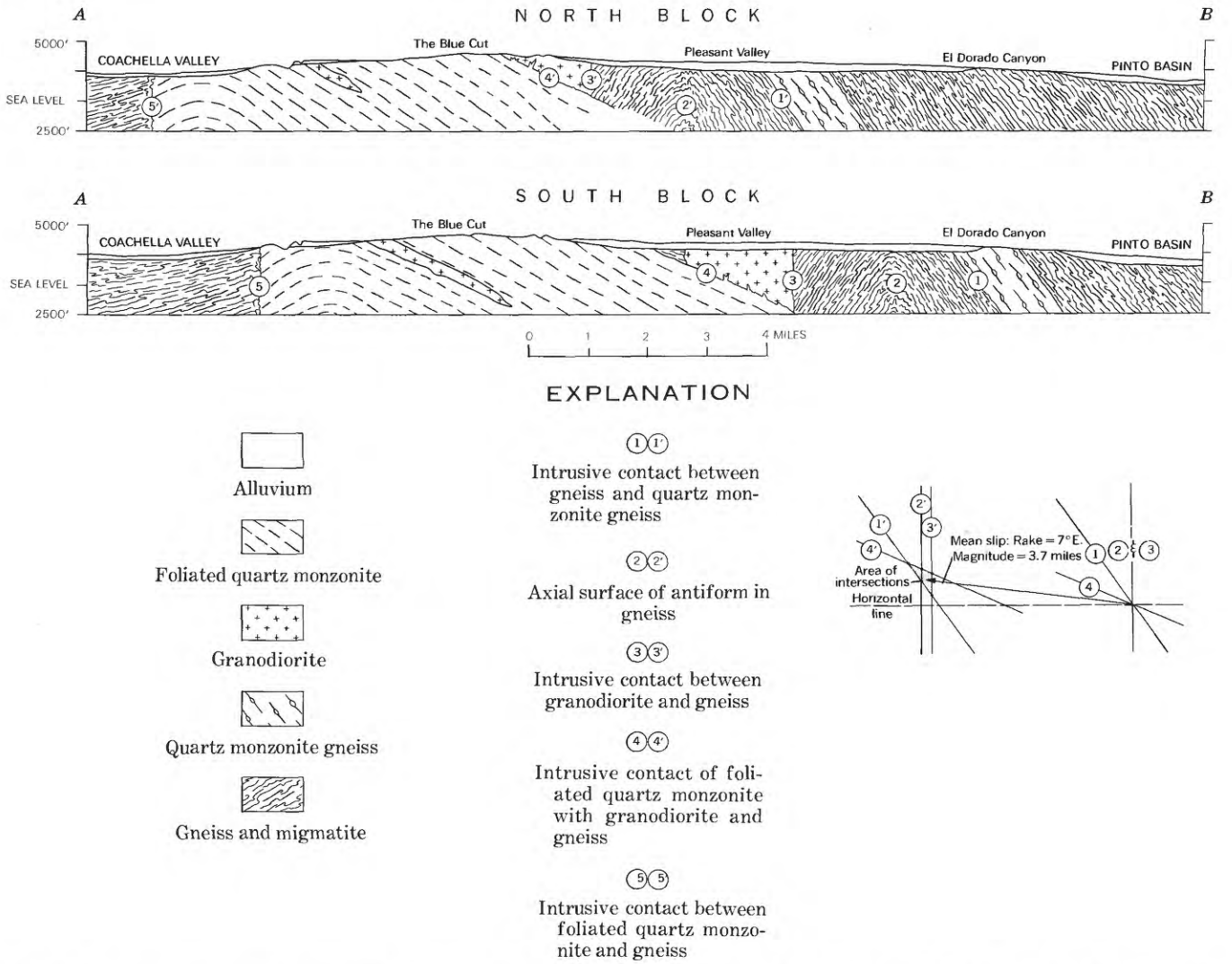

FIGURE 2.—Cross sections along western half of Blue Cut fault (between points *A* and *B* in fig. 1), and diagram of slip orientation and magnitude. Pairs of traces shifted so that all traces in south block intersect at a point. Distance and direction from this point to area where traces intersect in north block gives slip. Sections and diagrams are drawn at the same scale.

From what is now known, the fourth explanation seems most likely. The Sheep Hole fault forms a major lithologic boundary. The belt of quartzite and marble in the Eagle and Pinto Mountains trends eastward toward the southern Coxcomb Mountains, but does not occur there or anywhere else to the east (unless it is the equivalent of the post-Cambrian Maria Formation of Miller, 1944). The McCoy Mountains Formation of Miller (1944), a Paleozoic or Mesozoic unit containing metamorphosed clastic and volcanic rocks, is widespread to the east, but absent to the west. Faults which probably belong to the Sheep Hole fault zone cut the Coxcomb Mountains, and one of the faults offsets a steeply dipping septum of metasediments in a right-lateral sense by 0.8 mile. If we assume the displacement on the Sheep Hole fault to be mainly right lateral, and if the fourth explanation is correct, the eastern extension of the Blue Cut fault would exist farther south. Since the Blue Cut fault does not cut through the Coxcomb Mountains, it must have been offset at least 11 miles right laterally. There are some east-west faults farther southeast at the south tip of the Palen Mountains (see Jennings, 1967), but until more details are known, these bits of evidence are merely suggestive.

MOVEMENT HISTORY

The offsets described above must represent the net slip along the Blue Cut fault. This is so because traces formed in late Mesozoic time (the contact between metasedimentary rocks and Jurassic quartz monzonite,

and quite possibly the pair 4 and 4′ in fig. 2) are offset roughly the same amount as traces which probably existed during the Precambrian (the pair 1 and 1′ in fig. 2). The initial movement along the Blue Cut fault must have been later than the emplacement of the Jurassic quartz monzonite and earlier than the deposition of the older alluvium.

At only five places along the fault have late Cenozoic deposits been disturbed: (1) on an old alluvial fan east of the Blue Cut, stream channels bend in crossing small fault scarplets, but in no consistent direction; (2) hillocks at the east end of Pleasant Valley are underlain by Tertiary or Quaternary sedimentary rocks tilted as much as 90° and striking east-west; (3) just northeast of these hillocks, a ridge of fanglomerate has been formed by relative uplift of the south block of the fault; (4) the faults along the boundary between Pinto Basin and the Hexie Mountains are possibly a part of the Blue Cut fault zone; they cut older alluvium, but stream channels in the older alluvium are deflected in no systematic sense; (5) a cluster of low hills in western Pinto Basin outlines a north-northwest-trending anticline in Tertiary or Quaternary sedimentary rocks. This anticline could be considered a drag fold formed by left slip, but in the absence of any stronger evidence, it can only be said that there was faulting of unknown direction and amount after deposition of the Tertiary or Quaternary rocks, and of unknown direction and minor amount after deposition of the older alluvium.

OTHER WEST-TRENDING FAULTS

There is evidence for left slip on several other west-trending faults in the eastern Transverse Ranges. The Pinto Mountain fault, which forms the boundary between the eastern Transverse Ranges and the Mojave Desert to the north (fig. 1), has had a maximum of about 10 miles of left slip since the Late Cretaceous (Dibblee, 1967a). Along the Porcupine Wash fault in the central Hexie Mountains, a near-vertical contact between gneiss and granodiorite has been offset left laterally by 1.8 miles. Due east of here, in the central Eagle Mountains, the Substation fault has offset a swarm of Late Cretaceous or Tertiary dikes by about 2 miles left laterally. An unnamed fault in the eastern Pinto Mountains appears to have a 1-mile left-lateral offset, as measured on an albite-rich phase of the porphyritic quartz monzonite. Other faults and lineaments in this region are known, but more work is needed to determine their displacements.

REFERENCES

Dibblee, T. W., Jr., 1967a, Evidence of major lateral displacement on the Pinto Mountain fault, southeastern California [abs.]: Geol. Soc. America, Cordilleran Sec., 63d Ann. Mtg., Santa Barbara, Calif., 1967, Program, p. 32.

——— 1967b, Geologic map of the Morongo Valley quadrangle, San Bernardino and Riverside Counties, Calif.: U.S. Geol. Survey Misc. Geol. Inv. Map I–517.

——— 1967c, Geologic map of the Joshua Tree quadrangle, San Bernardino and Riverside Counties, California: U.S. Geol. Survey Misc. Geol. Inv. Map I–516.

——— 1968, Geologic map of the Twentynine Palms quadrangle, San Bernardino and Riverside Counties, California: U.S. Geol. Survey Misc. Geol. Inv. Map I–561.

Hope, R. A., 1966, Geology and structural setting of the eastern Transverse Ranges, southern California: Univ. California, Los Angeles, Ph.D. thesis, 201 p.

Jahns, R. H., 1954, Investigations and problems of southern California geology, [pt.] 1 *in* chap. 1 *of* Jahns, R. H., ed., Geology of southern California: California Div. Mines Bull. 170, p. 5–29.

Jennings, C. W., 1967, Geologic map of California, Olaf P. Jenkins, Salton Sea sheet: California Div. Mines and Geology, scale 1:250,000.

Miller, W. J., 1944, Geology of Palm Springs-Blythe strip, Riverside County, California: California Jour. Mines and Geology, v. 40, no. 1.

Pruss, D. E., Olcott, G. W., and Oesterling, W. A., 1959, Areal geology of a portion of the Little San Bernardino Mountains, Riverside and San Bernardino Counties, California [abs.]: Geol. Soc. America Bull., v. 70, no. 12, p. 1741.

BASIN CREEK UPLIFT AND HEART LAKE CONGLOMERATE, SOUTHERN YELLOWSTONE NATIONAL PARK, WYOMING

By J. D. LOVE and W. R. KEEFER,
Laramie, Wyo., Denver, Colo.

Work done in cooperation with the National Aeronautics and Space Administration

Abstract.—A major, but still largely buried structural feature, the Basin Creek uplift, and a previously undescribed sedimentary sequence, the Heart Lake Conglomerate (a new name in this report), provide new data for interpreting the geologic history of southern Yellowstone National Park. The uplift was initially folded at or near the close of Cretaceous time; in late Cenozoic time a major part of it, at least, was rapidly elevated. This later movement resulted in deposition of the Heart Lake Conglomerate, 70–330 feet thick, composed chiefly of Madison Limestone (Mississippian) fragments in a talc- and chlorite-rich matrix. The conglomerate may be of Pliocene or Pleistocene age.

A structural feature, the Basin Creek uplift, and a sedimentary sequence, the Heart Lake Conglomerate, both in southern Yellowstone National Park, have not previously been described in detail. They provide data necessary to reconstruct the structural and depositional history and one episode of the volcanic history of southern Yellowstone National Park.

BASIN CREEK UPLIFT

An arcuate exposure of Mesozoic and Paleozoic rocks, partly buried by rhyolitic flows and tuffs, has long been known in southern Yellowstone National Park (Hague, 1896; 1904). This feature was remapped between 1945 and 1949, and rocks that Hague had named the Sheridan Quartzite and had assigned to the Precambrian were found to be the Muddy Sandstone Member of the Thermopolis Shale and the sandstones of the Cloverly Formation that had been locally silicified (Love and others, 1955).

As a result of these studies and others made by Keefer in 1966–67 during the current U.S. Geological Survey investigation of Yellowstone National Park (Campbell, 1969), the arcuate exposure of pre-Tertiary rocks was recognized as the southeast flank of a major Laramide uplift that had been extensively modified by additional movements in late Cenozoic time. The name "Basin Creek uplift" is here proposed for this structural feature. Its exposed parts extend from Yellowstone Lake southward across the southern boundary of Yellowstone National Park (figs. 1, 2). Mount Sheridan, the Red Mountains, Flat Mountain, and areas to the north and west are capped by younger

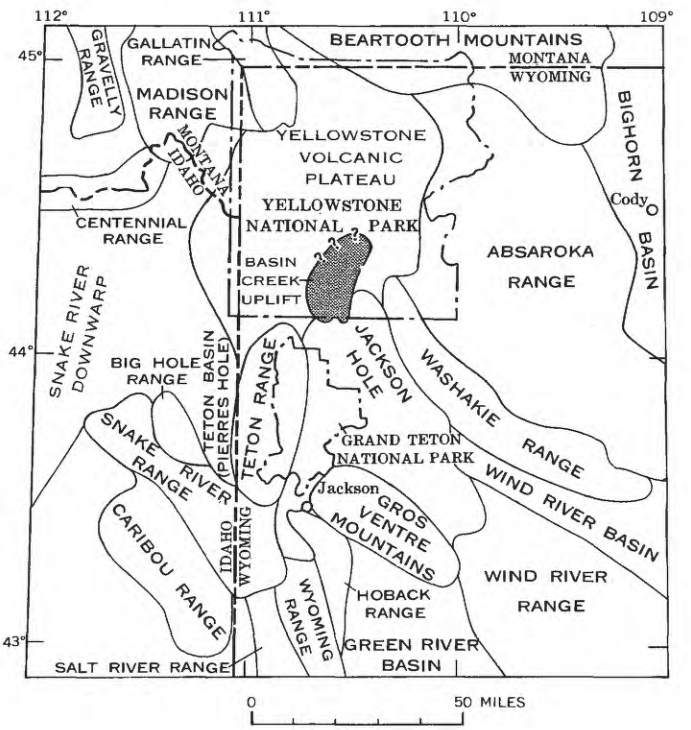

FIGURE 1.—Map showing relation of Basin Creek uplift (patterned) to surrounding uplifts and downwarps.

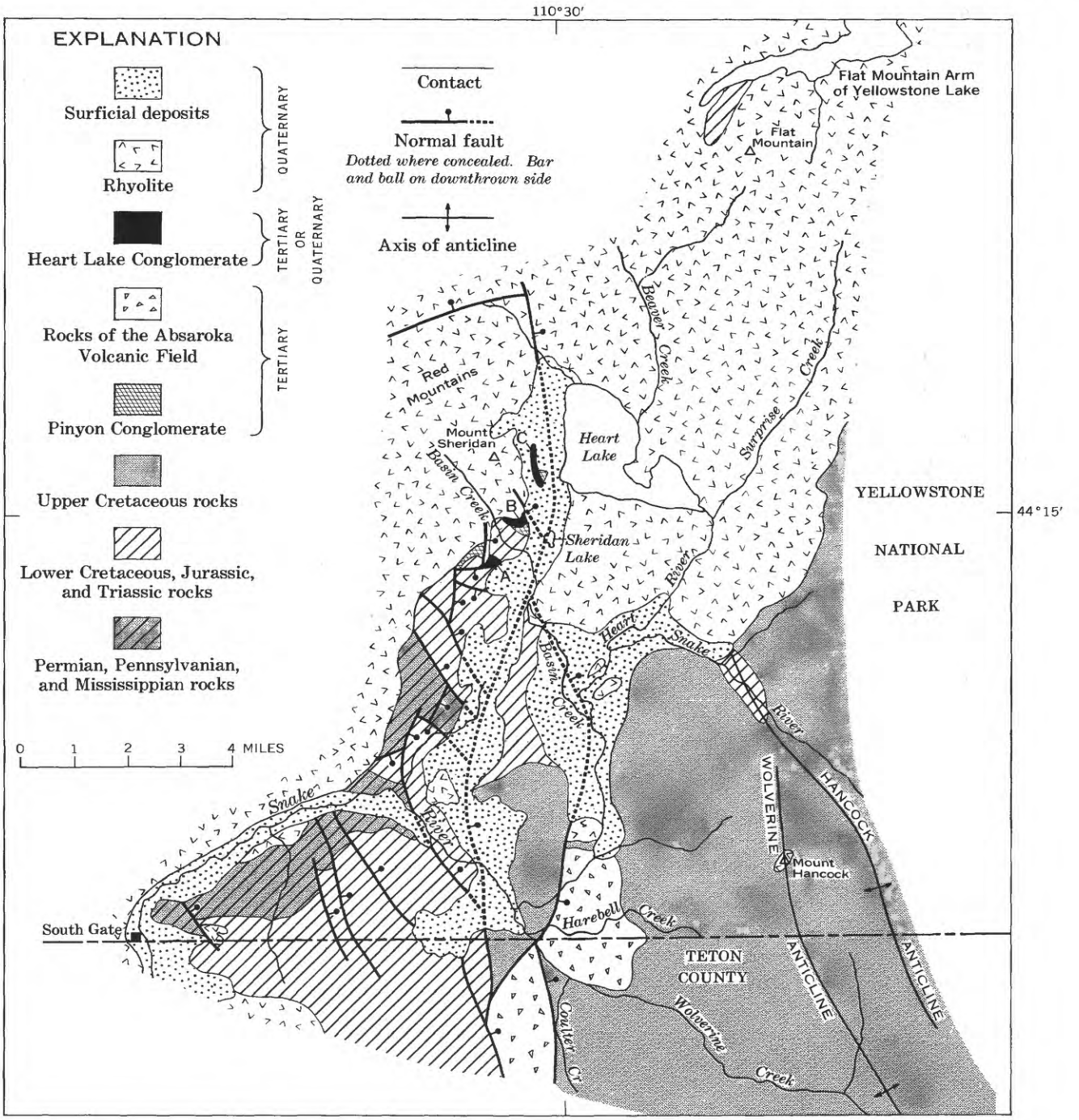

FIGURE 2.—Generalized geologic map of part of southern Yellowstone National Park and the area to the south. Localities *A*, *B*, and *C* are outcrops of Heart Lake Conglomerate referred to in text.

volcanic rocks that conceal the northern and western sides of the uplift. Basin Creek has cut a canyon across the southeast margin of the uplift south of Mount Sheridan.

The major vertical movement of the Basin Creek uplift occurred during Laramide deformation, probably at or near the end of Cretaceous time, and its amount can be estimated. The Harebell Formation (latest Cretaceous) in northern Jackson Hole (fig. 1) is about 10,000 feet thick; its upper part contains several zones of marine or brackish-water fossils (mollusks identified by E. G. Kauffman, written commun., 1967; hystrichomorphs and associated Cretaceous pollen identified by R. H. Tschudy and E. B. Leopold, written

359-403 O—69——9

commun., 1966–68). Deposition, therefore, took place at or near sea level in a subsiding basin. Inasmuch as there is no evidence that the uplift contributed debris to the Harebell Formation, the initial upwarping apparently followed deposition of the Harebell. When uplift of the Basin Creek area began, the base of the Harebell was more than 10,000 feet below sea level in the downwarp directly to the southeast. By the beginning of deposition of the Pinyon Conglomerate (Paleocene), however, all the Harebell and 6,000 feet of the older Mesozoic rocks had been eroded from the crest of the uplift. The Pinyon Conglomerate was then deposited across rocks at least as old as Jurassic along the east flank of the uplift (figs. 2, 3, 4), as well as across all of the Harebell Formation in the adjacent downwarp to the southeast. These relations suggest that the vertical movement in the southeastern part of the Basin Creek uplift during the Laramide orogeny was 12,000–15,000 feet.

At the beginning of the Pinyon Conglomerate deposition the uplift probably was a simple north- or north-northwest-trending elliptical fold, which had a moderately flat top and unfaulted south and east flanks. The nature of the west flank is not known; however, nearby major upwarps, such as the Washakie Range (fig. 1), and lesser folds, such as the Bailey (6 miles south) and Spread Creek (20 miles southeast) anticlines, were thrust westward or southwestward (Love, 1956a). Similar thrusting may have taken place along the

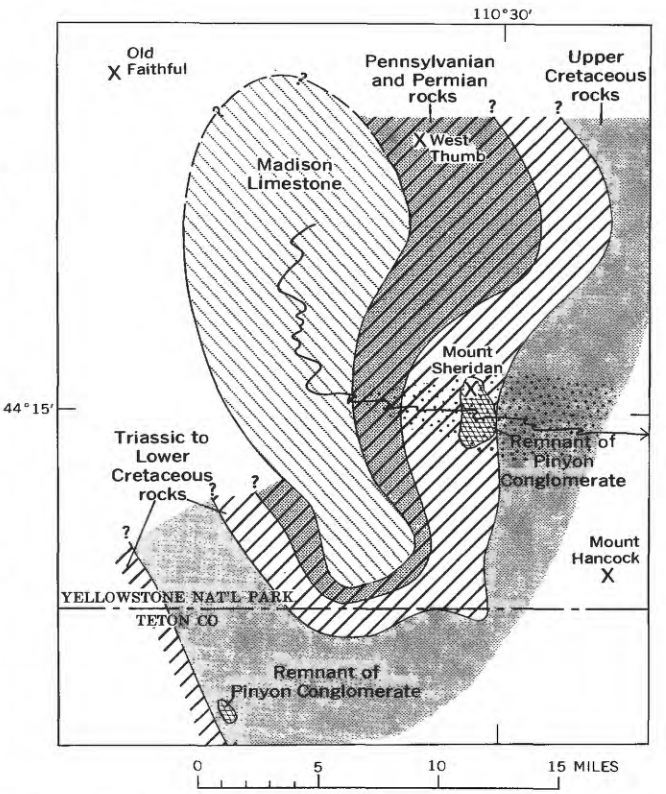

FIGURE 3.—Reconstructed geologic map of Basin Creek uplift at time of deposition of Heart Lake Conglomerate, before caldera formation to the north. Stippled area indicates hypothetical location of Heart Lake Conglomerate.

FIGURE 4.—Contact between highly silicified Pinyon Conglomerate (above) and Cloverly and Morrison(?) Formations undivided (below), indicated by line; man in center shows scale; locality B, Mount Sheridan measured section.

west margin of the Basin Creek uplift. A syncline with an amplitude of 6,000 feet developed at the same time as the Basin Creek uplift, between the uplift and the ancestral Teton Range to the southwest (fig. 1).

The original thickness of the Pinyon Conglomerate is not known, but one remnant on the southeast face of Mount Sheridan is 450 feet thick. The Basin Creek uplift appears to have been relatively quiescent during deposition of the conglomerate, as well as throughout the remainder of Tertiary time, for the preserved remnants of the Pinyon have not been extensively deformed.

During some part of late Cenozoic time, an area including at least the southern part of the Basin Creek uplift was rejuvenated. The movement triggered deposition of the Heart Lake Conglomerate and may also have been related to the initial stages of volcanism that resulted in vast outpourings of rhyolite which blanketed this and other areas to the north, west, and south. The extensive silicification of sandstones, siltstones, and shales in Lower Cretaceous and Jurassic rocks, as well as the alteration of the Pinyon Conglomerate (fig. 5) and clasts within the Heart Lake Conglomerate, may have been in part related to this volcanism. In many places, silicification of the Pinyon progressed to the point where its conglomeratic nature is now barely recognizable.

FIGURE 5.—Pinyon Conglomerate at locality B, Mount Sheridan measured section. Entire rock has been so completely impregnated with secondary silica that it is hardly recognizable as a conglomerate. One quartzite boulder is outlined below knife at upper right.

HEART LAKE CONGLOMERATE

A distinctive conglomerate which overlaps Mesozoic rocks and the Pinyon Conglomerate and consists largely of Paleozoic rock fragments and rhyolitic debris was found in the Mount Sheridan area by Love in 1949. Because the overlying rhyolites were then considered to be of Pliocene age, this conglomerate was called "Pliocene and Miocene" on the geologic map of Wyoming (Love and others, 1955).

The name Heart Lake Conglomerate is here proposed for this unique sequence; the Heart Lake overlies the Pinyon Conglomerate and underlies the main mass of rhyolite welded tuff on the steep east and south slopes of Mount Sheridan, west and southwest of Heart Lake. The conglomerate is known from three exposures (locs. *A*, *B*, and *C*, fig. 2), at each of which a section has been measured and sampled. At locality A, the conglomerate is either 70 or 125 feet thick, depending on correlation of beds; at B, about 330 feet thick; and at C, about 110 feet thick. Locality B is designated the type section (fig. 6 and stratigraphic section given below) at that locality the strata are exposed on a steep south-facing headwall at the base of the great bare precipitous slope that rises 1,700 feet to the top of Mount Sheridan. No opportunity was available to trench the type section or to describe it in detail; it is therefore subdivided into gross units with only approximate thicknesses. The rocks strike about north and dip about 15°W.

Type section of Heart Lake Conglomerate on east and south slopes of Mount Sheridan (loc. B, fig. 2)

Unit and description	*Thickness (feet)*
Rhyolitic sequence (Pleistocene):	
10. Rhyolite bedded tuff, altered, chalky-white; surface weathers to bright red, orange, and yellow; stands in conspicuous ragged sheer cliff; rock composed of clear crystals of glassy quartz and feldspar in spongy soft matrix containing chalky altered pseudomorphs of plagioclase crystals; many vugs, some with quartz crystals; unit dips west at about same angle as underlying rocks; rests on an irregular surface at top of underlying unit	200±
Sharp change in lithology; exposures too limited to show whether an unconformity is present.	
Heart Lake Conglomerate (Pleistocene or Pliocene):	
9. Conglomerate, yellowish-gray; composed of moderately small fragments of volcanic rock, chiefly rhyolite, and rounded pebbles, cobbles, and boulders of limestone and quartzite; unit is poorly exposed on slope at angle of repose and was not examined in detail	40
8. Conglomerate, yellowish-gray; lithified and forms hard cliff; chiefly rounded fragments of limestone, quartzite, and volcanic rocks, largely rhyolite; at top is 3 feet of bedded tuffaceous sandstone	20

FIGURE 6.—View north from locality A across Basin Creek toward the type section (locality B) of the Heart Lake Conglomerate. Indicated are the main mass of rhyolite welded tuff (Qr) on Mount Sheridan, the Heart Lake Conglomerate (QTh), marker bed (4) which is unit 4 in measured section, Pinyon Conglomerate (Tp), Cloverly and Morrison(?) Formations (KJm), dike of rhyolite mixed with Pinyon Conglomerate (Qrd), and landslide debris (Qls).

Type section of Heart Lake Conglomerate on east and south slopes of Mount Sheridan (loc. B, fig. 2)—Continued

Unit and description	Thickness (feet)
7. Conglomerate, yellowish-gray, soft; forms slope; may contain some claystone beds; coarse debris composed of rounded fragments of limestone, quartzite, and rhyolite(?) in a tuffaceous sandstone and probably claystone matrix	20
6. Conglomerate, yellowish-gray; forms hard ledge; roundstones are chiefly quartzite and are rarely more than 3 inches in diameter	20
5. Claystone, gray, bentonitic; soft, in lower part; grades up to yellowish-gray conglomerate which contains highly fractured roundstones that are smaller than those in overlying unit	20
4. Conglomerate and tuffaceous sandstone, brown, hard, bedded, noncalcareous; forms conspicuous ledge that extends across outcrop area; roundstones are of quartzite and Paleozoic rocks, smaller than in overlying units; many black rounded chert pebbles, probably derived from Madison Limestone (Mississippian); many gray waxy soft talc pebbles and gray clayey matrix	8
3. Conglomerate, mouse-gray, soft, poorly sorted; forms slope at angle of repose; fresh exposures in torrent gullies show that unit is a jumble of large and small fragments dumped together and tightly cemented with limy cement; about 75 percent is Paleozoic limestone (chiefly Madison) and remainder is Paleozoic quartzite and sandstone, Pinyon quartzite, and rhyolite; quartzite is conspicuous as lag gravel on slopes but is a minor lithology in fresh exposures; highly rounded boulders of fossiliferous Madison Limestone 1–2 feet in diameter are common but average size is 4–6 inches; numerous boulders of highly altered rhyolite(?) that disintegrate on outcrop; some highly rounded black chert pebbles, probably derived from the Madison Limestone; matrix is white, limy, with abundant white to pale-green waxy claystone; increasingly tuffaceous in upper part, with quartz crystals 30 feet below top; many pale-green to white rounded pebbles of waxy noncalcareous nondecrepitating talc; talc pebbles are so abundant 50 feet below the top that	

Type section of Heart Lake Conglomerate on east and south slopes of Mount Sheridan (loc. B, fig. 2)—Continued

Unit and description	Thickness (feet)
they make up nearly half the rock and give it a slippery feel	200±
Approximate total thickness of Heart Lake Conglomerate	330
Angular unconformity. Beds above dip 15° W., and those below 20° W. Actual trace of unconformity is covered or distorted by intrusion of rhyolite dike.	
Pinyon Conglomerate (Paleocene):	
2. Conglomerate; green and brown in lower part, rusty brown in upper part; hard, tightly cemented, highly silicified with secondary silica. Roundstones are chiefly quartzite boulders 8–15 inches in diameter; commonly gray, but some are black; others are tan and gray hard rounded boulders of sandstone; some are red and blue-green quartzite; many of the hardest boulders still have polish preserved; many are fractured and recemented; pressure scars are conspicuous; matrix is iron-rich coarse-grained sandstone; bedding planes poorly developed; entire sequence apparently is conglomerate	450±
Approximate total thickness of Pinyon Conglomerate	450
Angular unconformity. Beds above strike about north, dip 20° W.; those below strike N. 45° W., dip 15° SW. The actual unconformity is visible on the east side of the spur that bounds the east margin of the headwall where the overlying section was measured (fig. 4).	
Cloverly and Morrison(?) Formations, undivided (Lower Cretaceous and Upper Jurassic):	
1. Quartzite, white, very fine grained, hard, well bedded	10
Base of measured section.	

The section at locality A is exposed on a steep to sheer south-facing bare outcrop on the high hill nearly half a mile southwest of the sharp bend in Basin Creek canyon and 6,500 feet west-southwest of the outlet of Sheridan Lake. Dips are probably less than 5°W., and the entire section is on a west-tilted downthrown fault block.

Measured section, locality A (fig. 2)

Unit and description	Thickness (feet)
Rhyolitic sequence (Pleistocene):	
5. Tuff, altered white, platy, extremely hard; conchoidally fractured in part, granular; some layers have graded bedding; others are finely laminated with as many as 100 alternating light gray and black laminae per inch; some layers are black because of abundant finely comminuted carbonaceous material; samples collected for pollen and diatom study (no diatoms; pollen listed, p. D129); unit forms steep slope littered with white rock chips at top of sheer ragged rusty brown and white cliff	20

Measured section, locality A (fig. 2)—Continued

Unit and description	Thickness (feet)
4. Rhyolite tuff, white to rusty brown; forms ragged cliff; is soft, spongy, layered, with bedding planes conspicuous in lower part; basal beds appear to merge with much softer underlying unit	135±
Approximate total thickness of rhyolitic sequence	155
Heart Lake(?) Conglomerate (Pleistocene or Pliocene):	
3. Pumice breccia and claystone; upper 40 feet is white to gray pumice breccia composed of angular soft white and gray chunks of highly altered pumice and rhyolite in a soft chalky clayey matrix; many quartz bipyramids; much of rock looks as if it had been intensely altered by hydrothermal action; lower 15 feet is colloidally fine-grained soft plastic claystone with many pumice chunks and quartz bipyramids; white and black laminations, some very closely spaced. Pyrite concentrated in black laminae and in irregular finely crystalline masses; has sulfur odor. Sporadic pebbles and cobbles of quartzite, chert, limestone; black obsidian welded tuff, and other dense volcanic rocks have surficial sheen; some are as much as 6 inches in diameter, but none this large was seen above middle of unit	55
Heart Lake Conglomerate (Pleistocene or Pliocene):	
2. Conglomerate; rusty-brown and iron stained in upper 10 feet, chalky bluish white in remainder; coarser grained near middle. Roundstones are nearly all of Madison Limestone; some are 2 feet in diameter, 1-foot size is common, and average is about 4 inches; most are rounded to subrounded. Various Madison lithologies represented, from chalky white dolomite to dark-gray crinoidal limestone; corals are common; no Darby Formation (Devonian) roundstones noted, but one boulder is of mottled dolomite that might be Bighorn Dolomite (Ordovician); no Cambrian, Precambrian, or red Chugwater Formation (Triassic) observed; Pinyon type quartzite roundstones are present but sparse; some black obsidian welded tuff, hard dense volcanic rocks (chiefly rhyolite), Paleozoic chert, and Pinyon quartzite roundstones commonly have a conspicuous sheen; abundant rounded pebbles of talc and some chloritic claystone; slippery clayey matrix is probably predominantly talc and chlorite	70±
Angular unconformity. No evidence of Pinyon Conglomerate here but a few feet of it is present at this horizon several hundred yards to the northwest.	
Sundance Formation (Upper Jurassic):	
1. Shale, blue-gray, hard, chippy, interbedded with soft plastic gray claystone and mudstone	20+
Base of section.	

Corals and other fossils are common in many of the Madison Limestone boulders. One from unit 2 in the measured section at locality A yielded *Vesiculophyllum* sp. (identified by W. J. Sando, written commun., 1968). This form is of Mississippian age and is typical of the Madison Limestone.

The section at locality C is similar to the sections at localities A and B. Especially notable at locality C are the abundance of waxy gray talc and chloritic claystone pebbles and the presence of a clayey matrix in the limestone conglomerate. The conglomerate is about 75 feet thick. The overlying siltstones and claystones here are like those in the upper part of the type section at locality B but are much thinner. The underlying Pinyon Conglomerate is at least 300 feet thick, with the base not exposed, and is highly silicified and brecciated.

The most significant features of the Heart Lake Conglomerate are: (1) the dominance of rock fragments from sand size to boulders 3 feet in diameter (fig. 7), most of which were derived from the Mississippian Madison Limestone; (2) the abundance of waxy talc and chloritic claystone fragments in the conglomerate; and (3) the presence of rhyolitic debris, which is especially abundant in the middle and upper parts.

FIGURE 7.—Detail of Heart Lake Conglomerate at locality A. south Basin Creek measured section. Nearly all rock fragments are Madison Limestone. Matrix contains abundant waxy very fine grained gray claystone.

Spectrographic analyses of two samples of claystone in unit 3 at locality A show no unusually high amounts of trace elements, and are relatively low in magnesium, calcium, manganese, and sodium.

Samples of the pebbles suspected of being talc gave an X-ray diffractometer pattern of talc and calcite (Theodore Botinelly, written commun., 1968). Botinelly observed pale-green inclusions, possibly pseudomorphs after feldspar, in some talc pebbles. An X-ray diffraction pattern of the green-colored material indicates that it is chlorite.

It has been noted that the Jurassic and Cretaceous shales and sandstones, as well as the Pinyon Conglomerate, are highly silicified at locality B, whereas the limestones appear superficially to be little altered. Marine fossils in the Jurassic limestones are well preserved. In the Heart Lake Conglomerate, limestone roundstones containing Mississippian corals likewise show little conspicuous alteration. Nevertheless, representative samples of limestone from the lower part of the Sundance Formation of Jurassic age in unit 1 and a boulder of Madison Limestone from unit 6 of the Heart Lake Conglomerate in the measured section at locality B were submitted for carbon and oxygen isotopic analysis. The results are as follows (Irving Friedman, written commun., 1967):

Sample	O^{18} per mil SMOW	C^{13} per mil PDB
Jurassic limestone	−8.4	+1.3
Madison Limestone boulder	−1.4	−0.3

The oxygen analyses are reported relative to Standard Mean Ocean Water (SMOW), a standard water whose isotopic composition is close to that of mean ocean water. The carbon analyses are given in terms of the PDB standard. PDB is a Cretaceous belemnite, *Belemnitella americana*, from the Peedee Formation of South Carolina (Craig, 1957, p. 135). Friedman's communication stated:

> The O^{18} analysis shows that both samples are altered isotopically, the first [Jurassic] more than the second [Madison]. A normal value for Madison limestone would be +20 to +25 per mil SMOW. The carbon values of both samples are in the marine limestone range.

Most occurrences of talc in the Rocky Mountain region are associated with Precambrian rock terranes. A Precambrian metamorphic source for the talc in the Heart Lake Conglomerate, however, is virtually precluded by the fact that, despite careful search, neither Precambrian crystalline rocks nor Cambrian rocks were found in the formation. The close association of the talc and chlorite with abundant fragments of post-Cambrian Paleozoic carbonate rocks, particularly Madison Limestone, suggests strongly that the talc and chlorite were derived from metamorphosed impure dolomites within these strata. (See discussion by Cooper, 1957, p. 582–588.) Thick beds of dolomite occur in the Bighorn Dolomite (Ordovician) and Darby Formation (Devonian), as well as in the Madison Limestone. Some of these dolomites could have been partially transformed to talc and chlorite by the low-grade metamorphism that affected the Paleocene, Lower Cretaceous, and Jurassic rocks underlying the Heart Lake Conglomerate in the Mount Sheridan area. If the late Cenozoic rise of the Basin Creek area was

related to rhyolitic intrusion, this magma could have been responsible for the metamorphism, but it would have had to occur before the debris of the Heart Lake Conglomerate was eroded from the core of the uplift.

The Heart Lake Conglomerate rests with angular unconformity on the Pinyon Conglomerate of Paleocene age at localities B (fig. 2) and C, and on the Sundance Formation of Late Jurassic age at locality A. No conclusive evidence of an unconformity was found at the top of the conglomerate, and the progressive increase in rhyolitic(?) debris in the upper part suggests the possibility that the Paleozoic source area was being covered with rhyolite tuff during the later stages of deposition of the Heart Lake strata.

No fossils were found in the Heart Lake Conglomerate. Farther south in Jackson Hole the first abundant rhyolitic debris occurs in Pliocene rocks (Love, 1956a). In the type locality of the Teewinot Formation, 6,000 feet thick and dated as middle Pliocene by vertebrate, invertebrate, and plant fossils, are several zones containing roundstones of black and gray obsidian as well as crystallized rhyolitic lavas and welded tuff and thick beds of vitric and crystal tuff (Love, 1956b). Obsidian clasts from a bed in the upper part of this section yielded a potassium-argon age of 9.2 million years (Evernden and others, 1964, p. 185–186).

No vent areas of a size adequate to supply the middle Pliocene rhyolitic debris are known in Jackson Hole, so it is inferred that the debris came from vents in Yellowstone National Park. The Heart Lake Conglomerate might, therefore, be equivalent to some part of the Teewinot Formation. On the other hand, if additional work should demonstrate that the conglomerate grades into the overlying rhyolitic sequence of possible Pleistocene age (R. L. Christiansen, written commun., 1968) on Mount Sheridan, then it, too, might be Pleistocene.

The white platy slightly carbonaceous tuff comprising unit 5 of the measured section overlying the Heart Lake Conglomerate at locality A yielded the following flora of post-Oligocene age (E. B. Leopold, written commun., 1968):

Compositae, cf. *Ambrosia*, 3 grains
Chenopodiaceae, 13 grains
Pinus, 15 grains
Compositae, *Artemisia*, 1 grain

This assemblage is of little help in precise age determination, but it does indicate that pollen is present and that more extensive collecting might be rewarding.

SUMMARY OF INTERPRETATIONS

Because a large part of the Basin Creek uplift is covered by Pleistocene rhyolitic rocks, its reconstruction and its geologic history are necessarily based in part on indirect evidence and inference. Two episodes of uplift occurred, the first in Laramide time and the second in late Cenozoic time. The Laramide uplift was probably elliptical—elongated in a north-northwest direction—and relatively flat topped, and was eroded to the Jurassic before the deposition of the Paleocene Pinyon Conglomerate. The late Cenozoic area of uplift is believed to be at least partly coincident with the Laramide area of uplift; such a pattern would be consistent with the pattern for the adjacent Teton Range. The later movement of the Basin Creek uplift could have been either a fault block uplift or a simple rejuvenation by folding of a large segment of the original structural feature.

Observations made in the limited outcrop areas at localities A, B, and C (fig. 2) provide data for at least a partial reconstruction of the Paleozoic core of the Basin Creek uplift at the time of deposition of the Heart Lake Conglomerate. The large size and lack of sorting of the rock fragments indicate rapid erosion and transport by powerful streams from a nearby source of high relief; imbrication of slabs in the conglomerate shows that the streams flowed from the west. If it is assumed that the 3,000 feet of strata between the Cloverly Formation and the Madison Limestone all dipped eastward off the uplift at about 10° (because of later movements, the strata now dip 15°–25°W.) at this time, large areas of the Madison could have been exposed to erosion as near as 4–5 miles west of the present exposures of the conglomerate (locs. *A*, *B*, and *C*, fig. 2). The postulated shape of the uplift at the time of late Cenozoic tectonism and deposition of the Heart Lake Conglomerate, as shown in figure 3, is based on the above interpretations, on estimates of the volume of conglomerate deposited, and on regional structural trends in the Paleozoic and Mesozoic rocks to the west, south, and east. Data are entirely lacking on rocks to the north.

Following the deposition of rhyolite in Pleistocene time, the exposed parts of the Basin Creek uplift, as well as the adjacent areas, were offset by many large and small normal faults. These faults tend to disguise the configuration of the uplift before rhyolite deposition and the relation of the Heart Lake Conglomerate to the uplift.

REFERENCES

Campbell, A. B., 1969, Current U.S. Geological Survey research in Yellowstone National Park, *in* Abstracts for 1968: Geol. Soc. America Spec. Paper 121, p. 590.

Cooper, J. R., 1957, Metamorphism and volume losses in carbonate rocks near Johnson Camp, Cochise County, Arizona: Geol. Soc. America Bull., v. 68, no. 5, p. 577–610.

Craig, Harmon, 1957, Isotopic standards for carbon and oxygen and correction factors for mass-spectrometric analysis of carbon dioxide: Geochim. et Cosmochim. Acta, v. 12, nos. 1–2, p. 133–149.

Evernden, J. F., Savage, D. E., Curtis, G. H., and James, G. T., 1964, Potassium-argon dates and the Cenozoic mammalian chronology of North America: Am. Jour. Sci., v. 262, no. 2, p. 145–198.

Hague, Arnold, 1904, Atlas to accompany U.S. Geological Survey Monograph 32 on the Geology of Yellowstone National Park: U.S. Geol. Survey.

Hague, Arnold, Weed, W. H., and Iddings, J. P., 1896, Yellowstone National Park, Wyo.: U.S. Geol. Survey Atlas, Folio 30, [6] p.

Love, J. D., 1956a, Summary of geologic history of Teton County, Wyoming, during Late Cretaceous, Tertiary, and Quaternary times, *in* Wyoming Geol. Assoc., Guidebook, 11th Ann. Field Conf., 1956: p. 140–150.

——— 1956b, New geologic formation names in Jackson Hole, Teton County, northwestern Wyoming: Am. Assoc. Petroleum Geologists Bull., v. 40, no. 8, p. 1899–1914.

Love, J. D., Weitz, J. L., and Hose, R. K., 1955, Geologic map of Wyoming: U.S. Geol. Survey, scale 1:500,000.

RELATIONSHIPS BETWEEN THE DOTHAN AND ROGUE FORMATIONS, SOUTHWESTERN OREGON

By PRESTON E. HOTZ, Menlo Park, Calif.

Abstract.—In southwestern Oregon, sedimentary rocks of the Dothan Formation structurally underlie metavolcanic rocks of the Rogue Formation, which in turn underlie the Galice Formation of Late Jurassic age. Most authors have considered this to be an unbroken stratigraphic sequence of Late Jurassic age. Recent mapping has shown, however, that the contact between the Dothan and Rogue Formations is an eastward-dipping fault and that there is no stratigraphic continuity between the Dothan and the Rogue. Graywacke of the Dothan Formation is metamorphosed to contorted semischist in a narrow zone adjacent to the fault. Granitic rocks of Late Jurassic age (138 to 151 m.y.) that intrude the Rogue Formation do not intrude the Dothan Formation and are terminated by the fault. The fault is believed to be the northward extension from California of a fault of regional extent along which pre-Nevadan rocks of the Klamath Mountains province are thrust over post-Nevadan rocks of the Northern Coast Ranges.

One of the major geologic problems of southwestern Oregon has been the structural and stratigraphic relationship between the Upper Jurassic Galice Formation, its associated volcanic rocks, and the Dothan Formation. The age of the Dothan Formation has long been disputed because the formation is largely unfossiliferous and its stratigraphic position with respect to the Galice is uncertain. Some geologists regarded it as older than the Galice, others considered it to be younger, and some postulated that the Galice and Dothan are virtually equivalent in age. Recent reconnaissance (Hotz, 1969) has shown that a fault of regional extent separates the Dothan Formation from volcanic rocks associated with the Galice Formation, a relationship that was originally postulated by Irwin (1964) on the basis of studies in California. The contact has been studied in several critical areas northwest of Grants Pass, Oreg., that were relatively inaccessible to earlier students of the area but are now accessible by recently constructed logging roads. Excellent exposures have been provided by some of the roadcuts.

GEOLOGIC SETTING

Sedimentary rocks exposed near Galice, Oreg., on the Rogue River were named the Galice Formation by J. S. Diller (1907, p. 403). They are composed predominantly of dark-gray to black slate, subordinate amounts of interbedded fine- to medium-grained graywacke, and still less conglomerate. The Late Jurassic (Oxfordian to Kimmeridgian) age of the Galice Formation is well established by abundant fossils (*Buchia concentrica*).

Volcanic rocks are associated with the Galice Formation. To a minor extent they are interbedded with the sedimentary rocks, but in some large areas underlain by metavolcanic rocks, sedimentary rocks are rare. The metavolcanic rocks include flows, flow breccias, agglomerates, and tuffs, most commonly of andesitic composition, but including some dacitic to rhyolitic members (Wells and others, 1949, p. 4–5). Wells and Walker (1953) applied the name Rogue Formation to a sequence of metavolcanic rocks that lies between sedimentary rocks of the Galice Formation and the Dothan Formation in the canyon of Rogue River. The Rogue Formation seems to be continuous to the northeast with metavolcanic rocks interbedded with Galice sedimentary rocks (fig. 1), but this relationship is uncertain. According to Wells and Walker (1953) the Rogue Formation consists of tuffs, agglomerates, flow breccias, and flows that range in composition from andesitic to dacitic and rhyolitic. An amphibolite unit south of the Rogue River (fig. 1) is regarded by Wells and Walker (1953) as the metamorphic equivalent of the Rogue Formation.

A wide belt of sedimentary rocks lying to the west and northwest of the metavolcanic rocks that include the Rogue Formation was named the Dothan Formation by Diller (1907, p. 407) for Dothan Postoffice (now West Fork Station) on Cow Creek (fig. 1). These rocks include graywacke, shale, some conglomerate, and minor amounts of chert and limestone. A few lenticular

U.S. GEOL. SURVEY PROF. PAPER 650–D, PAGES D131–D137

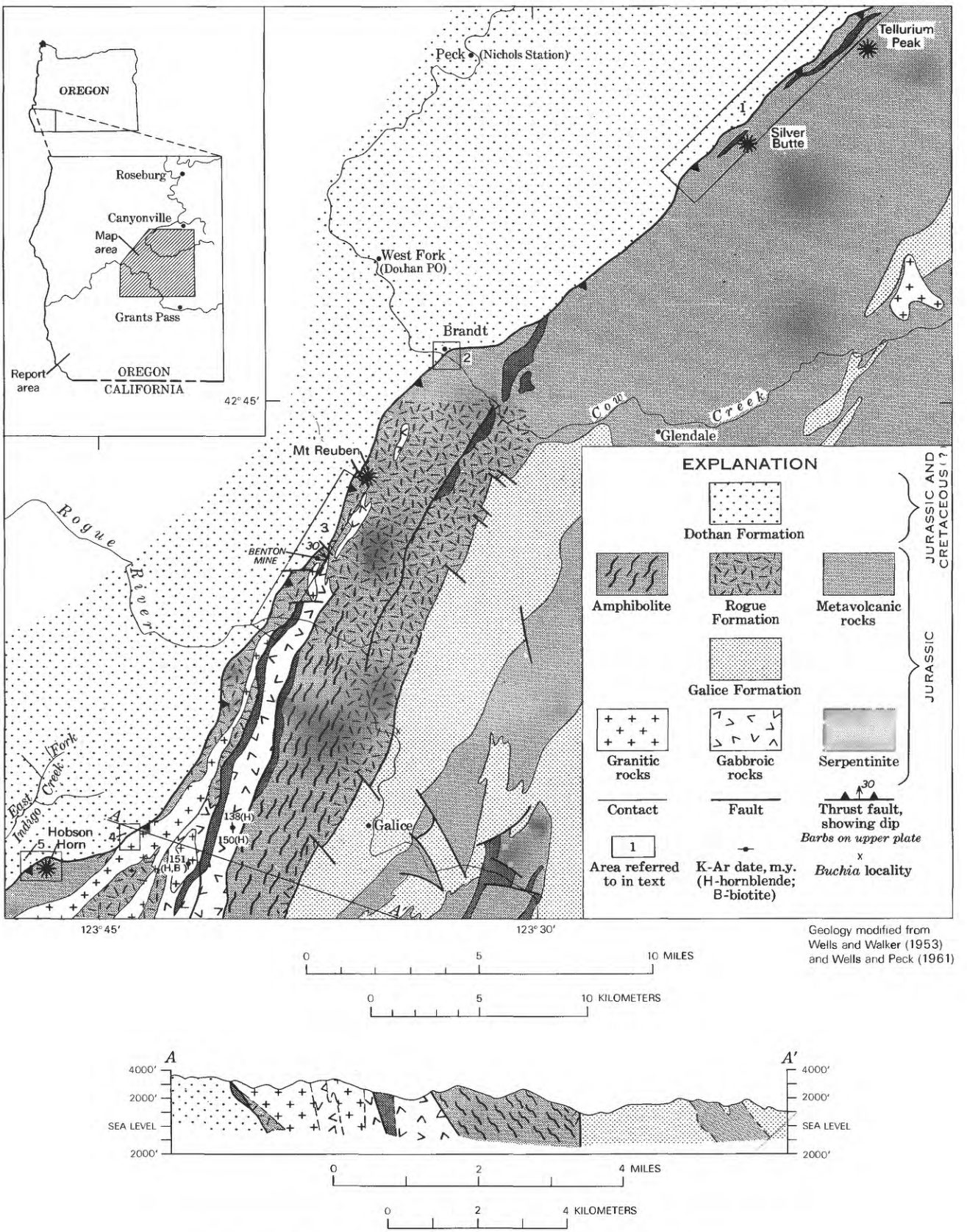

FIGURE 1.—Geologic map and section of part of southwest Oregon.

bodies of pillow basalt are interbedded with the sedimentary rocks in the type area; elsewhere they are more plentiful. A few fossil collections made by Diller (1907, p. 409–410) from beds he regarded as part of the Dothan Formation were later assigned to either the Galice Formation or the Myrtle Group (Wells and Peck, 1961).

Throughout this region the predominant trend of all the rocks is north-northeast to northwest, with steep to moderate southeastward dips. Structural details are poorly known, but locally at least the rocks are tightly folded, with the axial planes of folds also inclined to the southeast. In the succession from west to east the Dothan Formation underlies the Rogue Formation. Diller (1907, p. 410, 421), however, concluded that the strata are overturned and the Dothan is actually younger than the Galice and associated volcanic rocks. Taliaferro (1942, p. 81–83), after an examination of exposures along Cow Creek, decided that the section is a right-side-up normal succession and that the Dothan grades upward into the volcanic rocks with which sedimentary rocks of the Galice Formation are interbedded. From work in the Galice quadrangle, Wells and Walker (1953) also concluded that the Dothan Formation is right side up and older than the Rogue and Galice Formations. Dott (1965) and his students, after studying the geology of the coastal region of southwest Oregon, also were convinced that the Dothan Formation is part of a normal stratigraphic succession beneath the Rogue and Galice Formations.

FIELD OBSERVATIONS OF THE DOTHAN-ROGUE CONTACT

The following data on the nature of the contact between the Dothan Formation and volcanic rocks associated with the Galice Formation, including in part the Rogue Formation, were obtained from the examination of exposures in five areas in southwest Oregon, labeled 1 to 5 on figure 1.

Area 1 is southwest of Canyonville in the old Silver Peak mining area. The contact between sedimentary rocks of the Dothan Formation and metavolcanic rocks is on the northwest side of a northeast-trending ridge that includes Silver Butte and Tellurium Peak at the south and north ends, respectively. The contact is not well exposed, but its position can be estimated within a few feet at several places where it crosses spurs that project northwestward from the main ridge. The average strike of the contact is between N. 45° E. and N. 50° E., and its trace indicates that the dip ranges from practically vertical to as low as 40° SE. The Dothan Formation is composed of thick-bedded massive graywacke with thin partings and thicker interbeds of dark-gray shale that dip moderately to steeply southeast. Thin bodies of rhythmically bedded chert are exposed at two places near the contact. The contact can be most closely located at the north end of the ridge along an old road where exposures are nearly continuous. Here the contact is occupied by a body of sheared serpentinite approximately 10 feet thick, which cannot be shown at the scale of the map (fig. 1). On the northwest side of the contact is a zone approximately 100 feet wide of contorted semischist and a thin body of chert, beneath which are massive graywacke and shale. Southeast of the serpentinite are greenschist and massive metavolcanic rocks that dip moderately to steeply southeast. Narrow bodies of serpentinite also occupy the contact half a mile and approximately 2½ miles to the southwest, where narrow zones of poorly exposed semischist were observed on the Dothan side of the contact. Thin bodies of serpentinite also intrude metavolcanic rocks 1,000–2,000 feet southeast of the contact. All the mines and prospects of the Silver Peak district are in the metavolcanic rocks, and none are in rocks of the Dothan Formation. Shenon (1933) reported that mineralization at the Silver Peak mine is in schistose, altered rocks of the Dothan Formation, but the mine is three-fourths of a mile southeast of the contact of the Dothan with metavolcanic rocks, and all the rocks exposed at the mine are metavolcanics; none resemble the sedimentary rocks of the Dothan.

Area 2 is on Cow Creek near Brandt. Rocks southeast and northwest of the contact are well exposed in railroad cuts; the contact zone is exposed in numerous outcrops in the creek. Taliaferro (1942, p. 81–83) reported that "* * * unmistakable relations in this section indicate that the Dothan grades upward into the volcanics * * *." However, the evidence provided by the exposures does not support this conclusion. Dothan graywacke, shale, and some interbedded pillow lavas are exposed northwest of Brandt. Southeast of Brandt, well-foliated greenschist and a gabbroic intrusive are exposed in the cuts. The intervening area, exposed in the creek banks, consists of strongly sheared and contorted black mudstone containing detached blocks of graywacke. Close to the greenschist the rock is dark-gray semischist. The change to greenschist is abrupt, and there is no evidence of gradation or interfingering of the metavolcanic rocks with the sedimentary rocks.

Some of the most critical data on the nature of the contact between the Dothan Formation and volcanic rocks of the Rogue Formation come from area 3 north-northwest of Galice. North of the Benton mine (near the center of area 3), foliated, contorted, quartz-

veined greenschist dips eastward approximately 30° and overlies a zone approximately 1,000 feet wide of highly sheared dark shale and sandstone in which the least disturbed beds dip 25°–40° eastward. The contact between greenschist and the zone of sheared sedimentary rocks strikes northeast and dips approximately 30° SE. Granitic rocks intrude the greenschist but not the Dothan.

Near the northeastern end of area 3 west of Mount Reuben, the Dothan is strongly sheared over a width of approximately 300 feet adjacent to the contact with the Rogue. Although not actually exposed, the contact can be located within a few feet. The sheared zone contains small tectonic blocks of graywacke in which an incipient cleavage is apparent. The volcanic rocks east of the contact are metamorphosed to fine-grained foliated greenschist. Foliation planes in the greenschist and the sheared sedimentary rocks dip gently to moderately eastward.

Exposures in Rogue River canyon at the southern end of area 3 are good, and the area of the contact is easily accessible by trail. The contact is abrupt and can be located within approximately 50 feet. Adjacent to the contact the Dothan is highly sheared and contorted over a zone 500 to 1,000 feet wide. Small tectonic blocks of graywacke "float" in a very fine grained phyllitic matrix. East of the contact, schistose metavolcanic rocks dip 15°–30° eastward.

The relationships at area 4 are critical because the Dothan Formation is in contact with granitic rocks. K-Ar dates determined on hornblende and biotite from specimens of gabbro and quartz diorite plutons that intrude the Rogue Formation near here range from 138 million years to 150 m.y. (M. A. Lanphere, written commun., 1968). In roadside exposures the granitic rocks near the contact are highly fractured, altered, and cut by many white veinlets of clinozoisite. The contact is not exposed, but its position can be estimated within a few feet. No evidence of intrusion of the sedimentary rocks by the granitic rocks can be seen, and there is no apparent metamorphism at the contact. Next to the contact, however, the sedimentary rocks are highly sheared and some contorted semischist is exposed. Here, also, in this zone of sheared sedimentary rocks, is a sliver a few feet wide of sheared serpentinite and a large isolated block of hard, brecciated metavolcanic rock. Three hundred feet west of the contact are exposures of thick-bedded graywacke that has no obvious shear or foliation structure.

At area 5, near Hobson Horn, where the contact between the Dothan Formation and greenstones of the Rogue Formation passes through a topographic saddle, the contact is poorly exposed. Sheared serpentinite a few feet wide occurs at the estimated position of the contact. The metavolcanic rocks, which are contorted greenschists near the contact, are intruded by small brecciated gabbroic bodies. Sedimentary rocks of the Dothan are not obviously brecciated or metamorphosed.

On the basis of reconnaissance mapping, Wells (1955; Wells and Peck, 1961) showed a granitic pluton projecting northward into the Dothan Formation in the vicinity of Hobson Horn and the East Fork of Indigo Creek. However, now that logging roads have made the area accessible, it was found that only sedimentary rocks of the Dothan Formation are exposed in the East Fork of Indigo Creek; nor is the Dothan intruded by granitic rocks at Hobson Horn, although gabbro intrudes metavolcanic rocks of the Rogue Formation.

The field evidence in the five areas described here unquestionably supports the conclusion that the Dothan Formation is in fault contact with the Rogue Formation and other possibly equivalent volcanic rocks. There is no evidence that the metavolcanic rocks are either depositional on the Dothan or that they grade into one another, as suggested by Taliaferro (1942, p. 81–83) and Wells and Walker (1953). The limited data available from this reconnaissance indicate that strata of the Dothan Formation are closely folded, in some places isoclinally, and locally the beds are overturned with tops facing west. There is no evidence to support Diller's suggestion (1907) that the entire section is overturned.

PETROGRAPHY

Thin-section study of the rocks provides additional data on the nature and significance of the contact between the Dothan and the metavolcanic rocks. Typically, specimens of the graywacke of the Dothan Formation from exposures near the contact are composed of subangular to angular fragments in an almost unresolvable groundmass (fig. 2*A*). Borders of many grains are fuzzy and grade into the ground mass. Mineral fragments are mostly quartz and plagioclase, with minor amounts of sphene, epidote, muscovite, biotite, chlorite, and, rarely, tourmaline and zircon. Rock fragments are abundant and include very fine grained recrystallized chert, shale, altered volcanic rock, and limestone. Specimens from three places—the northern part of area 3, area 4, and an area approximately 2 miles west of area 4—contain a small percentage of K-feldspar grains, less than 1 percent to 2 percent. Two specimens contain fragments of serpentinite and grains of clinopyroxene. The groundmass contains secondary fine-grained chlorite, which also commonly mantles mineral and rock fragments at the interface with the groundmass. Pumpellyite, known to occur

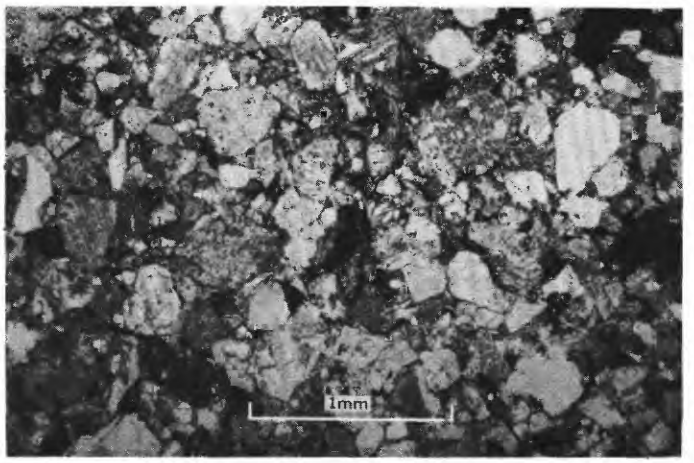

A

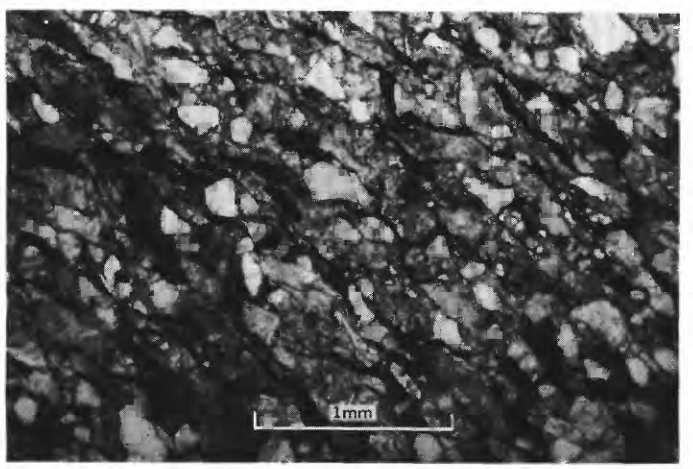

B

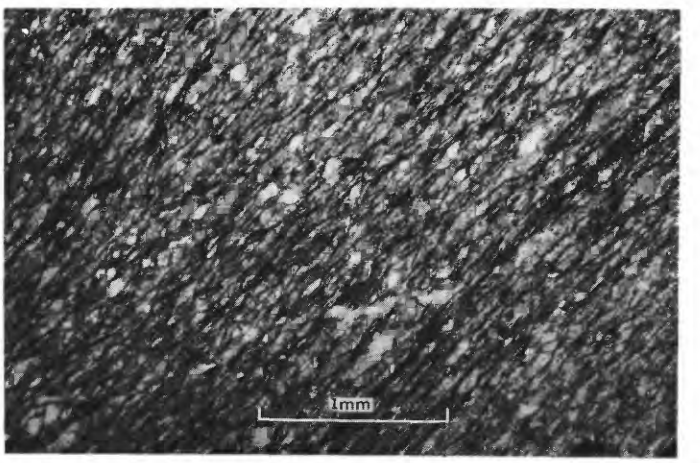

C

FIGURE 2.—Photomicrographs showing progressive development of metamorphic fabric in graywacke of the Dothan Formation. *A*, Typical graywacke of textural zone 1. *B*, Graywacke with incipient cleavage. Shows parallel orientation of mineral grains and rock fragments. Slight reduction in grain size from *A*. Dark streaks are cleavage laminae composed of opaque submicroscopic material (carbon?), and very fine grained mica. Lower part of textural zone 2. *C*, Fine-grained semischist showing closely spaced braided dark folia composed of opaque submicroscopic material and fine-grained colorless mica enclosing angular to subangular grains of quartz and albite. Textural zone 2.

at many places in the graywackes of the Dothan and Franciscan Formation in Oregon and California (Blake and others, 1967), was not observed in specimens from this area.

The faint cleavages that are megascopically visible in some of the sandstone near the contact and in tectonic blocks in the fault zone are apparent under the microscope as through-going but irregular folia of dark-brown to black, translucent to opaque, fine-grained dust and very fine-grained colorless mica (fig. 2*B*). In some specimens the rock and mineral fragments between the cleavages are unoriented, but in others the long axes of grains and fragments have a subparallel arrangement.

The semischist that is adjacent to the contact at several places has a well-developed planar structure composed of closely spaced braided folia of colorless mica and opaque material (carbon?) (fig. 2*C*). The folia wrap around microscopic angular to subangular grains of quartz and untwinned albite. Slight segregation layering has been developed in some specimens, made evident by a few very thin lamellae of recrystallized quartz and feldspar. X-ray diffractometer patterns obtained on minus-2-micron fractions from specimens of the semischist indicate the presence of well-crystallized muscovite and chlorite, presumably from the micaceous lamellae.

Petrographic data indicate that through a narrow zone adjacent to the fault, graywacke of the Dothan Formation is progressively metamorphosed from northwest to southeast. As the contact is approached from the northwest, an incipient cleavage appears in otherwise massive graywacke. Immediately adjacent to the fault, the graywacke is almost completely recrystallized to a very fine-grained muscovite-chlorite-quartz-albite semischist. The foliation dips southeastward more or less parallel to the fault, and the Dothan dips southeastward beneath the fault and the overlying metavolcanic rocks. Thus the metamorphism of the graywacke increases upward. The relationships are similar to those described by Blake, Irwin, and Coleman (1967) in the southern Klamath Mountains, where metamorphism of the Franciscan Formation increases upward toward a fault boundary between the California Coast Ranges and the Klamath Mountains and Great Valley provinces; the upward increase in metamorphism is regarded as due to cataclasis and recrystallization along the sole of a great eastward-dipping thrust fault. The semischist described above

corresponds to textural zone 2 of Blake, Irwin, and Coleman (1967); the graywacke with incipient cleavage is equivalent to the transition between their zones 1 and 2. The metamorphism is not as intense, however, as that which they describe in the southern Klamath Mountains (Blake and others, 1967). Lawsonite, which occurs in textural zone 2 rocks described by Blake (1967) and is indicative of the blueschist metamorphic facies, is not present in these rocks from Oregon. No completely recrystallized schist corresponding to textural zone 3 of Blake, Irwin, and Coleman (1967) has been recognized adjacent to the contact here. To the southwest near the Oregon-California State line, however, schists occur at the contact of the Dothan with the large Josephine ultramafic pluton.

CONCLUSIONS

The evidence indicates that the contact between the Dothan and Rogue Formations is an eastward-dipping thrust fault and thus does not support the hypothesis held by Taliaferro (1942), Wells and Walker (1953), and Dott (1965) that the Dothan is part of a stratigraphic succession that includes the Rogue and Galice Formations. Granitic and gabbroic plutons which intrude the Rogue Formation do not intrude the Dothan and are cut off by the fault between the Dothan and Rogue. Some of the Dothan graywacke contains grains of K-feldspar. These relationships suggest that deposition and deformation of the Dothan were later than the plutonic episode in the Klamath Mountains (Lanphere and others, 1968) that took place in the Middle and Late Jurassic. Ultramafic rocks intrusive into the Rogue and Galice Formations do not penetrate the Dothan in this area. The small discontinuous bodies of sheared serpentinite which occur in the fault zone are believed to be tectonic slivers.

Evidence that apparently conflicts with these conclusions has been presented by Dott (1965, p. 4693–4694), who reported a whole-rock K-Ar age of 149± 4 m.y. obtained on a sample from what he regarded as a rhyolite flow in the Dothan to the southwest near Collier Butte. The reliability of this evidence for the age of the Dothan seems somewhat questionable because the reported 0.18-percent K content (Dott, 1965, p. 4694) is anomalously low for rhyolite, and the sample showed only slight incipient devitrification, which would be highly unusual for a rock of this age. At another place in southwestern Oregon, Dott (1965, p. 4694) reported a rhyolite sill in the Dothan which yielded an age of 30±1 m.y.

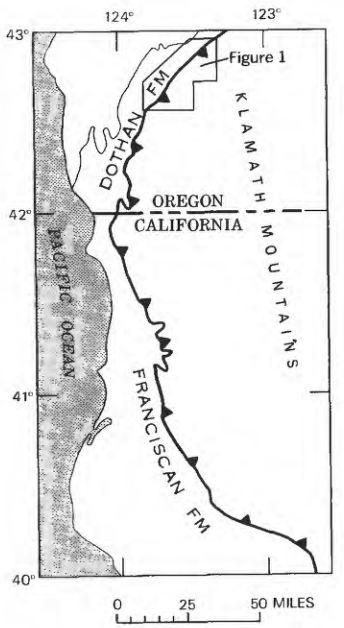

FIGURE 3.—Map of northern California and southwest Oregon.

The Dothan Formation is the northward extension (Wells and Peck, 1961) of rocks mapped as the Franciscan Formation in northern California (Strand, 1963; Bailey and others, 1964, p. 20, pl. 1; fig. 3, this report), part of which is known to be of latest Jurassic and Early Cretaceous age. Therefore, a latest Jurassic and probable Early Cretaceous age is postulated for the Dothan. The fault between the Dothan Formation and metavolcanic rocks that include the Rogue Formation is believed to be the northward continuation of the fault between the Franciscan and Galice Formations and associated metavolcanic rocks in California (Irwin, 1964; 1966, fig. 2; Blake and others, 1967) along which rocks of the Klamath Mountains were thrust westward over the Franciscan of the Northern Coast Ranges during the Late Cretaceous. Where the dip of the fault can be measured (area 3), it is inclined 30° eastward. Elsewhere its trace in relation to topography indicates that the fault dips eastward at moderate to steep angles (45°–60°) and may be near vertical locally. Hence, it is more properly termed a reverse fault at many places. The magnitude of displacement is unknown but may have amounted to tens of miles. Movement along the fault probably was accompanied by displacements through a wide zone to the east along parallel faults and belts of serpentinite in the Rogue-Galice sequence (Wells and Walker, 1953).

REFERENCES

Bailey, E. H., Irwin, W. P., and Jones, D. L., 1964, Franciscan and related rocks, and their significance in the geology of western California: California Div. Mines and Geology Bull. 183, 177 p.

Blake, M. C., Irwin, W. P., and Coleman, R. G., 1967, Upside-down metamorphic zonation, blueschist facies, along a regional thrust in California and Oregon, *in* Geological Survey Research 1967: U.S. Geol. Survey Prof. Paper 575–C, p. C1–C9.

Diller, J. S., 1907, The Mesozoic sediments of southwestern Oregon: Am. Jour. Sci., 4th ser., v. 23, no. 138, p. 401–421.

Dott, R. H., Jr., 1965, Mesozoic-Cenozoic tectonic history of the southwestern Oregon coast in relation to Cordilleran orogenesis: Jour. Geophys. Research, v. 70, no. 18, p. 4687–4707.

Hotz, P. E., 1969, Relations between the Dothan and Rogue Formations, southwest Oregon [abs.]: Geol. Soc. America, Cordilleran Sec., Ann. Mtg., Eugene, Oreg., 1969, Program, p. 27.

Irwin, W. P., 1964, Late Mesozoic orogenies in the ultramafic belts of northwestern California and southwestern Oregon, *in* Geological Survey Research 1964: U.S. Geol. Survey Prof. Paper 501–C, p. C1–C9.

——— 1966, Geology of the Klamath Mountains province, *in* Bailey, E. H., ed., Geology of northern California: California Div. Mines and Geology Bull., 190, p. 19–38.

Lanphere, M. A., Irwin, W. P., and Hotz, P. E., 1968, Isotopic age of the Nevadan orogeny and older plutonic and metamorphic events in the Klamath Mountains, California: Geol. Soc. America Bull., v. 79, no. 8, p. 1027–1052.

Shenon, P. J., 1933, Copper deposits in the Squaw Creek and Silver Peak districts and at the Almeda mine, southwestern Oregon: U.S. Geol. Survey Circ. 2, 34 p.

Strand, R. G. (compiler), 1963, Geologic map of California, Olaf P. Jenkins edition—Weed sheet: California Div. Mines and Geology, scale 1:250,000.

Taliaferro, N. L., 1942, Geologic history and correlation of the Jurassic of southwestern Oregon and California: Geol. Soc. America Bull., v. 53, no. 1, p. 71–112.

Wells, F. G., 1955, Preliminary geologic map of southwestern Oregon west of meridian 122° west, and south of parallel 43° north: U.S. Geol. Survey Mineral Inv. Field Studies Map MF–38, scale 1:250,000.

Wells, F. G., Hotz, P. E., and Cater, F. W., 1949, Preliminary description of the geology of the Kerby quadrangle, Oregon: Oregon Dept. Geology and Mineral Industries Bull. 40, 23 p.

Wells, F. G., and Peck, D. L., 1961, Geologic map of Oregon west of the 121st meridian: U.S. Geol. Survey Misc. Inv. Map I–325, scale 1:500,000.

Wells, F. G., and Walker, G. W., 1953, Geologic map of the Galice quadrangle, Oregon: U.S. Geol. Survey, Geol. Quad. Map GQ–25, scale 1:62,500.

PRELIMINARY REPORT ON THE PALEOZOIC AND MESOZOIC SEDIMENTARY SEQUENCE ON ST. LAWRENCE ISLAND, ALASKA

By WILLIAM W. PATTON, JR., and J. THOMAS DUTRO, JR.,
Menlo Park, Calif., Washington, D.C.

Abstract.—Preliminary investigations in the eastern part of St. Lawrence Island indicate the presence of a heretofore unreported sedimentary sequence possibly as much as 8,000 feet thick. The oldest strata are a thick sequence of Devonian dolomite and dolomitic limestone exposed along the Seknak River. On the Ongoveyuk River these strata appear to be succeeded disconformably by at least 1,000 feet of Upper Mississipian limestone and cherty limestone which in turn are overlain disconformably by a 400-foot shaly sequence that is definitely of Middle and Late Triassic age in the upper part and probably of Early Triassic or Permian age in the lower part. The youngest sedimentary rocks appear to be a thick section of graywacke and mudstone along the Ongoveyuk River, tentatively assigned a Jurassic or Cretaceous age. The Paleozoic and Mesozoic sequence shows strong lithologic and faunal similarities to coeval rocks in the Brooks Range; and some counterparts appear also to be present on the Seward and Chukotsky Peninsulas.

During the summer of 1968, the U.S. Geological Survey began reconnaissance mapping, stratigraphic studies, and geochemical sampling of the bedrock areas on St. Lawrence Island in the northern Bering Sea. These investigations are part of a broad program of onshore and offshore studies pointed toward assessing the mineral resources of the Bering Sea shelf (fig. 1). St. Lawrence Island by virtue of its unique geographic position serves as a valuable "window" to the subbottom geology of the shelf and is vital to the interpretation of marine geophysical data.

The purpose of this paper is to report briefly on a heretofore little known sequence of Paleozoic and Mesozoic rocks exposed in the eastern part of St. Lawrence Island. These rocks are of regional significance because they provide a stratigraphic tie between mainland Alaska and eastern Siberia and, hopefully, shed some light on the puzzling tectonic relationships between the North American and Asian landmasses. In addition, they are important to the search for new sources of petroleum because they suggest that large parts of the Bering Sea shelf may be underlain by a thick section of Paleozoic carbonate rocks.

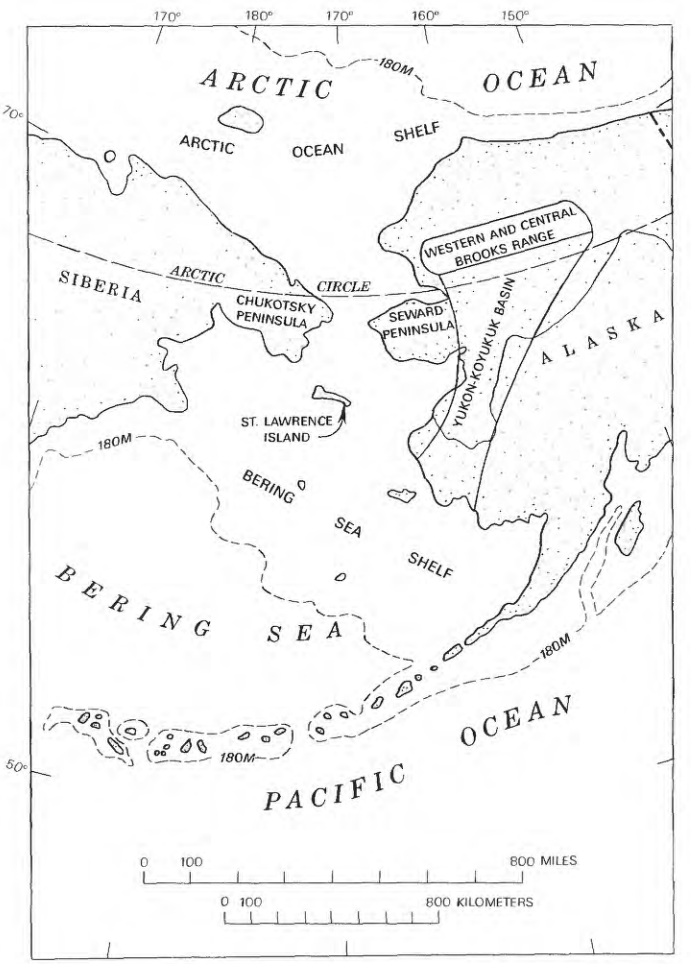

FIGURE 1.—Index map showing St. Lawrence Island and shelf areas of the Bering Sea and Arctic Ocean.

The stratigraphic data presented in this report are based on 3 weeks of fieldwork during July 1968. Inasmuch as only a small portion of the eastern part of the island has been critically examined thus far, these data should be regarded as preliminary and tentative.

Published information on the geology of St. Lawrence Island is confined to exploratory surveys along the coast (Dawson, 1894; Emerson, 1904, p. 38–42; Collier, 1906). Except for a brief mention of the Triassic strata by Martin (1926) and the information shown on the "Geologic Map of Alaska" (Dutro and Payne, 1957), no information has been published about the Paleozoic and Mesozoic sedimentary rocks.

GEOLOGIC SETTING

The eastern part of St. Lawrence Island is a broad, wave-cut bedrock platform now elevated a few feet to nearly 100 feet above sea level (fig. 2*A*). The surface of the platform is dotted with countless small shallow lakes and blanketed by a thin veneer of water-soaked mossy turf and peat. Several isolated groups of talus-covered hills, which are bounded by ancient sea cliffs and probably represent former islands, rise 1,000 to 2,000 feet above the surface of the platform.

The Paleozoic and Mesozoic strata are sparsely exposed along small drainages incised as much as 30 feet into the platform (fig. 2*B*). The best exposures of these rocks are found along the Ongoveyuk, Seknak, and Maknek Rivers and their tributaries (fig. 3). Even along these drainages, however, the exposures are discontinuous and the bedrock is largely reduced to frost-riven talus.

A

B

FIGURE 2.—Views of St. Lawrence Island, Alaska. *A*, Eastern part of St. Lawrence Island from north coast, showing wave-cut platform carved across folded Paleozoic and Mesozoic sediments. Hills in background composed chiefly of granitic intrusives. (Photograph by U.S. Navy.) *B*, Incised tributary of Ongoveyuk River with cutbank exposures of Mississippian and Triassic strata in foreground and middle distance and Jurassic-Cretaceous(?) strata in background. (Photograph by T. P. Miller.)

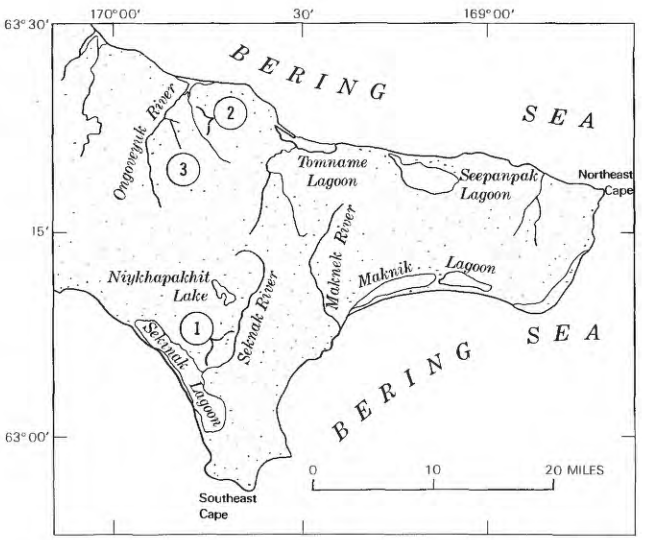

FIGURE 3.—Map of eastern St. Lawrence Island, showing location of Paleozoic and Mesozoic sections 1, 2, and 3 (see fig. 4).

Bedding attitudes where discernible indicate that the Paleozoic and Mesozoic strata are everywhere highly folded with dips locally as steep as 90°. The gross distribution of the rock units suggests that these strata have a north to northeast regional strike and a west to northwest regional dip. Examination of aerial photographs reveals that all the bedrock units are cut by two sets of lineaments trending approximately N. 50° E. and N. 25° W.

Granitic intrusives and volcanic rocks of late Mesozoic and Cenozoic age, which underlie all the hilly areas as well as large parts of the wave-cut platform, have thermally altered broad areas of the surrounding sedimentary rocks. In addition, all the sedimentary rock units are pervasively intruded by a variety of felsic and mafic sills and dikes.

DEVONIAN

The oldest rocks recognized in the eastern part of St. Lawrence Island comprise a thick sequence of dolo-

359-403 O—69——10

mites and dolomitic limestones of probable Devonian age. These rocks are widely exposed along the Seknak and Maknek Rivers on the south side of the island and in a small area along the Ongoveyuk River on the north side of the island.

The bulk of the exposed sequence (fig. 4) is composed of medium-gray to brown, laminated, locally brecciated dolomite and dolomitic limestone which contain poorly preserved *Amphipora*(?). In the upper part these beds grade into dark-gray to black, fine-grained, thin-bedded dolomite with abundant *Amphipora*(?) and corals. A few thin beds of black chert and black silty dolomite are intercalated near the top of the sequence.

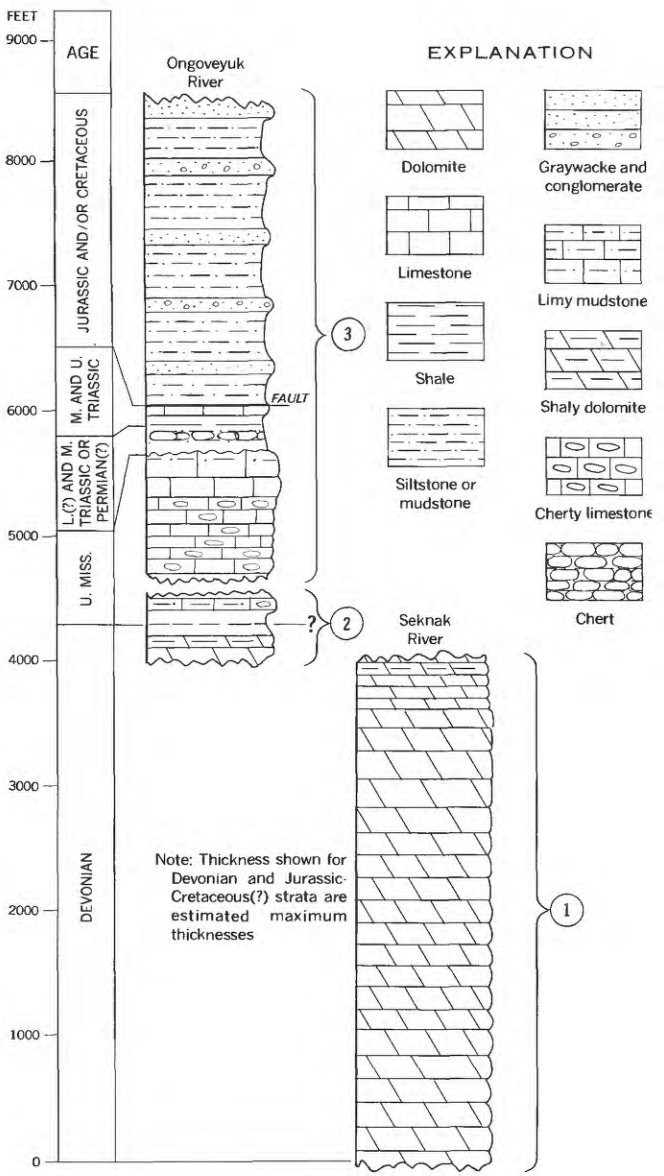

FIGURE 4. Generalized columnar section of Paleozoic and Mesozoic sedimentary rocks, eastern St. Lawrence Island (see fig. 3 for location of sections).

The sequence is best exposed along the lower Seknak River (fig. 3) in a series of discontinuous cutbanks. The beds strike uniformly north-northwest and dip on the average of 30° NE. Judging from the width of outcrop, the sequence may be as much as 4,000 feet thick. The top of the sequence is not exposed on the Seknak River. On the Ongoveyuk River, however, dark thin-bedded dolomites similar to those in the upper part of the Seknak River section are succeeded by cherty and sandy limestones of Late Mississippian age.

Five collections of stromatoporoids and corals from the Seknak River sequence were examined by W. A. Oliver, Jr. (written commun., 1968), who reports that they represent the stromatoporoid genus *Amphipora*(?) and tabulate corals including *Favosites* and thamnoporoid forms. He states that a Devonian age is strongly suggested, possibly Givetian or Frasnian, although these fossil groups range earlier into the Silurian.

MISSISSIPPIAN

Strata of Mississippian age are widely distributed along the Ongoveyuk River in the northern part of the island and occur in scattered rubble patches around the shores of Niykhapakhit Lake in the central part of the island. These rocks can be divided informally into two members (fig. 4): a thin-bedded dark cherty member below, and a thick-bedded light-colored limestone member above. The lower member, about 600 feet thick, contains abundant dark-gray chert nodules—as much as 35 to 40 percent in the upper 50 feet and 5 to 20 percent in the lower part. The upper member, about 350 feet thick, is nearly chert free and is composed chiefly of light- to medium-gray, medium to coarsely bioclastic limestone. Limy mudstone makes up about 30 percent of the top 50 feet of the member.

The total thickness of the Mississippian sequence in the Ongoveyuk River area probably does not exceed 1,500 feet. Nearly 1,000 feet of section, including the upper contact, is almost completely exposed on a small tributary of the Ongoveyuk River (fig. 3). The lower contact is not exposed at this locality, but on the east fork of the Ongoveyuk River, fossiliferous cherty and sandy limestones of Late Mississippian age are separated from dolomites of probable Devonian age by only a narrow covered interval (figs. 3 and 4).

Fossils of Late Mississippian age were found at several levels in the sequence. Among the more significant forms are the brachiopods of the genus *Gigantoproductus* that occur about 100 feet above the base of the upper member. This interval correlates broadly with the *Gigantoproductus* Zone in the upper part of the Alapah Limestone of the central Brooks Range sequence (Bowsher and Dutro, 1957, p. 5–6; Yochelson and Dutro, 1960, fig. 24).

Three collections near the base of the sequence contain many specimens of what is probably a new species of *Rugosochonetes*, together with a rich endothyroid microfauna of Viséan age, according to A. K. Armstrong (written commun., 1966). An assemblage from the lower 200 feet of the sequence (corals identified by W. J. Sando, written commun., 1968) includes:

Caninia sp.
Syringopora (*Kuiechowpora*) cf. *S. virginica* Butts
Zaphrentites sp. (large)
echinoderm debris, indet.
ramose bryozoans, indet.
Anthracospirifer sp.
productoid fragment, indet.

Sando states that the corals "* * * indicate a possible early Chester age, although a late Meramec age cannot be ruled out."

Another collection from an indeterminate level in the sequence contains *Ekvasophyllum*? sp. that suggests to Sando (written commun., 1968) either an early or middle Meramec age. A lithostrotionoid coral collected as float by T. P. Miller in 1966 was identified as *Lithostrotionella* aff. *L. mclareni* Sutherland by Armstrong (written commun., 1966), who suggested that it indicates a Meramec age. According to Armstrong, similar corals occur in the lower part of the Alapah Limestone in the central Brooks Range, together with Meramec age endothyroids and brachiopods.

Thus, the faunal evidence indicates that the sequence is approximately correlative with the Alapah Limestone, with an age range from early Meramec through possible early Chester. Foraminifera from eight of the collections made in 1968 were examined by Bernard Mamet, Université de Montréal, who states (written commun., March 31, 1969):

> The encountered microfauna is very poor. Widespread occurrence of the "*Brunsia*-facies" eliminates most of the foraminiferal markers * * *. All foraminiferal-bearing horizons have an age ranging from Early Late Visean to Early Late Late Visean; this correlates with the late Meramec-earliest Chester.

Collections from the lower 600 feet of the sequence contain foraminiferal assemblages assigned by Mamet to his Zones 14–15 (late Meramec). Two collections from the upper 300 feet of the sequence contain assemblages that may range as high as Mamet's Zone 16i (earliest Chester).

TRIASSIC

The Mississippian strata on the Ongoveyuk River are overlain by a 400-foot siltstone, shale, dark chert, and limestone section that contains Triassic fossils in the upper part. Similar rocks also were found at scattered localities along the streams that drain into Tomname Lagoon. Triassic fossils have been identified in float from the northwestern part of the island, but the presence of Triassic bedrock in this part of the island has not been established.

The upper 170 feet of the Ongoveyuk River section (fig. 4) is chiefly black shale and dark thin-bedded limestone and chert. Flat clams identified as *Daonella*, *Halobia*, and *Monotis* by N. J. Silberling (written commun., 1968) occur in vertical sequence and indicate a condensed section including beds of Ladinian, Karnian, and Norian age. The lithologic and faunal character of these beds is remarkably similar to that of the upper part of the Shublik Formaton (Limestone and Chert Members) in the Brooks Range of northern Alaska (Patton and Tailleur, 1964) (fig. 5).

The lower 225 feet of the Ongoveyuk River section is mostly thin-bedded chert and dark siltstone. These beds have yielded no fossils, but their lithologic character suggests a possible correlation with either the Shale Member (Early? and Middle Triassic) of the Shublik Formation or the Siksikpuk Formation (Permian) (fig. 5).

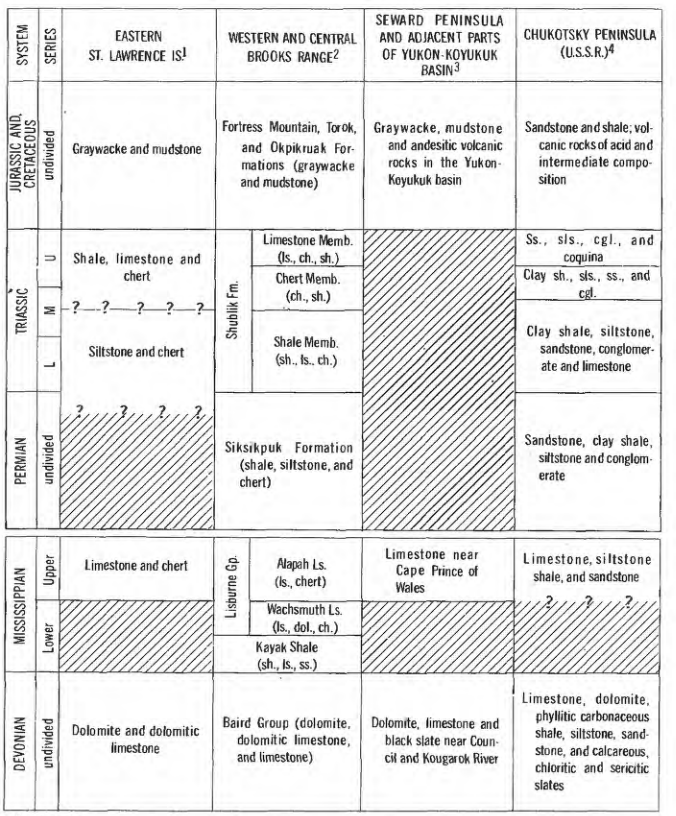

[1] This report.
[2] Patton and Tailleur (1964), Bowsher and Dutro (1957), and Tailleur, Brosgé, and Reiser (1967).
[3] Patton (1967), Steidtmann and Cathcart (1922), and Gryc, Dutro, Brosgé, Tailleur, and Churkin (1967).
[4] Sachs and Strelkov (1961), Markov and Tkachenko (1961), and Krasny (1964).

FIGURE 5. Suggested correlation of Paleozoic and Mesozoic sequences on eastern St. Lawrence Island, western Alaska, and Chukotsky Peninsula (U.S.S.R.).

JURASSIC-CRETACEOUS(?)

The youngest Mesozoic strata seem to be a thick sequence of graywacke and mudstone which is tentatively assigned a Jurassic or Cretaceous age. These rocks are extensively exposed along the middle course of the Ongoveyuk River and also occur in scattered patches of rubble along the streams that drain into Tomname Lagoon. As yet, however, they have not been identified elsewhere on the eastern part of the island.

Gross structural relationships clearly suggest that these graywacke and mudstone strata immediately overlie the Triassic beds, although the exposed contact on the Ongoveyuk River is complicated by faulting. The upper contact is not exposed, but it appears that these strata dip northwestward beneath the Cenozoic(?) volcanic rocks that crop out along the lower Ongoveyuk River.

No fossils have been found in the graywacke and mudstone beds, and their tentative age assignment is based on: (1) their apparent stratigraphic position above the Triassic strata and below the Cenozoic(?) volcanic rocks, and (2) the widespread occurrence of graywacke and mudstone of Jurassic and Cretaceous age in adjacent parts of mainland Alaska.

The graywacke, which makes up 15 to 25 percent of this unit, is typically a dark-greenish-gray, well-indurated, poorly sorted, fine-grained, muddy sandstone that locally displays sole markings, graded bedding, and other features characteristic of turbidites. Thin intraformational polymict granule-pebble conglomerate and shale-chip conglomerate are sparsely distributed through the unit. Both the graywacke and the mudstone are heavily sheared, in places so intensely that individual graywacke layers have been broken into disconnected, randomly oriented, slickensided blocks which are enveloped in a mudstone paste.

Accurate measurements of thickness of this unit are not possible because structure is locally complex and exposures are incomplete. The width of outcrop and the regional dip of the strata indicate that the unit may be as much as 2,500 feet thick.

CORRELATIONS

The Paleozoic and Mesozoic strata on eastern St. Lawrence Island show a marked resemblance to coeval rocks in the western and central Brooks Range, as indicated in figure 5. In addition, counterparts of some of the Paleozoic and Mesozoic strata appear to be present on the Seward and Chukotsky Peninsulas.

Devonian rocks are widely distributed in the Brooks Range and include a thick section of dolomite and limestone that bears a characteristic stromatoporoid and coral fauna (Tailleur and others, 1967). Similar carbonate rocks, of probable Devonian age, are reported on the Seward Peninsula, but few details of their stratigraphy are known. (Gryc and others, 1967.)

Upper Mississippian limestone and cherty limestone beds containing a coral and brachiopod fauna identical with that found on St. Lawrence Island are extensively exposed in the western and central Brooks Range (Bowsher and Dutro, 1957; Sable and Dutro, 1961). Coral-bearing limestone of probable Late Mississippian age has also been recognized in a small exposure near Cape Prince of Wales at the extreme western end of the Seward Peninsula (Steidtmann and Cathcart, 1922).

The Upper and Middle Triassic strata on St. Lawrence Island closely resemble the upper part of the Shublik Formation in the western Brooks Range, and the shaly beds underlying these fossiliferous strata may be correlative with the lower part (Lower? and Middle Triassic) of the Shublik Formation or with the Siksikpuk Formation (Permian). Triassic strata were thought to be present in the western Seward Peninsula, but recent investigations in this area by C. L. Sainsbury (oral commun., 1969) indicate that most, if not all, of the rocks previously mapped as Triassic (Dutro and Payne, 1957) are pre-Ordovician in age.

Graywacke and mudstone strata of Jurassic and Cretaceous age similar to those found on St. Lawrence Island are widely distributed in western and northern Alaska. Rocks of this character make up nearly all the Cretaceous strata of the Yukon-Koyukuk basin (Gates and others, 1968) and all the Jurassic and Early Cretaceous beds of the western and central Brooks Range.

REFERENCES

Bowsher, A. L., and Dutro, J. T., Jr., 1957, The Paleozoic section in the Shainin Lake area, central Brooks Range, Alaska: U.S. Geol. Survey Prof. Paper 303–A, 39 p.

Collier, A. J., 1906, Geology and coal resources of the Cape Lisburne region, Alaska: U.S. Geol. Survey Bull. 278, 54 p.

Dawson, G. M., 1894, Geological notes on some of the coasts and islands of the Bering Sea and vicinity: Geol. Soc. America Bull., v. 5, p. 117–146.

Dutro, J. T., Jr., and Payne, T. G., 1957, Geologic map of Alaska: U.S. Geol. Survey, scale 1:2,500,000.

Emerson, B. K., 1904, General geology; notes on the stratigraphy and igneous rocks [of Alaska], *in* Harriman Alaska Series, v. 4: Washington, D.C., Smithsonian Institution, p. 11–56.

Gates, G. O., Grantz, Arthur, and Patton, W. W., Jr., 1968, Geology and natural gas and oil resources of Alaska, *in* Natural Gases of North America (AAPG symposium): Am. Assoc. Petroleum Geologists Mem. 9, v. 1, p. 3–48.

Gryc, George, Dutro, J. T., Jr., Brosgé, W. P., Tailleur, I. L., and Churkin, Michael, Jr., 1967, Devonian of Alaska, *in* Oswald, D. H., ed., International symposium on the Devonian System, v. 1: Calgary, Alberta Soc. Petroleum Geologists, p. 703–716.

Krasny, L. I., 1964, Geologic map of the northwestern part of the Pacific mobile belt, sheet 4: U.S.S.R., Ministry of Geology. [In English]

Markov, F. G., and Tkachenko, B. V., 1961, The Paleozoic of the Soviet Arctic, *in* Raasch, G. O., Geology of the Arctic, v. 1 *of* Proceedings of the First International Symposium on Arctic Geology: Toronto, Toronto Univ. Press, p. 31–47.

Martin, G. C., 1926, Mesozoic stratigraphy of Alaska: U.S. Geol. Survey Bull. 776, 493 p.

Patton, W. W., Jr., 1967, Regional geologic map of the Candle quadrangle, Alaska: U.S. Geol. Survey Misc. Geol. Inv. Map I–492, scale 1:250,000.

Patton, W. W., Jr., and Tailleur, I. L., 1964, Geology of the Killik-Itkillik region, Alaska: U.S. Geol. Survey Prof. Paper 303–G, p. 409–500.

Sable, E. G., and Dutro, J. T., Jr., 1961, New Devonian and Mississippian formations in De Long Mountains, northern Alaska: Am. Assoc. Petroleum Geologists Bull., v. 45, no. 5, p. 585–593.

Sachs, V. N., and Strelkov, S. A., 1961, Mesozoic and Cenozoic of the Soviet Arctic, *in* Raasch, G. O., ed., Geology of the Arctic, v. 1 *of* Proceedings of the First International Symposium on Arctic Geology: Toronto, Toronto Univ. Press, p. 48–67.

Steidtmann, Edward, and Cathcart, S. H., 1922, Geology of the York tin deposits, Alaska: U.S. Geol. Survey Bull. 733, 130 p.

Tailleur, I. L., Brosgé, W. P., and Reiser, H. N., 1967, Palinspastic analysis of Devonian rocks in northwestern Alaska, *in* Oswald, D. H., ed., International Symposium on the Devonian System, v. 2: Calgary, Alberta Soc. Petroleum Geologists, p. 1345–1361.

Yochelson, E. L., and Dutro, J. T., Jr., 1960, Late Paleozoic gastropods from northern Alaska: U.S. Geol. Survey Prof. Paper 334–D, p. 111–147.

A TUFF CLAST FROM THE BIDAHOCHI FORMATION AT TONALEA, ARIZONA

By JAMES C. WRIGHT,[1] Beltsville, Md.

Abstract.—A block of tuff, partly altered to montmorillonite and 10 feet or more in diameter, at the trading post at Tonalea, Coconino County, Ariz., is tentatively interpreted as an eroded and transported boulder from the Pliocene Bidahochi Formation. The altered tuff is very similar to an altered tuff in the Bidahochi near Sanders, Ariz., about 120 miles southeast. Because the tuff boulder probably could not have survived transport for more than a few miles, a near-shore shelf environment favorable to accumulation of such tuff near Tonalea is implied. This supports earlier evidence that the lacustrine basin, in which the Bidahochi accumulated, originally extended nearly 80 miles northwest of its previously noted outcrops near Bidahochi.

FIELD OCCURRENCE

A roadcut on the north side of U.S. Highway 164 several hundred feet southwest of the trading post at Tonalea, Coconino County, Ariz. (fig. 1), exposes a block of partly altered vitric tuff. It is in unconsolidated alluvium of silt, silty sand, and pebbly stringers overlying consolidated rocks of Jurassic age. The exposure is about 5,500 feet above sea level. At this locality the alluvium is generally only a few inches to a few feet thick, but it locally fills a broad trough at least 15 feet deep in the bedrock. This alluvium-filled trough interrupts the exposures of Jurassic rock on both sides of the highway. Along the northwest side of the highway the trough is just over 100 feet wide; along the southeast side, about 75 feet wide. The trough crosses the highway in a northwest direction.

The base of the alluvium in the trough is not exposed in the roadcuts, and the steep ends of the trough are partly concealed by slumps. Probably the trough is a preserved remnant of a steep-walled scour channel cut on an old erosion surface. However, the sharp near-vertical walls may be fault contacts of a small graben; there is no other local evidence of vertical faulting, and late Tertiary vertical faulting, though known, is not prevalent on the Colorado Plateau. The Jurassic strata in the exposure are disturbed by bedding-plane gliding along thin layers of purple bentonite that are intercalated with dominant red sandstone and siltstone. Some strata are displaced horizontally at least 10 to 20 feet along these small faults, which are probably gravity slides; in one place Jurassic strata with purple bentonite at their base have been moved about a foot over unconsolidated alluvium.

The tuff block is more than 10 feet across horizontally and 5 feet thick. The block is rounded; its contacts are sharp against the alluvium. The silt and sand in the roadcut also contain a few small tuff blocks several inches across. Weathered remnants of several other tuff blocks about a foot in size are exposed on the

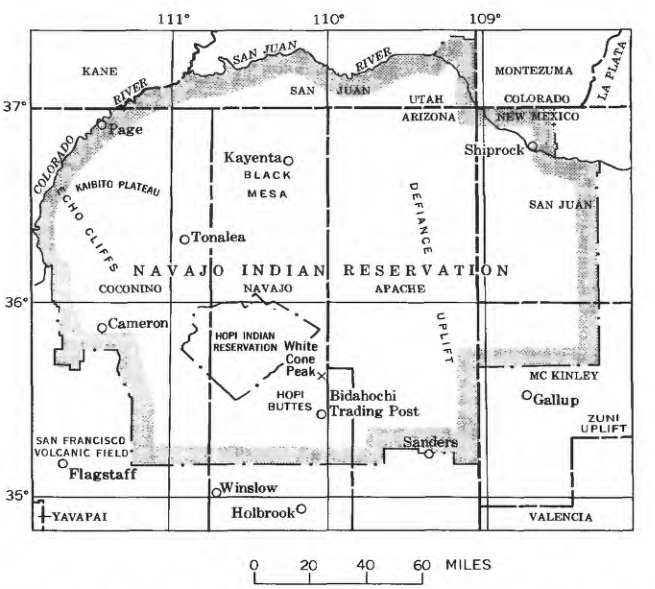

FIGURE 1.—Index map of northeastern Arizona and adjacent States.

[1] Deceased, August 18, 1968.

alluvium-covered surface within 300 feet southeast of the roadcut.

LITHOLOGY

The partly altered tuff is white, lightweight, massive, earthy, and noncalcareous. It is flecked with minute black spots about 0.5 to 1.0 millimeter across. Chips of the tuff about an inch across float on water for a few seconds, but slowly sink as surficial pore space fills with water. The bulk density is about 1.0. The densities of the component vitric shards and montmorillonite were not determined, but if they each are assumed to be approximately 2.3 (Berman and others, 1942, p. 11, 16) the porosity of the altered tuff exceeds 50 percent. In spite of this high porosity, the altered tuff is nearly impermeable, probably because of its fine grain and slight swelling of the clay induced by water. The massive, partly altered tuff breaks with a subconchoidal fracture. A macroscopically obscure preferred planar orientation of the platy glass shards is revealed by microscopic examination.

Most of the vitric shards which form roughly half the altered tuff are platy. Most are less than $\frac{1}{8}$ mm long, although a few are as much as $\frac{1}{2}$ mm long. A few shards are threads, forked threads, minute spheres, and intersecting platelets. The index of refraction of the glass is 1.503 ± 0.002; in natural volcanic glass of typical composition this indicates about a 72-percent silica content (George, 1924, p. 365).

The only abundant mineral in the tuff is dioctahedral montmorillonite, which has been identified by X-ray diffraction analysis. The clay, concentrated by settling out of the generally coarser vitric shards, is moderate to dark yellow (2.5*Y* 6/6 to 2.5*Y* 8/6, Munsell Color Co., Inc., 1954). The montmorillonite is presumably an alteration product of primary vitric shards (Kiersch and Keller, 1955, p. 482–490). A very small amount of quartz is recognized from a weak reflection at 3.33 angstroms, and a trace of illitic clay may be represented by a barely perceptible reflection at 9.9 A.

The tuff contains a few percent of material coarser than $\frac{1}{4}$ mm. This material is mostly well-rounded frosted quartz grains. These are clearly detrital contaminants in the tuff; they are similar in size, rounding, frosting, and coloration to grains of the indurated quartzose sandstone that underlies much of northeastern Arizona. Fine feldspar revealed by X-ray diffraction analysis of coarse concentrates from the tuff may be either volcanic or detrital. The minute black specks in the tuff are small clusters of clastic silt grains cemented by an abundant black matrix. Iron in the black clusters is revealed by a high background on the X-ray diffraction traces generated with copper radiation. Quartz and feldspar are present in the cemented clusters, but no crystalline iron or manganese minerals were noted. The black cement is interpreted as an amorphous phase or phases of hydrous iron oxide, and possibly manganese oxide.

PROPOSED CORRELATION

The tuff block at Tonalea is almost certainly derived from a tuff bed within the Bidahochi Formation. It was not eroded from Mesozoic or older rocks of the area, because tuffs of the older units have all been totally altered to argillaceous bentonite that differs markedly from the block at Tonalea in clay content, color intensity, and a characteristic, although small, content of biotite, feldspar, and quartz crystals. The partly altered tuff block at Tonalea is remarkably like an altered tuff in the Bidahochi Formation near Sanders, Ariz. (Nutting, 1943, p. 152; Kiersch and Keller, 1955). Kiersch and Keller (1955, p. 476) reported that the altered tuff in the Sanders area is the basal bed of the upper member (Repenning and Irwin, 1954, p. 1823) of the Bidahochi, filling erosional channels cut on the surface of the lower member. Numerous tuffs are interbedded in the lower member, but the tuff block at Tonalea particularly resembles the tuff from the base of the upper member in these features: (1) thickness exceeding several feet; (2) white color, earthy texture, and massiveness; (3) almost crystal-free vitric composition; (4) nearly similar index of refraction for fresh glass shards; 1.503 for the Tonalea glass, 1.498 for the Sanders material (Kiersch and Keller, 1955, p. 486); (5) partial alteration to montmorillonite—the X-ray diffraction trace of a glycolated whole-rock sample from the Tonalea block is nearly identical with that published for partly altered tuff from Sanders (Kiersch and Keller, 1955, fig. 8B, p. 485); and (6) specks of black cement which are probably hydrous iron and possibly manganese oxide (Nutting, 1943, p. 152). These similarities do not prove that the block at Tonalea was derived from the tuff at the base of the upper member of the Bidahochi, but they are petrographically consistent with such an origin.

The Bidahochi Formation, a lacustrine and partly fluvial deposit, is limited on the south by the Mogollon Plateau, on the east by the Zuni and Defiance uplifts, and on the north by Black Mesa (Repenning and Irwin, 1954, p. 1821; Kiersch and Keller, 1955, p. 477; Cooley and Akers, 1961; Cooley and Davidson, 1963, p. 25–27). The thick blanketlike "lens deposits" of altered tuff near Sanders formed on a broad shallow lacustrine shelf abutting the Defiance uplift. These clay deposits are now preserved at elevations between 5,900 and 6,100 feet (calculated from maps of Kiersch and

Keller, 1955, p. 472–473; and Cooley and Akers, 1961, p. C247). Smaller elongate deposits in the same area, now preserved at elevations of 6,300 to 6,600 feet, probably accumulated in fluvial channels feeding the ancient lake. Because of postdepositional erosion the western limits of the lacustrine deposition of the Bidahochi are unknown. The large tuff block at Tonalea probably could not have survived transport for more than a few miles at most, so a marginal lacustrine shelf area favorable for tuff accumulation probably was nearby. This shelf area may have included the west edge of Black Mesa about 3 miles east of Tonalea, and the high ground on the Kaibito Plateau 5–10 miles north and northwest of Tonalea. Subsequent erosion has removed all or most of the tuffaceous deposits that may have accumulated on shelves in this area, and therefore the eroded and redeposited block near Tonalea is one of the few preserved records west of Hopi Buttes of this stage of Pliocene lacustrine deposition, and is supporting evidence that the lacustrine basin, in which the Bidahochi Formation accumulated, originally extended some 80 miles northwest of its previously noted outcrops near Bidahochi.

M. E. Cooley (written commun., 1966) has noted the presence of the Tonalea outcrop and a few other locally preserved remnants which indicate that the Bidahochi Formation probably extended into the Tonalea area and westward nearly to Echo Cliffs. The channellike trough, in which the tuff blocks at Tonalea occur, probably was cut during the Black Point cycle of erosion, which followed deposition of the Bidahochi (Cooley and Akers, 1961; Cooley, written commun., 1966).

POSSIBLE ERUPTIVE SOURCE

The eruptive source of this and other tuffs in the Bidahochi Formation is unknown. However, the tuff is well dated paleontologically and also by isotope analysis. Constructive inferences may be made about the nature of the volcanic source and its probable location.

At White Cone Peak (near Bidahochi in Hopi Buttes) a land-mammal fauna, principally of beavers, just above the base of the White Cone Member of Shoemaker and others (1957) of the Bidahochi Formation (which equals the upper member) is at virtually the same stratigraphic level as the tuff. The fauna is Hemphillian provincial age of Wood and others (1941) (middle Pliocene age) or possibly early Blancan provincial age (late Pliocene age) of Wood and others (1941). A whole-rock potassium-argon isotope analysis indicates an age of 4.1 million years for a mafic lava flow from the volcanic member of the Bidahochi that is also nearly equivalent to the tuff (Evernden and others, 1964, p. 164, 190). The whole-rock isotope age determination, which depends on the retention of argon in feldspar crystals less than 0.03 mm long, is considered by Evernden and his colleagues as a minimum age; the true age may be as much as several million years greater.

Eolian crossbeds in the upper member of the Bidahochi Formation indicate that the prevailing wind direction then as now was from the southwest (Cooley and others, 1969); accordingly the eruptive center most probably was to the southwest—in southwestern Arizona, southeastern California, or northern Baja California.

The source is estimated to have been 50 to 500 miles from the Tonalea and Sanders localities because of the fineness of the vitric shards (predominantly less than $\frac{1}{8}$ mm), the paucity and small size of the volcanic feldspar crystals in the tuff (not more than 1 or 2 percent of the whole volume), and the textural similarity of the tuff at Tonalea to that at Sanders, which is 120 miles away. Median diameters of Tertiary and Quaternary ash falls were plotted as a function of distance from source by Fisher (1966, fig. 3, p. 710); tuffs 25 to 500 miles from their source had median diameters of $\frac{1}{8}$ mm to $\frac{1}{32}$ mm. The original median diameter of the unaltered vitric shards in the tuff at Tonalea was probably much less than $\frac{1}{8}$ mm, suggesting that the tuff was airborne from a source more than 100 miles away.

The glass is rhyolitic as judged from the index of refraction (1.503), and from its water-free 73-percent-silica content calculated from an analysis published by Nutting (1943, p. 183). The original volume of this thick and, presumably, once-extensive tuff bed was huge. The source of the tuff was most probably a large rhyolitic caldera of mid-Pliocene age. None of the nearby igneous centers fit this description. The igneous rocks of the Hopi Buttes between Tonalea and Sanders are ultramafic and mafic-alkalic rather than rhyolitic. The San Francisco volcanic field, about 100 miles southwest, consists primarily of mafic lavas with some limited amounts of intermediate rocks, but no large centers of rhyolitic volcanism.

The Thirteen Mile Rock (Hackberry Mountain) volcanic pile, about 150 miles southwest of Sanders, is probably the type of large center from which the tuff in the Bidahochi Formation was erupted (Sabels, 1960, 1962). However, the base of this pile has been dated by a potassium-argon determination on mica from a coarse tuff breccia as 14 million years old. It is unknown whether eruption associated with this center continued until deposition of the upper member of

the Bidahochi, about 4 to 8 million years ago. Other late Tertiary, but not precisely dated, centers of rhyolitic eruption are known throughout southwestern Arizona and adjacent States. Any of these may have been the source of the tuff in the Bidahochi Formation.

REFERENCES

Berman, Harry, Daly, R. A., and Spicer, H. C., 1942, Density at room temperature and 1 atmosphere, p. 7–26 *in* Birch, Francis, chm., Schairer, J. F., and Spicer, H. C., eds., Handbook of physical constants: Geol. Soc. America Spec. Paper 36, 325 p.

Cooley, M. E., and Akers, J. P., 1961, Ancient erosional cycles of the Little Colorado River, Arizona and New Mexico: Art. 237 *in* U.S. Geol. Survey Prof. Paper 424–C, p. C244–C248.

Cooley, M. E., and Davidson, E. S., 1963, The Mogollon Highlands—Their influence on Mesozoic and Cenozoic erosion and sedimentation: Arizona Geol. Soc. Digest, v. 6, p. 7–35.

Cooley, M. E., Harshbarger, J. W., Akers, J. P., and Hardt, W. F., 1969, Regional hydrogeology of the Navajo and Hopi Indian Reservations, Arizona, New Mexico, and Utah: U.S. Geol. Survey Prof. Paper 521–A, 61 p.

Evernden, J. F., Savage, D. E., Curtis, G. H., and James, G. T., 1964, Potassium-argon dates and the Cenozoic mammalian chronology of North America: Am. Jour. Sci., v. 262, no. 2, p. 145–198.

Fisher, R. V., 1966, Textural comparison of John Day volcanic siltstone with loess and volcanic ash: Jour. Sed. Petrology, v. 36, no. 3, p. 706–718.

George, W. O., 1924, The relation of the physical properties of natural glasses to their chemical composition: Jour. Geology, v. 32, no. 5, p. 353–372.

Kiersch, G. A., and Keller, W. D., 1955, Bleaching clay deposits, Sanders-Defiance Plateau district, Navajo country, Arizona: Econ. Geology, v. 50, no. 5, p. 469–494.

Munsell Color Company, Inc., 1954, Munsell soil color charts: Baltimore, Md., one volume, looseleaf [unpaged].

Nutting, P. G., 1943, Adsorbent clays, their distribution, properties, production, and uses: U.S. Geol. Survey Bull. 928–C, p. 127–221.

Repenning, C. A., and Irwin, J. H., 1954, Bidahochi formation of Arizona and New Mexico: Am. Assoc. Petroleum Geologists Bull., v. 38, no. 8, p. 1821–1826.

Sabels, B. E., 1960, Thermoluminescence correlation of rhyolitic tuffs [abs.]: Geol. Soc. America Bull., v. 71, no. 12, pt. 2, p. 1963.

——— 1962, Mogollon Rim volcanism and geochronology, *in* Weber, R. H., and Peirce, H. W., eds., Mogollon Rim region, east-central Arizona, Guidebook of the New Mexico Geol. Soc. 13th Field Conf., 1962: New Mexico Bur. Mines and Mineral Resources, p. 100–106.

Shoemaker, E. M., Hensley, F. S., Jr., and Hallogen, R. W., 1957, Diatremes on the Navajo and Hopi Reservations, Arizona: U.S. Geol. Survey TEI-690, p. 389–398, issued by U.S. Atomic Energy Comm. Tech. Inf. Service, Oak Ridge, Tenn.

Wood, H. E., 2d, and others, 1941, Nomenclature and correlation of the North American continental Tertiary: Geol. Soc. America Bull., v. 52, p. 1–48.

NEW LOCATIONS OF PLEISTOCENE (KANSAN) MOLLUSCAN AND OSTRACODE FAUNAS, DICKINSON COUNTY, KANSAS

By EDWIN D. GUTENTAG [1] and CARLOS GALLI-OLIVIER,[2]
Garden City, Kans., Lawrence, Kans.

Work done in cooperation with the State Geological Survey of Kansas and the Division of Water Resources of the Kansas State Board of Agriculture

Abstract.—Identification of the lithologic composition and faunal content of Pleistocene deposits at the Abilene and Chapman quarries indicates a Kansan age. The Pearlette Ash Member of the Sappa Formation found at the Abilene quarry is considered to be of late Kansan age. A study of the inferred habitats at the Abilene quarry shows a succession of habitats: (1) perennial stream, (2) lake or pond, (3) small pond with deposition of the ash, and (4) terrestrial. At Chapman the faunal data indicate aquatic habitats.

The Pleistocene deposits along the Smoky Hill River valley in Dickinson County, Kans., are extremely varied lithologically and spatially. These discontinuous and lithologically heterogeneous deposits are difficult to correlate without the aid of guide fossils or stratigraphic markers.

The purpose of this paper is to extend the knowledge of the early Pleistocene deposits in the region by describing the lithologic composition and faunal content of two quarries. The habitat preference of the contained fauna indicates the prevailing environmental conditions at the time that the associated sediments were deposited.

The Abilene quarry (fig. 1) is about 2.4 miles southeast of Abilene in the NW¼NE¼SW¼ sec. 26, T. 13 S., R. 2 E.; the Chapman quarry is about 2 miles east of Chapman in the SE¼SE¼ sec. 28, T. 12 S., R. 4 E., about 13 miles east-northeast of Abilene. These exposures were studied as part of a general reconnaissance of the Pleistocene deposits of the Smoky Hill River valley by Galli-Olivier.

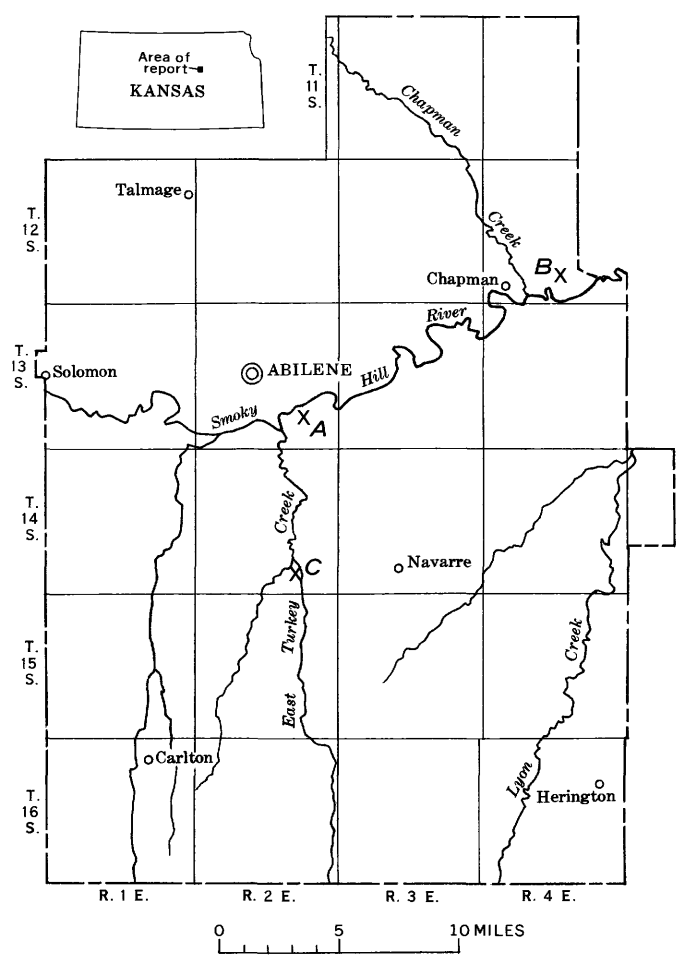

FIGURE 1.—Map of Dickinson County, Kans., showing locations of sites sampled. *A*, Abilene quarry; *B*, Chapman quarry; *C*, Turkey Creek site.

[1] U.S. Geological Survey.

[2] State Geological Survey of Kansas. Present address: Department of Geology, Wayne State University, Detroit, Mich. 48202.

Acknowledgments.—The authors wish to thank Messrs. C. K. Bayne and H. G. O'Connor, of the State Geological Survey of Kansas, and Mr. O. S. Fent, of Salina, Kans., for their suggestions and discussions concerning the Pleistocene deposits. Appreciation is expressed to Dr. Barry Miller, of Kent State University, for checking many of the gastropod identifications, and to Mrs. E. A. Waddell for preparing the microfossils for study.

The classification and nomenclature of the stratigraphic units used in this report are those of the U.S. Geological Survey and differ somewhat from those of the State Geological Survey of Kansas.

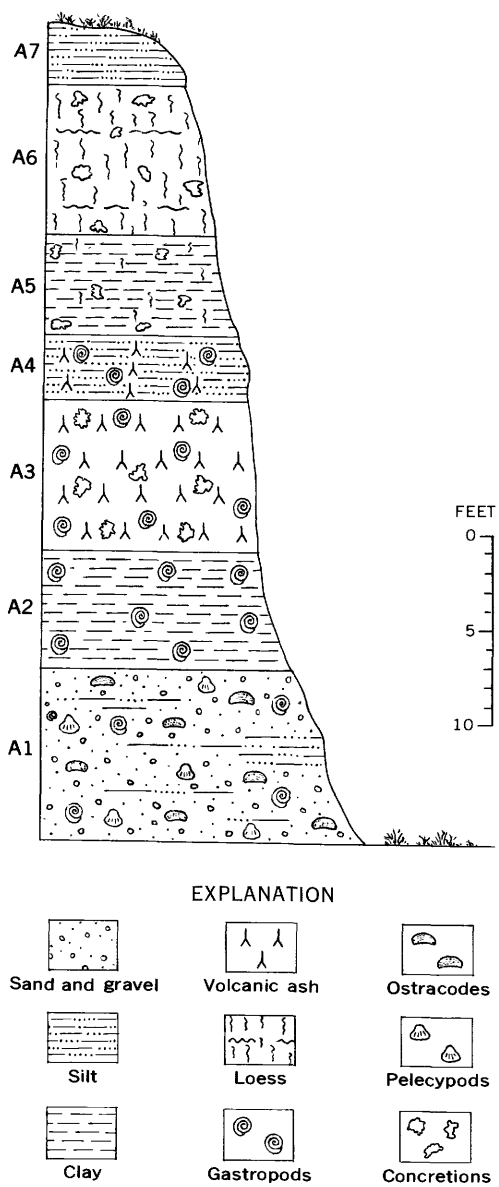

FIGURE 2.—Stratigraphic section of deposits of the Abilene quarry.

STRATIGRAPHIC RELATIONSHIP

Abilene quarry

The Pleistocene stratigraphic section of the Abilene quarry (fig. 2) described below was measured by Galli-Olivier in July 1968 on the walls of an inactive quarry in the NW¼NE¼SW¼ sec. 26, T. 13 S., R. 2 E., starting with the lowermost exposures of conglomerate and continuing into the next higher beds in adjacent walls.

Unit and description	*Thickness (feet)*
A7. Organic soil	Varied
A6. Silt (loess), yellowish-orange, friable; contains calcium carbonate concretions	8
A5. Clay, yellowish-brown, friable; contains calcium carbonate concretions	5
A4. Silt, ashy, very pale orange, friable, thin-bedded; contains calcium carbonate concretions; contains fossils (gastropods)	3. 5
A3. Ash, white, well-sorted, friable, thin-bedded, laminated; very fine angular shards; cut-and-fill structures on small scale, thinly cross laminated in parts; contains white rounded concretions of calcium carbonate in upper part; contains few fossils (gastropods); vertical walls	8
A2. Clay, yellowish-gray with moderate-brown stains, friable, thin-bedded; contains few subangular to subrounded pebbles of limestone, contains fossils (gastropods)	6
A1. Gravel, light-yellowish-gray, lenticular beds; yellowish-gray silt lenses; thinly crossbedded; weathers to vertical walls, includes fossils (gastropods, pelecypods, and ostracodes). Matrix is light yellowish gray, and consists of medium to coarse sand and fine gravel. Pebbles have maximum diameter of 6 centimeters, estimated mode of 5–7 millimeters; are mostly subangular to subrounded, a few very well rounded; surfaced with coating of calcium carbonate and limonite; composed of limestone (80 percent) and limonite sandstone, shale, siltstone, white opal and chert, crystalline quartz, and pink quartzite	9
Total	39. 5

The ash in unit A3 is correlated with the Pearlette Ash Member on the basis of the diagnostic properties of color, refractive index, and shard shape as described by Frye and others (1948). The ashy silt in unit A4 appears to contain reworked ash from the underlying unit.

Chapman quarry

The Pleistocene section of the Chapman quarry (fig. 3) described below was measured by Galli-Olivier in July 1968 on the walls of an active quarry in SE¼SE¼ sec. 28, T. 12 S., R. 4 E., beginning at the unconformable contact with a limestone of the Chase Group of Permian age.

Unit and description	Thickness (feet)
B6. Organic soil, grayish-black; contains white caliche in the lower part	4
B5. Clay, grayish-orange, moderate dry-strength; contains white hard concretions of caliche; caliche of the upper part is friable; weathered surfaces are split horizontally, possibly bedding planes; vertical joints are thinly coated by caliche and oxides of iron	12
B4. Clay, very-pale-orange to light-olive-gray, indurated, thinly laminated; lowermost part composed of 0.1 foot of green plastic clay; contains layer of white calcareous deposit; contains fossils (gastropods and pelecypods)	3
B3. Clayey silt, grayish-orange, sandy, indurated, massive, moderately plastic; sand grains fine to medium, rounded, some spherical and frosted; contains few pebbles and concretions of calcium carbonate	8
B2. Clayey silt, yellowish-red, poorly sorted, sandy, vertically jointed, moderate to high dry-strength, massive; contains fossils (ostracodes and gastropods); contains white rounded concretions, up to 8 centimeters thick, with associated limonite in the upper contact with unit B3	4.3
B1. Gravel, yellowish-orange, thin-bedded; in the upper part a yellowish-red sandy clay contains fossils and, at the upper contact with unit B2, white concretions of calcium carbonate, 3–4 cm thick. Matrix consists of yellowish-orange, very coarse sand to fine gravel. Pebbles have maximum diameter of 10–15 cm and estimated mode of 7 mm; angular to well rounded; some show luster; composed of limestone, sandstone, limonite, chert, quartz; contain fossils (gastropods, pelecypods, and ostracodes)	2.8
Total	34.1
Unconformity	
Limestone (Chase Group of Permian age)	

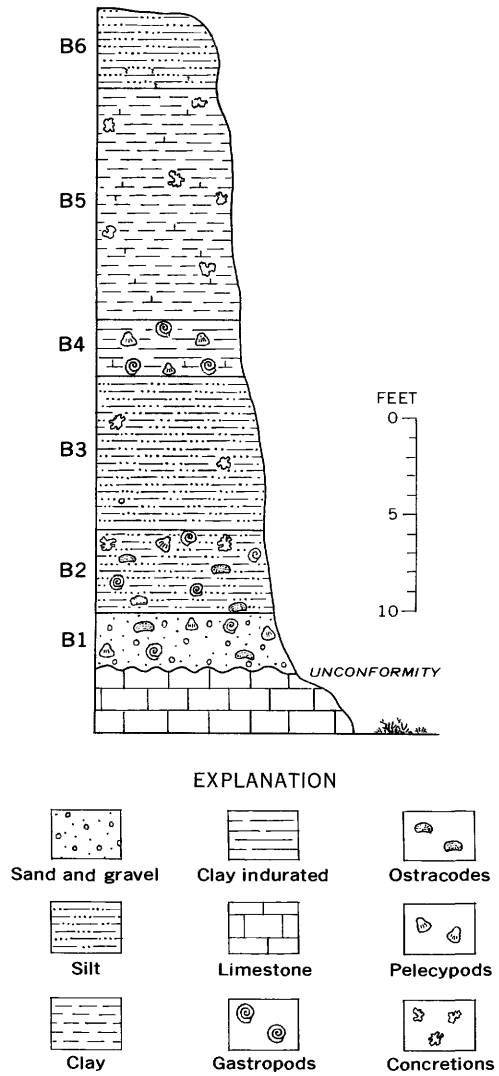

FIGURE 3.—Stratigraphic section of deposits of the Chapman quarry.

The measured sections at both quarries are Pleistocene deposits in terrace position. From lithologic data and stratigraphic position, unit A1 at the Abilene quarry seems to be equivalent to unit B1 at the Chapman quarry. A Kansan age is established at the Abilene quarry section by the presence of the Pearlette Ash Member (unit A3). At the Chapman quarry no such marker bed was found and, therefore, fossil data are the only useful tool.

AGE DETERMINATION

Index fossils of extinct invertebrates are rarely found in the Pleistocene deposits, and the useful vertebrate species are not widely distributed. However, some invertebrate and vertebrate species that exist unchanged from the Pleistocene to the present are used to reconstruct past environments because these species are restricted by climate and habitat. Beds that are lithologically distinct and areally widespread are generally used in stratigraphic dating. Where the marker bed is absent, the associated assemblage of species can serve to identify the stratigraphic unit. The fossil assemblage associated with the Pearlette Ash Member, a marker bed of unusually uniform lithology, serves to identify widely spread stratigraphic units.

Pearlette Ash Member

The Pearlette Ash Member is found in scattered localities in an area extending over eight states from Texas to South Dakota (Frye and Leonard, 1952). Leonard (1950) considered the Pearlette to represent Yarmouthian interglacial age and listed the mollusks

restricted to that period. However, in 1952 Frye and Leonard reported on mollusks restricted to Kansan glacial age that also included all the species previously listed by Leonard as indicative of Yarmouthian interglacial age.

Hibbard (1949a) considered the vertebrates of the Cudahy fauna, which is found in association with the Pearlette Ash, to be boreal, thus indicating a closing phase of a glacial age. In Meade County, Kans., the Borchers interglacial fauna of Yarmouthian age lies above weathered Pearlette Ash. Because of the great compositional difference between the Cudahy glacial and the Borchers interglacial faunas, Hibbard (1954) stated that considerable time elapsed after deposition of the ash and before deposition of the silts and clays containing the Borchers fauna. Swineford (1963) considered the deposition of the Pearlette Ash to represent a moment of time, perhaps a period of 3 days occurring during late Kansan time.

The association of the ostracode fauna with the Pearlette Ash was studied at four localities by Benson (1967). He differentiated two faunas associated with the Pearlette Ash; the one above the ash was considered as Yarmouthian; the one below the ash was considered as late Kansan. Benson's analysis was based on the suggestion by Jewett (1963) to place the Pearlette Ash Member arbitrarily at the boundary between Kansan glaciation and Yarmouthian interglaciation. In view of Swineford's concept of Pearlette Ash deposition occurring possibly over a few days and the fact that boreal vertebrates occur in the Cudahy fauna, it would be most fortuitous that the ash fall would correspond with the Kansan-Yarmouthian time line. The disruption of the normal ecologic succession of the pond fauna can be attributed to the catastrophic ash fall and not to a warming of the climate.

Molluscan fauna

In Dickinson County the occurrence of the Pearlette Ash Member and its associated molluscan fauna was reported by Leonard (1950) and Ho and Leonard (1961) from the roadcut exposure along East Turkey Creek in the SW¼SW¼SW¼ sec. 26, T. 14 S., R. 2 E. This site is located on a tributary of the Smoky Hill River and is about 6 miles south of the Abilene quarry (fig. 1).

Frye and Leonard (1952) reported 23 species of mollusks from the Turkey Creek site. Table 1 compares the Chapman and Abilene molluscan faunas to those from the Turkey Creek site. The faunal list has been amended with respect to synomyny changes given by Taylor (1960), Hibbard and Taylor (1960), and Miller (1966). The changes are summarized as follows:

Carychium perexiguum Baker=*C. exiguum* (Say)
Gyraulus labiatus Leonard=*G. parvus* (Say)
Menetus pearlettei Leonard=*Promenetus exacuous kansasensis* (Baker)
Planorbula vulcanata Leonard=*P. armigera* (Say)

TABLE 1.—*Comparison of molluscan faunas from Turkey Creek, Chapman, and Abilene sites, Dickinson County, Kans.*

[×, species present]

Molluscan species from Turkey Creek site [1]	Chapman site			Abilene site			
	B1	B2	B4	A1	A2	A3	A4
Carychium exiguum (Say)							
Euconulus fulvus (Müller)							
Gastrocopta armifera (Say)	×				×	×	
contracta (Say)							
tappaniana (C. B. Adams).							
Gyraulus parvus (Say)	×		×	×			
Hawaiia minuscula (Binney).		×		×	×		×
Helicodiscus parallelus (Say).		×				×	×
Helisoma trivolvis (Say)							
Lymnaea palustris (Müller)				×			
Oxyloma navarrei Leonard.							
Physa sp							
Planorbula armigera (Say)							
Promatiopsis cincinnatiensis (Lea).							
Promenetus exacuous kansasensis (Baker).	×	×					
umbilicatellus (Cockerell)							
Vallonia gracilicosta (Reinhardt).	×	×		×			×
pulchella (Müller)				×			
Valvata lewisi (Currier)							
Vertigo milium (Gould)							
ovata (Say)							
tridentata (Wolf)							
Zonitoides arboreus (Say)							

[1] Frye and Leonard (1952).

The three molluscan sites in Dickinson County have been compared with respect to species contained in common and are summarized in tables 1 and 4. The Chapman site has 6 species out of a total of 13 conspecific with those of the Turkey Creek site, whereas the Abilene site has 7 species out of 19 conspecific with those of the Turkey Creek site. The Chapman site has 10 species conspecific with those of the Abilene site. These data from tables 1 and 4 can be used to determine the taxonomic similarity, T, by the equation

$$T=\frac{100C}{N}$$

where C is the number of species common to two faunas, and N is the number of species in the smaller fauna.

The indices of faunal similarity (table 2) reveal that the Abilene and Chapman sites are markedly similar to each other. When the indices are compared, the Chapman site is more similar to the Turkey Creek site than is the Abilene site.

TABLE 2.—*Taxonomic similarity indices, T, of molluscan faunas from sites in Dickinson County, Kans.*

	Turkey Creek	Chapman	Abilene
Turkey Creek ($N=23$)		46	37
Chapman ($N=13$)	46		77
Abilene ($N=19$)	37	77	

On the basis of the contained molluscan fauna alone (the Pearlette Ash is not present at the Chapman site), the Chapman site has more affinity with the Abilene site and less affinity with the Turkey Creek site and is judged to be of Kansan age.

Ostracode fauna

Ostracodes are found in deposits of Pleistocene age throughout much of the High Plains and have been used to date some of these deposits (Gutentag and Benson, 1962; Gutentag, 1963). Benson (1967) described the ostracodes from 1 foot above and 1 foot below the Pearlette Ash at SW¼SW¼SW¼ sec. 26, T. 14 S., R. 2 E., at approximately the same place as Leonard's Turkey Creek molluscan site.

Benson (1967) reported four species of ostracodes from below the ash and seven species from above the ash. Table 3 compares the Chapman and Abilene ostracode faunas to those from the two zones at Turkey Creek. Additional ostracodes not found at Turkey Creek are shown in table 4.

TABLE 3.—*Comparison of ostracode faunas from Turkey Creek, Chapman, and Abilene sites, Dickinson County, Kans.*

[Except for totals, the presence of species is shown by × or expressed in percent]

	Turkey Creek		Chapman		Abilene	
	Below ash [1]	Above ash	B1	B2	A1	A2
Candona simpsoni Sharpe	65	-----	×	×	×	----
renoensis Gutentag and Benson.	-----	4	----	----	×	----
Ilyocypris gibba (Ramdohr)	-----	1	----	----	----	×
Physocypria pustulosa (Sharpe)	25	3	----	----	----	----
Cypricercus tuberculatus (Sharpe).	×	15	----	----	----	----
Cypridopsis vidua (O. F. Müller).	×	43	----	×	----	----
Cyprinotus sp.	-----	34	----	----	----	----
Uncertain cyprid	-----	×	----	----	----	----
Total specimens	20	829	4	12	14	6

[1] From Benson (1967, table 1, p. 236).

Candona simpsoni is considered by Benson to characterize the fauna below the ash. In the Abilene quarry (fig. 2 and table 3) unit A1 contained *Candona simpsoni* stratigraphically below the Pearlette Ash of unit A3. In the Chapman section (fig. 3 and table 3) where ash is not present, units B1 and B2 contained *Candona simpsoni*. Species considered by Benson as representative of the fauna commonly found above the ash are not present at either site. On the basis of contained ostracodes, the Chapman section is believed to be pre-Pearlette Ash and Kansan in age.

HABITAT

Mollusks and ostracodes have been used as a basis for inferring the prevailing climatic conditions at the time the associated sediments were deposited. It is generally assumed that climate is a primary factor in the distribution of nonmarine species and that the habitat preference of the species remains the same throughout their span of existence. The habitat requirements of the fauna summarized in table 4 are taken from Miller (1966) for similar species in the southern Great Plains. Ecologic data for living ostracodes are not as well known as for the mollusks. The ostracodes may represent both the perennial- and shallow-water habitats, but for convenience they have been included with the perennial-water habitat. It should be noted that both the ecologic requirements of extant members of the same species and the lithologic data are used to reconstruct the past habitats. If additional large-scale collecting such as practiced by Hibbard (1949b) is made at these sites, the habitats given in this paper could be subject to revision.

At the Abilene quarry, the sand and gravel unit A1 (fig. 2) indicates a combination of aquatic habitats—a permanent aggrading stream, shallower water near shore, and tributaries carrying in debris from nearby terrestrial habitats. The clay of unit A2 indicates an aquatic habitat of a lake or pond with a mud substrate bordered by grass and woodland near shore. The Pearlette Ash of unit A3 indicates a small pond with moist area and the woodland habitats on the edge. The ashy silt of unit A4 represents the terrestrial habitats of a moist area under organic litter and the almost dry habitat of truly terrestrial forms.

At the Chapman quarry, the fossil assemblage of the sand-and-gravel unit B1 (fig. 3) represents two aquatic habitats: a permanent moving aggrading stream and shallower water near shore. The terrestrial elements are from the near-shore woodland, grass, and dampground habitats. The faunas from the silt of unit B2 indicate an aquatic habitat of shallow quiet water near the shore of a small lake. The edge of the lake prob-

TABLE 4.—*Habitat and occurrence of molluscan and ostracode faunas in Chapman and Abilene sites, Dickinson County, Kans.* [×, species present]

Habitat	Species [1]	Chapman site			Abilene site			
		B1	B2	B4	A1	A2	A3	A4
Woodland: moist area under leaf litter, down timber, or in tall marsh grass.	*Cionella lubrica* (Müller)	×				×		
	Discus cronkhitei (Newcomb)		×		×			×
	Helicodiscus parallelus (Say)		×				×	×
	Nesovitrea electrina (Gould)				×			
Sheltered: 1.—In rocks, scrubs, grass, or in timbered areas.	*Gastrocopta armifera* (Say)	×				×	×	
2.—Species not restricted to a woodland habitat; can tolerate drier conditions.	*Helicodiscus singleyanus* (Pilsbry)							×
	Hawaiia minuscula (Binney)		×		×	×		×
	Pupoides albilabris (Adams)						×	
	Vallonia gracilicosta Reinhardt	×	×		×			×
	pulchella (Müller)				×			×
Marginal: wet mud, sticks, stones, or other debris along water's edge; shallow pools and other protected spots.	*Hendersonia occulta* (Say)					×		
Shallow quiet water: small ponds, streams, sloughs, or marsh with no current; or areas of rooted vegetation with little current; soft sand or mud bottoms; not subject to significant seasonal drying.	*Gyraulus parvus* (Say)	×		×	×			
	Amnicola limosa Lea	×	×		×			
	Physa anatina Lea				×		×	
	Promenetus exacuous (Say)	×	×					
	Lymnaea palustris (Müller)				×			
	**Pisidium casertanum* (Poli)	×						
	**Sphaerium transversum* (Say)				×			
Perennial water: streams or lakes with slow to moderate current; areas of still water; shallow spots with soft sand or mud substrate; not affected by seasonal drying.	*Helisoma anceps* (Menke)	×			×			
	Valvata tricarinata (Say)	×						
	**Pisidium compressum* Prime	×		×	×			
	**Spaerium striatinum* (Lamarck)				×			
	***Candona acuta* Hoff		×					
	** cf. *C. lactea* Baird				×	×		
	** *nyensis* Gutentag and Benson				×			
	** *renoensis* Gutentag and Benson				×			
	** *simpsoni* Sharpe	×	×		×			
	** *truncata* Furtos				×			
	***Cypricercus* cf. *C. reticulatus* (Zaddach)				×			
	** *vidua* (O. F. Müller)		×					
	***Ilyocypris gibba* (Ramdohr)					×		
	***Limnocythere reticulata* (Sharpe)				×			
	Total	11	9	2	20	6	4	6

[1] All are gastropods except as indicated otherwise: single asterisk (*), pelecypod; double asterisk (**), ostracode.

ably contained grass and brush. The indurated clay of unit B4 represents a small lake deposit with vegetation containing a sparse molluscan fauna.

CONCLUSIONS

At the Abilene quarry, faunal evidence and the presence of the Pearlette Ash Member of the Sappa Formation clearly indicate a Kansan age for the Pleistocene deposits. The Abilene quarry shows a succession from aquatic to terrestrial habitats as follows:

1. A perennial aggrading stream, shallower water near shore, and small tributaries carrying debris from nearby terrestrial sites of unit A1 (fig. 2).
2. A lake or pond with a mud substrate bordered by grass and woodland on the shore of unit A2.
3. A small pond with moist areas and woodland on the edges that was abruptly filled by the Pearlette Ash of unit A3.
4. A moist to almost dry terrestrial habitat as shown by the probable windblown ashy silt of unit A4.

At the Chapman quarry the Kansan age of the Pleistocene deposits is established by the contained fauna. The ostracodes indicate a pre-Pearlette Ash age for units B1 and B2 (fig. 3). The aquatic habitats at the Chapman site indicate a change from a permanent perennial stream with shallow water near shore of unit B1 to a small lake of unit B2. After the deposition of an unfossiliferous clayey silt, which may indicate windblown deposits and possible soil development of unit B3, a small lake developed with a mud substrate shown by unit B4.

REFERENCES

Benson, R. H., 1967, Muscle-scar patterns of Pleistocene (Kansan) ostracodes, *in* Essays in paleontology and stratigraphy: Kans. Univ. Dept. Geology Spec. Pub. 2, p. 211–241.

Frye, J. C., and Leonard, A. B., 1952, Pleistocene geology of Kansas: Kansas Geol. Survey Bull. 99, 230 p.

Frye, J. C., Swineford, Ada, and Leonard, A. B., 1948, Correlation of Pleistocene deposits of the central High Plains with the glacial section: Jour. Geology, v. 56, no. 6, p. 501–525.

Gutentag, E. D., 1963, Studies of the Pleistocene and Pliocene deposits in southwestern Kansas: Kansas Acad. Sci. Trans., v. 66, no. 4, p. 606–621.

Gutentag, E. D., and Benson, R. H., 1962, Neogene (Plio-Pleistocene) freshwater ostracodes from the central High Plains: Kansas Geol. Survey Bull. 157, pt. 4, 60 p.

Hibbard, C. W., 1949a, Pleistocene vertebrate paleontology in North America: Geol. Soc. America Bull., v. 60, p. 1417–1428.

——— 1949b, Techniques of collecting microvertebrate fossils: Michigan Univ. Mus. Paleontology Contr., v. 8, no. 2, p. 7–19.

Hibbard, C. W., 1954, A new *Synaptomys*, an addition to the Borchers interglacial (Yarmouth?) fauna: Jour. Mammalogy, v. 35, no. 2, p. 249–252.

Hibbard, C. W., and Taylor, D. W., 1960, Two late Pleistocene faunas from southwestern Kansas: Michigan Univ. Mus. Paleontology Contr., v. 16, no. 1, p. 1–223.

Ho, T. Y., and Leonard, A. B., 1961, Two new strobilopids from the Pleistocene of the High Plains: Nautilus, v. 75, no. 2, p. 43–49.

Jewett, J. M., 1963, Pleistocene geology in Kansas: Kansas Acad. Sci. Trans., v. 66, p. 347–358.

Leonard, A. B., 1950, A Yarmouthian molluscan fauna in the mid-continent region of the United States: Kansas Univ. Paleont. Contr., Mollusca, art. 3, 48 p.

Miller, B. B., 1966, Five Illinoian molluscan faunas from the southern Great Plains: Malacologia, v. 4, no. 1, p. 173–260.

Swineford, Ada, 1963, The Pearlette ash as a stratigraphic marker: Kansas Acad. Sci. Trans., v. 66, no. 3, p. 359–362.

Taylor, D. W., 1960, Late Cenozoic molluscan faunas from the High Plains: U.S. Geol. Survey Prof. Paper 337, 94 p.

CYTHEREIS EAGLEFORDENSIS ALEXANDER, 1929—A GUIDE FOSSIL FOR DEPOSITS OF LATEST CENOMANIAN AGE IN THE WESTERN INTERIOR AND GULF COAST REGIONS OF THE UNITED STATES

By JOSEPH E. HAZEL, Washington, D.C.

Abstract.—The ostracode *Cythereis eaglefordensis* Alexander, 1929, has been found in the middle part of the Britton Formation of Moreman (*in* W. S. Adkins, 1933) in Texas, the lower part of the Tropic Shale in Utah, the upper part of the Graneros Shale in New Mexico, the Greenhorn Limestone in South Dakota, and in the lower part of the subsurface Atkinson Formation of the Georgia-Florida area. Its Texas and Western Interior occurrences are consistent with the range zones of the ammonites *Sciponoceras gracile* and *Metoicoceras whitei*. The species appears, therefore, to be a useful biostratigraphic indicator for deposits of middle Eagle Ford age (latest Cenomanian). Its occurrence in the lower part of the Atkinson Formation, where ammonites are absent, indicates a middle Eagle Ford (middle Britton Formation) age for at least part of the lower Atkinson (the "Barlow fauna"), rather than a Woodbine age as has been previously suggested.

The distinctive ostracode species *Cythereis eaglefordensis* was described by Alexander (1929) from three localities in the Britton Formation of Moreman (*in* Adkins, 1933) of the Eagle Ford Group of Murray (1961) of north-central Texas (figs. 1 and 2). From the data given in Alexander (1929), Moreman (1927, 1942), Adkins (1933), and Adkins and Lozo (1951), Alexander's localities are all in the middle part of the Britton Formation in Moreman's zone of *Metoicoceras whitei* and his *Eucalycoceras bentonianum* subzone of the *Metoicoceras irwini* zone. Moreman's *Metoicoceras whitei* zone seems to equate with the *Romaniceras-Metoicoceras whitei* zone of Adkins (1933) and the *Metaptychoceras-Worthoceras* zone of Adkins and Lozo (1951). The *Eucalycoceras bentonianum-Mantelliceras* n. sp. zone of Adkins and Lozo (1951) and the *Eucalycoceras bentonianum-Borissiakoceras* zone of Adkins (1933).

The assemblage of ammonites and inocerami (particularly *Sciponoceras gracile*, *Metoicoceras whitei*, and *Inoceramus pictus* (= *I. fragilis* of Moreman, 1942)) illustrated and (or) listed from the forementioned zones by the authors cited suggests equivalency of these zones with the well-known *Sciponoceras gracile* zone of the Western Interior. Moreman (1942) considered the Britton to be lower Turonian. Adkins and Lozo (1951) placed the Cenomanian-Turonian boundary at the top of their *Neocardioceras* zone. On the basis of the occurrences of *Sciponoceras gracile* given by Adkins (1933) and Moreman (1942), the top of the *Neocardioceras* zone of Adkins and Lozo would be about in the middle of the local range zone of *Sciponoceras gracile* in the Britton Formation. Cobban and Reeside (1952) placed the *Sciponoceras gracile* zone in the Western Interior in the lower Turonian. On the basis of planktonic foraminifers, Pessagno (1967) placed the middle part of the Britton Formation at the top of the Cenomanian in the *Rotalipora cushmani-R. greenhornensis* zone. This interpretation is followed herein.

Acknowledgments.—I am grateful to E. G. Kauffman, of the Smithsonian Institution, and J. F. Mello and K. N. Sachs, Jr., of the U.S. Geological Survey, for critically reading the manuscript. D. L. Eicher, of the University of Colorado, kindly provided the Greenhorn Limestone samples.

WESTERN INTERIOR OCCURRENCES

Specimens of *Cythereis eaglefordensis* were found within the *Sciponoceras gracile* zone in the lower part of the Tropic Shale (locality *D* of fig. 1) of the Kaiparowits region of Utah. (See Swensen, 1962, for a discussion of the macrofauna of the Tropic Shale.) *Cythereis eaglefordensis* occurs in six samples from the Greenhorn Limestone of the northern Black Hills near Belle Fourche, S. Dak. (locality *F* of fig. 1; lithic units 3, 4, and 5 of Fox, 1954, p. 100). Cobban (1951) reports

359-403 O—69——11

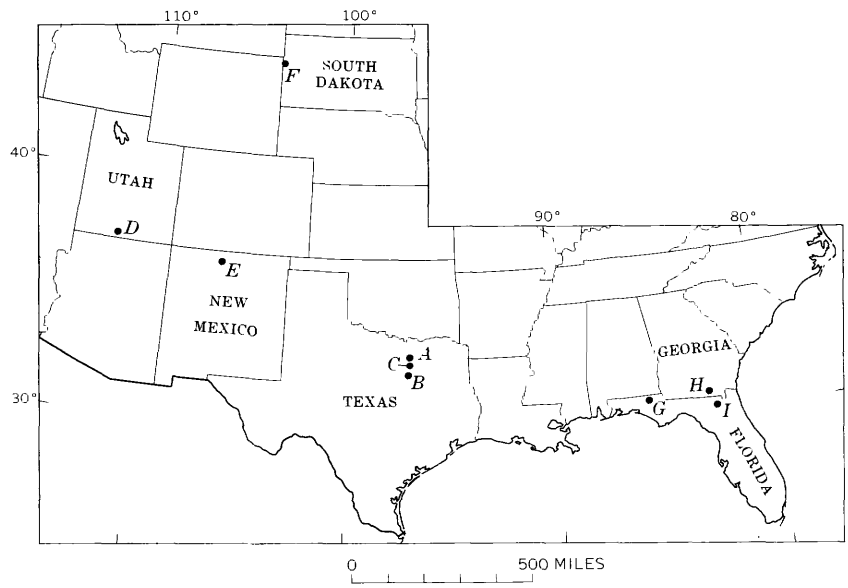

FIGURE 1.—Known geographic distribution of *Cythereis eaglefordensis* Alexander, 1929. Localities *A*, *B*, and *C* are localities 38, 39, and 40, respectively, of Alexander (1929); they are in the middle part of the Britton Formation in Denton, Ellis, and Dallas Counties, Tex. Locality *D* is in the lower part of the Tropic Shale, center N½SE¼ sec. 11, T. 43 S., R. 2 E., Nipple Butte quadrangle, Kane County, Utah; shale in exposures near dirt road about one-half mile east of Glen Canyon City, 30 feet above the base of the Tropic Shale (collected by Fred Peterson). Locality *E* is in the upper part of the Graneros Shale in Rio Arriba County, N. Mex. (locality 20 of Dane, 1960a, b). Locality *F* represents six samples collected from the Greenhorn Limestone near Belle Fourche, S. Dak. (units 3, 4, and 5 of Fox, 1954, p. 100; collected by D. L. Eicher). Localities *G*, *H*, and *I* are subsurface intervals in the lower Atkinson Formation in Jackson County, Fla., Echols County, Ga., and Suwannee County, Fla.; the locations of the wells and occurrences of *Cythereis eaglefordensis* are given in Swain and Brown (1964, p. 6–8).

Metoicoceras whitei and *Sciponoceras gracile* from the Greenhorn of the northern Black Hills.

These occurrences of *Cythereis eaglefordensis* in the Western Interior suggest that this microfossil is an indicator for the *Sciponoceras gracile* zone and valuable for determining this interval in areas where ammonites and inocerami are absent.

Elsewhere in the Western Interior, *Cythereis eaglefordensis* has been identified in a sample from the upper part of the Graneros Shale of Rio Arriba County, N. Mex. (locality *E* of fig. 1, this report; and locality 20 of Dane, 1960a, b), suggesting a *Sciponoceras gracile* age for this part of the Graneros in this area.

FLORIDA AND GEORGIA OCCURRENCES

In addition to the Texas localities for *Cythereis eaglefordensis* given by Alexander (1929), Swain and Brown (1964) have found the species in the subsurface of northern Florida and southern Georgia (fig. 1). The occurrences are in the lower part of the Atkinson Formation in the so-called Barlow fauna (the new biofacies of Applin, 1955). This part of the Atkinson Formation has been considered to be of Woodbine (middle Cenomanian) age by Applin (1955) and Applin and Applin (1967). However, the presence of *Cythereis eaglefordensis* indicates that the Barlow fauna part of the Atkinson correlates with the middle part of the Britton Formation of Texas and is late Cenomanian (*Sciponoceras gracile* zone) in age. This interpretation is corroborated by the presence of the planktonic foraminifer *Rotalipora cushmani* in the Barlow fauna (Applin, 1955, p. 196) which is a worldwide upper Cenomanian marker (Pessagno, 1967).

SUMMARY

The occurrences of the trachyleberidid ostracode *Cythereis eaglefordensis* with ammonites and inocerami of the *Sciponoceras gracile* zone suggest that this species is an indicator of that zone and that it is useful in determining that biostratigraphic level in areas where macrofossils are absent or not common. The presence of *Cythereis eaglefordensis* in the upper part of the Graneros Shale of Rio Arriba County, N. Mex., suggests that the upper part of the Graneros Shale (of Dane, 1960a, b) in New Mexico is younger

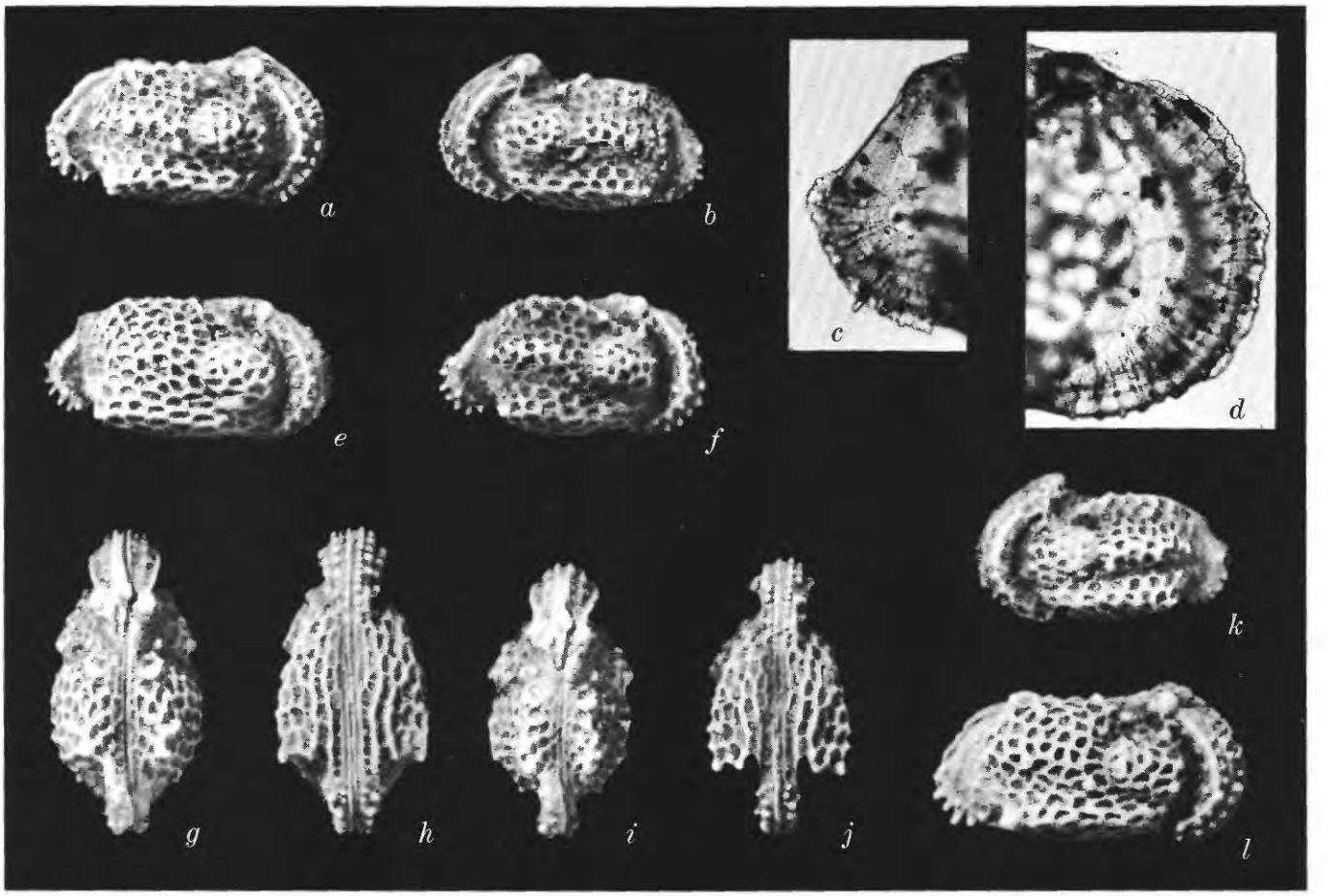

FIGURE 2.—*Cythereis eaglefordensis* Alexander, 1929. *a*, right lateral view female carapace, USNM 155237, Alexander's (1929) locality 39, Britton Formation, Ellis County, Tex., × 50. *b*, left lateral view female carapace, USNM 155240, lower part of Tropic Shale, Kane County, Utah (locality *D* in fig. 2), × 50. *c*, right lateral view posterior part of female valve, USNM 155238, Greenhorn Limestone near Belle Fourche, S. Dak. (rock unit 3 of Fox, 1954, p. 100), × 125. *d*, anterior part of same specimen as *c*, × 125. *e*, right lateral view female valve, USNM 162052, same locality as *d*, × 50. *f*, right lateral view female valve, USNM 132455, lower Atkinson Formation, Echols County, Ga., hypotype of Swain and Brown (1964), × 50. *g*, dorsal view male carapace, USNM 155236, same locality as *a*, × 50. *h*, ventral view same specimen as *g*, × 50. *i*, dorsal view same specimen as *a*, × 50. *j*, ventral view same specimen as *a*, × 50. *k*, left lateral view female valve, USNM 155239, same locality as *b*, × 50. *l*, right lateral view same specimen as *g*, × 50.

than the Graneros of the Colorado Front Range. The so-called Barlow fauna of the subsurface lower Atkinson Formation of Florida and Georgia contains *Cythereis eaglefordensis* which suggests a middle Eagle Ford (Britton Formation) rather than Woodbine age for that part of the lower Atkinson.

REFERENCES

Adkins, W. S., 1933, The geology of Texas; part 2, The Mesozoic systems in Texas: Texas Univ. Bull. 3232, p. 239–518.

Adkins, W. S., and Lozo, F. E., 1951, Stratigraphy of the Woodbine and Eagle Ford, Waco area, Texas, *in* Lozo, F. E., and Perkins, B. F., eds., The Woodbine and adjacent strata of the Waco area of central Texas, a symposium: Fondren Sci. Ser., no. 4, p. 101–164.

Alexander, C. I., 1929, Ostracoda of the Cretaceous of north Texas: Texas Univ. Bull. 2907, 137 p.

Applin, E. R., 1955, A biofacies of Woodbine age in the southeastern Gulf Coast region: U.S. Geol. Survey Prof. Paper 264-I, p. 187–197.

Applin, P. L., and Applin, E. R., 1967, The Gulf Series in the subsurface in northern Florida and southern Georgia: U.S. Geol. Survey Prof. Paper 524–G, 35 p.

Cobban, W. A., 1951, Colorado shale of central and northwestern Montana and equivalent rocks of Black Hills: Am. Assoc. Petroleum Geologists Bull., v. 35, no. 10, p. 2170–2198.

Cobban, W. A., and Reeside, J. B., Jr., 1952, Correlation of the Cretaceous formations of the Western Interior of the United States: Geol. Soc. America Bull., v. 63, no. 10, p. 1011–1044.

Dane, C. H., 1960a, The Dakota sandstone and Mancos shale of the eastern side of San Juan Basin, New Mexico, *in* Beaumont, E. C., and Read, C. B., eds., Guidebook of Rio Chama Country, 11th field conference, October 14–15, 1960: New Mexico Geol. Soc., p. 67–74.

Dane, C. H., 1960b, The boundary between rocks of Carlile and Niobrara age in San Juan Basin, New Mexico and Colorado: Am. Jour. Sci., v. 258-A (Bradley Volume), p. 46–56.

Fox, S. K., 1954, Cretaceous Foraminifera from the Greenhorn, Carlile, and Cody formatiaons, South Dakota, Wyoming: U.S. Geol. Survey Prof. Paper 254–E, p. 97–124.

Moreman, W. L., 1927, Fossil zones of the Eagle Ford of north Texas: Jour. Paleontology, v. 1, no. 1, p. 89–101.

——— 1942, Paleontology of the Eagle Ford group of north and central Texas: Jour. Paleontology, v. 16, no. 2, p. 192–220.

Murray, G. E., 1961, Geology of the Atlantic and Gulf coastal province of North America: New York, Harper and Brothers, 692 p.

Pessagno, E. A., Jr., 1967, Upper Cretaceous planktonic Foraminifera from the western Gulf Coastal Plain: Palaeontographica Americana, v. 5, no. 37, p. 245–445.

Swain, F. M., and Brown, P. M., 1964, Cretaceous Ostracoda from wells in the southeastern United States: North Carolina Div. Mineral Resources Bull. 78, 55 p.

Swensen, A. J., 1962, Anisoceratidae and Hamitidae (Ammonoidea) from the Cretaceous of Texas and Utah: Brigham Young Univ. Geology Studies, v. 9, pt. 2, p. 53–82.

NEGATIVE AEROMAGNETIC ANOMALIES OVER MINERALIZED AREAS OF THE BOULDER BATHOLITH, MONTANA

By W. F. HANNA, Menlo Park, Calif.

Abstract.—Aeromagnetic and rock magnetic studies in the Boulder batholith area indicate that several negative anomalies are associated with weakly magnetized plutonic and volcanic rocks, normally polarized, in contact with more highly magnetic plutonic rocks, also normally polarized. The amplitudes and extents of the magnetic lows, as well as their locations relative to surface geology, suggest that considerable volumes of batholithic rocks and lesser quantities of overlying volcanic rocks have been intruded by felsic bodies and silica-rich veins containing, in part, metalliferous mineral deposits. The weak magnetizations of these rocks are attributed to a depletion of iron oxides by magmatic differentiation and to hydrothermal alteration of magnetic iron oxides to more highly oxidized and hydrated nonmagnetic iron oxides within the intruded rocks.

The Boulder batholith area in southwestern Montana is underlain by Precambrian to upper Mesozoic sedimentary, metamorphic, and volcanic rocks that were intruded by late Mesozoic plutonic rocks and covered, in places, by Cenozoic volcanic and sedimentary rocks (fig. 1). Most igneous rocks in the area belong to one of three units: (1) the Cretaceous Elkhorn Mountains Volcanics, consisting of epiclastic and pyroclastic rocks, hypabyssal intrusives, and flows (Klepper and others, 1957; Smedes, 1966); (2) the Cretaceous Boulder batholith, consisting of plutons ranging from alaskite to gabbro, but composed mainly of quartz monzonite and granodiorite (Knopf, 1957; Knopf, 1964; Smedes and others, 1968; Tilling and others, 1968); and (3) the Eocene Lowland Creek Volcanics, consisting mainly of quartz latite and rhyolite (Smedes, 1962; Smedes and Thomas, 1965).

Several mineralized zones in the igneous rock complex are marked by active and former mining districts in and along the margin of the batholith. Although copper deposits at Butte are the most outstanding example of metalliferous mineralization, considerable quantities of silver, gold, copper, lead, zinc, and manganese ores have been produced in the area during bursts of mining activity over a 100-year period. Most economic mineral occurrences are concentrated in silica-rich veins of hydrothermal origin.

As an aid to interpreting subsurface geology in the Boulder batholith area, an aeromagnetic survey (Johnson and others, 1965) was made by the U.S. Geological Survey. The aeromagnetic survey was controlled by east-west flight paths spaced 1½ miles apart at a barometric elevation of 10,500 feet. A residual total intensity magnetic map (fig. 2) indicates that the batholith and associated volcanic rocks are in a major anomalous area 70 miles long and 35 miles wide. Edges of this northeast-trending anomalous area are characterized by local gradients of up to 100 gammas per mile, especially near contacts of batholithic and volcanic rocks with pre-Cretaceous and Cenozoic sedimentary rocks.

Of further importance to the geologic interpretation are gravity data compiled by Burfeind (1967) and Biehler and Bonini (1966). Results of this work show that a broad gravity low occurs over the batholith in approximate coincidence with the regional total magnetic intensity high. Other gravity features will be discussed later in the text.

NEGATIVE MAGNETIC ANOMALIES

Superposed on the generally high magnetic plateau associated with the Boulder batholith and neighboring volcanic rocks is a conspicuous series of negative magnetic anomalies near the center of the map area, extending from Wickes southwestward to Butte. Strong negative closures of 200 to 300 gammas within this series occur 1 mile northwest of Wickes, 3 miles northwest of Basin, 3 miles northwest of Elk Park, and at Butte. A fifth negative anomaly, displaced somewhat toward the northwest side of the belt, is centered 10 miles northwest of Butte. Other conspicuous negative

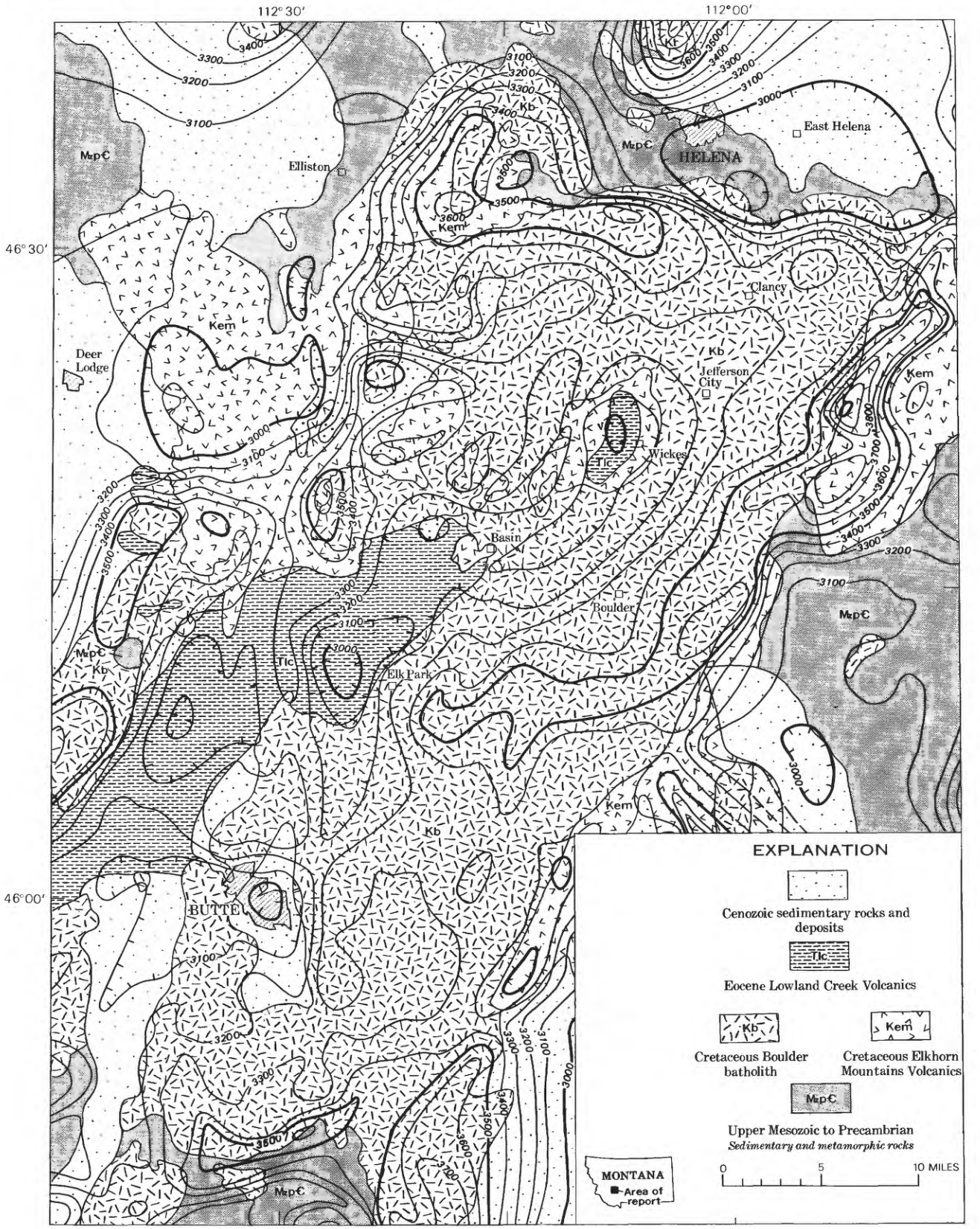

FIGURE 1.—Residual aeromagnetic and generalized geologic map of the Boulder batholith region. Contour interval 100 gammas. Contours compiled from regional aeromagnetic map (Johnson and others, 1965) by subtracting a regional magnetic field gradient of 6.5 gammas per mile in the direction N. 18½° E. (U.S. Coast and Geodetic Survey, 1965). Geologic map after Smedes (1962) and Smedes and others (1968).

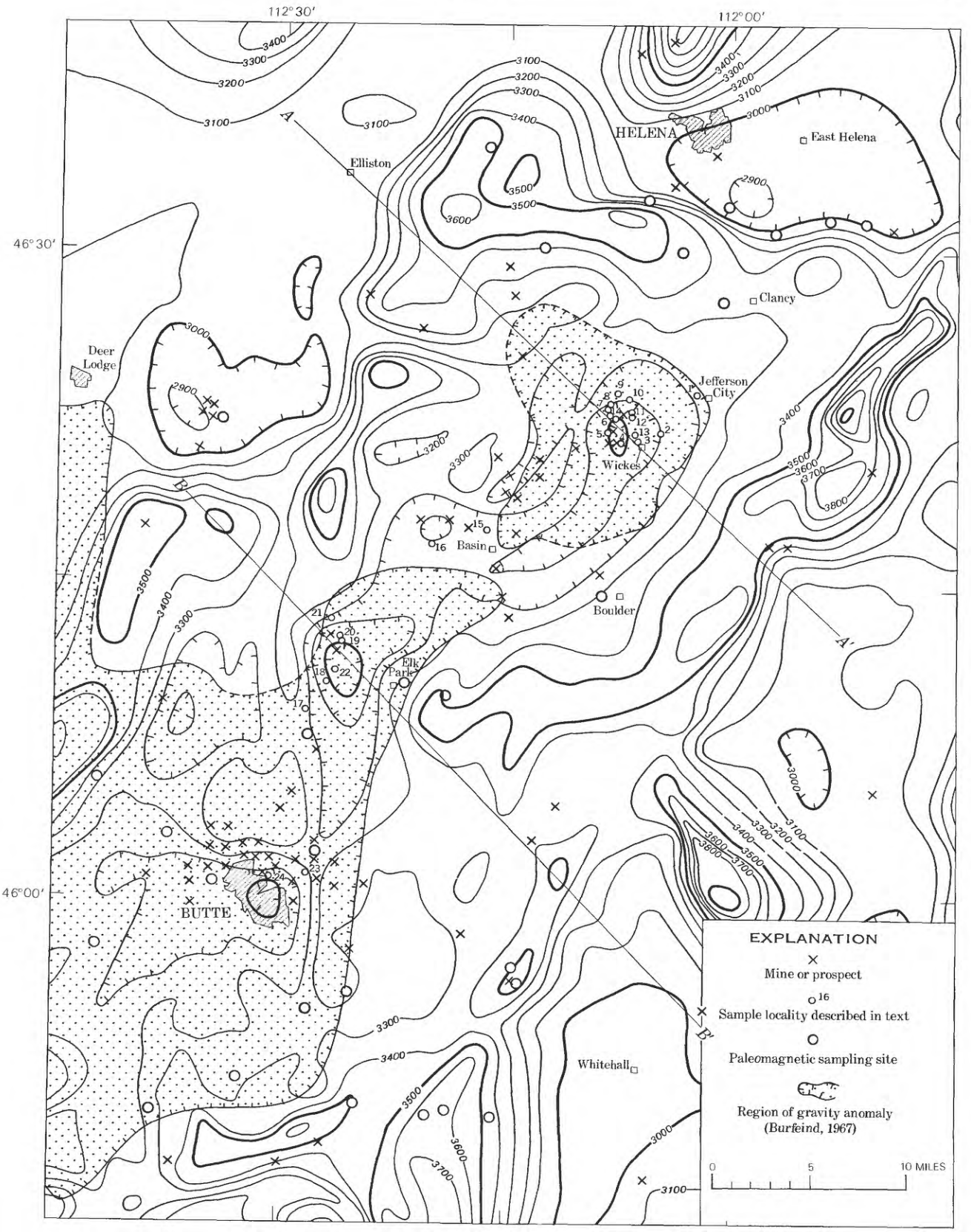

FIGURE 2.—Map showing sample locations, selected mining areas, lines of sections, and regions of strong negative Bouguer gravity anomalies. Aeromagnetic base same as in figure 1.

anomalies in the Boulder batholith area occur at the northwest and northeast boundaries of igneous rock outcrops, 6 miles east-southeast of Deer Lodge and 4 miles southeast of Helena. Weaker negative closures occur 7 miles northwest of Basin as well as along the northwestern and southeastern boundaries of the map area.

The train of negative anomalies over the batholith and its roof is associated with mining and prospecting areas. Four of the most conspicuous lows correlate with mineralized zones in the Elkhorn Mountains Volcanics, Boulder batholith, and Lowland Creek Volcanics. These lows occur over (1) the Elkhorn Mountains Volcanics and Lowland Creek Volcanics near Wickes (Becraft and others, 1963), covering a mining district which has produced silver, lead, gold, and some copper, (2) the Lowland Creek Volcanics northwest of Basin (Ruppel, 1963), approximately 1 mile east of a number of silver-lead mines and prospects, (3) the Lowland Creek Volcanics northwest of Elk Park (Smedes and others, 1962), centered near the once-active Ruby mine and associated prospects, and (4) batholithic rocks at Butte (Smedes, 1967; Smedes, 1968), covering open-pit and underground copper mines yielding considerable amounts of silver, gold, lead, and manganese ores in a district known as "the richest hill on earth" (Bateman, 1950). The negative anomaly over the Lowland Creek Volcanics northwest of Butte (Smedes, 1968), though not associated with a major mining district, is centered near several mining prospects.

Negative anomalies at the periphery of the major anomalous area are not generally associated with highly mineralized areas except for the conspicuous low east-southeast of Deer Lodge. This anomaly is centered over the Elkhorn Mountains Volcanics about 1 mile west of the Emery mining district (Robertson, 1953; Ruppel, 1961). The major low southeast of Helena is developed over Paleozoic and Mesozoic sedimentary rocks (Knopf 1963) which are not believed to be rich in metalliferous mineral deposits.

POSSIBLE SOURCES OF MAGNETIC LOWS

In general, negative magnetic anomalies may develop either as passive features over rocks that are less magnetic than surrounding rocks or as active features associated with relatively magnetic rocks polarized in a reversed sense. In particular, a magnetic rock source in southwestern Montana possessing a total magnetization (vector sum of induced and remanent magnetization) nearly parallel to the external field, called normal magnetization, gives rise to a positive magnetic anomaly and an associated weaker positive anomaly. This reversed total magnetization results from a reversed remanent magnetization which is stronger than the induced magnetization parallel to the magnetic field. Thus, for each negative magnetic anomaly in the Boulder batholith area, the following possibilities must be considered: (1) polarization low which is north of a positive anomaly associated with a normally magnetized rock source, (2) low over very weakly magnetic rocks surrounded by normally magnetized rocks, and (3) low developed over reversely magnetized rocks.

ROCK MAGNETIC MEASUREMENTS

To estimate the influence of intensity and direction of rock magnetization on the development of the negative anomalies, the magnetic properties of 24 oriented specimens of Elkhorn Mountains Volcanics, Boulder batholith, and Lowland Creek Volcanics were measured (table 1). Fourteen samples were collected from the Wickes mining district, 2 from northwest of Basin, 6 from northwest of Elk Park, and 2 from Butte. The sampling sites are shown as small open circles in figure 2. These data were supplemented by properties information obtained previously from more than 30 paleomagnetic sampling sites in the Elkhorn Mountains Volcanics, Boulder batholith, and Lowland Creek Volcanics nearby. Many of these paleomagnetic sampling sites are shown as large open circles in figure 2.

The data indicate that, in general, specimens of the Elkhorn Mountains Volcanics and the Boulder batholith possess normal remanent magnetizations, whereas those of the Lowland Creek Volcanics possess reversed remanent magnetizations. This relation is shown in the Wickes district (fig. 3) where four out of five Elkhorn Mountains Volcanics specimens, one Boulder batholith specimen, and one lithified alluvium sample are similarly magnetized in a normal sense, compared to six out of seven Lowland Creek Volcanics samples which are magnetized in a reversed sense (the remanent magnetization of the seventh sample is nearly horizontal).

Remanent magnetizations of the Elkhorn Mountains Volcanics and Boulder batholith, therefore, add to the induced magnetizations producing normal total magnetizations. Remanent magnetizations of the Lowland Creek Volcanics, in contrast, subtract from the induced magnetizations producing reversed or normal total magnetizations, depending upon whether the remanent magnetizations are stronger or weaker than induced magnetizations. It is of considerable interest that induced magnetizations of the Lowland Creek Volcanics are consistently stronger than remanent magnetizations, resulting in normally directed total magnetizations. Thus all the samples examined possess total

TABLE 1.—*Rock magnetic and other measurements of 24 oriented specimens from the Elkhorn Mountain Volcanics, Boulder batholith, Lowland Creek Volcanics, and lithified alluvium, Montana*

[Specimen locations are shown in figure 3. Measurements are defined in explanation]

Specimen MAA-	Measurements								
	REM D	REM I	REM J	K	Q	TOT D	TOT I	TOT J	ρ
Elkhorn Mountains Volcanics									
3	28	80	14.5	100	.25	20	73	71.8	2.74
8	2	6	6.91	33.0	.36	10	55	22.7	2.88
9	337	63	26.7	2.70	17.2	338	63	28.2	2.78
12	37	−47	.542	2.40	.39	27	48	1.22	2.85
13	11	30	4.05	10.0	.70	14	54	9.21	2.70
Boulder batholith									
1	4	55	13.4	20.0	1.16	9	63	24.6	2.74
15	313	66	47.2	280	.29	3	72	205	2.80
23	55	50	8.37	33.0	.44	36	66	26.7	2.80
24			.030	1.40	.038				2.84
Lowland Creek Volcanics									
4	119	−33	3.47	21.0	.29	58	65	1.05	2.50
5	130	−24	2.86	15.0	.33	71	66	7.60	2.56
6	166	−48	.040	4.80	.015	19	71	2.72	2.63
7	168	−34	.234	4.80	.085	26	73	2.59	2.73
10	155	−8	.110	2.70	.071	28	73	1.52	2.48
11	165	−66	7.36	76.0	.17	27	71	36.6	2.45
14	139	3	100	4.80	36.2	139	5	99.7	2.60
16	274	16	13.0	10.0	2.26	283	37	15.2	2.31
17	253	−30	.101	2.00	.038	6	72	1.09	2.20
18	243	−41	8.21	18.0	.79	275	45	6.31	2.47
19	102	−40	.797	1.40	.99	80	20	.073	2.54
20	177	40	.056	1.40	.069	22	74	.083	2.48
21	57	−10	.053	1.40	.066	25	68	.081	2.67
22	246	−54	2.68	1.40	.33	254	−44	1.99	2.46
Lithified alluvium									
2	32	74	7.62	25.0	.53	23	72	22.0	2.54

EXPLANATION

REM D: Declination of remanent magnetization, degrees east of north.

REM I: Inclination of remanent magnetization, degrees below horizontal.

REM J: Intensity of remanent magnetization, $\times 10^{-5}$emu/cc.

K: Apparent volume magnetic susceptibility, $\times 10^{-5}$emu/cc, measured with induction-type apparatus.

Q: Koenigsberger ratio of remanent magnetization intensity to induced magnetization intensity.

TOT D: Declination of total magnetization, degrees east of north.

TOT I: Inclination of total magnetization, degrees below horizontal.

TOT J: Intensity of total magnetization, $\times 10^{-5}$emu/cc.

ρ: Dry bulk density in g/cc, measured with improved Jolly balance.

Note: Remanent magnetizations measured with two spinner-type magnetometers. All remanent magnetization data are in situ.

magnetizations nearly parallel to the earth's magnetic field.

COMPARISON OF ROCK MAGNETIC DATA

Although rock sampling in the area of magnetic lows was only reconnaissance in scope, the data become more meaningful when compared with detailed information from paleomagnetic sampling sites nearby. For example, 80 specimens from 3 sites of the Lowland Creek Volcanics have an average susceptibility of about 5.0×10^{-5} electromagnetic units per cubic centimeter and a remanent intensity of 50×10^{-5} emu per cm^3. About 600 specimens from more than 25 sites of the Boulder batholith have an average susceptibility of about 250×10^{-5} emu per cm^3, and a remanent intensity of 50×10^{-5} emu per cm^3. More than 1,000 specimens of the Elkhorn Mountains Volcanics in southwestern Montana have given an average susceptibility of approximately 100×10^{-5} emu per cm^3, and a remanent intensity of 100×10^{-5} emu per cm^3 with major fluctuations according to rock type (Hanna, 1967; Hanna, 1968).

Comparison of average values of magnetization indicates that (1) the Lowland Creek Volcanics specimens from the negative anomaly belt have predictably low susceptibility values but unexpectedly low remanent intensity values, (2) the Boulder batholith specimens from the belt have lower susceptibility and remanent intensity values than other batholithic rocks nearby, and (3) the Elkhorn Mountains Volcanics specimens from the low intensity zone have lower susceptibility and remanent intensity values than those measured in similar rocks elsewhere. Reversed remanent magnetization is not of primary importance as a contributor to the negative aeromagnetic anomalies but only of secondary importance in that it tends to cancel the stronger induced magnetization of the Lowland Creek Volcanics. It is highly significant that, in general, rocks collected at sites of aeromagnetic lows in the area

possess anomalously weak total magnetization intensities.

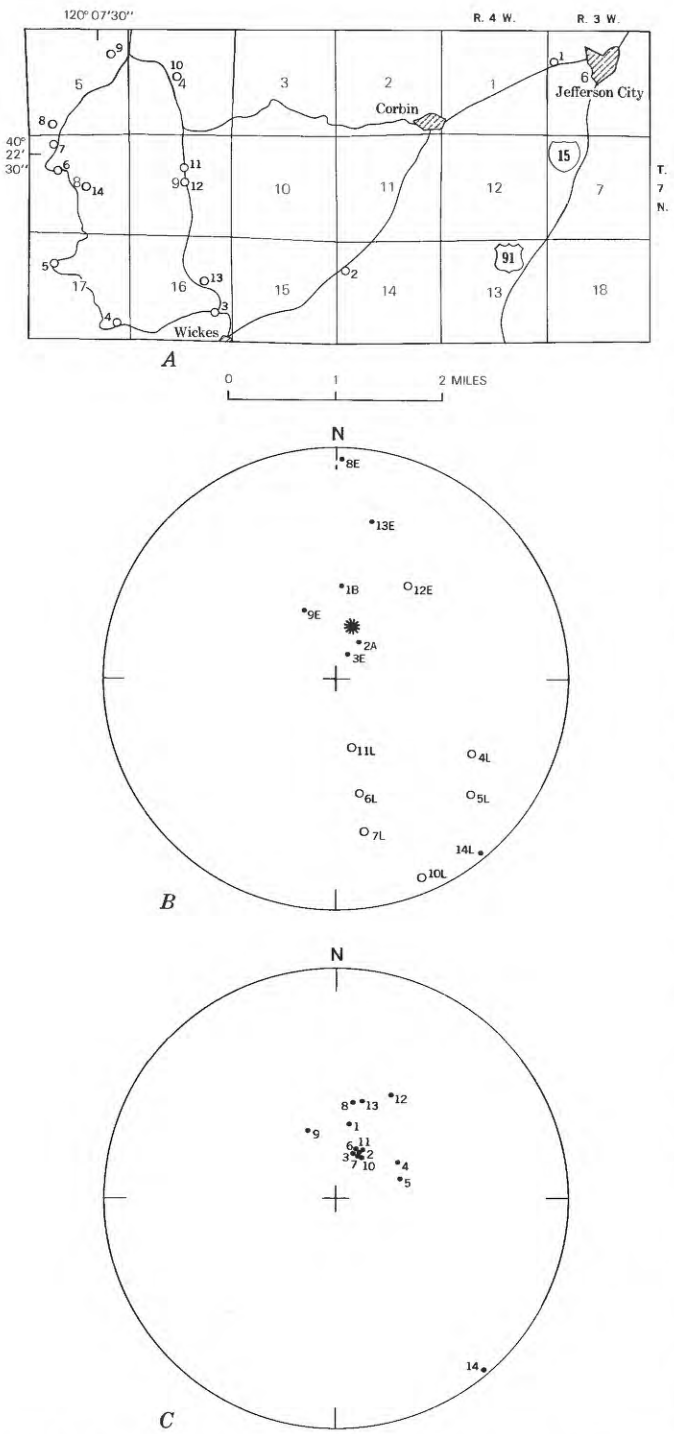

FIGURE 3.—Map and equal-area projections showing: *A*, sample locations in the Wickes mining district; *B*, in-situ directions of remanent magnetization; and *C*, in-situ directions of total magnetization. Open circles are on upper hemisphere; closed circles are on lower hemisphere. Asterisk is direction of earth's magnetic field. E, Elkhorn Mountains Volcanics, B, Boulder batholith; L, Lowland Creek Volcanics; A, lithified alluvium.

RELATION OF GRAVITY TO AEROMAGNETIC FEATURES

To further assist interpretation of the subsurface features, gravity and aeromagnetic profiles across the anomalous area near Wickes (A–A′) and Elk Park (B–B′) are compared on figure 4 (p. D166–D167). Gravity profile A–A′ is characterized by a broad 35-milligal low over the main mass of the Boulder batholith and subordinate fringe masses of Elkhorn Mountains Volcanics, by a weak depression in the gravity field associated with low-density Lowland Creek Volcanics, sedimentary rocks, and alluvium on the northwest, and by a decrease in gradient caused by low-density sedimentary rocks on the southeast. Breaks in slope near the center of the broad gravity low suggest that the lowest density rocks extend across a 12-mile area, from 4 miles southeast of Wickes to 8 miles northwest of this district as shown by the gravity contour line of figure 2. Aeromagnetic profile A–A′ indicates that the magnetic low at Wickes coincides with the deepest part of the broad gravity trough, and that relatively nonmagnetic rocks occur across an area 4 miles southeast of Wickes to 2 miles northeast of the district. The positive anomaly doublet immediately northwest, extending to a point 8 miles northwest of Wickes, is appreciably lower than the magnetic field over other parts of the batholith to the northwest and southeast, and probably is generated by weakly magnetized batholith rocks. Strong magnetic highs occur over the Boulder batholith and Elkhorn Mountains Volcanics along margins of the gravity low.

The broad gravity low over batholith rocks shown on profile B–B′ is marked by a conspicuous cup-shaped depression at the deepest part of the anomaly. This feature is probably caused by the combined effect of a graben filled with low-density upper Cenozoic basin deposits and a concentration of low-density material in batholith rocks beneath the graben. As along A–A′, increases in the gravity field toward the margins of the batholith are attributable to higher density rocks bordering the batholith at depth. A local gravity low associated with low-density sedimentary rocks occurs in the southeast part of the profile. The aeromagnetic profile along section B–B′ shows that the low northwest of Elk Park is centered at the northwest edge of this gravity low and extends for 3 miles northwest of the gravity depression. As along A–A′, the magnetic field over plutonic rocks northwest and southeast of the magnetic low is generally high, decreasing abruptly at the contact of batholithic and volcanic rocks with sedimentary rocks.

The gravity data, supported by density data of the 24 samples, indicate that there is little density contrast between most rocks of the Boulder batholith and the

Elkhorn Mountains and between most of the Lowland Creek Volcanics and sedimentary rocks. The most negative areas of the gravity field (Burfeind, 1967), outlined by the contour in figure 2, coincide to some extent with the train of aeromagnetic lows within the batholith, especially with individual lows at Wickes, northwest of Elk Park, and at Butte. No such correlation is observed with regard to aeromagnetic lows northwest of Butte and south-southeast of Deer Lodge.

CONCLUSIONS

The aeromagnetic and rock magnetic data suggest that negative magnetic anomalies over the Boulder batholith are associated with weakly magnetic rocks, normally polarized, in contact with more highly magnetic rocks, also normally polarized. The amplitudes and extents of magnetic lows at Wickes, northwest of Elk Park, and at Butte suggest that considerable volumes of plutonic rocks as well as smaller volumes of volcanic rocks are less magnetic than their counterparts elsewhere. Gravity data indicate that rocks in these areas are somewhat less dense than their counterparts elsewhere. It is believed that the anomalous magnetic features, and, to a lesser extent, the anomalous gravity features, are attributable to concentrations of felsic plutonic and volcanic rocks later intruded by silica-rich veins within the batholithic complex. The low magnetic intensities of these rocks are probably due to (1) low concentrations of magnetic iron oxides in primary magmatic and hydrothermal sources and (2) hydrothermal alteration of magnetic iron oxides to more highly oxidized and hydrated nonmagnetic iron oxides.

Other aeromagnetic lows in the batholith area are subject to various interpretations. Negative anomalies near Basin and northwest of Butte represent centers of major felsic and siliceous intrusions within the batholith and the Lowland Creek Volcanics. The major low east-southeast of Deer Lodge and the minor low northwest of Basin seem to be the only negative features that may be strongly influenced by reversed magnetization. Remanent magnetization directions of the Elkhorn Mountains Volcanics sampled in the Emery mining district southeast of Deer Lodge are nearly horizontal with a northeast declination, suggesting that other rocks in the area may be magnetically reversed. The negative anomaly southeast of Helena represents the only conspicuous polarization low north-northeast of the regional aeromagnetic high over the Boulder batholith. Shallow magnetic depressions at the northwest and southeast edges of the anomaly belt are developed over relatively nonmagnetic sedimentary rocks and deposits.

The association of magnetic lows with highly mineralized areas in the batholith has economic significance. In the Boulder batholith area as well as in other areas of comparable geologic terrane, it is important to evaluate negative anomalies in relation to their causes deduced from surface geology. Complete analysis of anomaly sources requires detailed magnetic measurements and geologic mapping supported by petrographic and geochemical investigations. Those anomalies which cannot be interpreted as polarization lows or as lows over reversely magnetized rocks may be associated with intrusions of felsic material, and sites of potential economic value. Thus the aeromagnetic map is a valuable aid in the search for ore deposits.

REFERENCES

Bateman, A. M., 1950, Economic mineral deposits, 2d ed.: New York, John Wiley and Sons, 916 p.

Becraft, G. E., Pinckney, D. M., and Rosenblum, Sam, 1963, Geology and mineral deposits of the Jefferson City quadrangle, Jefferson and Lewis and Clark Counties, Montana: U.S. Geol. Survey Prof. Paper 428, 101 p.

Biehler, Shawn, and Bonini, W. E., 1966, A geophysical interpretation of the Boulder batholith, Montana [abs.]: Am. Geophys. Union Trans., v. 47, no. 1, p. 192.

Burfeind, W. J., 1967, A gravity investigation of the Tobacco Root Mountains, Jefferson Basin, Boulder batholith, and adjacent areas of southwestern Montana: Indiana Univ., Bloomington, Ind., Ph. D. thesis, 146 p.

Hanna, W. F., 1967, Paleomagnetism of upper Cretaceous volcanic rocks of southwestern Montana: Jour. Geophys. Research, v. 72, no. 2, p. 595–610.

——— 1968, Remanent magnetization of two late Cretaceous glassy volcanic rocks from Montana [abs.]: Am. Geophys. Union Trans., v. 49, no. 4, p. 671.

Johnson, R. W., Jr., Henderson, J. R., and Tyson, N. S., 1965, Aeromagnetic map of the Boulder batholith area, southwestern Montana: U.S. Geol. Survey Geophys. Inv. Map GP–538, scale 1 : 250,000.

Klepper, M. R., Weeks, R. A., and Ruppel, E. T., 1957, Geology of the southern Elkhorn Mountains, Jefferson and Broadwater Counties, Montana: U.S. Geol. Survey Prof. Paper 292, 82 p.

Knopf, Adolph, 1957, The Boulder bathylith of Montana: Am. Jour. Sci., v. 255, no. 2, p. 81–103.

——— 1963, Geology of the northern part of the Boulder bathylith and adjacent area, Montana: U.S. Geol. Survey Misc. Geol. Inv. Map I-381, scale 1 : 48,000.

——— 1964, Time required to emplace the Boulder bathylith, Montana—a first approximation: Am. Jour. Sci., v. 262, no. 6, p. 1207–1211.

Robertson, F. S., 1953, Geology and mineral deposits of the Zosell (Emery) mining district, Powell County, Montana: Montana Bur. Mines and Geology Mem. 34, 29 p.

Ruppel, E. T., 1961, Reconnaissance geologic map of the Deer Lodge quadrangle, Powell, Deer Lodge, and Jefferson Counties, Montana: U.S. Geol. Survey Mineral Inv. Field Studies Map MF–174, scale 1 : 48,000.

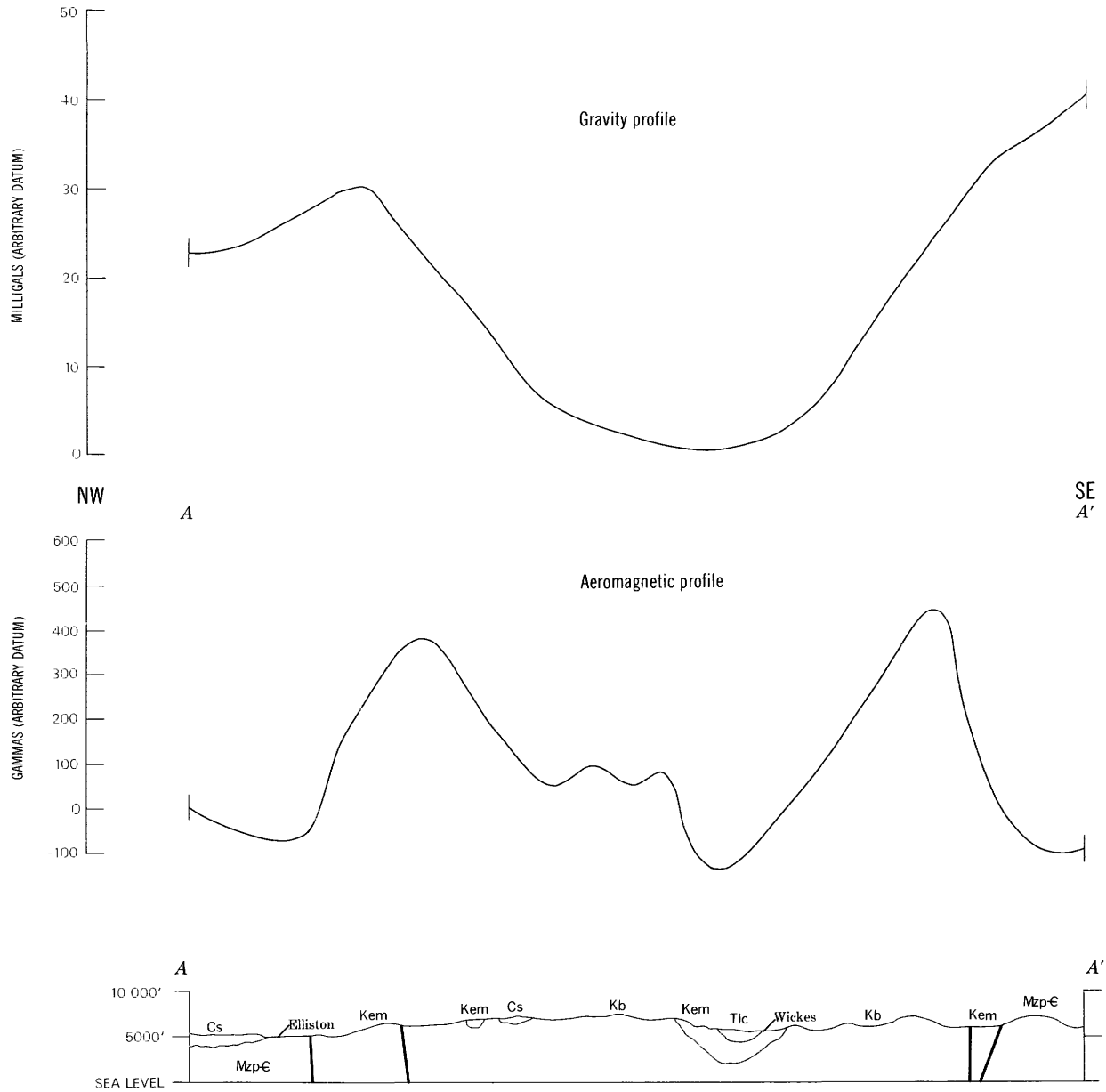

FIGURE 4.—Diagrams showing Bouguer gravity, aeromagnetic, and generalized surface geology profiles: Profile *A-A′*, above; profile *B-B′*, at right. Letter symbols are explained in figure 1; Cs, Cenozoic sedimentary rocks and deposits.

Ruppel, E. T., 1963, Geology of the Basin quadrangle, Jefferson, Lewis and Clark, and Powell Counties, Montana: U.S. Geol. Survey Bull. 1151, 121 p.

Smedes, H. W., 1962, Lowland Creek Volcanics, an upper Oligocene formation near Butte, Montana: Jour. Geology, v. 70, no. 3, p. 255–266.

——— 1966, Geology and igneous petrology of the northern Elkhorn Mountains, Jefferson and Broadwater Counties, Montana: U.S. Geol. Survey Prof. Paper 510, 116 p.

——— 1967, Preliminary geologic map of the Butte South quadrangle, Montana: U.S. Geol. Survey open-file map, scale 1: 24,000.

Smedes, H. W., 1968, Preliminary geologic map of parts of the Butte North quadrangle Silver Bow, Deer Lodge, and Jefferson Counties, Montana: U.S. Geol. Survey open-file map, scale 1:36,000.

Smedes, H. W., Klepper, M. R., Pinckney, D. M., Becraft, G. E., and Ruppel, E. T., 1962, Preliminary geologic map of the Elk Park quadrangle, Jefferson and Silver Bow Counties, Montana: U.S. Geol. Survey Mineral Inv. Field Studies Map MF-246, scale 1:48,000.

Smedes, H. W., Klepper, M. R., and Tilling, R. I., 1968, The Boulder batholith, Montana, *in* Geol. Soc. America Field Guidebook, Rocky Mountain Section, Description of geology: 21 p.

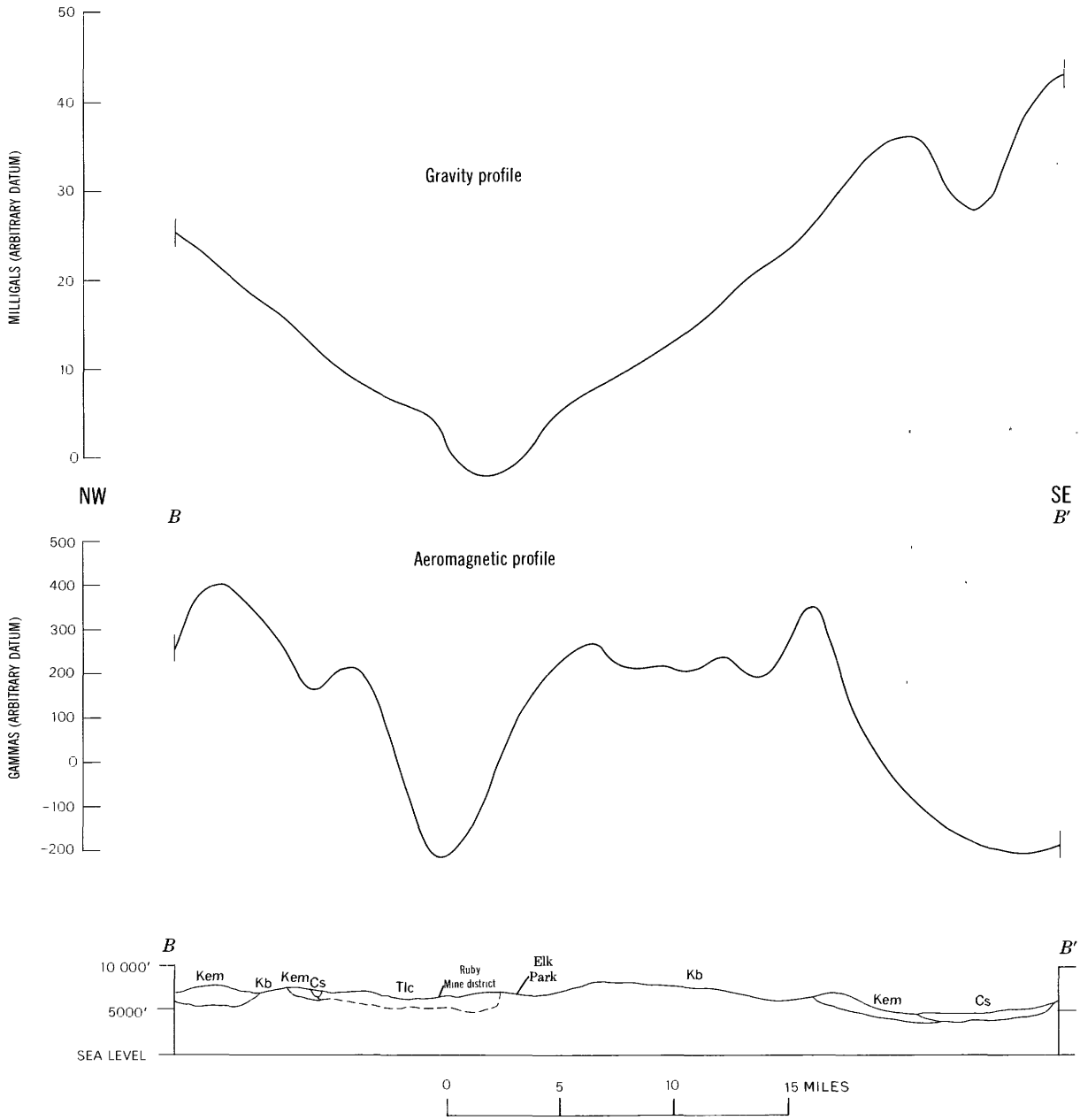

FIGURE 4.

Smedes, H. W., and Thomas, H. H., 1965, Reassignment of the Lowland Creek Volcanics to Eocene age: Jour. Geology, v. 73, no. 3, p. 508–510.

Tilling, R. I., Klepper, M. R., and Obradovich, J. D., 1968, K-Ar ages and time span of emplacement of the Boulder batholith, Montana: Am. Jour. Sci., v. 266, no. 8, p. 671–689.

U.S. Coast and Geodetic Survey, 1965, Total intensity chart of the United States, 1965.0: U.S. Coast and Geod. Survey Chart 3077f.

HAWAIIAN SEISMIC EVENTS DURING 1968

By ROBERT Y. KOYANAGI, Hawaiian Volcano Observatory,
Hawaii National Park, Hawaii

Abstract.—In Hawaii, 699 earthquakes having a magnitude of from 2.0 to 4.7 were recorded in 1968. Seismic activity continued beneath southeastern Hawaii during the year with prolonged volcanic eruptions and associated structural adjustments.

This is the seventh of a series of reports showing earthquake locations and other data compiled by the staff of the Hawaiian Volcano Observatory, U.S. Geological Survey (Koyanagi, 1964; Koyanagi and Endo, 1965; Koyanagi and Okamura, 1966; Koyanagi, 1968; Koyanagi 1969a, 1969b).

The locations of earthquakes having a magnitude of 2.0 and greater [1] occurring beneath the five volcanos on the island of Hawaii (fig. 1) and offshore along the Hawaiian Ridge from lat 18° to 23° N. and long 154° to 161° W. are shown in figures 2 and 3. The earthquakes are plotted in three depth groups (<10, 10–20, and 20–60 km) (fig. 4) and two magnitude groups (2.0–3.5, and >3.5).

The methods and limitations of locating earthquakes are consistent with the earlier reports. Hawaiian seismic-wave traveltime curves are applied to P-wave arrivals, and S-P values read to 1/10-second accuracy. Earthquakes beneath the island of Hawaii, having a magnitude of 2.5 or greater, are generally located within a 5-kilometer sphere of error; errors as great as 10 km may be expected from earthquakes located offshore considerable distances away from stations.

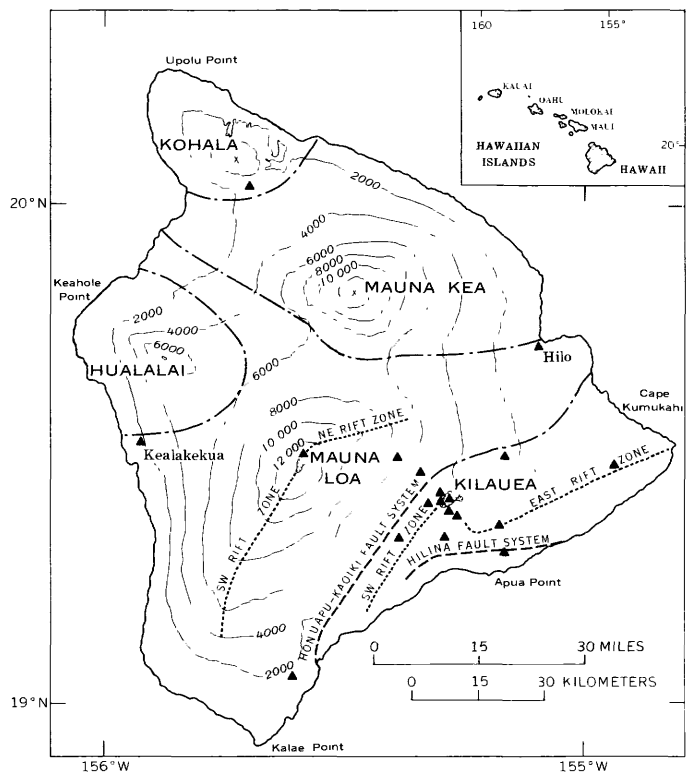

FIGURE 1.—Map of the island of Hawaii, showing the five volcanos and their principal structural features. Dot-and-dash lines are boundaries of volcanic systems. Location of seismograph stations is indicated by closed triangles. Contour interval is 2,000 feet, and datum is mean sea level.

DESCRIPTION OF 1968 SEISMIC EVENTS

Seismic activity for the year was climaxed by three eruptions of Kilauea Volcano, a long summit phase (Kinoshita and others, 1969) followed by two shorter flank phases. The long summit eruption at Halemaumau Crater started on November 5, 1967, and continued spasmodically until early July 1968. Periods of lava fountaining with continuous tremor lasting several hours to many days alternated with periods of degassing activity and relative volcanic quiescence. Tremor amplitudes generally diminished from one period of fountaining activity to the next. Between periods, during degassing at the lava lake, the seismic records showed numerous shallow shocks of low magnitude (about 0.1 or less). The end of the summit eruption in early July was followed by a pause of 6 weeks, after which Kilauea erupted again on August

[1] A modification of the Richter scale is used for magnitude determination (Koyanagi and others, 1966).

U.S. GEOL. SURVEY PROF PAPER 650-D, PAGES D168-D171

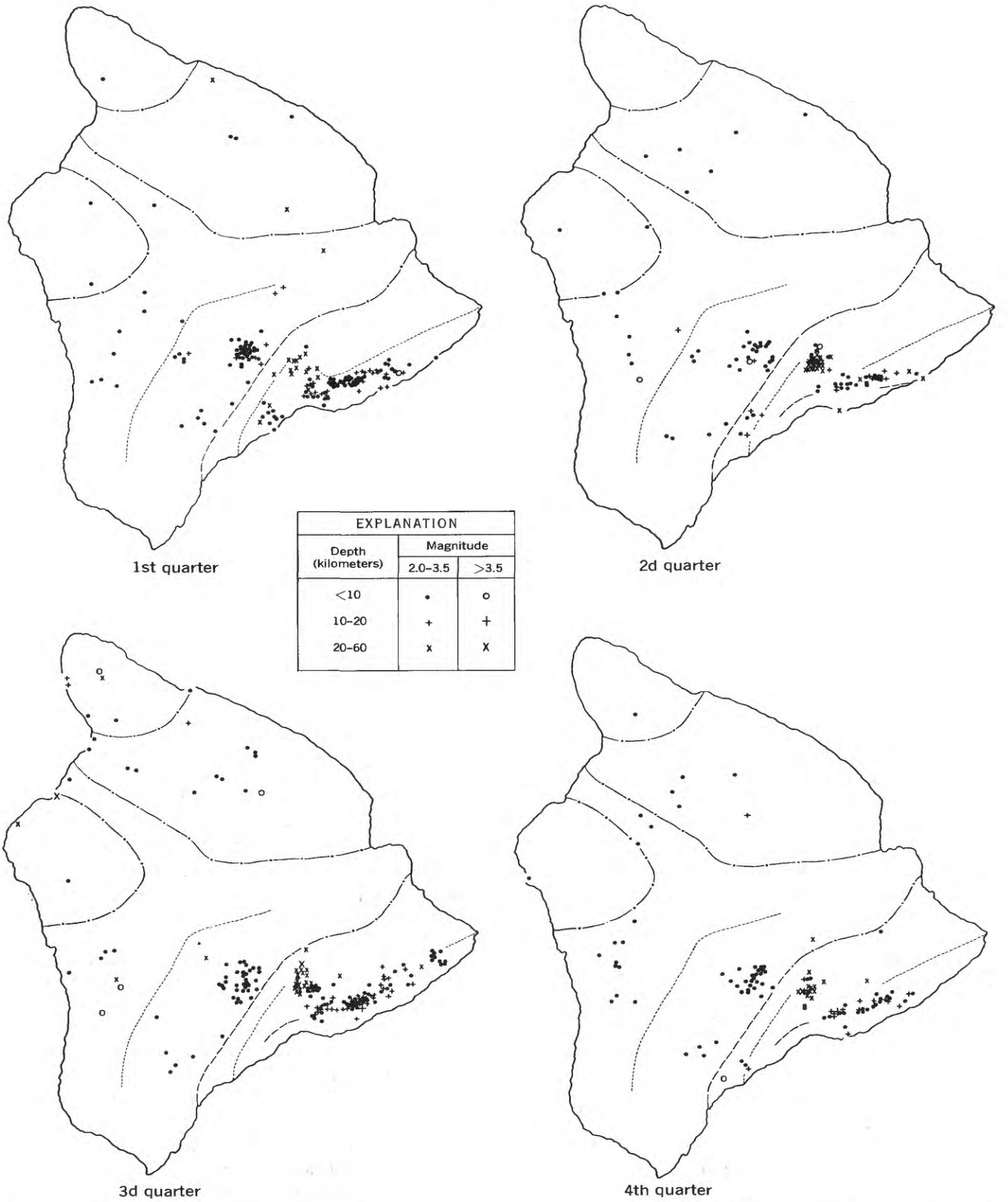

FIGURE 2.—Plot of epicenters of earthquakes having a magnitude of 2.0 or greater beneath the island of Hawaii during each quarter of 1968. Dot-and-dash lines are boundaries of volcanic systems, long-dashed lines are fault systems, and short-dashed lines are rift zones. Geographic names are shown in figure 1.

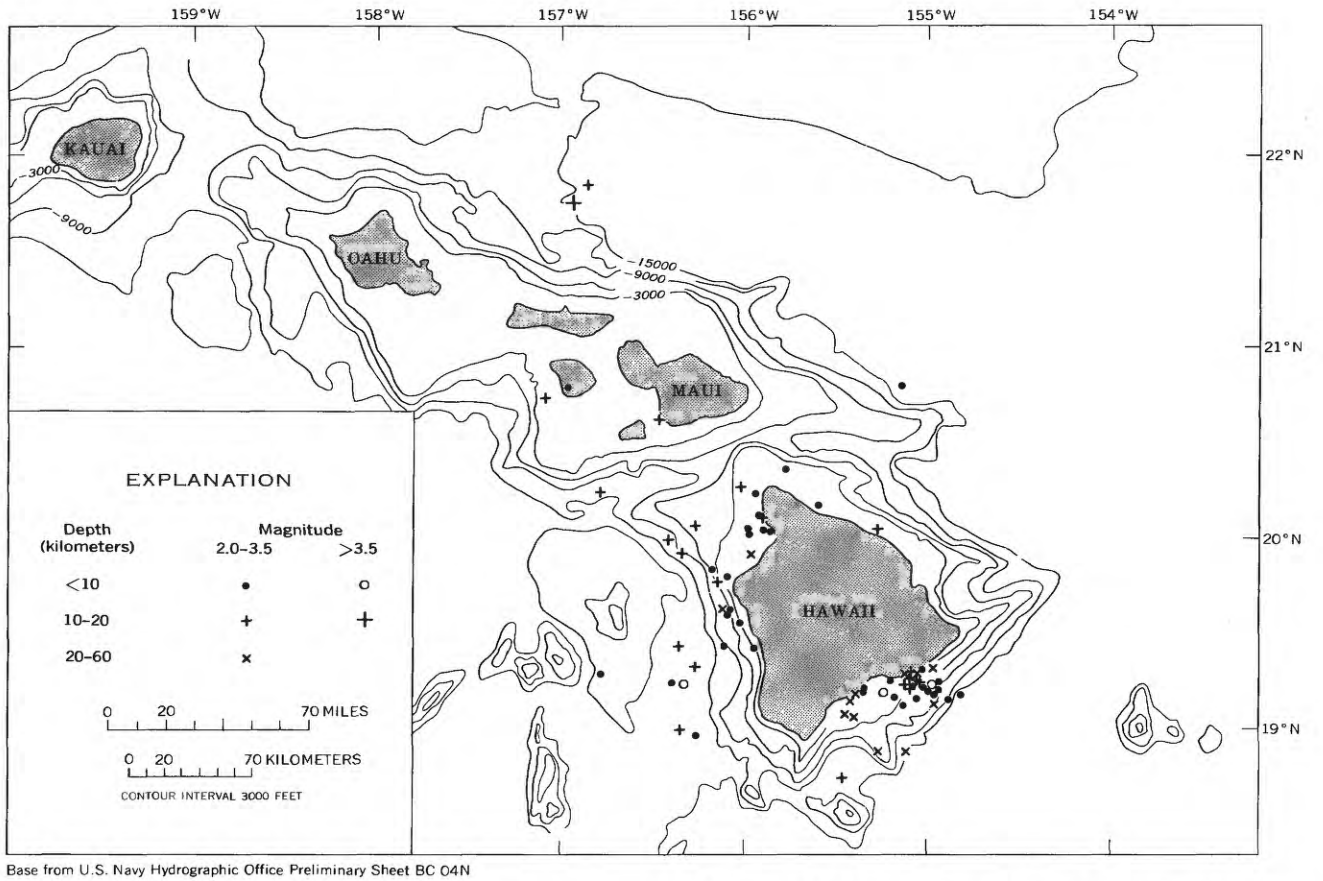

FIGURE 3.—Map of the Hawaiian Islands, showing epicenters of earthquakes having a magnitude of 2.0 or greater that occurred off the island of Hawaii during 1968.

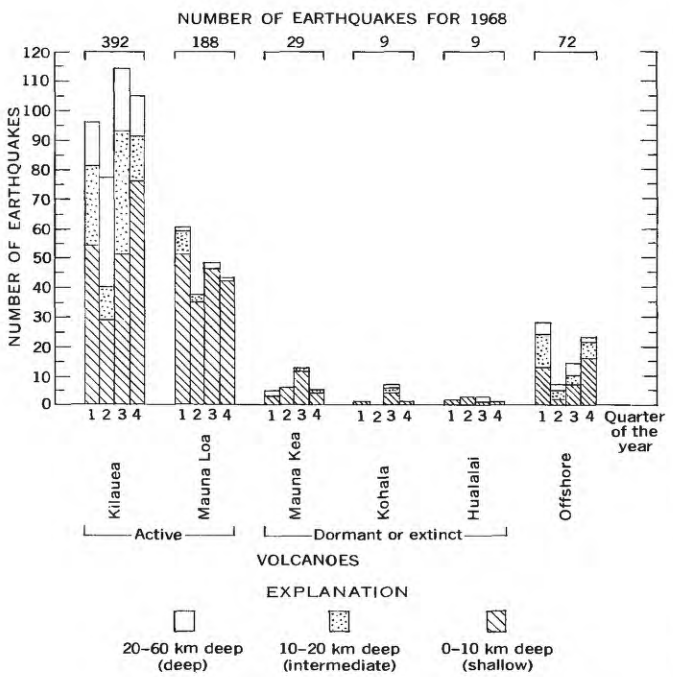

FIGURE 4.—Geographic location and distribution, with depth, of earthquakes having a magnitude of 2.0 or greater which occurred in the Hawaiian Islands during 1968.

22–26. This time the eruption took place 5 km southeast of the summit at Hiiaka Crater on the east rift. After another brief period of volcanic quiescence, the final outbreak of the year took place from October 7 to November 19, several kilometers downrift from the August event. In addition to sharp deflation of the summit, hundreds of shallow earthquakes and periods of harmonic tremor were characteristic of both flank eruptions.

During some periods of intense volcanic tremor in 1968, normal earthquake recording in the Kilauea summit area was somewhat disturbed, but probably only a few of the large earthquakes (magnitude of 2.0 or greater) were undetected. Tremor was localized and occurred at low intensities for long periods of eruption, so that normal monitoring of Kilauean earthquakes was undisturbed. During the first half of the year, the number of earthquakes originating beneath the flanks of Kilauea and from a source about 30 km beneath the summit of the volcano remained at moderate levels. On January 7–9, a swarm of more than 600 earthquakes occurred at a depth of about 10 km beneath the southeast flank; 12 of the larger shocks were registered at a

magnitude of from 2.0 to 2.8. In late April, when only weak tremor from the waning summit eruption was being recorded, a 4.5-magnitude earthquake originated 30 km beneath the southern part of the summit of Kilauea. This earthquake was felt islandwide at 04^h09^m, April 28, and in the five following days about 200 aftershocks were recorded.[2] During the 2d quarter, 33 earthquakes having a magnitude of 2.0 or greater originated at this deep source, and 3 of these had a magnitude greater than 3.5.

From early June, nearly a month prior to the end of the summit eruption, earthquake activity along Kilauea's flanks started to increase. Southwest-flank activity showed fluctuating highs in June, July, November, and December. However, the greatest increase was noted beneath the southeast flank. From June until the August east-rift eruption, southeast-flank earthquakes often numbered more than 50 per day. After the August eruption, the count dropped to about 30 per day, but it increased somewhat a few days prior to the final volcanic outbreak in October. During the October eruption, several hundred earthquakes outlined the eruptive area; 48 shallow earthquakes had magnitudes of from 2.0 to 2.7, but owing to difficulty in plotting, these were omitted from figure 2, 4th quarter.

Although the volcano remained quiet for the rest of the year, the frequency of southeast Kilauea earthquakes increased to new high levels in mid-December. At 16^h33^m, December 16, the largest earthquake of the year, with a magnitude of 4.7, occurred near the eastern end of the Hilina fault system. More than 150 aftershocks associated with this event occurred during the initial 14 hours of activity.

On December 19, an earthquake having a magnitude of 3.5 occurred about 10 km farther east and was followed by about 50 aftershocks within a few hours.

SUMMARY

In 1968, most of the earthquakes occurred beneath the southeast part of the Hawaiian Ridge. More than three-fourths of the earthquakes with a magnitude between 2.0 and 4.7 occurred near the two active volcanoes, Kilauea and Mauna Loa, and scattered epicenters extended off the west coast of the island of Hawaii. The earthquakes were related to the five volcanoes of the island of Hawaii as follows: 57 percent occurred beneath Kilauea, 27 percent beneath Mauna Loa, 4 percent beneath Mauna Kea, 1 percent beneath Kohala, and 1 percent occurred beneath Hualalai. The remaining 10 percent of the earthquakes occurred offshore; most were concentrated off the southeast coast, but some scattered earthquakes occurred off the west coast. Focal depth of 66 percent of the earthquakes was less than 10 km; 19 percent were 10 to 20 km deep, and 15 percent were 20 to 60 km deep.

During the year, 80 earthquakes were felt by Hawaii residents, and 5 of these, having magnitudes between 3.7 and 4.7, were felt islandwide. Of the 699 recorded earthquakes having a magnitude of from 2.0 to 4.7, 97 percent had a magnitude of from 2.0 to 3.5, and 3 percent had a magnitude exceeding 3.5. The following table shows the number of earthquakes according to magnitude and focal depth:

Magnitude	Depth (km)		
	<10	10–20	20–60
2.0–2.5	341	104	69
2.6–3.0	83	16	19
3.1–3.5	24	7	13
3.6–4.0	7	2	6
4.1–4.5	5	1	1
4.7	0	1	0

[2] Times are given in hours and minutes, Hawaiian standard time.

REFERENCES

Kinoshita, W. T., Koyanagi, R. Y., Wright, T. L., and Fiske, R. S., 1969, The 1967–68 summit eruption of Kilauea Volcano: Science. [In press]

Koyanagi, R. Y., 1964, Hawaiian seismic events during 1962: Art. 144 *in* U.S. Geol. Survey Prof. Paper 475–D, p. D112–D117.

——— 1968, Hawaiian seismic events during 1965, *in* Geological Survey Research 1968: U.S. Geol. Survey Prof. Paper 600–B, p. B95–B98.

——— 1969a, Hawaiian seismic events during 1966, *in* Geological Survey Research 1969: U.S. Geol. Survey Prof. Paper 650–B, p. B113–B116.

——— 1969b, Hawaiian seismic events during 1967, *in* Geological Survey Research 1969: U.S. Geol. Survey Prof. Paper 650–C, p. C79–C82.

Koyanagi, R. Y., and Endo, E. T., 1965, Hawaiian seismic events during 1963, *in* Geological Survey Research 1965: U.S. Geol. Survey Prof. Paper 525–B, p. B13–B16.

Koyanagi, R. Y., Krivoy, H. L., and Okamura, A. T., 1966, The 1962 Kaoiki, Hawaii, earthquake and its aftershocks: Seismol. Soc. America Bull., v. 56, no. 6, p. 1319.

Koyanagi, R. Y., and Okamura, A. T., 1966, Hawaii seismic events during 1964, *in* Geological Survey Research 1966: U.S. Geol. Survey Prof. Paper 550–C, p. C129–C132.

SIMULATED LUNAR CRATER FIELDS NEAR FLAGSTAFF, ARIZONA—THEIR GEOLOGY, PREPARATION, AND USES

By N. G. BAILEY, G. W. COLTON, and IVO LUCCHITTA,
Flagstaff, Ariz.

Work done on behalf of the National Aeronautics and Space Administration

Abstract.—Two crater fields were constructed in Cinder Lake near Flagstaff, Ariz., for experimental purposes connected with manned investigations on the moon. They are 1:1-scale replicas of parts of preliminary Apollo landing site II–P–6–1 in Mare Tranquillitatis. Realism was facilitated by the lack of vegetation in Cinder Lake, as well as by its flatness and cover of unconsolidated basaltic pyroclastic debris. Explosive charges of various predetermined sizes were buried at different depths in the ash and cinders, using Lunar Orbiter II photographs of site II–P–6–1 as a guide. The 569 craters excavated by detonation of the charges match, in size and distribution, the craters visible in the Orbiter photographs. The cratered fields are being used to test, and experiment with, tools and procedures for geologic exploration on the moon.

The U.S. Geological Survey is developing the following techniques for manned lunar exploration: (a) Defining objectives and setting up geologic traverse plans; (b) defining procedures to be used during the traverses; (c) setting up, testing, and perfecting an earth-based scientific data facility for recording and assimilating data obtained from the traverses, and for advising astronauts on what geologic methods and techniques to use.

Men will first land on one of the maria—large areas of gently rolling terrain pockmarked by craters of various sizes. The surface material of the maria consists of unconsolidated or poorly consolidated debris ranging in particle size from dust less than 1 millimeter in diameter to blocks several meters in diameter (Natl. Aeronautics and Space Adm., 1966, p. 32–33). Consolidated rock, possibly lava, may underlie the surficial debris layer at shallow depths. Impact-cratered terrane of this kind is uncommon on earth, yet an analog of mare terrane is invaluable as a test site for activities mentioned above—hence, the decision to construct one or more crater-field test sites that would duplicate as closely as possible parts of one of the prime Apollo landing areas.

The area selected for the test sites is Cinder Lake, 10 miles northeast of Flagstaff, Ariz., and 3 miles south of Sunset Crater National Monument (fig. 1). Cinder Lake is a barren plain of loose cinders and ash. The

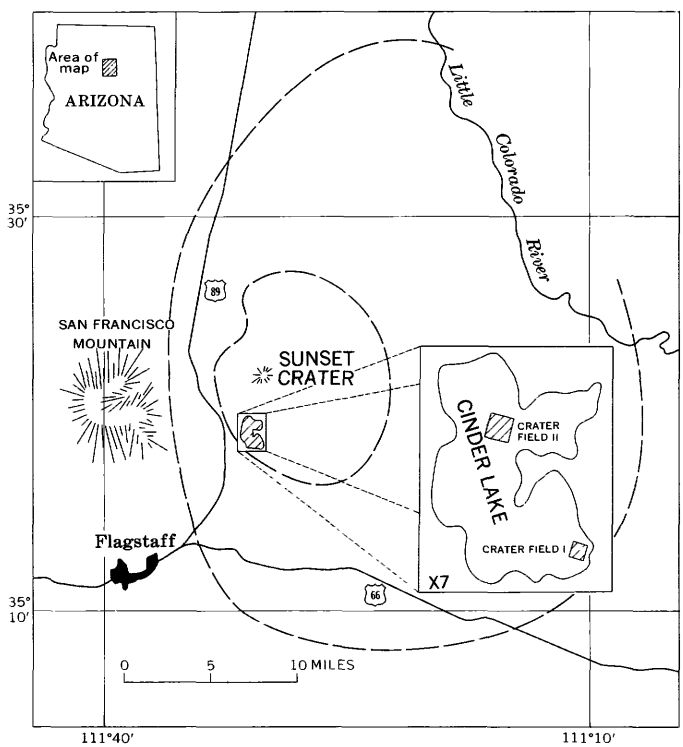

FIGURE 1.—Cinder Lake area. Lower inset shows the location of the simulated crater fields. Inner dashed line marks limit of continuous pyroclastic deposits from Sunset Crater, and outer dashed line the limit of discontinuous, dune deposits from Sunset Crater (both from Colton, 1932).

U.S. GEOL. SURVEY PROF. PAPER 650-D, PAGES D172–D179

area meets the following requirements: (a) Proximity to the U.S. Geological Survey Center of Astrogeology (in Flagstaff); (b) accessibility; (c) similarity to lunar maria because of subdued topography, unconsolidated surface cover of pyroclastic material, and lack of vegetation; and (d) temperate and relatively dry climate suitable for holding tests during most of the year.

Two crater fields were constructed under National Aeronautics and Space Administration (NASA) Contract No. T–65253G. Both are replicas of areas within the landing site designated by NASA as II–P–6–1, in Mare Tranquillitatis. A photogeologic map of this landing site has been prepared by Grolier (1968) from high-resolution Lunar Orbiter II and V photographs. The first crater field that was constructed measures 800 by 800 feet; the second one 1,200 by 1,200 feet. In addition, several test craters were excavated elsewhere in the Cinder Lake area for additional geologic and engineering studies.

GEOLOGIC SETTING

As the name "Cinder Lake" suggests, the area resembles a lake, but one filled with cinders and ash instead of water. It is surrounded on three sides by gently rolling hills and steep cinder cones, and on all sides by a dense growth of western yellow pine (*Pinus ponderosa*).

The pyroclastic material was provided by the violent subaerial eruption of basaltic tephra at the site of nearby Sunset Crater (fig. 1), in the year A.D. 1064 or 1065 (Smiley, 1958). Debris ranging in size from fine ash to blocks was ejected so violently that, with the aid of wind, it covered nearly 800 square miles of north-central Arizona (Colton, 1932, fig. 7). Most of the coarser material fell to the ground near the eruption site. The finer material—more susceptible to transport by wind—was carried greater distances from the orifice. At the orifice the debris accumulated to form a nearly perfect truncated cinder cone about 1,000 feet high—Sunset Crater.

In the 900 years since the eruption, little pyroclastic debris has been eroded from Sunset Crater. However, much erosion has occurred in the peripheral part of the ejecta blanket, where the material is finer grained. Colton (1932, fig. 1) distinguished between an inner area of continuous lapilli or cinder cover and an outer, larger area of discontinuous cinders arranged as dunes. Much of the material in the outer area has been removed or redistributed by wind and water.

Cinder Lake lies in the southwestern part of the area of continuous cinder cover (fig. 1). The Cinder Lake tephra are nearly uneroded owing to the level terrain and protected position of the area. Consequently, the original depositional layering is well preserved.

Construction of the simulated crater fields entailed digging more than 500 holes. Figure 2 shows a stratigraphic section typical of the nearly 500 that were examined in the holes. The three main divisions are the Sunset Crater eruptive sequence (most recent), a succession of weathered eruptive sequences (older), and a lava flow with its attendant squeezeups and flow ridges (oldest).

The Sunset Crater eruptive sequence ranged in thickness from 14 inches in holes dug in crater field I to 65 inches in holes in crater field II. The sequence is well stratified; as many as 17 distinct layers can be recognized by differences in color, particle size, degree of sorting, and coherency. Discrete layers increase in number and thickness northward toward the source. The upper half of the Sunset Crater sequence comprises at least 20 layers where exposed in an excavation two-thirds of a mile south of the base of Sunset Crater. By extrapolation, the total thickness of the sequence is estimated to be above 36 feet at this site. Within the Sunset Crater sequence, the thin bed of black ash near the middle serves as an excellent key bed for detailed correlation. This ash and a lithologically similar ash bed at the base of the sequence have been traced between the two fields and for several miles to the north and east. Another persistent unit is the 1½- to 2½-inch layer of resistant dark-brown material about 4 inches below the ground surface. It is present throughout the southern half of the area of continuous cinder cover. This layer is composed largely of coarse cinders but includes much volcanic ash and secondarily derived dust, all bound together in a matrix of humus further strengthened by plant rootlets. Nine hundred years of soil formation are represented by this thin humus-rich layer. This compact, relatively coherent layer probably increases the bearing strength of the surficial material in Cinder Lake. In its absence, wheeled travel might be much more difficult.

The materials immediately below the Sunset Crater sequence are also unconsolidated but are more compacted. They consist largely of layers of slightly weathered basaltic pyroclastic debris from older eruptions alternating with layers of this material in a highly altered state. These materials are logically grouped in genetically related pairs—a homogeneous cindery clay unit above and a unit of iron-stained bedded cinders below containing some ash. The total thickness of each pair represents the bulk of the pyroclastic material that accumulated during an eruption of some nearby vent. The clay-rich unit of each pair represents a prolonged period of in-situ weathering and

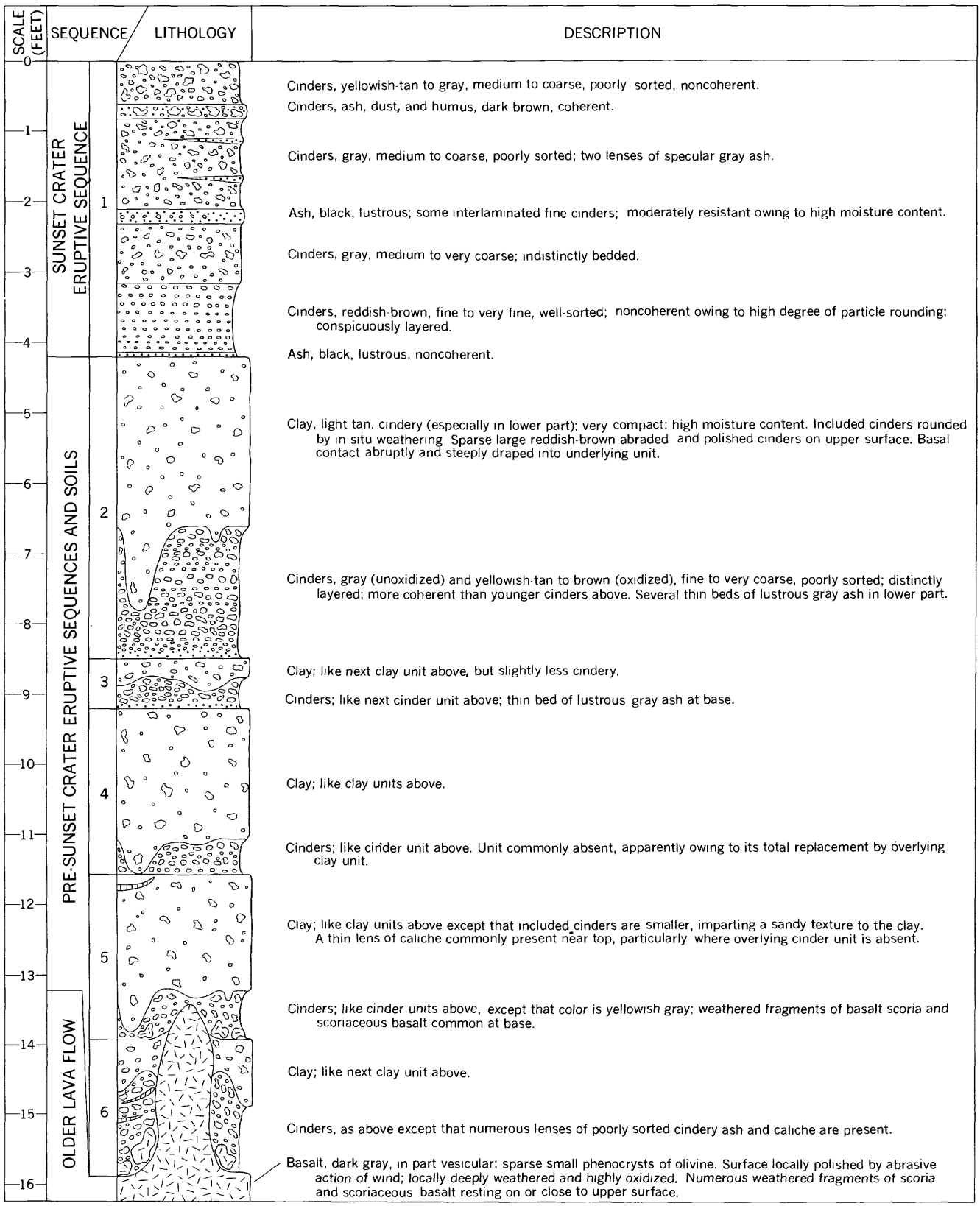

FIGURE 2.—Composite columnar section for Cinder Lake, near Flagstaff, Ariz.

soil development between eruptions. No bedding characteristic of deposition by alluvial processes has been observed. The contact at the top of each clay or paleosol unit therefore represents an ancient ground surface that formed between eruptions and was later buried by falling ash and cinders. Scattered potsherds and a few flint artifacts found in place at the top of sequence 2 (fig. 2) in a borrow pit at the north end of Cinder Lake are convincing proof of the existence of a former ground surface at this stratigraphic position. Counting the present surface and the incipient soil shortly below it, six such pairs are present in the deepest excavations in Cinder Lake. In addition, there may be others at greater depths.

All the Cinder Lake area is underlain at various depths by one or more flows of vesicular basaltic lava containing very small phenocrysts of olivine. Reconnaissance seismic surveys by H. D. Ackermann, of the U.S. Geological Survey (written commun., 1967, 1968), indicate that the average depth to lava in the crater fields is between 30 and 40 feet. The top of the lava, which normally is covered by irregular fragments of highly oxidized scoria or highly vesicular basalt, was reached in 11 holes in the two crater fields. It also crops out on many small knobs in Cinder Lake and along many of the hills that surround the "lake." In the aforementioned 11 holes, depths to the top of the lava ranged from 6 feet to about 17 feet. Consequently those holes that reached the lava flow—none of which exceeded 17 feet in depth—may be located on the crests and flanks of local tumuli, pressure ridges, or other prominences of unknown origin on the lava surface.

The contrast between the irregular topography of the top of the buried lava and the very gently undulating ground surface of Cinder Lake is marked. The difference in relief is due to the mantling effect of successive accumulations of airborne debris aided by the action of erosional and depositional processes which were operative during periods of accumulation and during intervals between eruptions. More material accumulated in depressions than on high areas, and relief became more subdued with time. The processes that subdue relief operated so consistently that subsurface highs on the lava correlate with slight but detectable thinning in the Sunset Crater sequence at the top of the stratigraphic column. The following generalization can be made on the basis of stratigraphic control afforded by many measured sections. If appreciable differences in thickness are measured in three or more holes spaced 8 feet or more apart and arranged in any pattern but a straight line, the top of the lava rises toward the hole in which pyroclastics are thinnest. This generalization holds true even where there is no visible surface expression of an underlying "high" on the lava.

CONSTRUCTION OF THE CINDER LAKE CRATER FIELDS

Orbiter photographs of several potential Apollo landing sites were studied to select lunar areas to be duplicated at a 1:1 scale, and two areas in landing site II–P–6–1 were chosen because of their surface smoothness and low density of craters greater than 6 feet in diameter. The position and size of the craters in each of the areas were determined from high-resolution Orbiter II photographs. The positions of the crater centers were then laid out on the crater-field sites by means of a planetable and alidade survey.

Crater field I, originally 500 by 500 feet in size, was constructed in July 1967 and later enlarged to 800 by 800 feet. It contains 143 craters that range from 5 to 58 feet in diameter.

The first group of shot holes (a total of 47) were dug by hand in 5 days; holes for the final 96 craters were dug with a backhoe in just 2½ days. All holes were loaded, covered, and detonated individually.

The charge size and depth of burial required to produce craters of a given diameter were determined earlier by experimentation near the crater-field site. These experiments indicated that depth of burial of the charge is the critical factor in determining crater size, given a charge large enough to throw the material out of the crater. Table 1 shows the depth and size of charge for all craters in crater field I.

Nitro-Carbo-Nitrate, a mixture of ammonium nitrate fertilizer and fuel oil, was used as a blasting agent for all except the 5-foot (planned diameter) craters. The mixture was primed by a 60-percent high-velocity gelatin dynamite, which in turn was detonated by electric blasting caps. The eight smallest craters were blasted by dynamite alone.

TABLE 1.—*Depth and size of charges for creation of craters at crater field I*

Planned crater diameter (feet)	Charge depth (feet)	Dynamite (pounds)	Nitro-Carbo-Nitrate (pounds)	Number of craters	Actual crater diameter[1] (feet)
5	1.1	2.0	----	8	9.6
8	1.6	.5	7	8	13.7
10	2.0	.5	8	32	14.8
15	3.2	1.0	30	32	19.4
20	4.2	1.5	65	16	19.8
25	5.3	1.5	130	22	22.6
30	6.2	1.5	185	15	25.4
35	7.1	2.0	315	5	33.1
40	8.0	22.0	480	3	43.3
50	10.0	44.0	950	1	47.0
60	12.0	45.0	1,580	1	57.5

[1] Rim crest to rim crest; measured in the field.

Crater field II was constructed in July 1968 and consists of 426 craters ranging in diameter from 6 to 72 feet. The shallow shot holes were dug by hand and the deeper ones with a backhoe. Digging the holes, burying the charges, and smoothing the surface took 10 days. Mr. Franklin H. Persse, an explosives engineer, U.S. Bureau of Mines, served as a consultant in determining the size and depth of burial of the charges, listed in table 2.

TABLE 2.—*Depth and size of charges for creation of craters at crater field II*

Planned crater diameter (feet)	Charge depth (feet)	Dynamite (pounds)	Nitro-Carbo-Nitrate (pounds)	Number of primers	Number of craters	Actual crater diameter [1] (feet)
6	1.0	0.5			63	6.6
9	1.1	1.5			93	9.1
12	1.8	4.0			68	12.4
15	2.0		25	1	61	19.5
18	3.2	5.0	25	1	37	21.3
21	4.2	15.0	50	1	35	24.6
24	5.3		100	1	28	29.2
27	5.9		150	1	9	35.2
30	6.6		200	1	8	33.1
33	7.0		275	1	5	36.8
36	8.0		350	1	5	39.8
39	8.9		475	2	5	39.6
45	10.7		750	2	3	46.7
48	11.5		850	2	1	50.0
53	12.1		1,200	2	1	52.0
60	13.6		1,750	3	1	62.0
63	15.6		1,900	3	1	62.0
66	16.4		2,350	3	1	66.0
69	17.0		2,900	3	1	72.0

[1] Rim crest to rim crest; measured on aerial photograph taken 6 days after craters were blasted.

M. J. Grolier, of the Geological Survey, made a detailed study of Lunar Orbiter II photographs of the landing site and found that there were three relative age groups of craters. To simulate these age differences in crater field II, the charges were detonated successively in three groups. A total of 354 charges in sites corresponding in position to the oldest lunar craters were detonated first; 61 corresponding to lunar craters of intermediate age were detonated next. Finally, the 11 charges corresponding to the youngest craters were detonated.

In the deeper holes the Nitro-Carbo-Nitrate was primed with ¾-pound charges of cast Pentolite, which were detonated by Primacord. The shallower holes were loaded with dynamite alone and also detonated with Primacord.

The planned diameters and the actual diameters of the craters of the two fields are compared in figure 3. Comparison of Orbiter II high-resolution photographs of the two lunar areas with aerial photographs of the two Cinder Lake crater fields (fig. 4) shows how successfully the simulation was achieved. The data obtained should enable increased accuracy in any future crater fields constructed in similar materials.

The northwest quarter of crater field II was later "salted" by adding foreign rock fragments to the rims and ejecta blankets of some craters, creating rays, and emplacing scattered rock fragments. The fragments

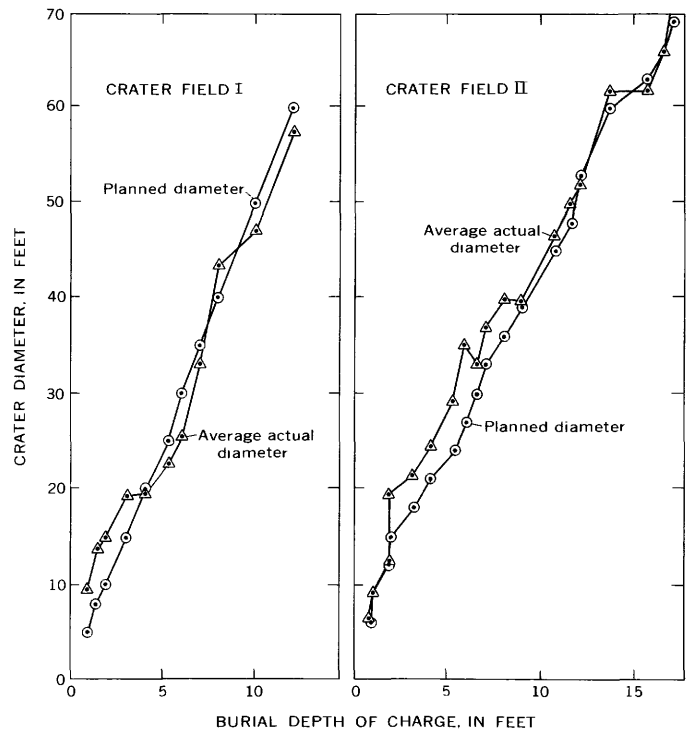

FIGURE 3.—Comparison of planned crater diameter and actual crater diameter related to depth of burial of charge.

were distributed so as to reflect a definite sequence of geologic events acting upon a specific geologic terrane, thus providing various geologic problems similar to those expected on the moon.

UTILIZATION OF THE CRATER-FIELD TEST SITES

The crater-field test sites and associated experimental craters have already been put to diverse uses with considerable success (fig. 5). These uses, as well as additional ones that are planned, are shown in tables 3 and 4.

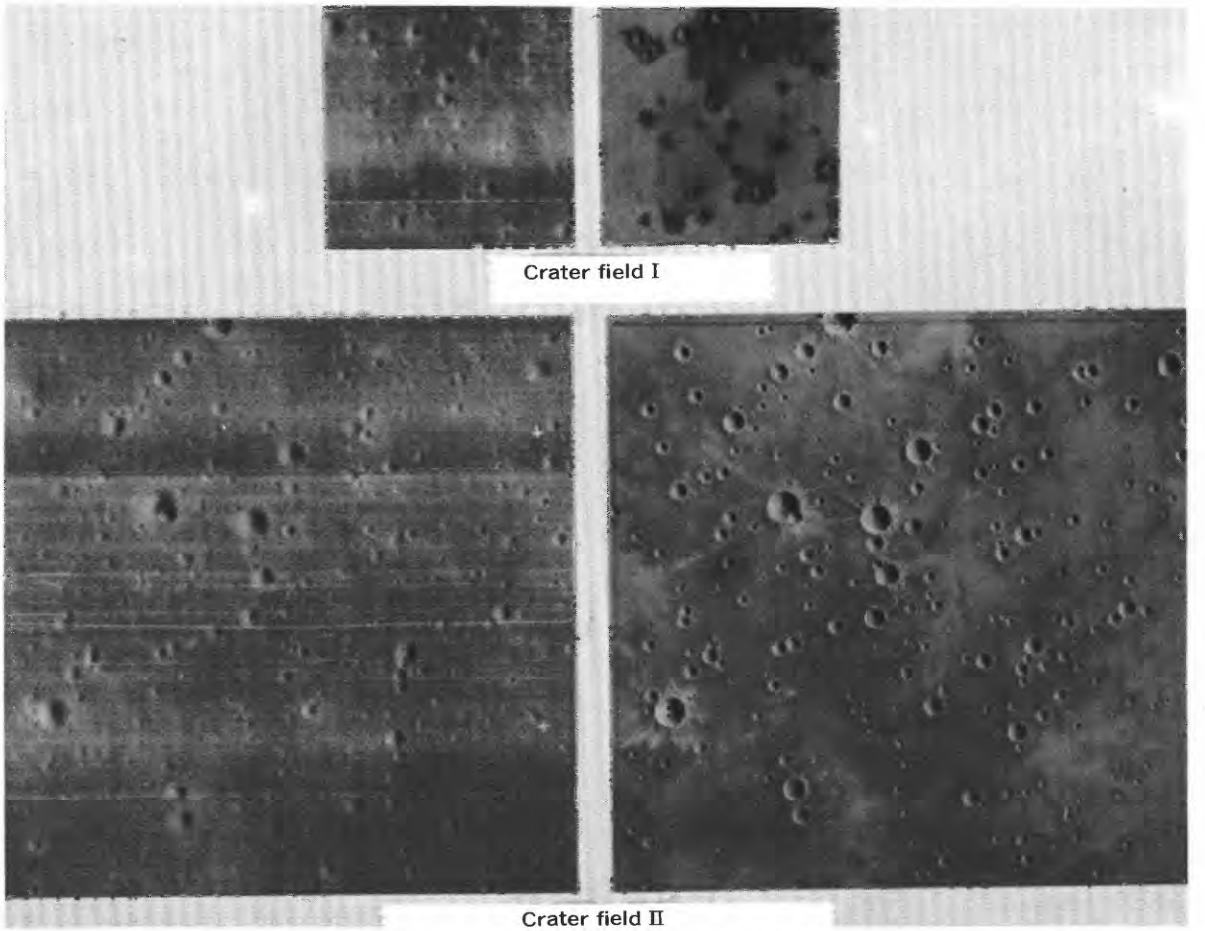

FIGURE 4.—Comparison of lunar areas selected for duplication and the resulting crater fields. Lunar Orbiter II high-resolution photographs on left. Aerial photographs of the Cinder Lake crater fields on right. The photograph of crater field I shows the original field of 47 craters that was later enlarged to 143 craters. The largest crater diameter in crater field I is 43 feet and in crater field II is 72 feet.

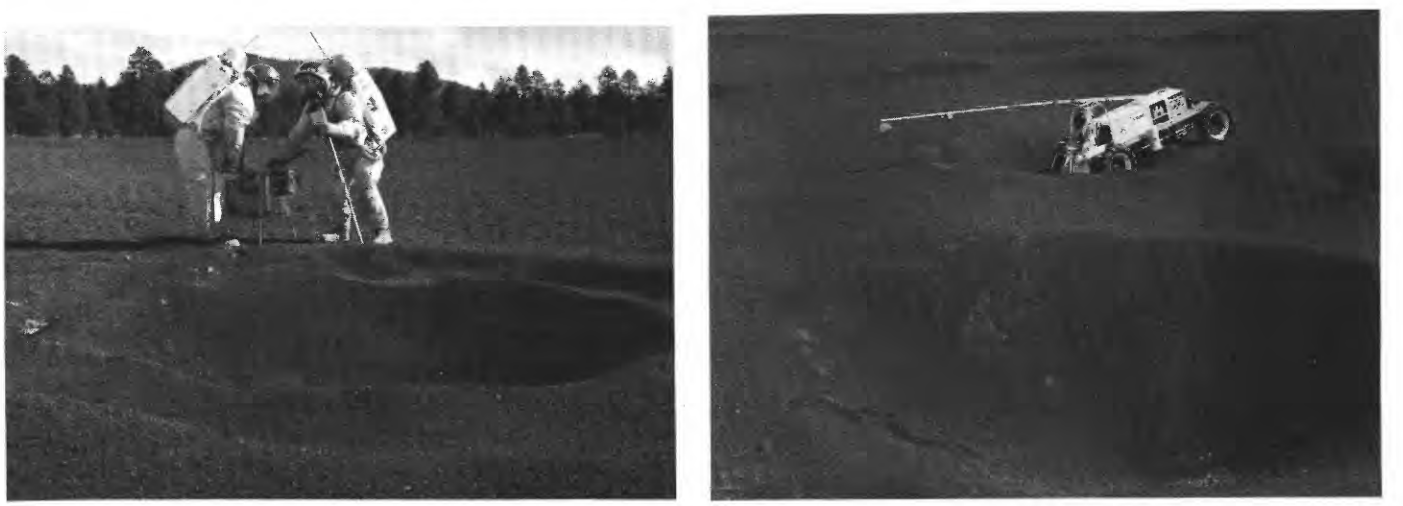

FIGURE 5.—Uses of crater field. Left, for suited field test; and right, for vehicle test.

TABLE 3.—*Uses already made of test areas*

Use	*Objectives*
	CRATER FIELDS
Location test (Bailey, 1967)	Determine how rapidly and how well test subjects can locate themselves by looking from the windows of a mockup of Lunar Landing Module and by using Lunar Orbiter photographs of area after which test site was patterned.
Performance of astronauts in pressure suits (fig. 5, left).	Determine how well two test subjects in pressure can manipulate tools and carry out out geologic tasks; how well they can walk around and see in a "realistic" landscape; how well they can see maps, photographs and other pictorial or printed material through the visor; and how well they can perform as a team.
Performance of tools, tool carrier, and so forth (fig. 5, left).	Determine how well prototypes of various geologic tools to be used on the moon perform their intended tasks under nearly realistic conditions of use.
Time-motion study (a)	Determine how quickly and how well test subjects can carry out preplanned traverses using various combinations of aerial photographs and photogeologic maps or using neither.
Time-motion study (b)	Determine how, and how often, test subjects perform certain tasks while doing geologic work similar to that on the moon, and how much time these tasks consume.
TV test	Evaluate utility of TV for locating and monitoring astronauts on a foot traverse from the the Lunar Landing Module, and its effectiveness in depicting geologic features.
Development and testing of Astrogeologic Data Facility (ADF).	Determine by means of testing in conjunction with a realistic site how the ADF should be constituted and how it should best function.
Part of test of Lunar Roving Vehicle (fig. 5, right).	By using the crater fields as stops on a much longer traverse, demonstrate and test procedures for (1) giving and recording information on a cratered area encountered during a long traverse, and (2) comparing and integrating this information with that obtained in other parts of the traverse.
Test of engineering properties of material in crater field.	Determine static bearing strength of undisturbed surface material, and compare it with that of disturbed material on rim of 80-foot crater.
Test of photogrammetric techniques	Determine how well photogrammetric data from Apollo-like traverses can be reduced and plotted.
Collection of samples to be tested in the Lunar Receiving Laboratory.	Provide samples, as well as description and photographic documentation thereof, collected in terrain similar to that of the moon, and in a manner analogous to that of an Apollo geologic traverse, to be used in a test run at the Lunar Receiving Laboratory, Houston, Tex.
Geologic studies	Study the geology and geologic history of the Cinder Lake-Sunset Crater area.
	SINGLE CRATERS
Test performance of simulated Lunar Roving Vehicle.	Determine how well the test vehicle built by the U.S. Geological Survey performs on a typical cratered surface. More specifically, how well it can cross craters, and how much the wheels are deflected from true course when a crater is crossed.
Training photogrammetric personnel	Provide training on use of AP–C plotter and other devices for mapping craters similar to those of the moon.
Cratering studies	Use geophysical methods to learn more about the geometry of the disturbed zones associated with an explosive crater.

TABLE 4.—*Future uses of test areas*

Use	*Objectives*
	CRATER FIELDS
Astronaut Training	Train astronauts for Apollo geologic traverses in landscape and geology that most realistically reproduce those of an actual landing site.
Tests on methods for studying specific lunar features and problems.	Determine most efficient methods for studying the geologic features and problems of the Apollo sites.
Development of Astrogeologic Data Facility (ADF).	Determine by means of tests in a realistic site (1) how the ADF should be constituted, and (2) how it should best function; train personnel involved.
Tests of Lunar Surveying Staff (a device for obtaining photographic, TV, and position data on a lunar traverse).	(a) Help provide information on the device before final specifications are written for flight hardware. (b) Determine how well topographic profiling and cartographic location can be obtained from tracking data. (c) Test near-real-time processing and mosaicking of Polaroid film images and their use for geologic interpretation at the ADF during the traverse. (d) Evaluate usefulness of TV as an aid to real-time monitoring and interpretation of geologic features by ADF personnel. (e) Explore potential new problems in data handling that the device may impose on the ADF.
Application of photogeologic mapping to mission simulations.	Determine what kinds of photogeologic maps are best suited for mission simulations and, hence, for lunar missions.
Crater morphology studies and terrain analysis.	Obtain a better understanding of how crater morphology may reflect mechanical properties of cratered material and how shape and distribution of small craters affect ease of travel and, hence, traverse planning.
Local navigation problems.	Determine ease and accuracy of location during a traverse in monotonous cratered terrain.
	SINGLE CRATERS
Sampling studies	Determine how best to sample craters for a maximum return of pertinent geologic information.
Photogrammetric studies	Continue studies to determine how well photogrammetric data can be reduced and plotted and how well positions can be determined by resection.

REFERENCES

Bailey, N. G., 1967, Cinder Lake crater field location test: U.S. Geol. Survey open-file rept., 15 p.

Colton, H. S., 1932, Sunset Crater—the effect of a volcanic eruption on an ancient pueblo people: Geog. Rev., v. 22, no. 4, p. 582–590.

Groiler, M. J., 1968, Preliminary geologic map of Ellipse II–6–1 and vicinity [scale 1:25,000]: U.S. Geol. Survey open-file rept.

National Aeronautics and Space Administration, 1966, Surveyor I—A preliminary report: Natl. Aeronautics and Space Adm. Spec. Pub. 126, 39 p.

Smiley, T. L., 1958, The geology and dating of Sunset Crater, Flagstaff, Arizona, *in* New Mexico Geol. Soc. Guidebook 9th Field Conf., Black Mesa basin, northeastern Arizona, 1958: p. 186–190.

THE USE OF SPECTRAL ANALYSIS IN DESCRIBING LUNAR SURFACE ROUGHNESS

By WESLEY J. ROZEMA, Flagstaff, Ariz.

Work done in cooperation with the National Aeronautics and Space Administration

Abstract.—The power spectral density (PSD) function has been investigated in recent years as a means of statistically describing land-surface roughness. Knowledge of the PSD functions of lunar topographic profiles is useful for analyzing the manner in which experimental lunar roving vehicles will respond to lunar terrain. In addition, the function enables comparison of the relative "roughness" of different types of terrain. Certain statisical problems are inherent in the determination of the PSD function, resulting in a variety of methods of estimating the function. Specific methods of determining the function were selected and applied consistently to several terrestrial and lunar topographic profiles. Superposition of the graphs of these functions provides an intuitive comparison of the "roughness" of terrestrial and lunar terrains.

The determination of a statistical description of the roughness of the lunar surface is vital for the design of lunar roving vehicles. Under the sponsorship of the National Aeronautics and Space Administration (NASA), Mason, McCombs, and Cramblit (1964) and Olivier and Valentine (1965) proposed the ELMS and ELMO, respectively, as statistical models of the lunar surface. Schloss (1965) suggested the use of curvature as a surface roughness characteristic.

Efforts toward generating a statistical description of the roughness of the lunar surface were begun for the U.S. Geological Survey by McCauley (1964). Using data derived photometrically from Earth-based photographs, Rowan and McCauley (1966) found the mean and standard deviation of slopes to be useful statistical parameters for the quantitative description of lunar surface roughness at Earth-based resolutions. However, in the design of a lunar roving vehicle, neither the aforementioned parameters nor data from the maximum-resolution Earth-based lunar photographs are completely adequate.

At present, lunar surface features as small as 0.6 meter can be resolved through photoclinometric reduction of Lunar Orbiter II and III photography. This degree of resolution is sufficient for lunar trafficability analysis. Furthermore, the power spectral density (PSD) function of a topographic profile has been found to be an especially useful statistic in the analysis of vehicular response to terrain. Spectral, or time series, analysis enables examination of the frequency content of the topographic profile. Although spectral analysis originated in communication engineering, in recent years it has been applied to other fields, including analysis of terrain roughness. Suggested by Bekker (1960) as one quantitative specificatin of terrain roughness, it has been applied to off-road hard ground by Kozin, Cote, and Bogdanoff (1963), and to the lunar surface, as photographed by Rangers VII and VIII, by Jaeger and Schuring (1966) and Van Deusen (1966).

Techniques for the derivation of the PSD function have been investigated as part of the Geological Survey's lunar trafficability project, sponsored by NASA (Purchase Order W–12,338, Amend. 2). The particular problems of analyzing a topographic profile by this method have been studied, and PSD functions for several terrestrial and lunar topographic profiles have been determined. This report summarizes the results.

Acknowledgments.—Appreciation is expressed to Dr. M. G. Bekker and Dr. Dietrich Schuring, of AC Electronics, Defense Research Laboratories, for advice and technical assistance during this study. Appreciation is also given to Dr. B. D. Van Deusen of the Defense

Operations Division, Chrysler Corp., for consultative advice. Finally, the writer is greatly indebted to Dr. Richard M. Jaeger of the National Center for Educational Statistics, U.S. Department of Health, Education, and Welfare, for his valuable advice and assistance during the course of this study.

POWER SPECTRAL DENSITY FUNCTION

Definition

Profiles of lunar and analogous terrestrial topography cannot be described by a specific functional relationship; thus, for the purpose of mathematical analysis, they are random profiles. The frequency content of such profiles is determined by spectral analysis. Nearby points on these profiles can reasonably be assumed to exhibit some degree of correlation, which, expressed as a function of the distance between them, can be stated mathematically as

$$R(v)=\frac{1}{N}\int_0^N h(x)\cdot h(x+v)dx, \quad |v|<N,$$

where $h(x)$ and $h(x+v)$ represent "neighboring" elevations at a distance v apart, and N is the total number of elevation points considered. $R(v)$ is called the autocorrelation function.

The value of $R(v)$ for specific values of v may contain information regarding the frequency content of a specific profile. For example, consider the unlikely (and nonrandom) surface profile of figure 1*A*. For distance $v=b$, $R(v)=0$ for all values of x, but for $v=2b$, $R(v)=\frac{1}{2}E^2$, since for half of the values of x, $h(x)\cdot h(x+2b)=0$, and for the remaining values of x, $h(x)\cdot h(x+2b)=E^2$. The graph of the autocorrelation function (fig. 1*B*) illustrates the presence of the frequency which has periodicity $2b$ in the surface profile.

From this very simple, nonrandom example, it is possible to extrapolate the concept of the power spectrum. The power spectrum is a measurement of the amount of variation of the profile height contributed by the various frequencies present. For the above example, only one frequency, $\frac{1}{2b}$ contributes to the variation of profile height, as can be seen from the autocorrelation function graph (fig. 1*B*). Hence, the graph of the power spectrum of this example would be a single spike representing power, $P(\omega)$, at the frequency $\frac{1}{2b}$ (fig. 1*C*).

Determination of the power spectrum for a nonperiodic function demands a rather lengthy mathematical development, but can be explained intuitively as follows: Any periodic function can be described by its Fourier series representation; thus, the autocorrelation function of figure 1*B* can be represented by a Fourier series of the form $R(v)=\sum_{n=0}^{\infty} F(n)\cos n\omega r$, where $\frac{2\pi}{\omega}$ is the period of the function. If the function is onperiodic, as is a random function, this concept can be extended by considering the periodicity to be infinite, and its representation becomes the Fourier integral over all frequencies:

$$R(v)=\frac{1}{\pi}\int_0^{\infty} P(\omega)\cos\omega v d\omega.$$

In electrical theory, power is proportional to the square of either the voltage or the current. This term can be applied to functions in general, and thus power is described as the mean square value of any function. If the function is periodic, the power contributed by any discrete frequency can be described as the square of the Fourier coefficient associated with the frequency. When $v=0$ in the autocorrelation function, the function becomes $\frac{1}{N}\int_0^N h^2(x)dx$, which is the mean square value, or power, of $h(x)$. Parseval's theorem then shows that the power spectrum is given by $P(n)=|F(n)|^2$.

If a random profile is considered as one in which a continuum of frequencies contributes to the variations

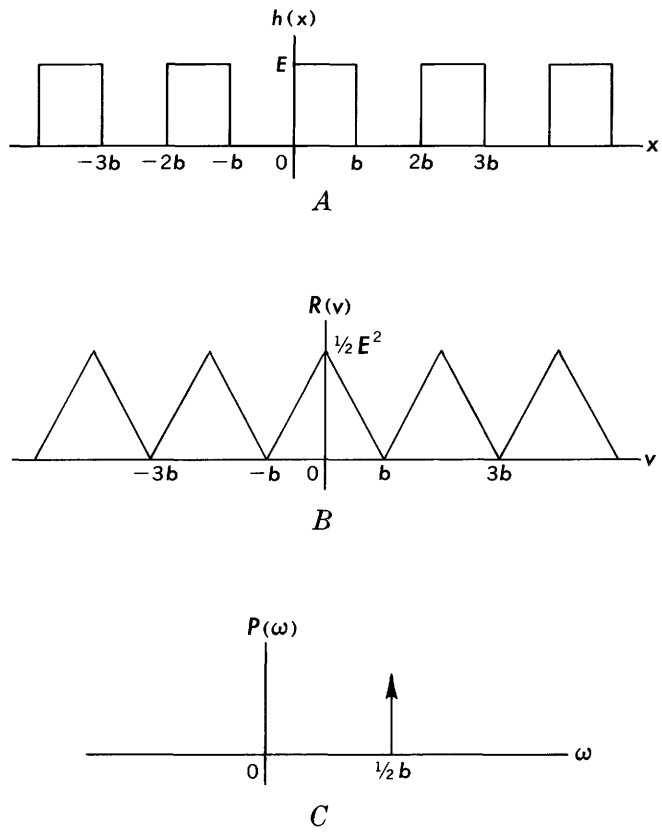

FIGURE 1.—Diagrams showing: *A*, arbitrary nonrandom surface profile; *B*, autocorrelation function of surface; and *C*, power spectrum of surface.

of profile height, it becomes obvious that the power contributed can be found only for bands of frequencies, and not for discrete frequencies. Thus, it is necessary to find the power spectral density (PSD)—the power per unit bandwidth—rather than the power spectrum. Since the autocorrelation function of a random profile is expressed as a Fourier integral, the PSD can be shown to be equivalent to its Fourier transform, $P(\omega)=2\int_0^\infty R(v)\cos \omega v dv$. Thus, given the autocorrelation function, the PSD function can be determined, and vice versa.

As a further illustration of the relationship of the autocorrelation and PSD functions, consider a terrain profile consisting of great amplitude differences in closely spaced points. The autocorrelation function for such a profile will show little correlation between "neighboring" points, but the PSD function will show great power in the high-frequency bands.

Assumptions

Two conditions must exist before a spectral analysis can be made of any given random profile. First, the profile must represent a stationary process, that is, its statistical properties will be unaffected by a change in the origin of the profile. This condition may be assumed to hold when a sample profile is obtained entirely within a single homogeneous terrain unit. Second, the mean value of the profile height must be zero; if it is not, it can easily be converted by normalizing the data.

Problems in spectral analysis

In the actual determination of the PSD function, several rather difficult problems arise. Basically, these are of two types: (1) instability in the spectral estimates resulting from sampling limitations, and (2) contamination of the "true" power spectrum by long trends in the profile.

Statistical estimation.—When a terrain profile is recorded, only a finite number of discrete data points can be obtained over a finite length. Consequently, the autocorrelation and PSD functions which are determined will of necessity be estimates of the "true" functions, as, mathematically, both are integrals over all frequencies or lags. This leads to the following problems of statistical estimation:

1. Profile heights can be read only at discrete points, resulting in loss of information. As illustrated in figure 2, if the sampling interval is Δx, frequencies in the profile greater than $\frac{1}{2\Delta x}$ cannot be detected. However, the power found attributable to the frequency $\frac{1}{2\Delta x}$ is actually compounded by all higher frequencies which are indistinguishable from $\frac{1}{2\Delta x}$ and are multiples of it. This aliasing problem can be corrected in signals produced by electronic devices by filtering out frequencies higher than $\frac{1}{2\Delta x}$ prior to sampling the data. In terrain profiles, however, aliasing can be avoided only by choosing a sampling interval smaller than any physically expected profile frequency. This, obviously, is not usually possible, particularly when considering lunar terrain profile limitations.

FIGURE 2.—Profile showing aliasing problem.

2. Since the profile record is of finite length, values for the autocorrelation function for large lags (the distance v between points on the profile) must be formed from very few observations. This produces a great deal of instability in the statistical estimates of the PSD function. To correct this, statisticians have devised several lag windows (weight functions) to be applied to the autocorrelation function, or similarly, spectral windows (kernels) to be applied to the PSD function. Generally, the lag windows apply decreasing weights to increasing lags in order to decrease the sampling error incurred by including the large lags in the autocorrelation function. Unfortunately, although these windows increase the stability of the estimate of the PSD function, they also increase the bandwidth of frequencies contributing to the power. Conversely, decreasing the bandwidth of frequencies also decreases the stability of the estimates. Many reliable windows have been proposed, as well as criteria for testing them, and the merits of each have been extensively debated.

Detrending.—A long-term trend affects the PSD function of a profile in two ways: (1) it may result in a nonstationary profile (a profile whose statistical properties are affected by a change in origin), and (2) since the amplitude of the profile associated with the low frequency of a long trend would likely be relatively large, enough power would be contributed by the low frequency to obscure that contributed by higher frequencies. Since the effect of low frequencies is irrelevant to vehicle response, profiles can be detrended (that is, long trends can be eliminated) in order to more accurately describe the power in the range of frequencies which are appropriate for vehicle response.

Several methods of detrending have been proposed: linear detrending (Parzen, 1964), parabolic fitting and linear running average (Kozin and others, 1963), and an exponentially weighted average (Van Deusen, 1966). For a detrending method to be effective, the data in the frequency range which best describes the terrain roughness must remain unaltered. However, in eliminating the power contributed by low frequencies, detrending also attenuates the power at some, if not all, of the higher frequencies. This problem is currently being investigated.

Interpretation

PSD functions of terrain profiles are usually plotted on log-log graph paper, with frequency units of cycles per meter and power units of square meters per cycle per meter. Terrestrial and lunar terrain samples both possess the same general characteristics, that is, the power contributed by lower frequencies is much greater than that contributed by higher frequencies. Van Deusen (1966) noted that, in general, PSD functions of terrain have a slope of -2 when plotted on log-log paper. There are, however, significant differences in some frequency ranges in the spectrums of the various terrain units, and the entire spectrum of one terrain may be greater than that of another by as much as an order of magnitude. Thus, the roughness of one terrain sample may be much greater than another over all frequencies.

The application of spectral analysis to vehicle design is accomplished by "shaping," in an analog computer, the power spectrum of a white-noise generator (the PSD of a random function) to approximate that of the power spectrum of the terrain under consideration. A simulated terrain profile is then generated by the computer, and is subsequently used as input into a system of differential equations which describe the dynamic response of a vehicle. The analog computer simulates the physical system, and can thus provide the design specifications for the vehicle that will be best suited for terrain of a given spectral composition.

TECHNIQUES USED

In the past, scientists who have determined the PSD functions of terrains have selected various spectral windows and have used various techniques to detrend profiles. It is doubtful whether valid comparisons of terrain roughness can be drawn from such studies. Consistent methods and techniques must be applied to all terrain units, both terrestrial and lunar, before valid comparisons can be made. Also, techniques should be used that will provide the stablest spectral estimates and that will least distort the "true" spectrum.

Spectral window

Since data samples for a terrain profile are not continuous, finite forms of the autocorrelation and PSD functions must be used. In this study the estimates suggested by Jenkins (1961) have been used:

$$R(v)=\frac{1}{N}\sum_{x=1}^{N-v} h'(x)h'(x+v),\ v=0,1,\ldots,M,$$

where

$h'(x)=h(x)-\overline{h(x)}$,
$\overline{h(x)}$=sample mean profile height, and
M=maximum lag.

$$P(\omega)=2\Delta\left[R(0)+2\sum_{v=1}^{M}\lambda(v)R(v)\cos\omega v\right],$$

where
Δ=sampling interval, and

$$\lambda(v)=\begin{cases}1-\dfrac{6v^2}{M^2}\cdot\left(1-\dfrac{v}{M}\right) & 0\le v<\dfrac{M}{2},\\[2ex] 2\left(1-\dfrac{v}{M}\right)^3 & \dfrac{M}{2}\le v\le M,\\[2ex] 0 & v>M\end{cases}$$

$\lambda(v)$ is the lag window suggested by Parzen (1961). This form of the PSD function $P(\omega)$ is the finite Fourier transform of the autocorrelation function.

In the results which follow, all spectral estimates have been made using a maximum lag of approximately 10 percent of the number of points in the terrain sample.

Detrending

In this study, the exponentially weighted average suggested by Van Deusen (1966, p. 57) has been used consistently to detrend the terrain profiles prior to determination of the PSD function. The values of the profile elevations after detrending are given by

$$h_d(x)=h(x)-\frac{\sum_{n=0}^{\infty}[h(x+n\Delta)+h(x-n\Delta)]e^{-n\Delta/\lambda}}{2\sum_{n=0}^{\infty}e^{-n\Delta/\lambda}},$$

where

$h(x)$=original profile height,
Δ=sampling interval, and
λ=arbitrary constant.

The choice of the value of λ greatly affects the amplitudes of the detrended profile. A value of $\lambda=15$ was used consistently in detrending all terrain profiles in this study.

RESULTS

In the initial phases of this study, the only lunar data available were elevation values, computed at the California Institute of Technology Jet Propulsion Laboratory, of the terrain photographed in the last P–3 frames of the Ranger VIII and IX flights, and a topographic contour map of the Surveyor III landing site which was developed by R. M. Batson, of the U.S. Geological Survey. Since there were many uncertainties as to the reliability of these data, they were used primarily as sources for exploratory investigations in detrending, maximum lag, and normality of the data distributions.

Use of the terrain data from the high-resolution Orbiter photography was anticipated for further spectral analysis of lunar topography. However, in processing the terrain data by the photoclinometric method (developed for spacecraft imagery by Watson, 1968, and Lambiotte and Taylor [1]), difficulties developed that delayed spectral analyses of most lunar samples. To date, four reasonably reliable lunar terrain samples have been processed; this report includes their spectral analyses. The four areas were chosen on Lunar Orbiter III photographs (fig. 3) and are in Apollo site III P–9, which is just north of the Mare Cognitum region.

PSD functions have also been determined for several terrestrial terrains. These include the undisturbed terrains of the Bonito lava flow, Flagstaff, Ariz. (fig. 4; data from a contour map by R. M. Batson, U.S. Geol. Survey) and of the Perth Amboy, N.J., microbadlands (fig. 5; data from a contour map by A. N. Strahler, Geology Dept., Columbia Univ.). Also included are the man-distorted terrains of the Perryman Mud Course at the Aberdeen Proving Ground, Md., and of the Yuma Proving Ground, Ariz. (data from Kozin, Cote, and Bogdanoff, 1963).

Finally, spectral analysis has been completed on two simulated lunar terrains: the Cinder Lake crater field near Flagstaff, Ariz., (fig. 6) and the Suffield test crater "Distant Plain," near Ralston, Alberta, Canada (data from a contour map courtesy of Dr. G. H. S. Jones, of the Defense Research Establishment Suffield, Ralston, Alberta). All the areas, lunar and terrestrial, have been sampled at an interval of approximately 0.6 meter.

Figure 7 shows graphs of the PSD functions for the four lunar terrain profiles. These surfaces are obviously similar in degree of roughness; however, the PSD curve of the framelet 933 profile indicates slightly lower power at all frequencies.

[1] J. J. Lambiotte and G. R. Taylor, 1967, A photometric technique for deriving slopes from Lunar Orbiter photography, *presented at* Space Systems for Planetary Geology and Geophysics Conference, Boston, 1967: Natl. Aeronautics and Space Adm., Langley Research Center, 22 p.

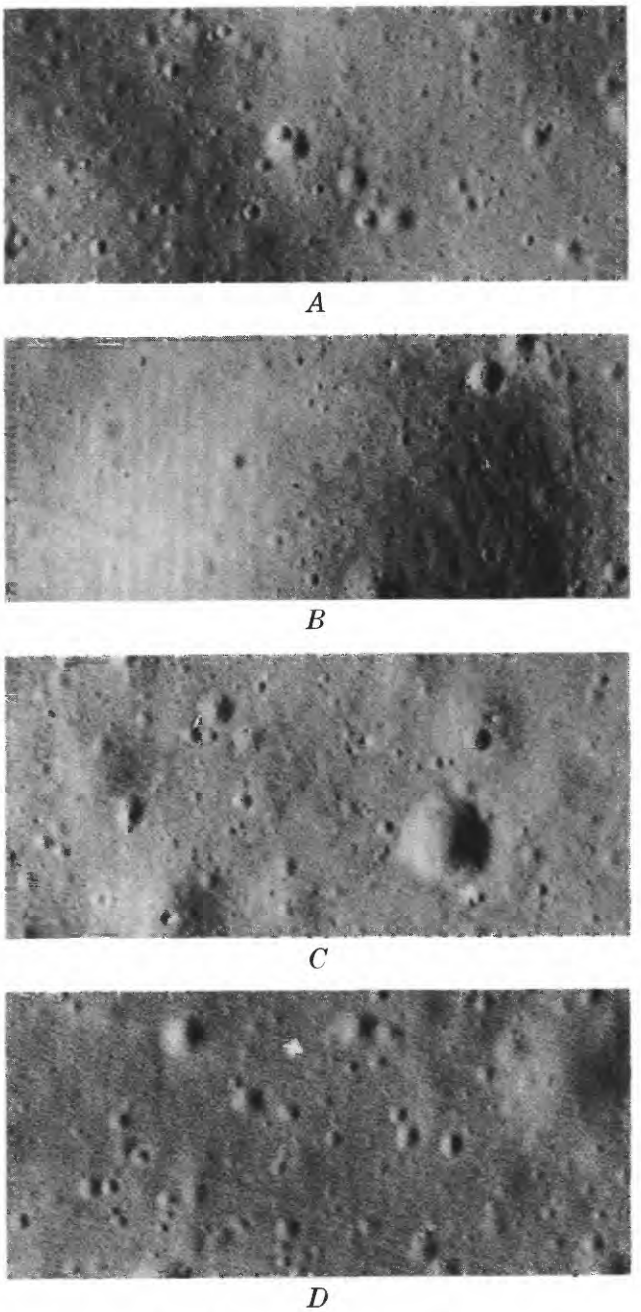

FIGURE 3.—Lunar terrain in four areas photographed by Lunar Orbiter III. *A*, frame H153, framelet 901; *B*, frame H154, framelet 027 (Surveyor III landing site); *C*, frame H153, framelet 914; *D*, frame H153, framelet 933.

One of the lunar PSD functions is compared with those of the undisturbed terrestrial terrains and that of the Suffield crater in figure 8. The lunar terrain appears to be much less rough than the terrestrial ones. The high power at all frequencies of both the Perth Amboy microbadlands and the Bonito flow indicates very rough terrains, and the very high power at the high frequencies in the Bonito flow PSD function indi-

FIGURE 4.—Bonito lava flow, Flagstaff, Ariz.

FIGURE 5.—Microbadlands topography, Perth Amboy, N.J. (courtesy of Dr. Stanley Schumm, Colorado State Univ.).

cates the extreme roughness of the area, as anyone who has observed the area can attest. It is interesting to note that the PSD function values for the Suffield crater are considerably greater at all frequencies than that of the lunar surface sampled.

Figure 9 compares the PSD functions of the "smoothest" lunar terrain profile, framelet 933, with those of the man-distorted terrestrial terrains and with that of the simulated lunar mare of Cinder Lake crater field. It is striking that the simulated lunar crater field PSD function shows greater power at almost all frequencies than that shown by the actual lunar terrain profile. It is also noteworthy that the lunar PSD function generally indicates less roughness than the Aberdeen and Yuma Proving Grounds profiles, and that these two areas are readily trafficable by many types of vehicles.

It should be remembered that although these PSD function graphs indicate power for frequencies from 0.01 to about 0.8 cycles per meter, the frequency range considered relevant to vehicle dynamics (Jaeger and Schuring, 1966) is from 0.05 to 0.5 cycles per meter. Thus, the topographic variations affecting vehicular response have wavelengths from 2 to 20 meters.

FIGURE 6.—Cinder Lake crater field, Flagstaff, Ariz.

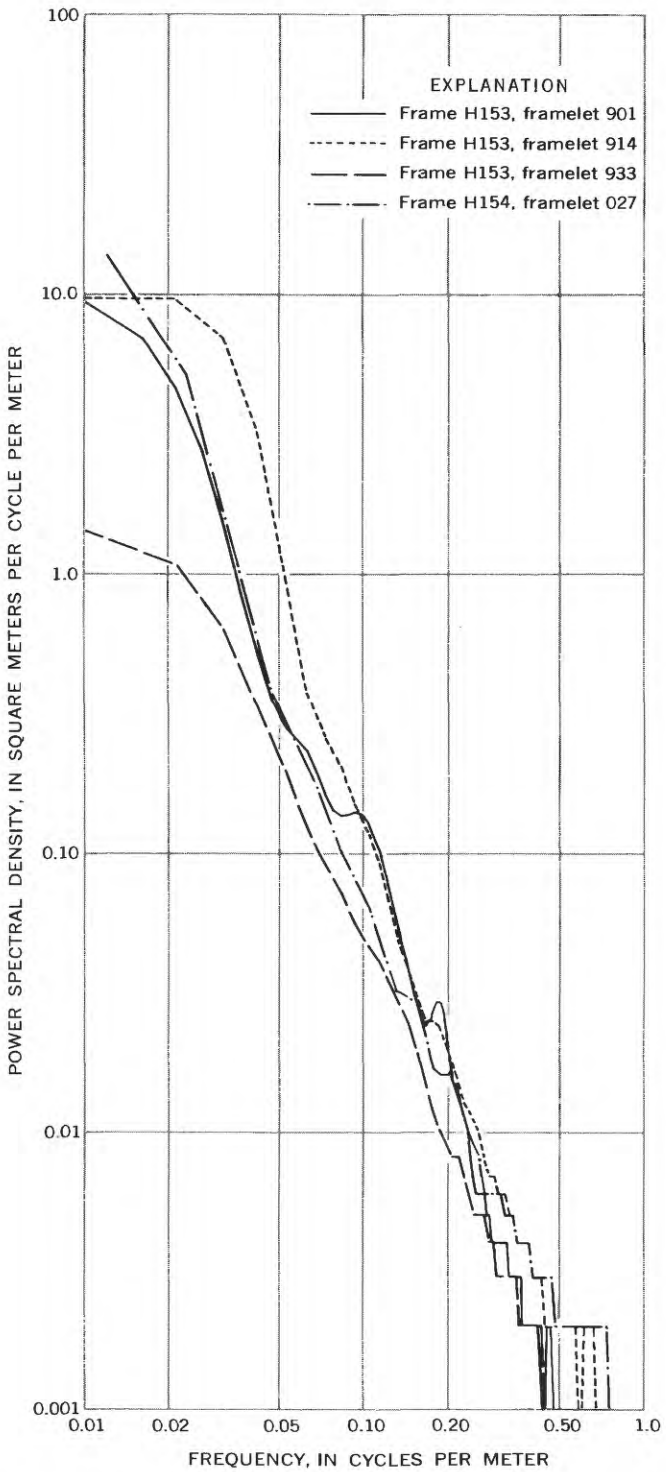

FIGURE 7.—Power spectral density functions for detrended lunar terrain profiles (from Lunar Orbiter III).

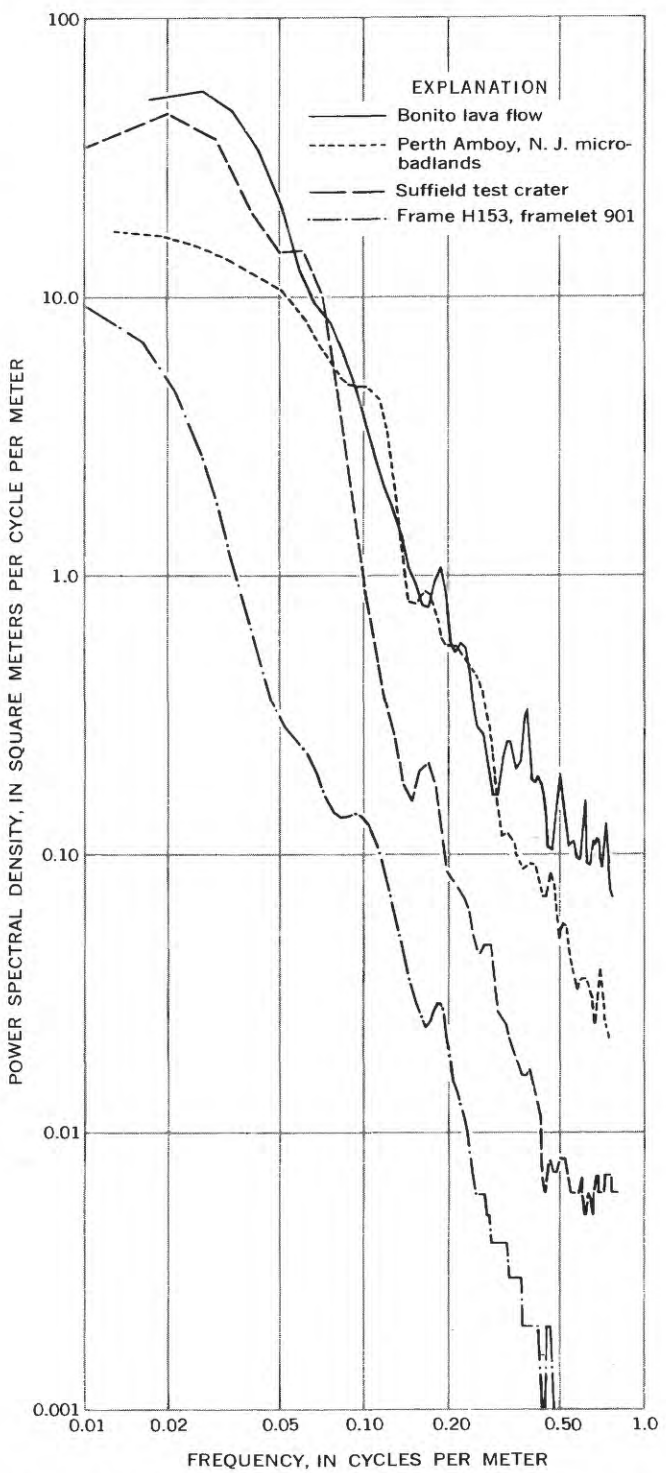

FIGURE 8.—Comparison of power spectral density functions for a detrended lunar terrain profile with those for detrended undisturbed terrestrial terrain profiles.

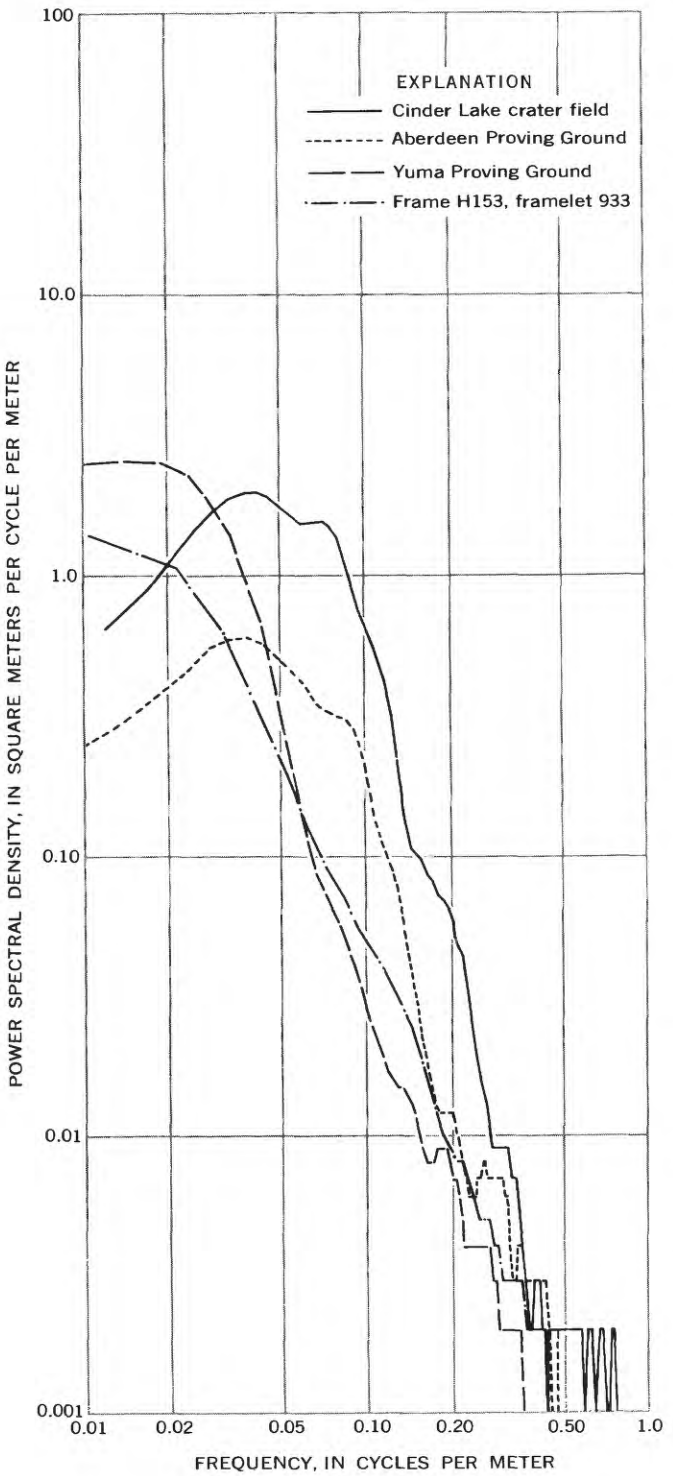

FIGURE 9.—Comparison of power spectral density functions for a detrended lunar terrain profile with those for detrended man-distorted terrestrial terrain profiles.

FUTURE APPLICATIONS

The results of this study suggest that the lunar surfaces sampled are no rougher than many surfaces on Earth, and are considerably smoother than many others. Other lunar surfaces should be investigated in order to gain a more complete picture of lunar trafficability.

A very important application of spectral analysis which has not yet been attempted is in geological terrain analyses. The PSD function may be useful for description of geomorphological types and therefore of many geologic map units, as well as for a statistical parameter of surface roughness.

REFERENCES

Bekker, M. G., 1960, Off-the-road locomotion: Ann Arbor, University of Michigan Press, 220 p.

Jaeger, R. M., and Schuring, D. J., 1966, Spectrum analysis of terrain of Mare Cognitum: Jour. Geophys. Research, v. 71, no. 8, p. 2023–2028.

Jenkins, G. M., 1961, General considerations in the analysis of spectra: Technometrics, v. 3, no. 2, p. 133–166.

Kozin, Frank, Cote, L. J., and Bogdanoff, J. L., 1963, Statistical studies of stable ground roughness: U.S. Army Tank Automotive Center, Rept. 8391, 160 p.

McCauley, J. F., 1964, Terrain analysis of the lunar equatorial belt: U.S. Geol. Survey open-file rept, 44 p. [1965].

Mason, R. L., McCombs, W. M., and Cramblit, D. C., 1964, Engineering lunar model surface: Natl. Aeronautics and Space Adm., Kennedy Space Center, Rept. TR–83–D.

Olivier, J. R., and Valentine, R. E., 1965, Engineering lunar model obstacles: Natl. Aeronautics and Space Adm., Kennedy Space Center, Rept. TR–145–D.

Parzen, Emanuel, 1961, Mathematical considerations in the estimation of spectra: Technometrics, v. 3, no. 2, p. 167–190.

——— 1964, An approach to empirical time series analysis: Radio Sci. Jour. Research, v. 68D, no. 9, p. 937–951.

Rowan, L. C., and McCauley, J. F., 1966, Lunar terrain analysis, in Lunar Orbiter—Image analysis studies report, May 1, 1965–Jan. 31, 1966: U.S. Geol. Survey open-file rept., p. 89–129.

Schloss, Milton, 1965, Quantifying terrain roughness on lunar and planetary surfaces: Am. Inst. Aeronautics Astronautics Paper 65–389, AIAA 2d Ann. Mtg., San Francisco, Calif., 22 p.

Van Deusen, B. D., 1966, A statistical technique for the dynamic analysis of vehicles traversing rough yielding and non-yielding surfaces: Chrysler Corp., Detroit, Mich., prepared for Natl. Aeronautics and Space Adm. under contract NASW–1287 by Advanced Projects Organization, 178 p.

Watson, Kenneth, 1968, Photoclinometry from spacecraft images: U.S. Geol. Survey Prof. Paper 599–B, 10 p.

ENERGY BALANCES FOR TRANSIENT WATER CRATERS

By K. L. R. OLEVSON, Menlo Park, Calif.

Work done in cooperation with the National Aeronautics and Space Administration under NASA contract R–66

Abstract.—Studies of transient craters in water, produced by falling water drops, show that significant amounts of energy are present as kinetic energy in a cylindrical wave which surrounds the crater when the crater has reached its maximum size. At maximum size, about 80 to 90 percent of the initial drop kinetic energy can be accounted for as potential energy, surface energy, and kinetic energy of the outwardly expanding cylindrical wave. The energy partitioning changes with velocity and crater size. For 14-milligram drops with velocities near 155 centimeters per second, surface energy is the most important energy sink, whereas potential energy is the most important energy sink at velocities near 566 centimeters per second. The percentage of kinetic energy in the cylindrical wave increases with increasing drop velocity and may exceed the percentage of surface energy for the highest velocities.

In the study of liquid-liquid impacts, the total energy of the system must remain constant and should be accountable. Previous workers do not fully account for the energy of the system. Since the descriptive works of Worthington (1882) and Worthington and Cole (1897), a number of investigators have accounted for part of the energy. Franz (1959) shows that a negligible amount is lost as acoustical energy. Moore, MacCormack, and Gault (1963) show that nearly half of the energy transforms to surface and potential energy in the cavity for 11- to 182-milligram drops impacting at 400 to 700 centimeters per second. Engel (1962) accounts for 20 to 50 percent of the initial drop energy which transforms to surface energy and potential energy in the crater and the cylindrical wave. Her data account for about 50 percent of the energy for drop velocities near 740 cm/sec and about 20 percent near 1,800 cm/sec for 38- to 60-mg drops.

This paper shows that for 14-mg drops with impact velocity in the range of 155 to 566 cm/sec, about 12 to 45 percent of the drop energy is present as kinetic energy in the cylindrical wave which expands continually outward while the temporary water crater is near maximum size.

CRATERING PROCESS

The cratering process for transient craters in water, produced by falling drops, can be divided into four stages: (1) initial impact and projectile deformation, (2) crater growth to maximum size, (3) crater collapse, and (4) growth of the central column or Rayleigh jet (Harlow and Shannon, 1967; Phillip, 1960).

Upon impact the water-drop projectile deforms, the leading edge first. Ejection of droplets commences and an upward and outward expanding conical sheet of water rises above a flattened cavity in the water. The cavity or crater continues to expand to maximum size at which time it is nearly hemispherical (fig. 1).

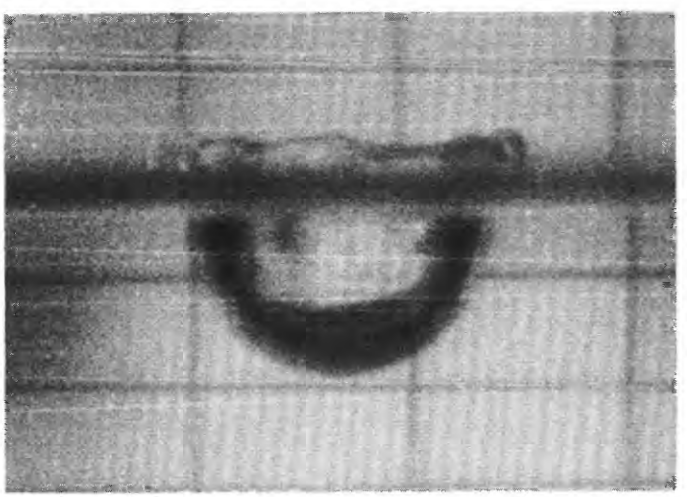

FIGURE 1.—Transient water crater produced by 14-mg drop at 367 cm/sec. Note the nearly hemispherical crater below the meniscus and the cylindrical wave, which is moving outward, above the meniscus. Rectangular grid lines in background are spaced ½ and 1 cm apart.

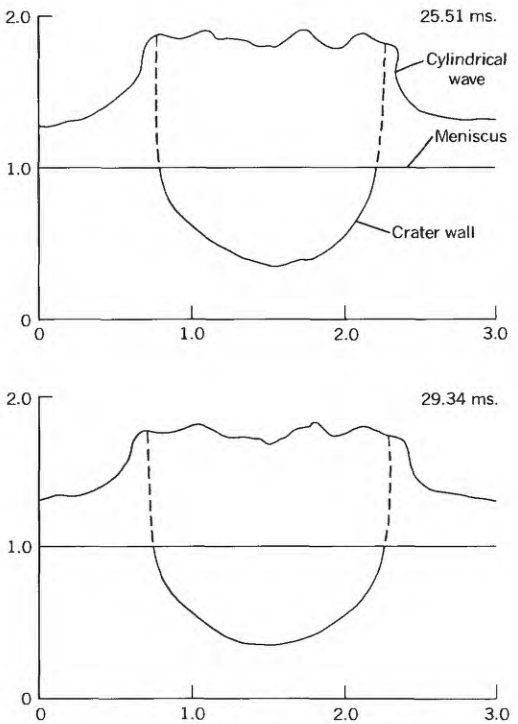

FIGURE 2.—Outward expansion and collapse of the cylindrical wave while the crater is at maximum size. Energy of the drop is 1,054 ergs; impact velocity of the drop is 384 cm/sec. Numbers in upper right of each diagram indicate the time in milliseconds after drop impact. Scales are in centimeters.

With growth of the crater, the conical sheet becomes a radially expanding cylindrical wave of water which reaches maximum height before the cavity reaches maximum size. It is important to stress that the cylindrical wave is moving outward before, during, and after the crater reaches maximum size (see fig. 2). After reaching maximum size the crater begins to collapse, the curvature of the floor reverses, the Rayleigh jet rises upward, and the amplitude of the cylindrical wave decreases as it continues to move outward.

EXPERIMENTAL CONDITIONS

Waterdrops with a mass between 6.4 and 14.1 mg were dropped into a small rectangular tank filled with tapwater. Velocity of the drops was computed from their fall height and was verified by using photographs taken by a high-speed camera framing between 1,970 and 4,860 pictures per second. Framing rate was established by using a timing light which recorded each millisecond on the edge of the film. Size of drops was controlled by using a hypodermic needle which normally produced drops with a mass near 14 mg. Drop size was verified by measuring it on the high-speed photographs.

Time of drop was synchronized with the photography by using the event synchronizer of the camera. After a predetermined interval during which the camera operates, the event synchronizer actuated a striker which knocked a preformed drop from the tip of the hypodermic needle. The drop then fell a known distance into the glass tank.

The tank measured 3¼ by 3¼ by 4 inches, which, according to May (1951), is large enough to avoid a size effect. May found empirically that the container width should be five times the width of the cavity. Additional evidence that container-size effect was not a factor is that the experimental results for the largest crater sizes in this report agree with previous data (Engel, 1961, 1962).

Measurement of drops, craters, and other features was facilitated by placing two bolts with 2-millimeter thread spacings in the plane of the impact and by using a grid behind the tank. Measurements showed that most drops were near 14 mg except for one which was determined to be 6.4 mg. Use of a long focal-length lens reduced refraction effects below the surface of the water so that crater dimensions measured by both the bolts and the grid were in good agreement.

PROCEDURES FOR ESTIMATING ENERGY

In order to account for the energy or work expended for craters at maximum size, the problem is divided into six parts: (1) potential energy of the crater, (2) surface energy of the crater, (3) potential energy of the cylindrical wave, (4) surface energy of the cylindrical wave, (5) kinetic energy of the cylindrical wave, and (6) the total energy of ejected droplets. For craters that are prolate hemispheroids, the potential energy of the crater is equal to the work expended in raising the water from the crater to the free surface against gravity (Moore and others, 1963; Engel, 1962). When z is used as the vertical axis, positive downward, and x as the horizontal axis, the work expended against gravity (W_{hh}) is

$$W_{hh}=\pi\rho g\int_0^b x^2 z\, dz, \qquad (1)$$

where

ρ=the density of water (1.0 g/cm^3),
b=the depth of the crater, and
g=the acceleration of gravity (980 cm/sec^2).

Integration of equation 1 for a prolate hemispheroid yields the total potential energy for the crater:

$$W_{hh}=\frac{\pi}{4}\rho g a^2 b^2, \qquad (2)$$

where

a=the radius of the crater, and
b=the depth of the crater.

Surface energy of the crater is the product of the surface area of the cavity and the surface tension of water less the initial surface energy originally over the crater (Engel, 1962). After this subtraction, the surface energy of the crater (SE_c) becomes

$$SE_c=\sigma\left(\frac{\pi ab}{\epsilon}\sin^{-1}\epsilon\right), \tag{3}$$

where

σ=the surface tension of water (72.4 dynes/cm^2), and
ϵ=the eccentricity of the elliptical profile of the crater $\left(1-\frac{a^2}{b^2}\right)^{1/2}$.

Potential energy of the wave is determined by calculating (1) the wave height from the continuity condition, which states that the wave height equals $-\frac{b^2}{3a}$ at the crater edge, and (2) the shape of the wave, for which wave height equals zero when x equals infinity. Continuity requires that the volume of the wave equal the volume of the crater:

$$2\pi\int_a^\infty hx\,dx=\text{volume of crater}, \tag{4}$$

where
h is the wave height as a function of x and may be expressed by

$$h=-\frac{1}{3}\frac{a^2b^2}{x^3}. \tag{5}$$

The potential energy of the wave (PE_w) becomes

$$PE_w=\pi\rho g\int_a^\infty\left(-\frac{1}{3}\frac{a^2b^2}{x^3}\right)^2 x\,dx$$

or

$$PE_w=\frac{\pi\rho g b^4}{36}. \tag{6}$$

Surface energy of the cylindrical wave is the product of surface tension and the sum of the new surfaces of the inner and outer sides of the wave. The difference in area of the outer surface and the original surface beneath the wave gives the new surface for the outer part (A_{ow}):

$$A_{ow}=2\pi\int_a^\infty x\left[1+\left(\frac{dx}{dh}\right)^2\right]^{1/2}dh-2\pi\int_a^\infty x\,dx, \tag{7}$$

which when combined with equation 5 gives

$$A_{ow}=2\pi\int_a^\infty\left[\left(\frac{a^4b^4}{x^6}+x^2\right)^{1/2}-x\right]dx. \tag{8}$$

Equation 8 requires graphical solution (Engel, 1962), which when combined with the empirical relationship from this study, $b=1.09966a$, yields

$$A_{ow}=0.650a^2,$$

and

$$SE_{ow}=0.650\,a^2\sigma,$$

where
SE_{ow} is the surface energy of the outer surface of the cylindrical wave.

The energy for the inside surface of the wave (SE_{iw}), which is the product of the wave height at $x=a$ and the circumference of the cavity, turns out to be

$$SE_{iw}=\frac{2}{3}\pi b^2. \tag{9}$$

In order to estimate the kinetic energy of the cylindrical wave, the wave is divided into two parts, upper and lower, because the parts move differently. The mass of these parts is graphically determined by projecting the cylindrical wave onto graph paper, summing the products of each incremental area and its distance from the crater axis, and assuming axial symmetry. The graphical estimates of the projected wave profile show that about a quarter of the mass displaced during cratering is in the upper part and three-quarters of the mass is in the lower part. The upper part moves mainly horizontally but with a small downward component. The lower part moves horizontally. Velocity of the cylindrical wave at the time of maximum size was determined using high-speed photographs covering an interval of time before and after the crater reached maximum size. Squares of the measured velocity of each of the two parts of the wave are then multiplied by half of its corresponding mass and summed to give the estimate of the kinetic energy of the wave. Estimates of wave kinetic energy cannot be made in the same experiment as those for surface energy and potential energy because the meniscus forms a visual barrier to measurement.

In a separate experiment, the kinetic energy and surface energy of ejected droplets, which separate from the cylindrical wave, are estimated by the combined use of high-speed photography and unexposed photographic film. High-speed photographs are used to estimate ejection angles. Photographic film is used to determine the number and size of droplets ejected to various heights above the crater. The number of droplets striking the unexposed film is determined for various heights above the water surface, and their size is determined by comparison of their spot size with that of calibrated standards (see also Hobbs and Kezweeny, 1967). Kinetic energy of the ejected drops is

TABLE 1.—*Experimental data*

Drop velocity (cm/sec)	Drop mass ($\times 10^{-3}$ g)	Drop energy (ergs)	Reynolds number ($\times 10^3$)	Crater width (cm)	Crater depth (cm)	Crater volume (cm^3)	Cylindrical wave velocity (cm)	
							Upper	Lower
155	12.7	171	4.5	0.80	0.55	0.18	----	----
156	14.1	193	4.68	----	.63	≈.52	19	----
180	10.5	187	4.86	.90	.55	.23	----	----
184	6.4	122	4.23	.83	.45	.16	----	----
248	14.1	464	7.44	1.15	.65	.45	----	----
294	11.6	519	8.23	1.35	.70	.67	----	----
343	14.1	850	10.29	1.40	.75	.77	----	----
367	14.1	971	11.01	1.38	.80	.76	----	----
384	14.1	1,061	11.52	----	.91	≈1.61	24	21
433	11.2	1,071	12.12	----	1.02	≈2.22	17	22
438	14.1	1,374	13.13	1.60	.80	1.07	----	----
448	14.1	1,436	13.44	1.65	.86	1.23	----	----
556	14.1	2,200	16.68	----	1.09	≈2.71	27	16
566	14.1	2,280	16.98	2.00	1.04	2.17	----	----
566	14.1	2,280	16.98	----	1.04	≈2.36	33	19

then estimated by using ballistic trajectories for ejection angles of 45° in combination with the known ejection heights. Surface energy is calculated from the measured drop size.

Consideration of the possible energy loss due to turbulence suggests that such loss is minor. The Reynolds number, determined from drop diameter, impact velocity, and kinematic viscosity of water, ranges from 4×10^3 to 17×10^3. This is near the region of turbulent flow (Vennard, 1966). Some evidence for turbulence is observed in the cylindrical wave at higher impact velocity. This additional energy is found to be immeasurable and is not included in the energy summations of this paper. However, the results of this study suggest that such loss is small.

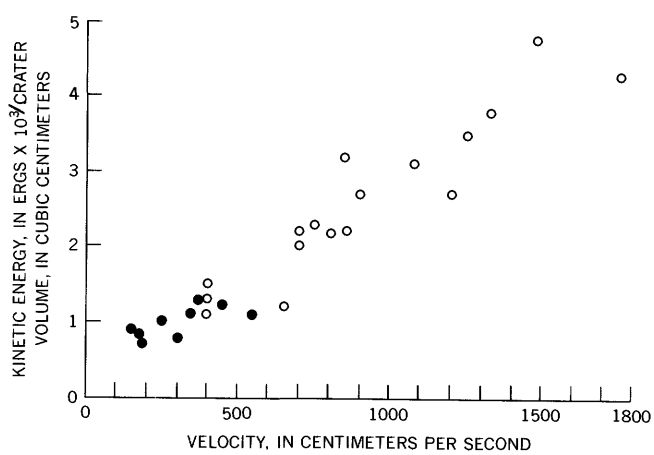

FIGURE 3.—Ratio of kinetic energy of falling drop at impact and volume of crater at maximum size plotted against velocity. Solid circles, data from this paper; open circles, data from Engel (1961, 1962).

RESULTS

The experimental data (table 1), combined with the data of Engel (1961, 1962), show a strong dependence between cratering efficiency (the ratio of kinetic energy of the drop and crater volume at maximum size) and the velocity of the drop (see fig. 3). Such a relationship between cratering efficiency and drop velocity implies a strong interdependence between energy expenditure, crater size, and drop velocity.

The equations of the previous section are used to partition the energy of the experimentally produced craters. A summary of the results of this analysis is given in table 2. These data show: (1) a strong dependence on potential-energy expenditure for the formation of the crater and the crater size (eq 2), and that the dependence becomes relatively more significant for the largest craters and highest drop velocities; (2) that the surface energy of the crater is dependent on crater size, (eq 3) but that this surface energy is only significant for the smallest craters; (3) that the potential energy of the cylindrical wave is strongly dependent on crater size, but the energy expended is only about one-ninth of the potential energy of the crater; (4) that surface energy expended in the cylindrical wave is roughly equal to that in the crater for all crater sizes studied; (5) that the kinetic energy of the cylindrical wave is relatively small for drops with the lowest velocities, but that this energy may be nearly equal to or may exceed the potential energy of the cavity for the highest drop velocities; and (6) that less than a few percent of the original kinetic energy of the drop is lost in the ejected droplets as surface energy and kinetic energy.

TABLE 2—*Energy partitioning, in percent*

Drop velocity (cm/sec)	Crater potential energy	Crater surface energy	Cylindrical wave surface energy	Cylindrical wave potential energy	Cylindrical wave kinetic energy	Energy accounted for	Estimated total energy
155	22	32	30	2		86	98
156					12		98
180	25	32	29	3		89	103
184	22	36	32	3		93	107
248	23	19	17	3		62	82
294	33	21	18	4		76	102
343	25	14	12	3		54	84
367	23	13	12	3		51	83
384					35		95
433					45		91
438	23	11	9	3		46	91
448	27	11	10	3		51	95
556					23		83
566	37	11	9	4		61	89
566					28		89

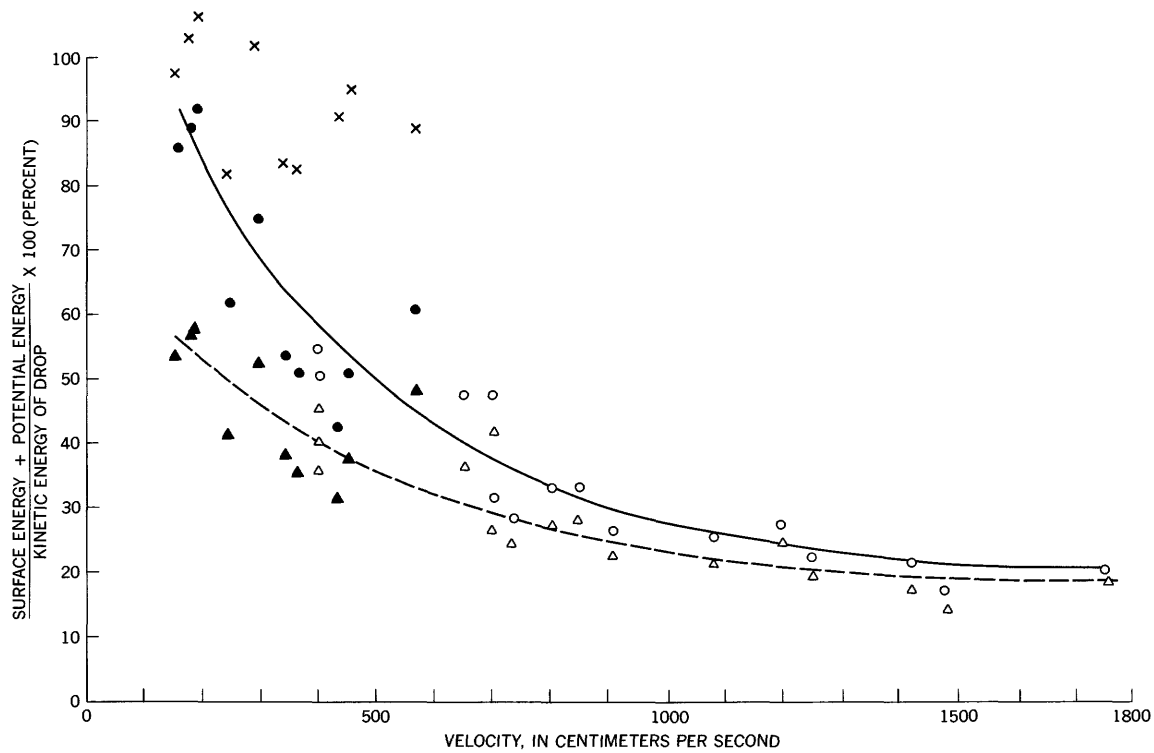

FIGURE 4.—Plot showing the percentage of drop energy which transforms to surface energy and potential energy while the crater is at maximum size. Circles represent potential energy and surface energy of the crater and the cylindrical wave for a given test; triangles represent surface energy and potential energy of the crater alone; x's represent estimated total energy accounted for in this study. Closed symbols represent data from this paper, and open symbols represent data from Engel (1961, 1962). Solid line approximates the trend of the circles, and broken line approximates the trend of the triangles.

Data from table 2, together with data from Engel (1961, 1962), show that the sum of potential energy and surface energy of the crater is strongly dependent on velocity for drops between 155 and 1,800 cm/sec, and a similar dependence is found when the potential energy and surface energy of the cylindrical wave are included in the sum (fig. 4). When the estimates of kinetic energy of the cylindrical wave for this study are included, the energy sum totals to 80 percent or more of the initial-drop kinetic energy (see table 2). Thus, the size of the craters is also strongly dependent on the kinetic energy in the cylindrical wave.

CONCLUSION

The sum of potential energy and surface energy of the crater and the cylindrical wave and the kinetic

energy of the cylindrical wave is nearly equal to the original kinetic energy of the falling drop when the crater has reached maximum size. For craters at maximum size produced by 14-mg drops at a velocity near 155 cm/sec, about 86 percent of the energy is potential and surface energy and 12 percent is kinetic energy of the cylindrical wave. At a higher velocity, between 40 and 60 percent of the energy is surface and potential and 20 to 40 percent is kinetic energy in the cylindrical wave. Although facilities available for the experiments reported here did not permit a drop velocity between 600 to 1,800 cm/sec, the change in energy partitioning for these high velocities, for which only 20 to 30 percent of the energy is represented by potential and surface energy, suggests that as much as 70 to 80 percent of the energy may be present as kinetic energy in the cylindrical wave.

REFERENCES

Engel, O. E., 1961, Collisions of liquid drops with liquids: U.S. Natl. Bur. Standards Tech. Note 89, 30 p.

——— 1962, Collisions of liquid drops with liquids—pt. II, Crater depths in fluid impacts: U.S. Natl. Bur. Standards Tech. Rept. WADD–TR–60–475, 52 p.

Franz, G. J., 1959, Splashes as sources of sound in liquids: Acoustical Soc. America Jour., v. 31, no. 8, p. 1080–1096.

Harlow, F. H., and Shannon, J. P., 1967, Distortion of a splashing liquid drop: Science, v. 157, no. 3788, p. 547–550.

Hobbs, P. V., and Kezweeny, A. J., 1967, Splashing of a water drop: Science, v. 155, no. 3766, p. 1112–1114.

May, Albert, 1951, The influence of the proximity of tank walls on the water-entry behavior of models: U.S. Naval Ordnance Lab., White Oak, Md., NAVORD Rept. 2240, 14 p.

Moore, H. J., MacCormack, R. W., and Gault, D. E., 1963, Fluid impact craters and hypervelocity—High-velocity impact experiments in metals and rocks: U.S. Geol. Survey open-file rept., May 1963, 29 p.

Phillip, A. G. D., 1960, Effect of viscosity on the splash caused by a drop of water falling into a mixture of glycerol and water: Jour. Applied Physics, v. 31, no. 4, p. 727–730.

Vennard, J. K., 1966, Elementary fluid mechanics, 6th ed.: New York, John Wiley and Sons, 516 p.

Worthington, A. M., 1882, On impact with a liquid surface: Royal Soc. [London] Proc., v. 33, p. 347–349; 1883, v. 34, p. 217–230.

Worthington, A. M., and Cole, R. S., 1897, Impact with a liquid surface, studied by the aid of instantaneous photography: Royal Soc. [London] Philos. Trans., ser. A, v. 189, p. 137–148.

GLACIAL ERRATICS AND THE PROBLEM OF GLACIATION IN NORTHEAST KENTUCKY AND SOUTHEAST OHIO—A REVIEW AND SUGGESTION

By LOUIS L. RAY, Washington, D.C.

Abstract.—The mode of transportation and emplacement of glacial erratics in northeast Kentucky and southeast Ohio, first reported in the early years of this century, has not been adequately explained despite the several proposed hypotheses. The problem is reviewed, and the suggestion is made that a glacial advance, possibly of Nebraskan age, extended somewhat beyond the mapped limits of glaciation in southern and southeast Ohio and into northern Kentucky. Such an advance would provide for emplacement of the glacial erratics through ice rafting. It is further suggested that until this problem is solved by field and laboratory studies, the regional Quaternary history can not be explained, nor can the Quaternary disruption of the preglacial Teays drainage system and the development of the present Ohio River.

Long ago it was predicted that "***a much broader territory in the Ohio Valley had been glaciated than has been supposed***" (Jillson, 1925, p. 20). This prediction, as yet neither verified nor rejected, was based on recognition of widely scattered erratics of exotic rock types in northeast Kentucky, far south of the mapped glacial border (Jillson, 1924a, 1925, 1929; Leverett, 1929; Flint and others, 1945). Boulders, cobbles, and pebbles of granite, granodiorite, porphyritic granite, gneiss, norite gneiss, schistose quartzite, and sandstone foreign to the region have been identified (W. F. Hunt and O. F. Poindexter, quoted in Jillson, 1924b, p. 129–131) and were reported to have been derived either from the Adirondack Mountains or that part of Canada north of the region between Ottawa and Quebec (Jillson, 1925; Leverett, 1929). All erratics were said to be in drainage basins of streams now tributary to the Ohio River, and at altitudes ranging from less than 800 feet to about 1,000 feet.

Small erratics have been reported by Tight (1903), Patton and Hicks (1925), Leverett (1929), and Ireland (1943) from presumably unglaciated southeast Ohio (see Goldthwait and others, 1961). The problem posed by the presence of erratics in southeast Ohio was summarized by Leverett (1929, p. 50), when he reported that he

> was disposed to refer their presence in this region to the work of Indians or other human agency. But since erratics have now been found in Kentucky at still greater distances outside the border of the till, and of a size entirely beyond that which is referable to human transportation, it seems well to look into the question of the mode of deposition of these small erratics noted in southeastern Ohio.

Since these erratics were first reported, no further important discoveries have been made in Kentucky. In southeast Ohio, beyond the mapped boundary of the oldest recognized ice sheet of Illinoian age, Rich (1939), on the basis of interpretation of aerial photographs, suggested the possibility of an ancient till plain in southern Ohio, west of the Scioto River (fig. 1). This suggestion has neither been confirmed nor rejected in later studies. Later, Ireland (1943) in his thought-provoking paper suggested that the position and weathering of erratics in southeast Ohio indicated deposition during a pre-Illinoian glaciation, probably of Nebraskan age. In the Hocking Valley, Kempton and Goldthwait (1959) reported terrace levels above those of Illinoian age and suggested that erratics described by Merrill (1953) on high hills above the level of the outwash of Illinoian age may possibly be "the only remaining traces found thus far of pre-Illinoian ice or water-laid deposits" (Kempton and Goldthwait, 1959, p. 137).

Thus, the problem posed long ago remains unsolved and seemingly forgotten today. Even the erratics in Kentucky shown on the "Glacial Map of North America" (Flint and others, 1945) have been removed from the later "Glacial Map of the United States East of the Rocky Mountains" (Flint and others, 1959). If, however, one accepts the assumption, which there seems to be no reason to doubt, that the erratics were ori-

U.S. GEOL. SURVEY PROF. PAPER 650-D, PAGES D195-D199

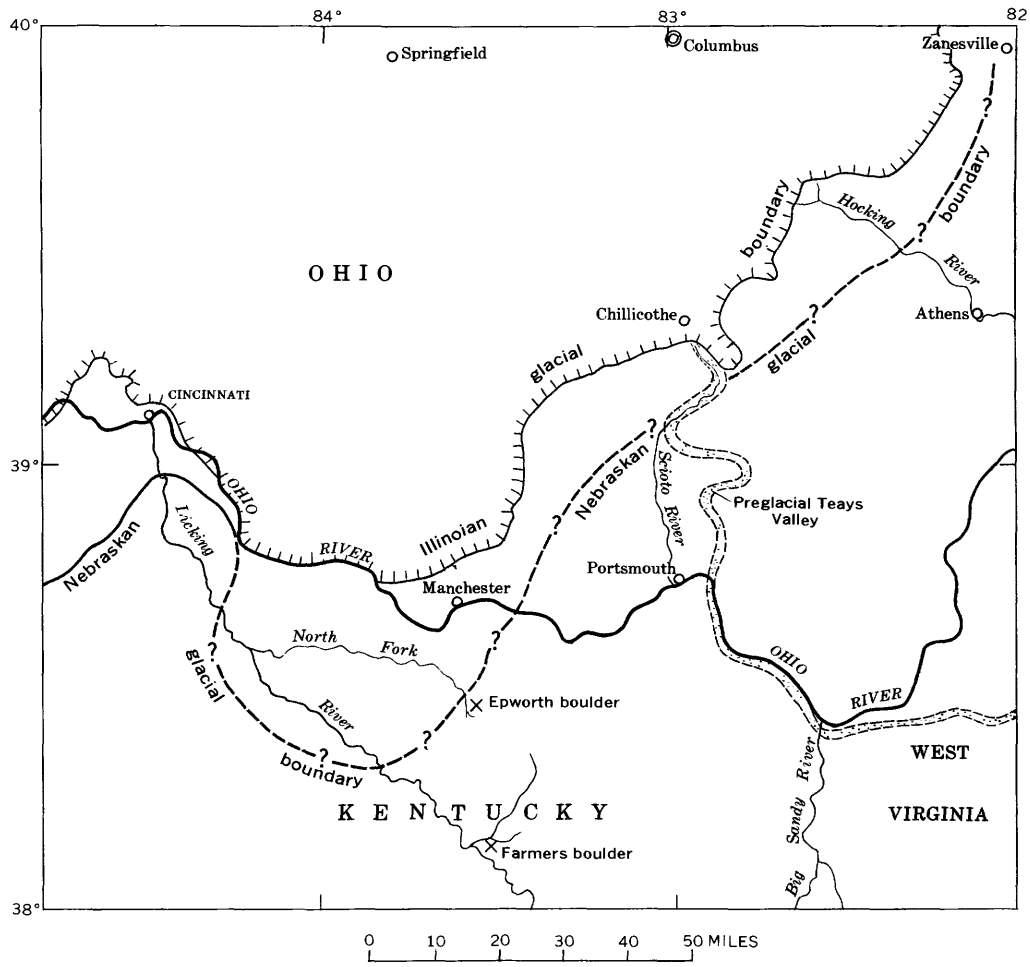

FIGURE 1.—Sketch map of parts of Kentucky, Ohio, and West Virginia, showing location of Epworth and Farmers boulders relative to drainageways and to proposed extension of Nebraskan ice sheet. Illinoian glacial boundary from Goldthwait, White, and Forsyth (1961), Nebraskan glacial boundary in part from Ray (1966), Teays Valley after Tight (1903).

ginally a product of glaciation, an explanation of their transportation and emplacement is essential for an understanding of the Quaternary history of a broad area in southeast Ohio, northeast Kentucky, and possibly in West Virginia. It is basic for determining the history of the disruption of the preglacial Teays drainage system and the development of the present Ohio River (see Leverett, 1902; Tight, 1903; Stout and others, 1943, p. 50–106).

Two major hypotheses, with variations, have been suggested for transportation and emplacement of the erratics: first, that they were ice rafted in glacially ponded proglacial drainage basins (Jillson, 1924a), and second, that they were deposited directly from an unrecognized glacial ice lobe that reached into northern Kentucky (Jillson, 1924b). Because the altitude of the largest known erratic requires glacially ponded drainage to an altitude higher than the highest overflow channels recognized between the ponded drainage basins, Jillson (1924a) suggested diastrophic uplift in Quaternary time. Leverett (1929), on the other hand, suggested marine submergence to explain this emplacement anomaly by ice rafting. Inasmuch as no corroborative evidence has been produced to indicate either a diastrophic uplift or a depression, one is left with the two major hypotheses—ice rafting in proglacially ponded drainage basins, or direct deposition from an unrecognized ice lobe, probably of Nebraskan age (Jillson, 1925).

Because precise data are lacking on the exact position and altitude of almost all erratics reported, only the two best known and described erratics in Kentucky are used to test critically the two hypotheses. These are the Epworth and Farmers boulders (fig. 1).

THE EPWORTH BOULDER

The Epworth boulder, the largest and best known of the erratics, is of porphyritic granite gneiss (W. F.

Hunt and O. F. Poindexter, quoted in Jillson, 1924b, p. 129–131). It is in Lewis County, Ky. (Burtonville quadrangle), at the head of a draw on the south-facing valley wall of Beechy Creek, a tributary of the North Fork of the Licking River, at an altitude of approximately 980 feet (Morris, 1965), some 200 feet below a dissected upland surface. Jillson (1924b) described the weathered boulder, which had been largely destroyed by blasting, as originally weighing about 16 tons and having dimensions of 8 × 6 × 4 feet (for photographs see Jillson, 1924b, or Leverett, 1929). The boulder rested on the Ohio Shale below its contact with the overlying Bedford Shale (Morris, 1965). Such a position suggests that it was not at its original depositional site, but had slumped, as noted by Jillson (1924b), possibly during dissection of the upland surface. If its original position was on the upland, it would seem to preclude its having been ice rafted into position, for no evidence has been reported of glacial ponding in the Licking River basin to that height. Its present location led Leverett (1929, p. 35) to conclude that its "topographic position as well as size***seem to be against its reference to flotation on ice blocks in ponded waters," for drainage divides regulating the level of ponding in the Licking River basin were presumably somewhat lower, probably near 900 feet (Leverett, 1929, p. 46).

It would appear, therefore, that the hypothesis of ice rafting in ponded proglacial drainage basins does not provide a satisfactory solution to the problem because the suggested diastrophic movements have been rejected for lack of critical supporting evidence.

The second hypothesis, that of direct deposition from glacial ice, was first rejected by Jillson (1924a) because there was no tangible evidence of glacial deposits near the Epworth boulder. However, in 1925 he concluded that as the glacial deposits must be of great age, possibly Nebraskan, they had been destroyed through weathering and erosion. As a result, he postulated an ice lobe extending far into Kentucky that encompassed an area from the West Virginia boundary almost to Louisville (Jillson, 1925, pl. 2). Detailed mapping by Morris (1965) in the vicinity of the Epworth boulder supports Jillson's belief in the lack of glacial deposits. Morris reported that the thin soils on the uplands indicate only a normal progression from fresh rock through a weathered zone to residual soil, and that if glacial deposits had formerly been present they have been completely removed by subsequent erosion.

Few have considered this proposed ice lobe to be a reasonable possibility because of the lack of supporting evidence, although Thwaites (1946, pl. 3) indicated a somewhat similar glacial lobe of Nebraskan age in northern Kentucky. Wayne (1956, fig. 10) likewise indicated a questionable extension of an ice lobe into Kentucky to encompass the sites of the erratics; he suggested that it is Kansan in age.

Available data indicate that the second hypothesis is no more satisfactory than the first in explaining the mode of transportation and emplacement of the Epworth boulder. As neither hypothesis can be categorically rejected on the basis of a single boulder, a critical appraisal of the Farmers boulder is required.

THE FARMERS BOULDER

The Farmers boulder, an erratic described and figured by Jillson (1924b) and Leverett (1929), is some 20 miles south of the Epworth boulder (fig. 1), near Farmers, Rowan County, Ky. (Farmers quadrangle). It is at an altitude near 720 feet in the bottom of a narrow, steep-sided ravine cut into the Ohio Shale below an upland surface developed on a more erosion-resistant sandstone (Borden Formation). The ravine is tributary to Triplett Creek from the south, near the creek's confluence with the Licking River. Broad, sloping, and dissected upland flats are locally present adjacent to the major streams at altitudes ranging from about 820 to 940 feet. Steep-sided "knobs" rise locally above the sloping uplands to altitudes of more than 1,200 feet.

The Farmers boulder is of schistose quartzite (W. F. Hunt and O. F. Poindexter, quoted in Jillson, 1924b) and has dimensions of 6 × 3 × 2 feet. It has been estimated to weigh 3 tons (Jillson, 1924b, p. 129–131). Although it appears to be relatively unweathered, there is evidence that it has been reduced in size by spalling. Obviously, this boulder, like the Epworth boulder, is not in its original depositional site, but has slumped into the ravine during dissection of the adjacent upland, locally at an altitude near 840 feet. If this upland is considered the original depositional site of the boulder, it is within the realm of possibility that the boulder could have been ice rafted into place. The distance from the parent ice front of the early glacier that ponded the Licking River near Cincinnati (fig. 1) and the circuitous nature of the ancient upland valley stretch one's credulity, however, for proglacial ice rafting. Furthermore, a brief reconnaissance of the local area by the writer and M. M. Leighton failed to reveal critical evidence for lacustrine deposits or ancient weathered glacial till on the upland flats. The emplacement of the Farmers boulder, like that of the Epworth boulder, cannot be readily explained by either of the two hypotheses on the basis of available field data.

SUGGESTED HYPOTHESIS FOR EMPLACEMENT OF ERRATIC BOULDERS

Inasmuch as available data are inconclusive for explaining the emplacement of the erratic boulders in northeast Kentucky and southeast Ohio, it becomes necessary to assess the problem regionally in the hope of suggesting a rational hypothesis. For this, several assumptions are made:

(1) That the erratics are of glacial origin and were removed from their parent ledges and transported for an unknown distance to the southwest by glacial ice;

(2) that the glacial ice sheet involved is pre-Illinoian in age, presumably Nebraskan, inasmuch as drift of Nebraskan age has been recognized as the earliest and most extensive on the relatively undissected uplands in northern Kentucky (Leighton and Ray, 1965; Ray, 1966);

(3) that since emplacement of the erratics the terrain has been deeply dissected by erosion;

(4) that the drift of Nebraskan age was composed largely of a fine-grained calcareous matrix with fragments of limestone, silty limestone, shale, and sandstone and with very few fragments of crystalline rock;

(5) that in southeast Ohio and northeast Kentucky there has been no appreciable diastrophism during Quaternary time; and

(6) that the advancing glacial ice sheet dammed and ponded stream basins draining to the north so that ponded waters of one basin rose to the level of the lowest divide separating it from adjacent basins.

It is suggested that future detailed field studies in "unglaciated" southern and southeast Ohio may reveal an extension of glaciation beyond the mapped boundary of the drift of Illinoian age (Goldthwait and others, 1961). Because the first and presumably the most extensive ice sheet to advance into Ohio is held to be of Nebraskan age and to have moved across an upland surface of relatively low relief, now dissected, it is suggested that relict deposits may be found only as deeply weathered drift on remnants of the dissected upland surfaces. This situation would be analogous to the deeply weathered drift of Nebraskan age on the dissected uplands of northern Kentucky between the Cincinnati and Louisville areas (Leighton and Ray, 1965; Ray, 1966). Because the glaciation of Nebraskan age in that area is the most widespread, it would appear reasonable to suggest that it was likewise the most widespread in southern and southeast Ohio.

Speculation places the margin of the ice sheet of Nebraskan age in Ohio, from the latitude of Zanesville to the Scioto Valley, a few to perhaps as many as 15 miles or more beyond the outer margin of the ice sheet of Illinoian age (fig. 1). It is suggested that the glacier crossed the Scioto Valley south of Chillicothe and continued to the southwest, crossing the present Ohio Valley between Portsmouth and Manchester (see Goldthwait and others, 1961). The later Illinoian ice is believed to have mantled and obscured the intervening drift of the less extensive Kansan glaciation.

In Kentucky, the ice boundary is suggested to have continued far enough to the south to have crossed and ponded the ancient high-level valley of the North Fork of the Licking River and possibly the main stem of the Licking River. The outer margin of the ice sheet may then have turned to the northwest, toward the area of Nebraskan drift in the Cincinnati region (Ray, 1966), where the Licking River is known to have been dammed by ice.

An ice lobe such as this would have been only temporary along the fluctuating outer margin of the glacier. It would, however, have provided for the pre-Illinoian terraces and ice-rafted erratics in southeast Ohio that appear to be related to upland channels and ponded stream basins. In Kentucky, the headwater reaches of the ancient North Fork of the Licking River are presumed to have been temporarily ponded to an altitude higher than that of the main stem of the Licking River and possibly as much as 200 feet or more higher than the ponded Teays drainage (fig. 1). Such ponding would have provided for ice rafting of both the Epworth and the Farmers boulders; it would likewise reduce the distance of ice rafting along the broad ponded drainageways on the relatively undissected uplands.

Such a proposed ice lobe at once raises a multitude of questions that cannot be answered on the basis of present knowledge. Where, for example, is the evidence of the glacial drift that must have been deposited on the uplands and in the ponded, ice-dammed drainage basins? It is believed that the glacial drift of the proposed ice lobe will be found only by detailed examination of residual deposits on the larger remnants of the now dissected uplands that were formerly ice mantled—uplands that have been subjected to subaerial weathering and erosion since dissipation of the ice sheet of Nebraskan age. Because the drift was dominantly calcareous, it may have been wholly leached, leaving only a residuum of clay, silt, sand, and cherty insolubles. Presumably, the minor crystalline rock constituents have been completely rotted, except where they are sufficiently protected by thick overburden or because they are of unusually large size. Analysis of the thickest surficial residuum may indicate, perhaps, introduced weathering-resistant minerals not locally derived. Likewise, thin lacustrine deposits in the now-dissected and well-drained upland channels may have

been largely removed by erosion or so modified by weathering that they have escaped identification and can be recognized only through detailed laboratory analyses.

It is hoped that future studies in field and laboratory may substantiate the speculative hypothesis here suggested. The problem will not be easily or quickly solved.

REFERENCES

Flint, R. F., and others, 1945, Glacial map of North America: Geol. Soc. America Spec. Paper 60, 37 p., 2 sheets, scale 1:4,555,000.

——— 1959, Glacial map of the United States east of the Rocky Mountains: New York, Geol. Soc. America, 2 sheets, scale 1:1,750,000.

Goldthwait, R. P., White, G. W., and Forsyth, J. L., 1961, Glacial map of Ohio: U.S. Geol. Survey Misc. Geol. Inv. Map I–316, scale 1:500,000.

Ireland, H. A., 1943, Pre-Illinoian glaciation in southeastern Ohio: Ohio Jour. Sci., v. 43, no. 4, p. 180–181.

Jillson, W. R., 1924a, Glacial pebbles in eastern Kentucky: Science, new ser., v. 60, p. 101–102 (*reprinted in* Kentucky Geol. Survey, ser. 6, v. 30, p. 123–125, 1927).

——— 1924b, Glaciation in eastern Kentucky: Pan-Am. Geologist, v. 42, no. 2, p. 125–133 (*reprinted in* Kentucky Geol. Survey, ser. 6, v. 30, p. 127–135, 1927).

——— 1925, Early glaciation in Kentucky: Pan-Am. Geologist, v. 44, no. 1, p. 17–21 (*reprinted in* Kentucky Geol. Survey, ser. 6, v. 30, p. 137–141, 1927).

——— 1929, Geologic map of Kentucky: Kentucky Geol. Survey, ser. 6, scale 1:500,000.

Kempton, J. P., and Goldthwait, R. P., 1959, Glacial outwash terraces of the Hocking and Scioto river valleys, Ohio: Ohio Jour. Sci., v. 59, no. 3, p. 135–151.

Leighton, M. M., and Ray, L. L., 1965, Glacial deposits of Nebraskan and Kansan age in northern Kentucky, *in* Geological Survey Research 1965: U.S. Geol. Survey Prof. Paper 525–B, p. B126–B131.

Leverett, Frank, 1902, Glacial formations and drainage features of the Erie and Ohio Basins: U.S. Geol. Survey Mon. 41, 802 p.

——— 1929, Pleistocene of northern Kentucky: Kentucky Geol. Survey, ser. 6, v. 31, p. 1–80.

Merrill, W. M., 1953, Pleistocene history of a part of the Hocking River valley, Ohio: Ohio Jour. Sci., v. 53, no. 3, p. 143–158.

Morris, R. H., 1965, Geology of the Burtonville quadrangle, Kentucky: U.S. Geol. Survey Geol. Quad. Map GQ-396, scale 1:24,000.

Patton, L. T., and Hicks, Clifford, 1925, Notes on occurrence of glacial material beyond the border of drift in Muskingum County, Ohio: Ohio Jour. Sci., v. 25, no. 2, p. 97–98.

Ray, L. L., 1966, Pre-Wisconsin glacial deposits in northern Kentucky, *in* Geological Survey Research 1966: U.S. Geol. Survey Prof. Paper 550–B, p. B91–B94.

Rich, J. L., 1939, A bird's-eye cross section of the central Appalachian Mountains and plateau, Washington to Cincinnati: Geog. Rev., v. 29, no. 4, p. 561–586.

Stout, W. E., Ver Steeg, Karl, and Lamb, G. F., 1943, Geology of water in Ohio (a basic report): Ohio Geol. Survey, ser. 4, Bull. 44, 694 p.

Thwaites, F. T., 1946, Outline of glacial geology: Ann Arbor, Mich., Edwards Bros., 129 p.

Tight, W. G., 1903, Drainage modifications in southeastern Ohio and adjacent parts of West Virginia and Kentucky: U.S. Geol. Survey Prof. Paper 13, 111 p.

Wayne, W. J., 1956, Thickness of drift and bedrock physiography of Indiana north of the Wisconsin glacial boundary: Indiana Geol. Survey Rept. Prog. 7, 70 p.

GLACIAL LAKE NORFOLK AND DRAINAGE CHANGES NEAR NORFOLK, CONNECTICUT

By CHARLES R. WARREN, Washington, D.C.

Work done in cooperation with the State of Connecticut Geological and Natural History Survey

Abstract.—In the Norfolk quadrangle, Connecticut, glacial drift has disrupted the preglacial drainage pattern in the headwaters of the Blackberry River, a west-flowing tributary of the Housatonic. Of four streams that flowed generally northward in preglacial time, three have been diverted so that their waters repeatedly cross inferred preglacial divides. Much of the glacial drift that diverts these streams was deposited in an ice-marginal lake, glacial Lake Norfolk.

The Blackberry River (fig. 1), in northwestern Connecticut, flows generally west-northwest to the Housatonic. Its southern tributaries therefore flow generally north, against the general direction of movement of the Pleistocene glacier ice. In preglacial time, four such streams apparently drained the northwest part of the Norfolk quadrangle, Connecticut, and three of these left the quadrangle independently. Glacial drift now diverts three of the four streams across preglacial divides. Much of this drift was deposited in a lake that formed between the retreating ice front and the preglacial divide to the south. This lake is here called glacial Lake Norfolk.

PREGLACIAL TOPOGRAPHY

The westernmost of the four stream valleys in the Norfolk quadrangle inferred to have drained to the Blackberry River in preglacial time is that of Roaring Brook (fig. 1). Perhaps because it trended north-northeast, almost transverse to the direction of advance of the ice, which came from the north-northwest, this valley does not contain any great amount of glacial drift, and the present course of Roaring Brook is apparently very nearly the same as its preglacial course. The three streams to the east, however, were all disrupted by thick drift.

The easternmost of the three streams inferred to have been diverted by glacial drift flowed north from what is now Spaulding Pond. North of the latitude of Norfolk village, the valley of this stream is so deeply buried under glacial drift that its route can only be guessed. However, I interpret the results of drilling by the Soil Conservation Service, U.S. Department of Agriculture (W. M. Brown, written commun., 1968) to mean that the stream drained northward, and that it passed east of Haystack Mountain. Wells drilled at the site of a proposed dam on Wood Creek, 0.3 mile above the mouth of the creek at the source of the Blackberry River, did not reach bedrock at depths as great as 67 feet. The elevation of the bottom of the deepest well was 1,104 feet, more than 30 feet below the elevation of the rock crossed by Wood Creek near its mouth. The preglacial drainage was therefore incised below that mouth, and the stream north from the site of Spaulding Pond must have left the quadrangle at some point north or northeast of Norfolk village, either where Wood Creek now enters it, or farther east as suggested on the map (fig. 1).

The divide west of this preglacial valley included Dutton Mountain, the rock hills east and north of the millpond in Norfolk, and Haystack Mountain. Presumably the low point along its crest was at or near the point where Wood Creek and Spaulding Brook join to become the Blackberry River. This rock saddle may have been lowered as the result of erosion by ice thrusting southeastward up the valley of Blackberry River.

The valley west of Dutton Mountain drained north into what is now the Blackberry River, and may be called the ancestral Blackberry River (fig. 1). The bedrock valley is now so deeply buried that its exact position can only be guessed, except at its northern end which is believed to be marked by an area of seepage springs on the south wall of the present valley of Blackberry River. In spite of a steep slope, these

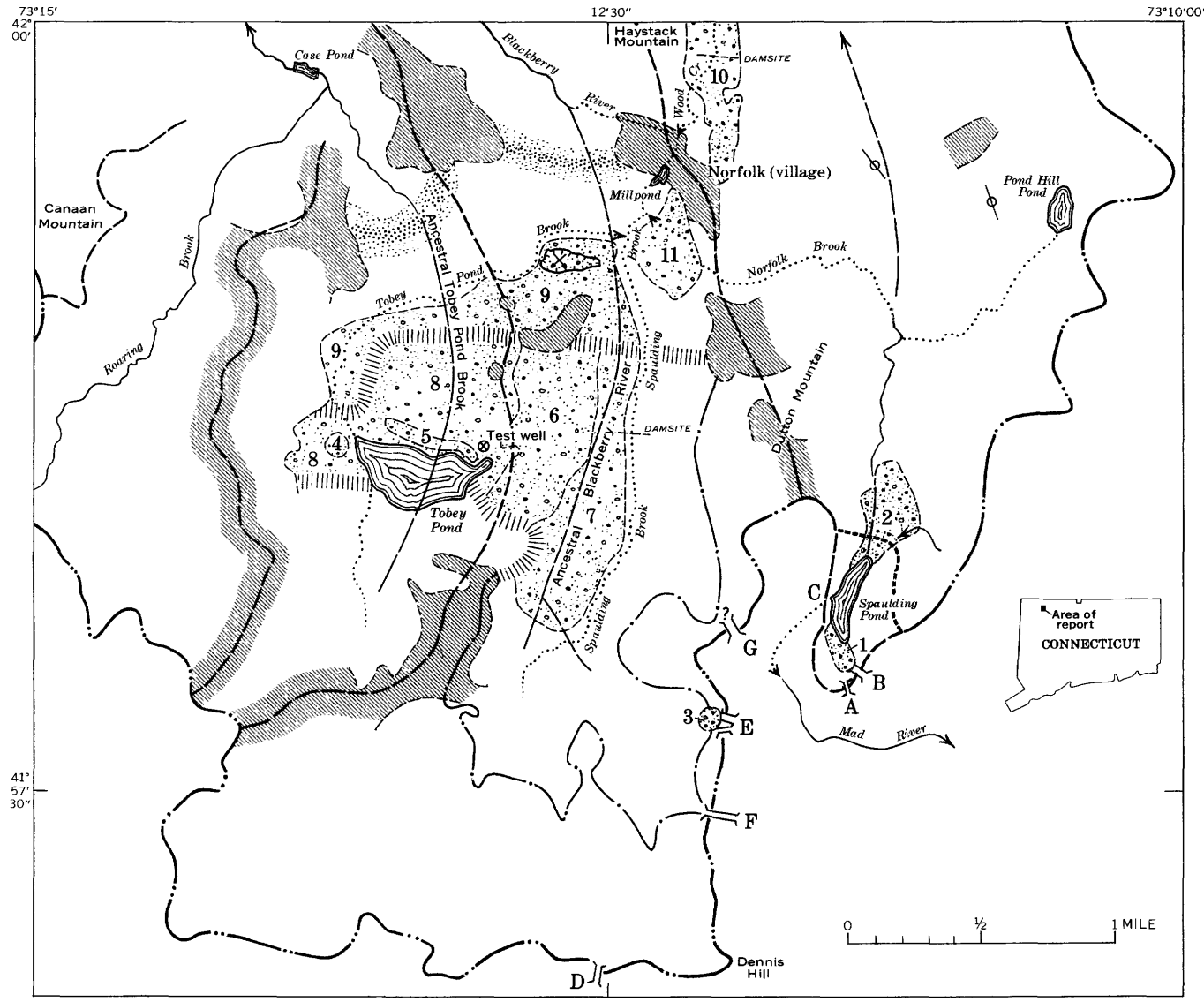

FIGURE 1.—Sketch map of that part of the Blackberry River basin that lies in the Norfolk quadrangle, Connecticut, showing glacial drainage changes and related glacial deposits.

springs keep the soil wet, so that it is covered by a stand of swamp alder rather than by one of the mixed forests normal on hillsides in the region.

Most of the preglacial divide west of this ancestral Blackberry River valley is also buried under glacial drift. However, rock outcrops at several places indicate the approximate location and trend of the former divide.

West of these outcrops, the bedrock surface lies much deeper. The distribution of kettles, some of which are deep, suggests the approximate position of the buried valley. A test well drilled at a location east of the inferred axis, northwest of the northeast spur of Tobey Pond, penetrated 123 feet of stratified drift without reaching bedrock (R. L. Melvin, written commun., 1969); its bottom was more than 60 feet lower than the lowest known point along the crestline of the inferred preglacial divide to the east. I believe that the buried valley marks the route of the ancestral Tobey Pond Brook (fig. 1), and that this brook drained northwest to a confluence with Roaring Brook.

MODIFICATION OF TOPOGRAPHY DURING GLACIATION

Effects of active ice

During the active phase of glaciation, ice from the north-northwest deposited thick till in what is now the northeast part of Norfolk village. The till forms a drumlin, or drumlinlike ridge (fig. 1), that completely blocks off the easternmost of the four preglacial valleys. The northward drainage from the site of Spaulding Pond was defeated, so that Norfolk Brook now spills westward across the preglacial divide into Spaulding Brook.

Another till ridge, in the lee of a bedrock hill, closed off the head of a smaller preglacial valley that was tributary to this easternmost north-flowing preglacial valley. This till ridge created the basin of Pond Hill Pond. The bedrock valley west or northwest from Pond Hill Pond is so effectively buried that its course can only be surmised.

A blanket of till was also deposited on the west slope of Dutton Mountain. The till here began the process of burying the valley of the ancestral Blackberry River. In the absence of subsurface data, the thickness of the till is unknown. If thick, the till may have buried the bedrock valley completely, so that the axis of the buried valley could lie east of Spaulding Brook, rather than west of Spaulding Brook as suggested in figure 1, or the valley could zigzag under the till.

Undetermined amounts of till are doubtless also present in the valley of the ancestral Tobey Pond Brook. This area is so deeply buried under younger stratified drift that only extensive subsurface exploration could determine what thickness of till may lie in it.

Spaulding Pond area

An esker south of Spaulding Pond leads up toward a spillway (*A*, fig. 1) at about 1,495 feet elevation. This esker, together with associated kettled stratified drift, *1*, that is apparently related to a nearby spillway, *B*, at about 1,455 feet, shows that the ice stagnated during its disappearance from this area. As soon as the ice had melted back from the line of the preglacial divide, water presumably became ponded between it and the rock to the south. At first this lake, an ancestral Spaulding Pond, drained through the spillway at *B*. As melting continued, however, a lower spillway became available at the low point in the rock divide around the head of the preglacial valley, namely the present outlet of Spaulding Pond, at *C*.

Spaulding Pond as it exists today is artificial, but its floor is thick peat; a natural pond must have occupied the site at the beginning of the Holocene. Rock encloses the sides and south end of the pond, but the north end is closed by a sand-and-gravel plug, *2*, that extends more than 1,000 feet to the north. Landforms of ice-contact origin in the north part of this stratified-drift plug show that it was deposited by melt water that came from ice in the valley just to the north.

This plug was built so high that it continued to impound the previously north-flowing drainage even after the ice finally went out; it forces the flow to continue to spill at *C*, the lowest point in the preglacial drainage divide, today. This diversion shifted the divide between the Housatonic and Connecticut drainage basins in this area.

At the present time, a brook that flows most of the year pours northwest onto the stratified-drift plug north of Spaulding Pond. There it sinks into the gravel and disappears to underflow except at times of unusual floods. The recharge keeps the water table in the gravel so high that water seeps continuously into Spaulding Pond. Although no surface water enters Spaulding Pond except during storms and the spring thaw, this ground-water inflow maintains its outlet, the source of Mad River, as a perennial stream.

Dennis Hill area

West of Dennis Hill, as at the divide south of Spaulding Pond, water doubtless became ponded as soon as the ice front had retreated north of the preglacial drainage divide. The resulting lake, a predecessor or early stage of glacial Lake Norfolk, stood at an elevation of about 1,435 feet; its water spilled southward at a saddle (*D*, fig. 1) half a mile west of the summit of Dennis Hill. The waters from spillway *D*

eventually reached the Housatonic River, south of the Norfolk quadrangle, by way of the Naugatuck River. Apparently plunge-pool erosion by a waterfall that developed in the spillway carved a rock basin, which is now occupied by a small round pond.

Spillway *D* was abandoned when, as melting continued, a lower drainage route became available. This route crossed the rock divide north of Dennis Hill and drained to the east, to the Connecticut River. For a time, drainage was by way of two spillways, at *E*. These spillways, at about 1,340 feet, crossed the preglacial divide at the head of Mad River about 0.9 mile north of Dennis Hill. A deposit of stratified drift, *3*, west of these spillways, indicates that ice stood nearby at least part of the time that they were in operation. However, I found no evidence to prove that the saddle, at *G*, one-third mile farther north, ever served as a spillway as Flint (1930, p. 131 and map) inferred. The topography at saddle *G*, the point where the former railroad grade crossed the divide, has been modified by cutting for the railroad and by grading for successive highways, but the available evidence suggests that before colonial days the surface was probably a few feet higher than that at the spillways designated *E*.

A still lower point in the crestline of the rock divide occurs 0.6 mile north of Dennis Hill, at *F*. Ice may have blocked this while the spillways to the north, at *E*, were in use, or the ground level may initially have been higher because of till deposits so that all three spillways functioned simultaneously. Whether through melting of ice or erosion of till, the low point at *F* soon came to be the controlling spillway so that it carried off the waters of glacial Lake Norfolk into Mad River. After this spillway was cut down to bedrock at about 1,325 feet elevation, the lake level was stabilized. As far as is known, this rock lip continued to control the level of glacial Lake Norfolk until so much ice melted out that a route to the west down the Blackberry River valley, around the north side of Canaan Mountain, was opened up.

Tobey Pond delta

The drift that buries the preglacial surface north and east of Tobey Pond is stratified and has the form of a kettled delta. This deposit, here called the Tobey Pond delta (*8* to *4*, fig. 1), is the principal evidence for the former existence of glacial Lake Norfolk. Melt-water streams entering glacial Lake Norfolk built the Tobey Pond delta after the ice front had retreated to a line that may have run east-west approximately half a mile north of Tobey Pond. A large block of stagnant ice, which later melted and left Tobey Pond as a kettle, limited the delta on the south. Numerous smaller kettles north of Tobey Pond record smaller blocks of ice that were surrounded or buried; the largest are inferred to mark the preglacial valley of ancestral Tobey Pond Brook.

The initial form of the delta surface is obscured both by the collapse due to melting out of buried ice and by Holocene erosion. Most of the delta lies east and north of Tobey Pond, but a gravelly hill, *4*, west of the outlet of Tobey Pond appears to be part of the same deposit. If so, its elevation of more than 1,360 feet makes it the highest preserved remnant. It stands more than 30 feet above the lake level that would be determined by the rock lip of spillway *F*, even after a reasonable allowance is made for the effects of postglacial tilt. The relations of this gravelly hill to the sloping delta surface north and east (*5* and *6*, respectively, fig. 1) of Tobey Pond suggest that it is the apex of the subaerial part of the delta, which had the form of a fan sloping east across the Tobey Pond ice block. The stream that deposited the bulk of the delta would seem, therefore, to have entered the basin of glacial Lake Norfolk near the gravelly hill at *4*. If so, it must have reached this point either across the ice to the northwest or across the divide east of Roaring Brook.

Nearly all the material in the delta and much of that in the associated fan is sand. For example, the test hole north of Tobey Pond (fig. 1) penetrated 113 feet of material that was almost entirely sand, after passing through 10 feet of interbedded sand and gravel at the surface (R. L. Melvin, written commun., 1969). Pebble gravel is present in the uppermost few feet of the combined deposit at most places except in the eastern face overlooking Spaulding Brook (*7*, fig. 1). Apparently pebble gravel characterizes the subaerial (fan) beds, but is scarce or lacking in the subaqueous foreset beds.

Other deposits probably related to glacial Lake Norfolk

The north edge of the Tobey Pond delta-fan deposit differs in appearance from the east edge. The east edge (*7*, fig. 1) appears to be a normal depositional foreset slope notched by scallops due to later erosion. The origin of the gentler slope, *9*, to the north is not fully understood. In a gravel pit at the northeast corner of what would seem to be the same deposit, gravel occurs in the upper beds, which overlie sand that contains little or no gravel. This is the same stratigraphic sequence that is usual farther south, but here the gravel lies more than 75 feet below lake level. The easiest explanation of the observed relations would seem to be that they are the result of over-ice deposition at lake level, followed by collapse. However, the sand strata do not show the usual internal evidence of collapse;

359-403 O—69——14

such evidence would perhaps be expected if these deposits had settled 75 feet by the melting of subjacent ice.

Lacustrine silts, *10*, in the valley of Wood Creek, in the north part of Norfolk village and to the north, may have been deposited in glacial Lake Norfolk, though they may also be older. They postdate the thick presumably subglacial till of the drumlinlike ridge to the east, but scattered stones, boulders, and patches of till seem to indicate that ice moved across them after they were deposited. This inference may be supported by the results of consolidation tests made for the Soil Conservation Service (W. M. Brown, oral commun., 1968), which have been interpreted as showing that in the vicinity of the proposed dam these lake silts (*10*, fig. 1) have been compacted by overburden. I suggest that this overburden was ice that has subsequently melted rather than strata that have subsequently been eroded. If ice overrode the lakebeds, two interpretations are possible. First, these lakebeds may be older than the glacial Lake Norfolk beds west of Dutton Mountain, which seem not to have been overridden. If so, the Wood Creek deposits must apparently have been under the ice cover throughout the lifetime of glacial Lake Norfolk. Alternatively, ice may have buried these silts as the result of a short-lived resurgence of ice movement just before glacial Lake Norfolk was drained.

I interpret several gravel knobs north of the Tobey Pond delta as kames, which indicate that after the delta had been built above lake level north and east of the ice block at the site of Tobey Pond, the ice confining the delta on the north melted out under stagnation conditions. However, ice was apparently still thrusting southeast up the valleys of Blackberry River and ancestral Tobey Pond Brook. Morainelike ridges (fig. 1) of drift, partly till and partly stratified, were deposited marginal to these valley lobes. These deposits seem to be retreatal moraines left by the last ice known to have been active in the Norfolk quadrangle.

Draining of glacial Lake Norfolk

When the ice melted out to the point where a route to the west down the valley of the Blackberry River became available, glacial Lake Norfolk was drained. The conditions attending this drainage are not known. I found no adequate evidence to establish Flint's inference (1930, p. 131 and map) of intermediate lake levels at 1,220 and 1,190 feet. On the contrary, Joseph H. Hartshorn (oral commun., 1968) has suggested that the lake may have emptied very rapidly.

If the initial westward leakage down the Blackberry River valley from the basin of glacial Lake Norfolk took a course through ice that was already decaying, the channel may have been enlarged rapidly, not only by normal stream abrasion processes in the crumbling ice, but also by melting, for the bottom waters of the lake may have been near the temperature of maximum density, 4°C., rather than at the melting point. Enlargement of the outlet might occur at an exponentially increasing rate. This would perhaps permit the suggested sudden emptying of the lake.

Sudden emptying of the lake, Hartshorn suggests, may account for the scalloped pattern in the foreset east face of the Tobey Pond delta (*7*, fig. 1). The saturated, rather fine-grained beds of the delta foresets would perhaps be unable to lose water by subdrainage as fast as the lake level was lowered, and sudden failure and movements of mudflow type could have resulted, and produced the scallops. Otherwise, postglacial erosion must have formed this pattern.

A deposit that has the form of a gently sloping fan (*11*, fig. 1) heads at the point where Norfolk Brook spills west across the preglacial divide into the valley of Spaulding Brook. The genesis of this feature as the result of turbidity currents under the waters of glacial Lake Norfolk seems unlikely, as the deposit includes gravel with 7-inch cobbles. On the other hand, I saw no supporting evidence to indicate that the level of glacial Lake Norfolk ever stood at 1,220 feet long enough for this deposit to accumulate as a delta, as Flint (1930, map) infers. Its origin in postglacial time also seems unlikely, as the present brook is incised below the fanlike surface. I therefore suggest that the deposit was constructed by mudflows at the time glacial Lake Norfolk was suddenly drained. Alternatively, it may have been built by torrential melt-water runoff after the lake was drained.

PRESENT DRAINAGE PATTERN

After glacial Lake Norfolk was drained, the runoff took a consequent course on the newly exposed surface.

In the easternmost preglacial valley, the stratified-drift plug (*2*, fig. 1) ponded the southern part and forced the ancestor of Spaulding Pond that existed in early Holocene time to drain across the preglacial divide, as discussed above. Farther north, the drumlinlike ridge blocked the valley and forced Norfolk Brook, in the middle segment of the former valley, to drain west across the preglacial divide into the valley of the ancestral Blackberry River. In the northern part of the former valley, north of the Norfolk quadrangle, other drift deposits, not yet mapped, blocked and reversed the preglacial drainage; east of Haystack Mountain, Wood Creek now drains south where the former drainage flowed north.

To the west, the Tobey Pond delta had largely obliterated the preglacial valley of ancestral Tobey Pond Brook. Kettles north of the outlet of Tobey Pond suggest that the present course of the upper part of Tobey Pond Brook may have been initiated along a line of collapse left when ice melted out from a former tributary of the main preglacial valley. At the longitude of the main preglacial valley (ancestral Tobey Pond Brook), the morainelike ridge blocking that valley forced the stream to continue eastward across the preglacial divide. Thus Tobey Pond Brook, like Norfolk Brook, became a tributary to the valley of the ancestral Blackberry River (fig. 1).

In the preglacial valley of the ancestral Blackberry River, Spaulding Brook followed the crease between the westward slope of till on the flank of Dutton Mountain on the east and the foreset beds of the Tobey Pond delta on the west. The delta apparently encroaches on the till slope, for drilling by the Soil Conservation Service at a proposed damsite west of Dutton Mountain (fig. 1) found that fine-grained soils, interpreted as lacustrine, thicken westward from beneath the alluvium of Spaulding Brook (W. M. Brown, written commun., 1968).

North of the latitude of Dutton Mountain, Spaulding Brook swung west around the foot of the Norfolk Brook fan (*11*, fig. 1). North of the fan, the morainelike ridge blocking the preglacial valley diverted Spaulding Brook, now augmented by the waters from the valleys to the east and west, and forced it to spill across the preglacial divide to the east. This diversion across bedrock accounts for the gentle gradient of Spaulding Brook above the point where it crosses the rock ridge, and for the picturesque waterfall in Norfolk village that descends from the preglacial divide to the junction with Wood Creek at the head of Blackberry River.

The drift deposits that blocked the northward exit down the preglacial valley east of Haystack Mountain prevented Spaulding Brook from draining northward from the foot of the waterfall in Norfolk village. Instead, uniting with Wood Creek, it spilled back across the former divide at the low point in its crest. Wood Creek cascades down on bedrock to reach the junction, and below the junction the Blackberry River flows on rock for more than 1,500 feet, all the way to the junction of the present valley with that of the ancestral Blackberry River.

REFERENCE

Flint, R. F., 1930, The glacial geology of Connecticut: Connecticut State Geol. and Nat. History Survey Bull. 47, 294 p.

AN ANASTOMOSING CHANNEL COMPLEX AT THE BASE OF THE PENNSYLVANIAN SYSTEM IN WESTERN KENTUCKY

By FRED R. SHAWE and BENJAMIN GILDERSLEEVE,
Berea, Ky., Bowling Green, Ky.

Work done in cooperation with the Kentucky Geological Survey

Abstract.—Mapping in western Kentucky has partly delineated a complex, anastomosing channel system at the base of the Pennsylvanian System. This channel complex is found at the margins of, and at altitudes reaching a maximum of about 120 feet above, a major westward-trending trunk channel. Fill in the main and subsidiary channels is dominantly sandstone, but it includes conglomerate, conglomeratic sandstone, siltstone, shale, and coal. The shape of channel walls is generally controlled by the varied resistance to erosion of different Mississippian rocks in which the channel is cut. In a few places, faults have controlled the position of a channel or the shape of a channel wall.

The most conspicuous feature at the base of the Pennsylvanian System in western and west-central Kentucky is a large westward-trending sandstone-filled channel cut into the Mississippian rocks. This channel has been traced along the southeast margin of the Illinois basin in Kentucky from near Willowtown to the vicinity of Woodbury, a distance of about 65 miles (fig. 1, area location). The channel was considered by Miller (1910) to be a probable Early Pennsylvanian connection between the Appalachian and Illinois basins. Burroughs (1923) recognized the channel character of conglomeratic sandstones in tributaries and distributaries of the channel in Hart County. Weller (1927) noted what he called subsidiary channels in the general area of the Brownsville and Reedyville quadrangles. Potter and Siever (1956), in their studies of crossbedding, showed that the sandstones and conglomerates had been deposited by currents flowing from east to west.

Recent mapping in the Brownsville and Reedyville quadrangles in Butler, Edmondson, and Warren Counties, Ky., has disclosed a complex system of anastomosing channels along the south flank of, and at altitudes reaching a maximum of about 120 feet above the floor of, the main channel (Gildersleeve, 1965; Shawe, 1966). This channel complex is cut into rocks of Late Mississipian age, which range from the Big Clifty Sandstone Member of the Golconda Formation to the lower part of the Menard Limestone. Rocks of the Caseyville Formation of Early Pennsylvanian age fill the channels (figs. 2 and 3). The network extends south of the main channel for at least 8 miles and has been traced for about 16 miles along the main channel. Fragmentary drill-hole records and current geologic mapping indicate a similar channel complex along the north side of the main channel.

The paleotopography of the channel complex was reconstructed—as nearly as possible—by contouring the interval between the Mississippian-Pennsylvanian uncomformity and the base of the Main Nolin coal (the lowest coal bed in the Pennsylvanian System in this area) to eliminate post-Main Nolin deformation. An altitude of 1,000 feet was assigned to the base of the Main Nolin coal to avoid negative numbers. The resultant map shows the subsidiary channel system; not enough data are available to depict the configuration of the main channel (fig. 1). Channels in the subsidiary system steepen abruptly 1–3 miles above their junctures with the main channel, although this is not evident on the map. Rarely, small subsidiary channels steepen abruptly just above their junctures with larger subsidiary channels. Distributary junctures seem as common as tributary junctures.

The channel system has a maximum relief of about 180 feet. Individual channels are crudely V-shaped with relatively narrow flat bottoms. The channels are generally symmetrical and have terraced walls; at some localities channels are asymmetrical in cross section and have only rudimentary terraces. The terraces are

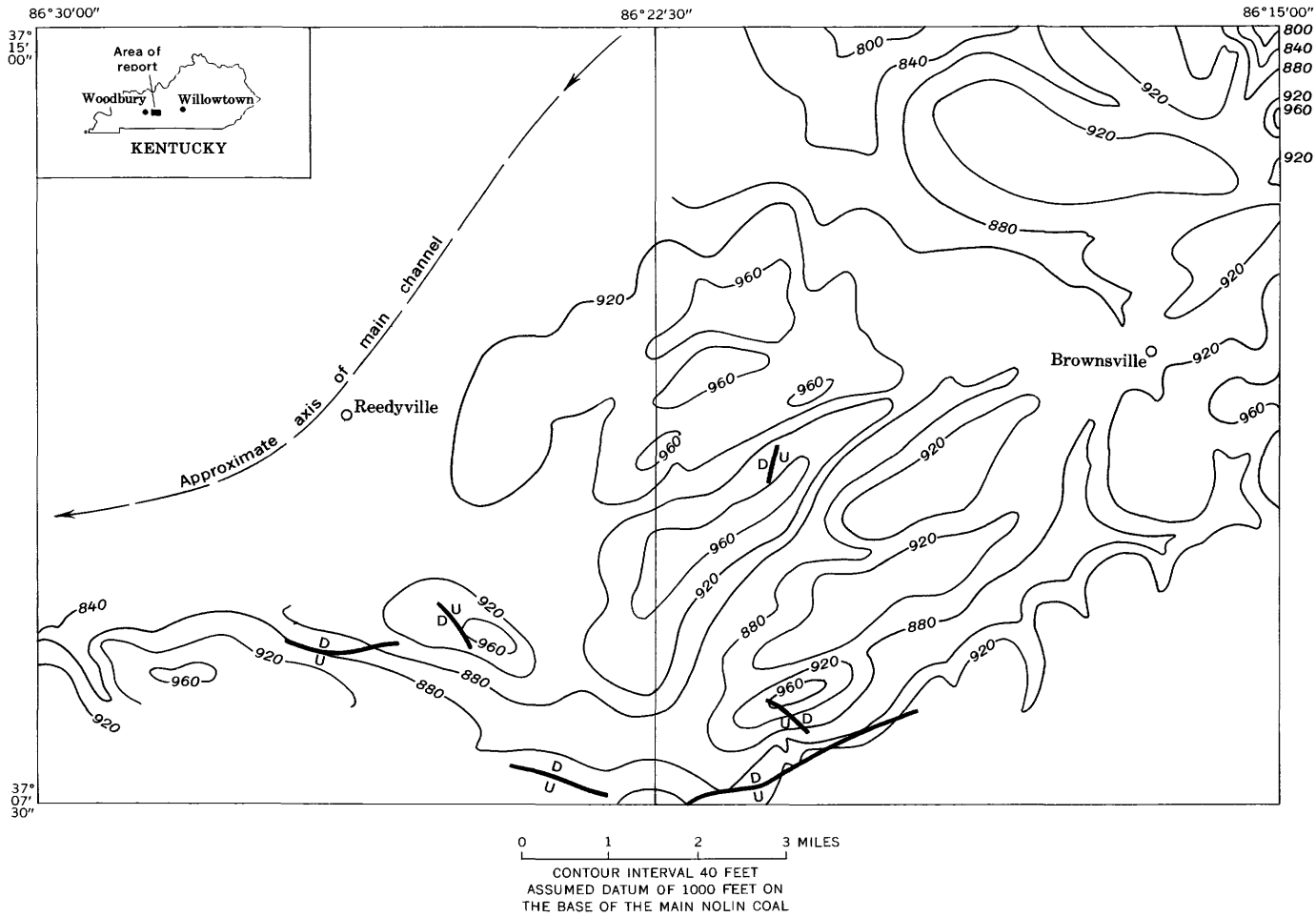

FIGURE 1.—Contour map of the Mississippian-Pennsylvanian unconformity, showing the configuration of the post-Mississippian channel complex and the location of pre-Pennsylvanian faults (D, downthrown side; U, upthrown side), Brownsville and Reedyville quadrangles, Kentucky. Data insufficient to contour main channel.

mostly the result of the varied resistance of different lithologies to erosion. Prominent terrace-forming units are the lower limestone beds of the Menard Limestone, the Vienna Limestone, and, to a lesser degree, the uppermost beds of the Glen Dean Limestone. The Haney Limestone Member of the Golconda Formation, the thick sandstone beds of the Hardinsburg Sandstone, and the Big Clifty Sandstone Member of the Golconda Formation are all about equally resistant to erosion and form relatively steep valley walls without terraces. Channels deep enough to have cut into any of these three lower units appear incised (fig. 3). Prechannel fault-line scarps modify the channel walls at several localities, and at one place, about 2½ miles south of Reedyville, the position of a channel is controlled by a fault for a distance of about 1 mile.

Fill in the channel complex consists of conglomerate, conglomeratic sandstone, and sandstone, as well as lesser amounts of siltstone and shale, and minor amounts of coal. The fill is characteristically conglomerate, conglomeratic sandstone, and sandstone where the channels are deepest and the channel sides are steepest; elsewhere, the fill may be shale, siltstone, sandstone, or conglomerate. At many localities, conglomerate is the lowest material exposed and grades upward into conglomeratic sandstone, sandstone, siltstone, and shale. Siltstone and shale occur throughout the area, generally in the upper parts of the channel fill, but locally they make up most of the channel fill. Coal in the channel fill is mostly the Main Nolin coal, which is confined to the area of the channel system. The highest interfluves in the channel area are higher than the Main Nolin coal.

Sand grains are subangular to subrounded quartz and range in size from very fine to very coarse; medium to coarse grain sizes predominate. Individual sand lenses range from very poorly sorted to well sorted. Conglomerate consists of beds, stringers, and lenses of well-rounded granules and pebbles of clear to milky quartz, commonly frosted and iron stained, in a matrix

of fine to very coarse quartz sand; pebbles are as much as 2 inches across but are mostly ¼ to ½ inch in longest diameter. Sandstone locally grades into conglomerate. A sparsely occurring conglomerate, made up of both locally derived limestone clasts as much as 1 foot in diameter and a few quartz pebbles in a matrix of limestone and quartz sand, is found mostly in the steepened reaches of the channels. At a few places this limestone conglomerate occurs on the terraced valley walls directly upon the limestone from which it was derived.

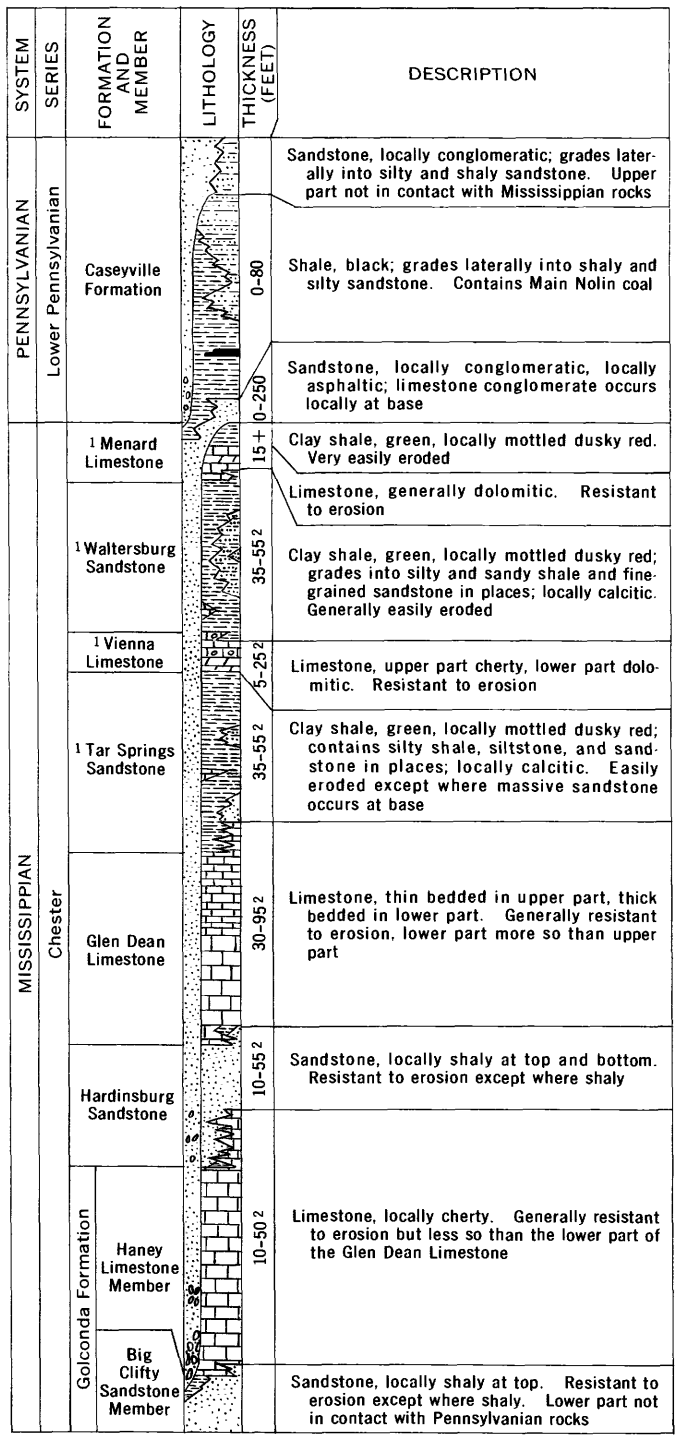

[1] Mapped as Leitchfield Formation in Brownsville quadrangle.
[2] Thickness where not directly overlain by Caseyville Formation.

FIGURE 2.—Generalized stratigraphic column of rocks exposed along the Mississippian-Pennsylvanian unconformity, Brownsville and Reedyville quadrangles, Kentucky.

Conglomerate, with the possible exception of the limestone conglomerate, and conglomeratic sandstone are crossbedded. Sandstone is both crossbedded and planar bedded; siltstone is rarely crossbedded. Channel fill consisting of crossbedded conglomerate or conglomeratic sandstone overlain by crossbedded sandstone, which in turn is overlain by planar-bedded sandstone, is not uncommon.

Contacts between channel fill and the Mississippian rock are sharp and generally "clean" in that there are very few areas of locally derived debris along the contact.

The field relationship between the pre-Pennsylvanian, faults and the channels and between the channels and the upland surface on either side of the channel complex shows that channel cutting took place relatively late during the post-Mississippian uplift. According to Siever (1951, p. 570–571), post-Mississippian uplift in the Illinois basin took place in two stages separated by a long period of erosion which reduced the surface to a peneplane; he related channel cutting in the Illinois part of the basin to the second stage of uplift. Channel cutting in the Kentucky part probably occurred at about the same time.

The origin of an anastomosing channel system cut into bedrock along the flanks of, and many tens of feet above, a major trunk channel is not well understood. Several somewhat similar stream patterns exist today, notably that of the Caroní River in Venezuela. The slightly similar Pleistocene stream pattern of the Washington scablands has been documented. Garner (1967) believes that the stream pattern of the Caroní River (and of some other present streams) is due to climatic change. Bretz and others (1956) associate the Pleistocene stream pattern of the Washington scablands with glaciation. The origin of the anastomosing channel complex in western and west-central Kentucky cannot be explained at this time; it is an intriguing problem.

REFERENCES

Bretz, J. H., Smith, H. T. U., and Neff, G. E., 1956, Channeled scabland of Washington; new data and interpretations: Geol. Soc. America Bull., v. 67, no. 8, p. 957–1049.

Burroughs, W. G., 1923, A Pottsville-filled channel in the Mississippian: Kentucky Geol. Survey, ser. 6, v. 10, p. 116–126.

Garner, H. F., 1967, Rivers in the making: Sci. American, v. 216, no. 4, p. 84–94.

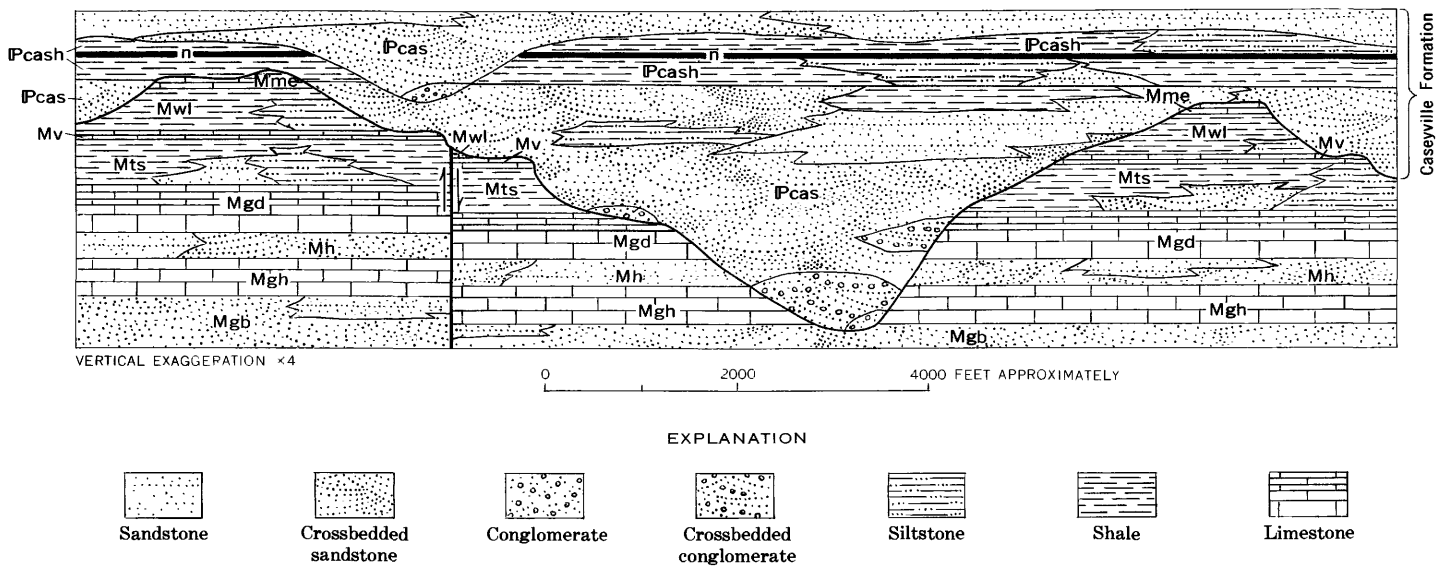

FIGURE 3.—Generalized cross section drawn across a buried pre-Pennsylvanian channel, showing the relation of Mississippian rock units to buried topography. Pcas, sandstone of Caseyville Formation; Pcash, shale of Caseyville Formation; n, Main Nolin coal; Mme, Menard Limestone; Mwl, Waltersburg Sandstone; Mv, Vienna Limestone; Mts, Tar Springs Sandstone; Mgd, Glen Dean Limestone; Mh, Hardinsburg Sandstone; Mgh, Haney Limestone Member of the Golconda Formation; Mgb, Big Clifty Sandstone Member of the Golconda Formation.

Gildersleeve, Benjamin, 1965, Geology of the Brownsville quadrangle, Kentucky: U.S. Geol. Survey Geol. Quad. Map GQ-411.

Miller, A. M., 1910, Evidence of former connection between eastern and western coal fields across central Kentucky: Geol. Soc. America Bull., v. 20, p. 621–624.

Potter, P. E., and Siever, Raymond, 1956, Sources of basal Pennsylvanian sediments in the Eastern Interior Basin. 1. Crossbedding: Jour. Geology, v. 64, no. 3, p. 225–244.

Shawe, F. R., 1966, Geologic map of the Reedyville quadrangle, western Kentucky: U.S. Geol. Survey Geol. Quad. Map GQ–520.

Siever, Raymond, 1951, The Mississippian-Pennsylvanian unconformity in southern Illinois: Am. Assoc. Petroleum Geologists Bull., v. 35, no. 3, p. 542–581.

Weller, J. M., 1927, Geology of Edmondson County: Kentucky Geol. Survey, ser. 6, v. 28, 246 p.

ACCURACY OF STREAMFLOW CHARACTERISTICS

By CLAYTON H. HARDISON, Washington, D.C.

Abstract.—Streamflow information, which is one of the end products of the Water Resources Division of the U.S. Geological Survey, may be obtained directly from a streamflow record or may be derived from base data by analytical methods. In either case, accuracy goals for the information obtained are needed to test the adequacy of the information and to design the data-collection system upon which the information is based. It is proposed that the accuracy goal for each streamflow characteristic be set equivalent to the accuracy with which that characteristic could be estimated from an observed record of some stipulated length. Curves and tables are presented in this paper to aid in setting such goals.

A streamflow characteristic as used in this paper is a characteristic of a population of flows, at a given site, of which the recorded flows are but a sample. Thus a streamflow information system, such as that operated by the U.S. Geological Survey, can only provide estimates of streamflow characteristics; that is, estimates of what flow may be expected in the future. These estimates are obtained either by analysis of the streamflow data collected at a specific site or by analytical methods, such as correlation and regression, that are used to extend or transfer streamflow information. Each estimate necessarily has an error associated with it that depends on the amount and kind of data and on the analytical methods used.

The accuracy of streamflow information required for specific uses, or a composite accuracy for all uses has never been determined. Studies are only now beginning that may eventually define the accuracy that will properly balance the cost of obtaining additional data and the project benefits accruing from streamflow information of increased accuracy. Until such studies have been made and evaluated, an interim means of setting accuracy goals is needed. It is proposed here that the accuracy goal for each streamflow characteristic be set equivalent to the accuracy that could be obtained from an observed record of some stipulated length..

This paper contains curves and tables from which the accuracy of streamflow characteristics based on records of stipulated lengths can be obtained.

A streamflow characteristic is anything that describes the flow to be expected at a given site. The 50-year peak flow, 20-year low flow, mean annual flow, mean monthly flow, and the standard deviation of the annual and monthly flows are examples of such characteristics. Streamflow characteristics can only be estimated; their true value can never be determined because there is a time-sampling error in every record of streamflow and a model error in every analytical method.

In this paper, the time-sampling errors of streamflow characteristics estimated from gaging-station records are computed using standard statistical methods and assuming no serial correlation between the annual occurrences. The measurement error in determining the discharge of the annual occurrence has been neglected as it is usually small in relation to the time-sampling error and, consequently, has only a minor effect on total error.

In the evaluation of the accuracy of streamflow characteristics given in this paper, the standard error of estimate of the characteristic is used as a single-valued index of accuracy. When the standard error of estimate is thus used, the reader should understand that only 68 percent of the estimates of that characteristic are within one standard error, plus or minus, of the true value. On the basis of theory of errors, he may also understand that about 95 percent of the estimates are within two standard errors of the true value, and that about 99.7 percent of the estimates are within three standard errors.

ACCURACY OF THE MEAN

The standard error of the mean of any item of hydrologic data can be obtained from the standard deviation of the annual occurrences of that item by the formula $SE=SD/\sqrt{N}$ in which SE is the standard error of the mean of the events, SD is the standard deviation of the annual events, and N is the number of events. The standard error of the mean in percent of the mean is given by

U.S. GEOL. SURVEY PROF. PAPER 650-D, PAGES D210-D214

$$\frac{100\,SE}{\overline{X}}=\frac{100\,SD}{\overline{X}\sqrt{N}}=\frac{100\,C_v}{\sqrt{N}},$$

in which C_v, equal to $SD/\overline{X}$, is the coefficient of variation and $\overline{X}$ is the mean of the annual events. This relation holds for all distributions. (The coefficient of variation is a dimensionless index of variability that allows the variability at several locations to be compared. It can also be averaged as a measure of regional variability.)

The relation between C_v and the standard error of the mean, in percent, is shown in figure 1 for five selected values of N. If, for example, the coefficient of variation of the annual discharge is 0.3, the standard error of the mean annual discharge based on 10 years of record is shown in figure 1 to be 9.5 percent.

If the logarithms of independent annual events, such as monthly or annual mean flows, are normally distributed, the coefficient of variation of the events can be estimated from I_v, the standard deviation of the common logarithms, by the relation

$$C_v^2=\exp[(2.3026\,I_v)^2]-1,$$

which is adapted from an equation given by Chow (1964, p. 17). Values of C_v for selected values of I_v based on this relation are given in table 1.

TABLE 1.—*Relation between standard deviation of the common logarithms, I_v, and the coefficient of variation, C_v, in a log-normal distribution*

I_v	C_v	I_v	C_v	I_v	C_v
0.06	0.139	0.32	0.849	0.58	2.22
.08	.186	.34	.920	.60	2.40
.10	.233	.36	.994	.62	2.58
.12	.282	.38	1.072	.64	2.78
.14	.330	.40	1.155	.66	3.01
.16	.381	.42	1.24	.68	3.26
.18	.432	.44	1.34	.70	3.53
.20	.486	.46	1.44	.72	3.82
.22	.540	.48	1.55	.74	4.15
.24	.598	.50	1.66	.76	4.51
.26	.656	.52	1.78	.78	4.91
.28	.718	.54	1.92	.80	5.36
.30	.782	.56	2.06		

ACCURACY OF THE STANDARD DEVIATION

The accuracy of the standard deviation for normal distributions of annual events is discussed first, and then by analogy the resulting equations are applied to log-normal distributions. These expressions for the accuracy of the standard deviation are later used in the computation of the accuracy of an estimated T-year event.

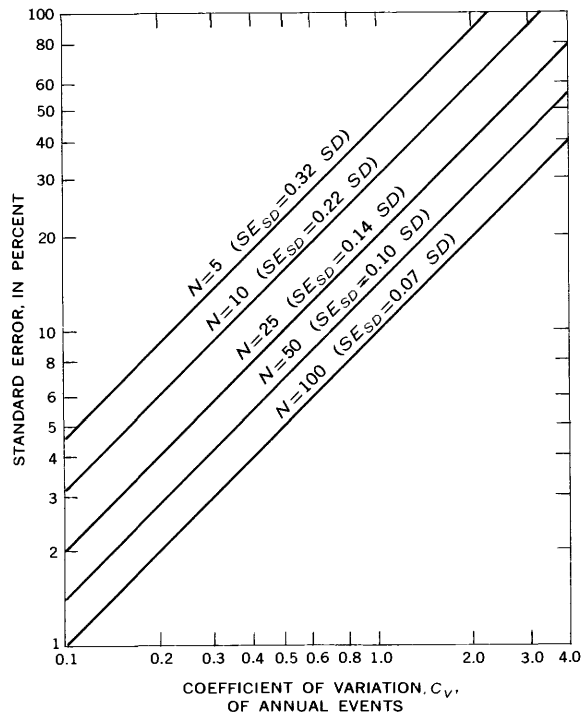

FIGURE 1.—Standard error of mean annual or mean monthly flow. Parameter, N, is number of years of record. Standard error of the standard deviation, SE_{SD}, for samples from a normal population is shown on parameter line.

For samples drawn from a normal population of annual events, the standard error of the standard deviation is given by

$$SE_{SD}=\frac{\sigma}{\sqrt{2N}},$$

in which σ is the standard deviation of the population and N is the number of annual events in the sample. Using SD, the standard deviation of the sample, as being the best estimate of the population, standard deviation gives $SE_{SD}=SD\sqrt{2N}$. As the ratio SE_{SD}/SD given by this equation is constant for a given N, the evaluation of SE_{SD} in terms of SD can be shown along the five lines in figure 1. As indicated in this figure, the SE_{SD} for a given N is obtained by multiplying the given constant by the standard deviation of the annual events; SE_{SD} in percent is 100 times the given constant.

For log-normal distributions, the standard error of the logarithms, I_v, can be substituted for SD in the equations for normal distributions, and the resulting standard error of the standard deviation, SE_{Iv}, will be in log units.

The coefficient of variation, C_v, is another commonly used measure of variability. If C_v is defined as $SD/\overline{X}$, the standard error of C_v for samples from normal populations is given by

$$SE_{C_v}=\frac{C_v}{\sqrt{2N}}\sqrt{1+2C_v^2}.$$

In this paper, C_v is used as a measure of variability of untransformed data, and I_v is used when a logarithmic transformation is applied to the data.

ACCURACY OF AN ESTIMATED T-YEAR EVENT

The standard error of a T-year event, such as the 10-year flood, estimated from a record of annual occurrences depends on the type of distribution, the error of the mean event, and the error in the slope of the frequency curve (the standard deviation is a measure of the slope). It is evaluated here by adding the variance due to error in slope to the variance of the mean event. This evaluation purports to give the standard error of T-year events based on samples of size N drawn from a normal population of known standard deviation. The magnitude of such T-year events would, of course, be computed from the mean and standard deviation of each sample, but the appraisal of their accuracy can be based on the standard deviation of the population, which is assumed to be known.

For samples from a normal population, the accuracy of estimated T-year events depends on the accuracy of the computed mean and of the computed standard deviation of the annual events in the sample. For a normal population of known standard deviation, the standard error of the sample mean equals $\sigma/\sqrt{N}$ and the standard error of the sample standard deviation equals $\sigma/\sqrt{2N}$ as discussed in the preceding sections. The variance due to error in slope at a point that is k standard deviation units from the mean may be computed as $(k\sigma/\sqrt{2N})^2$; tables of k values for a normal distribution are given in most statistical texts. By adding the variance of the mean event, $(\sigma/\sqrt{N})^2$, to the variance due to slope we obtain

$$SE_{x_T}=\sqrt{\left(\frac{\sigma}{\sqrt{N}}\right)^2+\left(\frac{k(\sigma)}{\sqrt{2N}}\right)^2}=\sigma\sqrt{\frac{1+k^2/2}{N}},$$

in which SE_{xT} is the standard error of the T-year event in the same units as σ.

For samples from a log-normal population, the standard deviation of the logarithms, I_v, can be substituted for σ to obtain

$$SE_{x_T}=I_v\sqrt{\frac{1+k^2/2}{N}},$$

in which k and N are the same as for normal distributions and SE_{xT}, the standard error of the T-year event, is in log units. This expression for the standard error defines the relations between variability of the annual events and the standard error of 2-, 10-, 20-, and 50-year events for selected lengths of record that are shown in figures 2 and 3.

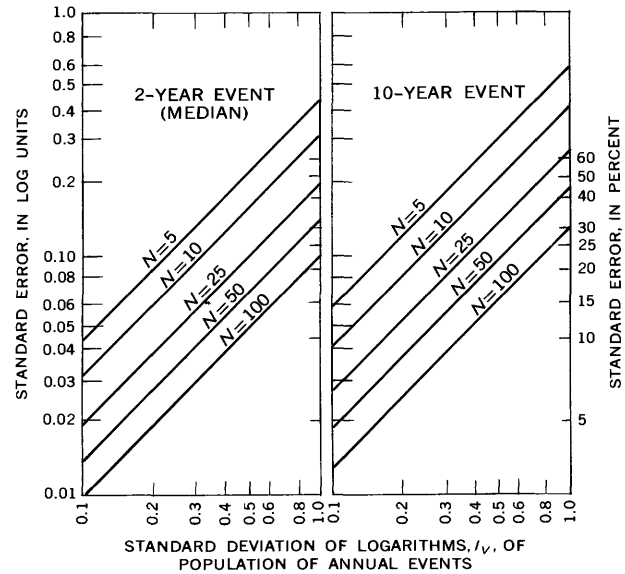

FIGURE 2.—Standard error of median and of 10-year event for log-normal distributions of annual events. Parameter, N, is number of years of record.

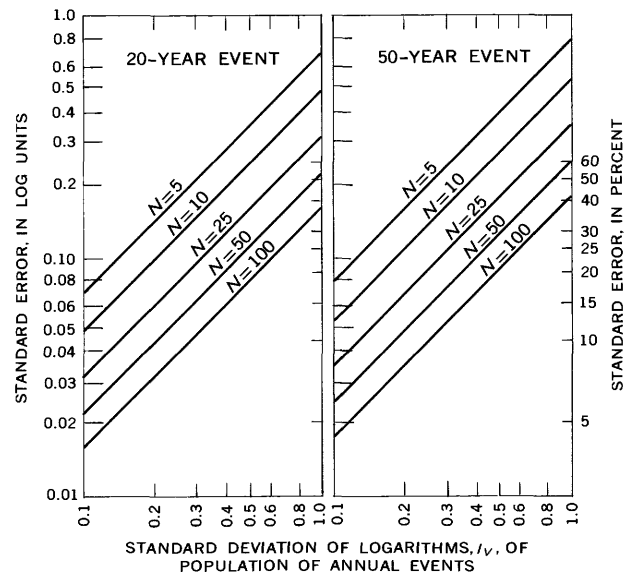

FIGURE 3.—Standard error of 20- and 50-year events for log-normal distributions of annual events. Parameter, N, is number of years of record.

The ordinate scales of figures 2 and 3 show the standard error in log units, and auxiliary ordinate scales show the standard error in percent. For a given number of log units, the standard error in percent is the average of the positive departure in percent and the negative departure in percent. The relation between log units and percentage is shown in table 2.

TABLE 2.—*Relation between log units and percentages*

Log units	Percentage			Log units	Percentage		
	Plus	Minus	Average		Plus	Minus	Average
0.01	2.3	2.3	2.3	0.16	44.5	30.8	37.6
.02	4.7	4.5	4.6	.17	47.9	32.4	40.1
.03	7.2	6.6	6.9	.18	51.4	33.9	42.6
.04	9.5	8.8	9.2	.19	54.9	35.4	45.1
.05	12.2	10.9	11.6	.20	58.5	36.9	47.6
.06	14.8	12.9	13.9	.21	62.2	38.3	50.2
.07	17.4	14.9	16.2	.22	66.1	39.7	52.8
.08	20.2	16.8	18.5	.23	69.8	41.1	55.4
.09	23.1	18.7	20.9	.24	73.8	42.5	58.1
.10	25.9	20.6	23.2	.25	77.8	43.8	60.8
.11	28.8	22.4	25.6	.26	81.9	45.0	63.5
.12	31.8	24.1	28.0	.27	86.2	46.3	66.2
.13	34.9	25.9	30.4	.28	90.5	47.5	69.0
.14	38.0	27.6	32.8	.29	95.0	48.7	71.8
.15	41.3	29.2	35.2	.30	99.5	49.9	74.7

Numerical values of the ratio SE_{xT}/I_v are given in table 3 for use in plotting working copies of the graphs in figures 2 and 3. If the distribution of annual events is normal instead of log-normal, the standard error of the T-year event, in cubic feet per second can be computed from the ratio SE_{xT}/σ shown in table 3.

TABLE 3.—*Ratio of standard error of T-year events to standard deviation of annual events for normal and log-normal distributions*

[For normal distributions, figures in table represent SE_{xT}/σ, in which σ is the standard deviation of the annual events; for log-normal distributions they represent SE_{xT}/I_v in which I_v is the standard deviation of the logarithms of the annual events]

Recurrence interval (years)	Length of record, in years				
	5	10	25	50	100
2	0.447	0.316	0.200	0.141	0.100
10	.604	.427	.270	.191	.135
20	.686	.485	.307	.217	.153
50	.788	.558	.353	.249	.176

To obtain the standard error in percent for T-year events based on normal distributions of annual events, the standard error in cubic feet per second obtained by use of table 3 must be divided by the average size of the T-year event, which equals $\mu+k\sigma$, in which μ is the population mean and σ is the population standard deviation. As shown by Nash and Amorocho (1966, p. 193), the standard error in percent could thus be related to C_v, the coefficient of variation of the annual events, in which case the entries in table 3 multiplied by $100C_v/(1+kC_v)$ give the standard error in percent. Values of k for normal distributions are given in most statistical texts.

For log-normal populations, the standard errors in log units obtained by multiplying the values in table 3 by I_v can be used to define curves such as those shown in figures 2 and 3 or they can be converted into percentage by use of table 2.

If the population from which the annual events are drawn is neither normal nor log-normal and if it is assumed to be a Pearson type-III distribution of known coefficient of skew, the standard error of T-year events can be computed by the following equation:

$$SE_{x_T}=\frac{\sigma}{\sqrt{2N}}\sqrt{b^2k^2+2.828\,rbk+2},$$

in which $b^2=(0.75C_s^2+1)$ varies with C_s, the coefficient of skew, k is from Harter's (1969) tables, and r is the correlation coefficient of the sample means and sample standard deviations. This equation is based on the equation for variance of the standard deviation given by Kendall (1952, p. 224) and the relation between β_1 and β_2 given by Elderton (1953, p. 57) for a Pearson type-III distribution. Values of r for use in this equation have been determined by sampling to be about 0.3 for C_s of 0.5, 0.5 for C_s of 1.0, and 0.65 for C_s of 1.5. For negative skew coefficients, values of r are opposite in sign to those for the corresponding positive skew coefficient. For log-Pearson type-III populations, I_v, the standard deviation of the logarithms of the annual events, can be substituted for σ and the coefficient of skew of the logarithms for C_s; the resulting SE_{x_T} will be in log units.

The error equation for Pearson type-III distributions is not evaluated here because in most regions and for most streamflow characteristics the standard error of T-year events obtained by assuming a normal or log-normal distribution will be sufficiently accurate for the proposed uses described in the next section.

USE OF THE RELATIONSHIP CURVES

It is obvious from figures 1, 2, and 3 that any appraisal of the accuracy of streamflow characteristics obtained from a gaging-station record requires that an index of variability of the population of annual events be known or assumed. Thus the index of variability used to enter the curves should preferably represent an average for a region.

Average indices of variability (C_v or I_v) for annual streamflow events in two separate regions have been used to obtain the standard errors for 25 years of record shown in table 4. Where appropriate, the type of distribution assumed for the population of annual events is shown by a letter symbol after the variability index. The standard errors for the first two characteristics in each region were obtained by entering the 25-year curve in figure 1 with the indicated C_v (the type of distribution is immaterial). The standard errors for the third characteristic were determined directly from the note along the 25-year curve. The standard errors for the remaining characteristics were determined by entering the appropriate 25-year curves in figures 2 and 3.

TABLE 4.—*Standard error of selected items of streamflow information obtained from 25 years of record in two regions*

[C_v is coefficient of variation of annual events, I_v is standard deviation of the logarithms of the population of annual events, *LN* indicates a log-normal distribution]

Flow characteristic	Potomac River basin			Part 8 in Texas		
	Variability index	Standard error		Variability index	Standard error	
		Log units	Percent		Log units	Percent
Mean annual	C_v=0.3		6	C_v=0.7		14
Mean monthly	C_v= .8		16	C_v=1.4		28
Standard deviation of annual and monthly means			14			14
50-year flood	I_v= .22 *LN*	0.078	18	I_v= .31 *LN*	0.11	26
Median annual 7-day low	I_v= .20 *LN*	.040	9	I_v= .47 *LN*	.094	22
20-year 7-day low	I_v= .20 *LN*	.061	14	I_v= .47 *LN*	.144	34

The variability indices for the 50-year floods shown in table 4 were obtained by plotting regional flood-frequency curves (peak in ratio to mean annual peak) for each region on log-probability paper and estimating an average I_v from the slope of the curves. The indices for the other items are the averages of those computed for the annual events observed during the period of record at several stations in each region. (The distribution of the logarithms of the annual 7-day low flows at several gaging stations in Texas appears to have a skew coefficient of about −1.0, but for the purpose of this appraisal were used as being log-normal). The variability of the monthly means in each region represent the average monthly C_v at several stations. Tables similar to table 4 could be prepared for other lengths of record by using the appropriate curves in figures 1, 2, and 3 or the appropriate ratios in table 3.

Results such as those shown in table 4 can be used to appraise the results of analytical methods, such as regional regression analysis of streamflow characteristics and hydrologic parameters, in terms of equivalent length of record. In addition, the standard errors provide realistic guides for use in planning surface-water information programs in that they show the accuracy that could be obtained with a feasible length of record. The question of what length of record to use in setting accuracy goals for various classifications and size of stream is outside the scope of this paper.

REFERENCES

Chow, V. T., 1964, Frequency analysis, pt. 1 *in* Statistical and probability analysis of hydrologic data, sec. 8 *of* Chow, V. T., ed. in chief, Handbook of applied hydrology: New York, McGraw-Hill Book Co., Inc., p. 8-1–8-42.

Elderton, W. P., 1953, Frequency curves and correlation, 4th ed.: Washington, D.C., Harren Press, 272 p.

Harter, H. L., 1969, A new table of percentage points of the Pearson Type III distribution: Technometrics, v. 11, no. 1, p. 177–187.

Kendall, M. G., 1952, The advanced theory of statistics, v. 1, 5th ed.: New York, Hafner Publishing Co., 457 p.

Nash, J. E., and Amorocho, Jamie, 1966, The accuracy of the prediction of floods of high return period: Water Resources Research, v. 2, no. 2, p. 191–198.

RELATION OF THE MANNING COEFFICIENT TO MEASURED BED ROUGHNESS IN STABLE NATURAL CHANNELS

By J. T. LIMERINOS, Menlo Park, Calif.

Prepared in cooperation with the California Department of Water Resources

Abstract.—The purpose of this study was to find an objective method of determining basic values of the Manning roughness coefficient, n, in channels with coarse bed material. Data used in this analysis were obtained from 50 current-meter measurements of discharge and appropriate field surveys at 11 sites on California streams. Characteristic bed-particle sizes, including the 16-, 50-, and 84-percentile sizes, for both minimum and intermediate axes were used to find the best relation between the roughness parameter, $\frac{n}{R^{1/6}}$ (where R is the hydraulic radius), and relative smoothness, $\frac{R}{d}$ (where d is a characteristic bed-particle size). The relations best fitting the field data were obtained when the characteristic particle size was either the 84-percentile (d_{84}) or a weighted composite size (d_w). Percentage differences for the 50 observed and computed values of n involving either d_{84} or d_w, had a standard deviation of about 19 percent. The form of the derived equations, using d_{84} or d_w, was virtually identical with theoretical equations presented by Chow in 1959 and Vennard in 1961 and with an equation derived from field data by Leopold and Wolman in 1957.

The Manning roughness coefficient, n, is an index of the resistance to flow in a channel, and as such, is an important element in many types of hydraulic computations. In streams with relatively stable boundaries the resistance to flow results from the interaction of many elements. Among them are particle size of streambed material, bank irregularity, vegetation, channel alinement, bed configuration, channel obstructions, converging or diverging streamlines, sediment load, and surface waves. With our present knowledge the quantitative effect of most of these factors is not determinable and must be estimated subjectively.

In many channels, however, streambed particle size exerts a major influence on the flow. Fortunately, the quantitative effect of this factor can be determined more accurately than most of the other parameters involved in resistance to flow. Engineering knowledge would be increased if an objective relation between Manning's n and streambed particle size could be shown. The purpose of this study was to derive such a relation. An objectively obtained value of the Manning coefficient was sought based only on the size of the streambed particles in a relatively straight uniform channel. This value of n could then be adjusted for any of the other flow-retarding effects mentioned in the preceding paragraph, in the manner described by Chow (1959, p. 101–113).

The retarding effect of a particle of given size is relative; it will have greater retarding effect on shallow flow than on deep flow. Therefore, instead of directly using the particle-size index, d, in this study, it was combined with the hydraulic radius, R, in the term, $\frac{R}{d}$, to provide an index of relative smoothness. The parameter $\frac{n}{R^{1/6}}$, rather than n, was used in this study because it is directly proportional to the square root of the Darcy-Weisbach friction factor, f, which is more widely used in theoretical studies of hydraulic friction. Thus the relation sought was one between $\frac{n}{R^{1/6}}$ and $\frac{R}{d}$. This course of action was consistent with that taken by the more recent investigators of friction in open channels.

Separate analyses involving characteristic particle size were made for two of the three diameters of a particle. The minimum diameter of the streambed particles was used in the study because a particle at rest on the bed invariably has its minimum diameter in the vertical position; that diameter is, therefore, the most representative measure of roughness height. The intermediate diameter of the streambed particles was studied because that is the diameter most easily meas-

U.S. GEOL. SURVEY PROF. PAPER 650-D, PAGES D215–D221

urable—either by sieve analysis or by photographic techniques—and is the diameter that had been used in previous studies by other investigators. The maximum diameter was not considered, it being the least effective of the three diameters, as a measure of roughness; the bed particles usually orient themselves so that the maximum diameter or axis of each particle is parellel to the streamlines.

BASIC DATA

Fifty current-meter measurements of discharge and appropriate field surveys were made for the purpose of computing the Manning roughness coefficient, n, from the equation

$$n=\frac{1.486AR^{2/3}S^{1/2}}{Q}, \quad (1)$$

where

A=cross-sectional area,
S=energy slope, and
Q=discharge.

The 11 study reaches used in this investigation were located near Geological Survey stream-gaging stations because facilities for measuring discharge by current meter were available at the stations. Seven sites are on streams in north coastal California, and the other four sites are on streams draining the west slopes of the Sierra Nevada. The test sites were selected to give a wide range in average size of bed material, and the discharges and surveys were made at such times as to provide data covering a suitable range in stream depth. All discharges tested were in the tranquil range, their Froude numbers being less than unity. The maximum discharge used at the various sites was that equivalent to a flood of about 1-year recurrence interval, but the ratios of depth to vertical height of streambed particles of median size reached values as high as 300. Because values of Manning's n—not to be confused with the roughness parameter, $\frac{n}{R^{1/6}}$—show little change with ratios greater than 30, the stream depths used in this study cover an adequate range.

The most important criteria in selecting a site for study was that it be relatively free from velocity-retarding influences other than those associated with the size and size distribution of streambed particles. The spacing and spacing pattern of roughness elements have an effect, of course, but were given no consideration in site selection. It was expected that the use of 11 sites would randomize the effect of natural particle spacing on the velocity. Sites that had an appreciable percentage of particles smaller than about three-quarters of an inch in diameter were, in general, eliminated from consideration to avoid the complication of having bed forms at a site—ripple, dune, or plane bed—that varied with discharge.

In other words, a basic value of the Manning coefficient was sought, that is, one that could be related to streambed particle size alone. Therefore, the following additional criteria were used in site selection:

1. Straight channel alinement with little increase in width in the downstream direction.
2. Minimal vegetation on the banks and in the channel.
3. Stable banks and bed, both devoid of major irregularities.
4. Relatively wide stream of simple trapezoidal shape that will contain the entire discharge without overflow.

Because the roughness parameter $\frac{n}{R^{1/6}}$ was to be related to characteristic bed-particle size, it was necessary at each site to (1) sample the bed material objectively, (2) obtain a cumulative frequency distribution of the dimensions of the particles, and (3) select sizes for study that corresponded to some predetermined percentiles of the distribution.

The sampling procedure used was patterned after the Wolman (1954) method. In each reach a grid system was established in the transverse and longitudinal direction of the channel to obtain 100 intersections. The streambed particle at each intersection was then measured along the implied minimum and intermediate diameters. Individual cumulative frequency-distribution curves were fitted graphically on logarithmic normal probability paper for the minimum and intermediate diameters of each sample of 100 particles. The three characteristic dimensions of streambed particles selected for study from the curves were those corresponding to the 16 percentile, 50 percentile (median), and 84 percentile. The 16 percentile (d_{16}) is a size that equals or exceeds that of 16 percent of the streambed particles; the 84 percentile (d_{84}) is a size that equals or exceeds that of 84 percent of the streambed particles.

Basic data pertinent to the analysis that follows are summarized in table 1.

RELATION OF ROUGHNESS PARAMETER TO RELATIVE SMOOTHNESS

Before the basic data are analyzed, a discussion of some of the previous investigations of channel resistance coefficients will be helpful. For a comprehensive report on such investigations, the reader is referred to a report by Carter and others (1963).

The results of theoretical studies made in the past, relating the roughness parameter, $\frac{n}{R^{1/6}}$, to relative

TABLE 1.—*Basic data summary showing range in values*

Hydraulic radius (feet)	Manning n	Statistical size distribution of bed material					
		Minimum diameter, d' (feet)			Intermediate diameter, d'' (feet)		
		84 percentile, d'_{84}	50 percentile, d'_{50}	16 percentile, d'_{16}	84 percentile, d''_{84}	50 percentile, d''_{50}	16 percentile d''_{16}
1.0–10.9	0.020–0.107	0.036–1.50	0.013–0.57	0.005–0.29	0.062–2.45	0.024–0.83	0.009–0.40

smoothness, $\frac{R}{d}$, are not entirely consistent. The results are basically similar in that they all show an inverse relation between the roughness parameter and relative smoothness, but there is usually variation in the form of the relation. For reasons that will become evident later, two theoretical investigations that showed agreement will now be cited. Chow (1959) obtained the following relation:

$$\frac{n}{R^{1/6}}=\frac{1}{21.9\log 12.2\frac{R}{k}}, \tag{2}$$

where

k=effective roughness height.

If we multiply numerator and denominator by 0.0926, and substitute for log 12.2, its equivalent value, 1.086, we obtain the equation

$$\frac{n}{R^{1/6}}=\frac{0.0926}{2.2+2.03\log\frac{R}{k}}. \tag{2a}$$

Vennard (1961) presented the following equation for flow in pipes:

$$\frac{1}{\sqrt{f}}=1.14+2.0\log\left(\frac{\text{pipe diameter}}{k}\right), \tag{3}$$

where

f=Darcy-Weisbach resistance factor.

If we substitute for $\frac{1}{\sqrt{f}}$ its equivalent, $\frac{0.0926}{\frac{n}{R^{1/6}}}$, we obtain

$$\frac{n}{R^{1/6}}=\frac{0.0926}{1.14+2.0\log\left(\frac{\text{pipe diameter}}{k}\right)}. \tag{3a}$$

Field corroboration of the theoretical relations has usually been hampered by the use of data that were inadequate in quality because they were originally collected for other purposes, or because the data were insufficient in quantity. Even with adequate data, complete agreement between field results and those derived from theoretical studies or laboratory experiments is not to be expected. Two reasons for this are: (1) The theoretical and laboratory-derived relations are predicated on the condition of uniform size and distribution of channel roughness elements—a condition that never exists in natural channels, and (2) complete freedom from the many velocity-retarding influences other than the size distribution of streambed particles cannot be achieved in natural streams. However, one field study particularly pertinent to this paper is that by Leopold and Wolman (1957). They developed an empirical relation, based on field data, between the resistance factor, f, and relative smoothness, $\frac{R}{d}$, the characteristic particle size used being d_{84} referred to the intermediate diameter. Their equation was

$$\frac{1}{\sqrt{f}}=1.0+2.0\log\frac{R}{d''_{84}}, \tag{4}$$

which can be transformed to

$$\frac{n}{R^{1/6}}=\frac{0.0926}{1.0+2.0\log\frac{R}{d''_{84}}}. \tag{4a}$$

The agreement in the form of relation derived from field data by Leopold and Wolman (equation 4a) and the theoretical equations presented by Vennard for flow in pipes (equation 3a) and by Chow (equation 2a) is noteworthy because relations of similar form evolved from the study being reported here.

Getting back to this study, the basic data referred to in table 1 were transformed for analysis to the type of data summarized in table 2. Corresponding values of n and R were combined to give values of the roughness parameter, $\frac{n}{R^{1/6}}$; corresponding values of d and R were combined to give values of relative smoothness, $\frac{R}{d}$. The two columns in table 2 showing relative smoothness in terms of a weighted particle size, d_w, will be discussed later.

Six correlations of roughness parameter versus relative smoothness were made by using values of d corresponding to the 84-, 50-, and 16-percentile bed-

TABLE 2.—*Summary of transformed basic data, showing range in values*

Roughness parameter $\frac{n}{R^{1/6}}$	Relative smoothness, $\frac{R}{d}$							
	Minimum diameter, d' (feet)				Intermediate diameter, d'' (feet)			
	$\frac{R}{d'_{84}}$	$\frac{R}{d'_{50}}$	$\frac{R}{d'_{16}}$	$\frac{R}{d'_w}$	$\frac{R}{d''_{84}}$	$\frac{R}{d''_{50}}$	$\frac{R}{d''_{16}}$	$\frac{R}{d''_w}$
0. 016–0. 093	1. 4–118	2. 8–327	5. 4–850	1. 8–163	0. 9–68	1. 9–177	4. 0–472	1. 2–94. 4

particle sizes, referred to both minimum and intermediate diameters. The following procedure was used for each correlation. Values of the roughness parameter, $\frac{n}{R^{1/6}}$ for each of the 50 discharge measurements were first converted to corresponding values of $\frac{1}{\sqrt{f}}$. Values of $\frac{1}{\sqrt{f}}$ versus $\frac{R}{d}$ were then plotted on semilogarithmic graph paper, the values of $\frac{1}{\sqrt{f}}$ being plotted as the dependent variable on the vertical natural-scale ordinate. The best fit to the plotted points of each set of data was a straight line that had an equation of the form

$$\frac{1}{\sqrt{f}}=a+b \log \frac{R}{d}, \tag{5}$$

where a and b are constants.

Equation 5 was then transformed to equation 6 below, by means of the relation between $\frac{1}{\sqrt{f}}$ and $\frac{n}{R^{1/6}}$:

$$\frac{n}{R^{1/6}}=\frac{0.0926}{a+b \log \frac{R}{d}}. \tag{6}$$

In all correlations except those involving only the 16-percentile size of bed material, the constant b was found to differ only insignificantly from 2.0, the coefficient in equations 2a, 3a, and 4a. Where applicable, therefore, the theoretical value of 2.0 was used as the coefficient of $\log \frac{R}{d}$.

The results of the correlations are given in table 3, and the relation involving d''_{84} is shown graphically in figure 1. None of the other curves of relation are shown in this report because of space limitations, but they all closely resembled that in figure 1, and the pattern of deviations of the plotted points was similar in all cases to that for the 84-percentile size.

For each of the relations obtained, the standard error of estimate and coefficient of correlation were computed. The standard error of estimate is in units of $\frac{n}{R^{1/6}}$ and, therefore, has very limited significance to the engineer who is interested in the percentages by which computed values of n differ from the observed values. Therefore, percentage differences were computed for each of the measured discharges. The percentage differences associated with each of the relations were found to be distributed about a mean value that differed only negligibly from zero percent. Therefore, the standard deviation of those percentage differences was used as an index of error, because it showed the approximate range within which the percentage differences for two-thirds of the measurements lay. The standard deviation of the percentage differences was the basis on which the equations were compared with respect to their adequacy for predicting values of n from particle size and hydraulic radius.

The three relations using individual characteristic particle sizes ignore all other characteristics of the distributions from which those individual sizes were selected. To give consideration to the entire cumulative frequency curve of particle sizes between the 84 and 16 percentiles, the 84-, 50-, and 16-percentile sizes were weighted and combined into a single composite size, d_w. Other methods of considering the cumulative frequency curve might have been used—for example, the three percentile sizes might have been used in a multiple correlation, or the slope of the cumulative distribution curve might have been used by including an additional term in the equation for either of the ratios, $\frac{d_{84}}{d_{50}}$ or $\frac{d_{84}}{d_{16}}$. It was thought, however, that the most desirable course of action would be to maintain the theoretical form of the equation, and consequently a single weighted composite size was used.

Two weighting methods were used. In one method each of the three percentile sizes was weighted in inverse proportion to the square of the individual standard errors of estimate listed in table 3. In performing that computation an adjustment was made to the

TABLE 3.—*Statistical summary of the correlations of* $\frac{n}{R^{1/6}}$ *versus* $\frac{R}{d}$

	Minimum diameter, d'				Intermediate diameter, d''			
	d'_{84}	d'_{50}	d'_{16}	d'_w	d''_{84}	d''_{50}	d''_{16}	d''_w
Value of a in equation 6	0.76	0	0.25	0.50	1.16	0.35	0.10	0.90
Value of b in equation 6	2.0	2.0	1.33	2.0	2.0	2.0	1.60	2.0
Coefficient of correlation	.89	.76	.65	.87	.88	.78	.67	.87
Standard error of estimate, in units of $\frac{n}{R^{1/6}}$	.0087	.0120	.0140	.0092	.0087	.0117	.0140	.0092
Mean (algebraic) of percentage differences	−.05	+.93	−.41	+.39	−.43	+1.79	+1.36	−.26
Mean percentage difference without regard to sign	15.1	18.4	19.9	15.6	15.5	18.3	20.6	16.1
Standard deviation of percentage differences	±18.6	±22.7	±25.5	±19.1	±19.0	±22.4	±25.7	±19.5

standard errors of estimate for the 16-percentile sizes, because those standard errors would have been larger had the theoretical coefficient (b) of 2.0 been used in the regression equations involving d'_{16} and d''_{16}. The second method of weighting was based on a rank correlation technique. The two methods gave results that agreed closely, and after averaging and rounding of the figures, the optimum weighting factors were found to be 6:3:1; in other words,

$$d_w = 0.6d_{84} + 0.3d_{50} + 0.1d_{16}.$$

Results of the correlations of $\frac{n}{R^{1/6}}$ versus $\frac{R}{d'_w}$ and $\frac{n}{R^{1/6}}$ versus $\frac{R}{d''_w}$ are shown in table 3.

DISCUSSION OF RESULTS

In general, the observed values of $\frac{n}{R^{1/6}}$ for each individual site had a fairly consistent plotting pattern with respect to all curves relating the roughness parameter to relative smoothness. The observed values of $\frac{n}{R^{1/6}}$ for four sites plotted consistently above the curves, values for four other sites plotted below the curves, and values for the remaining three sites straddled the curves. That consistent pattern suggests that systematic factors other than size of bed material affected the roughness coefficients at the sites, and that a curve of relation for basic values of $\frac{n}{R^{1/6}}$—that is, values based on size of bed material alone—should perhaps be drawn on the basis of the lowest plotted values of $\frac{n}{R^{1/6}}$. However, the 11 selected stream sites all gave the appearance of being relatively free of extraneous roughness effects, and an experienced hydraulic engineer viewing those sites would select n values on

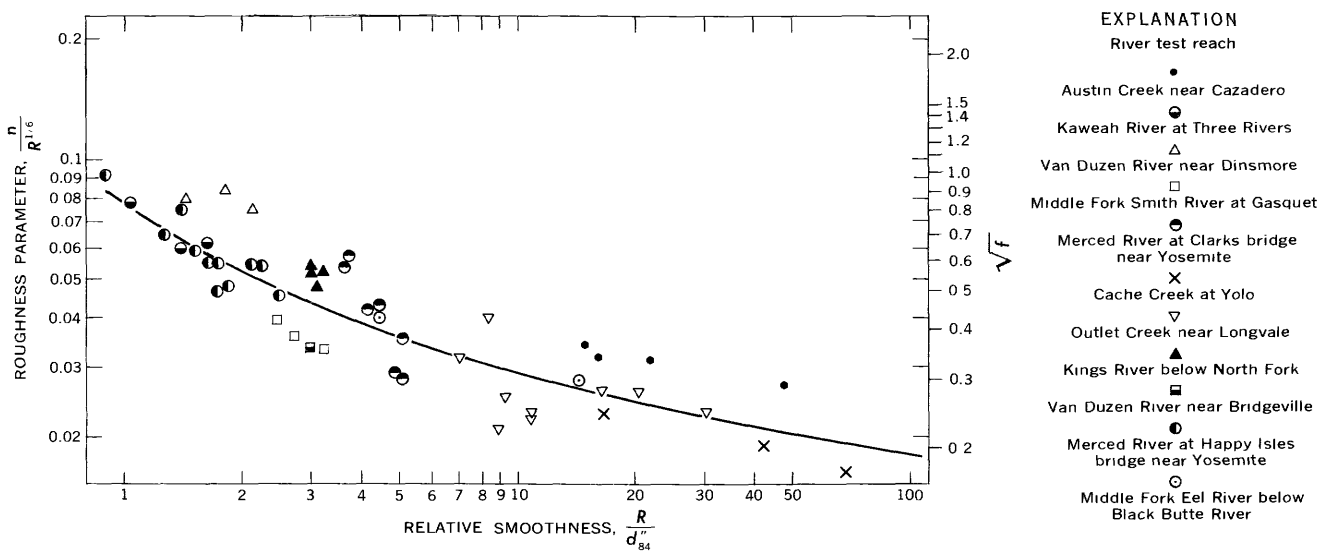

FIGURE 1.—Relation of roughness parameter to relative smoothness based on 84-percentile size of intermediate diameter, d'', of streambed particles.

the basis of bed-particle size alone. If the curves of relation are to be of practical value to engineers in selecting n values in the field it is therefore, necessary to assume, erroneously or not, that extraneous roughness effects were negligible at all 11 sites and that the scatter of all plotted points about the curves is random.

The possibility that some of the systematic scatter might be due to the positioning of the coarser bed material in individual reaches was also considered. However, no relation was apparent; for example, of the four sites whose values of $\frac{n}{R^{1/6}}$ plotted above the curves of relation, one site had its coarser material evenly distributed through the reach, two sites had their coarser material concentrated along the centerline or thalweg of the channel, and one site had its coarser material concentrated in the shallower water near the right bank.

The relations of $\frac{n}{R^{1/6}}$ to $\frac{R}{d}$ that best fit the field data were obtained using either of the two characteristic particle sizes, d_{84} or d_w. From the standpoint of best fit there was negligible difference between using intermediate or minimum diameter, but because of the relative ease of obtaining measurements of intermediate diameter—either by sieving or by photographic methods—it is expected that the relations using intermediate diameter will have more popular appeal.

It is not surprising that the larger particle sizes (d_{84}) were shown to have greater effect on flow retardation than the smaller particle sizes, because the influence of the larger particles extends over a relatively greater volume of channel. Furthermore, the smaller particles are often in the wake of the turbulence created by the larger particles. Leopold and others (1964) have stated that a single flow-resistance parameter involving bed-particle size should use a size larger than d_{50}. Finer particles in the channel also have a lesser retarding effect during high flow because at that time they may move as suspended or bedload material, although this fine material is commonly replaced by the deposition of material of similar size when the stage of the stream falls. Large quantities of fine material in suspension may also reduce the retardation effect by dampening turbulence, but in this study the sites were so selected that they were relatively free of bed material that was as fine as sand.

Table 3 shows that the equations using d_{84} gave slightly better results than those using d_w. The failure of the use of d_w to improve the results obtained using d_{84} is attributed to the fact that the pattern of scatter of points about the curves was consistent, regardless of the characteristic particle size used. Usually it is found that if the pattern of scatter varies in individual correlations involving each of several elements of similar type, an improved correlation results if a weighted composite value of the individual elements is used.

The standard deviation of the percentage differences between observed and computed values of $\frac{n}{R^{1/6}}$ was about 19 percent when d_{84} was used, and only slightly more than 19 percent when d_w was used. The slightly better results obtained by using d_{84}, combined with the fact that the computations using d_{84} are somewhat simpler than those using d_w, makes the use of d_{84} attractive. It is difficult, however, to rationalize the use of d_{84} because of the implication that the distribution of sizes is irrelevant and it matters not at all whether 84 percent of the bed material is sand or whether it is large cobbles, as long as 16 percent of the material is of greater size. Consequently, the author recommends the use of d_w rather than d_{84}, although there was no unanimity of opinion on this recommendation among his colleagues who reviewed this paper. The reader is free to make his own choice between the use of d_{84} and d_w.

SUMMARY

A satisfactory relation was found between a roughness parameter, $\frac{n}{R^{1/6}}$, and relative smoothness, $\frac{R}{d}$, where d is a characteristic bed-particle size obtained from a cumulative frequency distribution of the diameters of randomly sampled surficial bed material. The investigation was confined to channels with coarse bed material to avoid the complication of bed-form roughness that is associated with alluvial channels composed of fine bed material. Because basic values of n were sought—those attributable solely to the size and size distribution of bed material—the sites selected for study were relatively free of the extraneous flow-retarding effects associated with irregular channel conformation and streambank vegetation.

Three characteristic bed-particle sizes were investigated—the 84 percentile (d_{84}), the 50 percentile (d_{50}), and the 16 percentile (d_{16}). In addition, a weighted composite size (d_w) was tested, using a weight of 0.6 for the 84-percentile size, a weight of 0.3 for the 50-percentile size, and a weight of 0.1 for the 16-percentile size. Best results were obtained using either d_{84} or d_w, but it made little difference in the reliability of the results whether the study was confined to the minimum or to the intermediate diameter. The relations obtained between $\frac{n}{R^{1/6}}$ and $\frac{R}{d}$ were of the form

$$\frac{n}{R^{1/6}}=\frac{0.0926}{a+2.0\log\frac{R}{d}},$$

the only difference in the equations being in the values of the constant a, which varied with size (d_{84} or d_w) and diameter (minimum or intermediate) used. The above equation is virtually identical with the theoretical equations presented by Chow (1959) and Vennard (1961) and that derived from field data by Leopold and Wolman (1957).

REFERENCES

Carter, R. W., and others, 1963, Friction factors in open channels, progress report of the task force on friction factors in open channels of the committee on hydromechanics of the Hydraulics Division: Am. Soc. Civil Engineers Proc., Jour. Hydraulics Div., v. 89, no. HY2, pt. 1, p. 97–143.

Chow, V. T., 1959, Open-channel hydraulics: New York, McGraw-Hill Book Co., 680 p.

Leopold, L. B., and others, 1964, Fluvial processes in geomorphology: San Francisco and London, W. H. Freeman and Co., 522 p.

Leopold, L. B., and Wolman, M. G., 1957, River channel patterns; braided, meandering and straight: U.S. Geol. Survey Prof. Paper 282-B, 85 p.

Vennard, J. K., 1961, Elementary fluid mechanics: New York, John Wiley and Sons, Inc., p. 297–298.

Wolman, M. G., 1954, A method of sampling coarse river bed-material: Am. Geophys. Union Trans., v. 35, no. 6, p. 951–956.

PRECIPITATION AND BASE RUNOFF, BIG PIPE CREEK BASIN, MARYLAND

By FRANK W. TRAINER, Washington, D.C.

Abstract.—Base runoff from a small river basin in the Piedmont province in Maryland was studied through hydrograph separation during design of a study model depicting ground water and base runoff in part of the Potomac River basin. Subsequent base runoff derived from individual storms, believed to be approximately equal to ground-water recharge resulting from these storms, ranges from 25 to 31 percent of the precipitation in February-April to 7 to 9 percent in July-September. On the average, a given quantity of precipitation results in three to four times as much base runoff during winter and spring as during summer and autumn.

This report describes the relation between precipitation and base runoff in a small river basin in Maryland. The study on which it is based, a segment of a larger investigation in the Potomac River basin, is part of the design of a study model to depict ground water and the base runoff of the streams.

Big Pipe Creek drains an area of 102 square miles in the Piedmont province (fig. 1). It is tributary to the Monocacy River, which in turn is the chief tributary of the Potomac River in Pennsylvania and Maryland east of the Blue Ridge. Topography in the basin of Big Pipe Creek is gently rolling, with local relief commonly less than 200 feet. About 60 percent of the basin is underlain by metamorphic rocks, chiefly schists, of late Precambrian(?) age; the remainder is underlain by gently dipping Triassic sandstone, conglomerate, and shale. In all these rocks, water is stored in and transmitted through fractures. The bedrock is covered by a mantle of weathered material, which in many places is as thick as 50 to 75 feet. Water is stored in and transmitted through intergranular pores of this material. These two types of water-bearing material form a single ground-water reservoir in which the water probably is unconfined at most places. This reservoir is hydraulically connected with the streams, and ground-water discharge provides their dry-weather flow.

The climate of this region is temperate and humid. Although there are two principal types of precipitation events—cyclonic storms and thundershowers—the precipitation is rather evenly distributed by months through the year (fig. 2*C*). It averages about 41 inches annually. Most of the precipitation is rain. Snow commonly melts within a few days after it falls, so that storage of water as snow is a relatively unimportant aspect of the hydrologic cycle. Evapotranspiration is low in winter but high during the summer. The annual stream hydrograph is characterized by a period of above-average streamflow in winter and spring and a period of below-average streamflow in summer and autumn. (Fig. 2*A*, upper graph; for example, during calendar year 1948 average daily discharge was 140 cubic feet per second.) This general form reflects annual changes in the ground-water stage, and is thus indicative of ground-water storage (fig. 2*B*), which provides the base flow of the stream.

BASE RUNOFF

Base runoff is the part of the streamflow provided largely or entirely by ground-water discharge. In this region rains are typically frequent throughout the year, and base runoff can be observed directly, as the total streamflow, only during the longer rainless periods. In the present study, base runoff was estimated by hydrograph separation, a subdivision of the stream hydrograph into components believed to represent different parts of the subsurface-surface flow system. Numerous methods of hydrograph separation have been used; all are of necessity somewhat subjective and somewhat arbitrary. (For examples, see summaries by Kudelin, 1949, chap. 2; and Dickinson and others, 1967, p. 26.) The writer followed a graphical procedure based on use of a curve showing ground-water depletion or base-runoff recession (Horton, 1933; p. 449; Snyder, 1939, p. 728–730; Grundy, 1951, p. 215–216; American

U.S. GEOL. SURVEY PROF. PAPER 650-D, PAGES D222-D227

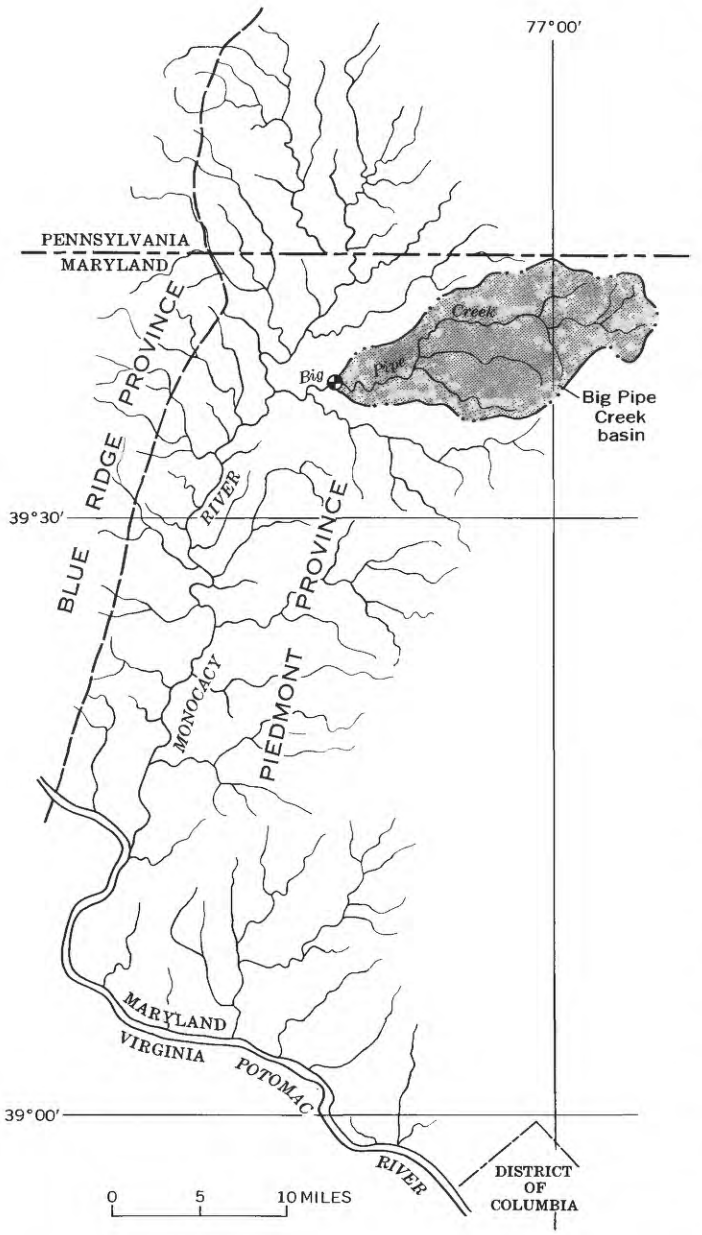

FIGURE 1.—Index map showing location of Big Pipe Creek basin above gage 800 feet west of village of Bruceville, Md.

Society of Civil Engineers, 1949, p. 72–73; Trainer, 1969). The curve obtained by this graphical determination was confirmed by a method of plotting recession values observed after 10-day periods of dry weather (Riggs, 1964, p. 354–355).

Some students have derived two base-flow recession curves, representing winter-spring and summer-autumn conditions, respectively, for a single river basin. In this study only one recession curve was found. This curve fits receding segments of the stream hydrograph (January 1948—September 1966) except during periods of 1 day to a few days, during several summers, when the stream hydrograph declined below the constructed recession curve as fitted to the preceding falling limb of the hydrograph. This departure is attributed to temporarily high evapotranspiration losses from shallow ground water in areas bordering the stream, with temporary decrease in ground-water discharge to the stream.

Considerable difficulty in the study of base runoff through interpretation of river hydrographs stems from the diversity in geologic environments and hydrologic regimes between and even within river basins. This diversity may make comparison of conclusions drawn from different basins problematical.

Diversity in geology is expressed as diversity in terrain transmissivity, which controls the response of a terrain to precipitation. A relatively permeable terrain favors infiltration and subsequent base runoff at the expense of direct runoff. A relatively impermeable terrain favors direct runoff. Many river basins, and most large ones, are underlain by more than one type of terrain. Riggs (1964, p. 353–354) has emphasized the complications in analysis which are introduced by the presence of diverse aquifers in a drainage basin. These complications are readily appreciated when one considers typical examples of contrasting aquifers found within single basins, as by the areal or stratigraphic juxtaposition of till and glaciofluvial deposits, of shale and carbonate rocks, of sandstone or porous basalt and metamorphic rocks.

Kudelin (1960, fig. 25a) has emphasized the manner in which the nature of ground-water discharge to the river is controlled by the presence or absence of hydraulic connection between aquifer and river, and by the hydraulic state of the aquifer (confined or unconfined). Probably most river basins of intermediate to large size, and many smaller ones, encompass more than one of the possible combinations of hydrogeologic conditions which determine the nature of ground-water flow into the river.

Diversity in hydrologic regime (that is, in the annual pattern of seasonal variations in discharge) results from differences in such climatic features as the amount of precipitation and its distribution within the year, the annual range in temperature and the seasonal distribution of its extremes, and the importance of snow or ice as a source of delayed runoff. These climatic factors govern the supply of water to a river basin and its removal from the basin. The regime of Big Pipe Creek is an example of Pardé's simple pluvial oceanic type (Pardé, 1955, p. 84–87; Ward, 1967, p. 350–351), characterized by a single period of above-average streamflow each year, in winter and spring, and one of below-average streamflow in summer and autumn.

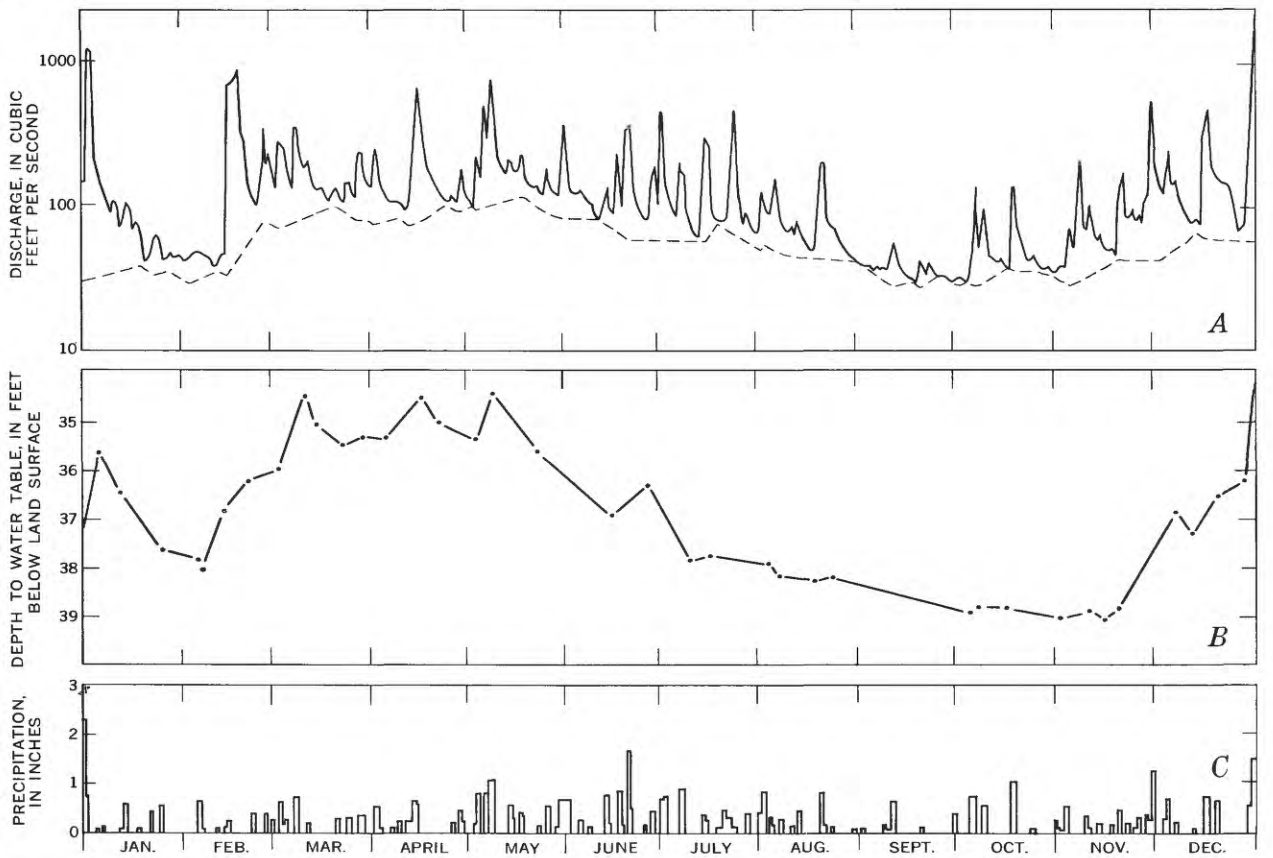

FIGURE 2.—Hydrographs and precipitation data for calendar year 1948.
A, Hydrograph, Big Pipe Creek at Bruceville, Md.; data from U.S. Geological Survey, 1952, p. 681–682. Dashed line is constructed base-flow hydrograph.
B, Ground-water hydrograph, well Fr-Cg 1, Johnsville, Md., about 4 miles south of the west end of basin of Big Pipe Creek; data from U.S. Geological Survey, 1951, p. 170.
C, Precipitation at Westminster, Md., at east end of basin of Big Pipe Creek; data from U.S. Weather Bureau, 1948

Precipitation is fairly evenly distributed through the year; however, the summer minimum reflects the influence of evapotranspiration. Other simple regimes are the glacial and nival types, whose maximum flows (in spring and summer) are derived from melting ice and melting snow, respectively.

The ground-water reservoir in the basin of Big Pipe Creek is unconfined and hydraulically connected with the streams. Under these conditions a principal consideration in hydrograph separation is the interpretation of bank storage. Data from streams in the Russian Plain (Kudelin, 1960), in Alberta, Canada (Meyboom, 1961), and in Washington State (Newcomb and Brown; 1961) show bank storage to be important along rivers characterized by snowmelt floods of long duration. Ground-water discharge to the streams probably ceases during a large part of such a flood, which may last as long as 1 to 3 months. Snowmelt is a relatively unimportant factor in the water budget of Big Pipe Creek, however, and when it does occur it is of a few days duration. Floods, in response to rain, are of short duration. The opportunity for delay of streamflow owing to bank storage of floodwater is therefore rather limited. The annual spring increase in streamflow must result in some bank storage, but the quantity of water which moves into and out of storage is believed to be relatively small because the rise in stage is small: a range of 2 feet encompasses the highest and lowest mean daily stages at the gaging station for more than 95 percent of the period January 1948-September 1966.

From these considerations of hydrogeology and hydrologic regime it is concluded that ground-water discharge to Big Pipe Creek probably does not cease during most periods of high streamflow. The arbitrary method of hydrograph separation used in this study is therefore believed to provide a good approximation to the base-runoff component of the stream hydrograph. (In this method a straight line is constructed from the antecedent base-runoff recession curve, beneath a flood peak, to the point on the falling limb of the hydrograph at which the new recession curve first approximates a straight line.)

A hydrograph of the base runoff of Big Pipe Creek was constructed for the period January 1948—September 1966. A 1-year segment of this graph is shown by the dashed line in figure 2*A*. The water-table hydrograph (fig. 2*B*) shows changes in stage which accompanied drainage of the ground-water reservoir by the stream during that 1-year period. The two hydrographs resemble one another in both their seasonal form and their response to some groups of rainstorms (fig. 2*C*). The base-runoff hydrograph is thus an expression of the continually-changing discharge from ground-water storage.

Over the period January 1948-September 1966, the average daily base runoff was 45 cubic feet per second of an average daily streamflow of 100 cfs. The range in base runoff was from about 1 cfs (September 1966) to about 190 cfs (May 1952), but commonly the base runoff was between 10 and 100 cfs. In terms of flow duration (total streamflow), a mean discharge of 45 cfs was exceeded on 61 percent of the days during the period January 1948-September 1966.

PRECIPITATION AND BASE RUNOFF

Horton (1933, p. 456–457) cited offset of the base-runoff recession curve after a storm and flood, from the trend of the recession just before the flood, as evidence of ground-water recharge during the storm. In the present study such offsets in the hydrograph were used to relate increment in base runoff (recharge, approximately) to precipitation. This method of construction, which was used earlier by Iwasaki (1934, p. 168) and by Grundy (1951, p. 216), consists of laying off two recession curves on the stream hydrograph, one along the antecedent trend of the base runoff which was interrupted by the storm-flood event and another along the hydrograph recession after the flood. In this study the pair of reecssion curves was extended downward to the level below which the space between them represents a daily base runoff of less than 0.5 cfs. The increment of base runoff enclosed by the pair of curves represents ground-water recharge (less evapotranspiration loss in the discharge area) as a result of that storm. This procedure was carried out for single floods and for groups of successive floods in which it is difficult to distinguish the individual floods in the hydrograph of total flow for the group. Most of the groups of storm-flood events occurred within a time span of a few days to 1 or 2 weeks; a few extended over periods of 3 to 5 weeks. Mean precipitation on the basin, for each storm or group of storms, was estimated to the nearest 0.1 inch from isohyetal maps prepared from data collected at six localities in and near the basin (U.S. Weather Bureau, 1948 and subsequent years).

In studies of river forecasting (for example, Kohler and Linsley, 1951) various parameters are used to take into account the influence of factors, such as soil moisture and potential evapotranspiration, which control the effectiveness of infiltration. In this investigation the base-runoff and precipitation data were classed in 12 groups, by month, to simplify the model and still take account of factors which depend on season. Where a storm or group of storms occurred in parts of 2 months, however, the data were used in the analyses for both months to make more data available for the graph drawn for each month. Data from a total of 129 storm-runoff events, or groups of events, were used; the number of events ranged from 8 to 19 per month. Figure 3*A* shows graphs drawn from monthly plots of base-runoff increment versus precipitation.

The curves in figure 3*A* cluster in two seasonal groups. Summer (June-September) is relatively less effective, and winter (November-April) much more effective in the transformation of precipitation into base runoff. May and October, and probably in some years, November, are transitional between these groups. These seasonal differences are attributed to the greater evapotranspiration of the summer season, which together with soil-moisture deficiency decreases the effectiveness of ground-water recharge in summer, and which also intercepts some ground water, near the streams, that would otherwise be discharged to form base runoff. The sequence of curves shows an orderly swing between the annual extremes. The increment in base runoff which results from a given quantity of precipitation is greatest in April and least in July. With the exception of February or March (one of which falls out of order) the curves lie in sequence between these extremes.

The two seasonal clusters of curves are fairly consistently related to one another in quantitative terms. Thus, in winter a given quantity of precipitation results in a subsequent increment in base runoff about three to four times as large as does the same quantity in summer. Average values of subsequent base runoff derived from precipitation range from 25 to 31 percent of the precipitation in February-April to 7 to 9 percent in July-September. (It is clear, therefore, that appreciable increments, and hence appreciable ground-water recharge, occur even during the summer and autumn.) Moreover, each seasonal cluster of data is fairly homogeneous. The data can therefore be lumped by seasons (fig. 3*B*) in order to simplify the hydrologic model.

Because the graphs in figure 3*A* represent ground-water discharge which resulted from the infiltration of water from specific storms or groups of storms, these

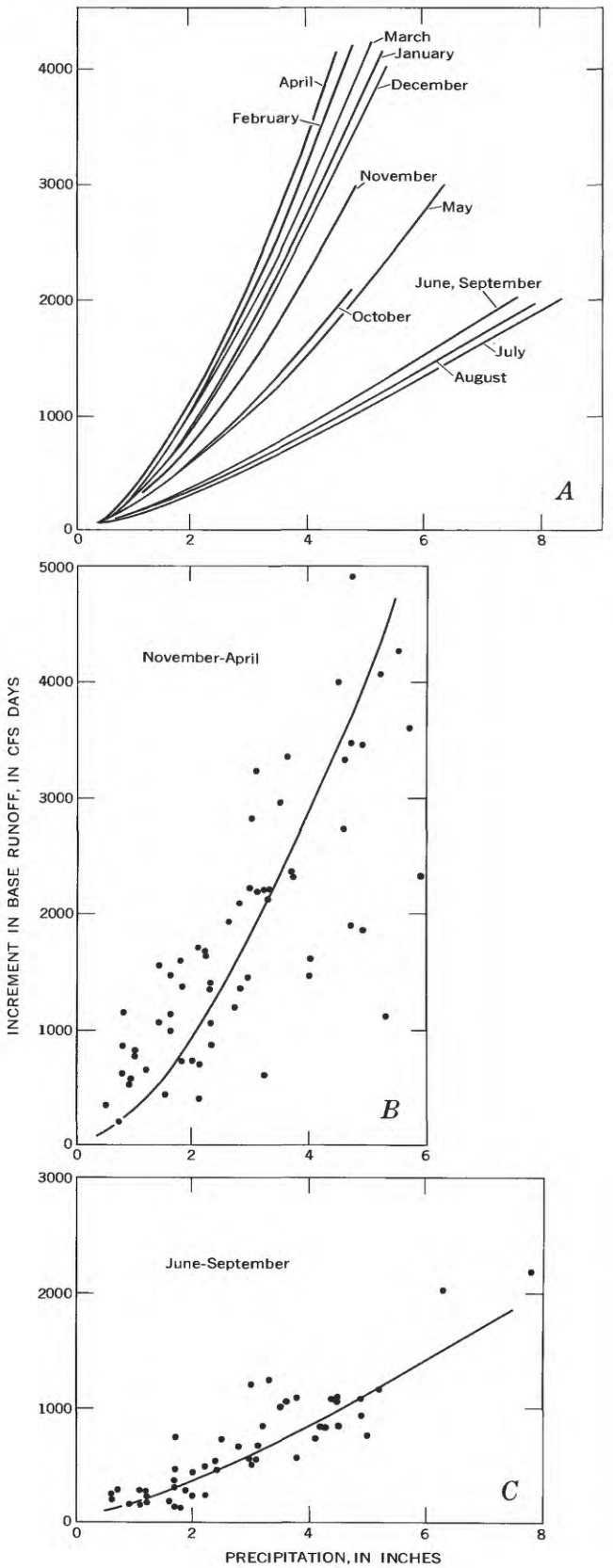

FIGURE 3.—Relation between precipitation and increment in subsequent base runoff in the basin of Big Pipe Creek, as determined for individual storms or groups of successive storms during the period January 1948-September 1966. Data plotted for months during which precipitation occurred. *A*, Monthly curves showing base-runoff increment versus precipitation; *B* and *C*, summary curves for periods November-April and June-September, respectively.

curves also serve as means of estimating ground-water recharge, provided allowance can be made for evapotranspiration losses from areas of shallow ground water. Estimates based on pan-evaporation rates at a station of the U.S. Weather Bureau at Beltsville, Md., about 35 miles south-southeast of this basin, taken in conjunction with the width of lowland along the stream channels in the basin, suggest that the annual water loss from the Big Pipe Creek basin, through evapotranspiration from the channel and from ground near it, is of the order of 10 percent of the stream discharge. For this reason, base-runoff increment as shown in figure 3 is believed to be representative of ground-water recharge. Although the numerical values given in figure 3 are at best approximate when applied to recharge, the curves are believed to show seasonal changes in recharge and in its relative magnitudes with reasonable accuracy.

Acknowledgments.—Helpful discussions of this study with R. R. Bennett and F. A. Watkins, and the assistance of L. E. Burgess in the compilation of data, are gratefully acknowledged.

REFERENCES

American Society of Civil Engineers, 1949, Hydrology handbook: Am. Soc. Civil Engineers, Manual of Engineering Practice No. 28, 184 p.

Dickinson, W. T., Holland, M. E., and Smith, G. L., 1967, An experimental rainfall-runoff facility: Colorado State Univ., Hydrology Papers, no. 25, 81 p.

Grundy, F., 1951, The ground-water depletion curve, its construction and uses: Internat. Assoc. Sci. Hydrology Pub. 33, p. 213–217.

Horton, R. E., 1933, The role of infiltration in the hydrologic cycle: Am. Geophys. Union Trans., v. 14, p. 446–460.

Iwasaki, Tomahisi, 1934, A stream flow study of the Tokyo water supply: Am. Water Works Assoc. Jour., v. 26, no. 2, p. 163–175.

Kohler, M. A., and Linsley, R. K., 1951, Predicting the runoff from storm rainfall: U.S. Weather Bur. Research Paper 34, 9 p.

Kudelin, B. I., 1949, Gidrogeologicheskiy analiz i metody opredeleniya podzemnogo pitaniya rek [Hydrogeologic analysis and methods of determining the ground-water alimentation of rivers]: Akad. Nauk SSSR, Laboratorii Gidrogeologicheskikh Problem im. F. P. Savarenskogo, Trudy, v. 5, 179 p.

——— 1960, Printsipy regional'noy otsenki yestestvennykh resursov podzemnykh vod [Principles of the regional appraisal of ground-water resources]: Moscow, Moscow University, 344 p.

Meyboom, P., 1961, Estimating ground-water recharge from stream hydrographs: Jour. Geophys. Research, v. 66, no. 4, p. 1203–1214.

Newcomb, R. C., and Brown, S. G., 1961, Evaluation of bank storage along Columbia River between Richland and China Bar, Washington: U.S. Geol. Survey Water-Supply Paper 1539–I, 13 p.

Pardé, Maurice, 1955, Fleuves et rivières: Paris, Librairie Armand Colin, 3d ed., 223 p.

Riggs, H. C., 1964, The base-flow recession curve as an indicator of ground water: Internat. Assoc. Sci. Hydrology, Pub. 63, p. 352–363.

Snyder, F. F., 1939, A conception of runoff-phenomena: Am. Geophys. Union Trans., v. 20, p. 725–738.

Trainer, F. W., 1969, Drainage density as an indicator of base flow in part of the Potomac River basin, *in* Geological Survey Research 1969: U.S. Geol. Survey Prof. Paper 650–C, p. C177–C183.

U.S. Geological Survey, 1951, Water levels and artesian pressure in observation wells in the United States in 1948; pt. 2, Southeastern States: U.S. Geol. Survey Water-Supply Paper 1127, 240 p.

——— 1952, Surface-water supply of the United States, 1949; pt. 1, North Atlantic slope basins: U.S. Geol. Survey Water-Supply Paper 1141, 745 p.

U.S. Weather Bureau, 1948–66, Climatological data, Maryland and Delaware: U.S. Weather Bureau.

Ward, R. C., 1967, Principles of hydrology: London, McGraw-Hill Publishing Co. Limited, 403 p.

CHANGES IN CHEMICAL QUALITY OF GROUND WATER IN THREE AREAS IN THE GREAT BASIN, UTAH

By A. H. HANDY, R. W. MOWER, and G. W. SANDBERG,
Salt Lake City, Utah

Work done in cooperation with the Utah Department of Natural Resources, Division of Water Rights

Abstract.—The chemical quality of ground water in three areas in the Great Basin, Utah, is known to be deteriorating. West of Kanosh in Pavant Valley, an increase in all major constituents except bicarbonate has been associated with a decline in water levels that has resulted from a high rate of pumping. In the upper artesian aquifer near Leamington, in the Sevier Desert, an increase in dissolved solids, mainly sodium and chloride, has resulted from a change in the chemical quality of the water that is recharging the aquifer. Between Beryl and Enterprise in Escalante Valley, an increase in the concentration of all major constituents also has been associated with a decline in water levels caused by a high rate of pumping.

General information about the chemical quality of ground water in the Great Basin of Utah has been collected since the early 1900's. Since 1957, however, water from selected wells in many areas in the Great Basin has been monitored regularly for changes in chemical quality. The Great Basin is mainly a semiarid region that receives an average of less than 15 inches of precipitation per year. Irrigation has been necessary for crop production in the basin since farming began in the middle 1800's. Ground water is the only source of irrigation water in some areas of the Great Basin, and ground water is used to supplement the water from surface sources in other areas.

Three areas where the chemical quality of the ground water is known to be deteriorating are the areas west of Kanosh in Pavant Valley, southwest of Leamington in the Sevier Desert, and between Beryl and Enterprise in Escalante Valley (fig. 1). Changes in the chemical character of ground water in the three areas may be the result of one or a combination of the following factors:

1. Surface water used for irrigation recharges aquifers. The surface water can be of much different type and concentration than the ground water.

2. Disintegrated crop-plant debris provides soluble nitrogenous matter and weak acids which are taken up by infiltrating water; the solvent power of the infiltrate may exceed that of natural recharge water.

3. Soil amenders and fertilizers afford soluble materials that may be dissolved in substantial amounts by infiltrating irrigation water.

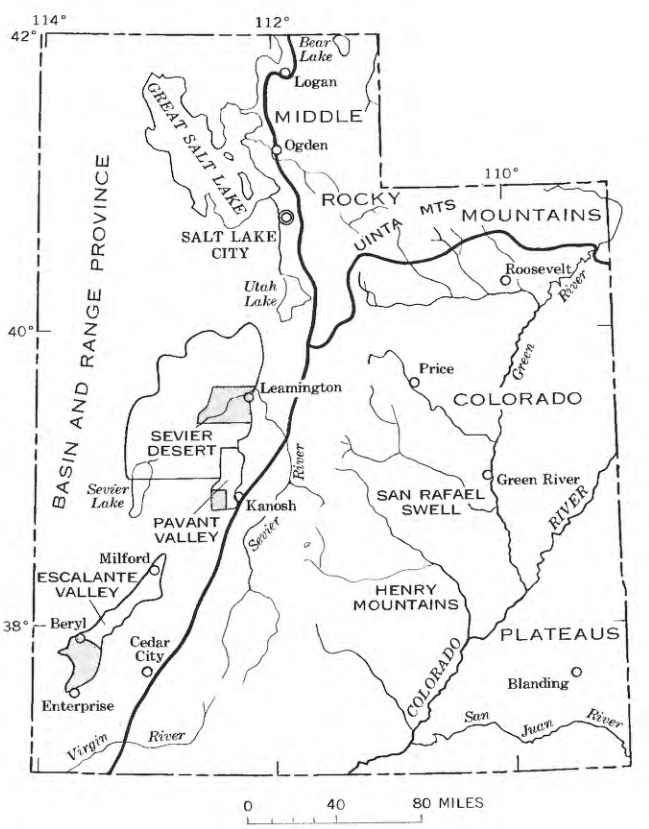

FIGURE 1.—Map of Utah showing the three ground-water areas (shaded) discussed in text.

4. Growing plants transpire a substantial amount of water but incorporate in their tissues only a minute portion of the mineral matter dissolved in that water. Most of the mineral matter originally in the transpired water remains in the soil or is carried downward, ultimately into the underlying ground-water body, by the water not transpired.

5. Some of the water applied for irrigation is recovered as ground-water recharge and may be reused for irrigation. Thus, mineral matter in recharge water from irrigation in the extreme lower parts of such areas may be several times more concentrated than it is in the headwater parts.

6. Discharge from a fresh-water body connected hydraulically to a saline-water body may result in migration of the saline water toward the well. If the fresh-water head is reduced sufficiently, saline water may rise or migrate laterally toward discharging wells.

PAVANT VALLEY

In the Kanosh ground-water district in the southern part of Pavant Valley the concentration of dissolved solids in the ground water has increased since 1957. Water samples from well (C–23–6)8abd–1 (fig. 2) indicate the changes found in the district. These changes are representative of changes found in other wells nearby (Mower, 1967, p. 19). The concentration of all major constituents except bicarbonate increased between 1957 and 1967. The largest gain was in the chloride ion, which increased from 802 to 1,610 milligrams per liter or 22.62 to 45.42 milliequivalents per liter. The specific conductance of the water increased from 3,660 micromhos per centimeter at 25°C in 1957 to 6,210 micromhos/cm in 1967 (fig. 3).

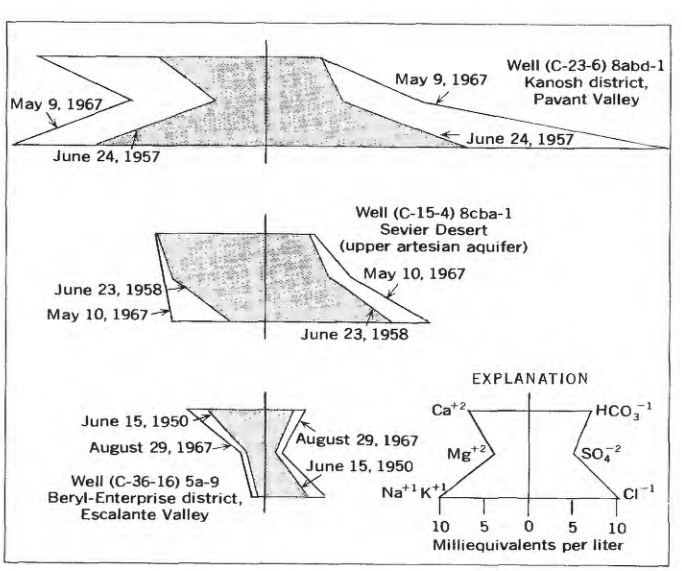

FIGURE 2.—Changes in chemical constituents in three selected wells in Pavant Valley, Sevier Desert, and Escalante Valley.

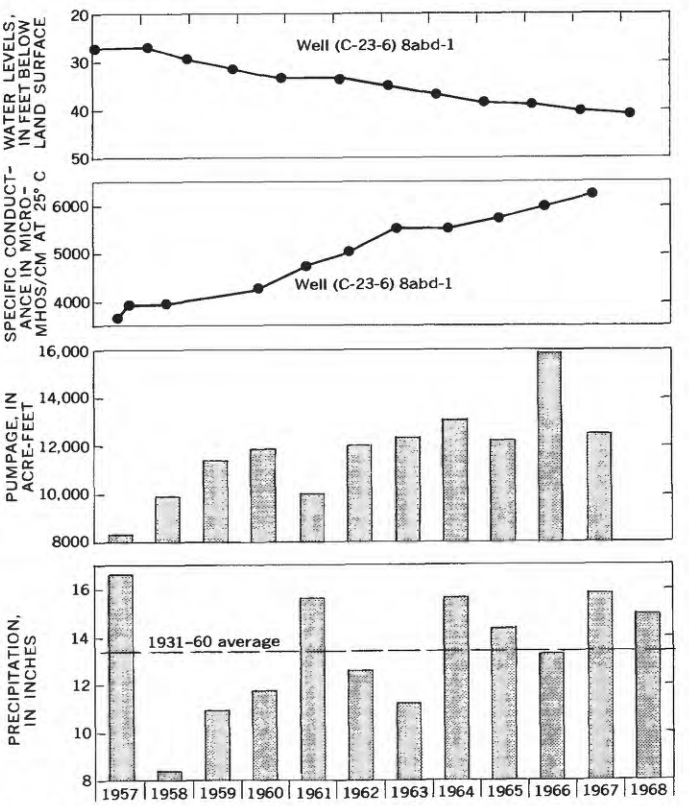

FIGURE 3.—Water levels and specific conductance of water in selected wells, annual pumpage in the Kanosh district, and precipitation at Kanosh, 1957–68.

Figure 3 also shows the changes in water levels in well (C–23–6)8abd–1, annual pumpage in the Kanosh district, and annual precipitation at Kanosh during the period 1957–68. Pumpage increased 50 percent from 1957 to 1967, even though precipitation reported by the U.S. Weather Bureau (1957–68) averaged near normal for the 11-year period. This increase in pumpage has been accompanied by a decline in water levels and an increase in concentration of dissolved solids (Baker and others, 1967, p. 69–70).

Pumping for irrigation in the Kanosh district began in 1946 when an estimated 200 acre-feet of water was pumped from one well. Pumpage in the district increased to 8,300 acre-feet in 1957 and to 15,900 acre-feet in 1966, but only 12,500 acre-feet was pumped in 1967 (fig. 3). The average annual natural recharge has been estimated to be 4,000 acre-feet (Mower, 1965, p. 45); therefore, ground-water discharge by wells has exceeded natural recharge at least since 1957 and ground water levels have declined every year since 1957. In well (C–23–6)8abd–1 the total decline between March 1957 and March 1968 was about 14 feet.

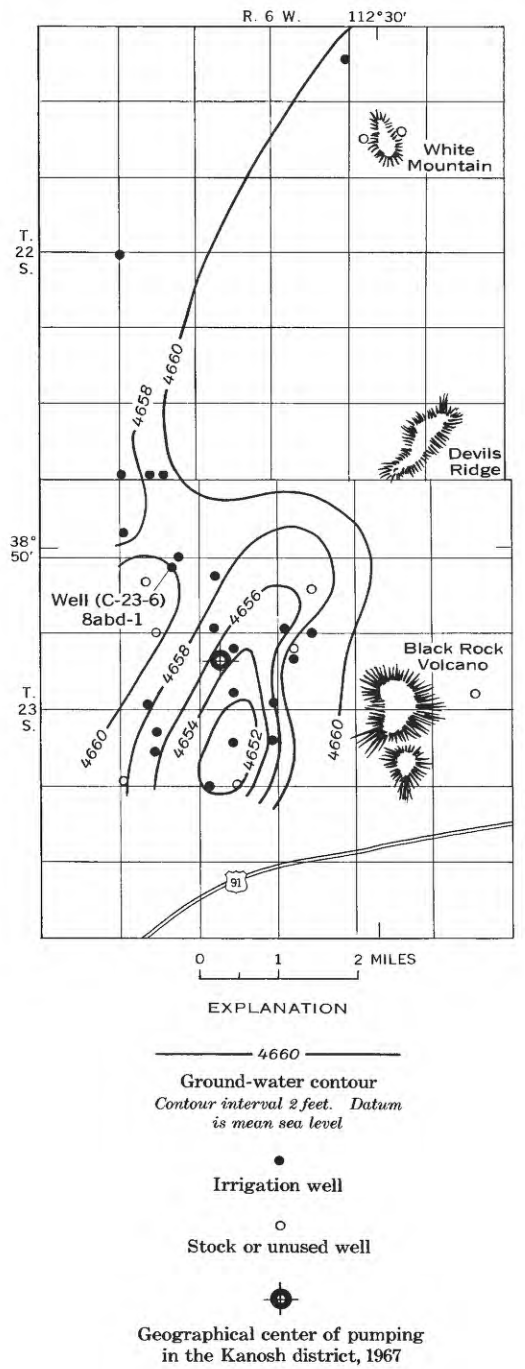

FIGURE 4.—Map of part of the Kanosh district, Utah, showing approximate ground-water contours, August 1967.

The decline in water levels has resulted in the formation of a depression in the water table (fig. 4). As this depression expands, ground water of poor quality from the north and west is drawn into it, causing a further deterioration of water quality. The water available for recharge in this area since formation of the depression has come mainly from recirculation of ground water that is pumped for irrigation. Water from wells north of (C–23–6)8abd–1 (downgradient) is of even poorer quality; water from several wells in the northern part of the district is reportedly unusable for irrigation. The best quality water obtainable in the Kanosh district is in the southern and southeastern parts of the district, upgradient from the center of pumping.

An estimated 25–50 percent of the irrigation water that is pumped from wells returns to the ground-water reservoir. Each time the water is used the concentration of dissolved solids is increased. The repeated reuse of residual water is the principal cause of the ever-increasing concentration of dissolved solids in ground water in the Kanosh ground-water district.

SEVIER DESERT

The Sevier Desert, near Leamington and Lynndyl, is underlain by two artesian aquifers (Mower and Feltis, 1968, p. 23). In the upper aquifer the dissolved solids increased and the water levels declined during the period 1961–68, even though the total annual precipitation reported by the U.S. Weather Bureau (1957–68) averaged near normal during the 8-year period (fig. 5). The water samples from wells (C–15–4)8cba–1

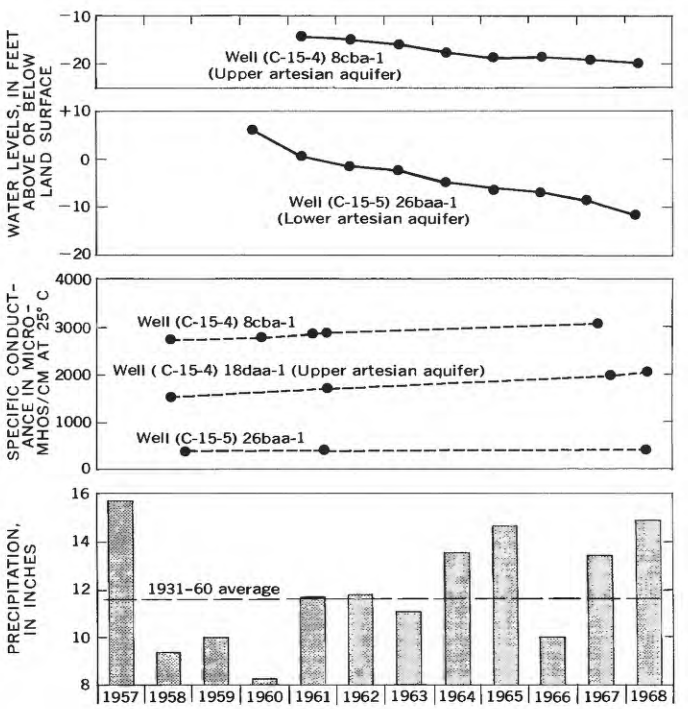

FIGURE 5.—Water levels and specific conductance of water in selected wells in the Sevier Desert, and precipitation at Oak City, 1957–68.

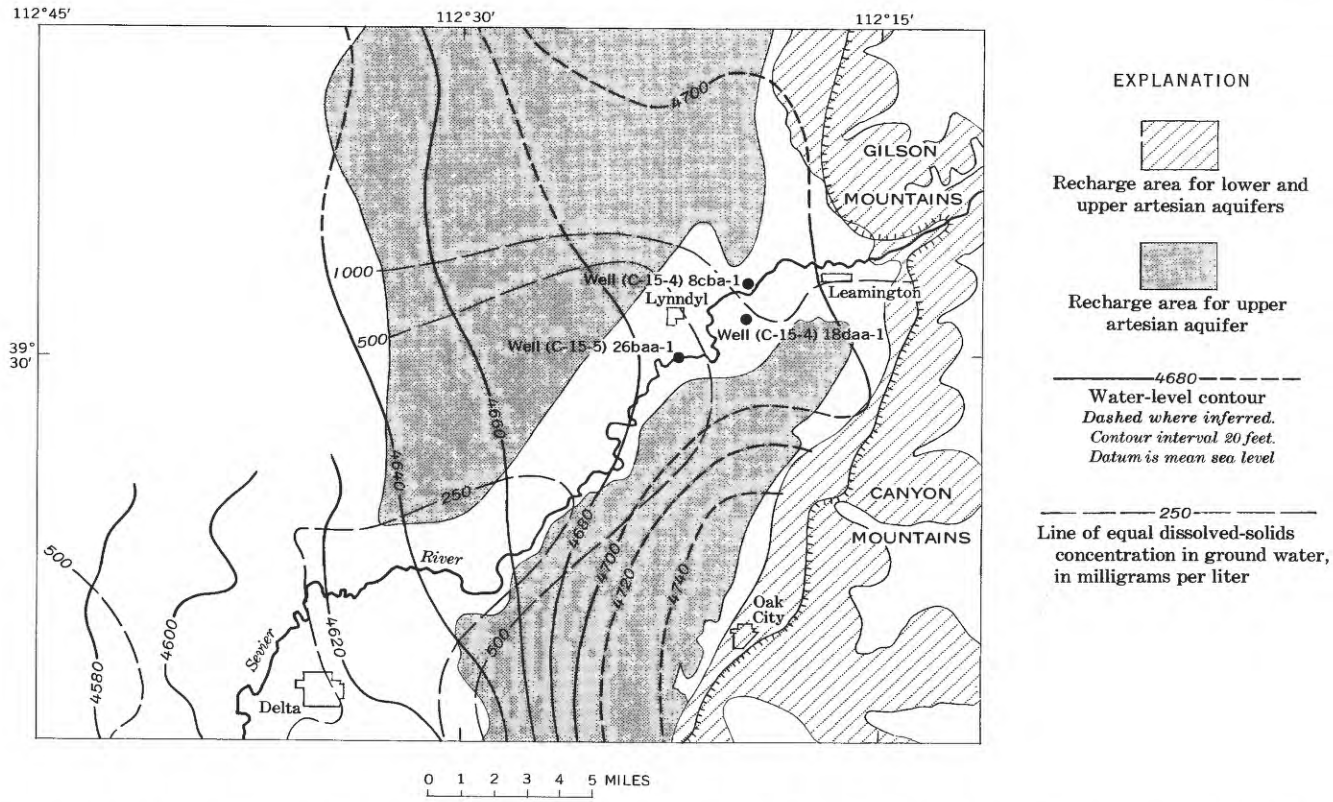

FIGURE 6.—Map of part of the Sevier Desert, showing recharge areas, dissolved solids in ground water, and ground-water contours in March 1964.

and (C–15–4)18daa–1 indicate the rate and magnitude of the increase of dissolved solids in the upper aquifer in this area (fig. 6). At well (C–15–4)8cba–1, the concentrations of calcium, magnesium, and bicarbonate increased slightly from 1958 to 1967 (fig. 2); the increase in concentration of sulfate was somewhat greater, and the largest increases were in sodium (as Na + K) and chloride. Sodium increased from 88 to 241 mg/l (3.84 to 10.46 meq/l), and chloride increased from 505 to 665 mg/l (14.24 to 18.76 meq/l); the specific conductance increased from 2,760 micromhos/cm in 1958 to 3,030 micromhos/cm in 1967 (fig. 5). The quality of the water differs in wells (C–15–4)8cba–1 and (C–15–4)18daa–1, but the magnitude of the change in water quality is about the same. The water is of poorer quality in well (C–15–4)8cba–1, which is nearer the recharge area.

The major factors causing the change in the quality of water in the upper artesian aquifer are the poor quality of the recharge water and the infiltration of excess water from irrigated fields. The Sevier River is the principal source of recharge water, both by direct infiltration from the river and associated canals where they cross the aquifer outcrops and by infiltration from fields irrigated with river water. The river water has a relatively high concentration of dissolved minerals because a part of the water is diverted several times for irrigation upstream from the Sevier Desert, and each time a part of the diverted water returns to the river. Thus the natural concentration of dissolved solids in the Sevier River water is increased severalfold, as shown in the table 1. The infiltration from fields in

TABLE 1.—*Concentration of dissolved constituents, in milligrams per liter, and specific conductance, in micromhos per centimeter at 25° C, of Sevier River water*

Constituent or characteristic	Maximum	Minimum	Weighted average
1967 water year (Oct. 1, 1966–Sept. 30, 1967)			
Sodium (Na+K)			285
Bicarbonate			276
Carbonate			0
Sulfate			345
Chloride			364
Dissolved solids			1,310
Hardness (Ca and Mg)			479
Specific conductance			2,080
Extremes for years 1951–67			
Dissolved solids	5,980	275	1,460
Hardness	1,970	188	556
Specific conductance (daily)	8,300	431	2,350

the Sevier Desert has been further concentrated by solution of mineral matter from the soil and by evapotranspiration. Ground water is a secondary source of irrigation water in the Sevier Desert, and recirculation and repeated reuse of the ground water adds to the deterioration of ground-water quality.

Water samples from well (C–15–5)26baa–1, which taps the lower artesian aquifer in this area, indicate virtually no change in the quality of water at this point in the aquifer (fig. 5). However, in the lower artesian aquifer the concentration of dissolved solids must be increasing at the eastern edge of the recharge area where the Sevier River enters the area because recharge to the aquifer is mainly from the Sevier River.

ESCALANTE VALLEY

Between Beryl and Enterprise in the Escalante Valley, water levels have declined and the concentration

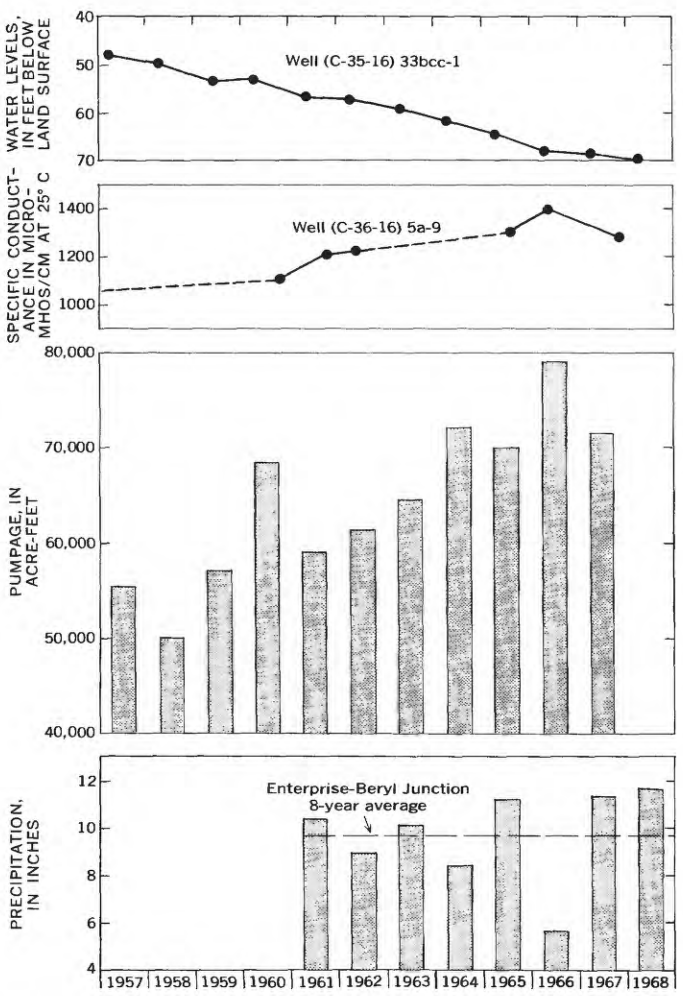

FIGURE 7.—Water levels and specific conductance of water in selected wells, annual pumpage in the Beryl-Enterprise district, and precipitation at Enterprise-Beryl Junction, 1957–68. See figure 8 for locations.

of dissolved solids in ground water has increased. Water samples from well (C–36–16)5a–9 indicate the magnitude of the changes in chemical quality found in the Beryl-Enterprise ground-water district, even though the quality varies slightly from well to well. From 1950 to 1967 the concentrations of all major constituents increased (fig. 2). The largest increases were in calcium and chloride. Calcium increased from 132 to 176 mg/l (6.59 to 8.80 meq/l) and chloride increased from 177 to 240 mg/l (4.99 to 6.77 meq/l). The specific conductance of the water increased from 994 micromhos/cm at 25°C in 1950 to 1,280 micromhos/cm in 1967 (figs. 2 and 7).

The increase in concentration of dissolved solids in the ground water is correlated in figure 7 with a decline of water levels caused by a high rate of pumping coupled with a low rate of precipitation reported by the U.S. Weather Bureau (1957–68). Ground water is virtually the sole source of irrigation water in the Beryl-Enterprise district, and pumpage from wells exceeds the recharge to the aquifers (Sandberg, 1966, p. 39). A depression in the water table was formed in the southern part of the district as a result of the heavy pumping, and the original gradient toward the north (as indicated by the water-level contours in fig. 8 for 1962) has been reversed (as indicated by the water-level contours in fig. 8 for 1967). Return flow from irrigation no longer flows to the north but is held in the area by the large depression in the water table. This depression has continued to deepen and to expand laterally since about 1964. If the depression remains, water quality will continue to deteriorate owing to repeated use and recirculation of the ground water.

Although the specific conductance of water from well (C–36–16)5a–9 and few other wells in the southern part of the Beryl-Enterprise district is relatively high, water in the southern part is generally of better quality than water in the northern part (Sandberg, 1966, fig. 12; Connor, Mitchell, and others, 1958, p. 86–91). The poorer quality water in the northern and eastern parts of the district will move toward the center of the depression and cause further deterioration of the water quality.

CONCLUSIONS

The quality of the ground water in the Kanosh and Beryl-Enterprise ground-water districts will continue to deteriorate as long as existing recharge-discharge relations persist and irrigation return flow is concentrated by transpiration, evaporation, and by leaching of the soils and soil amenders. Continued pumping at present (1968) rates will cause an increase in the depth and areal extent of the water-table depressions in the two districts. As the depressions expand, the area in

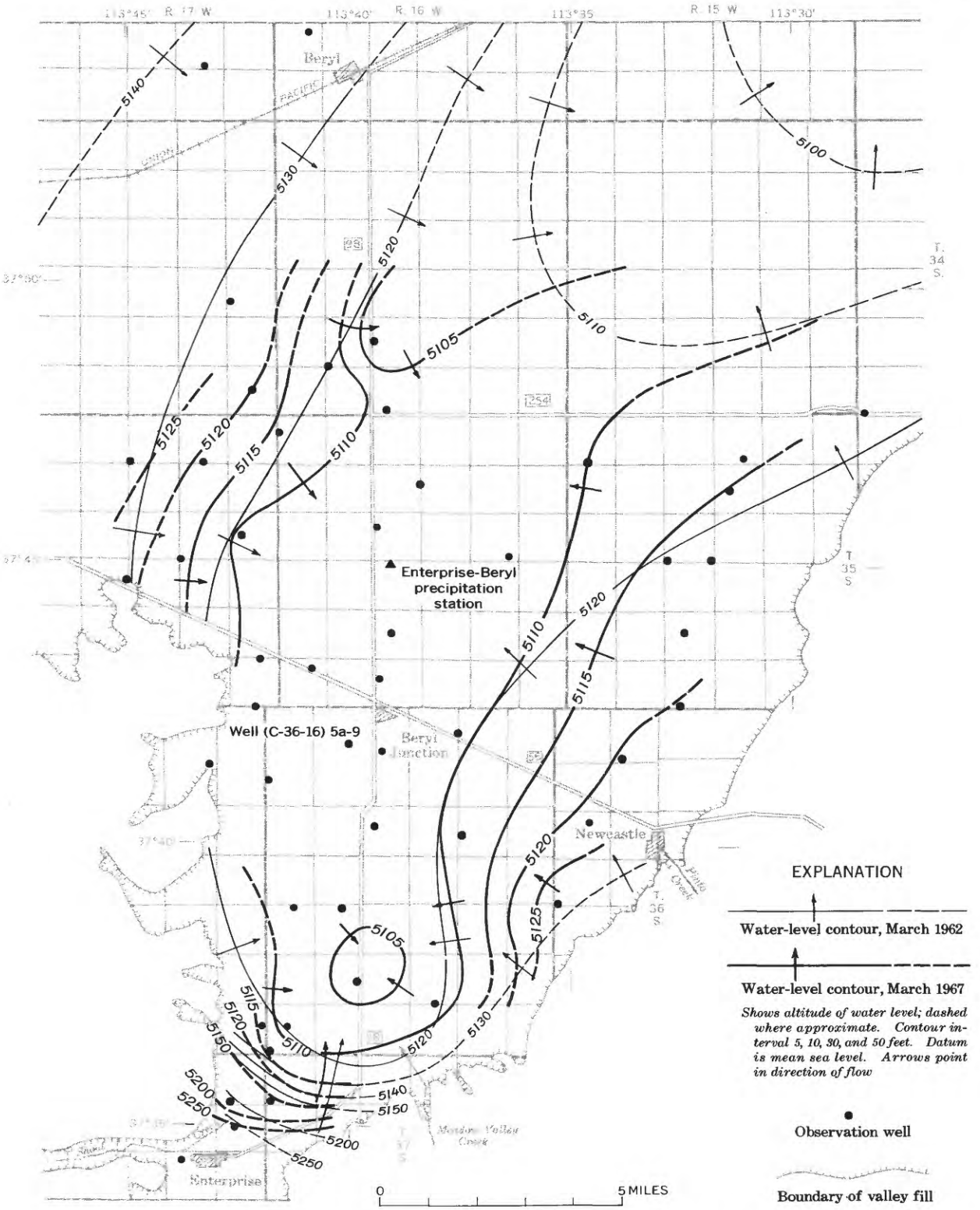

FIGURE 8.—Map of the Beryl-Enterprise district, Escalante Valley, Utah, showing water-level contours, March 1962 and March 1967.

which the chemical quality of ground water is deteriorating will also expand. The quality of the ground water in the Sevier Desert also will continue to deteriorate until the ground water is similar in quality to water from the Sevier River, and in some places may deteriorate further because of local concentration resulting from repeated reuse of ground water.

REFERENCES

Baker, C. H., Jr., Price, Don, and others, 1967, Ground-water conditions in Utah, spring of 1967: Utah Dept. Nat. Resources, Div. Water Resources Coop. Inv. Rept. 5, 89 p.

Connor, J. G., Mitchell, C. G., and others, 1958, A compilation of chemical quality data for ground and surface waters in Utah: Utah State Engineer Tech. Pub. 10, 276 p.

Mower, R. W., 1965, Ground-water resources of Pavant Valley, Utah: U.S. Geol. Survey Water-Supply Paper 1794, 78 p.

——— 1967, Causes of fluctuations in the rate of discharge of Clear Lake Springs, Millard County, Utah: U.S. Geol. Survey Water-Supply Paper 1839–E, 31 p.

Mower, R. W., and Feltis, R. D., 1968, Ground-water hydrology of the Sevier Desert, Utah: U.S. Geol. Survey Water-Supply Paper 1854, 75 p.

Sandberg, G. W., 1966, Ground-water resources of selected basins in southwestern Utah: Utah State Engineer Tech. Pub. 13, 46 p.

U.S. Weather Bureau, 1957–68, Climatological data, Utah: v. 59–70.

BIODEGRADATION OF DODECYLGUANIDINE ACETATE (DODINE)

By MARVIN C. GOLDBERG and ROBERT L. WERSHAW, Denver, Colo.

Abstract.—A two-part investigation of the biodegradation of dodecylguanidine acetate (dodine), a fungicide, showed that two soil organisms, a *Flavobacterium* sp. and an *Achromobacter* sp., utilize the material as the sole source of carbon. By use of C^{14}-labeled fungicide, the investigation also showed that the biological content of river muds typical of the Denver, Colo., area degrades up to 5 percent of a dodine charge within 68 days. Preconditioning the river muds to the fungicide neither enhanced nor decreased the amount of biodegradation in any of the samples tested.

Dodecylguanidine acetate (dodine) is typical of some of the thousands of compounds used yearly for agricultural purposes. These materials when sprayed onto soils and surface waters have the potential for impairing water quality throughout any given drainage basin. The consequences of these practices open two points of inquiry:

1. What is the residence time of the material on the soil surface or in water where ultraviolet light or micro-organisms under relatively high temperature can act as decomposition agents?

2. What is the residence time in aquifers where micro-organisms are less prevalent, light activation is absent, and generally low temperatures prevail? Usually, seasonal temperature variations are much greater in surface waters than in ground waters.

If one assumes that sorption is negligible, low decomposition rates would indicate the possibility of ground-water contamination. Also, low decomposition rates, even of highly sorbed material, indicate a potential impairment of surface-water quality through sediment transport and sorbant reexchange with the aqueous environment. Potential water-quality interactions depend on three factors: Molecular longevity, sorption reactions to different bed-sediment and soil compositions, and magnitude of solution equilibrium constants under various solute conditions.

Microbial decomposition of herbicides and fungicides is a major factor in the persistence of these compounds in soil. Herbicides can be degraded by specific microbial species (Audus, 1951; Brownidge, 1956; Dewey and Pfeiffer, 1959; Jensen, 1957; and Steensen and Walker, 1956), and even a fungicide can be broken down into other fungicidal substances by fungal organisms (Sijpesteijn and others, 1962).

Audus, (1951) lists 24 specific bacterial and fungal species capable of decomposing herbicides. Included are such compounds as 2,4-dichlorophenoxyacetic acid and some of its esters, 2,4-dinitrocresol, allyl alcohol, and Monuron. Significantly, some microbial species are capable of decomposing compounds whose chemical structures differ markedly from one another. One might expect that a fungicide could also be degraded by microbial species. This assumption is substantiated by the work done on C^{14}-labeled simazine (Ragab and McCollum, 1961), a selective urea herbicide, where part of the simazine breakdown is attributed to soil microbial action.

Urea and guanidine functional groups differ only in that a guanidine NH is replaced by an O atom in the urea; hence, the hypothesis that soil microflora could also decompose the guanidine compounds.

Additional studies with simazine and other urea herbicides (Cooke, 1956; Exer, 1958; Gast, 1958; Knusli, 1958) illustrate the radiochemical technique used in this study for determining small amounts of pesticide decomposition. Generation of CO_2 produced by metabolism of dodine was quantified by labeling the dodine with C^{14} in the liquid state and examining collected CO_2 gas for C^{14} content. If one makes certain that sterile control samples are simultaneously analyzed with the test samples and that the CO_2 generated by the sterile controls is subtracted from the CO_2 generated by the test samples, the fact that a C^{14}-labeled compound yields CO_2 is conclusive proof of metabolic oxidation. As in the previous studies, degradation of the urea herbicides by bacterial action was verified.

In this investigation, the authors sought to evaluate the biodegradability of dodine. Initially, a search was made for soil micro-organisms capable of metabolizing dodine, and then, metabolic decomposition rates were

U.S. GEOL. SURVEY PROF. PAPER 650-D, PAGES D235-D239

359-403 O—69——16

established on heterogeneous environmental materials from surface-water systems.

Acknowledgments.—The authors gratefully acknowledge the cooperation of the American Cyanamid Corp. for supplying ultrapure Cyprex and radiotagged Cyprex. We are also indebted to Dr. J. L. Tong, University of Denver, for independently verifying the results of the studies listed in table 1.

STUDY OF ORGANISMS CAPABLE OF METABOLIZING DODINE

Materials used

Dodecylguanidine acetate (dodine), a fungicide marketed as Cyprex by the American Cyanamid Corp., has the formula

$$n\text{-}C_{12}H_{25}NH\text{—}\overset{\overset{NH}{\|}}{C}\text{—}NH_2\cdot CH_3COOH$$

(Molecular weight, 287; melting point, 136°C)

It is slightly soluble in alcohol and water, and has an acute oral lethal dose to 50 percent of the rats tested (LD_{50}) of 1–2 grams per kilogram (Frear, 1963).

Within analytical limits of determination, the purity of the compound was 100 percent. It was analytical grade, lot 585-107-1 supplied by the American Cyanamid Corp.

The soil source for part one of this study was a test farm in Van Buren County, Mich. For a period of 2 years prior to the sampling date, the soil had been repeatedly sprayed with dodine. Eight soil samples were aseptically collected from a depth of 0–4 inches below the surface, and 8 samples were similarly collected from a depth of 4–8 inches below the surface.

Bacterial isolation and identification

Four bacterial culture media were prepared to optimize growth conditions for autochthonous (indigenous) and zymogenous (fermenting) soil bacteria. The basic salt medium used was identical with that described by Whiteside and Alexander (1960), with the addition of 0.1-percent yeast extract. A semisolid medium was obtained by the addition of 2-percent bacto agar to the yeast-extract salt medium. A dodine liquid medium and a dodine semisolid medium were formulated by substituting 100 milligrams per liter of dodine for the yeast extract in the two previous media. As a result, four bacteria culture media were available as follows:

Yeast-extract salt broth, *A*,
Yeast-extract salt agar, *B*,
Dodine-salt agar, *C*, and
Dodine-salt broth, *D*.

Each of the 16 Michigan soil samples was treated as follows: Two 1-gram samples of soil were transferred to 2 flasks containing yeast-extract salt broth. (*A*, fig. 1) One flask was incubated aerobically and the other anaerobically at 25°C. After 11 days, subcultures were made to a semisolid medium (*B*, fig. 1). (See fig. 1, part 1.) The purpose of the agar subculture was to isolate single species.

Once single species were isolated on agar plates, they were subcultured to dodine-salt agar (*C*, fig. 1) plates and dodine-salt broth (*D*, fig. 1) tubes and incubated for 15 days at 25°C. Organisms surviving on the dodine media were subcultured to the test media listed in table 1.

TABLE 1.—*Results of culture-media studies on organisms 1 and 2*

[All media used were Detroit Laboratories, Inc., Difco brand with exception of salt medium]

	Organism 1	*Organism 2*
Size	Width 0.8–0.9 micron, length 1.5–3.0 microns.	Width 0.6–0.7 micron, length 1.5–2.5 microns.
Strain	Gram negative rods	Gram negative rods.
Nutrient agar	Colonies 1–2 millimeters in diameter, completely round, raised, and creamy yellow.	Very prolific, flat, spreading, colorless growth.
Yeast-extract salt agar.	Small, opaque, raised, completely round colonies.	Prolific, flat, spreading, colorless growth.
Nutrient-broth growth.	Even turbidity	White, thick, friable pellicle.
Growth	At 25° and 37°C, aerobic and anaerobic.	At 25° and 37°C, aerobic and anaerobic.
Dextrose	No reaction	No reaction.
Mannitol	do	Do.
Lactose	do	Do.
Sucrose	do	Do.
Salicin	do	Do.
Methyl red	Negative	Negative.
Urea	do	Do.
Gelatin	Not liquified	Not liquified.
Litmus milk	No reaction	Alkaline after 3 weeks.
Motility	Nonmotile	Motile.

Discussion

Of the pure cultures studied, only two organisms were capable of surviving on dodine agar. The organisms were isolated aerobically and anaerobically from both the dodine-salt agar, *C*, and the dodine-salt broth, *D*.

A lag phase of approximately 7 days was noted in growth on dodine-salt agar (fig. 1, part 2). Additional incubation for 14 more days resulted in profuse growth. After conditioning the organisms to dodine by several subcultures in medium *D* (dodine broth) and medium *C* (dodine agar), subculture to mediums *A* and *B* (which contained no dodine) resulted in very poor growth of the organisms. Such a reaction indicates adaptation of the organisms to the pesticide.

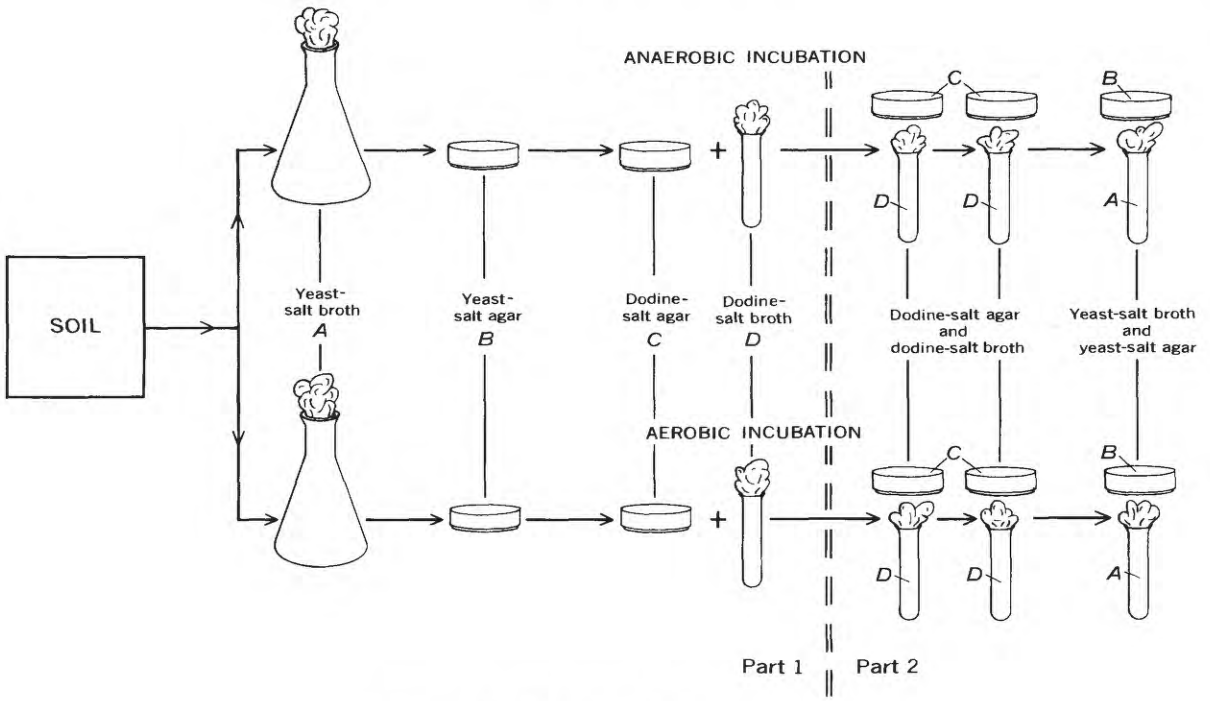

FIGURE 1.—Bacterial isolation flowsheet.

On the basis of descriptions in Bergey's Manual of Determinative Bacteriology (Breed and others, 1957), organism 1 was found to closely resemble *Flavobacterium peregrinum*. *F. peregrinum* is an aerobe, whereas, organism 1 grows under both aerobic and anaerobic conditions.

Organism 2 closely resembles *Achromobacter pestifer;* organism 2, makes litmus milk alkaline, whereas *A. pestifer* does not. This reaction was not observed until after 3 weeks of incubation and is therefore a minor consideration.

Isolation of two bacterial species capable of surviving when the sole source of carbon was in the dodine molecule indicates that dodine can be metabolized by microbial species in soils.

SOIL UPTAKE STUDIES

To determine dodine degradation under natural conditions, the decomposition of dodine by river muds from the Denver, Colo., area was studied.

A pesticide applied to soil can be absorbed by the soil materials, degraded by physical action such as photochemical decomposition or volatization, and metabolized by the biological environment (Sheets, 1964). Fortunately, in the laboratory it is possible to regulate the physical conditions and compensate for unwanted degradation effects by simultaneous examination of control samples. In these studies, the controls were obtained by sterilizing the soil system before addition of the dodine. Subtracting the nonmetabolic $C^{14}O_2$ production in the sterilized samples from the metabolic $C^{14}O_2$ production in the nonsterilized samples allows an accurate measurement of the $C^{14}O_2$ production due solely to metabolism.

Sample locations

Locations of mud samples used in this part of the study are listed as follows:

1. Seventh Avenue and Cherry Creek at the point where Cherry Creek enters the South Platte River; sample taken under 4 inches of flowing water.
2. Mud from feed-in canal to Cherry Creek Reservoir beneath bridge at East Hampden and Parker Road; sample taken under 10 inches of slowly flowing water.
3. Irrigation ditch entering the south end of Cherry Creek Reservoir. Sample taken 3 miles due south of the ditch-reservoir confluence under 5 inches of still water.
4. Ephemeral sand drainage ditch in Littleton, Colo. Sample taken under 0.5 inch of rapidly flowing water.
5. Bear Creek, about 4 miles west of Denver at Kipling and 8th Avenue; sample taken near bank under 6 inches of rapidly flowing water.

All samples from the five locations were treated within 1 day of collection, and each of the five samples was handled as follows: Three 50-gram portions of each sample were weighed separately into three Erlenmeyer flasks labeled 1, 2, and 3. The Erlenmeyer flasks contained a center well in the sample area (fig. 2). Five-tenths milliliter of saturated potassium hydroxide solution was added to the center well of the flasks. Flask 1 was sealed with a serum cap, then autoclaved at 15 pounds pressure per square inch for 15 minutes. After the flask cooled to room temperature, 1 ml of a solution containing 584 micrograms of C^{14}-radiolabeled dodine was aseptically added to the sample area. Flask 2 was then incubated for 76 days at 25°C.

To evaluate the effect of long-term contact between dodine and the environment, a pretreated sample was prepared. This procedure entailed placing dodine in contact with the soil for a period of 27 days before determining dodine degradability rates; hence, if a synergistic relationship or a conditioned response were operative it would be indicated by the decomposition rate change between the pretreated and untreated samples. The sample in flask 2 was the pretreated sample.

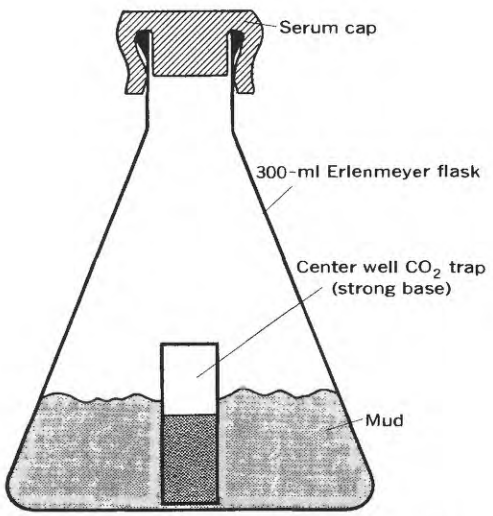

FIGURE 2.—Metabolic measurement flask.

The sample area of flask 2 contained 630 μg of nutagged dodine. The flask was sealed with a serum cap and incubated at 25°C for 27 days. Then 584 μg of O^{14}-radiolabeled dodine was added and flask 2 was incubated an additional 49 days.

Flask 3 was incubated at 25°C. It contained 584 μg of C^{14}-radiolabeled dodine in the sample area. Total incubation time was 68 days. During the incubation period, sterile air was added through the serum cap to obtain normal growth conditions.

After incubation, all three flasks were opened. One hundred lambda aliquots of solution were drawn out of the center wells and placed in liquid scintillation vials containing 15 ml of dioxane counting solution. The samples were counted in a Packard Tri-Carb liquid scintillation spectrometer for a length of time sufficient to ensure 0.5-percent statistical accuracy. Results are shown in figure 3.

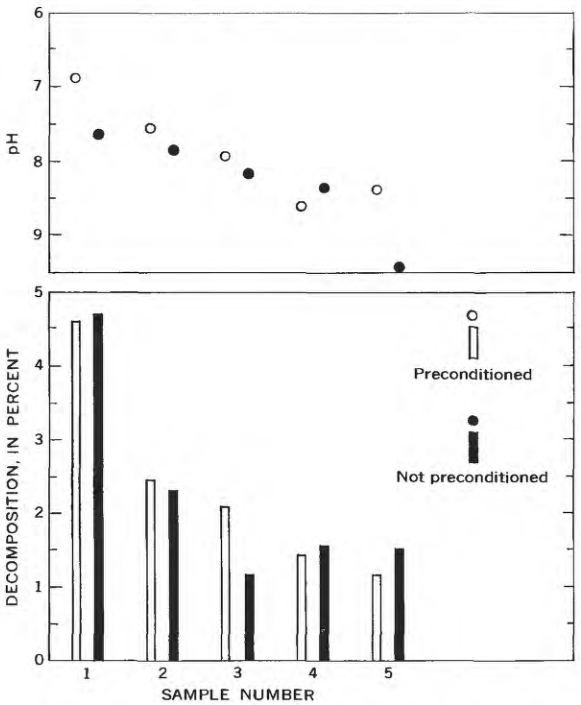

FIGURE 3.—Biodegradation of dodine by river sediments.

Discussion

The percentage decomposition of the 5 samples tested ranged from 1.15 to 4.55 for pretreated samples and from 1.8 to 4.66 for those not pretreated. No discernible difference in percentage decomposition is noted due to pretreatment. Examination of the pH data indicates that the samples having pH closest to the range 7.2–7.6 exhibit the largest degree of decomposition. Figure 3 is arranged to emphasize the trend between rising pH and declining percentage decomposition.

Examination of the chemical structure of the tagged compound suggests two mechanisms of oxidation as follows:

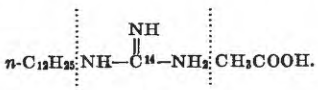

One mechanism consists of removing the acetate radical and allowing direct attack upon the guanidine group; the other mechanism, an oxidation mechanism such as beta oxidation, reduces the alkane chain

carbon by carbon and then allows attack on the guanidine group. At present, there is little to indicate which is the correct metabolic pathway; however, owing to the C^{14} tag of the guanidine carbon, it is certain that recovery of $C^{14}O_2$ has resulted in destruction of the guanidine complex. Residues of decane or acetic acid are not significant. The toxic properties of the molecule depend on the presence of the guanidine complex. Neither acetic acid nor decane is classified as a pesticide.

The extreme sensitivity of radioactive measuring processes makes it possible to detect a relatively small percentage decomposition of the radiolabeled molecule. Thus degradation reactions which proceed at low rates can be monitored. Curry (1962) took advantage of this fact to measure degradation of dodine on apple trees. He noted only a small percentage decomposition which correlates with the low percentage decomposition found in this study.

In natural systems, vaporization, sorption, photochemical decomposition, and other environmental reactions would tend to remove dodine from soils. The percentage degradation noted in this study is probably the minimum that one could expect from a natural system composed of a similarly bioactive soil.

CONCLUSIONS

Two organisms were identified and shown to be able to utilize dodecylguanidine acetate as a sole source of carbon. They are a *Flavobacterium* sp. and *Achromobacter* sp. Isolation and identification of two naturally occurring microbial species capable of utilizing dodine establishes the fact that natural biochemical reactions are able to decompose dodine in environmental systems.

Studies of preconditioned and nonpreconditioned muds established the fact that dodine biodegrades less than 5 percent during a 68-day period of incubation. There is no noticeable difference in biodegradability between the preconditioned river muds and those not preconditioned. In a natural system, it would be expected that dodine in contact with the soil would be slowly degraded. If roughly 5 percent was lost in 60 days, then if the same rate of decomposition prevails, 50 percent would be lost in 600 days.

REFERENCES

Audus, L. J., 1951, The biological detoxification of hormone herbicides in soil: Plant and Soil, v. 3, no. 2, p. 170–192.

Breed, R. S., Murray, E. G. D., Smith, N. R., 1957, Bergey's manual of determinative bacteriology, 7th ed.: Baltimore, Md., Williams and Wilkins Co., 1094 p.

Brownidge, N., 1956, Studies on the breakdown of 2,4-D and some related compounds by soil microorganisms: Univ. London, England, Ph. D. thesis.

Cooke, A. R., 1956, A possible mechanism of action of the urea type herbicides: Weeds, v. 4, p. 397–399.

Curry, A. N., 1962, Translocation and metabolism of dodecylguanidine acetate (Dodine) fungicide in apple trees, using C^{14} radiotagged Dodine: Agr. and Food Chemistry, v. 10, no. 1, p. 13–17.

Dewey, O. R., and Pfeiffer, R. K., 1959, Soil persistence and biological breakdown of 2,3,6 trichlorobenzoic acid: Internat. Symposium Crop Protection, 11th, Ghent 1959 Proc., p. 899–904.

Exer, B., 1958, Uber Pflanzenwachstrumsregulatoren. Der Einfluss von Simazin auf den Pflantzenstoflwechsel: Experientia, v. 14, no. 4, p. 136–137.

Frear, D. E. H., 1963, Pesticide index: State College, Pa., College Science Publishers, 193 p.

Gast, A., 1958, Uber Pflanzenwachstrumsregulatoren. Beitrage zur Kenntnis der phytotoxischen Wirkung von Triazinen: Experientia, v. 14, no. 4, p. 134–136.

Jensen, H. L., 1957, Decomposition of chloro-organic acids by fungi: Canadian Jour. Microbiology, v. 3, p. 151–154.

Knusli, E., 1958, Herbicides with triazine bases: Phytiat-Phytopharm. v. 7, p. 81–92.

Ragab, M. T. H., and McCollum, J. P., 1961, Degradation of C^{14} labeled simazine by plants and soil microorganisms: Weeds, v. 9, no. 1, p. 72–84.

Sheets, T. J., 1964, Review of disappearance of substituted urea herbicides from soil: Agr. and Food Chemistry, v. 12, no. 1, p. 30.

Sijpesteijn, A. K., Kaslander, J., and Van Der Kerk, G. J. M., 1962, On the conversion of sodium dimethyldithiocarbamate into its α-aminobutyric acid derivative by microorganisms: Biochim. Biophys. Acta, v. 62, p. 587–589.

Steensen, T. L., and Walker, N., 1956, Observations on the bacterial oxidation of chlorophenoxyacetic acids: Plant and Soil, v. 8, p. 17–32.

Whiteside, J., and Alexander, M., 1960, Measurement of microbiological effects of herbicides: Weeds, v. 8, no. 8, p, 204.

EFFECT OF INDUSTRIAL EFFLUENT ON WATER QUALITY OF LITTLE SIX MILE CREEK NEAR JACKSONVILLE, FLORIDA

By DONALD A. GOOLSBY, Ocala, Fla.

Work done in cooperation with the Florida Geological Survey, City of Jacksonville, and Duval County

Abstract.—A reconnaissance of Little Six Mile Creek near Jacksonville, Fla., made August 24–26, 1965, showed that acid industrial effluent has severely affected the entire stream, and during low flow, the upper Ribault River. The total acid load of the effluent during this reconnaissance was equivalent to 1.7 tons per day as sulfuric acid and the dissolved-iron load was equivalent to 0.4 ton per day. At times the acid effluent is neutralized by alkaline effluent from a tributary stream.

Little Six Mile Creek drains an area of 4.4 square miles in Duval County, Fla., northwest of Jacksonville (fig. 1). Drainage from this basin converges with drainage from the Six Mile Creek basin to form the Ribault River, a tributary to the St. Johns River. The Ribault River and Six Mile Creek are affected by ocean tides and the flow often reverses.

Water samples have been collected periodically at the gaging station on Little Six Mile Creek since March 12, 1965, as a part of a water-resources investigation in Duval and Nassau Counties. A comparison of chemical analyses shows the quality of water discharged from Little Six Mile Creek to be quite different from that of other basins in the area. The dissolved solids were much higher and the pH was much lower in Little Six Mile Creek than in other streams. Water samples collected at the gaging station on Little Six Mile Creek contained dissolved solids as high as 625 milligrams per liter and had a pH as low as 2.6 in contrast to water samples from Six Mile Creek which contained dissolved solids ranging from 66 to 176 mg/l and had an approximately neutral pH. A reconnaissance of the Little Six Mile Creek basin was made in August 1965, when flow conditions were near average, to determine the cause of the difference in quality. This report describes results of the reconnaissance.

METHODS OF INVESTIGATION

On August 24, 1965, preliminary field measurements of specific conductance and pH were made at numerous sites within the Little Six Mile Creek basin and on the Ribault River to select sampling stations. Sixteen sampling stations were selected; stations 1–11 in the Little Six Mile Creek basin, station 12 at the gaging station on Six Mile Creek, and stations 13–16 on the Ribault River (fig. 1).

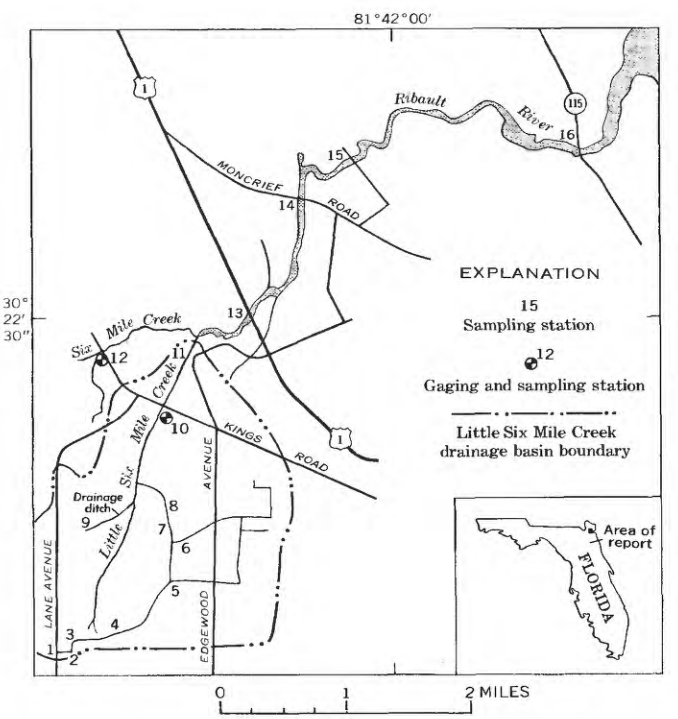

FIGURE 1.—Index map of the Little Six Mile Creek basin and Ribault River, showing the locations of sampling and gaging stations.

TABLE 1.—*Chemical analyses of water samples collected during August 25–26, 1965, reconnaissance of Little Six Mile Creek and Ribault River, Florida*

[Fe, reported as total iron]

Sampling station	Field pH	Total acidity as H_2SO_4 (mg/l)	Dissolved constituents (milligrams per liter)										Time (EST)
			Fe	Zn	Cu	Mn	Ca	Mg	Na	SO_4	Cl	DO[1]	
1	1. 9	2, 100	420	4. 8	0. 12	0. 3	60	25	20	2, 040	400	7. 5	1500
5	2. 1	1, 570	365	10	. 08	. 2	68	27	31	1, 300	490	6. 2	1700
7	2. 8	540	170	9. 0	. 00	. 1	64	20	25	740	78	6. 5	1730
8	3. 0	98	10	. 7	. 04	. 4	68	22	22	320	78	2. 8	1745
9	7. 3	0	. 03	. 0	. 00	. 0	60	26	17	174	17	------	1015
9[2]	12. 1	0	. 00	. 0	. 00	. 0	3. 8	. 0	730	154	30	3. 4	1030
10	6. 6	0	2. 7	. 1	. 00	. 0	62	22	18	220	38	2. 4	1415
12	6. 6	0	. 34	. 0	. 00	. 0	7. 7	2. 5	6. 3	10	12	5. 3	1300
13	6. 8	0	. 95	. 0	. 00	. 0	30	9. 9	19	90	30	. 4	1440
16	7. 2	0	. 42	. 0	. 00	. 0	35	34	235	95	478	4. 8	1710

[1] DO, dissolved oxygen.
[2] Collected on August 26, 1965; all other samples collected on August 25, 1965.

Field measurements of pH, specific conductance, and dissolved oxygen were made at all 16 stations between 1530 and 1925 hours on August 25, and water samples for laboratory analysis were collected at stations 1, 5, 7, 8, 10, 13, and 16. Stations 9 and 12 were also sampled on August 25 but not within the above time interval. All water samples were filtered through a 0.45-micron membrane filter to remove suspended material. Iron, copper, zinc, manganese, calcium, and magnesium were determined in the laboratory by atomic absorption spectrophotometry. The dissolved-oxygen measurements were made with an instrument utilizing a polarographic-type probe. In addition, discharge measurements were made at several of the sampling stations.

RESULTS

Chemical analyses of samples collected on August 25 between 1530 and 1925 hours are shown in table 1. Additional samples were collected on August 24, 25, and 26 at several sampling stations. These data, not shown in table 1, were used to determine if there were significant daily variations in pH and selected heavy metals.

The dissolved-iron concentration in all parts of Little Six Mile Creek would be toxic to most forms of fish life. Iron hydroxides and oxides precipitate on the gills of fish and cause death by suffocation. Heavy precipitates of ferric hydroxide may also smother fish eggs. According to McKee and Wolf (1963), 95 percent of the waters in the United States that support good fish fauna contain no more than 0.7 mg/l iron.

Iron in solution depends on the pH and oxidation potential of the solution. The oxidation potential is controlled, in part, by the amount of oxygen in solution. Generally as the pH rises (solution becomes less acid) or the dissolved oxygen increases, less iron can be retained in solution. The overall chemical reaction may be written as follows:

$$2Fe^{+2}+\frac{1}{2}O_2+5H_2O\rightarrow 2Fe(OH)_3+4H^{+1}. \quad (1)$$

Most of the iron precipitated before it reached station 10. From the chemical analyses and discharge data, it was estimated that the amount of iron that precipitated between stations 1 and 10 was approximately 750 pounds per day. Loss of iron from solution was the result of both oxidation and an increase in pH, and was evidenced by a thick rust-colored precipitate on the streambed and rusty deposits on overhanging vegetation. The precipitate was loose and several inches thick on the streambed and debris below the water surface.

The dissolved iron at station 1 ranged from 205 to 740 mg/l and averaged 512 mg/l. The concentrations, in milligrams per liter, of other heavy metals at station 1 were as follows:

	Minimum	*Maximum*	*Average*
Zinc	4. 4	8. 0	5. 5
Copper	. 12	. 16	. 14
Manganese	. 1	4. 8	. 3

On August 25, the average discharge at station 1 was approximately 0.3 cubic feet per second, all of which was effluent from an industrial plant. At the 0.3-cfs discharge rate, the total acid load as sulfuric acid at station 1 on August 25 was calculated to be 1.7 tons per day and the dissolved-iron load was 0.4 ton per day.

Figure 2, shows dissolved oxygen and pH versus distance downstream from station 1.

The variation in oxygen content between stations 1 and 7 is believed to be due to aeration of the water by its flowing through culverts and by inflow from drainage ditches. Oxidation of ferrous iron to ferric

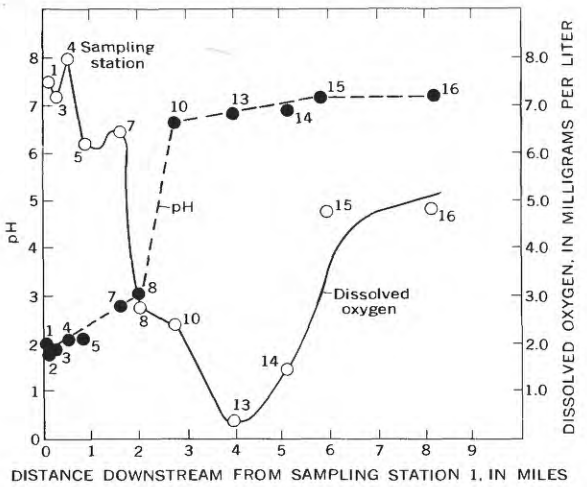

FIGURE 2.—Dissolved oxygen and pH versus distance downstream from sampling station 1.

iron was probably the main consumer of dissolved oxygen in this stream during the reconnaissance. Ferric iron may then precipitate as the hydroxide. A sharp decrease in dissolved oxygen between stations 7 and 8, figure 2, corresponds with a decrease in dissolved iron, figure 3. This reach of the stream is also where the heaviest iron hydroxide precipitate was observed.

Figure 3 shows the decrease in dissolved iron and acidity with distance downstream, and figure 4 illustrates the relation of iron in solution to acidity.

At station 1 the pH ranged from 1.8 to 2.5, and the average of the hydrogen-ion activity gave a corresponding pH of 2.0 for four different measurements.

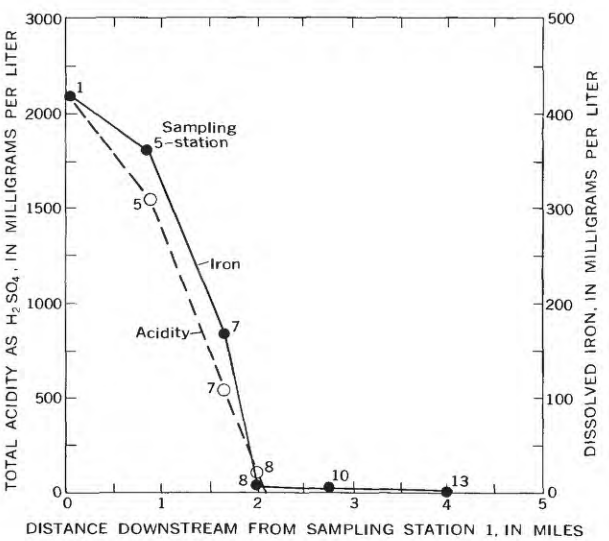

FIGURE 3.—Dissolved iron and total acidity as sulfuric acid versus distance downstream from sampling station 1.

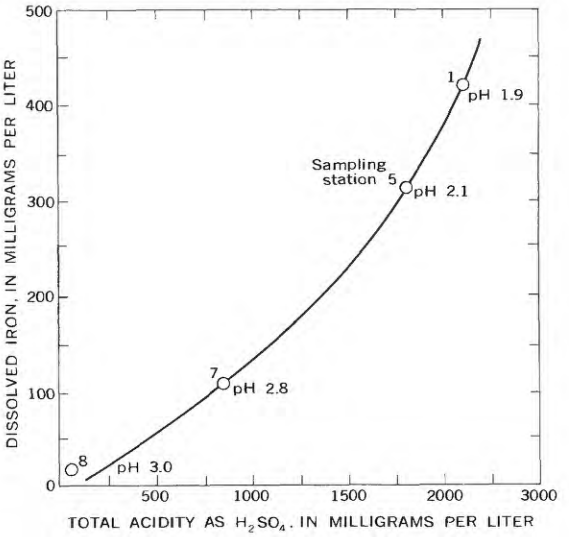

FIGURE 4.—Relation between dissolved iron and total acidity as sulfuric acid, constructed from data in table 1.

The pH rose slightly, to 3.0, between stations 1 and 8. The dissolved-iron content decreased to 170 mg/l at station 7, and to 10 mg/l at station 8. Between station 8 and the gaging station on Little Six Mile Creek (station 10), the pH rose sharply from 3.0 to about 6.6, and dissolved iron decreased to 2.7 mg/l.

The sharp rise in pH between stations 8 and 10 is due to neutralization by inflow of alkaline water from a drainage ditch between the two stations. The alkaline drainage was chiefly effluent and cooling water from a chemical plant located upstream from station 9. The pH of water from the drainage ditch (station 9) ranged from 7.3 to 12.1. The discharge at station 9 was 2.4 cfs on August 25. The highly alkaline water from the chemical plant consisted primarily of sodium hydroxide and appeared to be released in slugs several times a day.

Below the gaging station on Little Six Mile Creek (station 10) the pH continued to rise slightly; it leveled off to 7.2 at stations 15 and 16 on the Ribault River. The dissolved-iron concentration at station 16 was 0.42 mg/l.

Discharge measurements made during this reconnaissance show that approximately 65 percent (3.1 cfs) of the total discharge from the Little Six Mile Creek basin (4.71 cfs) came from industrial effluent. At low flow, discharge from Little Six Mile Creek would be almost entirely industrial effluent. The major neutralizing effect on the sulfuric acid effluent being released above station 1 at low flow would be the alkaline effluent released to the drainage ditch above station 9. Because the alkaline effluent is not released continuously and low flow occurs frequently, water discharg-

ing from Little Six Mile Creek into the Ribault River is often very acidic and contains appreciable quantities of dissolved iron. This is shown by the analysis of samples collected at station 10 prior to this reconnaissance. At station 10 on March 12, April 13, and May 28, 1965, the pH of the water was 2.9, 2.6, and 2.8, respectively, and the dissolved iron was 4 to 8 mg/l. On these dates, the discharges were 3.50, 2.66 and 3.99 cfs, respectively. As the flow increased, the pH also increased. On July 13, 1965, the discharge was 13 cfs and the pH was 6.7.

EFFECT OF EFFLUENT ON THE RIBAULT RIVER

Water entering the Ribault River from Little Six Mile Creek contained 2.4 mg/l dissolved oxygen, and water from Six Mile Creek contained 5.3 mg/l. The dissolved oxygen in the upper Ribault River was much lower, 0.4 mg/l at station 13 on August 25, 1965. The additional depletion of dissolved oxygen below the confluence of Little Six Mile Creek and Six Mile Creek was due to effluent discharged by industries located above and below station 13. The Ribault River is tidal and the flow reverses, therefore, both upstream and downstream industries affect stream conditions at station 13. The dissolved oxygen increased downstream from station 13. It was 1.5 mg/l at station 14, and 4.8 mg/l at station 16.

During this reconnaissance, the discharge from Little Six Mile Creek appeared to have little effect on the acidity and iron concentration of the Ribault River. Chemical analyses for stations 13 and 16 on the Ribault River are shown in table 1. The pH of the water at the two locations was 7.1 to 7.2 and the dissolved iron was less than 1.0 mg/l. At low flow, discharge from Little Six Mile Creek, when not neutralized by the alkaline industrial effluent, would lower the pH and increase the iron content in the upper reach of the Ribault River.

REFERENCE

McKee, J. E., and Wolf, H. W., 1963, Water quality criteria: California State Water Quality Control Board Pub. 3-A, 2d ed., 548 p.

THE RELATION OF TURBULENCE TO DEPOSITION OF MAGNETITE OVER RIPPLES

By RAUL S. McQUIVEY and THOMAS N. KEEFER,
Fort Collins, Colo.

Abstract.—Sorting of magnetite and other heavy minerals from predominantly quartz bed material occurs because of variations in turbulent shear stress from trough to crest of ripples and because for particles less than one-tenth millimeter in diameter critical shear stress is a function of density only. The sorted particles of heavy minerals tend to accumulate just upstream of ripple crests. It is suggested that artifically generated turbulence could be employed to sort small-sized heavy-mineral particles from sediment flows.

It has been known for some time that turbulence is a primary factor in the entrainment and transport of sediment. Only in the last 3 to 5 years have instrumentation and techniques been developed to make specific measurements of turbulence-related quantities in water. The purpose of this paper is to show how variations in the vertical distribution of turbulence may be related to bed shear stress and how this relation can be used to explain the accumulation of magnetite and other heavy minerals upstream of ripple crests in an alluvial streambed.

Before investigating the relationship between turbulence and shear stress we must look at the processes which cause particles of different specific gravities and sizes to become separated. This can be done by examining the relation between critical shear stress (shear stress needed to move a particle) and particle sizes of magnetite and quartz. This relation is shown in figure 1 (modified from Grigg and Rathbun, 1969). The median sieve diameters of the quartz and magnetite particles used in this study are represented by small circles. The physical importance of this relation can be seen as follows: Consider water flowing in an open channel with a bed consisting entirely of magnetite and quartz particles. Let these particles be thoroughly mixed and possess identical size distributions. Let the maximum particle diameter be 1 millimeter. It is apparent from figure 1 that if we vary the shearing stress on this hypothetical streambed from zero up to the lowest critical value for magnetite we can move all the quartz grains having a diameter less than one-half millimeter. When the shear stress is increased only slightly above this value all the magnetite and quartz can move. The following experiments will show that the variation of shear stress between the crest and trough of ripples is similar to this hypothetical model. The experiments also indicate that this variation in shear stress may be related to the variation in distribution and intensity of the longitudinal turbulent velocity fluctuations. The variation of boundary shear stress back and forth across the critical value for magnetite produces sorting of magnetite particles on the upstream side of ripples.

PROCEDURE

All experiments were carried out in a recirculating flume 20 centimeters wide by 20 cm deep by 10 meters long. Bed material for the flume was composed of white Ottawa quartz particles having a median sieve diameter of 0.19 mm and a median fall diameter of 0.210 mm. The flume was adjusted to give an average depth of flow of 4.50 cm over a ripple boundary under equilibrium conditions. This was obtained at a discharge of 2,035 cubic centimeters per second and a slope of 0.0021 meter per meter.

In order to study the way in which mineral accumulations form, 300 grams of magnetite with a median sieve diameter of 0.134 mm and a median fall diameter of 0.240 mm were sifted into the flow with a vibrating feeder. Particle movement was observed until equilibrium deposition patterns formed. This took about 2 hours. When equilibrium was reached the flume was shut off and deposits were photographed.

Because of difficulty in observing the movement of individual particles, additional observations were made

U.S. GEOL. SURVEY PROF. PAPER 650-D, PAGES D244-D247

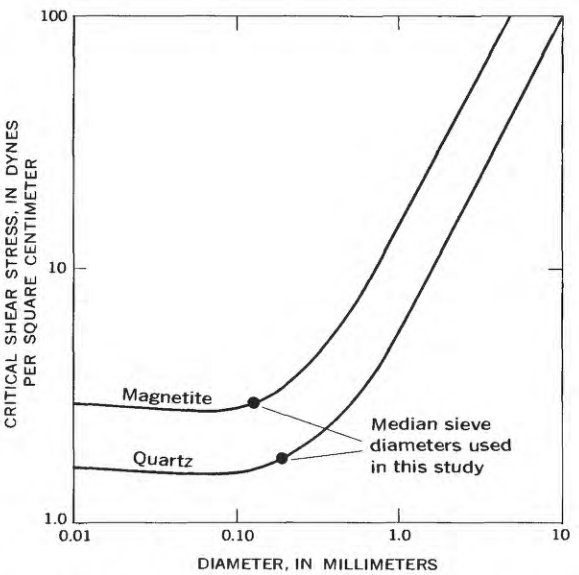

FIGURE 1.—Relation between critical shear stress in water at 20°C and grain diameter for spherical particles of magnetite and quartz (modified from Grigg and Rathbun, 1969).

under the same flow conditions with minerals marked with fluorescent dyes. Small amounts of garnet, lead, magnetite, and monazite were introduced into the flow from a salt shaker held beneath the water surface. Particle movement was then traced by ultraviolet light.

Measurements of turbulence were made using a constant-temperature hot-film anemometer system using techniques described by Richardson and McQuivey (1968). The vertical distribution of the longitudinal turbulent intensity (root-mean-square of the longitudinal velocity fluctuations, $\sqrt{\overline{u^2}}$ divided by the local mean velocity, $\bar{U}_L$) was measured over the trough, crest, and intermediate points of a number of ripples. All measurements were made at equilibrium flow conditions.

DATA

Figure 2*A* shows an overall view of typical magnetic accumulations in the flume. Figure 2*B* is a closeup view. Direction of the flow is from the top of the figure to the bottom in both parts of the figure. The two most important features of these accumulations are their location and distribution. Accumulations extend upstream from just behind the ripple crests for a distance approximately equal to one-third the ripple spacing. The accumulations generally extend across the entire width of a crest. Accumulations are thickest just upstream of the crest and taper out to zero in the upstream direction as shown in figure 3.

A

B

FIGURE 2.—Two views of magnetite deposits in 20-cm-wide flume. Flow is from top to bottom of photographs. *A*, overall view of deposits. *B*, closeup view of deposits upstream of ripple crests.

The vertical distribution of the longitudinal turbulent intensities, $\frac{\sqrt{\overline{u^2}}}{\bar{U}_L}$, and the local mean velocity, $\bar{U}_L$, are diagramed in figure 3. Wider variations in $\frac{\sqrt{\overline{u^2}}}{\bar{U}_L}$ occur over the trough than over the crest. Over the

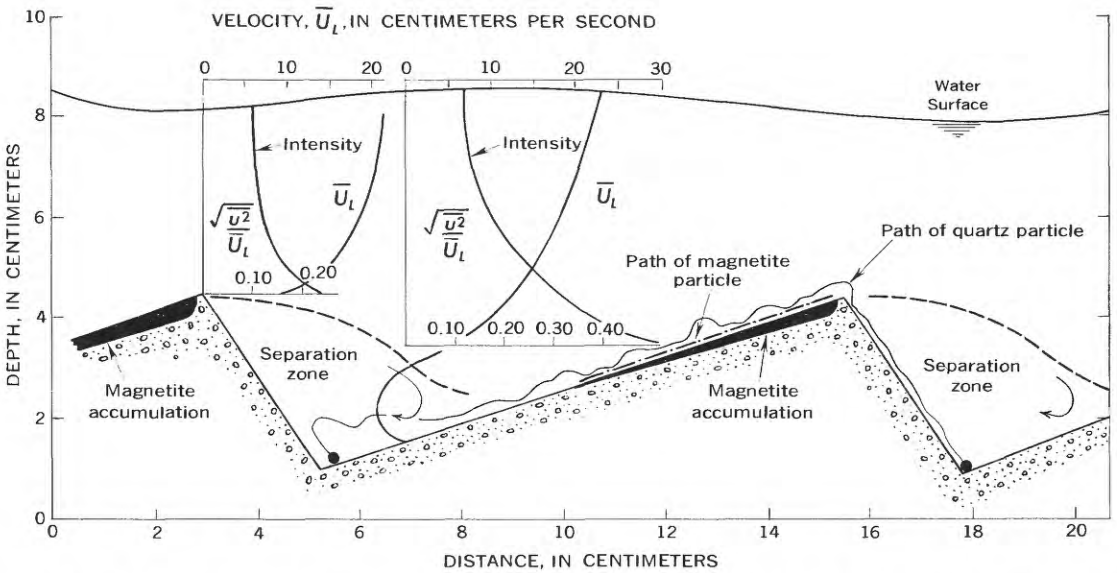

FIGURE 3.—Typical magnetite deposits on ripple bed. Distribution of longitudinal turbulent intensity and local mean velocity, and paths of magnetite and quartz particles are illustrated.

crest, intensity is nearly constant with a value of 0.10 in the region from the water surface to 0.40 of the total depth. Intensity increases to 0.15 near the bed. Over the trough of the ripple, intensity ranges from 0.10 at the water surface to 0.50 at the top of the separation bubble. The cross section average velocity is a maximum over the crest of a ripple and a minimum over the trough.

INTERPRETATION

Turbulence is related to shear stress in the following way. Boundary shear stress depends not only on the depth and slope, but also on the velocity gradient at the bed. High turbulent intensity at a given point is an indication of large local velocity fluctuations and large velocity gradients. Because fluctuations of 50 percent exist and because shear stress is approximately proportional to the local mean velocity squared, pulses of shear stress that have more than twice the predicted average stress may occur. Thus over the crest of a ripple, where the relative intensity of turbulence is low, a particle is subjected to less shearing stress than it is in the trough, where turbulence fluctuations are large. The variation of turbulence between crest and trough should not be confused with variation of mean velocity. The variation of mean velocity is accompanied by a variation of mean shear stress, but the variation of turbulence from trough to crest is precisely the reverse of the variation in mean velocity, as shown in figure 3.

Magnetite then does not move in precisely the same manner as quartz. After quartz particles are uncovered in the trough of a ripple they move by bouncing or sliding up the back of the ripple, avalanching over the crest and are again buried. The path of a typical particle is shown in figure 3. Magnetite particles are swept from the trough by the high turbulence level, but because of their size and the relation between this size and critical shear stress, they are not transported as far. Whereas large numbers of quartz grains avalanche over the crest, it is common to see magnetite drop just upstream of or barely beyond the crest of a ripple where the turbulence level (and shear stress) is least. The movement of magnetite is thus more cyclic in nature with particles moving from the edge of the separation zone where turbulence is high to the crest where turbulence is least. This is also shown in figure 3. A number of magnetite particles in any deposit do avalanche over the crest and mix with the remainder of the bed material. When these are uncovered as the ripple moves forward they again rejoin the accumulation behind the crest. Magnetite tends to remain nearer the surface than the average bed particle. Whenever magnetite particles in sizes less than approximately 0.2 mm in diameter are present, their density and size, coupled with the difference in turbulence between the trough and crest will lead to the formation of deposits upstream of the ripple crests. Observation of the fluorescent particles supports this hypothesis as reasonable for any heavy mineral.

CONCLUSIONS

Turbulence measurements offer the researcher a new and useful tool for the study of heavy-mineral trans-

port. Variations in the intensity of turbulence from the trough to the crest of ripples may be used to explain in part the segregation of magnetite and other heavy minerals behind the crest of ripples.

The relation between turbulence and hydraulic sorting of minerals suggests this as a profitable research area for separation techniques. It would seem feasible to develop new precise hydraulic sorting techniques using turbulence fields generated by grids or artificial bed forms. By entraining sediment of the proper size in the turbulence field, it may be possible to sort the size and density fractions by the variation of turbulent shear stress.

REFERENCES

Grigg, N. S., and Rathbun, R. E., 1969, Hydraulic equivalence of minerals with a consideration of the reentrainment process, *in* Geological Survey Research 1969: U.S. Geol. Survey Prof. Paper 650–B, p. B77–B80.

Richardson, E. V., and McQuivey, R. S., 1968, Measurement of turbulence in water: Am. Soc. Civil Engineers Proc., v. 94, no. HY2, p. 411–430.

EXTRACTION OF DISSOLVED CARBONATE SPECIES FROM NATURAL WATER FOR CARBON-ISOTOPE ANALYSIS

By JIM D. GLEASON, IRVING FRIEDMAN, and BRUCE B. HANSHAW,
Denver, Colo.; Washington, D.C.

Work done in cooperation with U.S. Army Research Office, Division of Environmental Research

Abstract.—The best method for separating the dissolved carbonate species from natural water in order to determine the δC^{13} value of carbon in the aqueous phase appears to be a direct-precipitation method. This method consists of adding ammonium hydroxide strontium chloride solution directly to the sample of natural water to be analyzed. The strontium carbonate thus formed precipitates, and is subsequently separated, dried, and analyzed for its δC^{13} value. The ammonium hydroxide strontium chloride solution can absorb carbon dioxide from the air; it is therefore extremely important that both the water sample and the prepared solution not be exposed to the air during handling and filtration. Exposure for a few minutes will cause contamination and give incorrect δC^{13} values.

One of the principal methods used in the extraction of total dissolved carbonate species from natural water for C^{14} age determination has been the gas-evolution method. In this technique (fig. 1), a sample of between 55 and 200 liters (depending on the carbonate-species concentration, Feltz and Hanshaw, 1963), contained in a large plastic drum, is acidified with concentrated sulfuric acid. Pure nitrogen from a gas cylinder is then slowly bubbled through the water. The water sample is heated to approximately 70°C by means of a submersible heater. The carbon dioxide that is evolved during acidification is swept out of the water with nitrogen gas. The gas mixture is then passed through a gas washing bottle containing a concentrated solution of strontium chloride in ammonium hydroxide. Experiments have shown that one gas scrub captures all the CO_2; a second wash is not needed. The extraction of carbon dioxide from the water is continued for not less than 4 hours. At the conclusion of this time, the strontinum carbonate is allowed to age for several days and is then filtered in a vacuum filter, dried, and used for C^{14} age determinations.

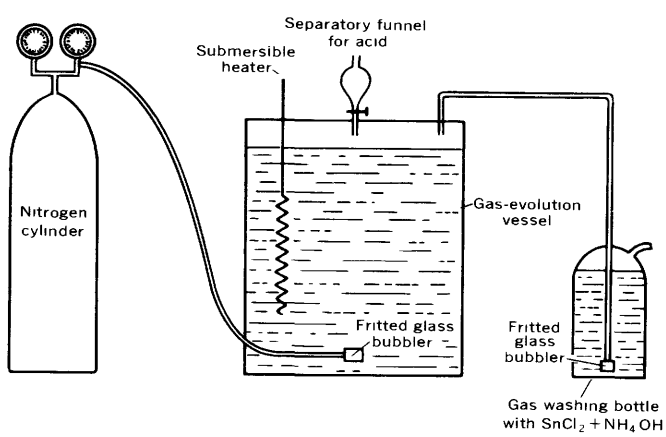

FIGURE 1.—Gas-evolution apparatus for extraction of dissolved carbonate species from natural water.

Usually, a small aliquot of the strontium carbonate is used for C^{13}/C^{12} analysis. C^{13}/C^{12} values are generally reported in the familiar δ notation where $\delta C^{13} = \left(\frac{C^{13}/C^{12}\ \text{sample}}{C^{13}/C^{12}\ \text{standard}} - 1\right) 1{,}000$. Carbon isotope ratios are reported as deviations from the PDB standard carbonate in parts per thousand (‰). The δC^{13} so determined is used in an adjustment equation (Pearson and White, 1967) to take into account the amount of "dead" carbon dissolved by the water during its contact with carbonate-containing rocks.

Recently, we decided that the gas-evolution technique should be checked by the use of another extraction technique to see if significant isotopic fractionation was occurring during this procedure. Accordingly, a number of wells were sampled in Florida,

and the gas-evolution technique was carried out as described on large-volume water samples. In addition, a second method, direct precipitation, was also carried out on 1-liter samples.

In the direct-precipitation procedure, the strontium chloride ammonium hydroxide solution is added directly to the 1-liter water sample. The water sample is shaken, and the strontium carbonate precipitate is allowed to settle. After 24–48 hours, most of the water is decanted, and the remaining strontium carbonate is collected on a filter, dried, and used for isotopic analysis. Evidence supplied from these 15 samples, as shown in table 1, indicates that the C^{13}/C^{12} analysis of the precipitate by the gas-evolution technique differs from the results of the analysis carried out by the direct-precipitation technique by approximately 2–6°/₀₀. Results of the gas-evolution technique are invariably isotopically lighter than those of the direct precipitation technique.

TABLE 1.—*Comparison of δC^{13} obtained by gas-evolution (G.E.) and direct-precipitation (D.P.) techniques*

[All ground-water samples from the Tertiary limestone aquifer of Florida]

Well location	Comments	δC^{13}G.E.	δC^{13}D.P.	$\Delta\delta C^{13}$
Arcadia	Gas evaluation trap=NaOH.	−9.7	−8.1	+1.6
Groveland	do	−10.8	−9.5	+1.3
Weeki Wachie Spring.	Gas evaluation trap=NH_4OH.	−15.7	−13.4	+2.3
Weeki Wachie No. 12.	do	−10.6	−4.0	+6.6
Yeehaw Junction	do	−8.4	−5.3	+3.1
Fort Pierce	do	−5.8	−2.4	+3.4
Cocoa No. 12A	do	−11.7	−8.9	+2.9
Clermont	do	−19.1	−10.0	+4.1
Frostproof	do	−13.2	−8.8	+4.4
Vero Beach	do	−8.9	−3.6	+5.3
Arcadia	do	−12.3	−8.1	+4.2
Container Corporation.	do	−15.3	−10.4	+4.9
Fort Clinton	do	−16.5	−10.4	+6.1
Sether	do	−14.7	−10.2	+4.5
N. E. Florida State Hospital.	do	−14.6	−10.0	+4.6

Experiments were then performed with sodium bicarbonate of known isotopic composition dissolved in water along with $CaCl_2$ and $MgSO_4$ to produce an artificial ground water. The dissolved carbonate species was collected by both the gas-evolution and direct-precipitation techniques. the δC^{13} results of the two techniques carried out in the laboratory did not agree. In addition, there seemed to be a large amount of δC^{13} scatter in samples from gas-evolution experiments. The δC^{13} determined on direct precipitates agreed fairly well with the δC^{13} of the $NaHCO_3$ standard, whereas the δC^{13} from gas-evolution samples varied greatly and was always isotopically lighter than the standard.

Thus it seemed advisable to examine the problem carefully and develop a technique that would give reproducible results. We observed that a precipitate forms in solutions of ammonium hydroxide strontium chloride that are exposed even briefly to the atmosphere; thus it seemed likely that contamination by atmospheric carbon dioxide during filtration might be a contributing factor in the differentiation of values.

Experiments were run exposing the ammonium hydroxide strontium chloride solution and carbon dioxide-free water to the air. It was found that as much as 200 milligrams of $SrCO_3$ was formed after 6 hours of exposure. This carbonate had extremely light δC^{13} values (−25°/₀₀). Experiments were also tried where the solution was exposed to the atmosphere through a very small opening. Approximately half as much $SrCO_3$ was formed in a comparable time. This $SrCO_3$ had heavier values (−7°/₀₀).

The importance of even short exposure to the atmosphere during handling and filtration of samples had not been taken into account previously. However, atmospheric contamination was considered a possibility for inconsistent values. Thus, a technique was sought in which the sample could be filtrated and handled without exposure to the atmosphere. Accordingly, a large sample of water was boiled to remove atmospheric carbon dioxide. Sodium bicarbonate of known isotopic composition, together with other salts, was dissolved in the carbon dioxide free water to simulate a natural mineralized water. The direct-precipitation technique was employed, and strontium chloride ammonium hydroxide solution was added directly to the simulated natural water. At various time periods after precipitation, the water and precipitate were shaken and an aliquot removed and filtered in a helium atmosphere to avoid contact with air. Results in table 2 show that the precipitate in all cases has exactly the same isotopic composition as did the sodium bicarbonate that was used to prepare the solution. One aliquot was filtered in air using a vacuum filter and exposed to the air for approximately 10 minutes. This sample was approximately 0.5 °/₀₀ lighter than the remaining samples (see table 2).

TABLE 2.—*Aliquot samples of δC^{13} values from simulated natural mineralized water at various times*

Hours from start	δC^{13}	Comments
0	−6.4	Starting $NaHCO_3$ before $SrCO_3$ precipitation.
¾	−6.5	$SrCO_3$ filtered out of contact with atmosphere.
2	−6.3	Do.
3½	−6.3	Do.
4½	−6.3	Do.
5¼	−6.3	Do.
5½	−6.8	$SrCO_3$ filtered in contact with air.

From these data it could be concluded that one of the major problems in the extraction and collection of carbon dioxide from natural water is the problem of uptake of atmospheric carbon dioxide by the ammonium hydroxide strontium chloride solution during handling and filtration. The absorption of atmospheric carbon dioxide would be a particularly serious problem in ground water that contains very little CO_2. Craig (1953) has also carried out experiments exposing strontium chloride ammonium hydroxide solution to the atmosphere. He has shown that the CO_2 extracted from the atmosphere is extremely light; values of -25 to $-35‰$ were obtained. This is in contrast to the C^{12}/C^{13} ratio of atmospheric CO_2 which is approximately $-7‰$. Craig (1953) pointed out that kinetic factors are very apt to cause large fractionation when air containing CO_2 is allowed to pass over an absorber. Therefore, great care must be taken in all applications to exclude atmospheric CO_2.

Our results indicate that the direct-precipitation technique gives correct isotopic compositions for 1-liter water samples. This would suggest that direct precipitation of total dissolved species from a large volume of water sample would be the best method of collection for radiocarbon work. To date, however, the direct-precipitation method on large-volume samples has not been successful. This is due to kinetic problems and to the coprecipitation of gelatinous flocs, principally of magnesium and aluminum hydroxides, which settle slowly and are difficult to filter. Therefore, our current technique is to process a large-volume (enough to give 3 grams total carbon) water sample by means of gas evolution for C^{14} age dating. A 1-liter water sample is prepared for δC^{13} analysis by direct precipitation and filtration in an inert atmosphere. If the $\Delta\delta C^{13}$ is large between the two methods, then the δC^{14} can be corrected for fractionation during collection. The δC^{13} from direct precipitation is also used in the adjustment equation given by Pearson and White (1967).

Acknowledgment.—We thank Meyer Rubin and Herman Feltz for their comments.

REFERENCES

Craig, Harmon, 1953, The geochemistry of the stable carbon isotopes: Geochim. et Cosmochim. Acta, v. 3, p. 53–92.

Feltz, H. R., and Hanshaw, B. B., 1963, Preparation of water sample for carbon-14 dating: U.S. Geol. Survey Circ. 480, 3 p.

Pearson, F. J., Jr., and White, D. E., 1967, Carbon-14 ages and flow rates of water in Carrizo Sand, Atascosa County, Texas: Water Resources Research, v. 3, p. 251–261.

DETERMINATION OF MERCURY IN NATURAL WATERS BY COLLECTION ON SILVER SCREENS

By MARGARET E. HINKLE and ROBERT E. LEARNED,
Denver, Colo.

Abstract.—A method for determining nanogram quantities of mercury in natural waters is described wherein mercury is collected on silver screens immersed in samples acidified with hydrochloric acid and the collected mercury is measured by heating the screens in a mercury-vapor absorption detector. As little as 10 nanograms of Hg in 100 ml of water can be detected by this procedure. The speed and simplicity of this method permit its use in hydrogeochemical surveys where mercury is utilized as a pathfinder element.

For several years mercury has been used as a pathfinder element to assist in the location of concealed ore deposits. Very small amounts of mercury have been measured in soils and rocks in the search for anomalous concentrations of mercury in mineralized areas and in areas not known to be mineralized (Hawkes and Webb, 1962, p. 73; Hawkes and Williston, 1962). Warren, Delavault, and Barakso (1966) found halos of mercury anomalies in the vicinity of mercury deposits and near base-metal, gold, and molybdenum deposits in British Columbia. Samples from the Cortez district, Nevada, showed mercury contents in direct correlation with gold contents (Erickson and others, 1966). Geochemical anomalies for mercury match the silver anomalies in the Tonopah and Silver Reef districts; in the Comstock district the mercury values are highest outside the principal silver-gold area, indicating possible undiscovered deposits (Cornwall and others, 1967).

Almost no use has been made of determination of mercury in natural water as a prospecting technique. The chief drawback has been the need to concentrate the mercury in the water in order to measure the small quantities present. Evaporation of the water or precipitation of metals from the water with hydrogen sulfide has been used to concentrate mercury; both procedures are time consuming and subject to analytical errors from sample loss or contamination. Small quantities of mercury have been extracted from water samples with dithizone and similar complexing agents (Lombardi, 1964; Beisova and others, 1965); however, extraction methods require several reagents and several steps in the sample treatment. X-ray (Marcie, 1967) and neutron-activation (Schutz and Turekian, 1965) analyses of mercury in water also require preconcentration of the mercury or extraction of the sample.

In the procedure described here, mercury is collected from an acidified water sample by displacement of silver in a silver screen. The screen is heated in a commercially available radiofrequency induction furnace, and the evolved mercury is measured in a mercury-vapor absorption detector (Vaughn and McCarthy, 1964).

The detector is basically an atomic-absorption instrument utilizing the 2537-angstrom line of mercury. To minimize interferences, the vapor to be measured is first passed over a silver amalgamator that is subsequently heated; the mercury vapor thus evolved is then passed into the absorption chamber of the detector.

As little as 0.1 part per billion of mercury or 10 nanograms (1×10^{-9} grams) in a 100-milliliter sample can easily be detected. Larger or smaller sample volumes can be used as desired.

EQUIPMENT AND REAGENTS

In addition to standard laboratory equipment such as beakers and volumetric ware, the following items are necessary:

Acetone
Hydrochloric acid, concentrated
Sulfuric acid, concentrated
Silver gauze screens, 2-inch diameter, 80 mesh
Shaking table
Screwcap jars for storing the silver screens

U.S. GEOL. SURVEY PROF. PAPER 650-D, PAGES D251-D254

359-403 O—69——17

Induction furnace, Leco model 523, operating at 14.6 megahertz
Vapor absorption detector

PROCEDURE

All glassware should be washed with 1:1 sulfuric acid between runs. The silver screens should also be cleaned between runs by heating in the radiofrequency induction furnace.

Place 100 ml of the sample, containing less than 500 mg of Hg, or a suitable aliquot diluted to 100 ml, in a 400-ml beaker. Add 10 ml of concentrated HCl and a clean silver screen to each beaker. For aliquots larger than 100 ml add 10 ml of concentrated HCl for every 100 ml of sample and run blanks of corresponding volumes. Oscillate the beakers on the shaking table for 1 hour. Then decant the sample solutions and rinse the screens three times with demineralized water and finally rinse them with acetone. Place the screens in clean jars and allow them to dry. When the screens are dry, cap the jars until ready for analysis in the vapor detector.

Place a screen in the induction furnace and vaporize the mercury. Then determine the nanograms of mercury in the sample measured by the detector:

$$\text{Mercury, in parts per billion} = \frac{\text{nanograms of mercury in sample}}{\text{sample aliquot in milliliters}}$$

DISCUSSION

Although the silver screens are routinely left in the sample solutions for 1 hour, the displacement reaction is complete within 30 minutes. The amount of mercury recovered is unchanged when the screens are left in the mercury solutions for longer times, even overnight.

Recovery of mercury was consistently 80–90 percent of the mercury contained in standard solutions. The same disparity in recovery applies both to solutions prepared from mercuric salts and to solutions prepared by adding mercury-saturated air to 1*N* HCl. The low recovery could be due to equilibrium between mercuric ions and the silver screens or mercuric ions and the glass beakers. The low recovery could also result from the methods for calibration of standard water solutions and of the mercury detector; standard solutions were prepared from mercuric salts, whereas the vapor-absorption detector was calibrated with different volumes of mercury-saturated air. A calibration curve may be prepared to accommodate this loss; the detector may be calibrated by vaporizing the mercury collected on silver screens immersed in standard solutions, and assuming 100 percent recovery. However, instrument calibration by injection of mercury-saturated air is more convenient than calibration by standard solutions carried through the analytical procedure. For mineral exploration, the consistent loss is not as significant as are anomalies in mercury content among the samples.

Sulfate ion has a repressive effect on mercury recovery. Table 1 gives a comparison of mercury recovered from sulfate solutions with that from chloride solutions; the values are averages of two or more runs. The percentage of mercury recovered from sulfate solutions more concentrated than 2 ng/ml of mercury decreases when hydrochloric acid is absent.

TABLE 1.—*Effect of sulfate on recovery of added mercury*

Mercury added (nanograms)	Mercury recovered from 100 ml (nanograms)				
	1*N* HCl	1*N* H_2SO_4	0.1*M* Na_2SO_4 no acid	0.1*M* Na_2SO_4 1*N* HCl	0.1*M* Na_2SO_4 1*N* H_2SO_4
50	47	45	23	44	51
100	100	117	44	84	88
200	191	200	110	189	154
400	367	399	258	388	317
800	814	469	545	746	558

Bromide-sulfate and iodide-sulfate solutions yielded erratic recoveries of mercury. In general the mercury recovery was highest with chloride, lower with bromide, and lowest with iodide. Approximately 1*N* HCl solutions gave the best recovery.

A composite mixture containing extremely high concentrations of ions found in some natural waters was prepared to check the interferences possible in unusual samples. The composite mixture contained the following ion concentrations: 12 parts per million F; 2,045 ppm B; 15 ppm I; 430 ppm Br; 1,700 ppm SiO_2; 460 ppm PO_4; 35 ppm NO_3; 80 ppm Fe; 1 ppm Se; 50,000 ppm Cl; 102,000 ppm SO_4; 11,800 ppm Na; 78,700 ppm K (Livingstone, 1963, tables 19, 20, 21, 22; White and others, 1963, table 27). From 50 to 800 ng of mercury were added to 100-ml portions of this mixture. Fifty to seventy percent of the added mercury was recovered, although some of the salts in the mixture were undissolved and in suspension. The lower mercury recovery possibly is due to adsorption of mercury on the suspended material.

Possible interferences from organic components of natural waters were checked by adding 400 ng of mercury to four amino acids. No change in mercury recovery was found in solutions of 0.1*M* alanine, 0.1*M* methionine, 0.001*M* cystine, or 0.001*M* cysteine.

During this investigation we found that mercury is adsorbed on the sample bottles soon after sample collection. A water sample stored for 1 month in a polyethylene bottle showed a tenfold decrease in mercury concentration. The empty sample bottle was washed

with 1*N* HCl. After four washings, each with fresh 1*N* HCl, the wash solution still contained significant quantities of mercury which had been adsorbed on the bottle. A new polyethylene bottle of the same brand yielded no mercury after each of four equivalent washings. To test mercury adsorption on glass, three natural-water samples from widely separated localities in Arizona were collected in new acid-washed glass bottles and stored 2 weeks before analysis. The empty sample bottles were rinsed three times with demineralized water, and the rinse water was discarded. The bottles were then washed with 300 ml of 1*N* HCl. Each HCl wash solution contained amounts of mercury that demonstrate significant adsorption on the bottle; the results are shown in table 2.

TABLE 2.—*Adsorption of mercury onto glass bottles from natural-water samples*

Sample	Mercury found (parts per billion)	
	Water	1*N* HCl wash
HL-1	0.4	0.7
HL-2	.2	.1
HL-3	.2	.1

Mercury also may be adsorbed on particulate or colloidal material in a water sample. Three natural-water samples were filtered by suction through 0.45-micron Millipore papers, and the filtrate was analyzed separately from the solids collected on the Millipore paper. The mercury was concentrated on the solids being transported by the waters; table 3 shows a comparison of mercury content in filtered and unfiltered aliquots of these samples. Well-mixed, unfiltered aliquots should provide the most representative sampling of water for exploration purposes, as the mercury carried in suspension may be more significant than the mercury in solution in natural water.

TABLE 3.—*Comparison of mercury found in filtered and unfiltered water*

Sample	Mercury found (mean values in micrograms per liter)		
	Filtered		Unfiltered
	Filtrate	1*N* HCl wash solution containing solids collected on Millipore filter	
C7216	0.1	0.5	0.5
C7217	.1	2.5	1.9
C7218	<.1	.7	.6

A sample could be treated in the field to minimize adsorption problems. A measured quantity of water could be collected in an acid-washed glass bottle, and an appropriate amount of HCl and a silver screen added. The bottle could be oscillated on the shaking table later in the day. The screen then could be removed, dried, and sealed in a jar for analysis by vapor detection at a convenient time.

RESULTS

The precision of the silver-screen method was tested by repeated analyses of solutions containing various amounts of mercury. Analyses were made on 0.1*M* sodium sulfate solutions to test mercury recovery from sulfate concentrations which might be found in natural waters (Livingstone, 1963; White and others, 1963). The range of values, mean values, and relative standard deviations are shown in table 4.

TABLE 4.—*Recovery of added mercury, 10 runs each*

Mercury added (nanograms)	Mercury recovered (nanograms)		Mean and standard deviation	Relative standard deviation (percent)
	High	Low		
50	51	39	45±3	6.7
200	218	163	193±17	8.8
400	388	322	369±23	6.2

Replicate analyses were made on nine natural water samples. The results (table 5) are reproducible considering the small quantities of mercury present in the samples.

TABLE 5.—*Mercury found in natural-water samples*

Sample	Number of runs	Mercury found (micrograms per liter)		Mean and standard deviation
		High	Low	
C7216	6	0.8	0.3	0.5±0.2
C7217	6	2.8	1.1	1.9±0.6
C7218	6	1.2	.4	.6±0.3
C6544	2	.8	.6	.7±0.1
C6545	2	.6	.6	.6±0
C6546	2	5.9	2.5	4.2±1.7
HL-1	7	.8	.2	.4±0.2
HL-2	4	.3	.1	.2±0.1
HL-3	2	.2	.2	.2±0

To test the accuracy of the silver-screen method, samples of natural waters were analyzed by this procedure and also by precipitation with hydrogen sulfide. The sulfide precipitates were analyzed by the vapor-absorption detector. On duplicate samples run simultaneously, H_2S precipitation commonly yielded analytical results with a tenfold spread between high and low values. Table 6 shows comparative results of analyses by the silver-screen method and by H_2S precipitation.

TABLE 6.—*Comparison of mercury found by silver-screen method and by H_2S precipitation*

Sample	Mercury found (mean values in micrograms per liter)	
	Silver-screen method	H_2S precipitation
C7216	0.5	1.2
C7217	1.9	2.8
C7218	.6	1.4
C6544	.7	None
C6545	.6	None
C6546	4.2	1.4

The silver-screen method is expected to be a useful procedure for hydrogeochemical surveys where mercury is utilized as a pathfinder element. Analyses are performed simply, rapidly, and economically. Analysis of samples larger than 100 ml will yield greater sensitivity, but will require more equipment and will be slightly more time consuming. For mineral exploration, the relative differences in mercury concentration among the samples are more important than absolute amounts.

REFERENCES

Beisova, M. P., Generalova, V. A., and Fesenko, N. G., 1965, Determination of mercury in natural waters in connection with evaluation of its contamination: Gidrokhim. Materialy, v. 40, p. 184–187 [In Russian]; *also*, Chem. Abs., 1966, v. 64, p. 17250e.

Cornwall, H. R., Lakin, H. W., Nakagawa, H. M., and Stager, H. K., 1967, Silver and mercury geochemical anomalies in the Comstock, Tonopah, and Silver Reef districts, Nevada-Utah, *in* Geological Survey Research 1967: U.S. Geol. Survey Prof. Paper 575–B, p. B10–B20.

Erickson, R. L., VanSickle, G. H., Nakagawa, H. M., McCarthy, J. H., Jr., and Leong, K. W., 1966, Gold geochemical anomaly in the Cortez district, Nevada: U.S. Geol. Survey Circ. 534, 9 p.

Hawkes, H. E., and Webb, J. S., 1962, Geochemistry in mineral exploration: New York, Harper and Row, Publishers, 415 p.

Hawkes, H. E., and Williston, S. H., 1962, Mercury vapor as a guide to lead-zinc-silver deposits: Mining Cong. Jour., v. 48, no. 12, p. 30–32.

Livingstone, D. A., 1963, Chemical composition of rivers and lakes, *in* Fleischer, Michael, tech. ed., Data of geochemistry [6th ed.]: U.S. Geol. Survey Prof. Paper 440–G, p. G1–G64.

Lombardi, O. W., 1964, Di-β-naphthylthiocarbazone (dinaphthizone) compared with dithizone as an analytical reagent for the determination of trace metals in natural waters—A preliminary investigation: Anal. Chemistry, v. 36, no. 2, p. 415–418.

Marcie, F. J., 1967, X-ray fluorescence determination of trace toxic elements in water: Environmental Sci. and Technology, v. 1, no. 2, p. 164–166.

Schutz, D. F., and Turekian, K. K., 1965, The investigation of the geographical and vertical distribution of several trace elements in sea water using neutron activation analysis: Geochim. et Cosmochim. Acta, v. 29, no. 4, p. 259–313.

Vaughn, W. W., and McCarthy, J. H., Jr., 1964, An instrumental technique for the determination of submicrogram concentrations of mercury in soils, rocks, and gas, *in* Geological Survey Research 1964: U.S. Geol. Survey Prof. Paper 501–D, p. D123–D127.

Warren, H. V., Delavault, R. E., and Barakso, John, 1966, Some observations on the geochemistry of mercury as applied to prospecting: Econ. Geology, v. 61, no. 6, p. 1010–1028.

White, D. E., Hem, J. D., and Waring, G. A., 1963, Chemical composition of subsurface waters, *in* Fleischer, Michael, tech. ed., Data of geochemistry [6th ed.]: U.S. Geol. Survey Prof. Paper 440–F, p. F1–F67.

DIFFERENCES IN SOIL CHEMISTRY INDUCED BY EVAPORATION AND FLOW OF GROUND WATER

By REUBEN F. MILLER, Denver, Colo.

Abstract.—Soil samples from a drainageway between two prairie potholes in North Dakota were analyzed to determine if and how migration of water through and upward from the saturated zone might influence the chemical composition of water flowing from the upper to the lower pond. Water in the unsaturated zone, that apparently achieves capillary equilibrium during the night, subsequently drains back down each day when equilibrium immediately above the water table is disrupted by transpiration. The salinity of water draining back to the water table is apparently increased as a result of transpiration. The proportion of sodium to calcium and magnesium in the water draining back to the water table is increased as a result of ion exchange. These processes produce an increase in both the salinity and proportion of sodium to calcium and magnesium of water arriving at the lower pond from the upper pond.

This investigation was conducted in conjunction with a study to determine the hydrology of the prairie potholes on the Coteau du Missouri in North Dakota (Eisenlohr and Sloan, 1968). The study site is in Ward County, in the NE¼ sec. 36, T. 152 N., R. 83 W, 9 miles north and 3 miles east of the town of Max.

The purpose of this investigation was to determine the influence of chemical processes in soil, under a shallow grassed drainageway connecting two ponds, on the chemical composition of water moving from the upper to the lower pond. The upper pond contained fresh water derived principally from runoff, whereas the lower pond contained saline water.

Differences in soil chemistry, moisture stress, and moisture-retention characteristics, both within and between the sampling sites (fig. 1) at the upper and lower ends of the drainageway, were determined.

The soil at both sites was sampled in consecutive vertical increments from the land surface to the water table and, at the upper site, in consecutive lateral increments just beneath the water table in the direction of flow.

The proportions and quantities of soluble sodium, calcium, and magnesium in individual soil samples were measured so that patterns and modes of recurring moisture migration through the soil could be defined as described by Miller and Ratzlaff (1965). The soluble calcium and magnesium in extracts from saturated samples of soil (Richards and others, methods 2 and 3a, 1954) were determined by versenate titration using Uni Ver, dry indicator-buffer-inhibitor powder, and Hexa Ver CDTA, sequestering agent (manufactured by Hach Chemical Co., Ames, Iowa).

Soluble sodium was determined with a Beckman flame photometer. Total soluble Na + Ca + Mg is reported as TSC (total soluble cations) in this paper, and Na/Na + Ca + Mg × 100 is presented as SSP (soluble sodium percentage). All ion concentrations were computed as milliequivalents per liter of extract from the saturated samples of soil.

Differences in levels of moisture stress in soil samples at the time they were taken from the unsaturated zone above the water table were determined using the filter paper method of McQueen and Miller (1968). Disks of filter paper (Schleicher and Schuell No. 589 White Ribbon) were first treated with 3-percent reagent-grade pentachlorophenol dissolved in ethanol and subsequently air dried. Pentachlorophenol was added to the papers to prevent their decomposition by soil organisms. One disk of treated filter paper was placed in contact with the top of each sample of soil in a

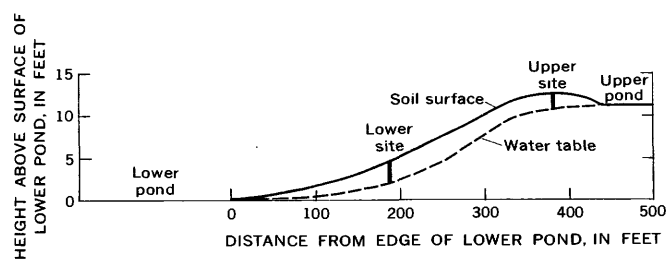

FIGURE 1.—Profile showing locations of sites at which columns of soil were sampled.

metal container. The lid of the container was sealed with plastic tape. Samples were then transported to the laboratory and stored at 20°C for more than a week to allow moisture equilibrium between the filter paper and the soil. After equilibrium was achieved, the filter paper was removed from contact with the soil and placed immediately in an aluminum weighing box, and the weight of the paper and the moisture it contained was determined. The weight of the filter paper was determined after drying it for 24 hours at 110°C.

The stress at which the moisture in each sample was retained by the soil was then determined from the moisture content of the filter paper. Moisture stress is reported as pF, and pF values were computed using relationships between pF and moisture content of filter paper defined by McQueen and Miller (1968). When the moisture content of the paper was less than 54 percent, $pF = \log_{10}S = 6.24617—0.0723M$. When the moisture content of the paper was greater than 54 percent, $pF = \log_{10}S = 2.8948—0.01025M$. S is the moisture stress in centimeters; M is the moisture content of the filter paper.

THEORY

To interpret the data obtained from this investigation, it is essential to understand mechanisms of ion distribution in soils, and how the mechanisms are influenced by the processes of moisture migration and moisture removal from soils.

In previous work, Miller and Ratzlaff (1965) concluded that patterns and modes of moisture migration through soil can be interpreted from relationships between SSP and TSC in soil profiles. Migration of moisture is more apt to leave a chemical imprint on soil profiles during the drying process than during the initial wetting process, because the drying process occurs last and at a time when ions move in closer proximity to exchange surfaces. Both the cation-exchange and salt-precipitation processes can cause progressive losses of multivalent calcium and magnesium from solution, with concomitant gains in monovalent sodium in the direction of moisture migration through soil. Resulting increases in SSP indicate direction of moisture migration. Movement of moisture as films closely adjacent to charged surfaces can also result in a decrease in TSC values in the direction of moisture migration. This process is called salt sieving. Salt precipitation as a result of evaporation can cause TSC values to increase in the direction of moisture migration.

Because a water table was present under the two soil profiles, it is essential to consider what influence moisture migration during the wetting process might have on the chemical composition of the soil. Brooks, Goertzen, and Bower (1958) found that during the wetting process, sodic water can produce a progressive decrease in SSP in the direction of moisture migration. This is the result of mass-action displacement of multivalent ions from exchange surfaces by a continuing supply of monovalent sodium ions. Kemper (1960) also found that there is no salt sieving, and that ion concentrations remain constant when water migrates through clay at degrees of wetness that occur during the wetting process.

It is also essential to understand the moisture-stress levels that might be expected in soil profiles underlain by a water table. McQueen and Miller (1968) report that calibration of filter papers for stress levels below 0.21 bars was determined from field samples obtained at known heights above a water table. A sampling program conducted in conjunction with a study of water use by phreatophytes on the Gila River in Arizona provided data for calibration. Eighteen profiles were sampled to the water table. Moisture stress in centimeters of water was determined from a tentative calibration curve and the stress plotted against height of sample above the water table in centimeters. Parts of several of these profiles could be represented by straight lines with similar slopes. The tentative calibration curve was adjusted to make the slopes of these lines approach a 1:1 relationship. The depths of the zero-stress intercepts of these lines were compared with known depth to the water table and were found to be in agreement. The adjusted calibration curve agreed with the data obtained with the pressure-plate assembly at 0.1 and 0.2 bars of stress. The intersection of the calibration curve developed from data above a water table is near the accepted "field capacity" moisture-stress levels of 0.1 and 0.3 bars. The abrupt change in slope of the calibration curves when plotted on semilogarithmic coordinates (fig. 2) represents a change in rate of curvature that would be evident if the data had been plotted by linear coordinates. This change in rate of curvature probably represents a change in energy level that occurs when gravity drainage or capillary migration upward from the water table is replaced by flow of moisture films over soil surfaces.

A measure indicative of the relative amount of surface available for adsorption and flow of moisture is provided by the saturation moisture capacity of soil samples. Stiven and Khan (1966) found that the SMC (saturation moisture capacity) of soil increases as the proportion of clay to silt and sand in the soil increases. Most of the surface area in soils is provided by clay and humus. Sand and silt provide much less surface per unit of weight than clay does.

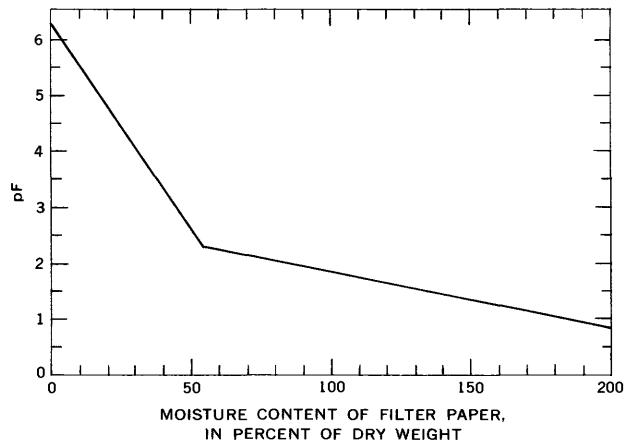

FIGURE 2.—Relation of moisture stress, pF, to moisture content determined for Schleicher and Schuell No. 589 White Ribbon filter paper treated with 3-percent pentachlorophenol in ethanol.

RESULTS AND CONCLUSIONS

The results indicate that the salinity of water, moving through or over the soil in the drainageway between the two ponds, increases as a result of either transpiration by vegetation or evaporation near the soil surface. They also indicate that the proportion of sodium as compared to calcium and magnesium also tends to increase as a result of ion exchange.

To facilitate interpretation of the results, SSP, TSC, pF, and SMC values obtained from the vertical part of the soil profile of each sampling site are plotted against height above the water table (figs. 3 and 4). The SSP, TSC, and SMC values obtained from the laterally sampled part of the upper site are plotted against distance in centimeters from the base of the vertical portion of the soil profile sampled at the upper site. The drop in the level of the surface of the water table is also illustrated (fig. 5).

Transpiration by vegetation apparently causes an increase in the salinity of water flowing through the soil in the drainageway between the two ponds. This is indicated by TSC values that are about twice as great for soil from immediately above the water table at the lower site (fig. 4) as compared with equivalent TSC values from the upper site (fig. 3). Removal of water by transpiration from the capillary fringe above the water table could account for the higher TSC evident just above the water table in both profiles (figs. 3 and 4).

The observed increase in salinity could result from ions being left behind when water is absorbed by roots.

Evaporation of water that migrates from the water table to the surface of the soil in the drainageway could also increase the salinity of the lower pond as compared with that of the upper pond. This is indicated by higher TSC values near the surface of both profiles than in the soil beneath (figs. 3 and 4). Water flowing over the surface of the drainageway would tend to flush salts from the surface soil into the lower pond.

The water draining through the soil in the drainageway from the upper pond into the lower pond should contain a higher proportion of sodium as compared to calcium and magnesium, as a result of ion exchange. This is concluded because SSP values in the soil immediately above the water table are approximately twice as great at the lower site as they are at the upper sampling site. An increase in SSP with distance from the base of the vertical soil profile at the upper sampling site is also evident (fig. 5).

The observations of Miller and Ratzlaff (1965) that SSP values increase in the direction of moisture migration apparently hold true at the sites sampled in this study. This is demonstrated by the observed increase

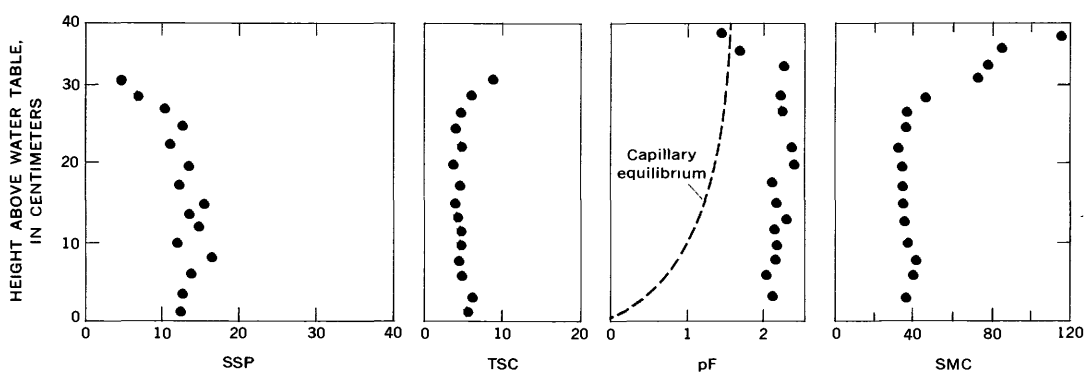

FIGURE 3.—Differences in SSP, TSC, pF, and SMC values with height above the water table, in centimeters, at the upper sampling site. SSP, soluble sodium percentage; TSC, total soluble cations; pF, moisture stress, in centimeters; SMC, saturation moisture capacity. The dashed line on the pF graph represents the pF gradient at equilibrium with the water table.

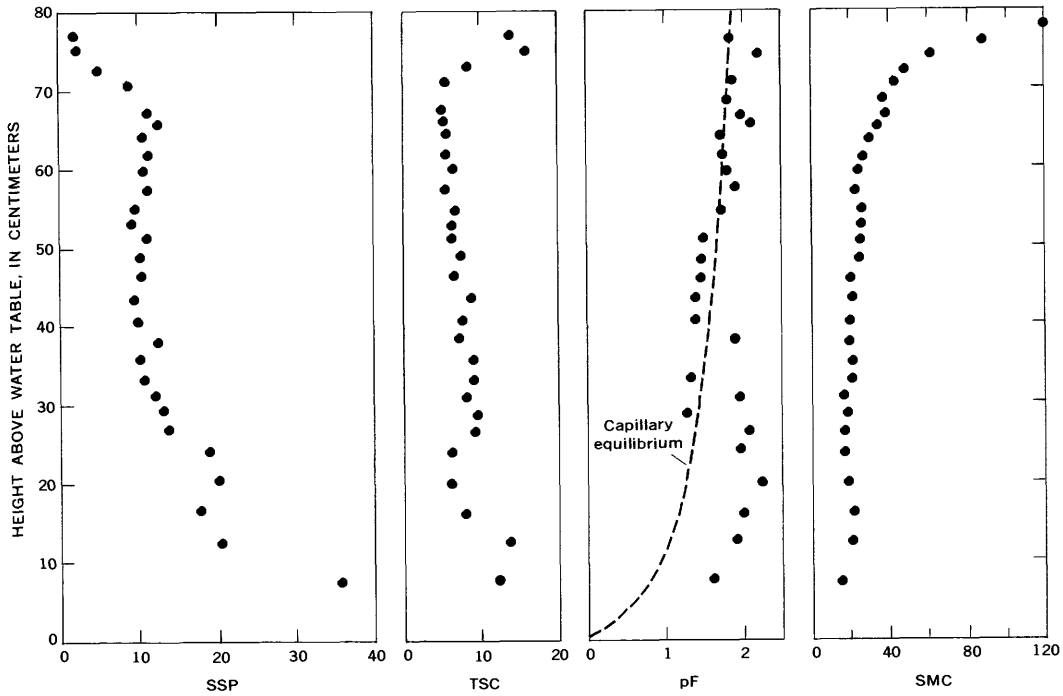

FIGURE 4.—Differences in SSP, TSC, pF, and SMC values with height above the water table, in centimeters, at the lower sampling site. See figure 3 for explanation of terms used.

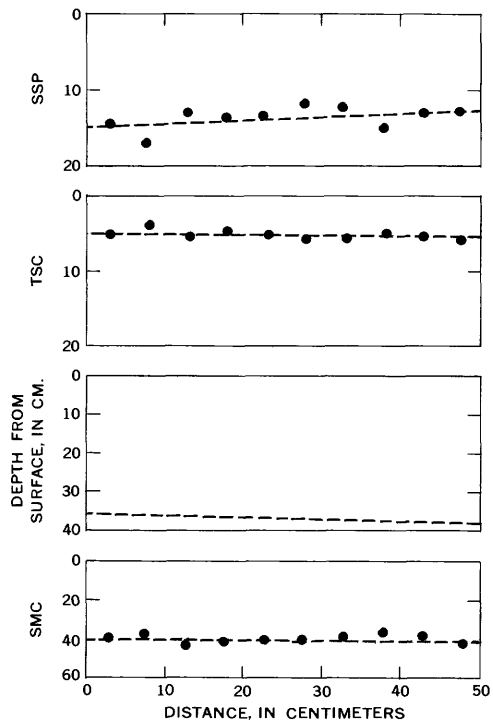

FIGURE 5.—Differences in SSP, TSC, depth to the surface of the water table, and SMC values that occurred with distance from the base of the vertical profile at the upper sampling site. See figure 3 for explanation of terms used.

in SSP values in the direction of lateral flow from the base of the column of soil sampled at the upper site. There apparently was not a high enough proportion of sodium to calcium and magnesium in the ground water to displace calcium and magnesium from exchange surfaces by mass action as observed by Brooks, Goertzen, and Bower (1958).

The lack of any discernible change in TCS in the direction of flow, even though SSP values increased, is in agreement with the findings of Kemper (1960). He found that salt sieving, or decreases in ion concentration, occurred only when moisture flowed in thin films across clay surfaces. He also found that salt sieving did not occur when moisture migrated by gravity flow, or at lower tensions where capillarity could occur.

Lateral flow in response to gravity across the 50-centimeter reach at the upper sampling site would be in response to a drop in head of approximately 1 centimeter whereas, vertical migration of moisture up into the soil above would be in response to capillary stress that would increase 1 centimeter for each centimeter of height above the water table. This tension gradient exists, however, only if capillary equilibrium has been achieved.

The dashed lines in figures 3 and 4 represent the change in pF values with increasing height above the water table at capillary equilibrium.

Vegetation in the drainageway apparently removes water from the capillary fringe above the water table during the day at a faster rate than the water can rise from the water table. This is concluded because, in the part of each of the two soil profiles closest to the water table, pF values are greater than would be expected at capillary equilibrium (figs. 3 and 4).

Capillary equilibrium is probably achieved during the night when transpiration is nil, because, in both soil profiles (figs. 3 and 4), the moisture nearer the surface is adsorbed at lower tensions than the moisture beneath, and pF values approach levels that would be expected at capillary equilibrium. They are considered to be a residual of conditions that existed the previous night.

Withdrawal of water immediately above the water table by transpiration of vegetation could destroy capillary equilibrium and permit drainage to depth in response to gravity. This is best illustrated by the pF data from the lower site (fig. 4). Water immediately above the depths at which withdrawal has apparently occurred as a result of transpiration is present at lower pF values than would be expected at capillary equilibrium whereas, moisture in the soil nearer the surface is adsorbed at higher pF levels. This indicates that moisture held at pF values lower than equilibrium is probably draining down in response to gravity from the depths where pF levels are higher.

This daily cyclic drainage of water from the surface toward the water table apparently results in the observed increase in SSP values from the surface of the soil toward the water table as a result of ion exchange.

The results also provide evidence that in the soil just below the water table (fig. 5) the amount of adsorptive surface present in the soil can have some influence on chemistry. A measure of the relative amount of adsorptive surface in soil is provided by its SMC. SSP values tend to decrease when SMC values increase, and SSP values increase when SMC values decrease. TSC values also tend to decrease and increase as SMC values increase and decrease.

The observed changes in SSP, as the adsorptive surface in soil varies, are more difficult to explain than the observed variations in TSC values. It seems logical that more ions should be adsorbed per unit of soil as the amount of adsorptive surface increases because there would be more negative charge to attract positively charged cations. The increase in the proportion of sodium in the soil as the surface area decreases, and the decrease as surface area increases must be influenced in some manner by the ion-exchange process.

An explanation of the observed differences would at best be speculation. More research would be required to explain the observed interactions between variations in amount of adsorptive surface and the proportions of monovalent and divalent ions in solution.

REFERENCES

Brooks, R. H., Goertzen, J. O., and Bower, C. A., 1958, Prediction of changes in the composition of dissolved and exchangeable cations in soils upon irrigation with high-sodium waters: Soil Sci. Soc. America Proc., v. 22, p. 122–124.

Eisenlohr, W. S., Jr., and Sloan, C. E., 1968, Generalized hydrology of prairie potholes in the Coteau du Missouri, North Dakota: U.S. Geol. Survey Circ. 558, 12 p.

Kemper, W. D., 1960, Water and ion movement in thin films as influenced by the electrostatic charge and diffusion of cations associated with clay mineral surfaces: Soil Sci. Soc. America Proc., v. 24, p. 10–16.

McQueen, I. S., and Miller, R. F., 1968, Calibration and evaluation of a wide-range gravimetric method for measuring moisture stress: Soil Sci., v. 106, no. 3, p. 225–231.

Miller, R. F., and Ratzlaff, K. W., 1965, Chemistry of soil profiles indicates recurring patterns and modes of moisture migration: Soil Sci. Soc. America Proc., v. 29, p. 263–266.

Richards, L. A., and others, 1954, Diagnosis and improvement of saline and alkali soils: U.S. Dept. Agriculture Handb. 60, 160 p.

Stiven, G. A., and Khan, M. A., 1966, Saturation percentage as a measure of soil texture in the lower Indus Basin: Soil Sci. 17, p. 255–263.

TWO-DIMENSIONAL DISPERSION IN A GRANULAR-MEDIUM DISK SOURCE EMITTING AT CONSTANT RATE

By AKIO OGATA, Honolulu, Hawaii

Abstract.—A solution of the two-dimensional differential equation of dispersion from a disk source is developed utilizing a point-source solution which appears frequently in heat-transfer problems. Because of the complexity of the solution, expressions applicable along a given axis ($r = o$ and $r = a$) were obtained to facilitate computation of the dispersion coefficients for a given laboratory test.

Two-dimensional dispersion in a granular medium has not been studied in any detail owing to both analytical and laboratory difficulties. In order to characterize dispersion in a porous medium in directions transverse and parallel to the flow, the process has been studied separately by employing simplified mathematical models, as for example, Harleman and Rumer (1962) and Ogata (1964). Because of the linearity of the differential equation governing the dispersion process this procedure is valid and values of the coefficient obtained should truly represent the components of the dispersion tensor. However, in study of dispersion in the laboratory it is generally more difficult to construct models that represent transverse dispersion only. Thus, this study is directed toward the development of expressions that may be readily calculated in order to compute the components of the dispersion.

The mathematical model assumes that tracer fluid is discharged from a circular disk source into a porous medium at a constant rate equal to the rate of flow of the surrounding fluid. The solution of the differential equation is readily obtained when the point-source solution is used. That is, because the equation is similar to the heat transfer equation with the addition of the convective transport term, solutions obtained in heat transfer problems can be directly utilized.

TERMINOLOGY

The terms used in the analysis are defined as follows:

C	concentration
C_0	reference concentration
D_z and D_r	dispersion coefficient in directions z and r
u	interstitial velocity or Darcy velocity divided by porosity
x, y, z, r	dimensional coordinates
t	time
Q	strength of source; rate of flow
a	radius of the circular surface source
$J_n(x)$	Bessel function of the first kind of order n
$I_n(x)$	modified Bessel function of the first kind of order n
$\mathrm{erf}(x)$	error function
$\mathrm{erfc}(x)$	$1-\mathrm{erf}(x)$=complimentary error function
$J(x, y)$	$1-x^{1/2}\int_0^\infty e^{-\tau}J_0(2\sqrt{\tau y})J_1(2\sqrt{\tau x})\frac{d\tau}{\sqrt{\tau}}$
α	$ux/4D_z$
β^2	$u^2t/4D_z$
γ^2	$4D_zD_r/u^2$
θ^2	$a^2/\gamma^2=a^2u^2/4D_zD_r$.

DIFFERENTIAL EQUATION AND SOLUTION

Assume that a finite circular disk of radius a, located at $z=0$, emits fluid of concentration $C=C_0$ into a semi-infinite medium from time $t=0$ to $t=t$. The governing differential equation for dispersion in a undirectional flow field, in cylindrical coordinates with radial symmetry, is (Bachmat and Bear, 1964)

$$D_z\frac{\partial^2 C}{\partial z^2}-u\frac{\partial C}{\partial z}+\frac{D_r}{r}\frac{\partial}{\partial r}\left(r\frac{\partial C}{\partial r}\right)=\frac{\partial C}{\partial t}, \qquad (1)$$

where $r^2=x^2+y^2$ and u is the interstitial velocity. The medium is assumed isotropic in regard to flow characteristics; hence, the dispersion coefficient is dependent only on direction and is independent of position vectors $\vec{z}$ and $\vec{r}$ and time t (Bear, 1961; Scheidegger, 1961).

If we substitute $Z=z-ut$ and $t=\tau$ in equation 1 and rewrite t for τ, the differential equation takes the form

$$D_z\frac{\partial^2 C}{\partial Z^2}+\frac{D_r}{r}\frac{\partial}{\partial r}\left(r\frac{\partial C}{\partial r}\right)=\frac{\partial C}{\partial t}. \tag{2}$$

Equation 2 is the more familiar diffusion or heat-flow equation for an anisotropic system. Solutions obtained for the heat transfer problems are applicable since the linear transformation $Z=z-ut$ does not rotate the frame of reference.

Since the problem is the same as that of a heat source located at $x=0$, the solution of equation 2 can be obtained readily by using the expression for an instantaneous point source in an anisotropic medium. The expression for an instantaneous point source as given by Carslaw and Jaeger (1959, p. 257, eq. 8) is

$$\frac{Q}{8(\pi^3 t^3 D_z D_x D_y)}\exp\left\{-\frac{1}{4t}\left[\frac{(z-z')^2}{D_z}+\frac{(y-y')^2}{D_y}+\frac{(x-x')^2}{D_x}\right]\right\}.$$

For a moving source, Carslaw and Jaeger (1959, p. 266) indicate that the coordinates $(x,y,z-ut)$ may be used. Hence, by writing the above equation in terms of $Z=z-ut$ and $r^2=x^2+y^2$ and also noting that because of symmetry, $D_x=D_y=D_r$, we can write the expression as

$$\frac{Q}{8(\pi^3 t^3 D_z D_r^2)^{1/2}}\exp\left\{-\frac{1}{4t}\left[\frac{(Z-Z')^2}{D_z}+\frac{r^2+r'^2-2rr'\cos\theta}{D_r}\right]\right\}.$$

To obtain solution for an instantaneous disk source the above equation needs to be integrated about θ from 0 to 2π and r from 0 to a, or

$$\frac{Q}{8(\pi^3 t^3 D_z D_r)^{1/2}}\exp\left(-\frac{Z^2}{4D_z t}\right)\int_0^a \exp\left(-\frac{r^2+r'^2}{4D_r t}\right) r' \int_0^{2\pi}\exp\left(\frac{2rr'\cos\theta}{4D_r t}\right) d\theta' dr'.$$

The results of the two integrations are shown by Carslaw and Jaeger (1959, p. 259, eq. 5, and p. 260, eq. 9).

For the specific case of the instantaneous disk source emitting with strength $Q=C_0\,u$ from a source of radius a, the solution is

$$\frac{C}{C_0}=\frac{ua}{2\sqrt{\pi D_z t}}\exp\left(-\frac{Z^2}{4D_z t}\right)\int_0^\infty e^{-D_r t\lambda^2} J_0(r\lambda)\,J_1(a\lambda)\,d\lambda. \tag{3}$$

Thus, if we replace Z by $z-ut$ and integrate expression 3 for all times between 0 and t, an integral equation for a continuous source is obtained, that is

$$\frac{C}{C_0}=\frac{ua}{2\sqrt{\pi D_z}}\exp\left(\frac{uz}{2D_z}\right)\int_0^t \exp\left[-\frac{z^2}{4D_z(t-\tau)}-\frac{u^2(t-\tau)}{4D_z}\right] \int_0^\infty e^{D_r(t-\tau)\lambda^2} J_0(\lambda r)\,J_1(\lambda a)\,\frac{d\tau}{(t-\tau)^{1/2}}d\lambda.$$

When we substitute

$$\xi^2=u^2(t-\tau)/4D_z,\ \alpha=uz/4D_z,\ \beta^2=u^2t/4D_z,$$

$$\gamma^2=4D_zD_r/u^2,$$

the above equation is written

$$\frac{C}{C_0}=\frac{2ae^{2\alpha}}{\sqrt{\pi}}\int_0^\beta e^{-\xi^2-\alpha^2/\xi^2} \int_0^\infty e^{-\gamma^2\xi^2\lambda^2} J_0(r\lambda)\,J_1(a\lambda)\,d\lambda d\xi.$$

This expression cannot be integrated without writing the second integral in terms of an infinite series. This procedure is extremely tedious, and the resulting expressions are too cumbersome to be used in analysis of data. The expression, however, may be written in two alternate forms which are useful in deriving approximate expressions. The first is obtained by noting that (Goldstein, 1953)

$$1-J(x,y)=x^{1/2}\int_0^\infty e^{-\tau}J_0(2\tau^{1/2}y^{1/2})J_1(2\tau^{1/2}x^{1/2})\frac{d\tau}{\tau^{1/2}}.$$

Hence,

$$\frac{C}{C_0}=\frac{2e^{2\alpha}}{\sqrt{\pi}}\int_0^\beta e^{-\xi^2-\alpha^2/\xi^2}\left[1-J\left(\frac{a^2}{4\gamma^2\xi^2},\frac{r^2}{4\gamma^2\xi^2}\right)\right]d\xi. \tag{4}$$

The J-function frequently occurs in diffusion and heat-flow problems and has been tabulated to some extent.

The alternate expression is obtained by writing equation 4 as

$$\frac{C}{C_0}=\frac{2ae^{2\alpha}}{\sqrt{\pi}}\int_0^\infty J_0(r\lambda)J_1(a\lambda)\int_0^\beta e^{-(1+\gamma^2\lambda^2)\xi^2-\alpha^2/\xi^2}d\xi d\lambda. \tag{5}$$

If we let $\zeta^2=(1+\lambda^2\gamma^2)\xi^2$, the second integral may be written

$$\int_0^{\beta\sqrt{1+\gamma^2\lambda^2}} e^{-\zeta^2-\alpha^2(1+\gamma^2\lambda^2)/\zeta^2}\frac{d\zeta}{\sqrt{(1+\gamma^2\lambda^2)}}.$$

Horenstein (1945) indicates that the above integral written in terms of the error function is

$$\int_0^a e^{-\eta^2-b^2/\eta^2}d\eta=\frac{\sqrt{\pi}}{4}e^{-2b}\operatorname{erfc}\left(\frac{b}{a}-a\right) \frac{\sqrt{\pi}}{4}e^{2b}\operatorname{erfc}\left(\frac{b}{a}+a\right).$$

Hence, equation 4 may also be expressed as

$$\frac{C}{C_0}=\frac{ae^{\frac{uz}{2D_z}}}{2}\int_0^\infty J_0(r\zeta)J_1(a\zeta)\left\{\exp\left(-z\sqrt{\frac{u^2}{4D_z^2}+\frac{D_r}{D_z}\zeta^2}\right)\operatorname{erfc}\left(\frac{z}{2\sqrt{D_zt}}-\sqrt{\frac{u^2t}{4D_z}+D_rt\zeta^2}\right)-\exp\left(z\sqrt{\frac{u^2}{4D_z^2}+\frac{D_r}{D_z}\zeta^2}\right)\operatorname{erfc}\left(\frac{x}{2\sqrt{D_zt}}+\sqrt{\frac{u^2t}{4D_z}+D_rt\zeta}\right)\right\}\frac{d\zeta}{\sqrt{1+\frac{4D_zD_r}{u^2}\zeta^2}}. \quad (6)$$

These expressions, equations 4 and 6, may be evaluated by complex numerical integration since subroutines of the Bessel function and error function are available. The numerical computation would require that estimates of the values of the dispersion coefficients in one of the two directions be known, because of the various groupings in which the terms D_z and D_r appear. However, for the purpose of evaluating the coefficients of dispersion using experimental data it would be desirable to obtain simpler expressions. Thus expressions applicable to steady-state condition and along $r = a$ and $r = 0$ are developed.

STEADY-STATE SOLUTION

For steady-state condition the concentration distribution can be obtained from equation 6 by first noting that

$$\operatorname{erfc}(-\infty)=2,\ \operatorname{erfc}(\infty)=0.$$

When we let $1/\delta=u\ a/2\ \sqrt{D_zD_r}$ and $\rho=r/a$, equation 6 reduces to

$$\frac{C}{C_0}=\int_0^\infty \exp\left[2\alpha(1-\sqrt{1+\delta^2\lambda^2})\right]J_0(\lambda\rho)J_1(\lambda)\frac{d\lambda}{\sqrt{1+\delta^2\lambda^2}}. \quad (7)$$

Here again no further reduction can be obtained. Numerical integration can again be carried out by writing the product of the Bessel function as a series and integrating term by term.

A special case of interest is when $D_z\to 0$. The term $4D_zD_r\lambda^2/u^2a^2$ becomes small; hence, the radical is approximated by $(1+\delta^2\lambda^2/2)$. Equation 7 becomes

$$\frac{C}{C_0}=a\int_0^\infty e^{-\alpha\delta^2\lambda^2}J_0(\lambda\rho)J_1(\lambda)\frac{d\lambda}{\sqrt{1+\delta^2\lambda^2}}$$

and for $D_z=0$, the expression further reduces to

$$\frac{C}{C_0}=a\int_0^\infty \exp\left(-\frac{D_rx}{u}\lambda^2\right)J_0(\lambda\rho)J_1(\lambda)d\lambda. \quad (8)$$

Equation 8 is the approximation obtained by Ogata (1961).

CONCENTRATION DISTRIBUTION ALONG $r = o$ AND $r = a$

The expressions previously obtained are generally cumbersome for use in the analysis of experimental data unless restrictive approximations are made. More readily computable expressions are obtained along the axis of symmetry, $r = 0$ and $r = a$. It would be of interest to first consider equation 4 from which expressions for steady-state condition can readily be obtained.

The J-function has been studied in detail by Goldstein (1953). A property which can be readily established is that

$$J(x, 0)=e^{-x}.$$

Hence, substituting the above expression into equation 4 gives

$$\left.\frac{C}{C_0}\right|_{r=0}=2\frac{e^{2\alpha}}{\sqrt{\pi}}\int_0^\beta \exp\left(-\xi^2-\frac{\alpha^2}{\xi^2}\right)[1-\exp(-a^2/4\gamma^2\xi^2)]d\xi. \quad (9)$$

The integral $\int_0^a \exp(-\eta^2-b^2/\eta^2)\,d\eta$ appeared in equation 5 and can be expressed in terms of the tabulated error function. With the use of the relationship the concentration distribution along $r=0$ is given as

$$\left.\frac{C}{C_0}\right|_{r=0}=\frac{1}{2}\left[\operatorname{erfc}\left(\frac{z-ut}{2\sqrt{D_zt}}\right)-e^{uz/D_z}\operatorname{erfc}\left(\frac{z+ut}{2\sqrt{D_zt}}\right)\right]-\frac{1}{2}\exp\left[\left(\frac{uz}{2D_z}\left(1-\sqrt{1+\frac{a^2D_z}{z^2D_r}}\right)\right)\right]\left[\operatorname{erfc}\left(\frac{\sqrt{z^2+a^2D_z/D_r}-ut}{2\sqrt{D_zt}}\right)\right]+\exp\left[\left(\frac{uz}{2D_z}\left(1+\sqrt{1+\frac{a^2D_z}{z^2D_r}}\right)\right)\right]\operatorname{erfc}\left(\frac{\sqrt{z^2+a^2D_z/D_r}+ut}{2\sqrt{D_zt}}\right)\Bigg]. \quad (10)$$

For steady state, that is as $t\to\infty$, $\operatorname{erfc}(-\infty)=2$, $\operatorname{erfc}(\infty)=0$ and equation 10 reduces to

$$\left.\frac{C}{C_0}\right|_{r=0}=1-\exp\left[\frac{uz}{2D_z}\left(1-\sqrt{1+\frac{a^2}{z^2}\frac{D_z}{D_r}}\right)\right]. \quad (11)$$

When steady state is realized the concentration distribution along $r=0$ is given by an exponential function, equation 11, that can be easily calculated. This expression indicates that when constant flow of contaminant into the semi-infinite medium is maintained the concentration of the circular source at $z=0$ is given by

$$\left.\frac{C}{C_0}\right|_{r=0} = 1 - \exp\left(-ua/2\sqrt{D_z D_r}\right).$$

The expression indicates that the value of the concentration ratio at $z=0$ is unity only at smaller values of $D_z D_r$. That is, for value $ua/2\sqrt{D_z D_r} \geq 4.7$ the concentration at $x=0$ may be taken as C_0.

The expression for concentration distribution along $r=a$ may be obtained by using equation 4. However, no simplification is realized; therefore, only the steady-state condition (where $t \to \infty$) will be considered. It is noted that (Luke, 1962)

$$J(x, x) = \frac{1}{2}\left[1 + e^{-2x} I_0(2x)\right],$$

which when we substitute it into equation 4 and let $\beta \to \infty$ gives

$$\left.\frac{C}{C_0}\right|_{r=a} = -\frac{e^{2\alpha}}{\sqrt{\pi}} \int_0^\infty e^{-\xi^2 - \alpha^2/\xi^2}\left[1 - \exp\left(-\frac{a^2}{2\gamma^2\xi^2}\right) I_0\left(\frac{a^2}{2\gamma^2\xi^2}\right)\right] d\xi$$

$$= \frac{1}{2} - \frac{e^{2\alpha}}{\sqrt{\pi}} \int_0^\infty e^{-\xi^2 - \frac{\alpha^2+\theta^2/2}{\xi^2}} I_0\left(\frac{\theta}{2\xi^2}\right) d\xi, \quad (12)$$

where $\theta^2 = a^2/\lambda^2 = a^2 u^2/4D_z D_r$.

In order to evaluate the integral in equation 12 we write (Erdelyi and others, 1953)

$$e^{-x} I_0(x) = {}_1F_1\left(\frac{1}{2}; 1; -2x\right) = e^{-2x}\, {}_1F_1\left(\frac{1}{2}; 1; 2x\right),$$

where ${}_1F_1\ (a;\ c;\ x)$ is the confluent hypergeometric function. ${}_1F_1$ by definition is represented by

$${}_1F_1(a; b; 2x) = \sum_{m=0}^{\infty} \frac{(a)_m}{m!(b)_m} (2x)^m,$$

where $(a)_0 = 1$, $a_m = a\ (a+1)\ (a+2)\ \ldots\ (a+m-1)$. Substituting the hypergeometric function into equation 12 gives

$$\left.\frac{C}{C_0}\right|_{r=a} = \frac{1}{2} - \frac{e^{2\alpha}}{\sqrt{\pi}} \int_0^\infty e^{-\xi^2 - \frac{\alpha^2+\theta^2}{\xi^2}} \sum_{m=0}^{\infty} \frac{(1/2)_m}{m!(1)_m} \left(\frac{\theta^2}{\xi^2}\right)^m d\xi.$$

If we change the order of summation and integration, the above expression becomes

$$\left.\frac{C}{C_0}\right|_{r=a} = \frac{1}{2} - \frac{e^{2\alpha}}{\sqrt{\pi}} \sum_{m=0}^{\infty} \frac{(1/2)_m}{(m!)^2} \theta^{2m} \int_0^\infty e^{-\xi^2 - \frac{\alpha^2+\theta^2}{\xi^2}} \frac{d\eta}{\xi^{2m}}. \quad (13)$$

The first term of the summation is

$$\frac{e^{2\alpha}}{\sqrt{\pi}} \int_0^\infty e^{-\xi^2 - \frac{\alpha^2+\theta^2}{\xi^2}} d\xi = \frac{1}{2} \exp\left(2\alpha - 2\sqrt{\alpha^2+\theta^2}\right).$$

Furthermore, if we let $\xi^2 = \lambda$ the integral in equation 13 becomes

$$\frac{1}{2} \int_0^\infty e^{-\lambda - \frac{\alpha^2+\theta^2}{\lambda}} \frac{d\lambda}{\lambda^{m+1/2}}.$$

The integral above is an integral representation of the modified Bessel function of the second kind, that is

$$K_\nu(az) = \frac{1}{2} a^\nu \int_0^\infty e^{-\frac{1}{2}z\,(t + a^2/t)} \frac{dt}{t^{\nu+1}};$$

$$Re\ z > 0,\ Re\ (a^2 z) > 0,$$

where $Re\ z$ indicates the real part of z. Thus, equation 13 may be written in terms of the Bessel function or

$$\left.\frac{C}{C_0}\right|_{r=a} = \frac{1}{2}\left[1 - \exp\left(2\alpha - 2\sqrt{\alpha^2+\theta^2}\right)\right]$$

$$- \frac{2e^{2\alpha}}{\sqrt{\pi}} \sum_{m=1}^{\infty} \frac{(1/2_m)}{(m!)^2} \frac{\theta^{2m}}{(\sqrt{\alpha^2+\theta^2})^{m-1/2}} K_{m-\frac{1}{2}}\left(2\sqrt{\alpha^2+\theta^2}\right). \quad (14)$$

Equation 14 is readily calcuated for any value of α^2 and θ^2 inasmuch as tables for the one-half order Bessel function are available. In addition, the Bessel function of the order one-half of an odd integer can be represented by an elementary function, that is,

$$K_{n+\frac{1}{2}}(z) = \left(\frac{\pi}{2z}\right)^{1/2} e^{-z} \sum_{k=0}^{n} (2z)^{-k} \frac{\Gamma(n+k+1)}{k!\ \Gamma(n+1-k)}.$$

The series, however, converges slowly for small values of $\sqrt{\alpha^2+\theta^2}$; for example, when $2\sqrt{\alpha^2+\delta^2} = 5$ the tenth term in the series is of the order 2.5×10^{-3}. The series, on the other hand, can be used effectively for α^2 large or z^2 large. Furthermore, in instances where the argument of the Bessel function is very large, only the first term in the series needs to be considered. Then equation 14 becomes

$$\left.\frac{C}{C_0}\right|_{r=a} = \frac{1}{2} - \frac{1}{2}\left(1 + \frac{\theta}{\sqrt{\alpha^2+\theta^2}}\right) \exp\left(2\alpha - 2\sqrt{\alpha^2+\theta^2}\right) \quad (15)$$

or

$$\left.\frac{C}{C_0}\right|_{r=a} = \frac{1}{2}\left.\frac{C}{C_0}\right|_{r=0} - \frac{\theta}{\sqrt{\alpha^2+\theta^2}} \exp\left(2\alpha - 2\sqrt{\alpha^2+\theta^2}\right).$$

Whenever equation 15 is valid, the dispersion coefficient can be computed readily when used in conjunction with equation 11. Computation of equation 14 is now being carried out. With its completion, data reported by the author previously (Ogata, 1964) will be reworked to determine the suitability of this approximation. In addition, solution for the boundary value problem $C = C_0$ for $0 \leq r \leq a$ is being developed.

REFERENCES

Bachmat, Y., and Bear, Jacob, 1964, The general equations of hydrodynamic dispersion in homogeneous, isotropic, porous medium: Jour. Geophys. Research, v. 69, no. 12, p. 2561–2567.

Bear, Jacob, 1961, On the tensor form of dispersion in porous media: Jour. Geophys. Research, v. 66, no. 4, p. 1185–1198.

Carslaw, H. S., and Jaeger, J. C., 1959, Conduction of heat in solids: Oxford Univ. Press, 510 p.

Erdelyi, A., Magnus, W., Oberhettinger, F., and Tricomi, F. G., 1953, Higher transcendental functions, v. II: New York, McGraw-Hill Book Co., 396 p.

Goldstein, S., 1953, On the mathematics of exchange processes in fixed columns: Royal Soc. (London) Proc., v. 219, p. 151.

Harleman, D. R. F., and Rumer, R. R., Jr., 1962, The dynamics of salt-water intrusion in porous media: Massachusetts Inst. Technology Hydrodynamics Lab. Rept., no. 55, 125 p.

Horenstein, W., 1945, On certain integrals in the theory of heat conduction: Quart. Applied Mathematics, v. 3, p. 183.

Luke, Y. L., 1962, Integrals of Bessel functions: New York, McGraw-Hill Book Co., 419 p.

Ogata, Akio, 1961, Transverse diffusion in saturated isotropic media: U.S. Geol. Survey Prof. Paper 411-B, 8 p.

——— 1964, The spread of a dye stream in an isotropic granular medium: U.S. Geol. Survey Prof. Paper 411-G, 11 p.

Scheidegger, A. E., 1961, General theory of dispersion in porous media: Jour. Geophys. Research, v. 66, no. 10, p. 3273–3278.

DIFFUSION FROM A GASEOUS SOURCE IN A POROUS MEDIUM—A FIELD AND THEORETICAL COMPARISON

By JOHN B. ROBERTSON, Idaho Falls, Idaho

Work done in cooperation with the U.S. Atomic Energy Commission

Abstract.—Small volumes of air containing a radioactive krypton-85 tracer were injected into fine-grained sediments at the National Reactor Testing Station, Idaho. Dissipation of the Kr^{85} gas away from the injection points was observed by recording the gamma radioactivity in the holes. A mathematical model was adapted from a heat-flow analogy to estimate the amount of molecular diffusion occurring in the system. The observed field data match the theoretical diffusion curves closely, indicating that most of the observed outflow was due to diffusion.

The injection and movement of gases underground are currently being investigated at the National Reactor Testing Station (NRTS), Idaho. Part of the study involves the evaluation of natural influences on gas flow through the unconsolidated surface sediments. In a series of field tests, small volumes of air traced with krypton-85 (Kr^{85}), a radioactive gas with a half-life of 10.8 years, were injected into fine-grained playa deposits and allowed to dissipate under ambient pressure and temperature.

The observed dissipation was thought to consist of two principal flow mechanisms—molecular diffusion and convective mass flow. The objective of this study is to evaluate the relative magnitudes of the two components. Any convective flow in the system must be due to buoyant effects or natural pressure gradients created by changes in temperature, wind velocity, barometric pressure, etc. The complexity of these gradients makes the convective flow component difficult to analyze quantitatively.

The theory of diffusive flow is well developed (Crank, 1956) and the experimental conditions in this study lend themselves to theoretical evaluation. This paper summarizes the approach and results of the diffusion analysis.

EXPERIMENTAL CONDITIONS

The tests were conducted in relatively fine-grained sedimentary deposits of the Birch Creek playa, a dry lake bed in the northern part of the NRTS. In the test area, the sediments are about 40 feet thick and are underlain by a thick sequence of basalt flows. The material is relatively uniform, consisting of 90 percent clay and silt. Four undisturbed samples, taken at depths of 3, 4, 4.5, and 5 feet, had an average porosity of 32.8 percent (ranging from 32.0 to 33.9 percent) and an average bulk density of 1.82 grams per cubic centimeter. Five other samples, collected at depths of from 2 to 10 feet, had the following average characteristics (range of values in parenthesis):

Moisture content=9.1 percent (7.3 to 10.7 percent)
Clay content (<0.004 millimeters)=48 percent (45 to 51 percent)
Silt content (0.004 to 0.0625 millimeters)=42 percent (36 to 51 percent) and
Sand content (0.0625 to 1.0 millimeters)=10 percent (2 to 13 percent).

These parameters showed no particular trends with depth. Theoretically the molecular diffusion properties of the medium depend primarily on its porosity and moisture content and are not directly dependent on permeability. These diffusional relationships are described more thoroughly later in the text.

The data above indicate that porosity and moisture content are rather uniform for the depths sampled. Subsequent sampling in some nearby similar playa sediments (about 3,000 feet away) displayed similar uniformity from depths of 5 feet to 29 feet. The major mineral constituents of these nearby samples were mixed layered clays, illite, montmorillonite, quartz, calcite, and hornblende. The sediments displayed a

fine-grained horizontal platy structure and vertical hairline fractures forming irregular prisms several inches in diameter. Walls of trenches cut into the sediments showed no evidence of conspicuous bedding, although there were a few subtle transitions in sediment characteristics. The structural patterns together with even the limited amount of bedding create heterogeneous and anisotropic permeability conditions in the sediments. However, because molecular diffusion is not directly related to permeability, the medium can be considered relatively homogeneous and isotropic in its diffusion properties.

Four injection holes and two observation holes, ranging in depth from 2.5 feet to 15 feet, were augered (fig. 1). A metal cage was installed in the bottom of each hole to maintain a cavity about 3 liters in volume. The hole was then filled to the surface with expanding cement. Figure 2 shows the construction of the injection holes. A Geiger-Müller tube, previously installed in the center of each cage, was used to measure radioactivity of the Kr^{85}. Each hole was equipped with a thermocouple for temperature measurement and three copper access tubes, ⅛-inch inside diameter, for the injection or removal of gas. A sealed pipe provided access for the tubes and wires to the land surface. Count rates and temperatures were recorded on digital punch tape and later processed and plotted by a computer.

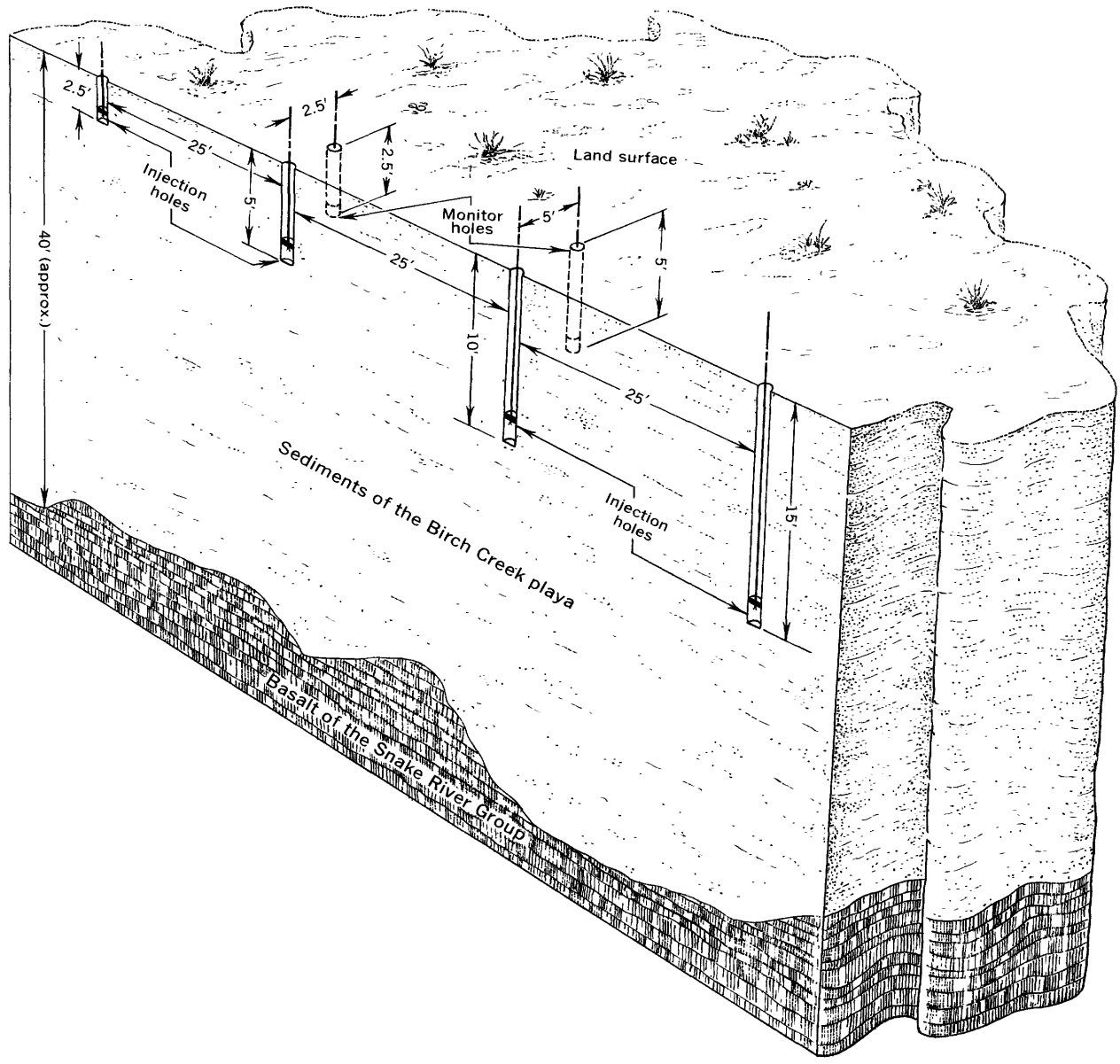

FIGURE 1.—Cutaway diagram showing the arrangement of injection and monitor holes in the Birch Creek playa, northern part of National Reactor Testing Station, Idaho.

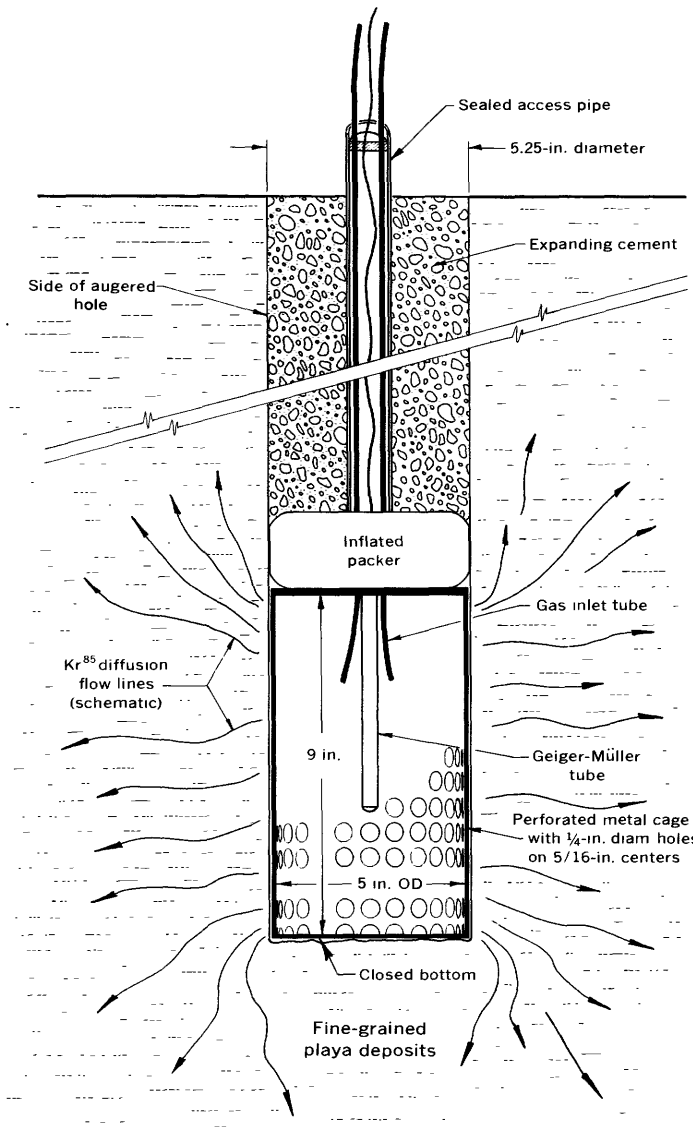

FIGURE 2.—Diagram of an injection hole.

Two tests were conducted; in each test, 3 standard liters of air containing 1 microcurie of Kr^{85} per liter were rapidly injected into each of the four injection holes. The detected diminution of radioactivity in the four injection holes resulted from outflow of Kr^{85}. Similarly, any significant inflow of Kr^{85} into the two observation wells would have caused an anomalous increase in activity above background. Test 1 had some instrument failure and lacked sufficient control. The evaluation described in this report is therefore restricted to test 2, which was much more reliable.

SUMMARY OF DIFFUSION THEORY

A theoretical estimate of the diffusive flow which should occur under the given field conditions can be developed from the basic laws of diffusion. The diffusion theory, as applicable to this problem, can be summarized by Fick's first and second laws. The first law states that the rate of transfer of a diffusing gas through a unit cross-sectional area is proportional to the concentration gradient normal to the section:

$$F=-D\frac{\delta c}{\delta x}, \tag{1}$$

where F is the unit flow rate; c, the concentration of diffusing gas; x, the normal direction; and D is the diffusion coefficient. The diffusion coefficient is assumed constant in this study but depends on the type of diffusing gas, the gas into which the first gas diffuses, and the nature of the porous medium. In this study, Kr^{85} diffused into the air. Henceforth, the symbol D_0 will be used to denote the diffusion coefficient of Kr^{85} into free air and D will denote the same property in the porous medium.

Fick's first law together with that for conservation of mass yields the second differential equation of diffusion (Fick's second law),

$$\frac{\delta c}{\delta t}=D\left(\frac{\delta^2 c}{\delta x^2}+\frac{\delta^2 c}{\delta y^2}+\frac{\delta^2 c}{\delta z^2}\right), \tag{2}$$

where t is time, and x, y, and z are the three normal coordinate directions. Solution of equation 2 will yield the concentration, c, of the diffusing gas at any time, t, and any position (x, y, z) in open space. Because a porous medium contains less open space for the diffusing gas to occupy (or less storage capacity) than a completely open medium, equation 2 must be altered to take this factor into account. This alteration is accomplished by dividing the diffusion coefficient by the gas-filled porosity.

Although this porosity effect has been noted previously by others (for example, Penman, 1940), it has been overlooked in many published studies; for this reason, a more detailed explanation is presented here. It was found that dividing the diffusion coefficient in equation 2 by the porosity of the medium would account for this effect. In a nonsteady diffusion system, such as in this test, the concentration of diffusing gas in a unit cube of porous medium (sediment) changes with time. For example, assume that the concentration increases from c_1 to c_2 in a given time; part of the diffusing gas increases the concentration. The amount expended depends on the magnitude of the increase and the porosity of the medium. This amount can be expressed mathmatically as concentration change times pore volume of the cube, or

$$(c_2-c_1)\times\theta=A, \tag{3}$$

where θ is the porosity and A is the quantity of diffusing gas taken into storage within the cube. For a unit

change in concentration, $c_2-c_1=1$. Therefore, the quantity, A, expressed for a unit concentration change per unit volume, would be $A=1\times\theta=\theta$. It could also be thought of as the amount of diffusing gas released from storage per unit volume per unit decrease in concentration. Thus, the rate of concentration change in equation 2 would be amplified by the factor $1/\theta$ for porous media so that

$$\frac{\delta c}{\delta t}=\frac{D}{\theta}\left(\frac{\delta^2 c}{\delta x^2}+\frac{\delta^2 c}{\delta y^2}+\frac{\delta^2 c}{\delta z^2}\right). \quad (4)$$

The term D/θ will henceforth be referred to as diffusivity, K. Equation 4 then becomes

$$\frac{\delta c}{\delta t}=K\left(\frac{\delta^2 c}{\delta x^2}+\frac{\delta^2 c}{\delta y^2}+\frac{\delta^2 c}{\delta z^2}\right). \quad (5)$$

For an open medium the porosity is equal to one and the diffusivity becomes equal to the diffusion coefficient.

The solution to equation 5 will yield the concentration of diffusing gas at any time, t, for any point (x, y, z) in a homogeneous isotropic, porous medium. The nature of the solution depends on the initial and boundary conditions of the particular system. Except for very simple situations, obtaining a solution becomes difficult. However, laws of diffusion flow are mathematically analogous to those of heat flow (Crank, 1956). Fick's first law (equation 1), for instance, is analogous to Fourier's law of heat flow,

$$Q=-K_t\frac{\delta T}{\delta x}, \quad (6)$$

where Q is the heat flux; k_t, the thermal conductivity of the medium; and $\delta T/\delta_x$, the temperature gradient in the direction of flow. Equation 5 also has a heat-flow equivalent. Solutions to a great number of heat-flow boundary-value problems have been published in a variety of sources. A solution to the subject diffusion problem might be adapted, therefore, from an existing solution of an equivalent heat-flow problem.

FIELD DIFFUSION CONDITIONS

The actual geometric boundary conditions in this problem, although relatively simple, cannot easily be duplicated mathematically. The process is further complicated by its nonsteady state. However, with certain simplifications, the boundary conditions can be approximated in a form that lends itself more readily to analysis.

First, the playa deposit, although only 40 feet thick, might be assumed to be of infinite extent in all directions when compared to the small size of the injection cavities and the small amount of Kr^{85} involved, particularly for the deeper injection holes (fig. 1). Second, the diffusivity of the playa material must be assumed to be homogeneous and isotropic; that is, the porosity, moisture content, and other factors affecting the diffusive properties are considered constant in space and time. These conditions were discussed and the assumptions justified earlier in the text.

The cylindrical geometry of the injection cavity (fig. 2) can be simplified by assuming it to be a sphere with the same surface area available for diffusion. The field injection cavities are 5.25 inches in diameter by 9.0 inches long with a wall area of 148 square inches and a volume of 195 cubic inches. A sperical cavity having the same surface area would have a diameter of 6.86 inches and a volume of 175 cubic inches.

Another necessary assumption is that the diffusion coefficient of Kr^{85} in the hollow, air-filled injection cavity is infinite relative to that in the porous medium. This is reasonable, first, because convective mixing probably occurs in the injection cavity, and secondly the diffusion coefficient in the cavity is about 50 times greater than that in the porous playa material, as will be shown later. This assumption is necessary for the further assumption that the radioactive count rate detected by the centrally-placed Geiger Müller tube is representative of the average Kr^{85} concentration (plus background) in the cavity. It may also be assumed that the initial charging of the injection cavity is instantaneous and affects only the interior of the cavity. Although the actual injection of the gas took a finite time of a few seconds, it could be considered instantaneous compared to the diffusion rates. Finally, it is assumed that there is no sorption or solution of the Kr^{85} gas on or in the mineral material or its contained moisture. This is probably reasonable in that Kr^{85} is a relatively inert noble gas.

The simplifying assumptions can be summarized in two statements:

1. The injection hole represents an instantaneous spherical source of inert Kr^{85}.
2. Diffusion proceeds from this source into a homogeneous, isotropic, porous medium of infinite extent.

Even with these simplifications, the solution of the problem is somewhat complex. Crank (1956, equation 3.8, p. 27) published a solution to equation 5 for an instantaneous spherical volume source in an infinite medium. That solution is for the simplified conditions described above except that the spherical source consists of a medium similar to that surrounding it rather than the more realistic hollow sphere. The equation is rather complex and tedious to evaluate. Carslaw and Jaeger (1959) provided a simpler solution to the

heat-flow equivalent of equation 5 for an instantaneous spherical surface heat source (rather than a spherical volume source). Their equation gives the temperature, T, at a point at any radial distance, r, from the center of the sphere:

$$T=\frac{Q'}{8\pi rr'(\pi K_t t)^{1/2}}\left[e^{-(r-r')^2/4K_t t}-e^{-(r+r')^2/4K_t t}\right], \quad (7)$$

where t is the time from the introduction of the instantaneous heat source; Q', the strength of the source; r', the radius of the source; and K_t, the thermal diffusivity of the medium. The diffusion equivalent of this equation was quantitatively compared to the more complicated Crank equation and found to give almost identical results for the conditions of this study. Although the initial conditions for the two equations are slightly different, they rapidly approach the same solution. The effect of the initial differences are short term and insignificant in this problem. Equation 7 was therefore selected as the most suitable model for relative simplicity without a significant sacrifice of accuracy.

To convert equation 7 to the appropriate diffusion equation, it is necessary only to replace the heat terms with analogous diffusion terms. Temperature is an index of heat concentration, so it is replaced by the concentration of Kr^{85}, as counts per minute (cpm), c. The r, r', and t terms remain the same for both cases. The thermal diffusivity, K_t, is replaced by the diffusion diffusivity, K, of the medium. The thermal strength, Q', of the source is defined as the temperature to which the total amount of heat liberated would raise a unit volume of the substance. It may be converted to the diffusion source strength, Q, by defining it as the concentration (or count rate) to which the total amount of Kr^{85} liberated by the injection cavity (source) would raise a unit volume of the playa material.

The converted diffusion equation would therefore be

$$c=\frac{Q}{8\pi rr'(\pi Kt)^{1/2}}\left[e^{-(r-r')^2/4Kt}-e^{-(r+r')^2/4Kt}\right], \quad (8)$$

where c is the concentration of Kr^{85} at any distance, r, from the injection hole and any time, t, after the injection of gas.

EVALUATION OF THE DIFFUSION EQUATION

In order to establish a theoretical Kr^{85} concentration-versus-time curve for any location at distance, r, from an injection well, it is necessary to evaluate the strength (Q) and diffusivity (K) for the actual field conditions.

Diffusion coefficient

The accurate determination of a diffusion coefficient in a natural porous medium requires complex equipment and sampling techniques and is quite difficult. A rather unsuccessful attempt was made to measure this property on five samples of the playa material at Harvard University by Dr. P. C. Reist (written commun., 1967). Successful determinations were made on only one sample, 10 inches square by 2 inches thick. The measurements were in the vertical direction. The average value measured was 0.00273 square centimeters per second (cm^2/sec) or 1.52 square inches per hour (in^2/hr) at field pressure and temperature. A value obtained from a single small sample is not necessarily representative of the entire playa deposit. Consequently, the diffusion coefficient for this system was estimated by another means.

Millington (1959) derived a method for estimating the diffusion coefficient, D, of one gas into air in porous media if the porosity, water content, and diffusion coefficient, D_0, of the gas in free air are known. His geometric derivation describes the effects of reduced area available for diffusion and increased path length, or tortuosity, caused by the porous medium. It appears reasonably valid; he assumes only that the pores of the medium represent approximate spheres of various sizes. His formula relating D to D_0 is

$$D/D_0=\left(\frac{n}{m}\right)^2(\theta_1)^{4/3}, \quad (9)$$

where θ_1 is the gas-filled porosity in a moist sample, and $\frac{n}{m}$ is the proportion of gas-filled pore volume to total pore volume.

The gas-filled porosity, θ_1, can therefore be related to total porosity, θ, so that $\theta_1=\frac{n}{m}\theta$. The n/m ratio can be calculated from

$$\frac{n}{m}=\frac{\theta-\frac{\text{volume of } H_2O}{\text{bulk volume}}}{\theta}, \quad (10)$$

where

$$\frac{\text{volume of } H_2O}{\text{bulk volume}}=\frac{V_W}{V_B}$$

$$=[H_2O \text{ content (dry wt. basis)}][\text{dry bulk density}]. \quad (11)$$

With a moisture content of 9.1 percent (the average of five samples previously described),

$$\frac{V_W}{V_B}=(1.82)(0.091)=0.165 \text{ cm}^3/\text{cm}^3; \quad (12)$$

and with a porosity of 0.328,

$$\frac{n}{m}=\frac{\theta-\frac{V_W}{V_B}}{\theta}=\frac{0.328-0.165}{0.328}=0.497, \quad (13)$$

$$\theta_1=\frac{n}{m}\theta=(0.497)(0.382)=0.163, \text{ and} \quad (14)$$

$$\frac{D}{D_0}=\left(\frac{n}{m}\right)^2(\theta_1)^{4/3}=(0.497)^2(0.163)^{4/3}=0.0221. \quad (15)$$

Bolch, Selleck, and Kaufman (1967, p. 79) give a value of D_0 for Kr^{85} in air of 0.157 cm²/sec at a pressure of 1 atmosphere and temperature of 300°K (27°C). This value of D_0 was then corrected to actual field temperature and pressure conditions by means of the Leonard-Jones equation (Bolch and others, 1967, equation 36, p. 23). The average pressure of the field area was 0.835 atm and the temperature between the depths of 5 feet and 15 feet in the playa sediment was 14°C (287°K). Corrected to these conditions, D_0 becomes 0.175 cm²/sec. The porous medium diffusion coefficient, D, is given, then, by $D=0.0221\ D_0=0.0221\ (0.175)=0.00387$ cm²/sec=2.16 in.²/per hr. The value measured vertically on one sample (1.52 in.²/per hr) is about 30 percent lower than the value calculated above. If the diffusivity is anisotropic, it would probably be higher horizontally than vertically because of grain orientation. Such an effect could explain the difference between the measured and estimated values. Such a difference could also be due to point-to-point variations in the medium which would average out on a large scale. Using the estimated value of D, the diffusivity, K, can be obtained from

$$K=D/\theta_1=\frac{2.16}{0.165}=13.1 \text{ in.}^2 \text{ per hr.} \quad (16)$$

Equation 8 can now be evaluated for field conditions using the estimate $K=13.1$ in.² per hr.

Injection holes

At an injection hole, $r=r'=3.43$ inches and equation 8 becomes

$$c=\frac{Q}{8\pi rr'(\pi Kt)^{1/2}}[1-e^{-(r+r')^2/4Kt}]. \quad (17)$$

The strength, Q, can be determined from

$$Q=\frac{\text{(initial count rate) (injection cavity volume)}}{\theta_1}. \quad (18)$$

For test 2 conditions, the average initial count rate in the injection holes was 4.0×10^5 cpm and the injection cavity volume 195 cubic inches so that

$$Q=\frac{(4.0\times10^5)\ (195 \text{ in}^3)}{0.163}=4.78\times10^8. \quad (19)$$

With the substitution of values of r, r', K, and Q equation 17 becomes

$$c=\frac{4.78\times10^8}{8\pi(3.43)^2(6.42)t^{1/2}}[1-e^{-(6.85)^2/4Kt}]$$

$$=\frac{2.52\times10^5}{t^{1/2}}[1-e^{-0.895/t}]. \quad (20)$$

By adding background radioactivity, c_b, to equation 20 and substituting time values, a gross-count-rate versus time curve can be obtained. However, the determination of the proper background value is a major problem. The background radiation was attributed primarily to radon-222 buildup in the sediments. Its intensity varied considerably with time and location and the tests themselves introduced additional disturbances. Because only gross activity could be observed during testing, it was impossible to differentiate background counts from Kr^{85} counts. The natural pretest background (measured in all six holes) generally followed a diurnal cyclic fluctuation; mean levels ranged from 200 to 2,000 cpm, with daily deviations of 10 to 30 percent. However, for simplicity in this analysis, it is desirable to use a level background value. Data before and after the field test indicate an average value near 1,200 cpm. Adding that value to equation 20 will yield the theoretical curve shown in figure 3. The sharp fluctuations in the curves for the 5-foot and 10-foot holes are instrumental variations rather than actual Kr^{85} or background radiation changes. Data for the 2.5-foot injection hole are not shown for two reasons. First, that hole deviates the most from the assumed boundary conditions and background value, and second, the figure is less cluttered without it.

The figure compares the theoretical curve to the actual curves obtained in the field from the three deepest injection holes. Figure 4 shows the same theoretical curve plotted with the observed curve from the 15-foot injection hole. Of the four holes, this one is considered to best fit the theoretical assumptions because it is the deepest and therefore farthest removed from atmospheric irregularities and boundary effects, and it had the least instrument variations. Therefore, it yielded the closest fitting curve to the theoretical plot. Also shown on figure 4 is the theoretical plot obtained by using the measured D of 1.52 in.² per hr in place of the estimated 2.16 in.² per hr.

Land-surface boundary effect

The assumption of an infinite medium in the vertical direction may not be valid because of the proximity of the ground-surface boundary. However, this boundary can be described mathematically with image theory.

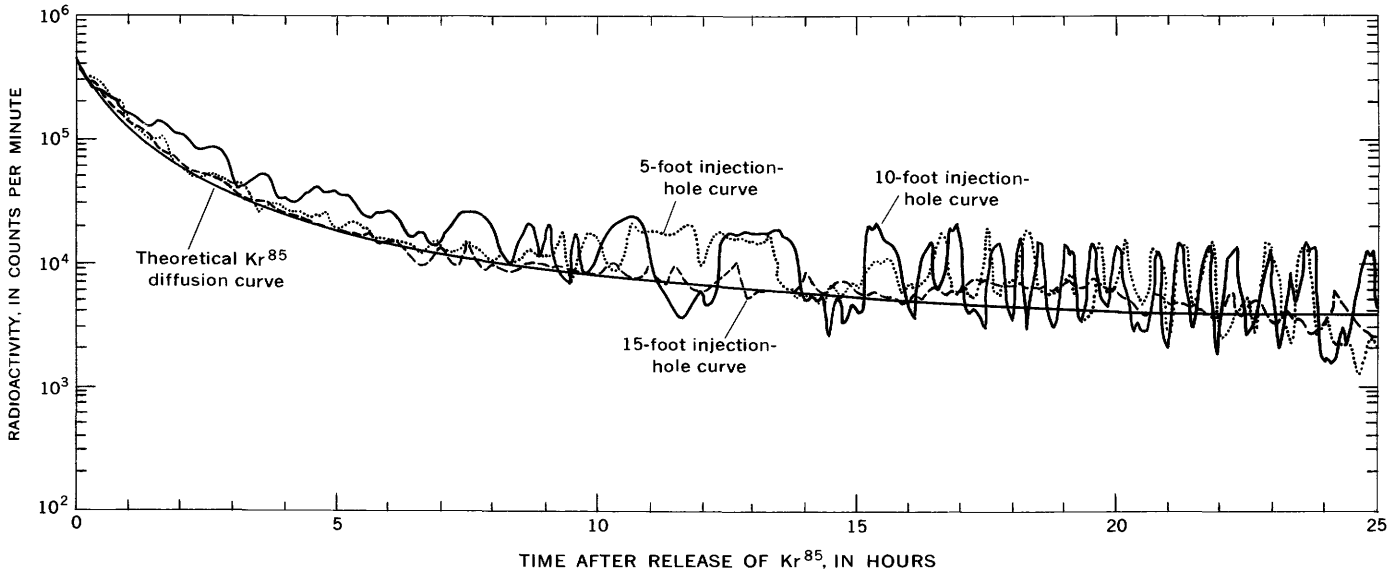

FIGURE 3.—Comparison of the theoretical diffusion curve (equation 20 plus background) to three field test curves.

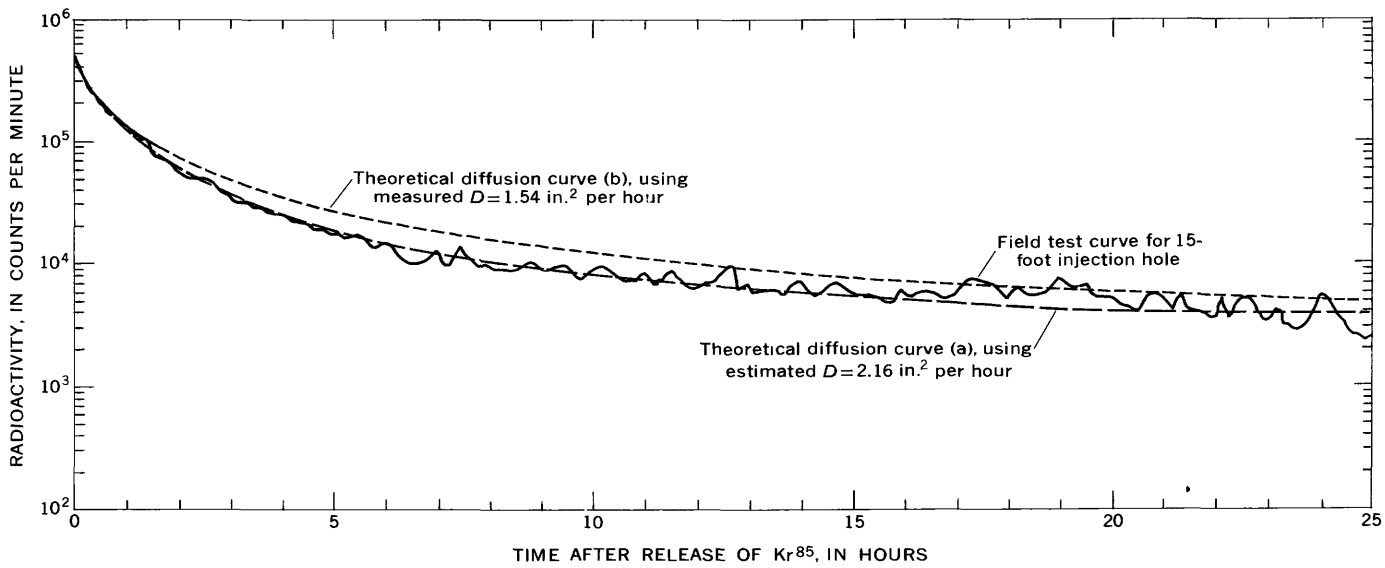

FIGURE 4.—Comparison of the field test curve for the 15-ft injection hole to two theoretical diffusion curves derived from (a) estimated diffusion coefficient of 2.16 in.^{2} per hour, and (b) measured diffusion coefficient of 1.52 in.^{2} per hour.

An imaginary diffusion sink above each injection hole at a height above ground equal to the hole depth, would provide the same effect as the boundary. The image sinks would have the same properties as the injection-hole sources, except their strength, Q (magnitude), would be opposite in sign. To include the boundary effect on the injection-hole count rate, the contributions from the image sinks have to be subtracted. For example, the image of the 2½-foot hole is 5 feet away. The image contribution would therefore be equation 8 evaluated for $r = 5$ feet. The maximum effect was calculated to be —161 cpm 50 hours after injection. It would be considerably less during the first 20 hours when the Kr^{85} diffusion is most important. The effects from the other image sinks would be much less, since they are farther removed. The influence of the ground-surface boundary, then, is clearly insignificant in comparison to the gross counts.

Monitor holes

Equation 8 can also be used to predict the concentration of Kr^{85} at any time in the monitor holes. The value of r is substituted to represent the distance from the bottom of the injection hole to the detection point in the monitor hole. The amount of Kr^{85} in a monitor hole would initially be zero, but would build up to a

maximum and then decrease as the wave of diffusing Kr^{85} passed.

Of the two monitor holes, the one near the 5-foot injection hole (fig. 1) should show a greater peak Kr^{85} concentration because it is nearer an injection point. That monitor hole is 2½ feet deep and the detection point is 42.4 inches away from the 5-foot-deep injection cavity. Therefore, equation 8 can be evaluated using $r=42.4$ inches. For these conditons, $Q=4.78\times10^8$ cpm in.^{3} and $K=13.1$ in.^{2} per hr. Equation 8, then, becomes

$$c=\frac{4.78\times10^8}{8\pi(42.4)(3.43)(\pi13.1)^{1/2}t^{1/2}}\left[e^{-(42.4-3.43)^2/4(13.1)t}\right.$$

$$\left.-e^{-(42.4+3.43)^2/4(13.1)t}\right]=\frac{2.05\times10^4}{t^{1/2}}\left[e^{-29.1/t}-e^{-40.1/t}\right]. \quad (21)$$

Figure 5 shows the plot of equation 21 plus a background of 600 cpm compared to the observed field curve of the 2½-foot monitor hole. The theoretical peak increase in Kr^{85} activity is about 460 cpm over background. This increase is less than background and even less than the normal fluctuations in background. Therefore, a buildup of 460 cpm from Kr^{85} in the monitor hole could be somewhat obscured by the erratic background. However, the field curve shows a rise coincident with the theoretical Kr^{85} increase. Any build-up in a more distant monitor hole would be less and would be further obscured. A boundary effect was also calculated for the monitor wells with image theory. However, the nearest image would be about 8 feet away and would have an insignificant effect (less than 50 cpm).

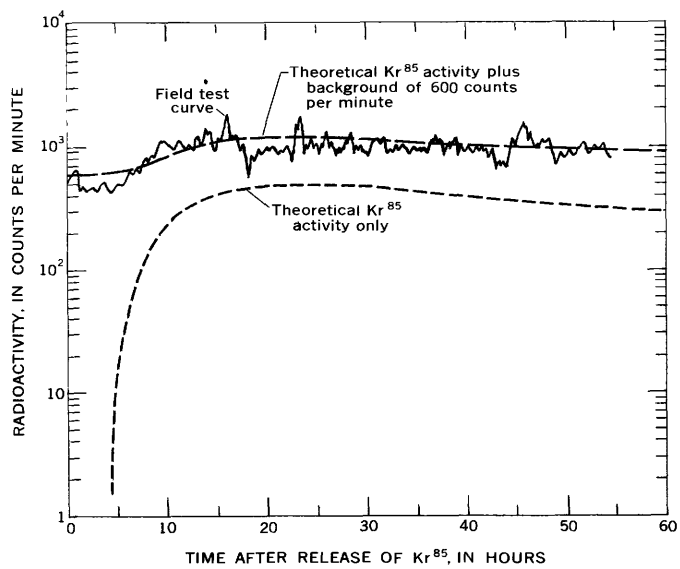

FIGURE 5.—Theoretical curves of Kr^{85} influx into the 2½-foot monitor hole, with and without background, compared to field test curve.

CONCLUSIONS

The observed field data match the theoretical plots rather closely on figures 3, 4, and 5. This suggests that the Kr^{85} dissipated from the injection cavities primarily by the diffusion process and that there was no significant convective flow. Because this is an indirect analysis, there is no conclusive proof that the flow was by diffusion alone. However, it does demonstrate that it is possible for diffusion to account for the field observations.

The principal restriction that prevents a more direct appraisal of diffusion with this approach is the lack of a reliable measured diffusion coefficient for the field medium. If the theoretically estimated value deviates greatly from the actual value, the resultant diffusion curves could be inaccurate; however, the estimated value for D appears to be reasonable.

The assumption of an isotropic medium may not be entirely valid as there undoubtedly was some anisotropy involved. Limited field observations and sampling indicated some anisotropic structural features, but the factors controlling diffusion were relatively uniform. Although vertical moisture variation was apparently small, horizontal variation could cause some heterogeneity. However, there is no evidence to indicate strong variations. Considerably more sampling areally and vertically would be needed to adequately verify the assumption of isotropic, homogeneous conditions.

Another source of error in the theoretical evaluation is the lack of accurate data on the background count which is added to the net count rate. As pointed out above, this is the principal problem preventing the determination of the net addition of Kr^{85} counts in the monitor holes. Due to the erratic variability of the background count in space and time, and instrument noise, it would be nearly impossible to accurately define it.

A simpler analysis of this diffusion problem could be made by assuming an instantaneous point source rather than a spherical source. This, however, would deviate further from the actual conditions and was not carried out in this study.

The field tests for this study were designed and conducted under the general direction of Mr. B. L. Schmalz, U.S. Atomic Energy Commission. His help is greatly appreciated.

REFERENCES

Bolch, W. E., Selleck, R. E., Kaufman, W. J., 1967, Gas dispersion in porous media, Peclet-Reynolds number correlations: SERL Rept. 67–10, Sanitary Engineering Research Laboratory, Univ. California, Berkeley, 124 p.

Carslaw, H. S., and Jaeger, J. C., 1959, Conduction of heat in solids: London, Oxford University Press, p. 259.

Crank, J., 1956, The mathematics of diffusion: London, Oxford University Press, 347 p.

Millington, R. J., 1959, Gas diffusion in porous media: Science, v. 130, p. 100–102.

Penman, H. L., 1940, Gas vapor movements in the soil: Internat. Jour. Agr. Sci., v. 30, p. 437–462.

RESPONSE OF GAS-PURGED MANOMETERS TO WATER-LEVEL SURGES

By J. R. BECK and C. R. GOODWIN, Menlo Park, Calif.

Prepared in cooperation with the California Department of Water Resources

Abstract.—This report describes tests conducted to evaluate the performance of bubble-gage servocontrolled manometers when operating in a lake or stream whose water level is oscillating at amplitudes and frequencies that are likely to be found at medium or high stages in streams or in larger bodies of water subject to wind action. Two types of units were tested—one made by the Exactel Instrument Co., and the other a U.S. Geological Survey manometer. Results of the tests indicate that gas-purged manometers produce an accurate record of water stage under static conditions but indicate a stage value less than the mean of the surge when surface waves of significant amplitudes and frequencies are present.

Bubble gages are used by the U.S. Geological Survey for sensing and recording water levels. Figure 1 is a diagrammatic sketch of a typical bubble-gage system. These sensing devices have several important advantages over float-type systems for recording water levels on continuous analog or digital recorders. Advantages include simplicity of installation, resulting in lower cost, since a float well is not required; relative ease of changing orifice location in unstable channels; and high salvage value when relocating or discontinuing a gaging station. Further, the manometer and recorder can be located some distance away from the orifice, free from the threat of floods.

In order to determine the effect of oscillating water-surface levels on the stage recorded by bubble gages, manometer response to both cyclic and abrupt changes in stage was tested. Cyclic tests included sinusoidal inputs to the orifice of approximately 2, 5, and 10 cycles per minute at amplitudes of 0.1 and 0.2 foot. The abrupt tests consisted of step inputs of 0.2 and 0.4 foot to the orifice.

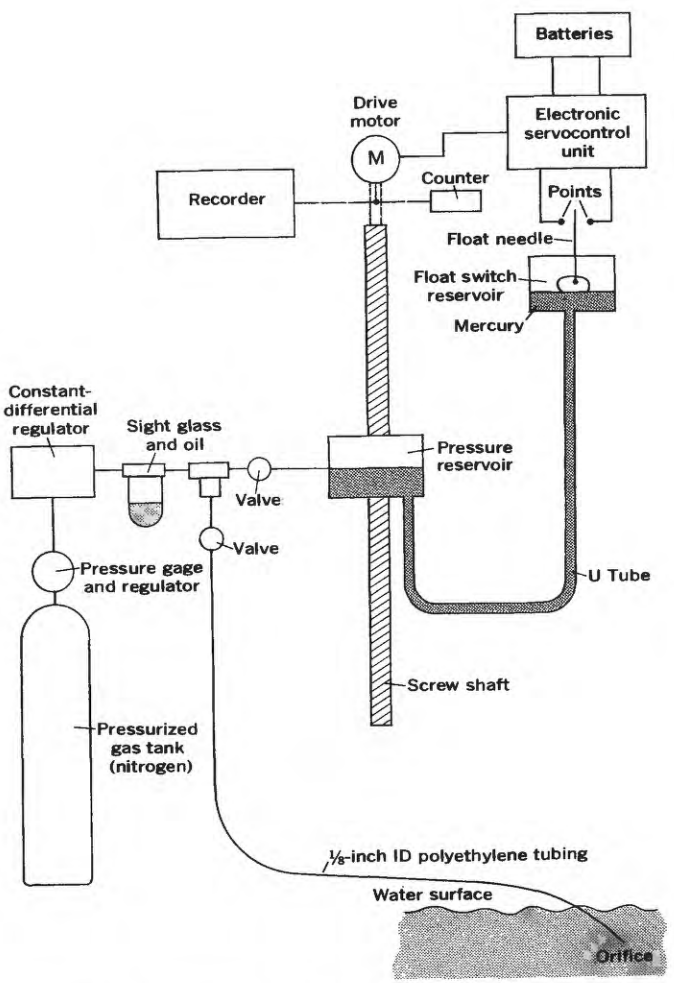

FIGURE 1.—Diagrammatic sketch of U.S. Geological Survey gas-purged manometer.

MANOMETER OPERATION

In a typical bubble-gage system, as diagramed in figure 1, bottled gas is forced into the system at a constant rate. The gas exits from a submerged orifice and rises as bubbles to the water surface. The greater the head of water above the orifice, the greater the pressure must be in the top of the pressure reservoir

to force the gas out of the orifice. When the head of water above the orifice increases, the pressure forces mercury through the U tube into the float-switch reservoir, thus activating the float switch. When contact is made by the float needle and points, the pressure reservoir is driven down by the drive motor, causing the mercury level in the float-switch reservoir to drop, thus centering the float needle and disconnecting the drive motor. Movement of the pressure reservoir is transmitted through a mechanical system to a counter and recorder. When the head of water above the orifice decreases, the system operates in reverse.

An investigation of the relation between water-surface oscillations and pressure changes at various depths was made because manometers indicate water-level changes by sensing pressure changes below the water surface. The relation between the subsurface and surface points is called the pressure response factor, K, and is the ratio of pressure variation at subsurface points to equivalent pressure change at the mean water surface. (Mean water surface is that surface which would obtain were there no oscillations.) Assuming two-dimensional irrotational theory of wave motion, K, can be obtained using the following equation:

$$K=\frac{\text{Cosh}\left[\frac{2\pi D}{L}\left(1-\frac{Z}{D}\right)\right]}{\text{Cosh}\,\frac{2\pi D}{L}}=\frac{\Delta P}{\Delta H} \quad (1)$$

where

D=depth to bottom water from mean water surface,
L=wave length,
Z=depth to orifice from mean water surface,
ΔP=pressure variation at orifice, and
ΔH=equivalent pressure at mean water surface corresponding to a wave height.

Figure 2 is a plot of these K values for various wave frequencies. From this plot, pressure variations at the orifice can be obtained if the surface oscillation amplitude and frequency are known.

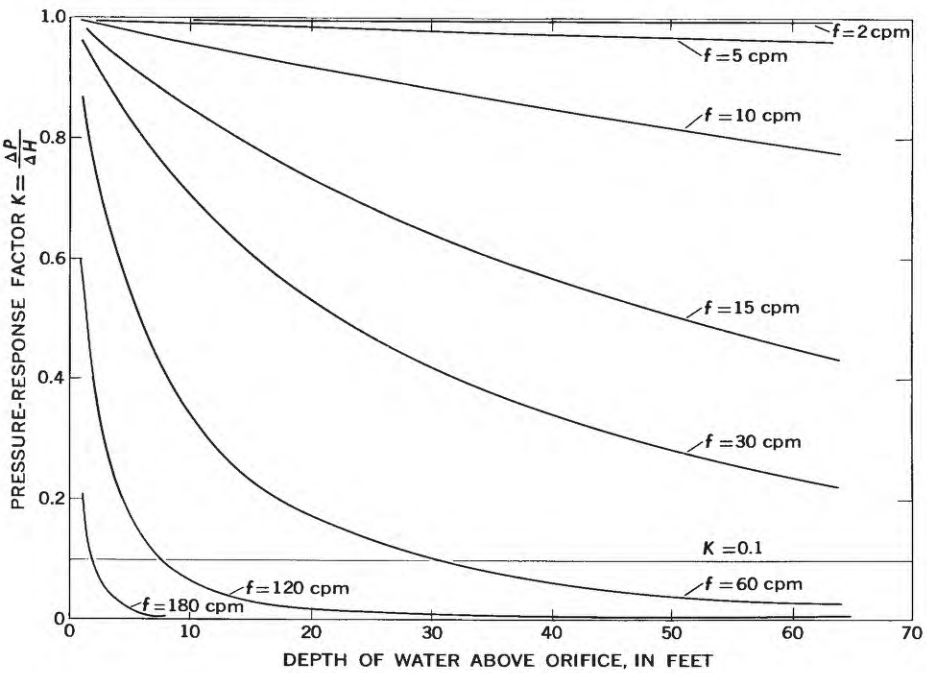

FIGURE 2.—Relation of pressure-response factor to depth of water for various wave frequencies. Cpm, cycles per minute.

TEST SETUP

The effect of an oscillating water surface was simulated by moving the orifice vertically in a water-filled cylinder (3 inches in diameter, 2½ feet in length) at various rates by means of a motor and disk crank to generate a sine-wave input to the orifice. An abrupt change of stage was simulated by moving the orifice rapidly from a minimum to a maximum head. Two Esterline Angus 0–1 milliampere recorders were used with a servocontrolled manometer of commercial design—one to record orifice cycling rate, and one to record manometer response. Both recorders operated from a potentiometer bridge connected between the manometer and recorder. A U.S. Geological Survey

manometer was tested using a Leupold and Stevens A–35 continuous chart recorder, driven by a motor through a gear train, for recording both orifice movement and manometer response. Tubing lengths of 50 and 100 feet were used to represent typical field installations. Tubing inside diameters were 1/8 and 3/16 inch.

RESULTS

Test data indicated that the mean value of the recorded stage was less than the mean value of the actual stage. The average error for the U.S. Geological Survey manometer ranged from about 0.08 foot of water at low bubble rates to about 0.02 foot of water at high bubble rates for an oscillating amplitude of 0.1 foot for all tests. When this amplitude was doubled the range of error was approximately doubled. Little difference was noted in the results when using 50- and 100-foot tubing lengths.

A delay circuit incorporated in the electronic servo-control unit is used to delay operation of the drive motor for approximately 35 seconds after contact is made by the float switch and points. This delay action prevents the recorder trace from oscillating unnecessarily when the water surface is oscillating. The recorder trace would thus indicate an average of the oscillations that would occur without the delay circuit. Tests were run on the U.S. Geological Survey manometer with the delay circuit both on and off. Magnitude of error was about the same in both tests.

ERROR PREDICTION

Prediction of error in stage recorded by a bubble gage may be obtained with a simplified mathematical approach. By making several assumptions, an analysis based on fluid-mechanics principles was established relating system pressure to elapsed time for a step input to the orifice. A differential equation using the mass-conservation principle was set up with rate of mass input of gas to the system equal to rate of mass output plus rate of change in mass storage of the system. The differential equation was developed and solved, resulting in the final exponential equation

$$P_s = Ce^{mt} - P_a,$$

where

P_s = static pressure inside system,
P_a = atmospheric pressure,
C = constant of integration,
m = rate of gas input per volume of system, and
t = elapsed time.

A sinusoidal plot of orifice movement, simulating oscillating water, was drawn in terms of water pressure or head, and a plot of system pressure obtained from the above equation was superimposed tangent to the lower portion of the orifice curve and drawn to intersect the next cyclic curve of the orifice pressure as shown in figure 3. For a sine-wave input to the manometer, the rising-stage sections of the curves were assumed to rise at rates sufficient to produce the maximum response obtained from the step input. The curve formed can be considered to be an approximation

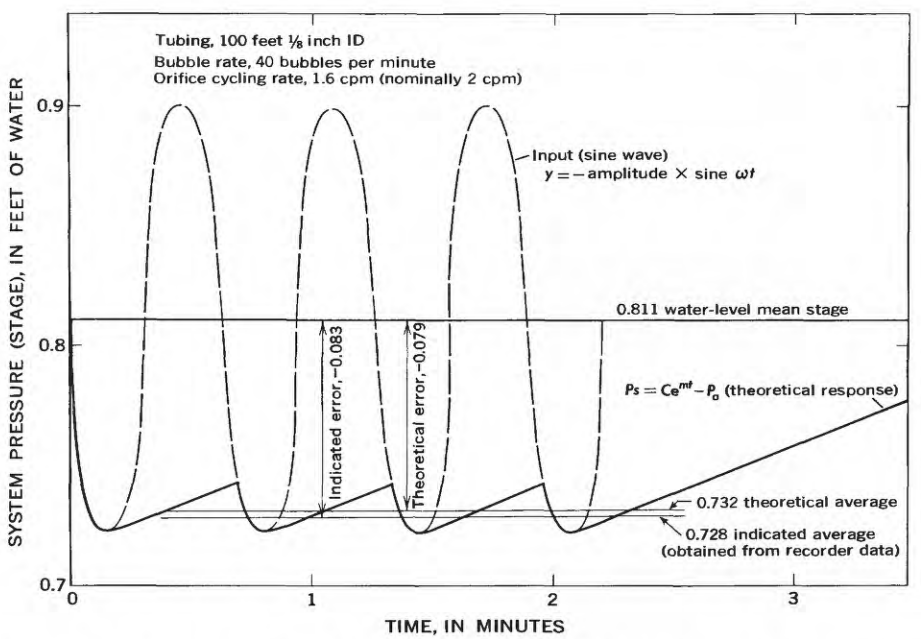

FIGURE 3.—Comparison of the average theoretical and average recorded responses of a gas-purged manometer system to a cyclic change in stage. cpm, cycles per minute.

to the trace recorded from cyclic operation in a typical manometer installation. A horizontal line can be drawn through the curve to obtain an average reading. The difference between this average line and the average orifice position can be obtained to give a predicted error in manometer-recorded water stage.

SUMMARY AND CONCLUSIONS

The stage indicated by a bubble gage is a reading equivalent to the internal pressure in the gas-purged part of the system. Under static conditions this internal pressure is an accurate analog of the water stage, but when oscillatory pressure variations occur at the system's orifice in response to short-period wave action, the average internal pressure of the system will not be equal to the average pressure head at the orifice. This is so because such systems adjust rapidly to decreasing pressures (falling-stage periods) and adjust slowly—at a rate controlled primarily by the purge rate—to increasing pressures (rising-stage periods). The net effect is that bubble gages do not record the mean of the surge, but underregister by a variable amount when subject to wave action.

The dominant factors controlling the magnitude of registration errors at a given installation are the size and frequency of the waves and the purge rate of gas flowing into the system. Other factors, which may vary with time or from system to system, are the depth of water over the orifice, the internal gas-filled volume of the manometer itself, and the length and size of tubing used to connect the manometer with the orifice.

Under adverse conditions, where the purge rate is less than 80 bubbles per minute, where the depth of water over the orifice is less than 50 feet (as is usual with the U.S. Geological Survey unit), and where wave frequency is greater than 5 cycles per minute, the gage height recorded may approach the trough of the waves. The magnitude of underregistration may be reduced by increasing the purge rate, but the laboratory tests reported herein still show significant errors at a purge rate of 160 bubbles per minute.

The significance of these registration errors must be assessed in relation to the characteristics of the body of water involved and the purpose for which the stage is being recorded. Stage records on lakes and reservoirs are generally used to document the exact elevation of the water surface. Registration errors in the records may consequently have considerable importance. For lake gages, the errors due to wave action would probably occur at random times coincident with periods of high wind. The magnitude of errors would be less at installations where wave frequency was high and the gage orifice was placed in deep water. In rivers the magnitude of wave action—sometimes referred to as surge—is a frequently repetitive phenomenon closely associated with the stage and discharge. At low stages, streams are typically calm with little or no wave action, while at high stages considerable turbulence develops and a consistent characteristic pattern of surge is apparent. If the primary purpose of the stage record on such a stream is for use in the computation of discharge records, then registration errors will probably be compensated for in the development of the stage-discharge relation and will be of no significance.

The significant findings of this study are that gas-purged manometer systems (bubble gages) indicate a stage value less than the mean of the surge when surface waves are present. In some instances these errors are negligible or may be compensated for by the manner in which the record is used. This report suggests a technique whereby the magnitude of errors may be predicted, but unless the wave characteristics are actually known, minor errors must be expected. A knowledge of this system characteristic should improve the quality of interpretation of stage records obtained by use of a bubble gage and permit corrective steps to be taken in instances where real problems exist.

AUTOMATIC WATER SAMPLING PROPORTIONAL TO STREAMFLOW

By P. H. CARRIGAN, JR.,[1] and W. F. JOHNSON,[2]
Washington, D.C., Oak Ridge, Tenn.

Work done in cooperation with the U.S. Atomic Energy Commission

Abstract.—Low-level radioactive wastes from the Oak Ridge National Laboratory are released to the Clinch River 2.3 miles downstream from Melton Hill Dam. Water samples proportional to river flow are composited at two stations, immediately and 8.6 miles downstream from the dam, to monitor radioactivity in the river. Sampling at the stations responds immediately to rapid changes in waste dilution owing to power releases at the dam. The sampling equipment frequently diverts aliquots of river water into a container, the duration of diversion being proportional to river flow. The flow is measured by the turbine flowmeter in the dam powerhouse and by a vane-deflection meter, developed in this study, at the respective stations.

Liquid wastes containing variable low-level concentrations of radionuclides from the Oak Ridge National Laboratory (ORNL), Tennessee, are released to the Clinch River from Whiteoak Creek. (See fig. 1.) The Clinch River Study Steering Committee, a group comprised of a representative from each participating Federal and State agency and having general supervision of the study, recommended that monitoring of radionuclide concentrations of these wastes in the river water, begun in 1943, be continued (Churchill, and others, 1965). Furthermore, the Steering Committee recommended that two automatic water-sampling stations be designed and installed on the Clinch River near Oak Ridge, Tenn., for the monitoring. River-water samples collected at these stations are analyzed to provide data on the mean weekly concentration of radionuclides in this water. Automatic sampling equipment appeared to be the most practical means of sampling the river water for determination of the rapid

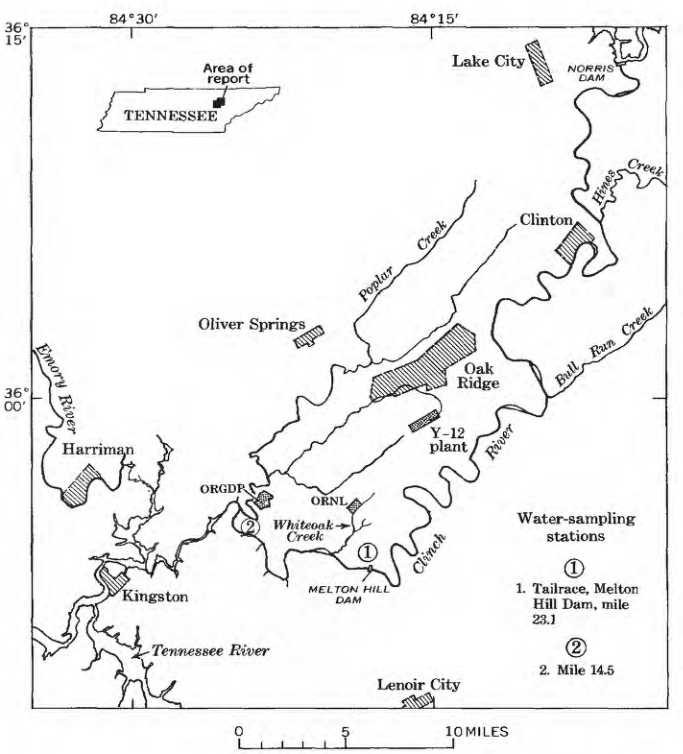

FIGURE 1.—Map showing location of automatic water-sampling stations on the Clinch River.

fluctuations in radionuclide concentrations caused by fluctuating power releases from Melton Hill Lake (Melton Hill Dam at mile 23.1 on the Clinch River).

The effect of simulated power releases on the dilution of a dye (simulating radioactive wastes) released from Whiteoak Creek, 2.3 miles downstream from the dam, may be seen in figure 2. The release simulation, an idealized composite of expected summer release patterns, was 16,000 and 8,000 cubic feet per second for 0600–1300 hours and 1800–2200 hours, respectively, on

[1] U.S. Geological Survey.

[2] Instrumentation and Controls Division, Oak Ridge National Laboratory. Research performed at Oak Ridge National Laboratory by Union Carbide Corp. under contract with U.S. Atomic Energy Commission.

U.S. GEOL. SURVEY PROF. PAPER 650-D, PAGES D278-D282

weekdays and no flow at other times of the week. Actual power release patterns are more variable from day to day and week to week than those simulated. The pulses in dye concentration (fig. 2) are in response to the power-release pulses. Dye pulses diminish during the week as dye retained in the creek during the weekend (Aug. 24–25) is periodically depleted.

The water-sampling intake for one station is located in the tailrace of Melton Hill Dam. Data on radionuclide concentrations in water samples collected at this section provide monitoring data on radioactivity originating from upstream sources in the Clinch River watershed. The intake for the other station is located in a section of the river near the water-supply intake for the Oak Ridge Gaseous Diffusion Plant (ORGDP) at mile 14.5. The ORGDP water supply is the first withdrawal of water from the Clinch River containing low-level radioactivity released from Whiteoak Creek.

In order to provide a weekly composite sample of river water for laboratory determination of the mean weekly concentration of radionuclides, the Steering Committee recommended that samples be collected continuously at a rate directly proportional to the river-flow at the sampling stations. The instruments, designed to continuously measure the flow and the equipment to reasonably satisfy the requirement for continuous collection of water samples at a rate directly proportional to the flow, are described in this paper.

Acknowledgments.—Development of the sampling stations was part of a cooperative research project, known as the Clinch River Study, which was financed by the Division of Reactor Development and Technology, U.S. Atomic Energy Commission. Funds for electronic design were secured, and arrangements for the fabrication and installation of the sampling stations were made by F. L. Parker, Leader, Radioactive Waste Disposal Research Section, ORNL, and E. G. Struxness, Assistant Director, Health Physics Division, ORNL.

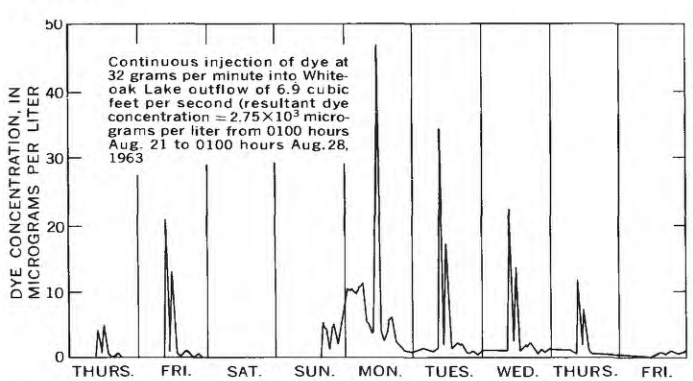

FIGURE 2.—Observed variation in Rhodamine B dye concentration with time during period August 22–30, 1964, in Clinch River at mile 14.5 (from E. G. Struxness and others, 1967).

The design concept of the vane-deflection meter is based on information furnished by E. L. Cook, U.S. Geological Survey (written commun., 1944). The equation for the deflection of the vane was checked and modified by B. J. Frederick, U.S. Geological Survey.

CONTINUOUS FLOW MEASUREMENT

At both sampling stations the essential feature of the flow-measuring instruments is that they produce an output signal of 0–100 millivolts which is directly proportional to the flow. This signal is the input signal to instruments which control the water-sample collection rate.

The flow-measuring instrument for the station located immediately downstream from the Melton Hill Dam powerhouse is the turbine flowmeter in the powerhouse. A full-scale signal of 100 mv from the flowmeter is directly proportional to a flow of 24,000 cfs.

At the other sampling station (mile 14.5) the water level is almost completely a function of backwater from Watts Bar Dam on the Tennessee River (52.3 miles downstream). Unless floods occur, the backwater conditions are virtually constant in Watts Bar Lake. Hence, flow at the station is almost directly proportional to the mean velocity because of its nearly constant cross-sectional area. (A change in release at Melton Hill Dam of 0–18,000 cfs produces less than 1.3 feet change in mean depth of 22 feet at station.) The mean velocity at this station is measured with a vane-deflection meter.

As shown in figure 3, the vane-deflection meter is a device whose rotation, due to the drag force on the vane, is resisted by a counterweighting system. The angle of rotation is a nonlinear function of the local velocity at the vane.

By equating the expression for the torque produced by the drag on the vane to that for the torque of the resisting counterweight system, the relation between deflection of the vane and the local velocity acting on the vane is found as follows:

The torque produced by drag on the vane is the product of the drag force and its lever arm, that is

$$T_v=\left(\frac{1}{2}\,C_d\rho A_v\cos\alpha V^2\right)\left(\frac{b}{2}\cos\alpha\right),$$

where

T_v = torque produced by drag,
C_d = coefficient of drag,
ρ = density of water,
A_v = area of vane,
V = velocity of flow,
α = deflection of vane from normal to the flow, and
b = width of vane.

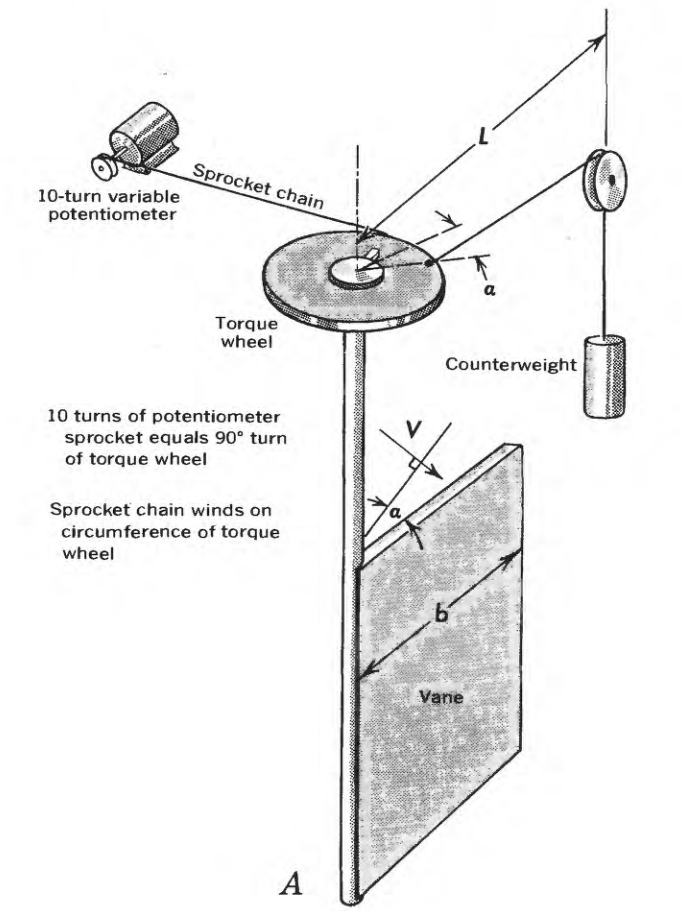

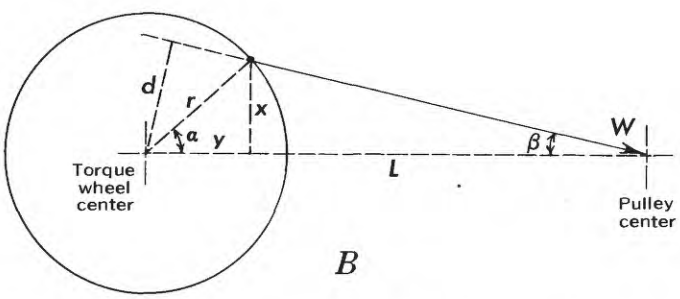

FIGURE 3.—Vane-deflection meter. *A*, schematic sketch; *B*, geometric relation of d to L, r, and α. Letter symbols are explained in text.

As shown in figure 3, the resisting torque T_w is produced by the counterweight, W, and its lever arm, d. The length of the lever arm is a function of the distance, L, between the vane axis and the counterweight pulley, the radius, r, of the torque wheel, and the deflection, α, of the vane from the line between centers of the torque wheel and of the pulley. Because

$$\frac{d}{L}=\sin\beta,\ \frac{x}{r}=\sin\alpha,\ \frac{y}{r}=\cos\alpha,\ \text{and}\ \frac{x}{L-y}=\tan\beta,$$

$$d=L\sin\beta=L\sin\left[\tan^{-1}\left(\frac{x}{L-y}\right)\right]$$

$$=L\sin\left[\tan^{-1}\left(\frac{r\sin\alpha}{L-r\cos\alpha}\right)\right]$$

$$=L\sin\left[\sin^{-1}\left(\frac{r\sin\alpha/(L-r\cos\alpha)}{1+(r^2\sin\alpha/(L-r\cos\alpha)^2)}\right)\right]$$

$$=\frac{rL\sin\alpha}{\sqrt{L+r^2-2rL\cos\alpha}},$$

then

$$T_w=Wd=\frac{WrL\sin\alpha}{\sqrt{L+r^2-2rL\cos\alpha}}.$$

By equating T_v and T_w and solving for V, the relationship between V and the other variables is

$$V=\left[\left(\frac{W}{\rho A_v brL}\right)\left(\frac{\sin\alpha}{\cos^2\alpha\sqrt{\frac{L+r^2}{2rL}-\cos\alpha}}\right)\frac{1}{C_d}\right]^{1/2} \quad (1)$$

For the vane-deflection meter at mile 14.5 on the Clinch River, equation 1 is computed to be

$$V=1.40\left[\frac{\text{Sin}\,\alpha}{\cos^2\alpha(1.30-\cos\alpha)^{1/2}}\right]^{1/2}\frac{1}{C_d^{1/2}}, \quad (2)$$

where C_d is empirically determined and V is in units of feet per second.

Through study of data from field calibration tests, equation 2 was modified so as to combine the influence of C_d as well as the relation of the mean velocity $\overline{V}$, instead of the local velocity V, to α in one constant term. The relation is

$$\overline{V}=1.29\left[\frac{\sin\alpha}{\cos^2\alpha(1.30-\cos\alpha)^{1/2}}\right]^{1/2}(1.10)^{\alpha/12}. \quad (3)$$

Through use of a specially wound, 10-turn potentiometer, mechanically linked to the vane shaft, the rotation of the vane is transformed to an output signal ranging from 0–100 mv which is directly proportional to $\overline{V}$, hence, directly proportional to the flow. A signal of 33mv is equivalent to a flow of 20,000 cfs. The potentiometer was wound so that the relation between its output voltage (input voltage, 100 mv) and α would satisfy equation 3.

SAMPLE COLLECTION EQUIPMENT

The sample collection equipment was designed to collect a sample volume directly proportional to the riverflow at frequent intervals. A sampling interval of 15 minutes was arbitrarily selected as an adequate frequency for sampling variations in riverflow. At the time of sampling the river water is pumped at about 8 milliliters per second into a sample container for a period whose duration is directly proportional to the flow. Thus, the equipment produces a discharge-weighted composite sample for any period desired.

The components of equipment for sample collection at both stations are a pump, sampling solenoid valve, sampling-interval selector, pulse-duration timer, recorder, and a sample container (fig. 4). A flow diagram showing the relation between these components is given in figure 5.

The jet pump is operated continuously to lessen chances of water freezing in the pump intake line (diameter 1 inch) and to prevent deposition of sediment particles less than 1 millimeter in diameter.

The solenoid valve opening is actuated by selected electric pulses of variable duration released through the pulse duration timer. The duration of the pulse (0–12 seconds) is directly proportional to the voltage output signal from the flow-measuring instrument (0–100 mv). These pulses of variable duration are generated every 15 seconds by the timer. Each pulse from the timer is counted by the sampling interval selector (a pulse-signal counter). At a preselected number of counts one pulse passes through the interval selector to the solenoid valve. The count may be varied from 1 (every 15 seconds) to 400 (every 100 minutes).

The recorder houses the pulse-duration timer and records the output signal from the flow-measuring instrument.

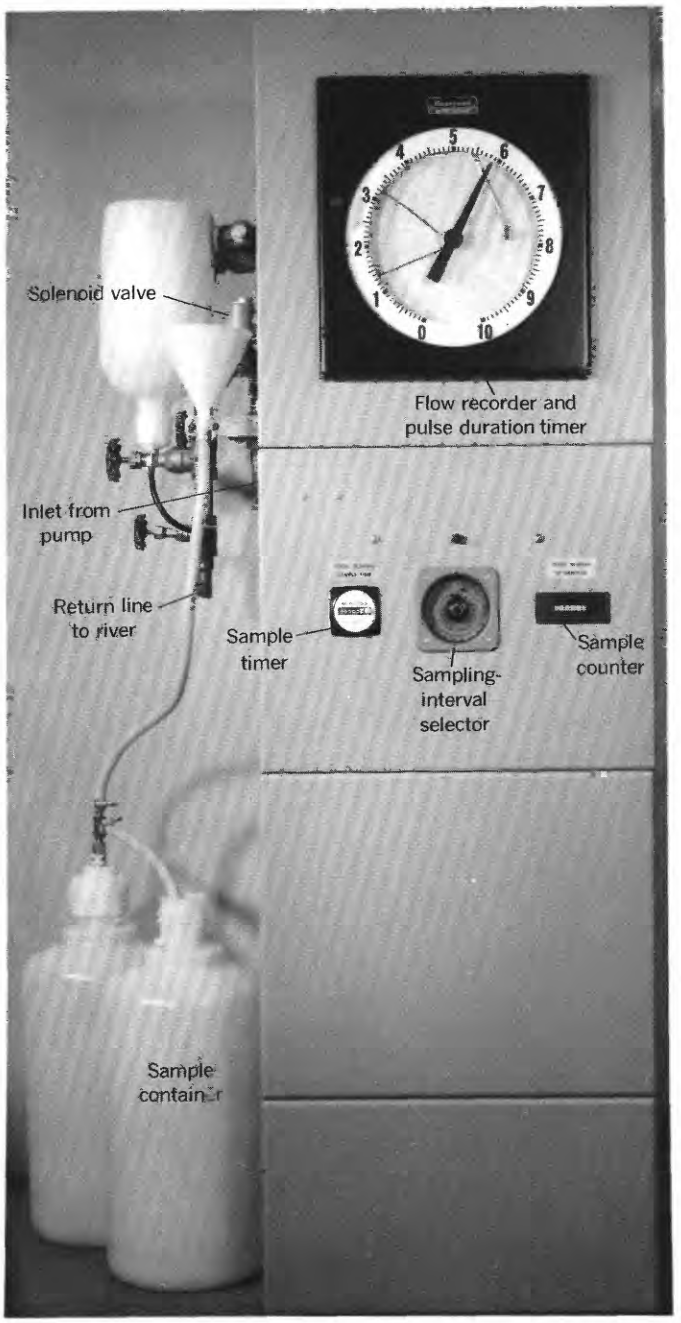

FIGURE 4.—Photograph showing sampling-equipment console (ORNL photograph).

SUMMARY

Automatic water-sampling stations were designed to collect at frequent intervals (nominally 15 minutes) a sample volume of Clinch River water directly proportional to the flow at the sampling station. Frequent sampling of a volume proportional to the flow was required on the lower Clinch River because of rapid changes in dilution of radioactive contaminants produced by fluctuating power releases at Melton Hill Dam.

The volume was proportioned by controlling the period of time each sample was diverted into a container from a pump continuously operating at a constant rate. The period of time for diversion was determined by measuring the flow at the sampling section and converting the output signal from the measuring instrument into an electric pulse having a duration proportional to the flow.

The sampling equipment was installed at the sampling station immediately downstream from Melton Hill Dam in 1965, and it has operated satisfactorily through 1968. The other set of equipment (vane-deflection meter and sampling equipment) was installed at the station 8.6 miles downstream in July

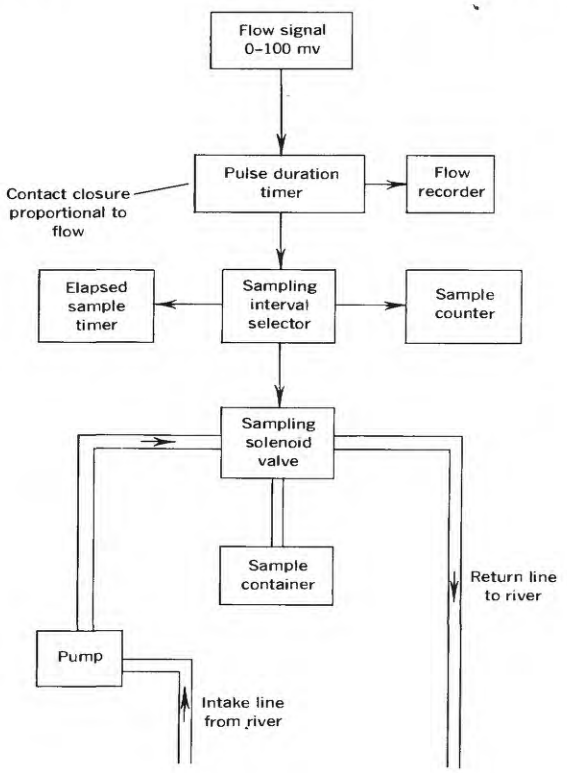

FIGURE 5.—Flow diagram showing the equipment components that control the sampling volumes.

1968 and it was operating satisfactorily as of the end of 1968. Comparison of daily discharge measured by the vane-deflection meter to that measured below Melton Hill Dam indicates an average difference of ±1 percent.

REFERENCES

Churchill, M. A., Cragwall, J. S., Jr., Andrew, R. W., and Jones, S. L., 1965, Concentrations, total stream loads, and mass transport of radionuclides in the Clinch and Tennessee Rivers: Oak Ridge National Laboratory, ORNL–3721, Suppl. 1, 78 p.

Struxness, E. G., Carrigan, P. H., Jr., Churchill, M. A., Cowser, K. E., Morton, R. J., Nelson, D. J., and Parker, F. L., 1967, Comprehensive report of the Clinch River Study: Oak Ridge National Laboratory, ORNL–4035, 121 p.

MEASUREMENT OF ATMOSPHERIC PRESSURE AND SUBSURFACE-GAS PRESSURE IN THE UNSATURATED ZONE OF THE BANDELIER TUFF, LOS ALAMOS, NEW MEXICO

By J. L. KUNKLER, Santa Fe, N. Mex.

Work done in cooperation with the U.S. Atomic Energy Commission and the Los Alamos Scientific Laboratory

Abstract.—Pressure transducers, power supplies, and potentiometric recorders were assembled into portable pressure-monitoring systems which measured pressures in the field with an accuracy of about 0.3 percent. The performance of some of the components was affected by fluctuations in field temperatures; hence these components were operated in a constant-temperature chamber. The data from this study show that the subsurface-gas pressures responded to changes in the atmospheric pressure to depths of 35 meters in the Bandelier Tuff; the response was completely attenuated at some depth between 35 and 89 m.

Several years ago a study was made at Los Alamos, N. Mex., of the gas-storage characteristics of the zone of aeration (unsaturated zone) in the Bandelier Tuff. This study, composed of several phases and covering a period of about 3 years, was sponsored by the U.S. Atomic Energy Commission and the Los Alamos Scientific Laboratory. Studies were made at two test sites, designated as TA–50 and TA–52. A description of TA–52 and of test holes constructed at the site is given in a separate paper (Kunkler, 1969, p. B186). Test site TA–50 is about 2 kilometers south of Los Alamos and about 300 meters north of test site TA–52. The physical and geologic conditions, and the construction of test holes at the TA–50 site, are almost identical with those at the TA–52 site.

During the studies at the test sites, considerable effort was devoted to the problem of designing and constructing pressure-monitoring systems. These systems, composed of several components that could be interchanged to suit the occasion, were used to monitor more or less continuously the atmospheric pressure and the borehole gas pressures of isolated and sealed test zones in the rock.

An accurate, reliable pressure-monitoring system is not difficult to build if the system can be operated indoors where the environmental temperature is rigidly controlled; however, several problems arise if the system is made portable and is operated exposed to the elements. This paper gives an account of some of these problems and their solutions.

SYSTEM COMPONENTS

Subsurface-gas pressures can be measured with gages, manometers, or pressure transducers. Of these instruments the pressure transducers, which convert pressure changes to electric signals, are the most difficult to use in the field; however, they are capable of sensing very small changes in pressure, and if coupled to a recorder they provide a continuous record of the measurements.

Several types of pressure transducers were tested during this study, and it was decided that the strain-gage types were most suitable. A strain gage is a thin strip of an alloy which has the property of changing its electrical resistance when placed under strain (Stein, 1964, p. 132–135). The mechanism of a simple strain-gage pressure transducer is illustrated in figure 1. The transducer is fitted with four strain gages (Rg_1–Rg_4) which are wired into a Wheatstone bridge circuit. Two temperature-compensating resistors (Rt) are added to the circuit within the transducer to compensate for ambient temperature changes or the thermal effect.

Pressure transducers are classified into two categories according to their mechanical configuration. One type is used to measure absolute pressures, and the second type is used to measure differential pressures

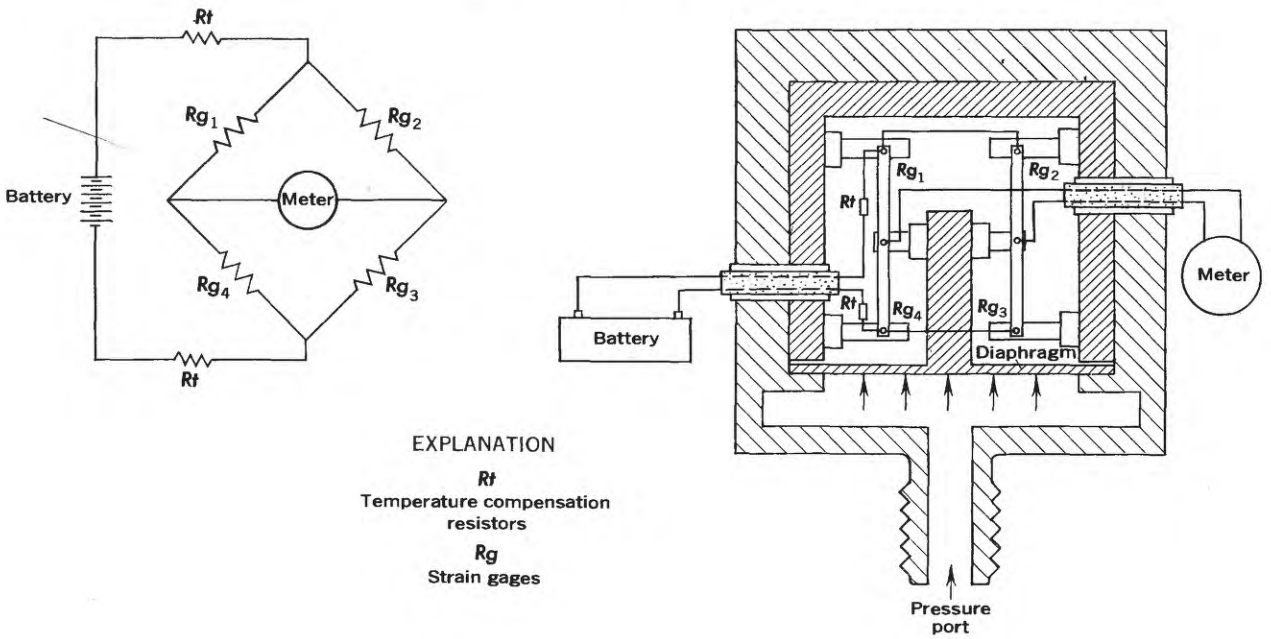

FIGURE 1.—Schematic configuration of a strain-gage pressure transducer.

(the difference in pressure between two sources). Both types were used during this study. The differential-pressure transducers differ in design from the absolute-pressure transducers by having a more complex mechanical configuration and greater sensitivity.

When used, the differential-pressure transducers were referenced to a fixed pressure datum by applying a constant and known reference pressure to one of their pressure ports. The reference pressure can be attained in several ways. For some applications where the ambient temperature is constant it is satisfactory to seal the reference pressure side of the transducer at a desired pressure. A better method, which was used during the study, is to supply an external reference pressure which is attained by pumping a stream of air through a manostat, a sensitive pressure regulator, to the reference pressure port of the transducer.

The electromotive force (emf) of signals from high-quality transducers is a linear function of the pressure, and the newest transducers are advertised as having this characteristic over a wide range of ambient temperatures. The transducers used for this study had lost their temperature-compensating capabilities, but they were capable of providing a linear relation between pressure and the output signal if the ambient temperature was held constant. The histories of these transducers is unknown. It is possible that they had been severely abused by former usage which had caused them to lose most of their temperature-compensating ability. Because their histories are unknown it is unfair to identify them by name. There is little doubt that these instruments had once been of finer quality. A typical pressure-versus-signal relation is shown for an absolute-pressure transducer in figure 2. The same relation for a differential-pressure transducer at reference pressures of 0, 30, and 59 centimeters of mercury is shown in figure 3.

The maximum range of the output emf of the transducers was 0 to 40 millivolts when they were activated with a 10 volt direct-current power supply. It was convenient to operate at lower input voltages so that the range could be adjusted to a convenient pressure scale on the recorder chart; the usual activating emf was about 7 v dc.

The pressure transducers were activated by a rectifier or from a series of batteries. Rectifiers tend to be unsatisfactory for this application; hence several mercury batteries such as Burgess Hg–42R were hooked in series

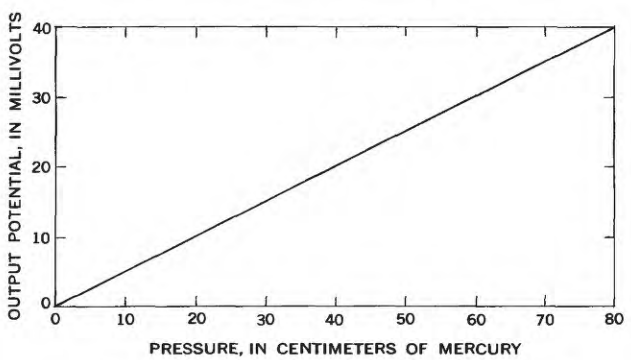

FIGURE 2.—Pressure versus output potential of an absolute-pressure transducer (range 0–80 cmHg).

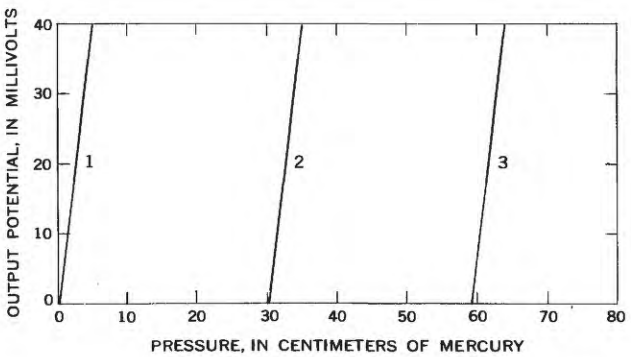

FIGURE 3.—Pressure versus output potential of a differential-pressure transducer at three reference pressures, 1, 2, and 3, which are 0, 30, and 59 cmHg, respectively.

with a variable resistor which could be adjusted to give the proper output emf.

Two types of multirange recorders were used to record the signals from the pressure transducers. The first type had a small zero-displacement capability and was suitable for recording only the signals from a differential-pressure transducer. The second type, an MR recorder (E. H. Sargent and Co.) had a very large zero-displacement capability and was suitable for recording the signals from either type of transducer.

Several methods are used to compensate for the thermal effect of transducers, and most designs incorporate one or more of these methods. Because none of the transducers used during this study had adequate thermal compensation, their ambient temperatures were controlled by placing them in a constant-temperature chamber. The battery potentials and the manostat pressure controls were also affected by changes in temperature. Hence the batteries, the manostat, and its associated air pump were placed in the constant-temperature chamber.

The diagram shown in figure 4 represents a pressure-monitoring system with an absolute-pressure transducer that is continuously monitoring the atmospheric pressure and the subsurface-gas pressure from one test zone. This system was revised for intermittent monitoring by adding eight solenoid valves to the pressure manifold, and by replacing the switching control mechanism with another designed to activate at about 80-minute intervals. While activated, the pressures at nine test points and the atmosphere were measured sequentially.

The pressure-monitoring systems were calibrated intermittently with sensitive manometers. During calibration, the output emf of the battery pack was adjusted with the variable resistor (fig. 4) so that the output emf of the transducer corresponded to a convenient pressure scale on the recorder, and this emf was maintained throughout the monitoring period by frequent adjustments of the variable resistor. Data from a typical calibration are shown in figure 5.

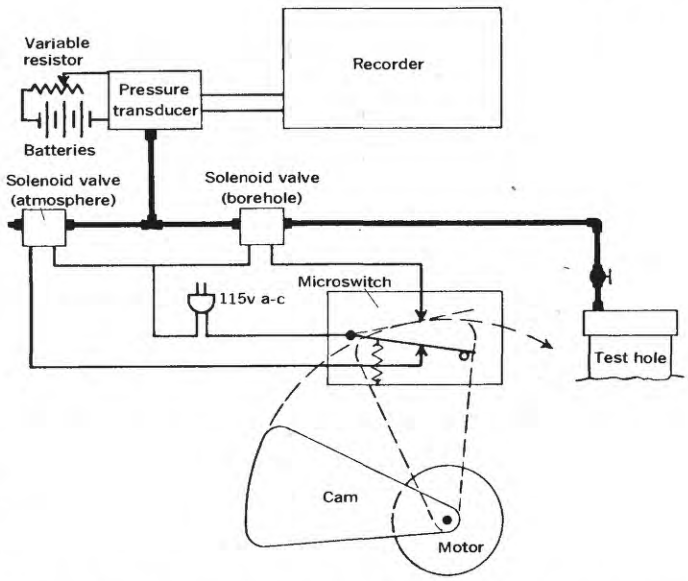

FIGURE 4.—Schematic diagram of a pressure-monitoring system.

DISCUSSION OF DATA

Subsurface-gas pressures and atmospheric pressures were monitored periodically for several months at the TA–50 and TA–52 test sites. It was expected that the

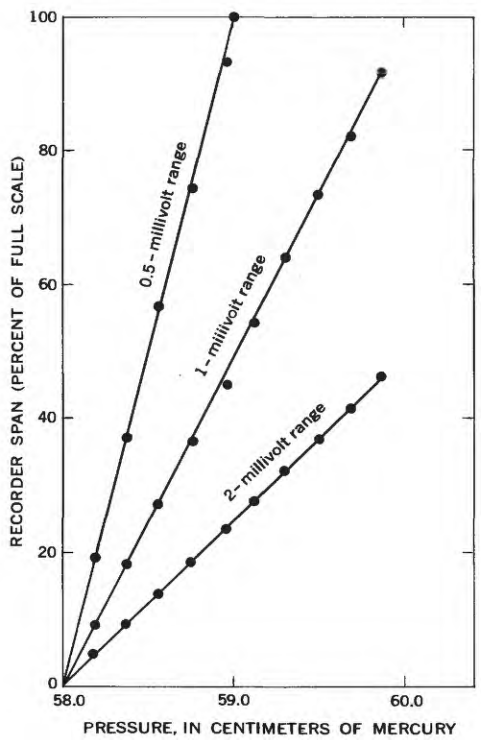

FIGURE 5.—Calibration of an absolute-pressure transducer at three recorder ranges.

subsurface-gas pressures would respond to changes in the atmospheric pressure, and that this response would be attenuated with depth until it would be undetectable at a depth of 30 m. The data showed that the gas pressure in the rock does respond to atmospheric pressure changes; however, there was no recognizable attenuation of this effect at depths less than 35 m, but the pressure changes were completely attenuated at a depth of 89 m. There were no pressure measurements in the interval between 35 and 89 m.

The response of the subsurface-gas pressures to changes of atmospheric pressure was obvious; however, a detailed study of these records showed that the relation was very complicated, and that the complexity increased with the depth of the test zone. For example, it was impossible to predict the beginning, the end, or the magnitude of a given response at depths greater than 10 to 15 m; however, in all recorded events the response at these depths was approximately proportional to the magnitude of the atmospheric-pressure change. This problem was studied for many months, and its cause was finally identified from data of a related study, which indicated that the subsurface gas was exchanged with the atmosphere along both the horizontal and vertical axes of the test zones. Both test sites are on narrow mesas, and the horizontal distance between some test zones and the land surface is not much greater than the vertical distance to the land surface. It was reasoned, therefore, that some, if not most, of the complexity of the relation between subsurface-gas pressures and the atmospheric pressure was due to the topography of the test site (Kunkler, 1969, p. 187).

It was necessary to pump gas from the test zones for various reasons. At times, gas was pumped for chemical and isotope analyses. At other times the test zones were pumped to remove atmospheric contamination or to obtain gas permeability data. The types of pumps and the pumping rates varied with the occasion; the greatest pumping rate was about 20 liters of gas per minute. During some pumping intervals, the borehole gas pressure was monitored; however, a study of these measurements indicates that the data have very little value; hence they are not reported. Copies of the pressure recordings are difficult to present as illustrations; it was necessary to either photograph the recorder charts and trace the pertinent data from the photographs or to plot the data from the charts as bar graphs.

An example of a record traced from a photograph of the recorder chart is given in figure 6. The atmospheric pressure and the subsurface-gas pressure were monitored using a cycle of 1 minute. The atmospheric pressure was monitored for 40 seconds, and the subsurface-gas pressure was monitored for 20 seconds.

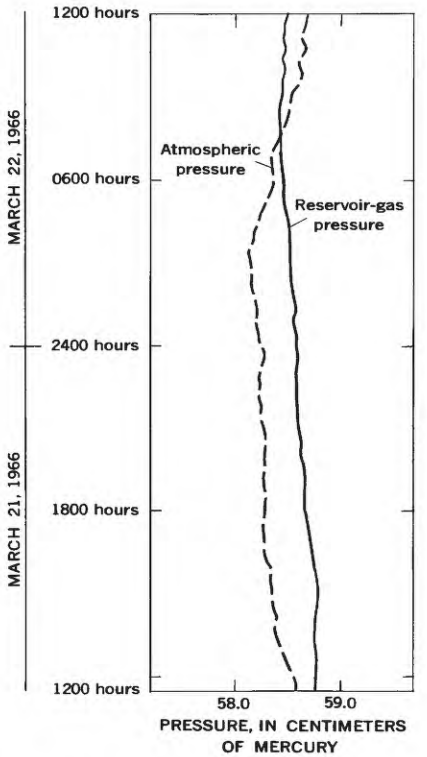

FIGURE 6.—Record of atmospheric and subsurface-gas pressures in test zone 24.7 to 26.2 m below land surface at test hole TA–50–29.

When the atmospheric pressure was monitored contemporaneously with the gas pressure of several test zones, the measurement cycle was only 2 minutes long, repeated at 80-minute intervals. Intermittent monitoring at 80-minute intervals did not provide much useful data because the pressure fluctuations of interest were of shorter duration. A typical problem in interpreting the data is shown in figure 7 where the gas pressure of two test zones only 0.9 m below land surface appears to have been consistently lower than the atmospheric pressure for a period of 2 hours and 42 minutes. This situation is possible but improbable. It is more likely that at times between the periods of monitoring the atmospheric pressure was significantly lower than shown.

ACCURACY OF MEASUREMENTS

All pressure measurements were made at the same datum and at a constant temperature. Recorded atmospheric pressures were checked with a mercury barometer located about 200 m from the test holes. Usually these measurements checked within 1 millimeter of mercury but varied at times by as much as 3 mmHg.

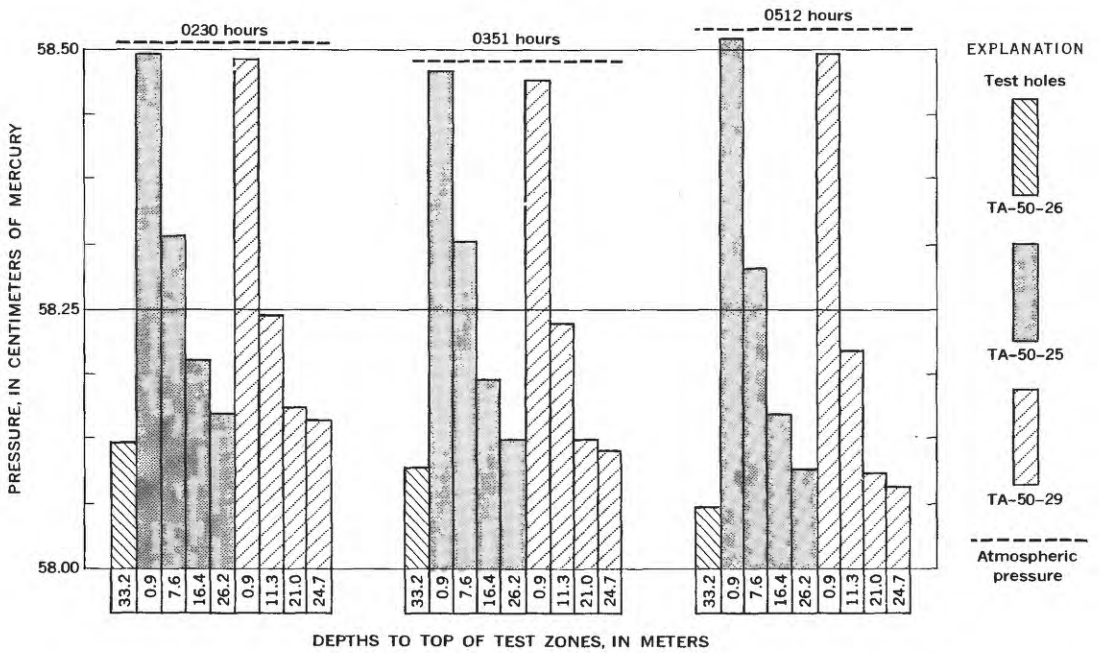

FIGURE 7.—Atmospheric pressure and subsurface-gas pressure of various test zones at 0230, 0351, and 0512 hours, November 4, 1965.

During some of the periods of monitoring at the TA–50 test site, where only the differential-pressure transducer was used, the air pump which supplied the reference pressure was not operating properly. This type of malfunction created an error in the measurement of absolute pressures of about 2 mmHg; however, the differential error between a series of pressure measurements probably did not exceed 0.2 mmHg, which is about equal to the sensitivity of the recorder adjusted to measure a full-scale pressure range of 25 mmHg. The average atmospheric pressure at the test site was about 58.9 cmHg; hence the error of absolute-pressure measurements may be about 0.3 percent, but the error of differential-pressure measurements (between the atmosphere and borehole) may be only one-tenth of this amount or about 0.03 percent.

A pressure-monitoring system containing an absolute-pressure transducer was used at the TA–52 test site. Measurements made with this system were about as accurate as those made at the TA–50 test site where a pressure-monitoring system with a differential-pressure transducer was used because the uncertainty in the value of the reference pressure was sufficient to overcome the greater sensitivity of the differential-pressure transducers.

Most of the difficulties in monitoring gas pressures and atmospheric pressures were related to the large temperature fluctuation in the field; therefore, many problems could have been avoided if a climate-controlled shelter had been provided for the instruments.

REFERENCES

Kunkler, J. L., 1969, The sources of CO_2 in the zone of aeration of the Bandelier Tuff near Los Alamos, New Mexico, *in* Geological Survey Research 1969: U.S. Geol. Survey Prof. Paper 650–B, p. B185–B188.

Stein, P. K., 1964, Material considerations for strain gages: Instruments and Control Systems, Oct. 1964, Rimbach Publications, Div. of Chilton Co., Philadelphia, Pa., p. 132–135.

ASH CONTENT AND COMPOSITION OF MILLIPORE HA FILTERS [1]

By D. W. SPENCER [2] and F. T. MANHEIM,[3] Woods Hole, Mass.

Abstract.—Analyzed Millipore HA brand of micropore filters contained about 0.04 percent ash. The main constituents of the ash were Na, Ca, Si, Mg, K, and P. More than 1 percent Fe, Cu, Cr, Zn, and Al oxides were also present; these may influence analysis of suspended detritus in sea water.

Microfilters are being used increasingly in all phases of analytical chemistry. In particular, the analysis of suspended material in sea water is frequently accomplished by collection of the material on filters having pore diameters between 0.45 and 3 microns (Joyner, 1964; Riley, 1965). Recently we have been concerned with the composition of suspended matter in sea water, attempting to determine trace elements on as little as 10 milligrams of solids. Though sometimes referred to as being "ashless," the ash of the filter (0.03–0.05 percent of dry weight) makes up a sufficiently large proportion of the ashed sample that knowledge of the composition of the filter ash may be necessary to determine feasibility of trace-element analysis and possibly to apply corrections to the results.

Acknowledgments.—We thank Mr. Richard Cotton, vice president of the Millipore Corp., for his cooperation. This work was supported in part by grant No. AT(30–1)–1918 from the U.S. Atomic Energy Commission (AEC). AEC Report No. NYO–1918–178.

METHOD

Through the courtesy of the Millipore Corp., we obtained about 500 grams of their MF-HA material remaining as scrap after filter disks had been cut from rectangular sheets. We were assured by the manufacturer that all precautions had been taken to avoid contamination during packing and shipping of the polyethylene-wrapped material. In our procedure the filter material was handled only with platinum-tipped tongs, and care was taken at every step to exclude dust. The Millipore Corp. recommended that the material be charred with pure ethyl alcohol before being ashed. Approximately 200 milliliters of alcohol was consumed in charring. To check on possible contamination from this source, 100 ml of alcohol was evaporated to 10 ml and aspirated into an atomic absorption spectrophotometer. None of the metals analyzed by this technique (table 2) could be detected in the alcohol.

Aliquots of the charred filter material were ashed successively in a large platinum dish, at 500°C, for at least 2 hours. We found that about 500 g of filter material left about 0.2 g of white ash. The results (table 1) gave a figure of about 0.04 percent of ash in terms of original filter weight, not significantly different from values obtained earlier as an average for individual filter circles.

TABLE 1.—*Ash content of Millipore filter material*

Year [1]	Number of samples	Weight of ash (mg)		Weight of filter material (mg)		Ash weight / Filter weight ×100
		Mean	Standard deviation	Mean	Standard deviation	
1965	30	0.040	0.004	92	2	0.045
1966	10	[2] 0.026	[2] 0.006	92	3	.028
1967		195.19		4,477.6		.041

[1] Year of purchase of filters.
[2] Deviations due in part to weighing procedure which was less reproducible in 1966 than in 1965.

The techniques for analysis of the ash are outlined below. Fifty milligrams of ash was fused with lithium tetraborate and internal standards (Be and Sb); the resulting glass was ground and mixed with graphite, and analyzed by high-voltage spark on a direct-reading emission spectrometer. The method was modified from that of Landergren, Muld, and Rajandi (1964). Fifty mg of ash was heated successively at 110°–120°, 500°, and 1,000°C in an electric furnace, and weight losses were determined at each temperature. Partial fusion occurred at 1,000°C, owing to the high percentage of

[1] Contribution No. 2326 of the Woods Hole Oceanographic Institution.
[2] Woods Hole Oceanographic Institution.
[3] U.S. Geological Survey.

alkali salts. The ignition loss at 1,000°C, the average major cation values (including MnO calculated as Mn_3O_4), and the values of P_2O_5 and SO_3 were used to calculate the sum.

Two 25-mg samples were placed in platinum crucibles; to each was added 1 ml of concentrated hydrofluoric acid and 2 drops of concentrated sulfuric acid (reagent grades). After the crucible contents were evaporated to dryness, the residue was dissolved in 1 ml of pure 4*N* hydrochloric acid and 10 ml of distilled deionized water. After dilution to 15 ml, the solutions were analyzed by atomic absorption spectrophotometry.

Total sulfur was determined by high-temperature combustion and subsequent titration of evolved SO_2 by the standard LECO apparatus, using the sodium azide addition technique (Bremanis and other, 1967) to minimize influence of small amounts of chloride.

RESULTS

The results of the analyses (table 2) show that sodium, calcium, silicon, magnesium, and potassium are the dominant cations in the ash (reported as constituent oxides). The excess on summation may be ascribed chiefly to inhomogeneity in the ignition and analytical aliquots, and partly to analytical error. The results suggest that no major cation is present that has not been determined. That these constituents form the main part of filter ash from batch to batch is confirmed by semiquantitative analyses by the Millipore Corp. from earlier years (written commun., 1967). The unexpectedly large amounts of chromium which were found may be introduced from tools used in the cutting process. Very high chromium values were obtained by Robertson (1968) on Millipore filters; his results are included for comparison with ours (reported as elements) in table 3. Data by Hallett, Bressan, Roy, and Corless (1967) suggest that some of the copper in the filters may be water soluble.

TABLE 2.—*Results of analyses, in weight percent, of Millipore filter ash*

	Method of analysis				Average	Standard deviation
	Emission spectrometry	Atomic absorption 1	Atomic absorption 2	Other		
SiO_2	9.7				9.7	
Al_2O_3	1.3				1.3	
Fe_2O_3	1.9	1.99	2.26		2.05	0.19
Cr_2O_3	1.1	1.02	1.18		1.10	.08
MnO	.14	.16	.19		.16	.03
CaO	20.6	20.6	20.8		20.7	.12
MgO	7.7	6.44	6.53		6.89	.70
SrO	.13	.118	.120		.123	.006
CuO	1.3	1.37	1.68		1.45	.20
ZnO	[1].48	.80	1.12		[2].96	.23
K_2O	6.3	5.25	5.32		5.62	.59
Na_2O		26.0	25.4		25.7	.42
P_2O_5	3.7				3.7	
H_2O (110°C)				0.7		
SO_2				5.5	5.5	
Ignition loss (500°C)				2.0		
Ignition loss (1,000°C)				17.3	17.3	
Sum					102.2	
Ba	0.049					
Ni	.074	0.080	0.095			
Ti	.023					
Ag	.012					
Mo	.02					
Co		.005	.006			
Li		.0035	.0037			
Pb	.082	.087				

[1] Low result probably due to loss on fusion.
[2] Average of two results by atomic absorption spectrophotometry.

TABLE 3.—*Concentration of elements in Millipore filter material*

[In parts per million of original filter]

Element	This work	Robertson (1968)	Element	This work	Robertson (1968)
Si	18.5		Na	77.7	
Al	2.8		P	6.6	
Fe	5.9	0.33	S	9.0	
Ca	60.2		Ba	0.20	
Mg	17.0		Ni	.34	
Mn	0.51		Ti	.094	
Cr	3.1	17.6	Ag	.049	<0.00005
Sr	0.43		Mo	.082	
Cu	4.8		Co	.025	.013
Zn	3.15	2.37	Li	.015	
K	19.1		Pb	.35	

REFERENCES

Bremanis, E., Deering, J. R., Mead, C. F., and Keyworth, D. A., 1967, Elimination of nitrogen and chloride interferences in the iodometric determination of sulfur as sulfur dioxide: Materials Research and Standards, v. 7, p. 459–460.

Hallett, D. W., Bressan, D. J., Roy, L. D., and Corless, J. T., 1967, Copper contamination from microfilters: Rhode Island Univ., Graduate School of Oceanography, Kingston, R.I., 6 p. [Preprint]

Joyner, Timothy, 1964, The determination and distribution of particulate aluminum and iron in coastal waters of the Pacific Northwest: Jour. Marine Research, v. 22, p. 259–268.

Landergren, Sture, Muld, William, and Rajandi, Benita, 1964, Analytical methods, *in* Landergren, Sture, On the chemistry of deep-sea sediments: Repts. Swedish Deep-Sea Expedition, v. 10, Spec. Inv., Fasc. 4, p. 148–151.

Riley, J. P., 1965, Analytical chemistry of sea water, *in* Riley, J. P., and Skirrow, George, eds., Chemical oceanography, v. 2: New York, Academic Press, p. 295–424.

Robertson, D. E., 1968, Role of contamination in trace element analysis of sea water: Anal. Chemistry, v. 40, p. 1067–1072.

RADIO-CONTROLLED SIGNAL LIGHT

By THOMAS O. DANDO, Washington, D.C.

Abstract.—A radio-controlled signal light for topographic-mapping field operations has been developed to operate with conventional two-way radios. At the transmitter station, a small audiofrequency tone generator is held near the microphone. The audio tone received at the remote station is fed through a narrow-band filter to an amplifier which activates the command-control relay. The command-control circuit uses little power because it is passive except for the moment the tone signal is being received. Normal voice transmission will not activate the control; therefore, the radios can also be used for normal communications. Tests of the prototype model have shown 100-percent response form a distance of 43 miles. Use of five different audio tones permits independent, selective switching of five different lights.

For decades signal lights have been used as targets for nighttime observations in triangulation surveys. For this application, many different lamps have been used.

The advent of electronic distance-measuring (EDM) equipment has brought about a need for better target signals because the EDM equipment is most often operated in daylight, in traverse surveys rather than triangulation. This type of operation makes the usual type of passive signal, erected at considerable cost, impractical. What was needed was an easily erected portable signal that could be seen and identified at distances often exceeding 15 miles. A first approach to this type of signal light was made in 1961 by U.S. Geological Survey engineers who combined a simple transistorized control circuit and a small lamp to provide a flash pattern for positive signal identification. The controlled lamp flashes were readily distinguished from sun reflections and other false signals. However, the lamp used was of low power and could not reach out to the great distances spanned today.

NEW DESIGN

The signal lamp described here retains the desirable features of earlier models but incorporates all the flexibility required by modern, rapid-pace surveys. The lamp can be controlled on site by an operator or by a clock timer, or it can be controlled remotely by radio. It can take either of two sizes of sealed-beam lamps, precisely positioned within the lamp housing. The lamp housings are machined with parallel top and bottom surfaces so that several lamps can be stacked vertically over a station and pointed in different directions, as shown in figure 1. The remote control of on-off switching can also be used for other electrical equipment that does not require an operator on site.

CONSTRUCTION

The outer housing, the bulb mount, and the circuit box are made of anodized aluminum. The hard-coat anodizing process provides not only a hard surface comparable to that of nitrided steel but also electrical insulation. The top and bottom surfaces of the main housing, which are subject to contact, rotation, and wear, are provided with an additional permanent coating of dry lubricant. For mounting on a tripod, the housing is designed to adapt to a standard theodolite tribrach so that it can be precisely leveled. Or the housing can be mounted directly on a tripod and leveled by means of a bulls-eye bubble in its base.

The bulb mount within the outer housing accommodates either PAR-36 or PAR-46 sealed-beam lamps, and the filament of either is positioned exactly in the vertical axis of the lamp housing. Both sizes of lamp are available in a variety of wattages, including one imported quartz-halogen unit that delivers 300,000 beam candlepower at a power drain of only 55 watts. Precise vertical tilting motion is provided by a tangent screw.

Functional elements of the system are diagramed in block form in figure 2. All the electrical circuitry is contained in a control box fixed inside the lamp housing proper and sealed with a rubber gasket to make it weatherproof. Sockets and switches provide for the

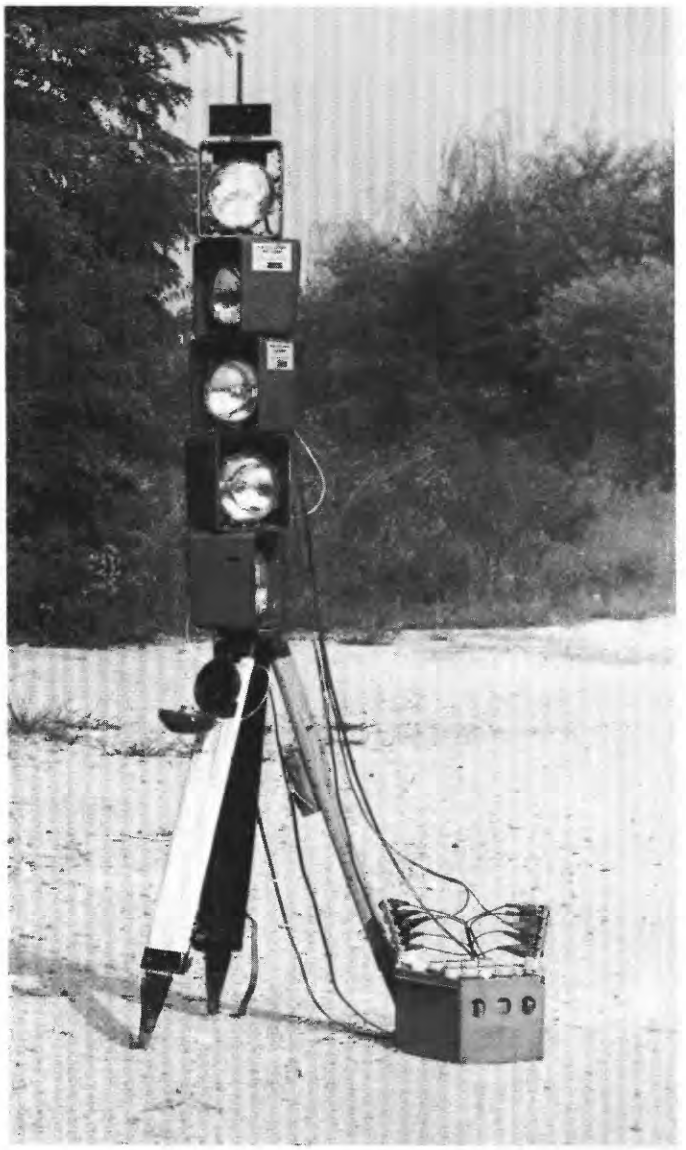

FIGURE 1.—Radio-controlled signal light. Height of instrument and tripod is about 6½ feet.

various functions: (1) power input from a battery; (2) power output for the lamp or other equipment; (3) on-off switch; (4) flash-steady switch; (5) flash rate control; and (6) radio patch-cord sockets for remote signals.

The power-input cord is conventionally coded red (positive) and black (negative); if polarity is accidentally reversed, the control box will not operate, and no damage will result, because of a protective circuit. Output polarity is not important for the lamp but may be critical for other controlled equipment.

The momentary-type on-off switch provides local control of the lamp. Once a command is given by pushing the switch, about 15 seconds must elapse before another effective command is given. This delay feature is needed to avoid false commands in remote-control operation.

The flash-steady switch permits selection of controlled-rate flashing output or continuous output. Flashing output is generally preferred for the lamp, but continuous output is needed for other equipment.

OPERATION

Operation locally is very simple. After the lamp is set up on the tripod, and all connections are made, the lamp is sighted in the desired direction by means of a peepsight on the bulb housing, and the switch is pushed to turn on the lamp. In most operations, there is radio communication between stations, so that the lamp pointing can be refined as directed by the observer at the theodolite station.

For a fixed off or on period at the lamp station, a 24-hour clock timer with an 8-day movement can be plugged in to give a measured period ranging from 15 minutes to 23 hours 45 minutes.

Ultimate flexibility is provided by radio remote control. In this mode, a pure audio tone of selected frequency is sent over a standard transmitter to a monitor receiver at the lamp station. The audio tone is generated by a miniature piezoelectric tuning fork. The receiver output is fed to the lamp control box. Here, it passes through a narrow-band filter that uses a tuning fork to match the audio signal frequency. An amplifier takes the signal passed by the filter and builds it into an impulse to turn the lamp on or off. The compact monitor receiver, mounted on top of the lamp housing, is built to withstand rugged use and to consume low power.

The small hand-held tone generator contains five tuning forks operated selectively by pushbuttons. At present, each tone is used for a separate command, so that five lights can be controlled by the one box. Additional commands can be obtained by adding more tuning forks or by using the available forks in various combinations, so that two or more simultaneous tones are required to generate a single command. Since the filter circuit at the lamp responds only to the selected frequency, which must be sustained for at least 3 milliseconds, voice communication between stations will not cause false commands. Also, it should be noted that the response frequency of an individual control circuit is not necessarily permanent, as the tuning forks are plug-in components. To change the frequency, it is only necessary to change tuning forks.

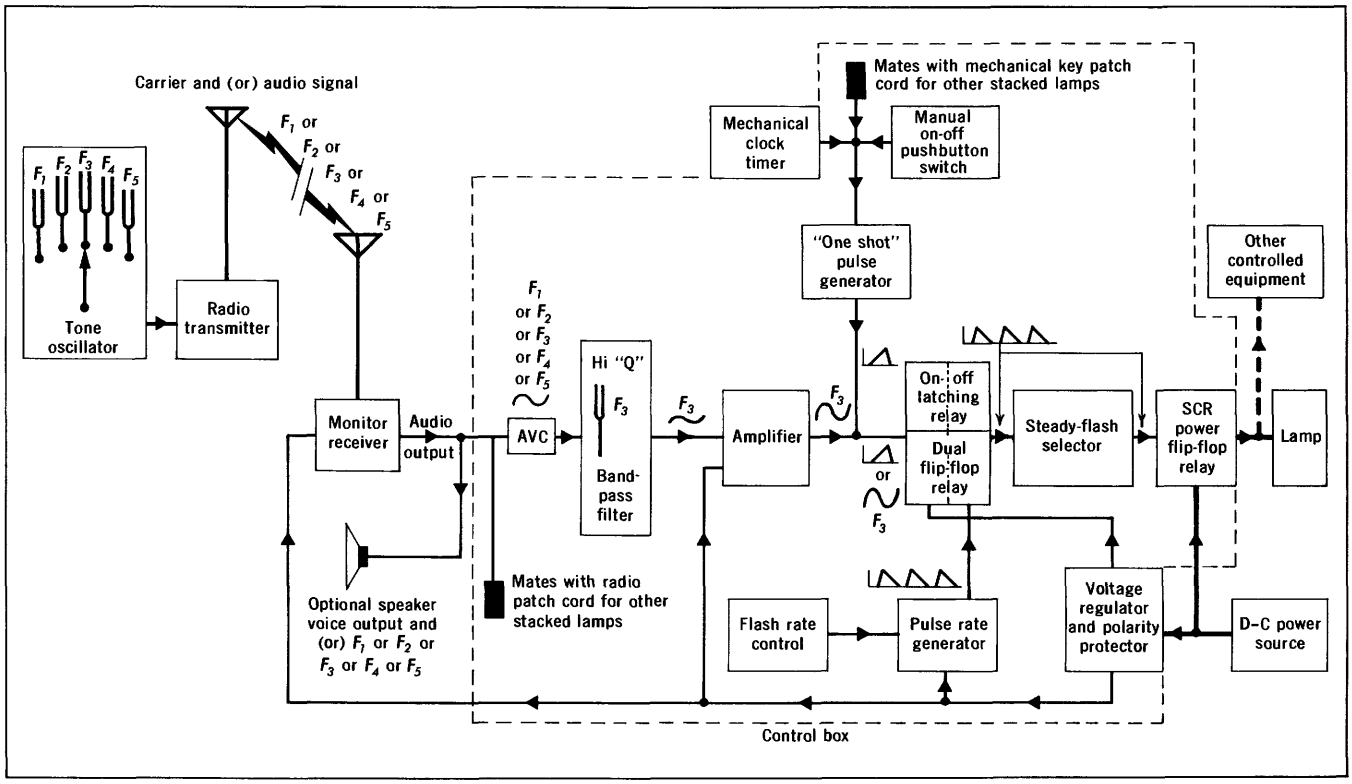

FIGURE 2.—Functional parts of the signal light.

CONCLUSION

The type of signal lamp described here seems to meet all the requirements of modern electronic traverse, with a flexibility of control not available before. The basic design has been kept simple, to meet present needs, but with the possibility of future elaboration. Technical details about components and the functioning of individual circuits have been avoided because they are not of general interest.

SUBJECT INDEX

[For major headings such as "Economic geology," "Mineralogy," "Surface water," see under State names or refer to table of contents]

AUTHOR INDEX

U.S. GOVERNMENT PRINTING OFFICE : 1969 O—359-403